DOE/NV/03624--0102

FY2017 Annual Report

Site-Directed Research & Development

Strategic Opportunity Research
Exploratory Research

NEVADA NATIONAL
NNSS
SECURITY SITE

DOE/NV/03624--0102

NEVADA NATIONAL SECURITY SITE

Site-Directed Research and Development

Fiscal Year 2017 Annual Report

This work was done in part by National Security Technologies, LLC,
under Contract No. DE-AC52-06NA25946,
and by Mission Support and Test Services, LLC,
under Contract No. DE-NA0003624,
with the U.S. Department of Energy and supported
by the Site-Directed Research and Development Program.

Report Date: April 2018

Disclaimer

Contents

Strategic Opportunity Research

Exploratory Research

Material Studies and Techniques

Instruments, Detectors, and Sensors

Computational and Information Sciences

Photonics

Appendix: SDRD Performance Metrics

Unpublished Summaries
Available from SDRD Program Office,
Las Vegas, NV 89193-8521

Flexible Intelligent Multi-Node CBRN Environment Simulator
Richard Hansen

Advanced Algorithms for Nuclear Weapon Performance Analysis
Marylesa Howard

SDRD: Advancing Our Site's Vision

In 2017, the Nevada National Security Site (NNSS) won an R&D 100 award. This was possible because of the strong technical talent we have and through our Site-Directed Research and Development (SDRD) program funding. This not only impressed me because of the national recognition it achieved, but more importantly, because it is exactly the type of research we should be doing at the NNSS. SDRD provides an opportunity to invest in areas of research we view as important. This chance to set the direction is a precious commodity in a world where sponsors largely control program research and promising opportunities may go unexplored. Because SDRD is such a valuable resource, great care must be exercised in targeting our SDRD investments to align with our strategic research directions and mission needs.

Also in 2017, the NNSS transitioned to a new management and operating entity, and I am proud to be one of the new senior leaders shepherding us to the future. Our name, Mission Support and Test Services, LLC, has come to mean different things to different people. Let me explain what it means to me as it applies to SDRD and the realms of Science and Technology and R&D:

1. **We enable subcritical experimentation and dynamic material studies for our national laboratory partners, providing new diagnostic and test systems to ensure the safety and security of our nuclear stockpile and help maintain our nation's strategic deterrent.**
2. **We develop sensors, diagnostics, and algorithms to assess the global threat of proliferation of nuclear weapons and special nuclear materials.**
3. **We develop new detection systems and techniques to monitor ports, borders, and other areas of interest for radiation signatures.**
4. **We develop communication methods and systems that overcome national and global issues of geography and security.**
5. **We develop tools and training to prepare first responders and others to recognize weapons of mass destruction threats as they enter new global situations.**

Our solutions to these national and global challenges encompass an incredibly broad spectrum of science, technology, and analysis. It is so broad, in fact, that I am personally dedicated to ensuring we are investing in areas that are advancing our site's vision and the NNSA mission while remaining complementary to the programs within the nuclear security enterprise. Our projects should be a springboard to new and strengthened laboratory and strategic partnership program customer relationships. By focusing our efforts towards our fields of strength, and going even deeper into those technologies, we add more value to the national interest. This is the path that increases the site's relevance to the national platform, now and in the years to come.

John Benner
Vice President and Chief Operating Officer

This page left blank intentionally

Introduction

NEVADA NATIONAL SECURITY SITE: EMPHASIS ON MEASURED RESEARCH AND DEVELOPMENT

Meeting current and emerging national security demands requires the willingness to take nontraditional approaches and push boundaries. Forward-looking research and development leads to innovation and creates new opportunities. At the Nevada National Security Site (NNSS), our advanced R&D program not only fulfills our missions, it achieves breakthroughs in every facet of our scientific, technological, and engineering efforts. The Site-Directed Research and Development (SDRD) program lies at the heart of discovery and innovation for NNSS national security missions. SDRD uses a robust, balanced combination of leadership-driven strategic initiatives and staff-driven exploratory R&D to provide the maximum impact for our national security missions. The success of this approach is clearly reflected in the project activities and research presented in this report.

In early 2017, we issued our first-of-its-kind broad site announcement (BSA), which included four key strategic initiatives: nuclear event detection, nuclear safety theory, material equation of state studies, and electromagnetic effects. This BSA, which formed the basis of our FY 2018 strategic proposal call, encouraged researchers to propose projects in these areas, where we seek to make the most directed investments. The value of intentional investment in R&D has been documented in multiple studies and backed by both industry and government. The SDRD program continues to be a vital part of our enterprise, a key component for meeting future requirements and emerging demands.

STRATEGIC OPPORTUNITY RESEARCH BUILDS CAPABILITY

Assessing the value of R&D is a perennial subject of debate—one that requires regular analysis, certainly careful measure beyond a survey of return on investment. In the case of our recently completed inaugural strategic opportunity research projects (appearing in the first section of this annual report), we achieved early success and made technical infrastructure enhancements that are flourishing now and will continue to do so for the foreseeable future. These projects were high-risk ventures, but we felt strongly that our investments would pay off. This is exactly the type of bold risk-taking required in advanced R&D. In both projects, we see that scientific and technical platform development has led to new opportunities and has significantly raised our overall capabilities.

We have often described our two main objectives as providing “ground truth and discovery.” Our exploratory research (featured in the second section of this report) exemplifies these two themes and drives much of our progress. This research complements and enhances our strategic efforts. Delivering ground truth and discovery requires the ability to conduct very complex, high-value experiments and gain the knowledge of underlying processes. This is shown in multi-discipline investigations (see “SDRD to Stockpile Stewardship Success: Understanding Ejecta from Shocks” on page ix). Likewise, we are employing computational techniques in new ways to help us understand complex datasets and extract highly valuable information for critical decision making (see “SDRD to Global Security Success: Machine Learning for Automated Analysis of Threats” on page xii).

PROJECT SELECTION PROCESS AND FUTURE PROGRAM DEVELOPMENT

At the heart of SDRD lies our proposal and project evaluation and selection process, which we routinely scrutinize and optimize for best performance. We strive to maximize efficiency and implement continuous improvement based on data. The FY 2018 proposal call again used the two-phase process as described in our previous annual reports. We saw further growth in submissions, up 13% over last year, thus making three consecutive years of increased numbers of pre-proposals. We invited 72 full proposals, minimally higher than last year, but still suggesting we are realizing sustained improvements based on these measures. We reduced the proposal technical review teams from three down to two, by focusing on our major missions in stockpile stewardship and global security. A new combined and integrated team performed the final review of the invited proposals. We also utilized more formal external peer review (provided by partner laboratories) of our strategic research proposals and, as usual, supplemented all proposal evaluations with assistance of our advisory level committee. These refinements have further enhanced a streamlined and efficient process that once again allowed us to implement thorough proposal assessment and final project selection.

In our last annual report, we mentioned many of the major elements introduced into the SDRD program since its inception in 2001. We also discussed planning for the next decade regarding how R&D investments will be crucial to realizing the innovations needed to accomplish our mission. SDRD is an enduring program, and envisioning the future is an absolute necessity to ensure long-term impacts. In some ways, SDRD stands at a crossroads. Our first strategic projects are coming to the end of their life cycles, and we must make decisions about where to invest next. Investing more into our strategic efforts would seem to be the most prudent choice based on our needs and the effectiveness demonstrated to date. A small 0.5% increase, above our current 2.5% rate, would raise our current $9.2M budget to approximately $11M. Keeping a healthy balance between strategic efforts and exploratory R&D will be necessary and feasible given the discretionary nature of SDRD.

FY 2017 ANNUAL REPORT SYNOPSIS

The reports that follow are for project activities that occurred from October 2016 through September 2017. Project life cycle is indicated under the title as well as the original proposal number (in the following format: site abbreviation--ID #--originating fiscal year, e.g. STL-###-YR).

These reports describe the status and progress of our activities, and each one illustrates the discoveries as well as challenges that arise in these endeavors.

2017

First SOR projects complete

Inaugural directed research projects end their 3-year life cycles with proven results and desired R&D capability enhancements. New SOR projects moving forward in 2018 and beyond.

2015

Strategic opportunity (SOR) projects

Implemented a new category of directed R&D projects with emphasis on strategic outcomes. The majority of our investments were maintained under the exploratory research (ER) category.

2014

Increased investment

Raised the investment rate for the first time in the history of the program due to successes and outcomes.

2010

“Work for Others”

Included non-DOE agency funds for the first time into the base of SDRD allowable funding source. This increased and broadened the portfolio of NNSS R&D.

2009

Multi-year lifecycles

Implemented and allowed selectable 1-year to 3-year project life cycles to enhance flexibility. Prior to 2009 projects were limited to one year.

SDRD to Stockpile Stewardship Success: Understanding Ejecta from Shocks

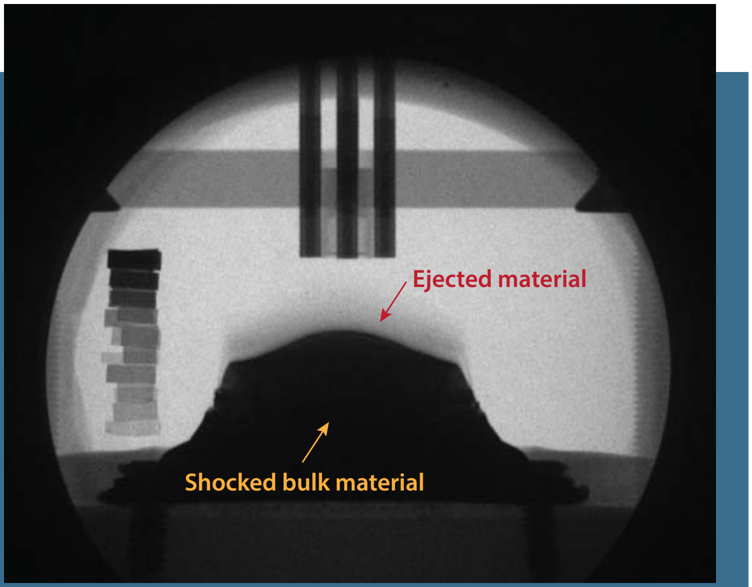

Soft x-ray radiograph of a high explosive–driven shock experiment showing ejected material

The ability to accurately model a nuclear explosion fortifies our confidence in the safety and security of the nuclear weapons stockpile. Modeling all the physical processes without full-scale testing presents unique challenges. However, some material conditions such as mix—the amount and configuration of metal in a gas—can be measured. Mix arises mainly from ejecta, tiny bits of metal injected into the gas when the shock releases at an uneven (rough) surface. Such ejecta are also of great interest to the fusion community, as metal in the gas impedes the fusion process.

Particle ejecta size and velocity distributions are fairly well understood, and we are now studying the more elusive transport and the erosion processes that affect ejecta sizes and locations of particles in the imploding cavity. Researchers want to know if the ejecta can become entrained in a shock front and whether particles erode due to chemical processes at the particle surface or the drag or "friction" that occurs as they travel. With the Neutron Science and Technology Group at LANL (P-23), SDRD principal investigators have done several major projects in this regard. We are using shock platforms, high-speed visible and infrared framing cameras, and new diagnostics to understand the mix phenomena.

A current SDRD project uses Coherent anti-Stokes Raman Spectroscopy (CARS) to measure ejecta cloud temperatures in a gas that has a Raman shift (see pages 161−168). Anti-Stokes scattering lines are measured with a spectrometer viewing hydrogen gas shocked by an aluminum plate driven with a high explosive. Feasibility of the system was proven and enhancements are underway to improve data quality. Also a laser-induced breakdown spectroscopy (LIBS) diagnostic is being designed to evaluate the materials present in an ejecta cloud from a shock releasing at the interface between two different metals.

We are also studying ejecta cloud emissivity with infrared cameras, which supplies temperature data for pyrometry diagnostics.

Mie scattering for measuring particle sizes may become more feasible than the more complicated holography with its optical lensing requirements. Using one laser wavelength we can ascertain average particle diameter; our results have compared well with holography data. We have begun investigating two-color Mie scattering, which may tell us about the fraction of scattering particles with diameters below the diffraction limit, an important quantity but one that is very hard to obtain.

Under a current collaborative LDRD project, we are studying conversion of ejecta through hydriding in surrounding gas, which should increase the rate of ejecta breakup. The idea is to produce ejecta from metals with different reactivities and test them in reactive and non-reactive gases with similar molecular weights, namely deuterium (D_2) and helium. Infrared imaging has showed that cerium hydrides rapidly in D_2 gas. But other diagnostics indicate that the cerium ejecta travel farther in the D_2 than those from tin. All combined, these efforts are yielding new knowledge and understanding of this important element of material dynamics.

— Contributed by **Lynn Veeser**

SDRD, by its nature, is a high-risk venture that seeks to fund new ideas and opportunities that may result in transformational knowledge and/or techniques. We have stated many times before that weighing success versus failure in R&D is counterintuitive. Efforts that do not seem to come to fruition are a valid part of R&D that can often lead to new exciting paths of discovery.

In summary, the SDRD program, now in its 17th year, continues to be a vital engine for innovation with potential only limited by the imagination of the individuals who contribute their time and talent. The 28 reports published here describe the efforts of the principal investigators and their teams pursuing advanced studies and utilizing their talents to push the boundaries of the "state of the art." Creativity, backed by resources, is capable of meeting significant challenges. To that end, SDRD seeks to return the highest value possible.

ACKNOWLEDGMENTS

SDRD requires a talented team of individuals to ensure success from year to year. Without their support none of this would be possible. Special acknowledgement and appreciation goes out to

SDRD Project Wins R&D 100 Award for "Geometrically Enhanced Photocathodes for Improved High-Energy Efficiency in X-Ray Detectors"

Dr. Kathy Opachich, with Robert Guyton in the lab, holds a sample of the structured photocathode. The cathode is plasma etched in silicon with a thin gold coating on the surface.

An FY 2015–2016 SDRD project led by Principal Investigator Kathy Opachich (Livermore Operations) has won a 2017 R&D 100 Award. This is the second time a Site-Directed Research and Development project has won the prestigious award.

Dr. Opachich and her team conceived a new way to push the limits of efficiency and performance of x-ray photocathodes, which are the critical component in x-ray streak cameras. These cameras are fundamental diagnostic systems utilized in a variety of plasma physics and fusion experiments. In fact, innovations in this area have been called for in the 2017 Department of Energy (DOE) National Diagnostics Plan and are needed across many DOE laboratories and NNSA facilities. The hallmark technology developed here using geometrical enhancement, breaks a barrier in the quantum efficiency, or light conversion efficiency, of these photocathodes, which has been limited to the 1%–10% range in the soft x-ray region.

Most x-ray detectors operate at normal incidence (i.e., x-ray photons are at a 90° incidence angle to the photocathode) and suffer a loss in quantum efficiency at energies greater than 5 keV. Improvements in yield have occurred with grazing incidence geometry due to the larger path length of the x-ray photons, which better matches the secondary electron escape depth within the photocathode material.

The recessed geometrically enhanced photocathode takes further advantage of increased path length by achieving grazing incidence through lithographically fabricated microstructures. This new structure radically increases the total electron yield by up to 3 times in the important 1–12 keV energy range. Using shallower angles can also potentially improve the yield further (i.e., up to 10 times).

Dr. Opachich worked with her NNSA colleagues and collaborators from Lawrence Livermore National Laboratory, Lawrence Berkeley National Laboratory, General Atomics, and Nanoshift LLC, to develop the geometrically enhanced photocathode design.

Michele Vochosky, assisted by editors Jill Gibson and Sierra Cory, for technical communications and compiling, editing, and publishing this report; to Katina Loo for providing conceptual document design, graphics, and book layout; to Tom Graves and Emma Gurr for project management and cost accounting efforts; to Newell Ramsey and Kathy Gallegos for information system support; to Janet Lux for financial data reporting; to Larry Franks, Rob Hixson, and Lynn Veeser for technical guidance and support; and to our SDRD site representatives and technical review committee: Jesse Bonner, Frank Cverna, Daniel Frayer, Paul Guss, Marylesa Howard, Jeff Koch, Craig Kruschwitz, Brandon La Lone, Aaron Luttman, Mary O'Neill, Alex Plionis, Mike Reed, Patrick Sawyer, Jerry Stevens, and Rusty Trainham. And a final special thanks goes to members of our external advisory board, Larry Franks, Carl Ekdahl, Damon Giovanielli, Ralph James, Paul Rockett, Maurice Sheppard, and Gerry Yonas, who graciously give their time and provide ongoing, valuable recommendations.

Howard A. Bender III
SDRD Program Manager

Marylesa Howard receives the SDRD MVPI award from Raffi Papazian, Jim Holt, and Howard Bender

Marylesa Howard, FY 2017 MVPI

Dr. Marylesa Howard is one of the NNSS's top performing researchers. Her research productivity, her impact on the NNSA and academic communities, and her contributions to the standing and reputation of the SDRD program warranted her the award "SDRD Most Valuable PI" for FY 2017.

During the last two and a half years, Dr. Howard and her team have developed new algorithms for segmenting image data into different classes of materials, which has a broad range of applications. She has developed both a partial differential equations–based approach and a frequentist method for segmentation, both of which have been incorporated into a software tool that the NNSS is now licensing (at no cost) to DOE and university partners. Her work has also led to two new journal publications, one which focuses on advanced algorithms and another on an important application in shock physics.

The segmentation software tool Dr. Howard created has now been licensed by LANL and is being used in the development of new techniques for validating weapons models against legacy data. At the NNSS, we are using the tool to process current subcritical experiment data, including the recent Eurydice experiment. The software has also been licensed to Sandia National Laboratories for use in their thermal battery development program and by MIT for academic research.

Dr. Howard's work on image segmentation has been featured in numerous presentations and symposiums. She is among the leading publishers of research in the company, having authored nine peer-reviewed research journal articles on SDRD-related work in the last three years. Additionally, Dr. Howard has given more than 25 invited and conference presentations on her work and has helped establish new research partnerships at major universities and enabled new recruiting pipelines for young STEM talent.

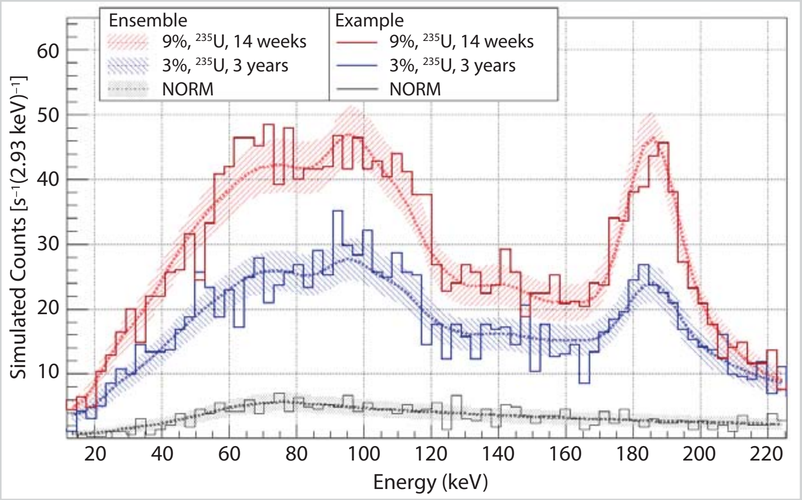

GADRAS models were created of the gamma ray energy spectrum emitted from an IAEA Type-5A transportation cylinder containing either 9% ^{235}U 14 weeks after production or 3.3% ^{235}U. Ensembles of 10^4 simulations of each spectrum were created. The average and spread of these simulations is illustrated as dashed and hatched curves. A single example of a 1-second observation is shown as solid lines.

SDRD to Global Security Success: Machine Learning for Automated Analysis of Threats

A new NNSS data science initiative based on modern machine learning methods has emerged in response to the challenging problem of locating illicit special nuclear material. Namely, there exists a need to perform radiation source detection and spectral identification under narrowly defined yet challenging conditions. An FY 2016 SDRD feasibility study (see figure) took the first step toward solving this issue, and recently new work has started under a DOE NA-22 project for FY 2017–2019 (Signal Studies Algorithms and Methods) looking at specific case studies augmented by targeted data collections. Fundamental work continues via a three-year SDRD effort (see pages 185−192) to generalize some of these techniques to the broader community.

Neural network–driven machine learning methods are realizing a recent renaissance empowered by the advent of so-called “deep learning” methods and the availability of open source tools such as Google’s Tensor Flow. Having established the application of data-driven, unsupervised machine learning methods for the Technical Nuclear Forensics community using Laplacian Eigenmap methods, NNSS scientists are now well positioned to exploit supervised methods to a greater extent than ever before. This is due to not only the maturity and wide availability of the tools, but also to the NNSS’s unique access to data sources via its ongoing Nuclear Incident Response and Defense Nuclear Nonproliferation R&D projects that involve operational, testing, and experimental data sources.

Targeted machine learning applications are only as effective as the CONOPS used to employ them. Fortunately, there are new complimentary technologies that can allow these new methods to flourish in ways that could upend the existing paradigm for illicit nuclear materials detection. The data science initiative has led to multiple new ideas for Intelligence Advanced Research Projects Activity, the Department of Homeland Security, and Defense Nuclear Nonproliferation R&D (NA-22). In each of these, novel and targeted machine learning algorithms are embedded into persistent, distributed, and multi-modal surveillance systems. These proposed systems feature broad multidisciplinary efforts that fully leverage capabilities across the NNSS enterprise and beyond.

— Contributed by **Lance McLean** and **Alex Plionis**

Strategic Opportunity Research

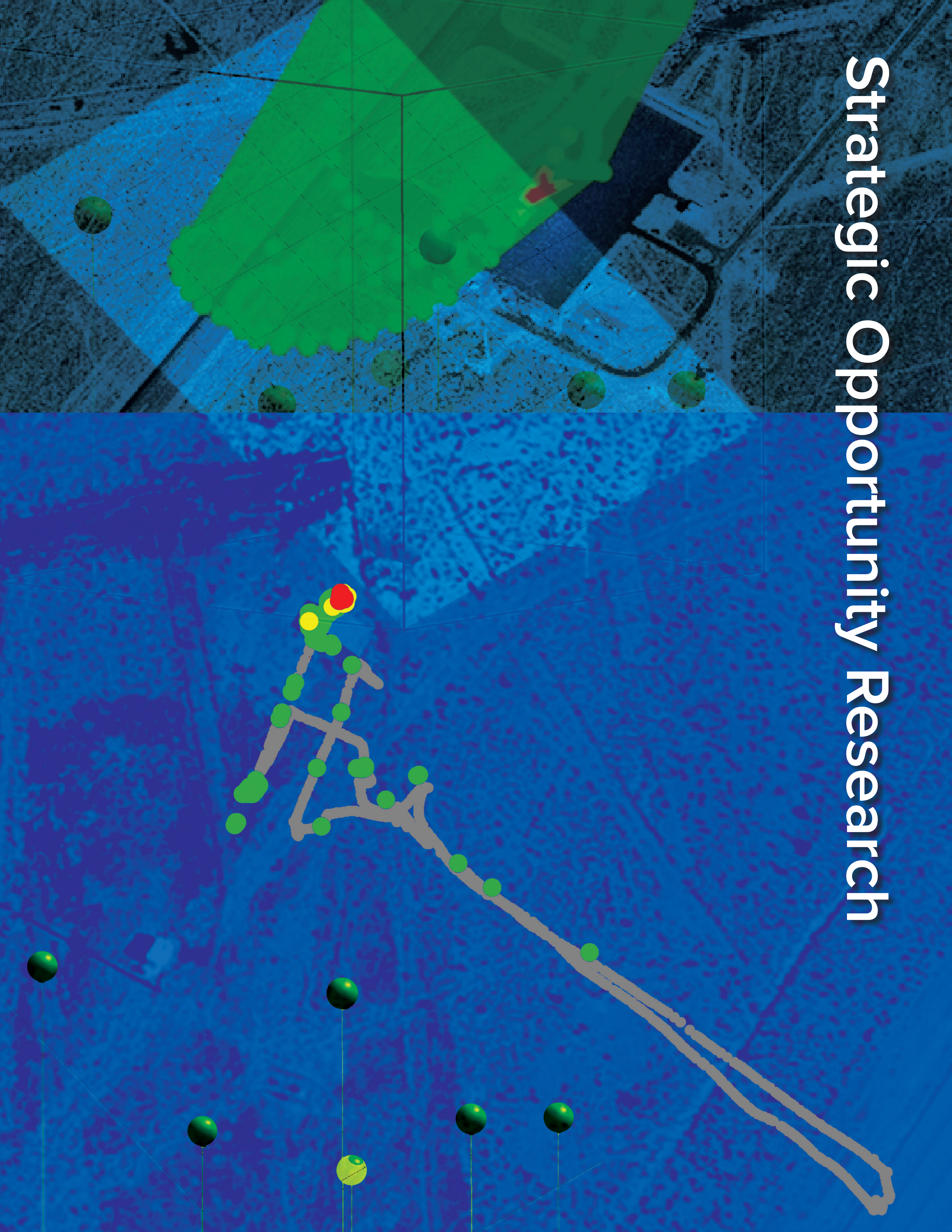

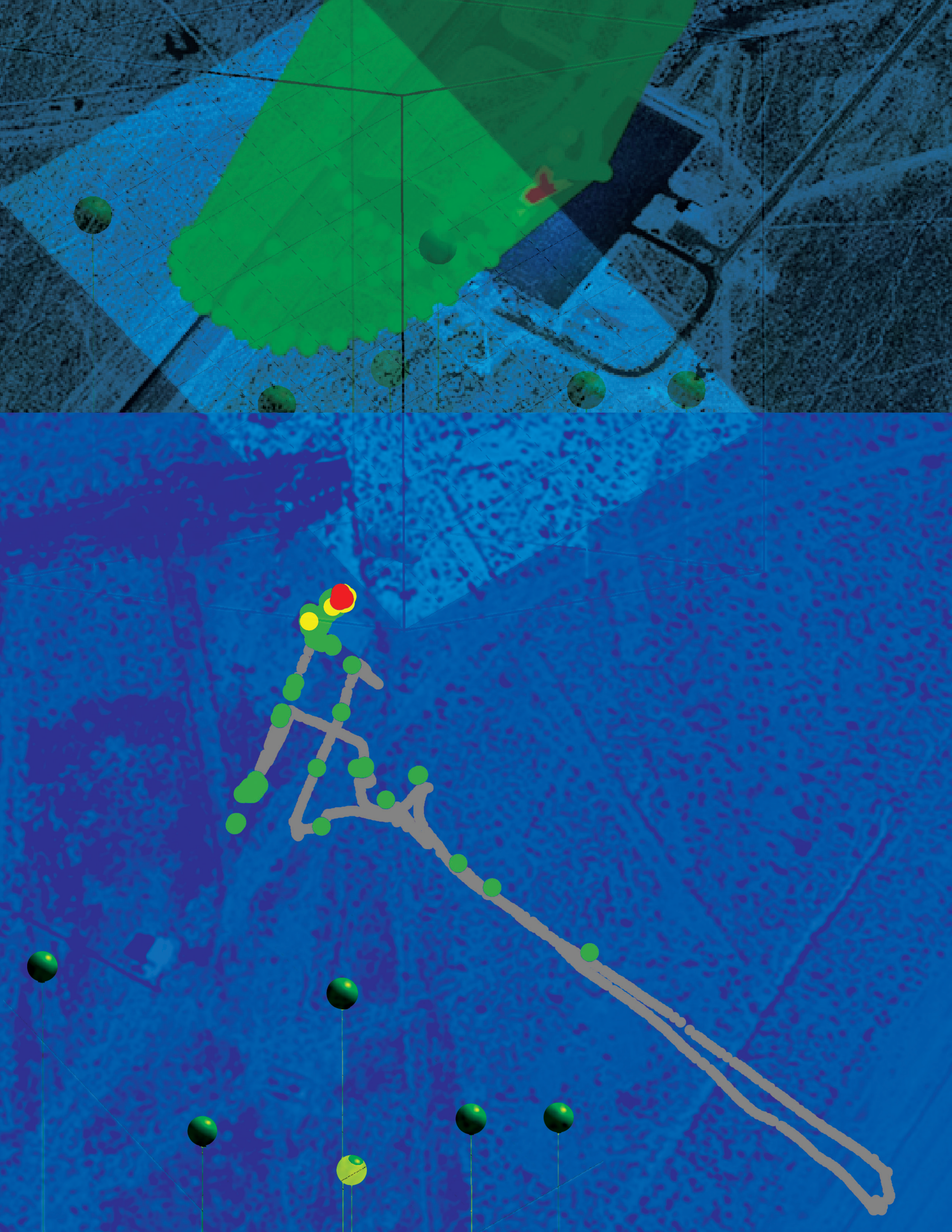

Enhanced Dynamic Materials Research

LAO-19-15 ■ Year 3 of 3

Brandon La Lone,[1,a] **Gerald D. Stevens,**[a] **Dale Turley,**[a]
Lynn R. Veeser,[b] **and Robert S. Hixson**[b]

[1]lalonebm@nv.doe.gov, (805) 681-2046
[a]Special Technologies Laboratory
[b]New Mexico Operations–Los Alamos

We have initiated a research program in dynamic materials properties to address some key outstanding shock physics issues. This three-year research project has examined the spall strength of copper single crystals and investigated the pressure and temperature melt boundary of shocked tin in collaboration with Caltech. To carry out our research, we acquired a new research-quality propellant launcher, which was installed at the Special Technologies Laboratory (STL) gas gun and small-scale explosives campus. The launcher became operational in FY 2017, and a first dynamic test is planned for November 2017. This new launcher is the same bore diameter as the existing STL light gas gun (40 mm) but triples the maximum velocity achievable from 0.8 to 2.5 km/s. With this new capability, we will initiate new dynamic materials research directions that are rigorous and will improve fundamental physics models used in large hydrodynamic codes. Such codes are routinely used to simulate dynamic events, but results are only as good as the input physics models. We found that the spall strength of [100] oriented copper crystals was linearly dependent on the peak compressive stress and the tensile strain rate, and this was the first such study to separate these two effects. Our measurements of the tin melt boundary were of sufficient accuracy to validate some of the theoretical models in the literature and show that other models were incorrect.

BACKGROUND

This strategic initiative SDRD project had several objectives that addressed important issues in shock wave physics (Hixson 2016, La Lone 2017). One objective was to examine the anisotropic response of metals by performing experiments on single crystals. Another objective was to measure the temperature

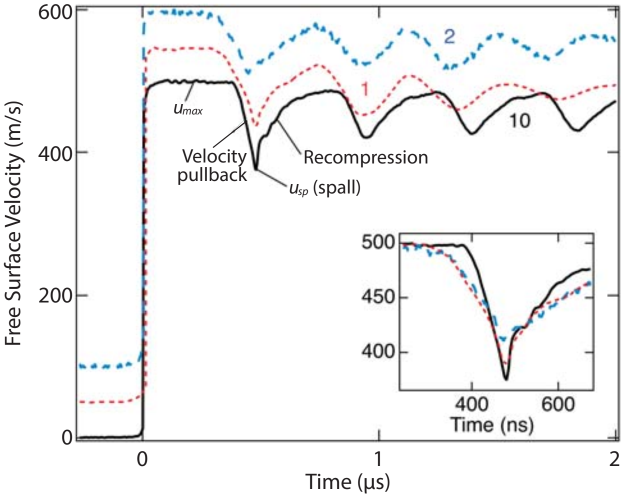

Figure 1. Free surface velocities for the three orientations of copper crystals studied. The colored numbers by the wave forms are the shot numbers in Table 1. The top two traces are offset by multiples of 50 m/s for clarity. The inset shows a magnified view of the spall signatures.

and pressure of a phase boundary during shock wave loading. A third objective was to build a new dynamic compression platform to perform the experiments.

In the first two years, we began studying the spall response of single-crystal copper, and this year we completed that investigation by performing three more experiments and writing a publication (Turley 2018). In FY 2015 and 2016, we also successfully identified the melt boundary of shock-compressed tin in a collaboration with Caltech. In FY 2017 we obtained another dataset that built on the earlier work and strengthened the results; a publication focused on the tin experiments is being prepared. In FY 2015 and 2016, we also initiated the purchase of a new propellant launcher, acquired it, and had it installed. This year we acquired the storage magazine and completed the explosive site plan; the propellant launcher is now operational.

Project

Single-Crystal Metal Physics

Metals used in engineering applications are made from polycrystalline materials, where the sample is composed of small "grains" of single-crystal metal. If such materials are not made correctly, it is possible to have grains oriented in a way that is not purely random. This can lead to anisotropic mechanical response of the metal, where the properties depend on the orientation of the sample relative to the stresses applied. In the first year of this project, we performed scoping studies on three different orientations of single-crystal copper to explore elastic and plastic wave speed and spall strength anisotropies. Based on those results (Hixson 2016), we decided to examine in detail the spall strength of [100] oriented copper crystals in the remaining two years of this work.

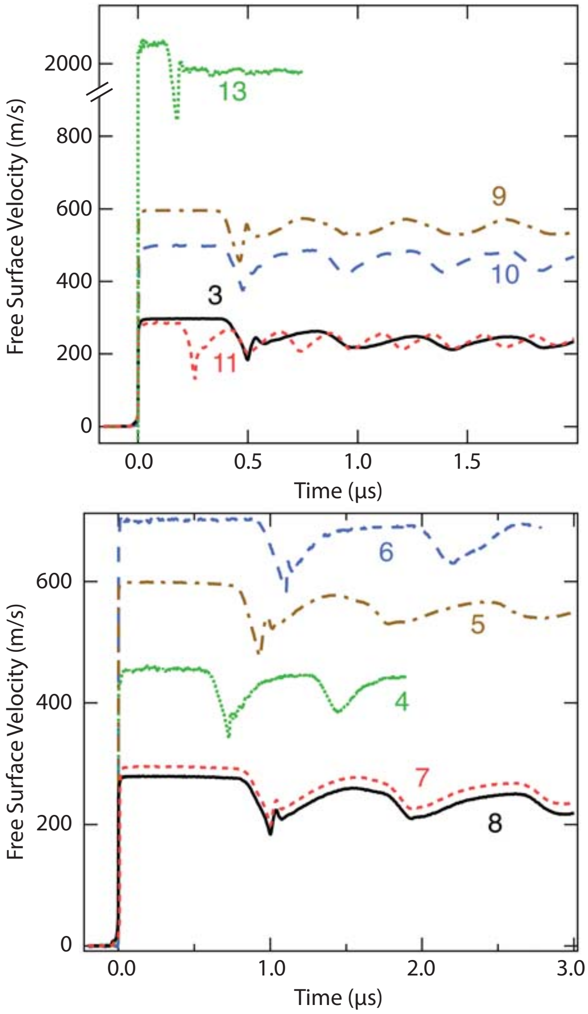

Figure 2. Free surface velocity record for spall along [100] oriented copper crystals

Metals are put under tension when release waves collide during high-explosive and gas gun–driven shock wave experiments. When the tensile stress exceeds the tensile strength of the metal, it will spall—meaning the sample will tear itself apart. The spall strength for polycrystalline metals has been reported to depend on the peak compressive stress prior to tension, the tensile strain rate as tension is applied, and the dwell time, defined as the time between the compressive and tensile pulses. The variables that affect the spall strength of single-crystal copper have not been thoroughly investigated. Minich (2004) reported a peak compressive stress dependence; however, the tensile strain rate also varied in these experiments, so it is not possible to untangle the two effects from their data alone. Our initial results from FY 2015 indicated the strain rate had at least some effect on the spall stress.

We designed and executed a series of plate impact experiments to begin to look for dependencies of spall strength upon the various parameters. This led us to conduct a carefully designed series of experiments where the goal was to hold the tensile strain constant and vary the peak stress for copper crystals. We did this by changing the sample thicknesses and the impact velocity for each experiment. Thicker samples result in lower tensile strain rates, whereas higher impact velocities increase the peak stress and the strain rate. Table 1 shows the experimental parameters used in our experiments (most experiments are the [100] orientation) and is a combination of data from all years of the project.

All experiments used impactors that were half the thickness of the target. Both the targets and impactors were made from copper crystals (99.99%) purchased from MTI Corporation that were polished to a specular finish and were flat and parallel to within 10 microns. The surface normal was always within ±2 degrees of the studied crystal orientation according to vendor specifications. Impactors were launched using the Special Technologies Laboratory (STL) light gas gun, except for the highest velocity experiment (170613-1), which was performed on the Caltech single-stage propellant gun. The free surface velocity was recorded using standard photonic Doppler velocimetry (PDV) techniques with two-fiber PDV probes.

The free surface velocity records comparing the three orientations are shown in Figure 1. The spall signature of the copper crystals is unique in that there is a high-frequency oscillation associated with the compression pulse that follows the pullback signal. This is most pronounced in the [100] orientation, which also has the highest spall strength. A detailed study of this signature will be performed in future work. The

Table 1. Experimental parameters for the [100] copper spall experiments

SHOT NO.	EXPER. NO.	IMPACTOR THICKNESS (mm)	TARGET THICKNESS (mm)	CAL. STRAIN RATE $\dot{\varepsilon}$ (μs^{-1})	FREE SURFACE VELOCITY (m/s)	PULLBACK VELOCITY $\Delta u_{PULLBACK}$ (m/s)	PEAK STRESS (GPa)	SPALL STRENGTH (GPa)
1	150306[a]	1	2	--	496	108	9.6	1.9
2	150313[b]	1	2	--	494	85	9.7	1.5
3	150820-2	1	2	1.3	297	121	5.5	2.1
4	160524-1	1.5	3	0.95	456	110	8.8	1.9
5	150820-1	2	4	0.72	598	120	11.7	2.1
6	160524-2	2.5	5	0.62	701	118	14.1	2.1
7	150819-1	2	4	0.65	294	95	5.5	1.7
8	150818-2	2	4	0.70	279	96	5.2	1.7
9	150819-2	1	2	1.5	595	147	11.8	2.6
10	170201-1	1	2	1.4	498	124	9.6	2.2
11	170201-2	0.5	1	2.2	286	157	5.3	2.8
12	160525-1[c]	1	2	--	595	--	11.9	--
13	170613-1	0.5	1	3.8	2036	209	49.6	3.7

[a] Experiment used [110] oriented impactor and target; [b] Experiment used [111] oriented impactor and target;
[c] A sapphire window backed the target rather than a free surface

remainder of the experiments were performed on the [100] orientation because it has the most distinctive features.

The free surface velocity records for the copper experiments are shown in Figure 2. Of interest to the present study are the tensile strain rates, the free surface velocity plateau (0–350 ns), and the total velocity depth or pullback velocity that is a measure of the spall stress. Tensile strain rates at the spall plane were calculated using hydrodynamic computer simulations with CTH. These values are listed in Table 1. The free surface and pullback velocities were converted to peak stress and approximate spall strength using standard impedance matching methods. Figure 3 shows a 3-D plot of the spall strength as a function of peak compressive stress and deceleration from all [100] spall experiments except for the highest velocity experiment (170613-1). Surprisingly, all data were well fit by a single plane, indicating that the spall strength, in the ranges shown, is linearly dependent on both the peak compressive stress prior to tension and the tensile strain rate. The equation for the plane is $\sigma_{sp} = \kappa_0 + \kappa_1 \cdot P + \kappa_2 \cdot \dot{\varepsilon}$, with best fit parameters $\kappa_0 = 0.97$ (19) [GPa], $\kappa_1 = 0.05$ (1), and $\kappa_2 = 0.66$ (9) [GPA μs].

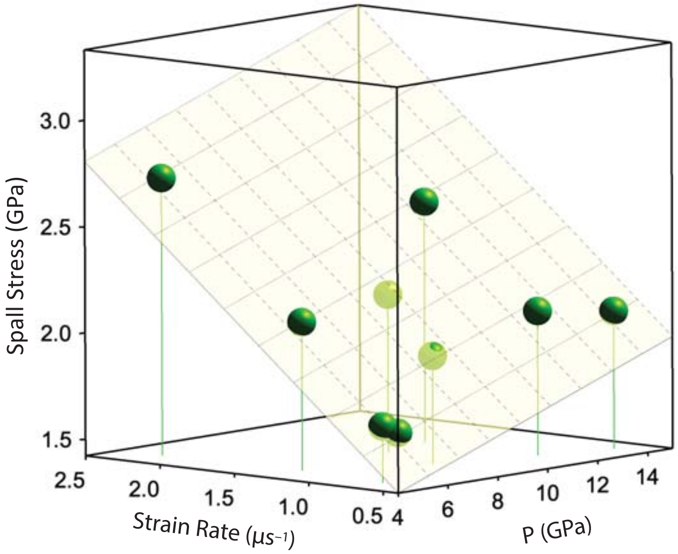

Figure 3. [100] oriented copper spall stress as a function of peak compressive stress (P) and the calculated strain rate. A single plane accurately fits all of the data.

When we add the highest stress point from experiment 170613-1, the data no longer lie on a plane; consequently, the linear dependence indicated by the planar fit has a limited range of validity. Nonetheless, it clearly shows that the effects of peak compressive stress and strain rate on the spall strength of copper crystals are separable and are both important to the spall process. Prior investigations into spall failure of copper crystals never separated these two effects.

Tin Temperature Measurements

The measurement of phase transition boundaries is an important aspect of equation of state (EOS) development for weapons physics because the way a material responds under dynamic loading depends on its phase and its strength in that phase. The locations of solid-solid and melt phase boundaries are necessary for developing phase-aware physics models. Dynamic melt determinations for metals have most frequently been performed using the rarefaction overtake method (McQueen 1982), in which the sound speed is measured as a function of shock stress, and the change in sound speed that accompanies the loss of shear strength upon melt is observed. This method requires experiments over a relatively large range of shock states to determine the point where the shock Hugoniot and melt curve cross. This approach does not provide a direct measurement of the melt temperature. This lack has driven the dynamic materials community to devise simpler, cost-effective methods to pinpoint where materials melt both on and off the principal Hugoniot. Other dynamic melt diagnostics (x-ray diffraction [Morgan 2010, Gorman 2015], velocimetry [Mabire 2000], and reflectivity [Elias 1988]) also lack a way to measure temperatures, with one exception. Researchers led by Partouche-Sebban (2005) made dynamic pyrometric measurements on lead using samples shocked to near melt (either 49 or 57 GPa) and reflected from windows of different shock impedance. They obtained temperature-pressure points around 12 (polymethyl methacrylate), 30 (lithium fluoride [LiF]), and 50 GPa (sapphire) from the radiance and reflectance after the shocks reflected from the various windows. They also included one point for tin with melt at T = 1400 ±50 K and 14.4 GPa.

Melt curves have also been measured statically using diamond anvil cells (DAC), tungsten carbide (WC) anvil cells, laser heating, and x-ray diffraction, and are often calculated using molecular dynamic simulations or density functional theory (DFT) calculations. For metals at high pressures, there is often serious disagreement about the location of the melt boundary, sometimes thousands of degrees, between DAC data,

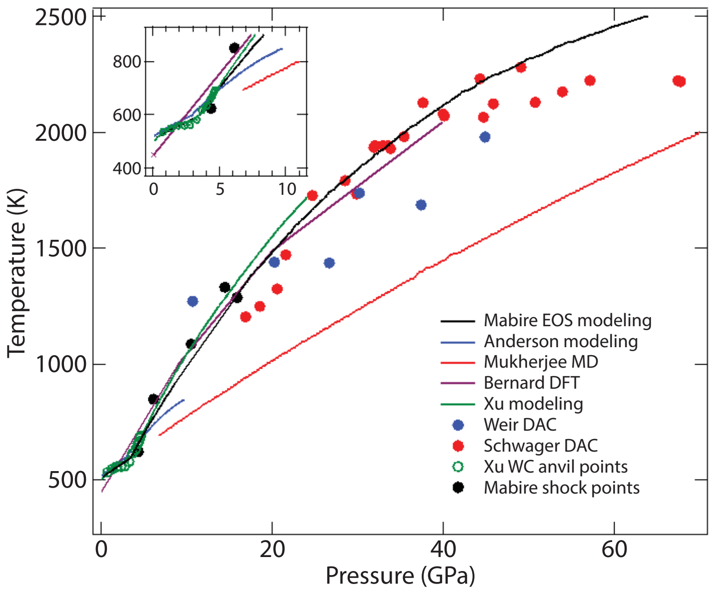

Figure 4. Theoretical models (solid curves) including molecular dynamics (MD) and density functional theory (DFT) calculations, dynamic melt data, and diamond anvil cell (DAC) and tungsten carbide (WC) anvil data for tin at high pressures showing a substantial amount of scatter. The inset shows a zoomed in view around the β-BCT [body-centered tetragonal]-melt triple point where there is generally good agreement.

theory, and dynamic measurements. Figure 4 shows a survey of tin melt data from various references, highlighting the significant amount of scatter and the need for more accurate melt boundary diagnostics.

In this project, in collaboration with Caltech, we demonstrated a melt boundary identification technique using radiometry, integrating sphere reflectometry, and velocimetry to measure the temperature, emissivity, and stress histories of shocked compressed tin with few-nanosecond time resolution. The sample is shocked to an elevated temperature and pressure in its solid phase, and, as the pressure is released, the sample melts. This technique provides a continuous, highly accurate melt boundary measurement.

The experimental technique, detailed in previous SDRD reports (Hixson 2016, La Lone 2017), is therefore only briefly described here. A 1.3 mm thick copper impactor, backed by low-impedance syntactic foam, impacts a 3 mm thick tin target backed by a LiF window. Loctite 326 is used to bond the window to the tin. In a set of experiments, the tin-LiF interface reflectance is measured with our flash lamp integrating sphere technique. In another set of measurements, the thermal radiance of the tin-LiF interface is measured. The interface velocity is measured in every experiment using PDV. The combination of reflectance and thermal radiance provides a measure of the interface temperatures, and the velocity is converted to stress using standard impedance matching techniques. This year, we reanalyzed data from prior years using measured corrections for motion in the reflectance diagnostic, which changes the reflectance by up to 3%. We also performed one additional high-stress radiance experiment (shot 4R in Table 2); however, we did not measure the reflectance

Table 2. Shock parameters for radiance and emissivity experiments on shocked tin at the Caltech powder gun

SHOT NO.	COPPER PROJECTILE VELOCITY (km/s)	INTERFACE VELOCITY (km/s)	SHOCK STRESS IN TIN (GPa)	INITIAL STRESS AT INTERFACE (GPa)
1R	1.727	1.258	31.0	22.5
2R	1.965	1.424	36.7	26.3
3R	2.108	1.516	40.3	28.7
4R	2.290	1.649	45.0	32.1
1E	1.829	1.319	33.4	24.2
2E	1.961	1.413	36.6	26.3
3E	1.973	1.427	36.8	26.5
4E	2.042	1.475	39.6	27.6

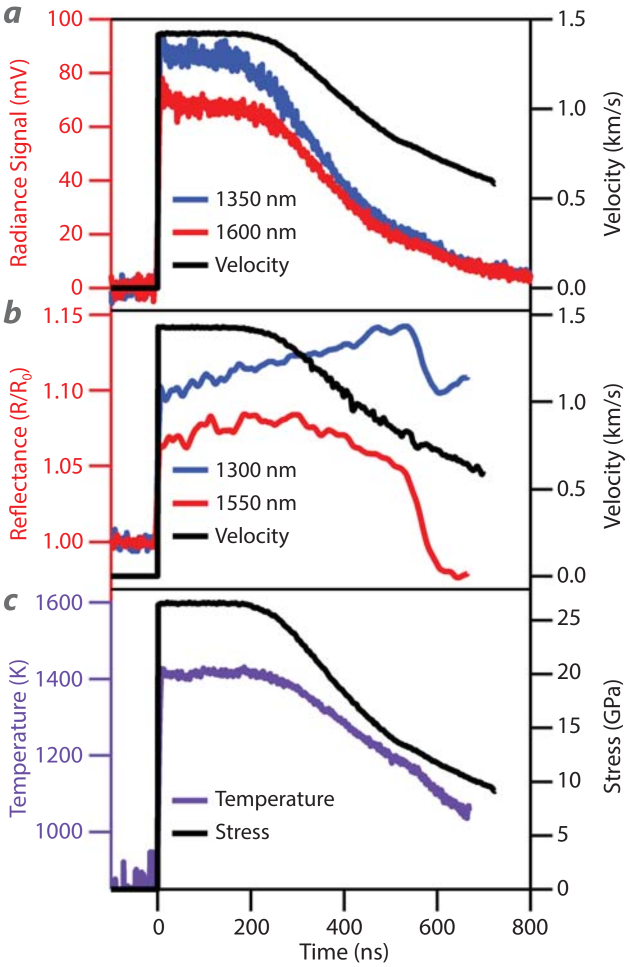

Figure 5. (a) Radiance data and velocity from shot 2R, (b) reflectance data and velocity from shot 2E, and (c) temperature calculated from a combination of radiance and reflectance data along with stresses

(emissivity) for this experiment. Because we did not measure reflectance, temperatures were calculated assuming the emissivity was constant and the same as shot 3E while the interface was on the melt boundary.

Table 2 lists the shock parameters for the four radiance (R) and four reflectance-emissivity (E) experiments. Figure 5 shows typical dynamic radiance data and velocity data from shot 2R, reflectance data and velocity from shot 2E, and temperatures and stresses calcu-lated from a combination of both experiments. When the shock reaches the window interface at time t = 0 in the figure, the tin transforms almost immediately to the body-centered tetragonal (BCT) phase, and its reflectance increases by 5%–15%. About 500 ns later there is a subsequent drop in reflectance when the release path intersects the tin melt boundary. These sudden emissivity changes indicate that, at least for tin, the reflectance alone is a good phase-change indicator.

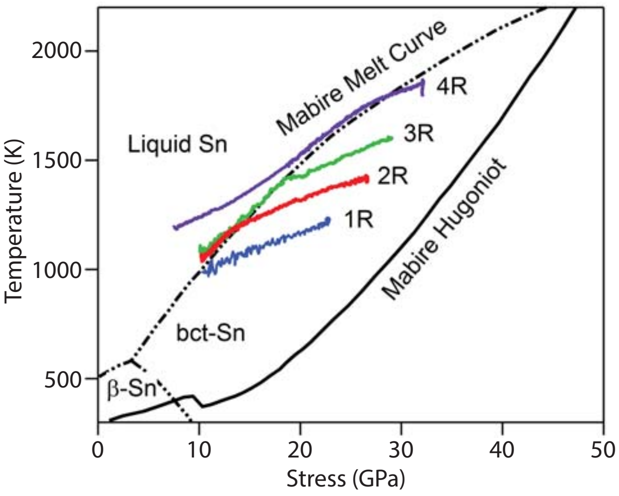

Figure 6. Measured temperature versus stress release paths for tin (color) and the calculated phase diagram (black) of Mabire (2000). Initial shock is to a point on the Hugoniot curve. The three highest-stress shots agree well with the calculated melt curve. The lowest curve is from an experiment that did not release enough to melt. The highest stress experiment likely fully liquefied along the release and began to depart from the melt curve and release into the fully liquid state.

We combine the temperature curves for the two detectors and merge the result with the stress curve to obtain a temperature versus stress release path for each radiance experiment. The temperature-stress curves appear in Figure 6 superimposed upon the calculated phase diagram of Mabire (2000). Our measured temperature curves release from right to left in the figure. The release curves begin at a partially released state, lower than the Hugoniot, from the shock reflecting off the lower impedance LiF window. Starting from this partially released state, a time-dependent release originated from the rear surface of the impactor allows us to track a release path to a much lower stress. These release paths follow an isentrope and therefore unload along the melt curve after intersecting it. Melt is indicated by an abrupt change in the slope (steepening) of the release curves as they transition from releasing in the solid phase to releasing along the melt boundary. The steeper portion of the release, where the curves are on the melt boundary, is in good agreement with the calculated melt curve of Mabire (2000). Temperature uncertainties are estimated to be ±4% with generally lower uncertainty on the melt curve than in the solid phase.

Propellant Launcher Initiative

The 40 mm bore light gas gun at STL is routinely used for shock wave studies and diagnostic development; however, this gun has an upper velocity limit of approximately 800 m/s. One of our key goals is to reach shock wave stresses that are roughly equivalent to those occurring in high-explosive detonation, which can drive shock wave stresses as high as ~50 GPa in some metals. To reach this performance requires higher impact speeds than those achievable by the STL light gas gun. We therefore looked in detail at propellant launcher systems that were roughly equivalent in launch tube bore but had a much higher impact speed capability, ultimately acquiring a 40 mm propellant launcher from Physics Applications, Inc., as a "turnkey" system. The launch tube is 5.5 m long and has an outer diameter of 146 mm, and the target chamber and catch tank are a combined 2.6 m long and 0.9 m in diameter. The launcher is designed to use up to 700 g of smokeless propellant for launching 40 mm diameter projectiles between 0.5 and 2.5 km/s, greatly expanding our velocity range for performing shock compression studies. This launcher has been delivered and installed in Building 229 at STL, which is the same building that houses the light gas gun. A photograph of the installed gun is shown in Figure 7. We also installed the necessary propellant storage magazine and a dedicated propellant loading shed.

Figure 7. The new propellant launcher, installed in Building 229 at STL, is capable of launching projectiles at 0.5 to 2.5 km/s, which expands the velocity range considerably for shock compression experiments

CONCLUSION

The purpose of this strategic SDRD was to improve our understanding of materials subjected to dynamic compression and ultimately to improve the physics models in weapons simulations. In particular, we focused our research on two topics: the role of crystal anisotropy on the spall behavior of shock-compressed metals and a new method for locating the high-pressure phase boundaries of shock-compressed metals. Both of these issues are poorly constrained in existing physics models.

To examine the role of crystal anisotropy, we explored factors that influence the spall strength of single-crystal copper using the 40 mm bore gas gun at STL. We first compared three different crystal orientations of copper, [100], [110], and [111]. Of these the [100] had the highest spall strength. We further explored the role of peak compressive stress and tensile strain rate on the spall strength of [100] oriented crystal copper. Our results indicate that the spall strength of [100] copper is linearly dependent on both the peak compressive stress and the release rate as the sample goes into tension for peak stresses up to about 14 GPa. This is the first such study that separated these two effects. Some departure from linearity is seen at higher stresses. While copper alone is of some interest to the scientific community, perhaps more importantly the methods we used for the parameterization study could be applied to materials of interest to the weapons community—not just to crystalline metals but also to polycrystalline metals. To determine the location of a high-pressure phase boundary, we have obtained very accurate temperature data on tin across the center of the Mabire (2000) phase diagram—temperatures from 1000 to 1400 K and stress from about 9 to 30 GPa. The temperatures were obtained using a combination of reflectance and pyrometry measurements. Using the temperature measurements we determined the location of the melt boundary from an inflection in the release paths. The techniques we used to identify the location of a melt boundary are the first of their kind and can be directly applied to materials of interest to the weapons community.

To upgrade the dynamic compression capability of the NNSS, a new propellant launcher acquired in FY 2016 was installed at STL. The first dynamic experiments are planned to occur in November 2017. The launcher will enable projectile velocity measurements from 0.7 to 2.5 km/s, so that we can generate shock wave stresses comparable to what can be done with high explosives but with a more controlled, one-dimensional drive. Both Los Alamos and Livermore National Laboratories have already expressed interest in teaming with us on performing experiments with the new launcher.

ACKNOWLEDGMENTS

We gratefully acknowledge the help of Ben Valencia and Mike Grover in performing the single-crystal copper experiments. We also acknowledge Oleg Fatyanov and Michael Burns at Caltech for their help with the tin temperature measurements. Finally, we acknowledge very useful conversations with Saryu Fensin and Rusty Gray of Los Alamos National Laboratory.

REFERENCES

Anderson, W. W., F. Cverna, R. S. Hixson, J. Vorthman, M. D. Wilke, G. T. Gray, K. L. Brown, "Phase transition and spall behavior in β-tin," *AIP Conf. Proc.* **505** (2000) 443–446.

Bernard, S., J. B. Maillet, "First-principles calculation of the melting curve and Hugoniot of tin," *Phys. Rev. B* **66** (2002) 012103.

Elias, P., P. Chapron, B. Laurent, "Detection of melting in release for a shock-loaded tin sample using the reflectivity measurement method," *Opt. Commun.* **66** (1988) 100–106.

Gorman, M. G., et al., "Direct observation of melting in shock-compressed bismuth with femtosecond x-ray diffraction," *Phys. Rev. Lett.* **115**, 9 (2015) 095701.

Hixson, R. S., B. La Lone, G. D. Stevens, W. D. Turley, L. R. Veeser, "Enhanced dynamic materials research," in *Site-Directed Research and Development*, FY 2015, National Security Technologies, LLC, Las Vegas, Nevada, 2016, 15–29.

La Lone, B., G. D. Stevens, D. Turley, L. R. Veeser, R. S. Hixson, "Enhanced dynamic materials research," in *Site-Directed Research and Development*, FY 2016, National Security Technologies, LLC, Las Vegas, Nevada, 2017, 1–9.

Mabire, C., P. L. Héreil, "Shock induced polymorphic transition and melting of tin," *AIP Conf. Proc.* **505** (2000) 93–96.

McQueen, R. G., J. W. Hopson, J. N. Fritz, "Optical technique for determining rarefaction wave velocities at very high pressures," *Rev. Sci. Instrum.* **53** (1982) 245.

Minich, R. W., J. U. Cazamias, M. Kumar, A. J. Schwartz, "Effect of microstructural length scales on spall behavior," *Metallurgical and Materials Transactions A* **35A**, 9 (2004) 2663–2673.

Morgan, D. V., M. Grover, D. Macy, M. Madlener, G. Stevens, W. D. Turley, "Observations of shock-loaded tin and zirconium surfaces with single-pulse x-ray diffraction," *Powder Diffr.* **25** (2010) 138–142.

Mukherjee, D., K. D. Joshi, S. C. Gupta, "Shock wave induced melting of tin: Ab-initio study," *AIP Conf. Proc.* **1349** (2011) 821.

Partouche-Sebban, D., et al., "Measurement of the shock-heated melt curve of lead using pyrometry and reflectometry," *J. Appl. Phys.* **97** (2005) 043521.

Schwager, B., M. Ross, S. Japel, R. Boehler, "Melting of Sn at high pressure: Comparison with Pb," *J. Chem. Phys.* **133** (2010) 084501.

Turley, W. D., S. J. Fensin, R. S. Hixson, D. R. Jones, B. M. La Lone, G. D. Stevens, S. A. Thomas, L. R. Veeser, "Spall response of single copper," *J. Appl. Phys.* **123** (2018) 055102.

Weir, S. T., M. J. Lipp, S. Falabella, G. Samudrala, Y. K. Vohra, "High pressure melting curve of tin measured using an internal resistive heating technique to 45 GPa," *J. Appl. Phys.* **111** (2012) 123529-1–123529-5.

Xu, L., Y. Bi, X. Li, Y. Wang, X. Cao, L. Cai, Z. Wang, C. Meng, "Phase diagram of tin determined by sound velocity measurements on multi-anvil apparatus up to 5 GPa and 800 K," *J. Appl. Phys.* **115** (2014) 164903.

Unmanned Aircraft System for Remote Contour Mapping of a Nuclear Radiation Field

RSLN-15-15 ■ Year 3 of 3

**Russell Malchow,[1,a] Karen McCall,[a] Paul Guss,[a] Rick Fischer,[b]
Michael Lukens,[a] Mark Adan,[a] Michael Howard,[a] Eric Wagner,[a]
Ki Park,[a] Rusty Trainham,[c] Paul Oh,[d] and Pareshkumar Brahmbratt[d]**

[1]malchorl@nv.doe.gov, (702) 295-8770
[a]Remote Sensing Laboratory–Nellis
[b]Remote Sensing Laboratory–Andrews
[c]Special Technologies Laboratory
[d]University of Nevada, Las Vegas

Nuclear radiation detection and monitoring are vital to public safety, particularly for nuclear disasters involving radioactive contamination. Among the advantages an unmanned aerial system (UAS) has are quick deployment, low-altitude flying that enhances sensitivity, no radiation exposure health safety restriction, and the ability to access highly hazardous or radioactive areas. Additionally, the UAS can be configured with nuclear detecting sensors optimized to measure the hazards associated with the event. For this project, small UAS platforms were obtained for sensor payloads for radiation detection and electro-optical systems that were specifically developed for UAS research, development, and operational testing. The sensor payloads have been optimized for the contour mapping of a nuclear radiation field, which resulted in a formula for low-cost UAS platform operations with built-in formation flight control. The focus of the FY 2017 work was to continue testing and sensor integration with greater emphasis on increasingly more realistic scenarios. Autonomous flight was achieved on several platforms.

BACKGROUND

Unmanned aerial systems (UASs) have many advantages and provide significant operational benefits. It is a common argument that UASs are better suited for “4D” tasks: dull, dirty, dangerous, and deep (Barnhart 2012a). The “dull” aspect refers to repetitive missions. “Dirty” refers to environments in

Figure 1. NNSS UAS platforms obtained from FY 2015 through FY 2017

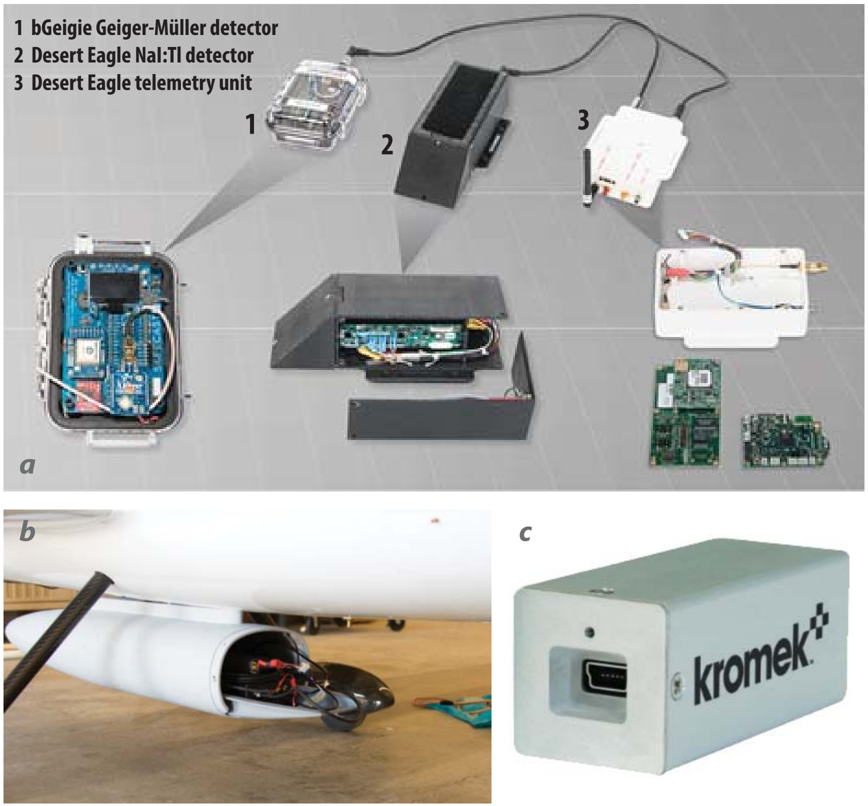

Figure 2. (a) Detectors used in the UAS program, (b) $LaBr_3$:Ce detector in detector pod, and (c) the Kromek CZT detector

which there are nuclear, biological, and chemical threats. The tasks deemed "dangerous" are those in which there is a high risk to the aircraft and aircrew. "Deep" tasks are those that are beyond the range of current manned aircraft (Franklin 2008). Low-cost UASs (Di 2011a) are becoming increasingly popular in both research and practical applications. And, lately, UAS research is becoming a notable area with a growing number of papers focused on system modeling, navigation, flight control, path planning, and other topics. Moreover, with the rapid development of electronics and wireless communication technology, civilian remote sensing becomes practical by installing inexpensive sensors on UASs.

UASs are used for remote sensing applications in many different areas, such as water management, forest fire detection, wetland monitoring, and crop identification (Chao 2009). Compared with a single UAS, the cooperative UAS system performs with more safety and efficiency (Geramifard 2011; Han 2013a, 2014a). Multiple UASs can share information with each other by wireless communication (Abdessameud 2010), so optimal algorithms like gradient searching can be implemented (Gan 2011).

The central tenet of the UAS is that the cockpit does not have an operator onboard the aircraft; therefore, control of the aircraft must take place by other means. The approach to command and control can be separated into three distinct forms: (1) ground control or remote piloting, (2) semi-autonomous control, and (3) autonomous control.

A small UAS (sUAS) system (maximum weight of 55 lb) can employ sensors to not only perform remote sensing, but also assist with the autonomous or semi-autonomous navigation and operation of the sUAS (Beard 2012). Under autonomous control, the onboard computer is in control—not a human being (Gupta 2013). Goplen (2015) has enumerated the types of data that UASs collect for U.S. Geological Survey use and archives: 3-D modeling, color infrared orthophotography, contour map generation, digital surface models, feature extraction, keyhole markup language, normalized difference vegetation index, orthophotography point cloud generation, and volumetric measurements.

UAS designs are usually one of two types: fixed-wing (Di 2011a) and rotary-wing. Fixed-wing UASs can cooperate (Di 2011b) to fulfill the requirements of many practical applications (Han 2013b, 2014b, 2014c) and are popular for tasks requiring endurance (Chao 2010), as they can fly for long periods. Vertical takeoff and landing (VTOL) UASs combine advantages of fixed- and rotary-wing aircraft, requiring a small area for takeoff and landing. Compared with fixed-wing UASs, VTOL UASs have hovering capability and little space restriction for takeoff and landing, which are beneficial for applications in search and surveillance as well as static image capturing or remote sensing.

UAS payloads may be either sensors or cargo (Barnhart 2012b). For sUASs, typically, the payloads are sensors. Designers of electro-optical sensor payloads for sUASs are under intense pressure to evolve their technologies to keep pace with the fast-moving trends in the sUAS industry. Perhaps in no other market is there a need for ever-smaller, lighter, and less expensive payloads as in the sUAS industry.

PROJECT

The motivation of this work is to detect the level of nuclear radiation in a timely way through efficient use of low-cost UASs. Table 1 presents the mission statement, project objectives, and an update on our progress during FY 2017.

We acquired two fixed-wing Sandstorm UASs in FY 2015 and in FY 2016 acquired two small fixed-wing T-28s, two rotary-wing 3DR quadcopters, and one Tarot octocopter (Figure 1). In FY 2017 a DJI Matrice, a heavy-lift hexacopter, was added. The systems are capable of performing normal and operational scenario flight maneuvers. The systems are self-contained, have an independent capability to control or terminate the flight, use autonomous waypoint navigation, support line-of-sight operations, and have the flexibility to integrate COTS and government-furnished sensors.

Table 1. Summary of UAS Strategic Initiative Project

DOMAIN AND SDRD UAS STRATEGIC INITIATIVE	FY 2017 STATUS
Mission Statement By FY 2018, the NNSS will operate a UAS with a detector, returning data relevant to determining radiological hazards on the ground, demonstrating the ability to integrate systems and detectors into the system.	Demonstrated with several platform/detector configurations.
Environment Will fly low and slow to allow for radiological detection but above or around obstacles.	Demonstrated during flights at the NNSS.
Awareness and Navigation Will be programmed using standard autopilot waypoints and actively monitored.	Established capability to fully simulate programmed flights before flight program is uploaded to platform.
Sensors Will incorporate a radiological and other sensor for reporting on the presence of, and identification of, radiological hazards and other hazards.	Several detectors have been successfully integrated into fixed-wing and rotary-wing platforms.
Communication Will communicate in real time or near-real time relevant navigation and detection information. Information will be formatted and relayed so as to be useful for a current software platform or platforms.	Infrastructure established and data telemetry successfully tested.
Architecture Will implement a current architecture or architectures.	Formed a team to establish standards for sensor integration.

System control, telemetry, and subsystems meet minimum federal requirements for aerial flight missions. The system was also configured to provide real-time sensor data and metadata for processing and recording.

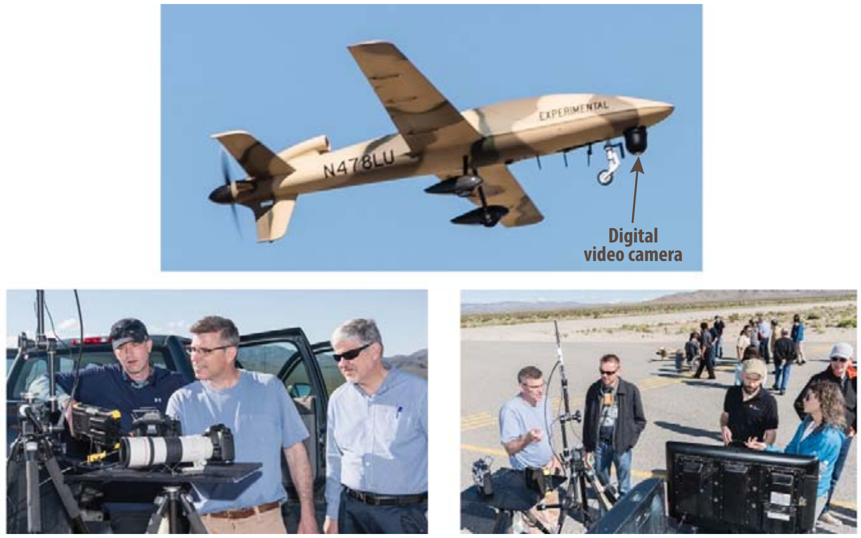

Figure 3. UAS digital video camera and ground monitoring system showing real-time data

NNSS UAS Training, Testing, and Data Collection

In FY 2017 operator training and sensor integration continued. Pilots and flight planners continued making progress on autonomous flights. Simulation software was obtained to plan flights and fly virtual UASs in realistic virtual environments. These tools enable fine-tuning of flight parameters without risk, and promote the engagement of pilots and programmers before an actual flight takes place. Several photographic-only missions were flown, which demonstrated the ability to plan, program, and execute autonomous flights over known terrain. This is an important step toward the longer-term goal of flights that are beyond visual line of sight.

In addition to the 1″ × 1″ Desert Eagle thallium-doped sodium iodide (NaI:Tl) detector and the Safecast bGeigie Geiger-Müller (GM) detector, a 3″ × 6″ NaI:Tl detector, a 3″ × 3″ cerium-doped lanthanum bromide ($LaBr_3$:Ce) detector, and a 1 cc cadmium zinc telluride (CdZnTe or CZT) detector were successfully integrated and flown on the UAS platforms. These detectors are shown in Figure 2.

Data Collection

During the radiation detection tests with the Sandstorm fixed-wing aircraft, the Safecast and 1″ × 1″ NaI:Tl Desert Eagle radiation detectors were mounted inside the platform with the components of the digital video camera. All the sensors were individually battery powered, and the data from the sensors were sent to ground stations situated nearby.

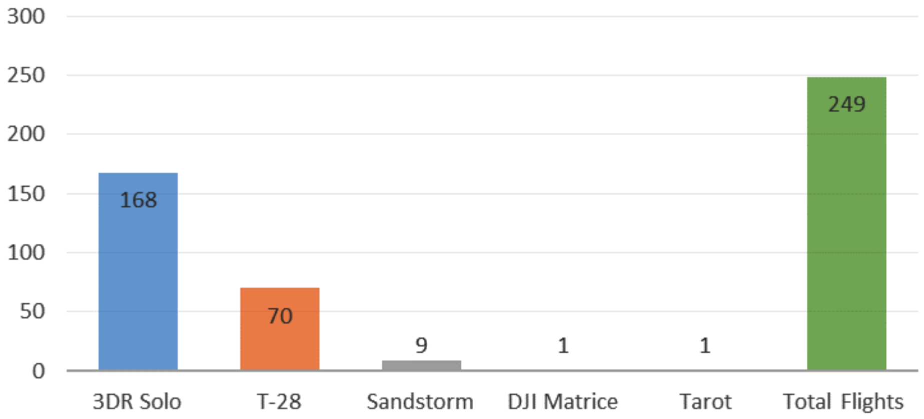

Figure 4. UAS training and data collection flights during FY 2017 for this SDRD project by UAS type

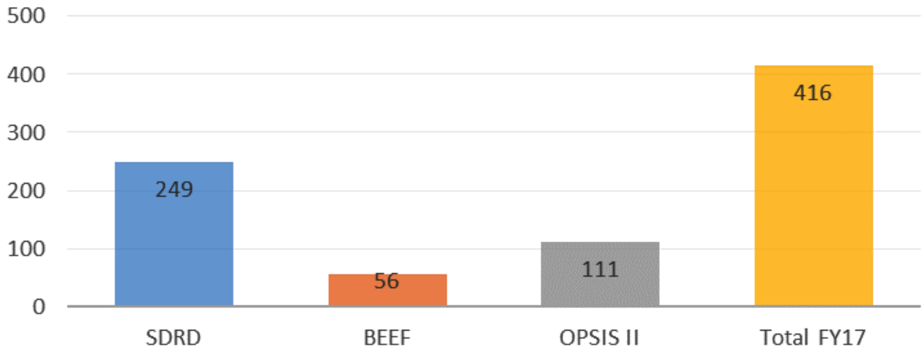

Figure 5. UAS total flights during FY 2017 for all projects

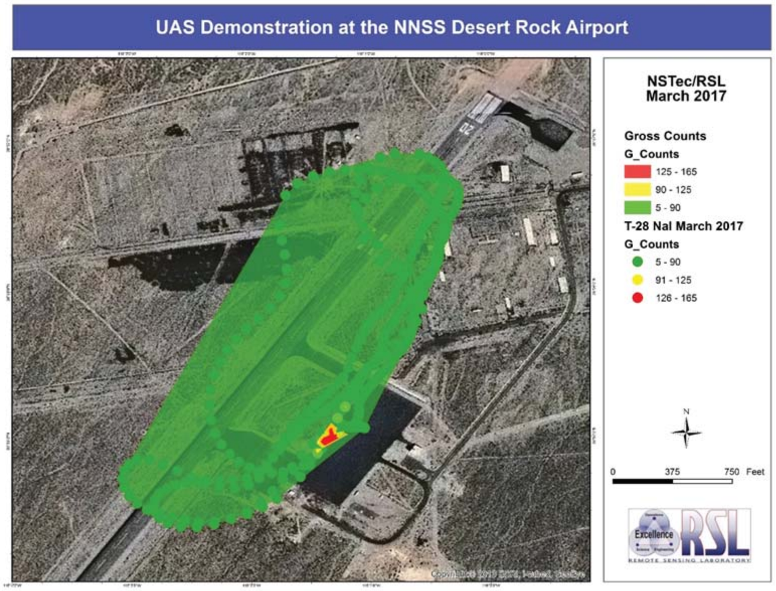

Figure 6. Map showing contour plot of gross gamma count rates collected with the 1″ × 1″ NaI:Tl detector mounted on a T-28 UAS. The position of a ^{137}Cs source is indicated by elevated count rates, shown in red.

The Safecast's bGeigie Nano is a mobile radiation detector that uses a pancake GM tube to measure alpha, beta, and gamma radiation. The bGeigie Nano incorporates a GPS receiver, and it can send data wirelessly over Wi-Fi, Bluetooth, and other protocols with the addition of an XBee module from Digi Corporation. For incorporation into the Sandstorm, we acquired the transmitter/receiver hardware and successfully demonstrated the integration of this hardware with RaptorX software (RaptorX 2015). After the real-time system was demonstrated, we began the integration into the Remote Sensing Laboratory (RSL) Advanced Visualization and Integration of Data (AVID) acquisition and analysis system.

The Desert Eagle is a low-power multichannel analyzer/spectra transmitter device. When combined with the 1″ × 1″ NaI:Tl detector, it enables an sUAS to collect and transmit real-time isotopic gamma ray spectra. This government off-the-shelf radiation detection system is a low-power mobile spectral detector system. This device not only integrates into the Special Technologies Laboratory RaptorX package, but it also interfaces with the AVID system. This is a critical milestone on the proof-of-concept pathway to demonstrate and use the technology to autonomously perform a radiological survey using an sUAS. It collects 1024-channel spectra at 0–3 MeV and sends the spectra acquired at 1 Hz to a ground station for real-time mapping, breadcrumb tracking, or isotope identification.

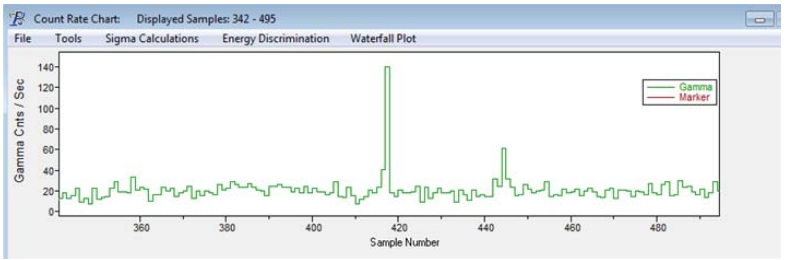

Figure 7. Time series of total count rate from the flight shown in Figure 6

The NNSS UAS platforms have not only been equipped with radiation detectors, but we have also integrated and tested complementary hyperspectral, thermal, and visual optical systems. For instance, during the radiation detection mission, there was a digital camera mounted on the bottom of the front nose of the Sandstorm (Figure 3). The data from the camera was streamed real-time to a ground station. The data were taken in conjunction with the radiation data but recorded on separate ground units. A future goal would be to have an integrated system for recording, displaying, and analyzing multiple sensor data types.

In addition to the digital video camera, the project acquired a high-definition still digital camera and an unmanned aerial vehicle lidar camera for data collection on the Sandstorm and Octocopter platforms. These sensors have been researched for terrain reconstruction, obstacle sensing, and developing 3-D maps.

UAS Flights in FY 2017

In FY 2017 a total of 249 UAS training and data collection flights were performed. Flights as a function of platform are shown in Figure 4. The 249 flights totaled more than 39 hours of flight time, with 168 3DR Solo flights, 70 T-28 flights, 9 Sandstorm flights, and a single flight each for the DJI Matrice and the Tarot. The DJI Matrice was grounded after its maiden flight and it is presently awaiting a modification of its flight control hardware. The Tarot suffered

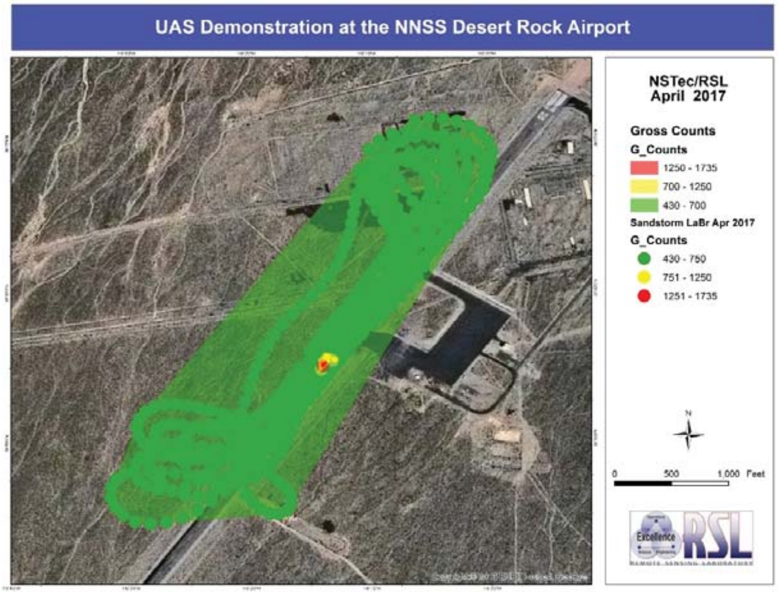

Figure 8. Map showing contour plot of gross gamma count rates collected with the 3″ × 3″ $LaBr_3$:Ce detector mounted on a Sandstorm UAS. The position of a ^{137}Cs source is indicated by elevated count rates, shown in red near the center of the map.

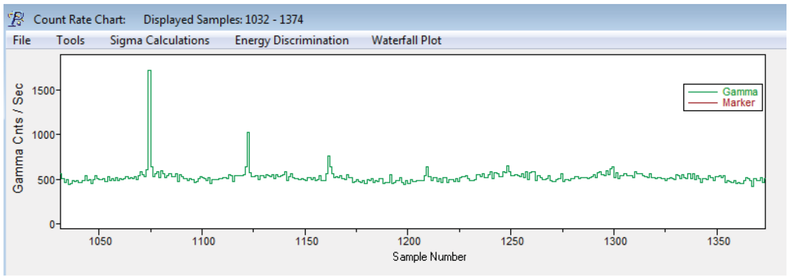

Figure 9. Time series of total count rate from the flight shown in Figure 8

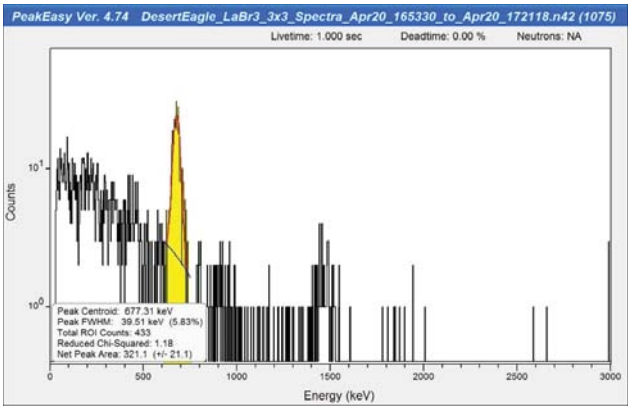

Peak Centroid: 677.31 keV
Peak FWHM: 39.51 keV (5.83%)
Total ROI Counts: 433
Reduced Chi-Squared: 1.18
Net Peak Area: 321.1 (+/- 21.1)

Figure 10. Spectrum from sample number 1074 of Figure 9. ^{137}Cs is clearly identifiable.

a hard landing during its first flight and has not been returned to service.

In addition to training and data collection flights, the UASs were flown in support of other projects at the NNSS at BEEF (56 flights) and OPSIS II (111 flights), for a total of 416 flights this year (Figure 5).

Data Analysis Results

Measurement campaigns begun in the first two years continued in FY 2017 at the NNSS. The goals were to improve data collection and telemetry and test the systems in more realistic scenarios—that is, explore what real operational use of the UASs would look like.

Figure 6 shows the result of a T-28 flight over a 40 mCi ^{137}Cs source at the NNSS. On board the UAS was the Desert Eagle 1″ × 1″ NaI:Tl detector. The flight path is indicated by the dots on the map (known as breadcrumbs) colorized by total gamma count rate. Individual data points have been contoured. The location of the source is clearly indicated by the red area near the middle of the map. Figure 7 shows the gross count rate time series from this flight. Times that the T-28 was over the source are indicated by peaks in the count rate, with larger peaks indicating a closer (i.e., lower altitude) pass over the source. This flight is an example of the ability of a UAS-mounted detector to successfully collect and telemeter data, and locate radiation anomalies.

Figure 11. Image from video shot by the 3DR Solo during a source investigation demonstration. The Solo was manually flown around the building for situational awareness. Location of the sources is indicated by the yellow arrow.

A 3″ × 3″ $LaBr_3$:Ce detector mounted on one of the Sandstorm platforms was flown over a 40 mCi ^{137}Cs source at Desert Rock Airport. The UAS made several passes at different altitudes and offsets from the source, as seen in Figure 8. Figure 9 shows the gross count rate time series from this flight, and Figure 10 shows the spectrum collected during the closest approach of the Sandstorm to the source; a ^{137}Cs signal is clearly visible.

This flight is significant because it shows the utility of a long flight time UAS (i.e., fixed-wing) to detect a mission source on the ground. This capability was tested, again at Desert Rock Airport, by placing a source in a location unknown to the pilots. The source was located with the T-28, and the location of the source was relayed to the 3DR Solo pilot. The 3DR, equipped with the Kromek 1 cc CZT detector, flew to the source, where it hovered and collected a long dwell spectrum. Because the 3DR was also carrying a camera, it telemetered pictures of the source, providing situational awareness to the pilot. Figure 11 is a still image captured from the video taken from the 3DR as it flew around the building where the source was located. While the flight was conducted within the visual line-of-sight of the pilot, it still demonstrates the well-known advantage of using drones for collecting imagery and other data (such as radiological) in dangerous or denied environments. Figure 12 shows the flight path of the 3DR colorized by count rate. Radiological information like this, monitored in real time, can be used to guide the UAS as a long dwell is collected. Figure 13 displays the spectrum collected using the Kromek CZT on this flight, showing the excellent resolution obtainable from an aerial platform.

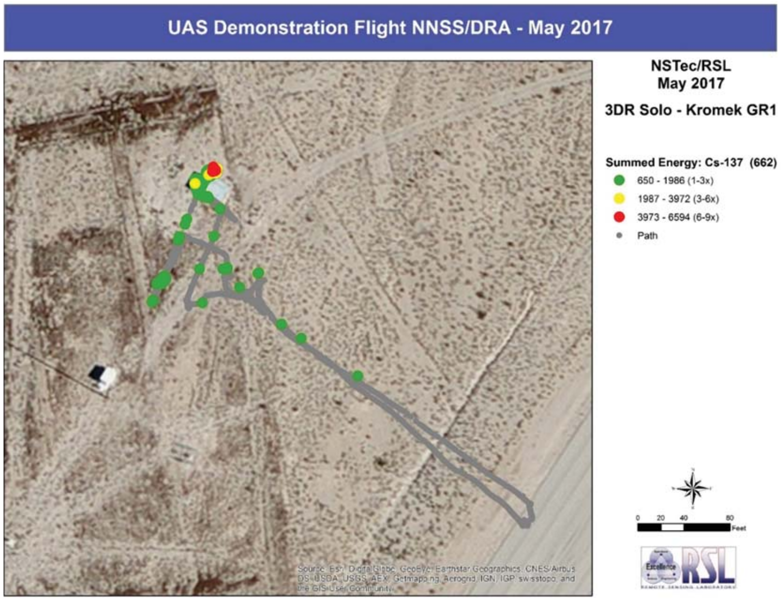

Figure 12. 3DR path manually flown during the source investigation demonstration. The building in Figure 11 is in the upper left of the image, and the location of the source is seen in red.

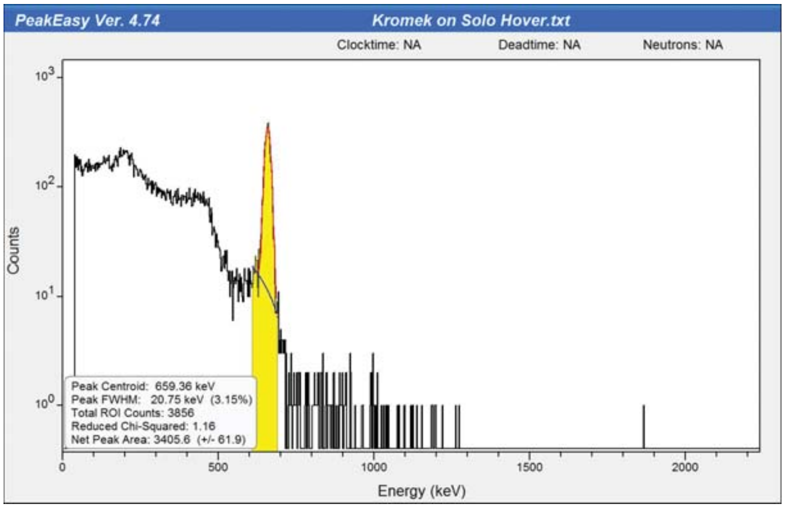

Figure 13. Spectrum collected from a ^{137}Cs source using the Kromek CZT detector mounted on a hovering 3DR Solo UAS

CONCLUSION

This project's scope was to engineer a UAS concept for remote sensing with several UASs. In FY 2015, we received authorization to acquire two UAS platforms and subsequently acquired five additional platforms in FY 2016. The field missions described above look promising and illustrate the potential to make significant remote sensing radiological measurements using sUAS platforms. In FY 2017 we continued development of mission planning and execution algorithms and initiated a comprehensive sUAS remote sensing operations program using the acquired seven UAS platforms.

This project was successful in several ways. It has given us invaluable experience in learning how to integrate detector packages onto a variety of UASs, has driven a more detailed examination of UAS radiological mission space, and has brought us into the wider community developing and deploying UASs. Detector integration continues with existing collaborative projects and proposals with laboratory and university partners. A better understanding of a requirement-driven mission space will help us make UASs operational in radiological emergency response scenarios and integrate UAS data with more traditional data streams; these efforts will continue.

Vendor delays and scheduling conflicts highlighted the pitfalls of dependence on subcontractors for a reliable emergency response capability. It is for this reason that NNSA owns its own aircraft for manned aerial radiological measurements. This model of taking responsibility and control of equipment, maintenance, and training should be emulated by the UAS program.

Secure communications and encrypted data transfer from detectors and UAS platforms will be an ongoing issue. Cybersecurity will continue to play an important part in the UAS program, particu-larly with regard to firmware embedded by manufacturers. These last issues emphasize the need for continued work developing counter-UAS strategies.

ACKNOWLEDGMENTS

We would like to thank Lance McLean, Michael Madlener, Chris Joines, Michael Toland, Susan Roberts, Emmanuel Avaro, David Carder, Shawn Cadwell, and Dave Krausnick for their contributions to this work.

REFERENCES

Abdessameud, A., A. Tayebi, "Formation stabilization of VTOL UASs subject to communication delays," 49th IEEE Conference on Decision and Control, Atlanta, Georgia, December 15–17, 2010, 4547–4552.

Barnhart, R. K., B. Hottman, D. M. Marshall, E. Shappee, *Introduction to Unmanned Aircraft Systems*, RCR Press, Boca Raton, Florida, 2012a, 2.

Barnhart, R. K., B. Hottman, D. M. Marshall, E. Shappee, *Introduction to Unmanned Aircraft Systems*, RCR Press, Boca Raton, Florida, 2012b, 24.

Beard, R. W., T. W. McLain, *Small Unmanned Aircraft Theory and Practice*, Princeton University Press, Princeton, New Jersey, 2012, 288.

Chao, H., A. M. Jensen, Y. Han, Y. Chen, "AggieAir: Towards low-cost cooperative multispectral remote sensing using small unmanned aircraft systems," in Advances in Geoscience and Remote Sensing, G. Jedlovec, ed., InTech, Vukovar, Croatia, 2009, 463–490, https://www.researchgate.net/publication/221905354_AggieAir_Towards_Low-cost_Cooperative_Multispectral_Remote_Sensing_Using_Small_Unmanned_Aircraft_Systems, accessed January 5, 2016.

Chao, H. Y., Y. C. Cao, Y. Q. Chen, "Autopilots for Small Unmanned Aerial Vehicles: A Survey," *International Journal of Control, Automation, and Systems* **8**, 1 (2010) 36–44.

Di, L., Y. Chen, "Autonomous flying under 500 USD based on RC aircraft," *Proc. of 2011 ASME/IEEE International Conference on Mechatronic and Embedded Systems and Applications*, Washington, D.C. (2011a).

Di, L., H. Chao, J. Han, Y. Chen, "Cognitive multi-UAS formation flight: Principle, low-cost UAS testbed, controller tuning and experiments," *Proc. of 2011 ASME/IEEE International Conference on Mechatronic and Embedded Systems and Applications*, Washington, D.C. (2011b).

Franklin, M., "Unmanned combat air vehicles: Opportunities for the guided weapons industry?" Royal United Services Institute for Defence and Security Studies (2008), https://rusi.org/sites/default/files/200808_op_unmanned_combat_air_vehicles.pdf, accessed January 6, 2016.

Gan, S. K., S. Sukkarieh, "Multi-UAS target search using explicit decentralized gradient-based negotiation," IEEE International Conference on Robotics and Automation, Shanghai, China, May 9–13, 2011.

Geramifard, A., J. Redding, N. Roy, J. P. How, "UAS cooperative control with stochastic risk models," American Control Conference, San Francisco, California, June 29–July 1, 2011.

Goplen, S. E., J. L. Sloan, "National unmanned aircraft systems project office," U.S. Geological Survey Fact Sheet, FS-2015–3013, 2015.

Gupta, S. G., M. M. Ghonge, P. M. Jawandhiya, "Review of unmanned aircraft system (UAS)," *International Journal of Advanced Research in Computer Engineering and Technology* **2**, 4 (2013) 1646–1658, http://www.uxvuniversity.com/wp-content/uploads/2014/04/Review-of-Unmanned-Aircraft-System-UAS.pdf, accessed January 6, 2016.

Han, J., Y. Q. Chen, "Cooperative source seeking and contour mapping of a diffusive signal field by formations of multiple UAVs," *Proc. IEEE 2013 International Conference on Unmanned Aircraft Systems*, Atlanta, Georgia, 2013a.

Han, J., Y. Xu, L. Di, Y. Q. Chen, "Low-cost multi-UAS technologies for contour mapping of a nuclear radiation field," *J. Intell. Robot. Syst.* **70** (2013b) 401–410.

Han, J., Y. Q. Chen, "Multiple UAV formations for cooperative source seeking and contour mapping of a radiative signal field," *J. Intell. Robot. Syst.* **74** (2014a) 323–332.

Han, J., L. Di, C. Coopmans, Y. Q. Chen, “Pitch loop control of a VTOL UAS using fractional order controller,” *J. Intell. Robot. Syst.* **73** (2014b) 187–195.

Han, J., “Cyber-physical systems with multi-unmanned aerial vehicle-based cooperative source seeking and contour mapping,” Doctoral Thesis, Utah State University, 2014c.

RaptorX, https://raptorx.org, 2015, accessed September 30, 2015.

This page left blank intentionally

Exploratory Research

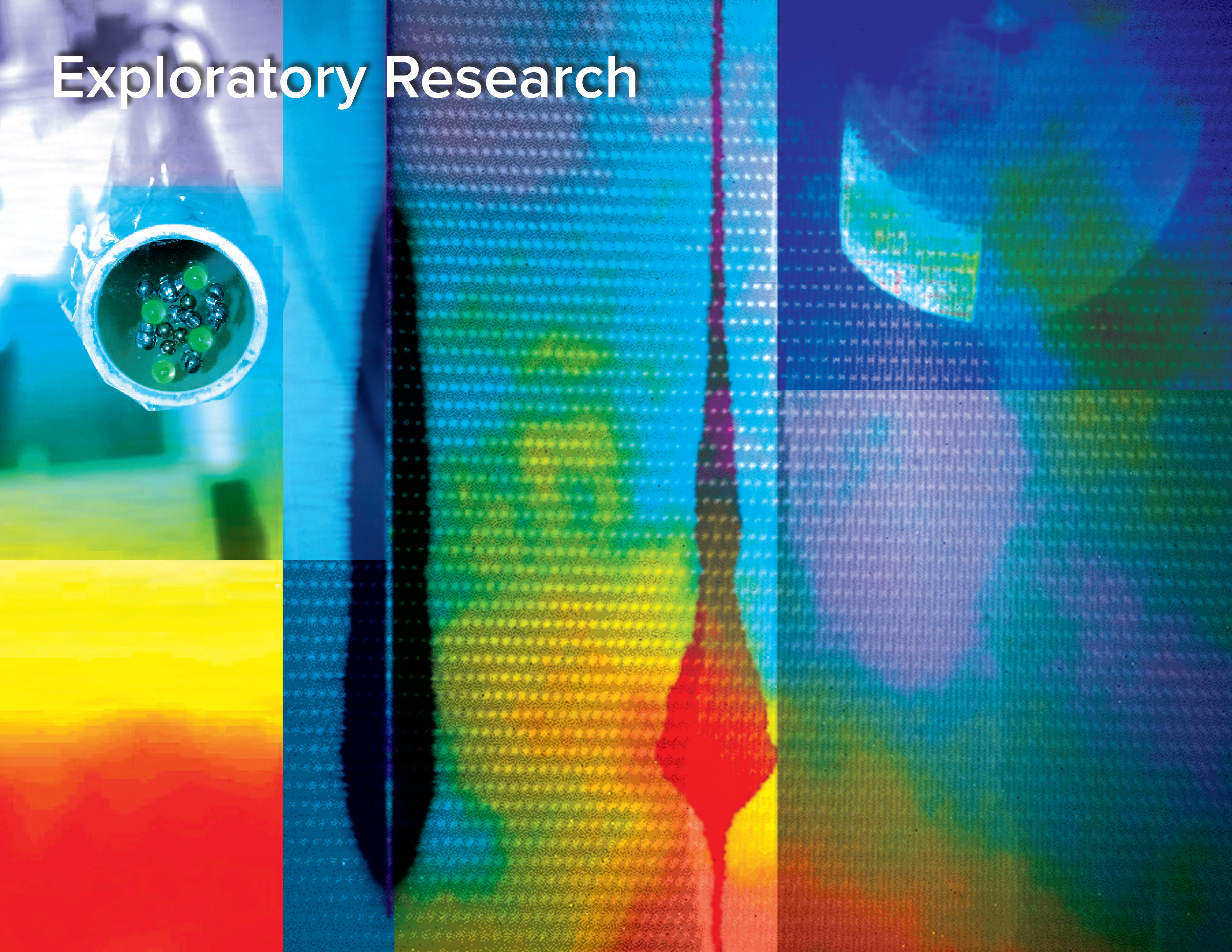

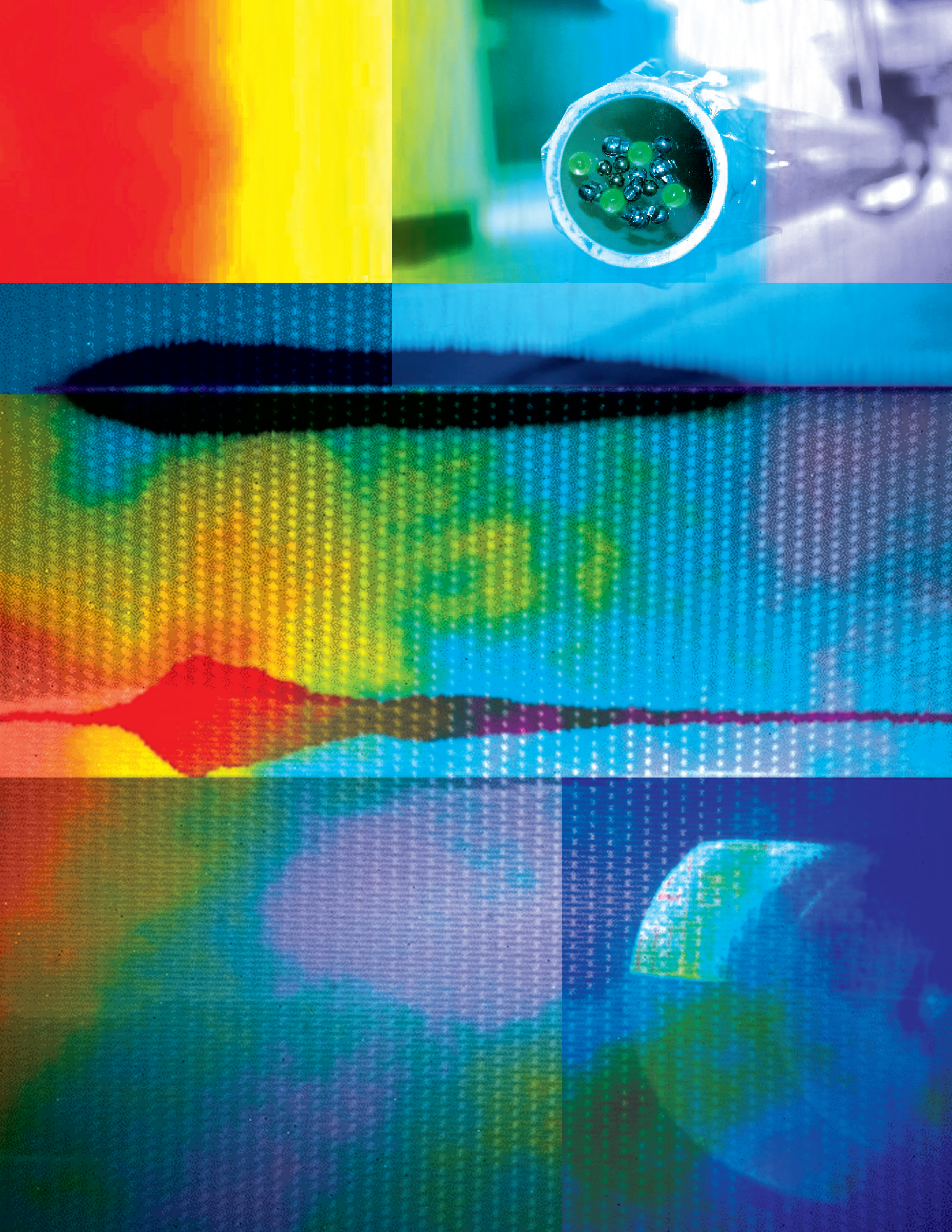

Simultaneous Raman and Pyrometric Temperature Measurements of a Shock Wave–Compressed Material

STL-009-17 ■ Continuing in FY 2018 ■ Year 1 of 2

Gene Capelle,[1,a] Brandon La Lone,[a] and Jason Mance[a]

[1]capellga@nv.doe.gov, (805) 681-2522
[a]Special Technologies Laboratory

To better understand the equation of state of dynamically compressed materials, it is necessary to have an accurate temperature measurement of the shock-compressed state. We have demonstrated a temperature measurement technique that is entirely different from the traditional pyrometry method normally used in shock wave measurements. The new technique, based on Raman spectroscopy, does not depend on surface emissivity and provides an independent way of measuring temperature. In FY 2017 we performed an experiment to measure the temperature of a shock-compressed liquid using both pyrometry and Raman spectroscopy so that the techniques could be cross-compared. A thin layer of toluene sandwiched between sapphire windows was shock compressed using a single-stage light gas gun to a peak stress of ~9 GPa. While the toluene was in the shock-compressed state, it was probed with a pulsed (532 nm, 35 mJ, 12 ns) laser, and the Raman spectrum was captured with a spectrometer and an intensified CCD camera. By analyzing the resulting Stokes/anti-Stokes emission, a temperature was calculated. Additionally, the toluene sample, while visibly transparent, had a strong radiance emission in the mid-wavelength infrared, which enabled our pyrometric temperature measurement of the same volume and at the same time. The temperatures measured with both techniques were in reasonable agreement at 600 K ±100 K. More work is needed to reduce the temperature uncertainty for both techniques.

BACKGROUND

One of the goals of the Stockpile Stewardship program is a better understanding of the behavior of materials during shock wave loading. Temperature is a critical variable in understanding and modeling the equation of state (EOS) of various materials. In EOS experiments relevant to the stockpile, pyrometry has been the predominant method used to measure the temperature of the shocked surface. Pyrometry involves measuring the optical emission from a shock-heated sample in a selected visible, near-infrared, or mid-wave infrared (MWIR) spectral band (or bands). By correcting the measured output by the sample's emissivity factor and comparing it to the output of an ideal black body, a best-fit temperature can be calculated.

Unfortunately, the emissivity of the shock-heated sample is not usually known, and it can vary in time throughout the shock process as the sample undergoes density and/or phase changes, adding some uncertainty to the calculated temperature. Additionally, there can be non-thermal sources of light emission, such as window fractoluminescence that can contaminate the pyrometry signal. For these reasons, an alternate temperature-measuring technique is needed, one that ideally would be independent of emissivity. If an independent method of measuring temperature could be demonstrated, its results could be compared to and give validity to pyrometry-based results. So important is this need that it was specifically called out in the *NNSS R&D Technology Needs Assessment* under Stockpile Stewardship: Temperature, and it was identified as a top priority at the Matter-Radiation Interactions in Extremes (MaRIE) temperature workshop in October 2016 (Lacerda 2016).

For this project we chose to use Raman spectroscopy to obtain the temperature of a shock-compressed sample (Pangilinan 1997). In a Raman-active material the intensity ratios of Stokes to anti-Stokes Raman emission line pairs are known to be dependent on the material temperature. We chose toluene, a Raman-active material that also has MWIR emission so we could simultaneously perform a pyrometric temperature measurement for comparison.

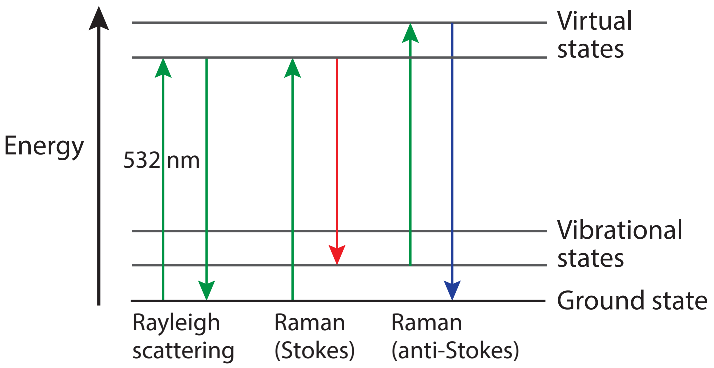

Figure 1. Simplified diagram illustrating Raman scattering

PROJECT

Theory

Figure 1 is a simplified schematic of light scattering from a visibly clear Raman-active liquid illuminated with a pulse of 532 nm laser light. Most of the light is transmitted. A small amount, however, is absorbed into a higher-energy "virtual" state, from which it immediately decays by emission of a photon. The transition is normally back to the ground state, resulting in the emission of a photon of the same wavelength; this is known as Rayleigh scattering. In a small number of cases, the decay can instead populate a higher energy level vibrational state. The resulting photon then carries less energy and is red-shifted to a longer wavelength from the input light. There may be a number of such lines, and they are called Stokes-shifted Raman lines, or just Stokes lines. Prior to laser excitation, the upper vibrational levels will also be populated, though not significantly at room temperature, according to a Boltzmann distribution. A small number of the input laser photons can also cause transitions from these low-lying vibrational states to upper virtual states. The photon that is re-emitted can transition back to the ground state, resulting in a blue-shifted shorter wavelength photon. These are called anti-Stokes Raman lines.

At higher temperatures, more of the upper vibrational states will be populated, and the anti-Stokes emission will increase. This gives us a way to deduce the temperature. Anti-Stokes lines are normally very weak at room temperature, as can be observed, as well as deduced from the formula presented later. As temperature increases, populations in the various molecular modes increase (the molecule becomes more active), so the anti-Stokes lines increase relative to their Stokes counterparts. The lines associated with the small Raman shifts increase the most at first. At higher temperature, higher molecular vibrational levels become populated, so anti-Stokes lines with larger Raman shifts become more pronounced.

Experiment

Experiments were first carried out in the laboratory at room temperature and pressure to develop and test a measurement technique. Toluene was selected as the experimental test liquid, with cyclohexane also a possibility. Toluene is visibly transparent, Raman active with at least some Raman lines free from other interferences (such as Raman emission from window material), not fluorescent when pumped at 532 nm, readily available, not excessively toxic, and has MWIR emission that works for simultaneous pyrometry measurements.

Because the project goal was to carry out shocked material (i.e., high temperature and pressure) tests at the Special Technology Laboratory (STL) gas gun facility, the lab tests were an opportunity to sort out the special constraints placed on the sample, the most stringent of which was sample size. In the dynamic experiments a "ring up" technique was used to achieve the desired temperature and pressure state in the toluene sample. A thin layer of toluene is loaded between two thick sapphire windows. When a shock wave exits the first sapphire window, it shock compresses the toluene and is then reflected by the other sapphire window back into the toluene. These reverberations cause the toluene sample to "ring up" in pressure and temperature. The challenge is to make the sample thin enough to allow multiple reverberations before release waves from the edge of the window enter the sample and drop the pressure. To accomplish this goal the sample was limited to a thickness of 0.5 mm.

For the laboratory tests, a small pulsed laser (Big Sky model CFR400, 532 nm, 35 mJ, 12 ns) focused ($f = 1000$ mm lens) to about a 2 mm diameter beam at the sample was used to excite Stokes and anti-Stokes emissions from the toluene sample placed in a 1 mm path length quartz cuvette. The illuminated area was imaged into a ~0.3-meter length of 1.5 mm core quartz fiber. An intermediate set of optics at the opposite end of the fiber collimated the exiting light for transmission through a 532 nm notch filter. The light was then re-imaged (1:1) into a fiber bundle; the other end of the bundle terminated in a line of fibers that filled the entire active height of the input slit of an IsoPlane 160 imaging spectrograph; an intensified CCD (ICCD) detector mounted to the spectrograph provided needed gain and a short time gating capability. Raman signals are prompt, so gating around the 12 ns laser pulse eliminates some of the background light. A series of measurements was made on toluene, and it was determined that a small but usable Raman signal could be collected from the thin layer of sample during a single laser pulse. The signal included a number of usable Raman Stokes/anti-Stokes line pairs within the available spectral window from approximately 494 to 576 nm.

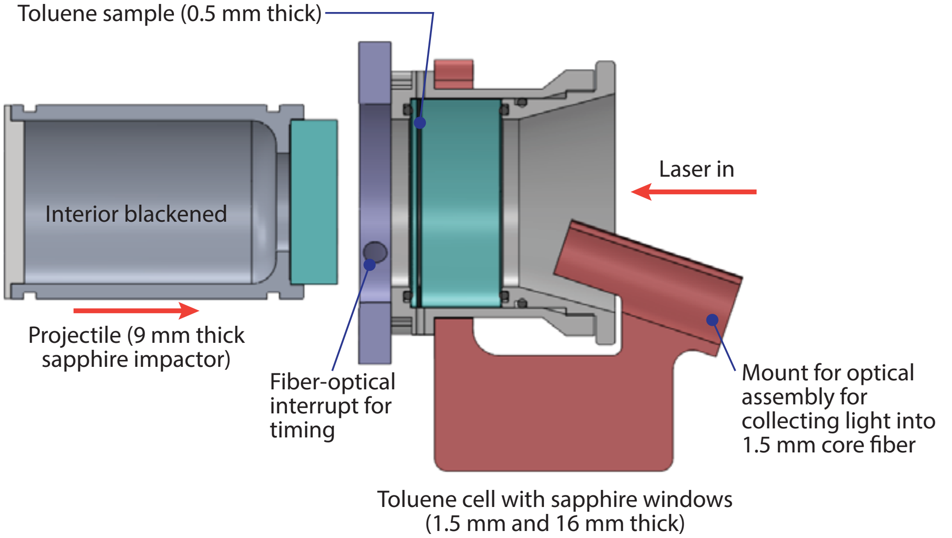

Figure 2. Design for the gas gun Raman spectroscopy experiment

A cell was then designed for the gas gun experiment; the final design is as shown in Figure 2. The cell contains a 1.5 mm thick front sapphire window, a 0.5 mm thick layer of toluene, and a 16 mm thick rear sapphire window; all layers in the cell were 41 mm in diameter. The impactor was a 9 mm thick, 32 mm diameter piece of sapphire. The design was such that after impact, the toluene is surrounded by a large quantity of sapphire to facilitate the "ring up" (multiple reflections of the compression wave) and to maintain the shock pressures as long as possible. An opening was made behind the sapphire impactor to allow the laser beam to pass into the projectile interior, which was blackened to decrease scattering. The laser beam was sent into the gas gun chamber through a Suprasil window, then off a mirror and into the cell at normal incidence to decrease scatter into the collection optics

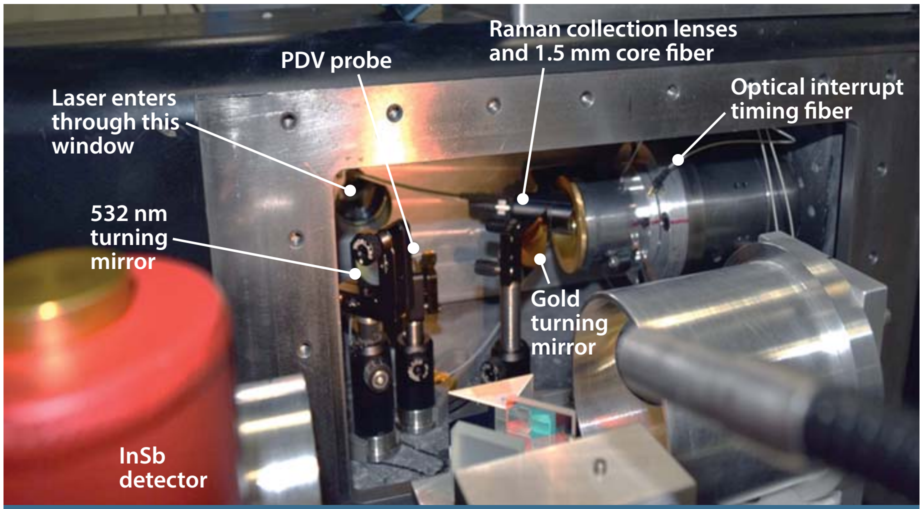

Figure 3. Optical arrangement for simultaneous Raman, pyrometry, and PDV measurements on shocked sample at STL gas gun facility

that collected the Raman scattered light approximately 20° off normal. The collection optics, consisting of two small lenses mounted in a 0.5″ diameter tube, slipped into the mount shown in Figure 2, gathered light from the illuminated section of toluene, and filled the full 0.22 NA of the 1.5 mm core fiber. A gold mirror mounted below the laser illumination zone directed thermal radiance from the toluene out through a sapphire port window on the opposite side of the gun experiment chamber to the indium antimonide (InSb) pyrometry detector. The InSb detector is a 300 µm, liquid nitrogen–cooled, amplified detector built at STL. A small spot on the sample is imaged onto the detector via a pair of 50 mm diameter off-axis parabolic mirrors. In the collimated space between the parabolic mirrors, we placed an optical filter that passes all wavelengths beyond 2.4 µm. A photonic Doppler velocimetry (PDV) probe (to measure velocity history) and an optical interrupt fiber were added to trigger the laser at the correct time. The full experimental setup at the gas gun facility is shown in Figure 3.

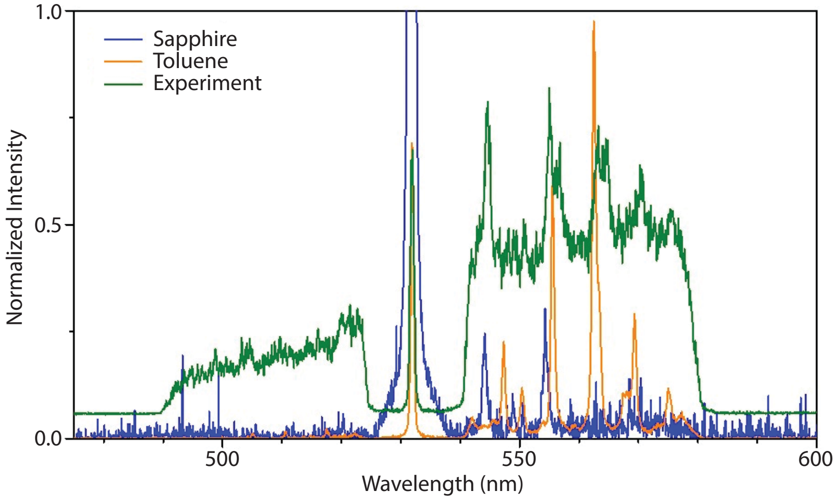

Figure 4. Raman spectrum with one laser pulse from 0.5 mm thick layer of toluene; same vertical scale for both orange and green traces. Laser line at 532 nm, Raman Stokes lines are at right, anti-Stokes at left. Cutoffs near 490 and 580 nm are due to edge of ICCD. The green line shows gas gun shot performed August 15, 2017; the yellow line is the signal before the shot (room-temperature toluene); and the blue line is the background Raman from sapphire (different scale and conditions).

Data

Figure 4 shows data from a gas gun experiment as well as a pre-experiment (room-temperature toluene) measurement. The Raman lines shift slightly during the compression. While the Stokes lines are only slightly less intense in the compressed state, the anti-Stokes lines are much stronger, as would be expected at higher temperatures, and the background has increased significantly. Also note the strong interference lines from sapphire. A measurement on a sapphire window (taken under different conditions) is shown and illustrates the sapphire lines, which are quite strong in the toluene compression. All of this suggests that there was more laser scatter during the dynamic experiment than under ambient conditions.

Figure 5 shows the PDV record converted to stress, and the pyrometry record for two different emission band assumptions (discussed below). The laser firing occurs at t = 0 s (some electrical noise is seen on the pyrometry data when the laser fires).

Pyrometry Analysis

Prior to the experiment, the InSb pyrometer detector was calibrated using a black body source with most of the optical elements in place except for the toluene layer. Sapphire's optical transmission cuts off at about 4.5 µm. Therefore, combined with the 2.4 µm long pass filter, the system was effectively viewing an optical bandpass from 2.4 to 4.5 µm. Experimental signal voltages were converted to temperatures using two different emission band assumptions for the toluene. One assumption (low temperature curve in Figure 5) was that the toluene was a black body emitter (emissivity = 1) across the entire 2.4–4.5 µm band of the detector. The other assumption (upper temperature curve in Figure 5) was that the toluene only radiates about its C-H stretch mode vibration bands, where we are confident toluene is strongly emissive, from 3.1 to 3.7 µm. These assumptions set reasonable upper and lower temperature bounds for the experimental data.

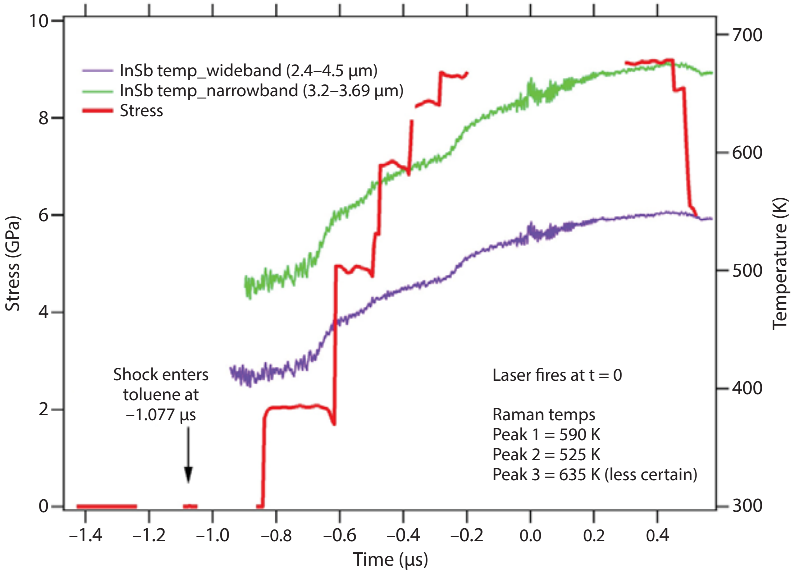

Figure 5. PDV record of compression (red), converted to stress (left vertical scale) and InSb pyrometry record (right vertical scale), assuming emission in the 2.4 to 4.5 µm band (green line) and a 3.2 to 3.69 µm band (purple line)

Raman Analysis

The temperature of the material is determined by comparing the ratio of the intensities of the Stokes and anti-Stokes lines in the Raman spectrum. This ratio is related to the temperature according to the equation (Long 1977)

$$\frac{I_{anti\text{-}Stokes}}{I_{Stokes}} = \left(\frac{v_0 + \Delta v}{v_0 - \Delta v}\right)^4 exp\left(-\frac{h\Delta v}{k_B T}\right), \qquad (1)$$

where v_0 is the frequency of the laser, Δv is the Raman shift frequency, h is the Plank constant, k_B is the Boltzmann constant, and T is the temperature. The ratios of the lines are determined using nonlinear least squares fitting (NLSF), assuming each peak has a Lorentzian profile of the form

$$I(v) = \frac{2A}{\pi}\frac{w}{4v^2 + w^2}, \qquad (2)$$

Before fitting the peaks, background must be subtracted from the spectrum. This is done assuming the background is slowly varying and iterated until the baseline of the fit matches the baseline in the data. An important added constraint to the fitting algorithm is that the Stokes-to-anti-Stokes ratios of all peaks in the Raman spectrum must yield the same temperature (for lines emanating from the same material). Initial fits in which the NLSF was allowed to determine all amplitudes independently were made; it was apparent that constraining the lines to a shared temperature largely reduces the uncertainty in the results, especially when the signal-to-noise ratio is low and background subtraction is difficult. This constraint was added by using Equations 1 and 2 to express the amplitude of the anti-Stokes lines in terms of the Stokes amplitude and temperature. The fitting equation is then as shown in Equation 3.

In Equation 3 the sum n is over the number of peak pairs in the spectrum, and it is assumed that the line pairs have the same width. The Rayleigh scattered peak at $\Delta f = 0$ is omitted from the equation for simplicity but was added in practice.

NLSFs were performed using OriginLab software. Figure 6 shows this technique applied to a room-temperature sample of toluene, which resulted in a temperature of 290 K (note that the scale has been changed to frequency space). Figure 7a shows the data, fit, and resulting temperatures in the toluene sample and the sapphire window for the dynamic gas gun experiment performed on August 14, 2017. Figure 7b shows what the fit would be like for different temperatures. The sapphire is near room temperature, as would be expected, and the compressed toluene was

$$I(f) = \frac{1}{2\pi}\sum_{n=1}^{13} \underbrace{A_n\left(\frac{f_0 + \Delta f_n}{f_0 - \Delta f_n}\right)^4 \left(\frac{w}{(f-(f_0+\Delta f_n))^2 + (w/2)^2}\right) exp\left(-\frac{h\Delta fn}{kT}\right)}_{\text{Anti-Stokes Peaks}} + \underbrace{A_n\left(\frac{w}{(f-(f_0-\Delta f_n))^2 + (w/2)^2}\right)}_{\text{Stokes Peaks}} \qquad (3)$$

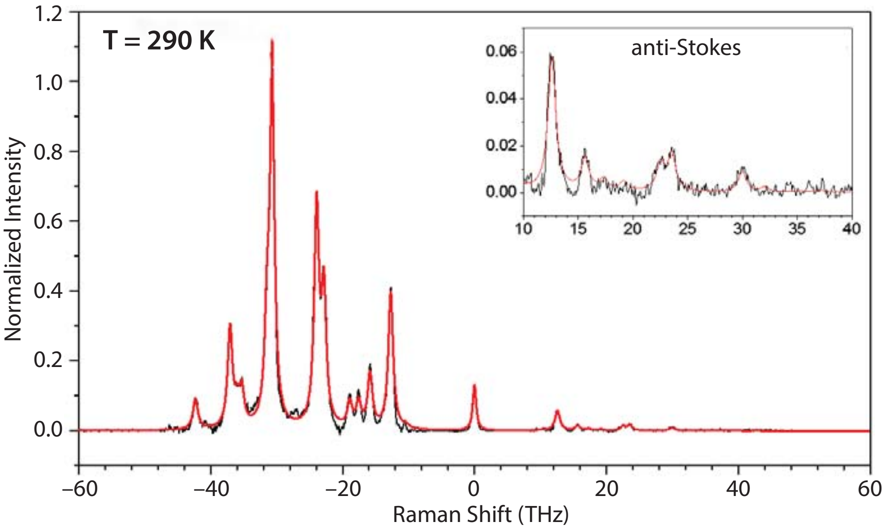

Figure 6. Raman spectra, NLSF results, and temperature from measurements (average of 20 laser shots) made on a room-temperature toluene sample

measured to be 610 K. From Figure 7b we qualitatively estimate that our temperature is accurate to within approximately 100 K. Future work will seek to improve on the accuracy of the measurement by investigating methods to increase the signal-to-noise ratio of the data.

CONCLUSION

A small toluene sample was multiply compressed between sapphire windows to about 9 GPa. The temperature near the peak of the compression process was estimated from measured Raman ratios to be between 550 K and 650 K. A simultaneous pyrometry measurement using an InSb detector was in apparent agreement with an estimated temperature of between 530 K and 630 K. While this conclusion is preliminary due to a limited number of experiments, the proposed Raman temperature measurement technique appears to work. As this project continues in FY 2018, we aim to conduct additional experiments to confirm the results and improve measure-ment accuracy. Also, both the Raman and pyrometry measurements presented represent temperatures of the compressed material (i.e., the volume of the liquid). Because most shock compression experiments of interest to us involve opaque materials such as tin, where pyrometry measures only the surface temperature, modifications to the experimental design will provide a method for simultaneously measuring volume and surface temperature for comparison.

ACKNOWLEDGMENTS

We wish to thank Eric Larson for his help with the pyrometry measurements, and Ben Valencia and Mike Grover for their help in designing,

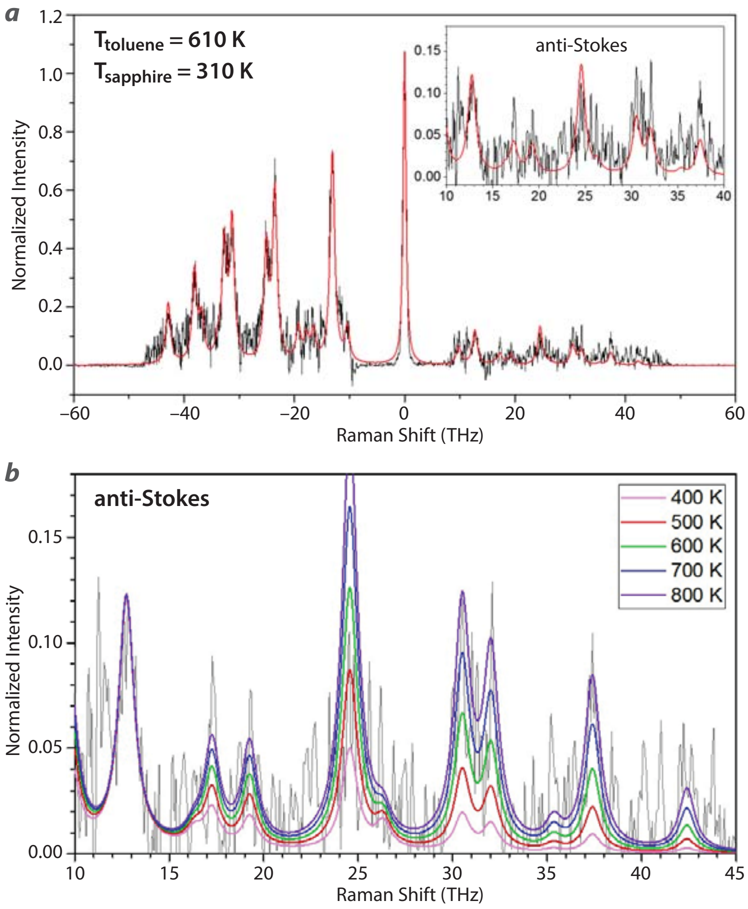

Figure 7. (a) Data, fit, and resulting temperatures for the gas gun experiment, and (b) detail of anti-Stokes portion showing potential fits for different temperatures

building, and fielding the experimental cell at the gas gun facility.

REFERENCES

Lacerda, A., et al., “New techniques for dynamic thermometry,” MaRIE Summer 2016 Workshop Series, September 28–29, 2016, http://www.lanl.gov/science-innovation/science-facilities/marie/_assets/docs/workshops/new-techniques-dynamic-thermometry.pdf, accessed November 1, 2017.

Long, D. A., *Raman Spectroscopy*, McGraw-Hill, London, 1977, 84.

Pangilinan, G. I., Y. Gupta, “Use of time-resolved Raman scattering to determine temperatures in shocked carbon tetrachloride,” *J. Appl. Phys.* **81** (1997) 6662.

This page left blank intentionally

A Multi-Axial Time-Resolved Spectroscopic Technique for Magnetic Field, Electron Density, and Temperature Measurements in Dense Magnetized Plasmas

LO-001-16 ■ Continuing in FY 2018 ■ Year 2 of 3

Eric C. Dutra,[1,a] Jeffrey A. Koch,[a] Radu Presura,[b] William Angermeier,[c] Timothy Darling,[c] Roberto Mancini,[c] and Aaron Covington[c]

[1]dutraec@nv.doe.gov, (925) 960-2584
[a]Livermore Operations
[b]New Mexico Operations–Sandia
[c]University of Nevada, Reno

The scope of this three-year project is to develop a multi-axial time-resolved spectroscopic technique for simultaneous measurement of magnetic field strengths, electron densities, and temperatures of dense magnetized plasmas for Z-pinch and dense plasma focus applications. These plasma properties are determined by analyzing experimental emission spectra with a code that includes Zeeman splitting as well as collisional and Doppler broadening. With increasing electron densities and temperatures, collisional and Doppler broadening dominate the measured line profiles, making it difficult to separate the Zeeman component. Two approaches can be used to make Zeeman splitting measurements under such conditions: the first employs a polarization technique to separate out the circularly and linearly polarized components, where the circular component is more affected by Zeeman Splitting (Stambulchik 2007, Tessarin 2011, Blesener 2012); the second is the technique used in this work, and it is based on the different widths of Zeeman-split fine structure components (Rochau 2010, Gomez 2014). In the second year of the project, we focused on code development on the Zeeman splitting fine structure, magnetohydrodynamic modeling of Z-pinches, and performing proof-of-principle laser ablation Z-pinch experiments. In Year 3 of this project, we plan to refine this technique, improve spectral simulations, and collect data at higher plasma temperatures.

BACKGROUND

Spectroscopic techniques in the visible wavelength range are often used in plasma experiments to measure magnetic field–induced Zeeman splitting, electron densities via collisional broadening, and temperatures from Doppler broadening. Pulsed power research Z-pinch machines, such as the Sandia National Laboratories Z machine, the NNSS dense plasma focus (DPF), and the University of Nevada, Reno (UNR) Zebra, produce dense magnetized plasmas using a Marx bank to drive current through a wire or gas. These machines can have an electric current rise time on the order of hundreds of nanoseconds, with target performance that is magnetically driven and dependent on the current that travels along the outer sheath of the plasma column formation. This current induces a magnetic field that compresses the plasma, thereby increasing plasma electron density and temperature. Spectroscopy provides a noninvasive way to make these measurements. The characterization of magnetic fields, field symmetries, and electron densities and temperatures provides information about the current distribution and current loss across the anode-cathode gap. These plasma parameters can be used to validate modeling codes used in the design of new pulsed power Z-pinch machines.

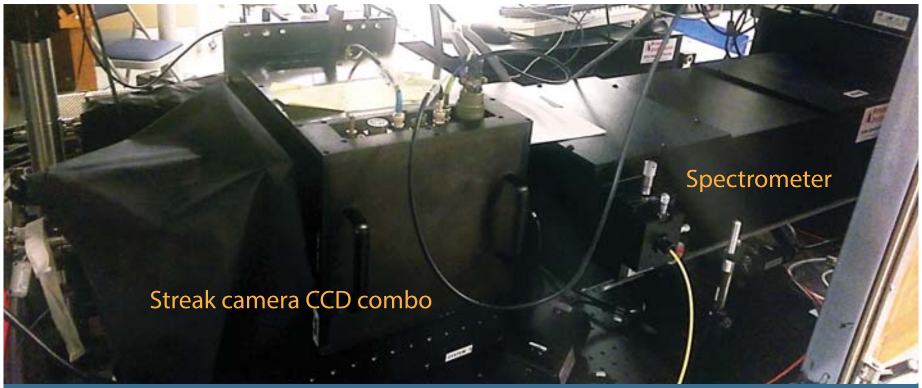

Figure 1. Acton SpectraPro SP-2750 spectrometers coupled to an NNSS-built optical streak camera (L-CA-24)

In the first year of this SDRD project, we worked with UNR to develop a Zeeman splitting spectroscopic model. This model allowed us to identify relative broadening or splitting induced by the magnetic field (Dutra 2016). The spectroscopic model guided us in identifying the spectroscopic equipment requirements for our experiment. We continued to develop the spectroscopic model so that it could be used to post-process our data. We purchased, assembled and characterized a streaked spectroscopy system, as seen in Figure 1, and used it to record initial time-resolved emission spectra from dense magnetized plasmas. These measurements were coupled with spectral emission modeling and used to develop an analysis procedure for estimating magnetic field strengths, electron densities, and temperatures.

The spectral line emission from the plasma sheath can be measured using time-resolved spectroscopy. However, when plasma temperatures and densities are high, collisional and Doppler broadenings dominate line profiles, making it difficult to measure the Zeeman component. In general, two techniques provide a measurement of both the collisional and the Doppler and Zeeman components. The first method measures both the linearly polarized components of the spectra, which are dominated by collisional and Doppler broadening, and the circularly polarized components, which are affected by Zeeman broadening. Measurement of the circularly polarized emission spectra allows a deconvolution of the collisional and Doppler broadening from the Zeeman broadening, enabling a simultaneous measurement of the magnetic fields, electron densities, and temperatures (Rochau 2010, Gomez 2014).

The second approach investigates the fine structure components of a given multiplet, which are split differently due to the magnetic field. The energy shift due to both the L and S coupling and the magnetic field is given by the Hamiltonian (H),

$$H = AL \cdot S + (L + 2\omega)\ B, \tag{1}$$

where the first term, L is the orbital angular momentum, S is the spin-orbital momentum, and A is a constant and multiplies the spin-orbit coupling. The second term makes up the magnetic field operator, where B is the magnetic field, and ω is the magnetic moment. The Hamiltonian can then be used to calculate the energy shifts. This can be done using two methods. The first method uses a perturbative expansion, which depending on the number of terms in the expansion, can be used to approximate either a weak or a strong field case. These techniques were both discussed in the FY 2016 SDRD final report

(Dutra 2017). Alternatively, one can solve the Hamiltonian exactly. This is done by compiling the Hamiltonian matrix, diagonalizing the matrix, and calculating the energy eigenvalue of the diagonalized matrix. Using the selection rules, one can then map the emission transitions onto a calculated line profile given by the collisional- and Doppler-broadened terms. This approach will be discussed in more detail in the spectral modeling section of this report. Because the doublet components have similar collisional and Doppler broadening in the same plasma, the difference in the line broadening of the two doublets depends solely on the magnetic field, along with the *L* and *S* components of the Landé g factor (Stambulchik 2007, Tessarin 2011, Blesener 2012).

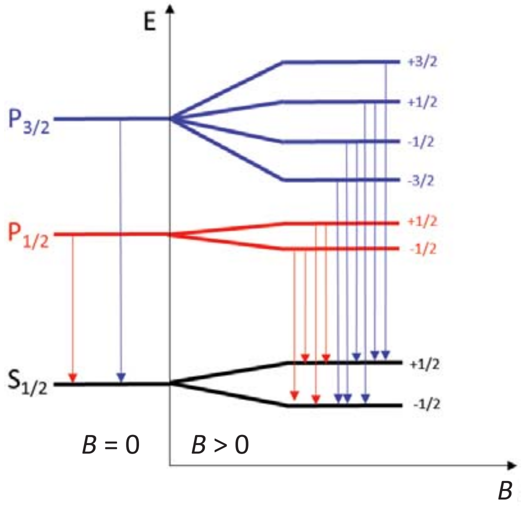

Figure 2. The transitions of 4P $^2P_{3/2}$ to 4S $^2S_{1/2}$ and 4P $^2P_{1/2}$ to 4S $^2S_{1/2}$ in the regions where $B = 0$ and $B > 0$

PROJECT

In experiments conducted at UNR's Nevada Terawatt Facility (NTF) using the 1 MA Z-pinch (Zebra), we explored the response of Al III, C IV, Ti IV, and O VI doublets, and 4P $^2P_{3/2}$ to 4S $^2S_{1/2}$ and 4P $^2P_{1/2}$ to 4S $^2S_{1/2}$ transitions. Optical light emitted from the pinch was fiber-coupled to high-resolution spectrometers. The dual spectrometers were coupled to two high-speed visible streak cameras to capture time-resolved emission spectra from the plasma. The data reflect emission spectra from 120 ns before the current peak to 100 ns after the current peak, where the current peak is approximately the time at which the pinch occurs. The Al III, C IV, and O VI doublets were used to measure Zeeman-, collisional-, and Doppler-broadened emissions with the method described in the second approach. The modeling, experimental method, data analysis, and results obtained in FY 2017 are described below.

Spectral Modeling

The spectral line emission modeling of collisional and Doppler broadening is available from Prism Computational Science in two software packages, PrismSPECT and SPECT3D. PrismSPECT is a geometrical radiation transport code, whereas SPECT3D can incorporate complex geometries, electron density, and temperature distribution. SPECT3D can also use magnetohydrodynamic (MHD) output files that include densities and temperature profiles, as input files for simulating radiation transport. SPECT3D will become more useful in the final year of the project. In the first year of the project, we began developing a spectral line emission code for Zeeman splitting, mainly focusing on the P → S transition, 4P $^2P_{3/2}$ to 4S $^2S_{1/2}$ and 4P $^2P_{1/2}$ to 4S $^2S_{1/2}$, for the Al III doublet. In the second year, we expanded our model to include other transitions (C IV, Ti IV, and O VI) as well as collisional and Doppler broadening into the model. Unfortunately, radiation transport codes that include Zeeman splitting are not readily available, so we have had to develop our own.

The new Zeeman line emission code calculates the Doppler broadening of the line profile assuming a Gaussian distribution, where the FWHM is proportional to the ion temperature. The code then calculates the collisional broadening with a Lorentzian profile with a FWHM that is proportional to the electron density. The Lorentzian and Gaussian distributions are then convolved, yielding a Voigt distribution. Next, we calculate the Zeeman splitting, which arises from emission in an external magnetic field. The Zeeman effect removes the degeneracy of the energy levels with respect to the magnetic moment and results in an energy splitting in the line emission that is directly proportional to the magnetic field strength. The Hamiltonian can then be used to calculate the energy shifts. To do this, we solve the Hamiltonian exactly by compiling our Hamiltonian matrix, diagonalizing the matrix, and calculating the energy eigenvalue of the diagonalized matrix. The energy shift is directly proportional to the magnetic field, *B*. This is illustrated in the schematic energy-level diagram in Figure 2, which shows the P → S transition modeled both with zero magnetic field, $B = 0$, and with the magnetic field, $B > 0$. The energy level diagram in the $B = 0$ region represents the P → S transition from only the spin-orbit coupling.

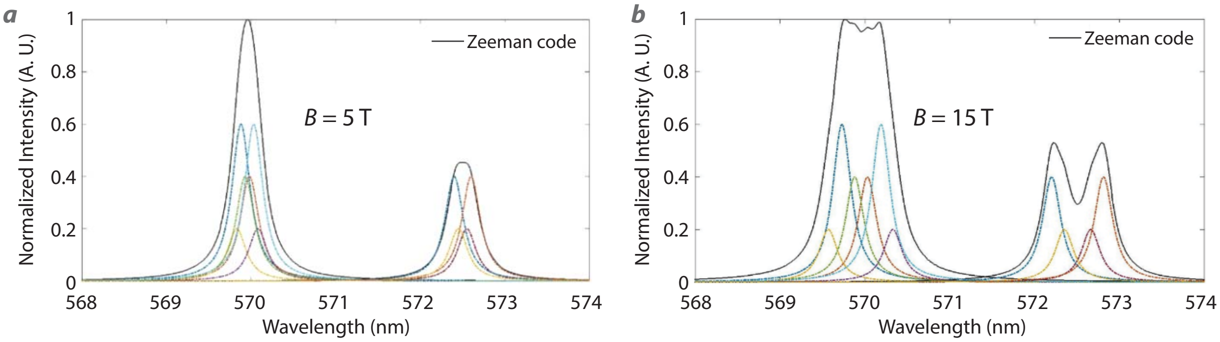

Figure 3. Zeeman line emission–modeled spectra of the 4P $^2P_{3/2}$ to 4S $^2S_{1/2}$ and 4P $^2P_{1/2}$ to 4S $^2S_{1/2}$ with constant temperature and constant electron density for (a) magnetic field strength B = 5 T and (b) magnetic field strength B = 15 T

The difference in energy, or the transition, from the J = 3/2 and J = 1/2 energy level to the S = 1/2 energy level results in a spectral emission line. As the magnetic field is turned on and increased, the degeneracy of the energy level is removed. This results in the splitting of the energy levels as seen in the $B > 0$ region of the diagram. The difference in energy of the transition from the new energy levels of the J = 3/2 and J = 1/2 to the S = 1/2 results in spectral emission lines, where the selection rules will determine the transitions observed.

The Zeeman line emission code then maps the calculated emission lines from the Zeeman splitting onto the Voigt distribution calculated from the collisional and Doppler distributions. Figures 3a and 3b are examples of the line emission at different magnetic fields. The collisional broadening was calculated using an electron density, $n_e = 5 \times 10^{16}$ cm^{-3} and an ion temperature, $T = 10$ eV. The magnetic field, B, is varied from 5 Tesla to 15 Tesla.

Figures 4a and 4b show the variation of the line width if the magnetic field and the temperature are kept constant, and the electron density, n_e, is varied. The temperature is $T = 10$ eV and the magnetic field is $B = 15$ T. The electron density is varied from $n_e = 1 \times 10^{16}$ cm^{-3} to $n_e = 5 \times 10^{17}$ cm^{-3}. As the electron density is decreased, we can start to resolve the Zeeman split line structure; however, as the electron density increases, the structure becomes less defined. It is important to note that the FWHM of each of the broadened line spectra is different. This difference still allows a measurement of the magnetic field even when the broadening due to high electron density or temperature obscure the Zeeman split structure, as seen in Figure 4b.

Next, the Zeeman line emission code was compared to PrismSPECT. PrismSPECT does not include Zeeman splitting. However, we can compare the spectral line broadening from their code to our code, with a zero magnetic field. The temperature and density that define the line shape of the distribution should be the same. This is shown in Figure 5. Here we vary the electron density (Figure 5a is $n_e = 7.5 \times 10^{16}$ cm^{-3} and Figure 5b is $n_e = 2.5 \times 10^{17}$ cm^{-3}) in our code and plot alongside PrismSPECT output for the same parameters. When compared to electron density that is within the range

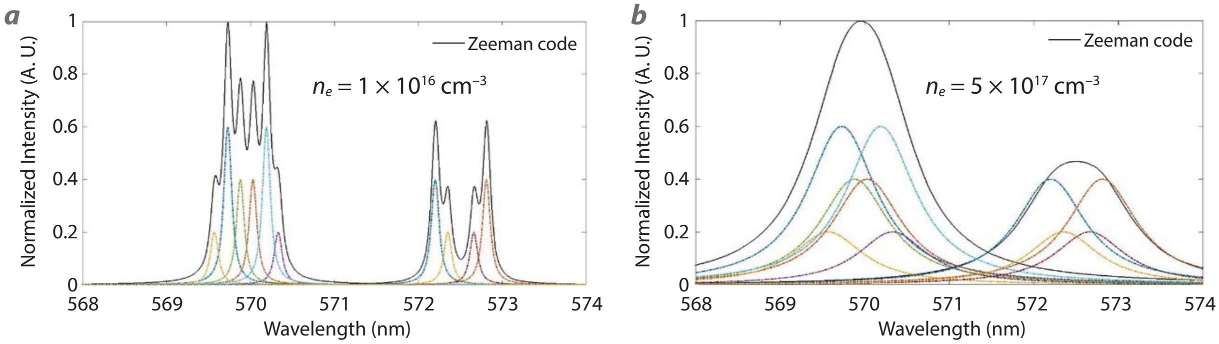

Figure 4. Zeeman line emission–modeled spectra of the 4P $^2P_{3/2}$ to 4S $^2S_{1/2}$ and 4P $^2P_{1/2}$ to 4S $^2S_{1/2}$ with constant temperature and constant magnetic field for (a) electron density $n_e = 1 \times 10^{16}$ cm^{-3} and (b) 5×10^{17} cm^{-3}

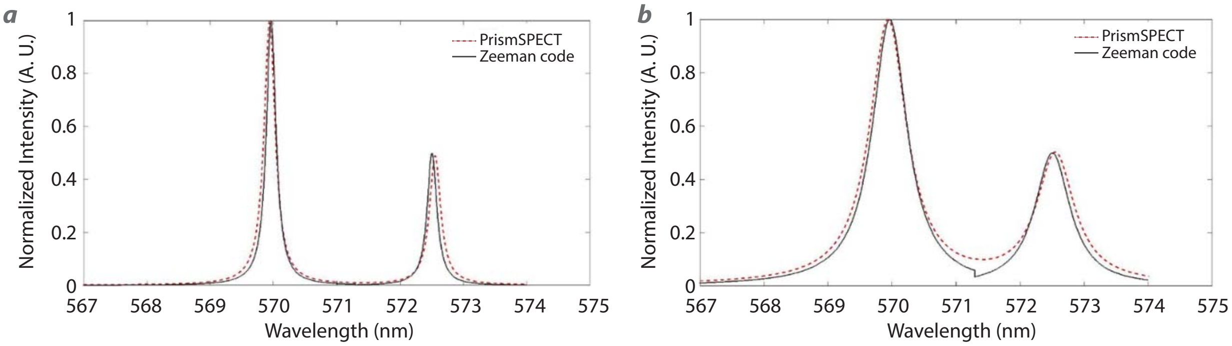

Figure 5. Zeeman line emission–modeled spectra of the 4P $^2P_{3/2}$ to 4S $^2S_{1/2}$ and 4P $^2P_{1/2}$ to 4S $^2S_{1/2}$ with no magnetic field and T = 10 eV compared to PrismSPECT for (a) electron density $n_e = 7.5 \times 10^{16}$ cm^{-3} and (b) $n_e = 2.5 \times 10^{17}$ cm^{-3}

of the experimental parameters, they are in good agreement.

Magnetohydrodynamic (MHD) Modeling

MHD simulations were added to the SDRD project to help create more accurate radiation transport models. The SPECT3D software can use MHD output files that include density and temperature profiles as input files for detailed simulation of radiation transport. Modeling the plasma and the radiation transport helps us understand variations in emission occurring at different locations in the plasma that are within the field of view of our spectroscopic diagnostic. This allows us to strategically place or align our optical probes to regions we wish to study. Moreover, the MHD codes used in conjuction with spectroscopy packages allow us to more accurately interpret experimental results.

MHD simulations were carried out using the MACH2 code. Two-dimensional simulations of the exploding wire pinch were performed for a 50 µm single aluminum wire, and the resulting plasma evolution is shown at different times in Figure 6.

We can validate the MHD modeling by comparing the simulated electron density distribution with the electron density distribution measured using a laser-based Mach-Zehnder interferometry diagnostic (Ivanov 2011). The initial wire experiments were performed in FY 2017, and the model was shown to be in reasonable agreement with the interferometric data in the bulk of the region of interest. However, we are still addressing unresolved issues at the boundary regions of the simulations. We have also moved forward with modeling the laser ablation Z-pinch experiments in a collaboration with Cornell University. We are currently working on comparing our data and preliminary MACH2 MHD models to the extended PERSEUS MHD modeling (Hamlin 2016) that Cornell is simulating for our experimental parameters.

Laser Ablation Z-Pinch Experiments

Laser ablation Z-pinch experiments were conducted at the NTF with the Zebra pulsed power generator coupled to the Leopard laser. The Leopard laser produces energies of up to 30 J with a 0.8 ns pulse width at a wavelength of 1057 nm. In this configuration, the laser ablates a target and creates an ionized plasma plume. The plume then expands across the anode-cathode gap and creates a conduction path

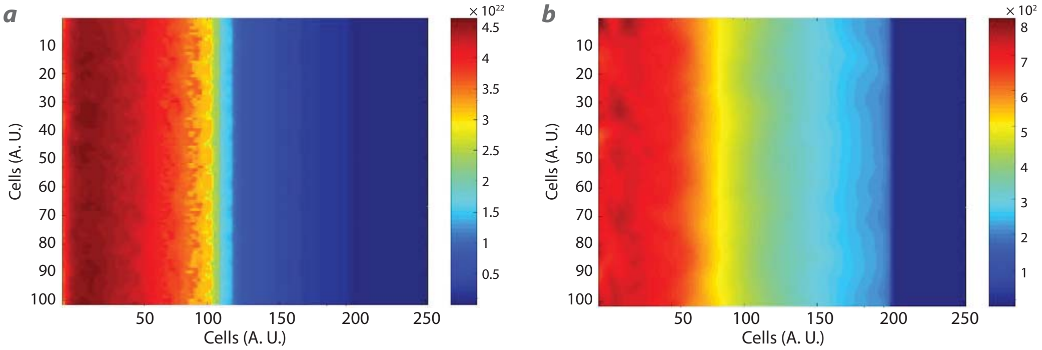

Figure 6. 2-D images of MACH2 MHD exploding wire simulation for (a) t = 5 ns and (b) t = 30 ns

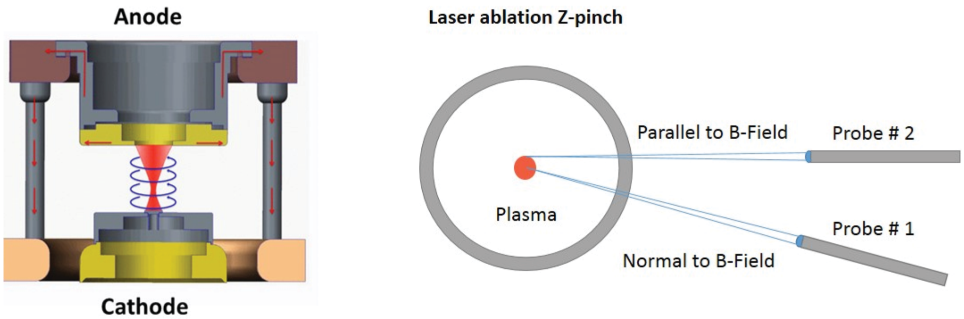

Figure 7. The laser is focused through the top of the anode plate onto the sample target placed on top of the cathode; when Zebra is triggered, current travels through the plasma and creates the $J \times B$ force radially inward toward the z-axis

on which Zebra's 1 MA current travels. Framing camera images indicate that the current flows through the outer shell of the ablation plume along the z-axis, producing a magnetic field in the azimuthal direction. The magnetic field is indicated by the arrows around the plasma column in Figure 7. The current and magnetic field create a $J \times B$ force that compresses the plasma and produces a pinch onto the z-axis. Optical probes were carefully arranged to collect visible light emitted from the plasma source. The alignment of the optical setup is illustrated in Figure 7. B-dot probes were located 14 cm from the center chamber, and optical probes were located 40 cm from the center chamber. A new probe design using off-axis-parabolic (OAP) lenses allowed us to place fibers outside the chamber and increased our light collection efficiencies while enabling a smaller focal spot ~0.5 mm. A plano-convex optical lens is used in conjunction with the OAP adapter to focus on the location identified in Figure 7. The optical setup is configurable, and probes can be aligned radially to the center of the plasma column, perpendicular to the magnetic field direction, or they can be slightly shifted from the radial optical probe and aligned parallel to the magnetic field direction.

One of the benefits of the laser ablation experiments is straightforward load fabrication. Traditional wire array configurations are limited to the availability of the wire material and thickness. Building the wire loads can be challenging and time-consuming, and wire loads tend to break easily. In the laser ablation experiments, we tested Al, copper (Cu), polyethylene (C_2H_4), deuterated polyethylene (C_2D_4), sodium chloride (NaCl), aluminum oxide (Al_2O_3), and titanium deuteride (TiD_2). For Al, Al_2O_3, C_2H_4, C_2D_4, and TiD_2, the Al III, C IV, Ti IV, and O VI P → S optical transitions were identified through modeling as possible emission lines that could be used for the spectroscopic broadening measurements across a wide range of plasma conditions. The data analysis section of this report will focus on the data collected on the Al_2O_3 target.

Data Analysis for Al_2O_3

Figure 8 is an image taken with the streaked spectrometer system on a laser ablation Z-pinch experiment with a compressed Al_2O_3 powder laser target. In the figure, time progresses from the bottom to the top with increasing Z-pinch current. As the current increases over time, the plasma heats rapidly, and the observed intensity of visible transitions evolves rapidly. Two transitions of interest have been identified and are circled in green. The first one is located around 570 nm and has been identified as the Al III doublet studied intensively last year. These transitions allow us to benchmark our data from the laser ablation Z-pinch

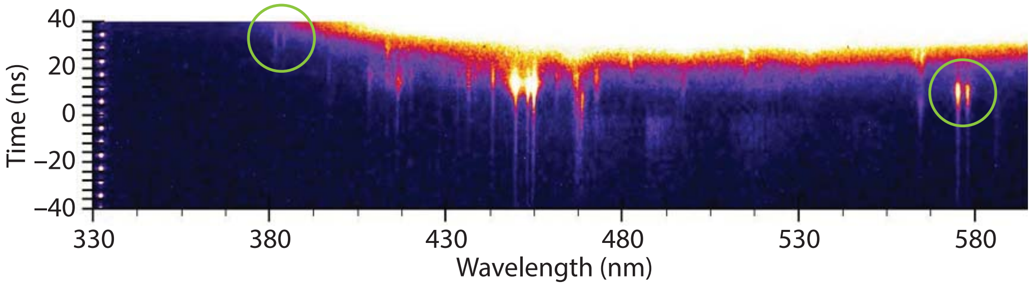

Figure 8. Laser ablation Z-pinch of Al_2O_3 using the broad survey grating (150 line/mm) in the streaked spectrometer system

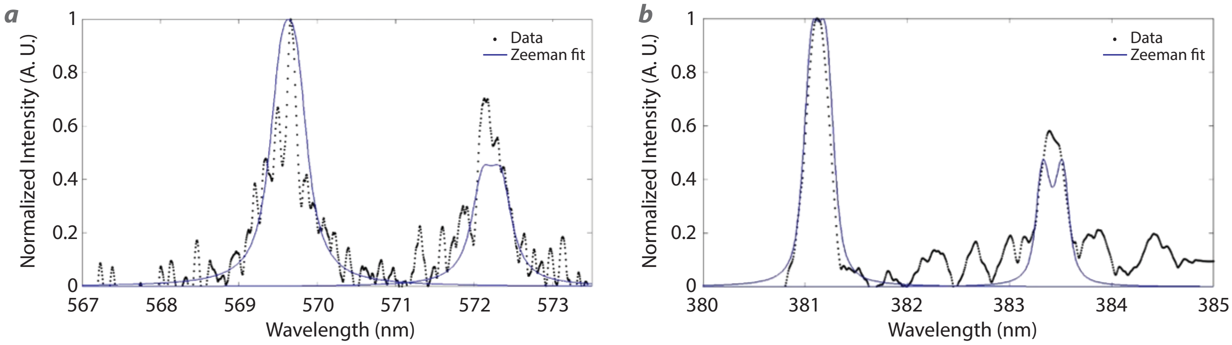

Figure 9. Lineouts from streaked spectrometer system of (a) Al III doublet and (b) O VI doublet with the associated magnetic fields *B* = 7 T and *B* = 12 T, respectively

(LAZE) campaign to prior work conducted with Al wires. The second circle is located at 380 nm and is identifield as the O VI doublet. This line is important because it is the only transition clearly visible at much higher temperature later in the pinch. Preliminary analysis indicates the plasma conditions are ~3 times hotter than those where the Al III doublet was measured. We can also compare the timescale of the two transitions. We see that the O VI doublet emission occurs approximately 24 ns after the Al III doublet emission. Therefore, a measurement of the O VI doublet emission should allow for higher magnetic field measurements that occur further into the current rise than we have been able to measure with this technique to date; this measurement capability increases the dynamic range of the diagnostic.

Data were also acquired using the high-resolution grating (2400 line/mm) in the streaked spectrometer system. The lineouts were analyzed for both the Al III doublet and the O VI doublet $^2P_{3/2}$ to $^2S_{1/2}$ and $^2P_{1/2}$ to $^2S_{1/2}$ transitions. Figure 9a shows a typical lineout taken from one of the high-resolution images for the Al III doublet. The Zeeman line emission code was applied to the data and gave an ion temperature T_i ~10 eV, electron density $n_e \sim 4 \times 10^{17}$ cm^{-3}, and corresponded to a magnetic field strength $B = 7$ T. Figure 9b is a lineout taken from one of the high-resolution images for the O VI doublet. The Zeeman line emission code was applied to these data and yielded an ion temperature T_i ~50 eV, electron density $n_e \sim 1 \times 10^{17}$ cm^{-3}, and the magnetic field strength was $B = 12$ T. It is also important to note that O VI doublet emission spectra are taken approximately 24 ns after Al III emission ends. Therefore, the higher current corresponds to an increase in the *B*-field in the plasma, demonstrating that multiple ionic species are needed to follow the increasing magnetic field strength with increasing time.

CONCLUSION

We have developed a spectroscopic model that incorporates both collisional broadening, Doppler broadening, and Zeeman splitting. The model was then benchmarked against the PrismSPECT code across a range of experiment parameters. Spectroscopic measurements of laser ablation Z-pinches have been made using Al III, C IV, Ti IV, and O VI doublets, and 4P $^2P_{3/2}$ to 4S $^2S_{1/2}$ and 4P $^2P_{1/2}$ to 4S $^2S_{1/2}$ transitions. We have reported on the Al III and the O VI doublet in this report. Using the Zeeman line emission code that we have developed, we measured the evolution of temperatures, electron densities, and magnetic field strengths with increasing pinch current. The results of these efforts were presented at the International Conference on Dense Z-pinches and at the American Physical Society Dense Plasma Physics conference.

In FY 2018 of this project, experimentally we will focus on higher temperature transitions such as the O VI doublet. We will also refine our MHD modeling capability and incorporate radiation transport modeling into Zeeman code. We will also use the MHD output as a parameter for radiation transport modeling using SPECT3D with the goal of creating a robust experimental and modeling capability for use on a wide range of plasma platforms.

ACKNOWLEDGMENTS

The authors would like to thank the support staff and graduate research assistants at the UNR NTF for help in fielding diagnostics, running the Zebra machine, and providing facilities for our experiments. We would like to gratefully acknowledge support from the State of Nevada Governor's Office for Economic Development (GOED) via the Knowledge Fund and the

Nevada Center for Applied Research (NCAR). These matching funds help to share the costs of staffing, equipping, and conducting experiments at the NTF.

REFERENCES

Blesener, K. S., S. A. Pikuz, T. A. Shelkovenko, I. C. Blesener, D. A. Hammer, Y. Maron, V. Bernshtam, R. Doron, L. Weingarten, Y. Zarnitsky, "Measuring magnetic fields in single aluminum wire plasmas with time-resolved optical spectroscopy," *High Energy Density Physics* **8**, 3 (2012) 224–226.

Dutra, E. C., J. A. Koch, R. Presura, W. A. Angermeier, T. Darling, S. Haque, R. C. Mancini, A. M. Covington, "Development of a spectroscopic technique for simultaneous magnetic field, electron density, and temperature measurements in ICF-relevant plasmas," *Rev. Sci. Instrum.* **87**, 11 (2016) 11E558.

Dutra, E. C., J. A. Koch, R. Presura, W. Angermeier, T. Darling, R. Mancini, A. Covington, "A multi-axial time-resolved spectroscopic technique for magnetic field, electron density, and temperature measurements in dense magnetized plasmas," in *Site-Directed Research and Development*, FY 2016, National Security Technologies, LLC, Las Vegas, Nevada, 2017, 23–32.

Gomez, M. R., S. B. Hansen, K. J. Peterson, D. E. Bliss, A. L. Carlson, D. C. Lamppa, D. G. Schroen, G. A. Rochau, "Magnetic field measurements via visible spectroscopy on the Z machine," *Rev. Sci. Instrum.* **85**, 11 (2014) 11E609.

Hamlin, N. D., C. E. Seyler, "Relativistic modeling capabilities in PERSEUS Extended-MHD simulation code for HED plasmas," *IEEE Trans. Plasma Sci.* **44**, 7 (2016) 1112–1126.

Ivanov, V. V., et al., "Measurement of the ionization state and electron temperature of plasma during the ablation stage of a wire-array Z pinch using absorption spectroscopy," *Phys. Rev. Lett.* **106**, 2 (2011) 225005.

Rochau, G. A., J. E. Bailey, Y. Maron, "Applied spectroscopy in pulsed power plasmas," *Physics of Plasmas* **17**, 5 (2010) 055501.

Stambulchik, E., K. Tsigutkin, Y. Maron, "Spectroscopic method for measuring plasma magnetic fields having arbitrary distributions of direction and amplitude," *Phys. Rev. Lett.* **98**, 22 (2007) 225001.

Tessarin, S., et al., "Beyond Zeeman spectroscopy: Magnetic-field diagnostics with Stark-dominated line shapes," *Physics of Plasmas* **18**, 9 (2011) 093301-1–093301-9, http://plasma-gate.weizmann.ac.il/uploads/bibman/tessarin:2011a.pdf, accessed January 18, 2017.

Correlation between Hot Spots and 3-D Defect Structure in Single and Polycrystalline High-Explosive Materials

NLV-035-16 ■ Continuing in FY 2018 ■ Year 2 of 3

Cameron Hawkins,[1,a] Oliver Tschauner,[b] Zachary Fussell,[a,b]
Jason McClure,[b] and Seth Root[c]

[1]hawkinmc@nv.doe.gov, (702) 295-9807
[a]North Las Vegas
[b]University of Nevada, Las Vegas
[c]Sandia National Laboratories

A novel approach that spatially identifies inhomogeneities from microscale (defects, conformational disorder) to mesoscale (voids, inclusions) is developed using synchrotron x-ray methods: radiography, Lang topography, and micro-diffraction mapping. These techniques provide a nondestructive method for characterizing millimeter-sized samples prior to shock experiments. These characterization maps can be used to correlate continuum-level measurements in shock-compression experiments to mesoscale and microscale structures. In FY 2016, we began the process of analyzing high-explosive analogous materials and developing software that can be used as a diagnostic tool pre- and/or post-shock for samples that are recoverable. We continued in FY 2017 by examining high-explosive material samples of C4 as well as pentaerythritol tetranitrate (PETN) and also expanded the capabilities of the software with continued development. In FY 2018 we intend to tie the developed software directly to the beam line and to perform research to prove the capabilities of the software.

BACKGROUND

Knowing how hot spots form in high-explosive (HE) materials during the initial stages of detonation is one of the keys to understanding the detonation process. HE materials are usually not refined single crystals, but compounds of crystallites of one to a few HE compounds and binders. Impedance mismatch between binder and crystallites can influence the response of material to shock. In addition, accidental but unavoidable inhomogeneities such as cracks, voids, grain boundaries, inclusions of fluid or solid phases in the crystallites, and crystal lattice defects can affect the initial response of the material to shock and can operate as locations for hot spot formation. Thus, correlating the given, initial inhomogeneities to hot spot formations is key to understanding the initial stages of detonation (Cawkwell 2008, Kuklja 2014). Such correlation, quantitatively established, helps to provide an understanding of the performance of HEs, allowing them to become more reproducible, more reliable, and safer.

During dynamic compression, localized stress and temperature in aggregate samples are affected by defects, voids, impurities, and other heterogeneities that exist prior to shock. These crystal lattice defects produce weak points by inducing lattice strain. In a solid without internal structural degrees of freedom, such as a face-centered cubic metal, such local strain would induce small-scale reverberations. In molecular solids, such as most HE materials, the local strain around the defects can be relaxed by changes in the conformational state of the molecules. In other words, the excess free energy from induced strain will be converted in part into an increase in internal energy. In HE materials, different conformational states of molecules have different sensitivities to shock (Tsyshevsky 2016). Thus, defects induce local strain, which then induces changes in sensitivities. We examine the extent of such changes of conformation around defects in HE materials as well as the nature of these conformational changes in terms of sensitivity.

Local changes in the molecule structure that have higher sensitivity to shock can therefore lend themselves to detonation. Researchers have examined the surface of β-HMX crystallites and concluded that the presence of a layer of δ-HMX, which is highly sensitive, as well as the thickness of this layer, controls the bulk sensitivity of HMX (Surber 2007, Chen 2014, You 2015). Current techniques of spatially resolved defect characterization (transmission electron microscopy [TEM] dark field, Leeds) are destructive and cannot be applied to samples prior to shock experiments. Furthermore, these methods are restricted to very small length scale (nm), whereas characterization of samples prior to shock needs to extend to mm-scale or beyond. Characterization of voids and impurities in HE samples is presently restricted to sub-mm length scale and lacks correlation of impurity location with impurity phase identification. There is a need for nondestructive characterization techniques that cover the mesoscale (mm to µm) and microscale (µm to nm) to provide a way to understand the stress and temperature evolution upon shock loading.

PROJECT

A combination of x-ray radiographic and topographic techniques along with a highly spatially resolved structure analysis were used to map mesoscale and microscale structures and defects, such as voids and inclusions. These techniques use the high-energy micro-focused synchrotron beam line 16-IDB at the High Pressure Collaborative Access Team (HPCAT) within the Advanced Photon Source (APS) at Argonne National Laboratory. Available energies beyond 30 keV provide full transmission of the x-rays through samples of cm-scale thickness and radial extension.

Synchrotron x-ray radiography provides a 2-D electron density distribution over the entire sample thickness with micron-scale resolution, which can be applied to single-crystal, polycrystalline, and/or powdered samples. This method detects voids and cracks on the mesoscale as well as density differences in polycrystalline aggregates of single or multiple phases. The radiography map can be used to identify regions that could generate local temperature or stress excursion during shock.

The topography technique builds on recent Lang topography innovations to provide a fully 3-D quantitative assessment of defect structure, orientation, and induced strain in polycrystalline aggregates. Lang topography is a single-crystal diffraction-based technique of mapping defect location and density in solids, which probes variation in Bragg intensity as a function of local strain (Klapper 2000, Giacovazzo 2002). The Lang method shows the spatial distribution of crystal defects (point defects, dislocations, domain walls) through the strain that these defects induce in a particular crystal lattice plane. The sample is oriented such that the intensity of a selected Bragg reflection of a certain lattice plane is maximized on an x-ray–sensitive area detector. Defects deform the lattice plane and thereby tilt the plane slightly out of optimal Bragg diffraction conditions. Thus, at any location of a defect, the Bragg signal will be reduced. In the Lang approach, the Bragg intensity is mapped as a function of the location in a crystal, and thus the distribution of defects in the crystal becomes visible without damaging the crystal.

The radiography and topography techniques both benefit from the development of a software algorithm to speed up and automate the process to establish a method for routine sample characterization prior to shock experiments. The software will tie directly to the beam line for on-the-flight capture of images and be used for analysis post-beam line. This is a

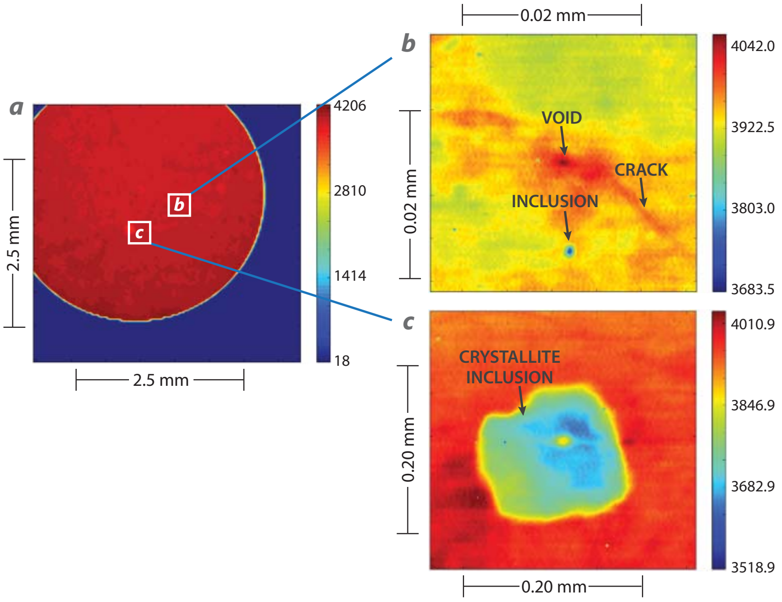

Figure 1. (a) Radiogram of an HE C4 sample (full view of sample surface); (b) radiogram of an HE C4 sample (close-up view showing a crack, void, and inclusion); and (c) radiogram of an HE C4 sample (close-up view showing an inclusion)

major advance toward developing diagnostics for understanding meso- and microscale effects during extreme dynamic compression and a usable preshock diagnostic tool.

Radiography and Topography of C4

Measurements of C4 samples were taken using radiography and Lang topography with the developed and tested compressed sensing software. Examination specifically focused on local structural changes to more sensitive forms of an HE component in the vicinity of defects. The samples under study were from three separate batches of C4 dated 2010, 2014, and 1976, the last being chosen due to its excellent detonation properties. The other two samples were considered to exhibit standard properties.

Individual samples were pressed into a ring and mounted onto a post. Each sample was approximately 3 mm in diameter and 0.5 thick. A camera system was used to test for tilt to ensure the sample was flat for the camera, which ensured the sample was normal with respect to the x-ray beam. The center of the sample was calculated to be centered on the beam. The post was then placed on a motorized stage. This provided a way to position the sample so images could be collected on the entire surface. The radiograms were collected with a beam of 0.3738 Å wavelength that was focused from 1 × 2 μm^2 to 2 × 4 μm^2 with a diode located behind the sample. Using x-ray absorption contrast, the sample could be centered on the single-axis goniometer to within a 3 to 4 micrometer circle of confusion over the angular range that was used.

The radiographic images, some of which are shown in Figure 1, are used to select regions of interest (ROIs) for performing topography. A radiogram of the sample is shown in red with the copper mounting ring shown in blue in Figure 1a. This looks like a fairly homogeneous sample until an ROI is magnified, as shown by Figures 1b and 1c. These magnified images show regions that have mesoscale defects such as voids, cracks, and inclusions. The micrometer resolution scans were collected using compressed sensing techniques, which provide sub-micrometer spatial resolution of density contrasts (voids, cracks, inclusions) and improves the efficiency of collection by a factor of 10 to 50 without compromising the spatial resolution. This provides a more time-efficient method for radiographic imaging, which allows much larger-sized samples to be characterized.

In comparison to conventional in-house Lang topography, the Lang method was significantly improved by (a) using fast x-ray area detectors with 2.4 ms readout time instead of conventional image plates and collecting Lang maps in time series rather than by correlated sample detector motion; (b) using a strongly focused, high-energy synchrotron x-ray beam instead of a collimated in-house x-ray source; and (c) developing software for fast processing of the time-series Lang maps. Our improvements have resulted in an increase of spatial resolution of Lang defect mapping by three orders of magnitude. We also, for the first time, saw crystallites as small as 50 μm in diameter and the first simultaneous Lang topographic mapping of several Bragg reflections, which allows determination of the Burgers vectors of dislocations. This ultimately leads to a reconstruction of the 3-D defect structure in a crystal, which is the next step of data analysis and will also be implemented in the software.

In the Lang topograms, dislocation kernels are marked by shifts of the phase factor or the Bragg intensity. The micro-focus hard x-rays are focused to 1 × 2 μm^2 at monochromatic x-ray energies typically between 30 and 40 keV. This technique provides a fully 3-D quantitative assessment of defect structure,

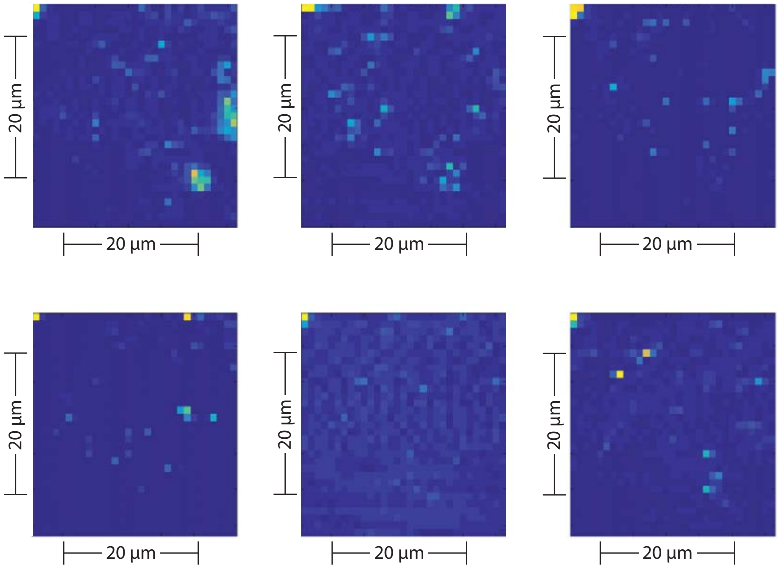

Figure 2. Topograms of ammonium nitrate showing dislocation kernels (pixel width = 2 µm)

orientation, and induced strain in polycrystalline aggregates. On-the-flight capture of frames were used with micron-sized frame rates that provided ~100 times higher spatial resolution than the conventional approach with detector translation. The topogram of ammonium nitrate in Figure 2 shows these dislocation kernels (bright spots), providing an indication for dislocation correlation. These topograms will be collected for the HE materials in FY 2018, the third year of the project. Once radiography is used to find ROIs, single-crystal x-ray diffraction (XRD) is used to index the crystal. The peak intensity can point to the direction of defects, then the Lang topograms are collected on specific crystal locations and translated across the crystal to determine changes in the intensity or strain. The intensity can be correlated to the strain quantitatively, identifying the location and orientation of the dislocations by phase-factor shifts. The crystal orientation and structural species present can be determined with Lang topography, which shows intrinsic defects, impurity phases, and strain (obtained from crystal lattice deformation).

Figure 3 shows an analysis on one of the C4 samples; the strain evolution across the crystal is shown in the top five images. In this particular sample, the technique allows for the identification of the phases present: β-HMX, γ-RDX, and γ-HMX. The developed software will be used to automate this process and point out the changes that exist in the crystal. It will also be used for obtaining the defect location and orientation from the Lang topograms. Each topogram is just one crystal, so the software is needed and used to collect a large amount of data on every crystal in the sample.

Figure 4 shows the user interface of the software (written in Python 2.7) and can be used to construct topograms from single-crystal diffraction patterns.

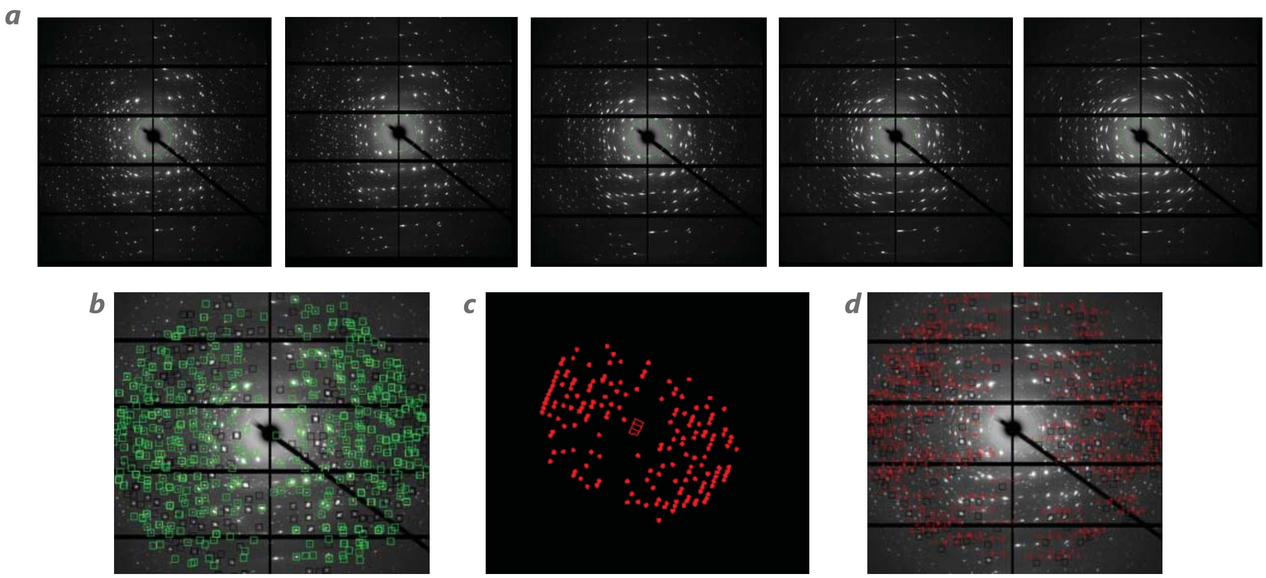

Figure 3. Diffraction patterns of an HE C4 sample using GSE ADA/RSV software (Przemyslaw 2013); (a) collected along a trajectory from center to border of an RDX crystallite, (b) pattern with indexed reflections, (c) reciprocal space projection, and (d) selected reflections

The software can be used after data are collected at the APS beam line, or it can be tied to the beam line directly to collect data of interest. An executable for the software, being written to work easily with the beam line, can function cross-platform (Windows, Mac, Linux). Current features of the software include import of beam line experiment log file, peak selection and centroid fitting, peak list for topogram creation, mapping of integrated peak areas across all diffraction patterns, and a separate topogram plotting window coded to allow independent viewing of selected Bragg reflections and created topograms.

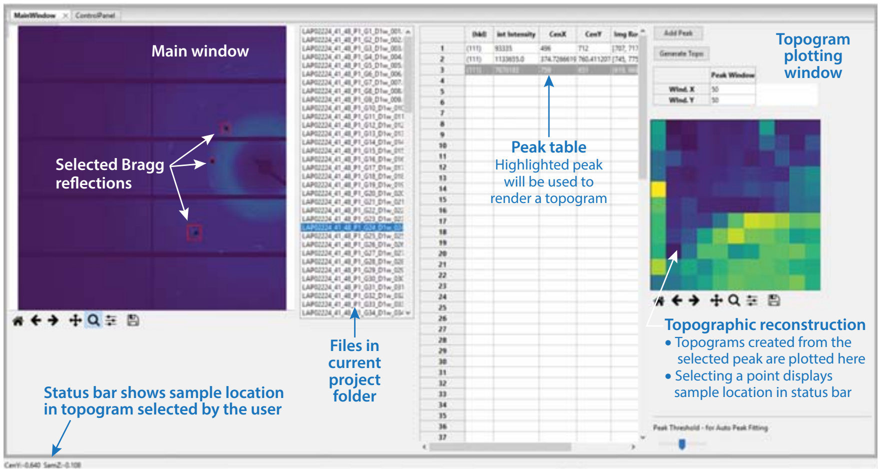
Main window

Selected Bragg reflections

Peak table
Highlighted peak will be used to render a topogram

Topogram plotting window

Topographic reconstruction
- Topograms created from the selected peak are plotted here
- Selecting a point displays sample location in status bar

Files in current project folder

Status bar shows sample location in topogram selected by the user

Figure 4. Lang topography code user interface

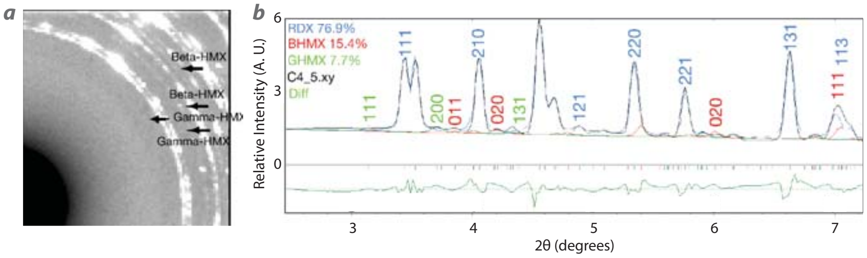

Figure 5. C4 “excellent performance” sample (a) x-ray diffraction and corresponding (b) integrated pattern showing the correlation between raw data (C4_5.xy) and models of RDX and HMX

Three samples of C4 were analyzed by radiography and topography techniques, as described above. Two of the samples were of standard detonation, and one performed excellently. The C4 with excellent performance was shown to be of much finer grain size than the others, with no γ-RDX crystals beyond a few microns. We analyzed the XRD pattern to assess impurities and conformational disorder, which presented locations of β-HMX and γ-HMX, as shown in Figure 5. The integrated pattern shows a fairly good fit; the experimental data in black, and the corresponding models are shown in colors for RDX (blue), β-HMX (red), and γ-HMX (green). However, the powder diffraction intensities were not sufficiently smooth for a rigorous fitting of peak intensities by structure modeling and subsequent refinement. It is likely that γ-RDX exhibits rotational disorder of nitro-groups, but we cannot exclude a lesser degree of saddle-crown shape conformational disorder, although this implies a marked increase in internal energy. In Figure 6, an integrated pattern is shown where α-HMX and β-HMX are present with a disordered RDX, which indicates conformational disorder. Research is continuing to determine if this is indeed the case by using single-crystal structure analysis approaches rather than powder diffraction methods.

Diffraction patterns of PETN showed a homogeneous film of crystallites with an average grain size of <1 µm. We examined the diffraction patterns by Rietveld refinement and observed a modest preferred orientation along [102]

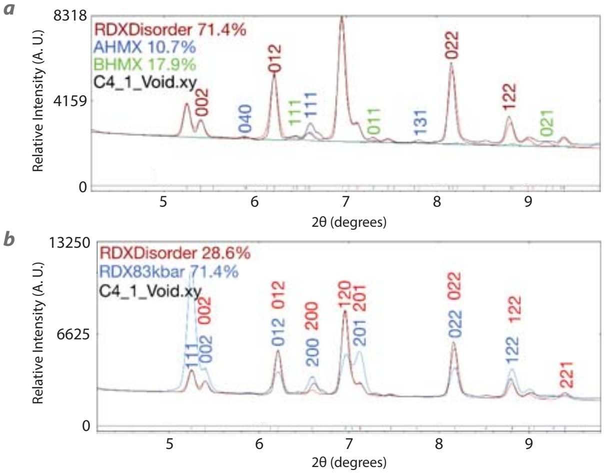

Figure 6. Integrated patterns for C4 “standard performance” sample showing the correlation between raw data (C4_1_Void.xy) and models of (a) disordered RDX and HMX and (b) disordered RDX vs. non-disordered RDX

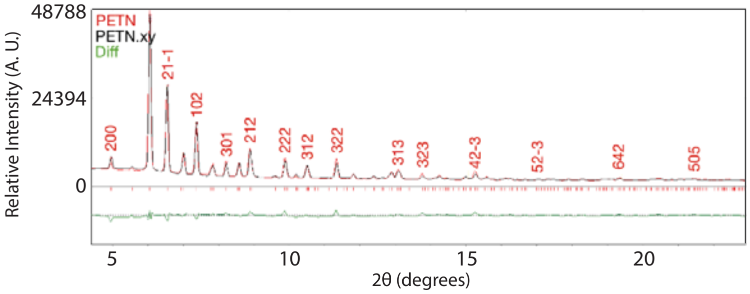

Figure 7. Integrated pattern (red line is calculated pattern) for PETN showing that the raw data (PETN.xy) correlates well to the PETN model

and rotational disorder of nitro-groups (about 7% to 13% of oxygen atoms 1 and 2 are rotated along the C-N bond axis). The refinement converged to an RWP of 7.15 (the deviation between the calculated and observed values). Figure 7 shows the integrated pattern.

Shock-Recovery of High-Pressure Bismuth Phases

Bismuth (Bi) is a non-HE material that can assist in the understanding of the stress and temperature evolution upon shock loading, and we continued to analyze it this year. Bismuth was selected, in part, because it has five different phases between 0 and 10 GPa. The complex phase diagram of Bi helps provide constraints on pressure and temperature conditions reached based on the melting and structures present.

Shock compression experiments were performed at the University of Nevada, Las Vegas shock lab, and the samples were analyzed using radiography, XRD, scanning electron microscopy (SEM), and electron backscatter diffraction (EBSD) to identify the phases present in the shocked samples. Samples were prepared with voids expected to reach local high temperatures up to three times greater than the bulk temperatures. Shock-induced melting was identified using SEM, after which EBSD and secondary electron techniques were used to examine the sample topography on a sub-micron scale, as well as examine regions of possible transformation of Bi to high-pressure phases through increased electron density. XRD at APS showed strong indicators of Bi-II on the shocked sample. Figure 8 shows the Bi sample and the four techniques used to analyze it.

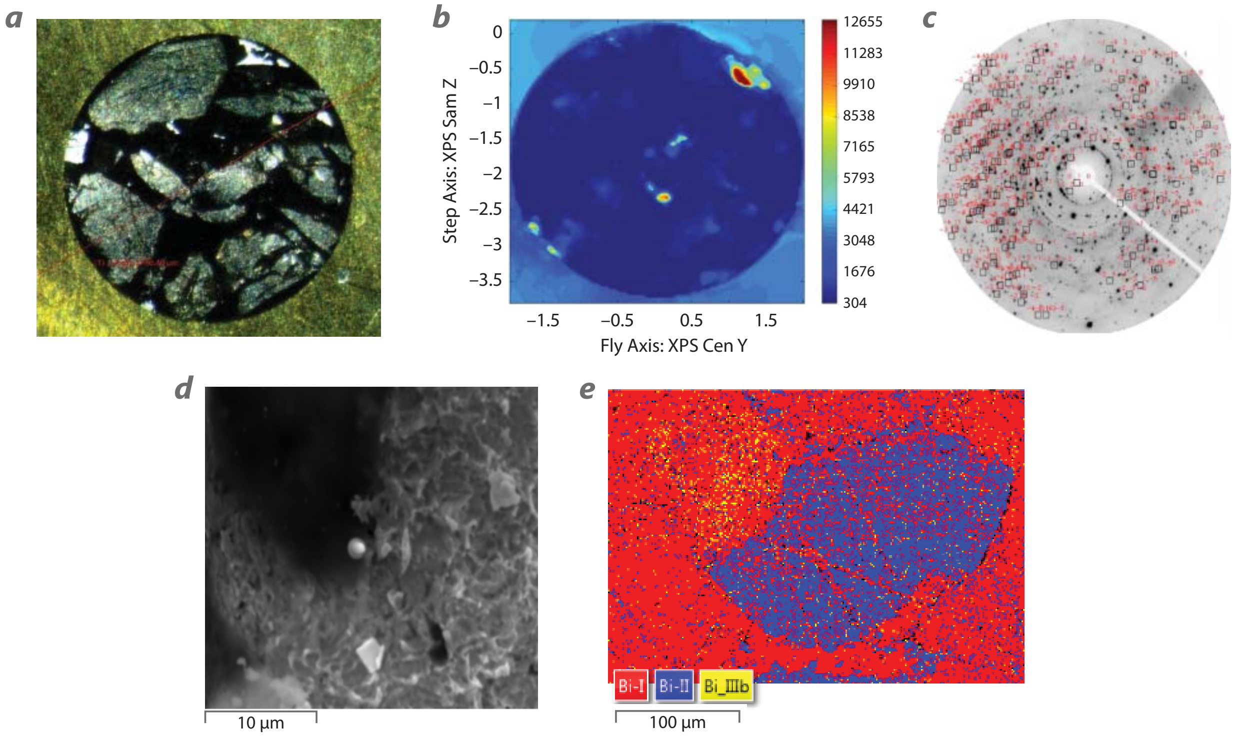

Figure 8. (a) Bismuth polycrystalline sample loaded into brass ring, (b) x-ray radiogram, (c) XRD from APS, (d) SEM image with void, and (e) EBSD map

CONCLUSION

The main result of this work is an advancement in the creation of nondestructive 3-D characterization of defects and crystal orientation of polycrystalline and heterogeneous materials that is performed prior to shock experiments. Several HE materials were analyzed using the techniques of radiography, Lang topography, and micro-diffraction mapping using the software developed over the course of the project. Bismuth samples were studied to advance knowledge and understanding of the stress and temperature evolution upon shock loading.

By analyzing C4 samples, it was shown that the main component, γ-RDX, exhibited conformational disorder and applies to the fine-grained fraction (i.e., weak zones such as those along cracks). The insensitive β-HMX, which is the minor component in C4, is evident, as is the more sensitive α-HMX. The end result is that fine-grained and coarse-grained RDX is resolved on the 10–100 micron scale and sub-micron scale, respectively. The analyzed PETN films are fine grained, homogeneous, and showed some preferred orientation as well as modest rotational disorder of nitro-groups.

ACKNOWLEDGMENTS

We would like to thank Jesse Smith (Advanced Photon Source), Robert Hixson (NNSS), Stuart Baker (NNSS), Edward Daykin (NNSS), Adam Iverson (NNSS), Doug Clark (NNSS), Timothy Rearich (NNSS), Darrin Valentine (NNSS), Mark Knickerboker (NNSS), and Rick Gustavsen (LANL) for their contributions to this work. Portions of this work were performed at HPCAT (Sector 16), Advanced Photon Source (APS), Argonne National Laboratory. Operations support of HPCAT from DOE-NNSA under Award No. DE-NA0001974 and DOE-BES under award No. DE-FG02-99ER45775, with partial instrumentation funding by the National Science Foundation. The Advanced Photon Source is operated for the DOE Office of Science by Argonne National Laboratory under contract No. DE-AC02-06CH11357. HiPSEC support for the project was provided from the Department of Energy through Cooperative Agreement DE-NA-0001982.

REFERENCES

Cawkwell, M. J., T. D. Sewell, L. Zheng, D. L. Thompson, “Shock-induced shear bands in an energetic molecular crystal: Application of shock-front absorbing boundary conditions to molecular dynamics simulations,” *Phys. Rev. B* **78** (2008) 014107.

Chen, M.-W., S. You, K. S. Suslick, D. D. Dlott, “Hot spots in energetic materials generated by infrared and ultrasound, detected by thermal imaging microscopy,” *Rev. Sci. Instrum.* **85**, 2 (2014) 023705.

Giacovazzo, C., H. L. Monaco, G. Artioli, D. Viterbo, F. Ferraris, G. Gilli, G. Zanotti, M. Catti, *Fundamentals of Crystallography*, 2nd edition, Oxford University Press, New York, 2002, 793; 799–801.

Klapper, H., “Generation and propagation of dislocations during crystal growth,” *Mater. Chem. Phys.* **66**, 2–3 (2000) 101–109.

Kuklja, M. M., “Quantum-chemical modeling of energetic materials: Chemical reactions triggered by defects, deformations, and electronic excitations,” in *Advances in Quantum Chemistry*, J. R. Sabin, E. Brändas, eds., Academic Press, Cambridge, Massachusetts, 2014, 71–146.

Przemyslaw, D., K. Zhuravlev, V. Prakapenka, M. L. Rivers, G. J. Finkelstein, O. Grubor-Urosevic, O. Tschauner, S. M. Clark, R. T. Downs, “High pressure single-crystal micro X-ray diffraction analysis with GSE ADA/RSV software,” *High Pressure Research* **33**, 3 (2013) 466–484.

Surber, E., A. Lozano, A. Lagutchev, H. Kim, D. D. Dlott, “Surface nonlinear vibrational spectroscopy of energetic materials: HMX,” *J. Phys. Chem. C* **111**, 5 (2007) 2235–2241.

Tsyshevsky, R., O. Sharia, M. Kuklja, “Molecular theory of detonation initiation: Insight from first principles modeling of the decomposition mechanisms of organic nitro energetic materials,” *Molecules* **21**, 2 (2016) 236.

You, S., M.-W. Chen, D. D. Dlott, K. S. Suslick, “Ultrasonic hammer produces hot spots in solids,” *Nat. Comm.* **6** (2015).

This page left blank intentionally

Systematic Studies in Dynamic Material Response – Early-Career Postdoctoral Research

LAO-065-16 ■ Year 2 of 2

Sarah Thomas[1,a] and Robert S. Hixson[a]

[1]thomassa@nv.doe.gov, (505) 663-2068
[a]New Mexico Operations–Los Alamos

In our FY 2017 research, we chose to examine wave speeds in copper (equation of state), strength in aluminum (compressive strength), and spall in iron (tensile failure). Our "top hat" method for measuring wave speeds was refined from previous years, and we gathered quality data on wave speeds in copper using this technique. We also took strides to improve our strength measurement techniques, which show promise for the future, although no quality results were obtained this year. Finally, our work on spall in iron provided quality data that we were able to include in a manuscript, to be submitted for publication in early 2018.

BACKGROUND

Weapons physics requires good input physics models to inform computer simulations of dynamic events. Computer simulations are used for the stockpile stewardship program. Many material properties used in simulations need improvement. More work is warranted to improve fundamental input physics models for large-scale hydrodynamic codes, which would thus improve prediction capabilities for integrated experiments that require better diagnostic methods, new experimental techniques, and a great deal more fundamental data.

The research we conducted this year directly addresses dynamic material properties issues that are called out in the *NNSS R&D Technology Needs Assessment*. It supports a fundamental understanding of dynamic material properties relevant to the NNSA mission and enhances development of robust physics models. Improving our ability to do high-fidelity simulations of dynamic events is a long-term goal of the national laboratories and the NNSA, and this work directly contributes to that goal. Data obtained on how materials yield in both compression and tension, shock wave velocities, and on the dislocation dynamics of materials as they yield, will allow more robust equations of state (EOS) to be developed.

Work carried out in FY 2016 paved the way for work done this year. We began development of our "top hat" wave speed measurement technique, a joint effort in cooperation with the "Enhanced Dynamic Materials Research" strategic initiative SDRD (Hixson 2016;

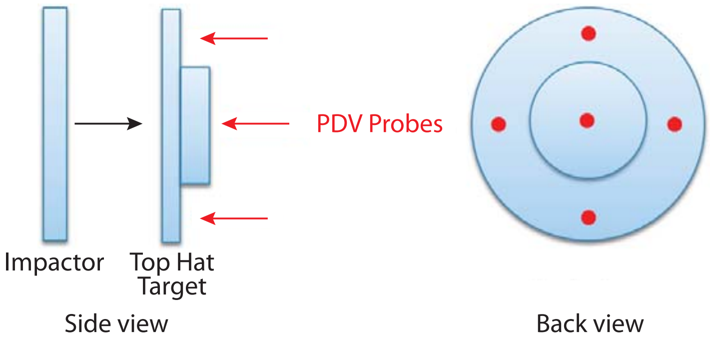

Figure 1. Geometry of copper wave speed experiments

La Lone 2017, 2018). We also measured spall in polycrystalline copper, which supplemented the body of data we have put together on both polycrystalline and single-crystal copper. We also began work to measure the strength of materials using reverse ballistic shot geometries, which we continued this year (Thomas 2017a).

PROJECT

Over the course of the project this year, we conducted three experiments: wave speed in polycrystalline and single-crystal [110] copper, strength of aluminum, and low-stress wave speeds and spall in iron. This research complements similar work being done in the strategic initiative SDRD project "Enhanced Dynamic Materials Research" (Hixson 2016; La Lone 2017, 2018) and at Sandia National Laboratories for the Z-materials project. Each experiment and its results are discussed in the following sections.

Copper Wave Speeds

While the EOS for copper has been fairly well studied, wave speeds at low stress are not as well known. Systematic errors may be present in the data presented in the Marsh (1980) compendium, the standard manuscript in the community, due to the use of the flash gap method when collecting the data. We undertook experiments to measure wave speeds in polycrystalline and single-crystal [110] copper at low pressures. As shown in Figure 1, a copper flyer plate impacted the base of a copper "top hat." The polycrystalline top hat was cut from a single piece of material. However, the single-crystal top hat was made from two crystals, the smaller diameter piece glued to the center of the larger diameter piece. We then used five channels of photonic Doppler velocimetry (PDV), four around the brim, and one in the center of the top, to measure the free surface velocity at these points.

Data from the four channels around the brim helped us determine the time that the elastic and plastic waves entered the base of the top part of the top hat. The center probe recorded the times the elastic and plastic waves exited the back of the top hat. The five channels of PDV allowed accurate cross timing. Using timing data and thickness parameters of the top part of the top hat, we determined the speeds of the elastic and plastic waves. The wave profile in Figure 2 shows elastic and plastic waves labeled as E1 and P1.

Having measured elastic wave speed, we compared it to the measured longitudinal sound speed of the material and found it to be in very good agreement, lending credence to our subsequent shock speed measurements. We calculated the elastic wave speed (u_s) by recording the time the elastic wave entered the top section of the top (the same as the time the wave exited the back of the brim) and subtracted from it the time it exited the top, then divided the time difference by the top thickness. A similar calculation determined the plastic shock speed, as seen in Figure 3.

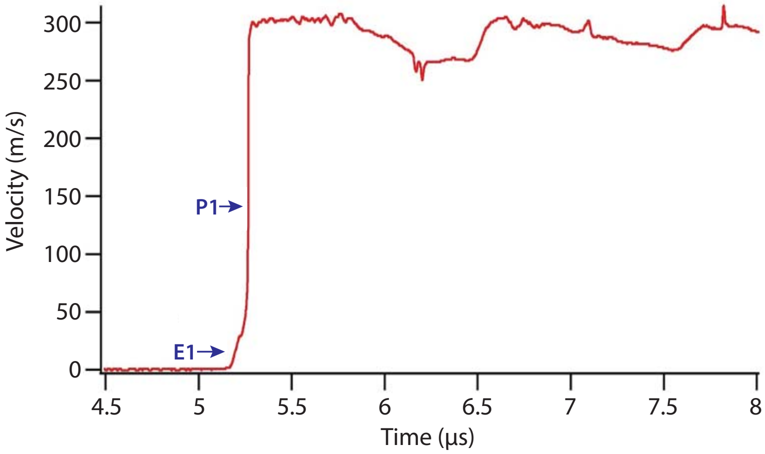

Figure 2. Wave profile extracted from PDV data taken at the brim of the target

Values for shock speed vs. particle speed are plotted in Figure 4 along with data taken from the Marsh compendium and data from FY 2016. We believe the error in these data is about 1%, though further error analysis is necessary. As seen in Figure 4, both the polycrystalline and single-crystal data agree within likely error with the Marsh data and our last year's

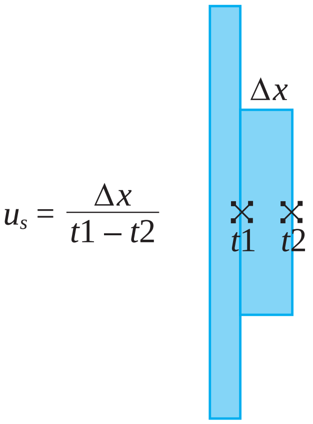

Figure 3. Calculation diagram of copper wave speed experiments

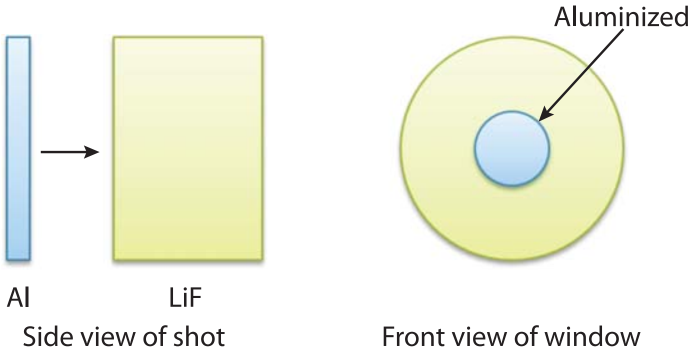

Figure 5. Geometry of aluminum front surface impact experiments

data. We tested the single-crystal orientation [110], the orientation with the least deviation in wave speeds from polycrystalline copper. It may be that completing the same measurements on [100] or [111] single-crystal copper would give different results, and this is something that should be explored further.

Dislocation Dynamics/Strength of Aluminum

Previous work by Winey et al. (2009) has shown that elastic wave evolution in aluminum alloys is different for 1050 Al compared to 6061-T6 Al; primarily the Hugoniot elastic limit (HEL) wave becomes steady more quickly in 6061-T6 AL. Because the evolution of plasticity in ductile metals such as Al is controlled by dislocation processes, this might imply that 6061-T6 has much faster dislocation dynamic processes than does 1050 Al. We chose to do front surface impact shots to look at the precursor decay directly. Because of the difficulty in acquiring 1050 Al, we instead chose to look at 1100 Al, which is still very pure.

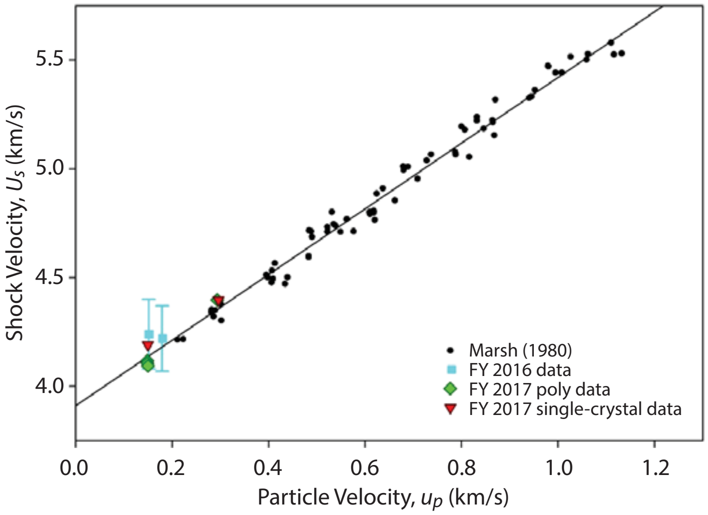

Figure 4. Copper shock Hugoniot EOS plot shows good agreement among the Marsh data (1980) and data we collected in FY 2016 and FY 2017 for polycrystalline and single-crystal copper

Figure 5 shows the geometry of the aluminum shots carried out in FY 2016, which was done in the so-called "front surface impact" geometry. An aluminum flyer plate strikes the front surface of a LiF window that has an aluminized face. A piezoelectric pin triggered the diagnostics. One collimating PDV probe looked down the barrel of the launcher to measure projectile velocity. Another dual-fiber probe looked through the ~19 mm thick LiF window at the back of the very thin aluminized layer on the impact surface. Data from these shots was expected to give a sharp increase in velocity as the impactor hit the target, with the initial velocity overshooting the steady state, and then relaxing into the steady state. This precursor decay would give information on the dislocation dynamic process times. The data collected from those shots were very noisy, which we attributed to both the large thickness of the window (19 mm) and the window material (LiF). This year we altered both the window's thickness and material to learn if these were indeed causing the noise. Z-cut quartz windows 6.5 mm thick were used in follow-up shots; but again, large amounts of noise occurred, as can be seen in Figure 6.

With the noise level the same, we turned our attention to the aluminized layer on the surface of the window; we thought it might be breaking up on impact due to imperfections in the impactor surface. We diamond-turned

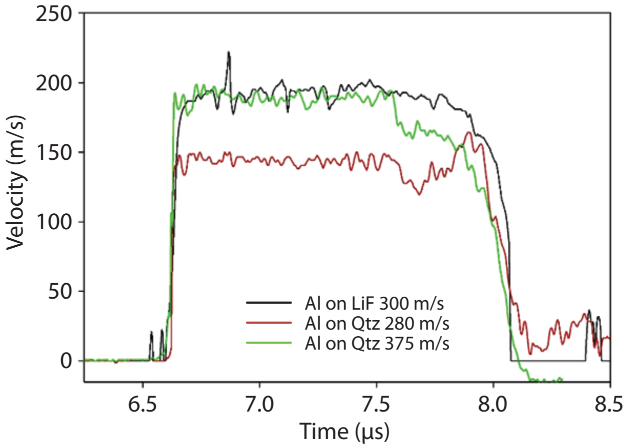

Figure 6. Wave profiles of front surface impact aluminum shots from FY 2016 (black) and FY 2017 (green and red) show that noise levels were not reduced by changing window thickness or material

the impactor surface and redid shots with and without an aluminized layer on the surface of the window. Our results were much improved on both shots (with and without aluminized layer as seen in Figure 7, respectively), proving that diamond-turning the surface of the impactor is critical to the success of these shots.

Unfortunately, we were still unable to see the precursor decay, even with improved signal-to-noise ratio, possibly due to either the signal not being very large (because of the relatively small HEL), or because the decay happened too fast to detect. It would be interesting to repeat this experiment with a different material of interest, for instance steel or tungsten, which both have larger HELs.

Spall in Iron

Tensile failure, or spall, in a material is governed by a number of factors—strain rate, peak stress, dislocation dynamics, and others. Tensile failure is an important and little-understood factor in fundamental physics models. In particular, iron is of interest because it undergoes a phase transition from alpha to epsilon at 130 kbar. Understanding the difference in spall behavior between the two phases is lacking. We began a study of spall in the alpha-phase of iron, with a view to examine epsilon-phase behavior in the future.

Figure 8 shows the experimental setup for the iron spall experiments. A symmetric impact (target and impactor of the same material) was generated in which the impactor was half the thickness of the target. With these dimensions, the spall plane forms in the center of the target. A single two-fiber PDV probe measured the free surface velocity at the center of the rear side of the target. A collimating PDV probe, glued into a hole in the target holder and looking at the oncoming projectile, measured impact velocity. Four shorting pins were set at opposition around the target in the target plate to measure tilt.

We executed three shots, one each at nominal velocities of 200, 300, and 400 m/s. The resulting wave profiles are shown in Figure 9.

Each profile holds information about a number of properties of the material. From the elastic wave, we were able to calculate the HEL, or compressive strength of the material (~9 kbar). The spall signature gave tensile or spall strength (~19 kbar). The period of ringing in the spall scab gives the scab thickness. And from the elastic and plastic waves, we were able

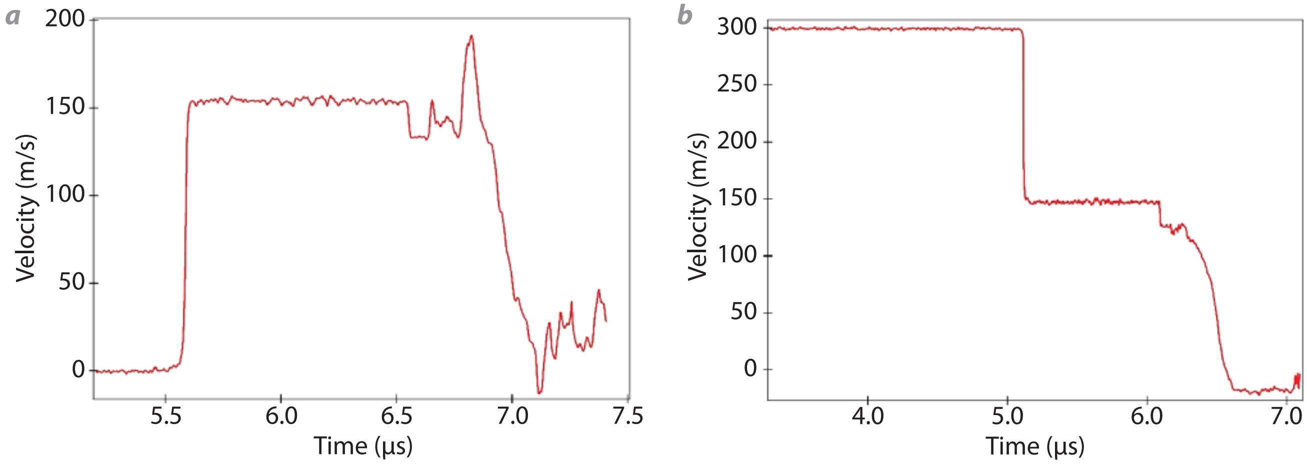

Figure 7. Wave profiles of diamond-turned aluminum on Z-quartz window (a) with and (b) without an aluminized surface

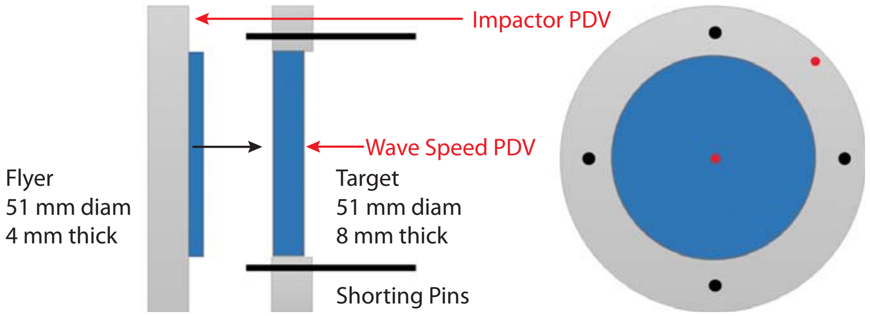

Figure 8. Iron spall experiment diagram

to determine the shock speed. All of this information complements other work done on various types of steel alloys. Combining our iron spall data with previous data on steel, we could plot the shock Hugoniot of the alpha-phase of iron and steel (Figure 10).

The data are shown in red in Figure 10. While there has not been much research into the alpha-phase shock Hugoniot of iron, work by Barker (1974, 1975) gives the equation for the alpha-phase Hugoniot as $U_s = 4.63 + 1.33\ u_p$. Our calculation was a bit different at $U_s = 4.53 + 1.38\ u_p$. Both are significantly different from the epsilon-phase Hugoniot, which is $U_s = 3.935 + 1.578\ u_p$; this shows that a distinction between the phases must be made in hydrodynamic codes that attempt to simulate iron behavior.

This work will be advanced by making more precise, accurate measurements of the shock Hugoniot of iron and steel in the alpha-phase. These measurements will be done using the technique we developed and described for copper wave speed experiments. We also plan to measure spall in the epsilon-phase, which will require a faster launcher.

CONCLUSION

Building on similar studies in FY 2016, in FY 2017, we studied copper wave speed, strength in aluminum, and iron spall. Our new method (developed under Brandon La Lone's strategic SDRD, Hixson 2016; La Lone 2017, 2018) for making low-pressure shock Hugoniot measurements has been improved over the course of this SDRD, and will be used in future work on other materials. Our work on spall in iron provided quality data that have been drafted into a submission to the *Journal of Applied Physics* for consideration for publication (Thomas 2017b).

The copper studies added to our body of work on polycrystalline and single-crystal copper wave speeds and spall. We have also refined our method of measuring the strength of materials. While we did not see the dislocation dynamics unfold in aluminum, we believe our improved technique holds promise for

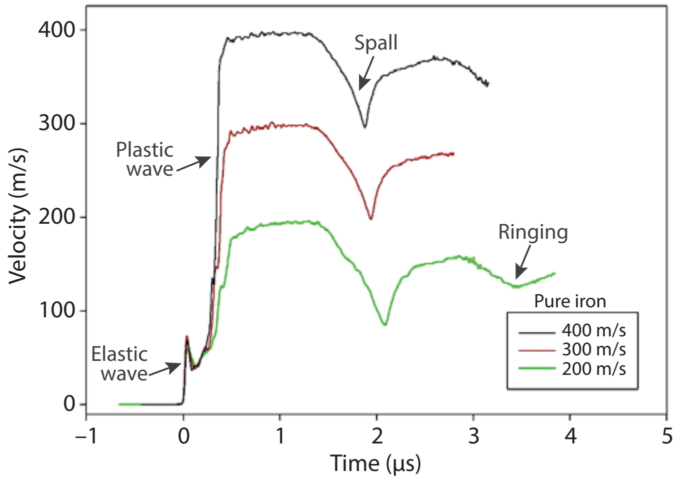

Figure 9. Iron spall wave profiles

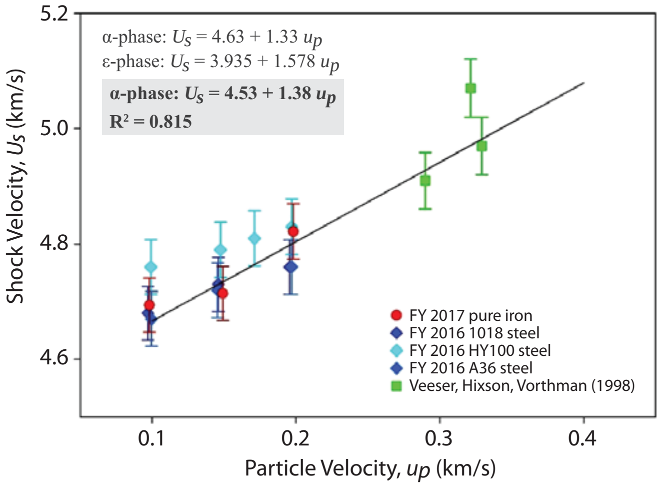

Figure 10. Alpha-phase shock Hugoniot of iron and steel

other materials. Iron spall measurements done this year complement work on steel also carried out this year, all suggesting a slightly different alpha-phase shock Hugoniot than the accepted value. Further study of spall and wave speeds in the epsilon-phase of iron would be of use to the shock physics community.

ACKNOWLEDGMENTS

We would like to thank Jeff Cates, Ed Daykin, Tom Graves, Mike Grover, Cameron Hawkins, Russ Howe, Melissa Matthes, Carlos Perez, Jason Scharff, Jerry Stevens, Dale Turley, Ben Valencia, and Lynn Veeser for their contributions to this work.

REFERENCES

Barker, L. M., R. E. Hollenbach, “Shock wave study of the α ⇄ ε phase transition in iron,” *J. Appl. Phys.* **45** (1974) 4872.

Barker, L. M., “α-phase Hugoniot of iron,” *J. Appl. Phys.* **46** (1975) 2544.

Hixson, R. S., B. La Lone, G. D. Stevens, D. Turley, L. R. Veeser, “Enhanced dynamic materials research,” in *Site-Directed Research and Development*, FY 2015, National Security Technologies, LLC, Las Vegas, Nevada, 2016, 15–29.

La Lone, B., G. D. Stevens, D. Turley, L. R. Veeser, R. S. Hixson, “Enhanced dynamic materials research,” in *Site-Directed Research and Development*, FY 2016, National Security Technologies, LLC, Las Vegas, Nevada, 2017, 1–9.

La Lone, B., “Enhanced dynamic materials research,” in *Site-Directed Research and Development*, FY 2017, National Security Technologies, LLC, and Mission Support and Test Services, LLC, Las Vegas, Nevada, 2018, 1–8.

Marsh, S. P., *LASL Shock Hugoniot Data*, University of California Press, Berkeley, California, 1980.

Thomas, S. A., R. S. Hixson, “Systematic studies in dynamic material response – Early-career postdoctoral research,” in *Site-Directed Research and Development*, FY 2016, National Security Technologies, LLC, Las Vegas, Nevada, 2017a, 53–58.

Thomas, S. A., M. C. Hawkins, M. K. Matthes, G. T. Grey III, R. S. Hixson, “Dynamic strength properties and alpha-phase shock Hugoniot of iron and steel,” 2017b, submitted to *J. Appl. Phys.*, 2017.

Veeser, L. R., R. S. Hixson, J. E. Vorthman, unpublished data gathered at LANL, 1998.

Winey, J. M., B. M. La Lone, P. B. Trivedi, Y. M. Gupta, “Elastic wave amplitudes in shock-compressed thin polycrystalline aluminum samples,” *J. Appl. Phys.* **106** (2009) 073508.

Dynamic Measurement of Chemical Composition and Chemical Reaction with Surrounding Gas of Shock Wave–Generated Ejecta Particles

STL-011-17 ■ Continuing in FY 2018 ■ Year 1 of 2

Dale Turley,[1,a] Jason Mance,[a] Gene Capelle,[a]
Brandon La Lone,[a] Mike Grover,[a] and Ruben J. Valencia[a]

[1]turleywd@nv.doe.gov, (805) 681-2239
[a]Special Technologies Laboratory

The goal of this work is to dynamically determine the content of a shock wave–generated ejecta cloud as well as observe chemical reactions of ejecta with a surrounding gas. This year we have demonstrated the use of laser-induced breakdown spectroscopy as a diagnostic for measuring the atomic content of an ejecta cloud composed of pewter (a mixture of tin, copper and antimony). Spectra observed with ejecta were not consistent with spectra taken statically in the solid pewter sample prior to detonation. Ejecta spectra showed no evidence of the presence of antimony and reduced contributions from copper. Further work in FY 2018 will be done to examine whether this disagreement reflects a change in the composition of the ejecta compared to that of the bulk metal. Additionally, in FY 2018 we plan to study chemical reactions of ejecta in deuterium gas by measuring the temperature of the gas using coherent anti-Stokes Raman spectroscopy.

BACKGROUND

Determining ejecta contributions to weapons performance remains a priority to the weapons community. Prior studies have not considered the effect of ejecta composition and chemical reaction on the transport of ejecta in pressurized gases. Nuclear weapon simulations (specifically transport models) can be limited if there is uncertainty in the material composition of the ejecta cloud. The primary goals of this work are to develop diagnostics to determine ejecta composition and to apply these techniques in dynamic experiments to further the understanding of ejecta interactions with gases.

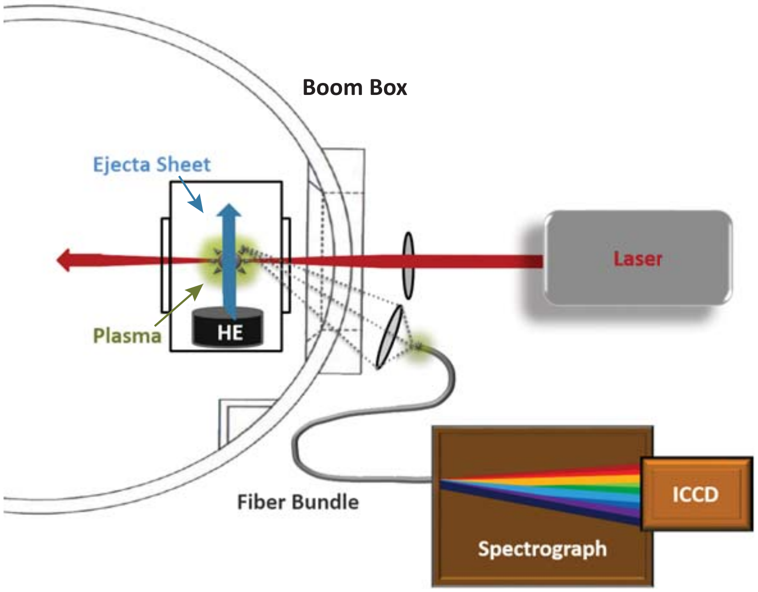

Figure 1. LIBS measurement experimental setup at the Special Technologies Laboratory Boom Box

PROJECT

In FY 2017 good progress was made in the development of the laser-induced breakdown spectroscopy (LIBS) and coherent anti-Stokes Raman spectroscopy (CARS) diagnostics. A CARS optical system was developed and tested statically in a hydrogen gas cell. In FY 2018 this system will be used to field CARS in a dynamic ejecta experiment. Also, in FY 2017 a LIBS system was assembled and used in both static and dynamic experiments to test the feasibility of this method as a diagnostic for measuring the atomic composition of an ejecta cloud.

LIBS

In a LIBS measurement, a laser beam is focused on a target material with sufficient energy to break down the target and create a plasma. As the plasma cools, the free electrons recombine with the atoms and emit photons with energies characteristic of the element. The elemental content of the material can be determined by measuring the spectrum of the light emitted from the plasma. A diagram of the LIBS ejecta experiment is shown in Figure 1. The laser outputs a single 10 ns long pulse with a wavelength of 1064 nm and energy of 80 mJ, which is focused onto the sheet of ejecta. The LIBS emission is then imaged out to a fiber bundle that is coupled to a spectrometer, and the spectrum is measured with an intensified CCD (ICCD) camera.

It was necessary to develop a package to hold the target and high explosives (HE) that would also allow optical access for diagnostics. The package design, shown in Figure 2, was developed in collaboration with our Los Alamos National Laboratory colleagues and optimized to create and observe ejecta using a variety of diagnostic techniques, namely x-ray radiography, piezo electric pins, photonic Doppler velocimetry (PDV), and framing camera imaging. The target, pewter in this case, is created by polishing a thin disk then cutting a 3 mm wide strip of triangular grooves into the material. Each groove, spaced apart by 100 µm, has a peak-to-valley depth of 24 µm. This groove pattern mimics prior dynamic ejecta experiments in order to produce a predictable ejecta quantity (Zellner 2007). HE are mounted under the disk and detonated to create a shock

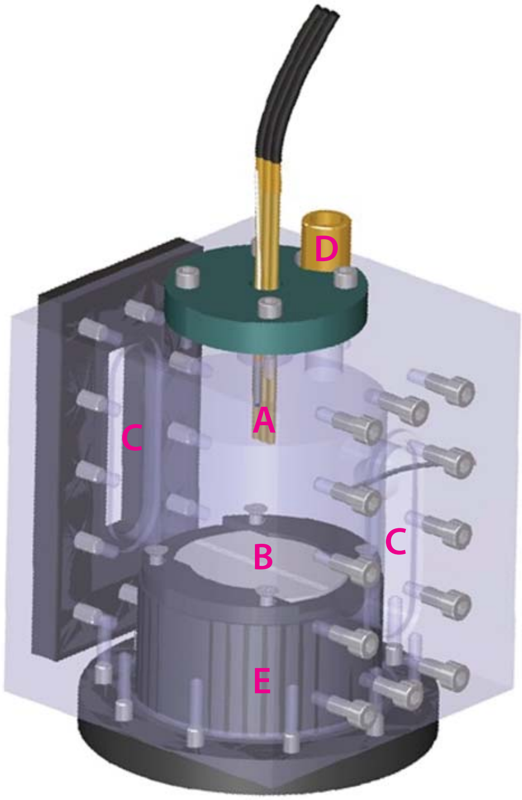

Figure 2. Package design for ejecta experiments showing (A) diagnostic feedthroughs for PDV, (B) the pewter disk with grooves cut for creating ejecta, (C) windows for laser access and spectral acquisition, (D) gas tube for pulling vacuum, and (E) a housing for placing HE under the pewter disk

wave that launches ejecta particles from the apex of the grooves at around two times the speed of the metal surface. We chose pewter as the material for composition measurements because it contains three metals of various percentages (92% tin [Sn], 7.5% antimony [Sb], and 0.5% copper [Cu]) and is composed primarily of Sn, which is known to create ejecta. Two design considerations were the transit time for the shock waves to reach the windows and containment of explosive burn products, both of which can obstruct the field of view required for optical measurements.

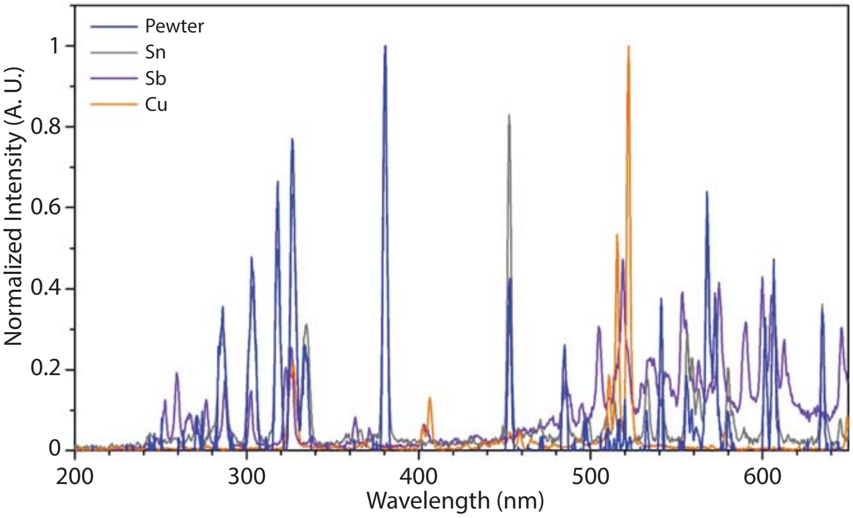

Figure 3. LIBS spectra in pure samples of Sb, Sn, Cu, and the pewter alloy (92% Sn, 7.5% Sb, 0.5% Cu)

Spectral Properties of the LIBS Signal

The LIBS signal was initially studied in a static environment in order to determine the appropriate timing and spectral resolution required to observe each of the three metal constituents in pewter. First, LIBS spectra were gathered from pure samples of Sb, Sn, and Cu and compared to spectra in pewter. The resulting spectra, shown in Figure 3, facilitated the identification of spectral regions where strong lines from each of the three components were present and distinguishable from other lines in the pewter LIBS spectrum.

Next it was necessary to obtain higher-resolution spectra in order to completely resolve the individual lines. This was accomplished by switching from the 150 groove/mm spectrometer grating, used to take the data in Figure 3, to a 2400 grooves/mm grating. But the corresponding increase in resolution demands a smaller spectral window. Several spectral windows were investigated, and a window centered at 522 nm was eventually chosen. Further LIBS data was taken in this region on pure samples and in pewter, and assignments of the lines in the pewter spectra were determined. The spectra and line assignments are shown in Figure 4. Note that some of the lines are second-order reflections off of the spectrometer grating. Second order lines were identified by taking spectra with a UV-blocking filter in place and observing which lines disappeared. Remarkably, the ratios of the line intensities in the pure metal spectra are consistent with those in the pewter spectra, indicating that the LIBS spectra in the pewter alloy are well approximated by the sum of the LIBS spectra of the pure constituents. All line assignments were cross-checked and are in agreement with those reported in the literature.

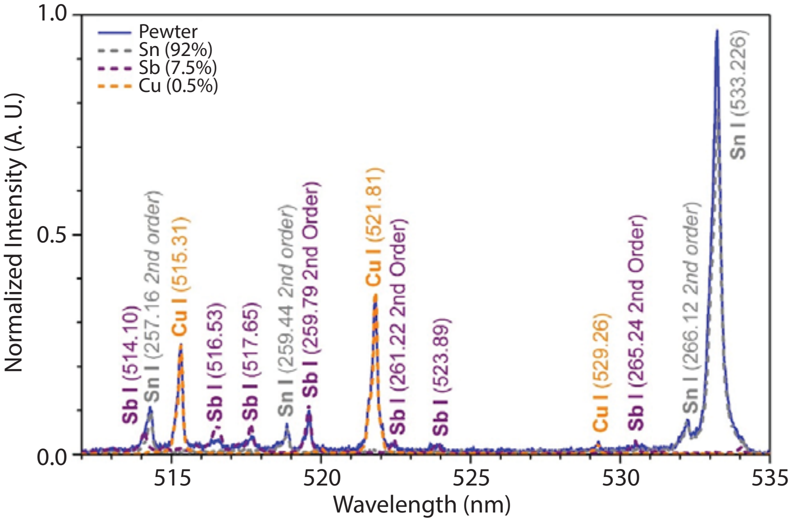

Figure 4. Static LIBS spectra and line assignments in the spectral region determined appropriate for carrying out dynamic ejecta measurements

Temporal Dynamics of the LIBS Signal

The temporal evolution of the LIBS signal was studied in order to determine the appropriate delay and integration times for the dynamic ejecta experiments. Figure 5 shows a time-

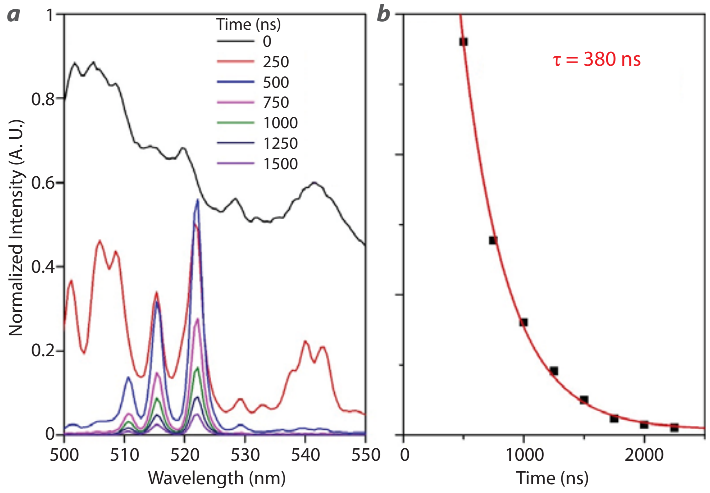

Figure 5. (a) Temporal evolution of the LIBS spectra of Cu at 250 ns intervals and (b) a fit to the intensity of the peak near 522 nm, indicating a lifetime of 380 ns

resolved LIBS spectrum in Cu. Initially the LIBS spectrum exhibits a broad background with short-lived broadened spectral lines. The longer-lived lines do not become prevalent until ~500 ns after plasma initiation. For this reason, a delay of several hundred ns was chosen for the dynamic experiments. Additionally, the lifetime of the longer-lived lines is in the hundreds of nanoseconds, which gives little benefit to extending the integration time of the detector beyond ~2 μs. Figure 5 illustrates the evolution of the LIBS signal in Cu along with an exponential fit to the peak intensity at 522 nm vs. time, indicating a lifetime of 380 ns. Similar studies done with the other metals and with pewter, gave similar lifetimes.

Dynamic LIBS Experiments in Ejecta

Dynamic experiments were carried out at the STL Boom Box where additional diagnostics were used to determine and corroborate timing. Care had to be taken to time the arrival of the laser pulse to spatially overlap the ejecta without hitting the free surface of the bulk metal sample. In the dynamic experiment, a 0.5″ × 0.5″ cylinder of 9501 HE was attached to the bottom of the pewter sample and initiated with an RP-1 detonator. Once the shock wave reaches the top of the sample, it interacts with the grooves to create ejecta particles that travel ahead of the free surface. The ejecta field can then be interrogated after it has been given enough time to travel away from the free surface. The ejecta and free surface were recorded with an imaging camera, and their velocities were measured using PDV.

The dynamic experiment is illustrated in Figure 6. The oscilloscope traces (Figure 6a) show the timing for the dynamic experiment. The experiment is initiated by a trigger, after which the detonator fires to ignite the high explosive. After about 7 μs the framing camera receives a series of triggers to capture

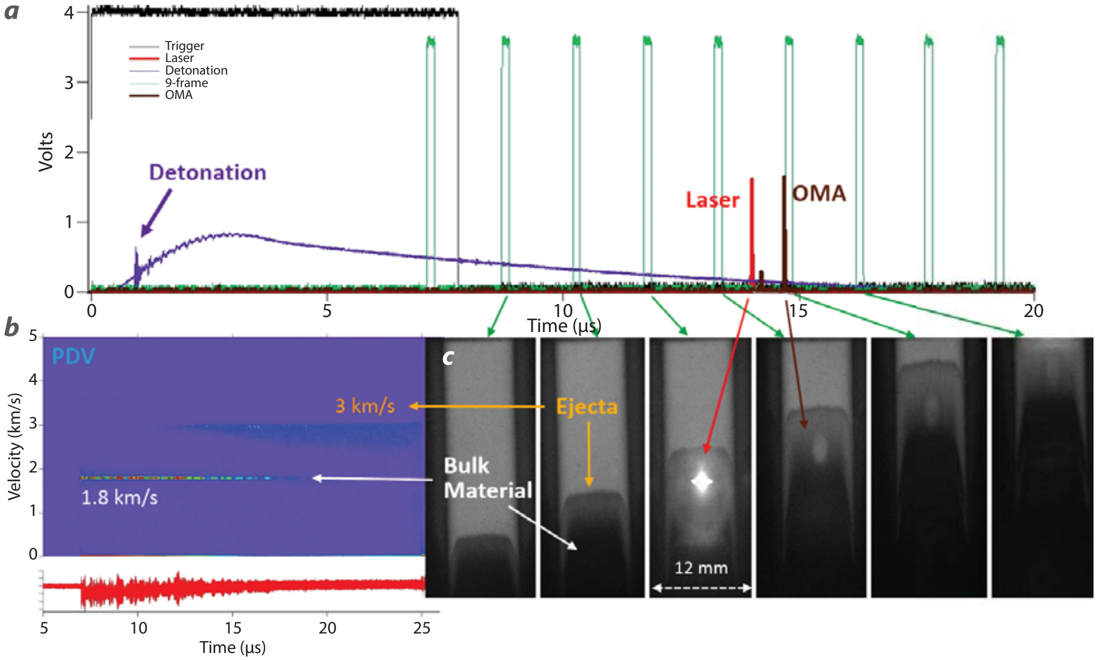

Figure 6. (a) Oscilloscope timing signals, (b) PDV data, and (c) 9-frame camera images

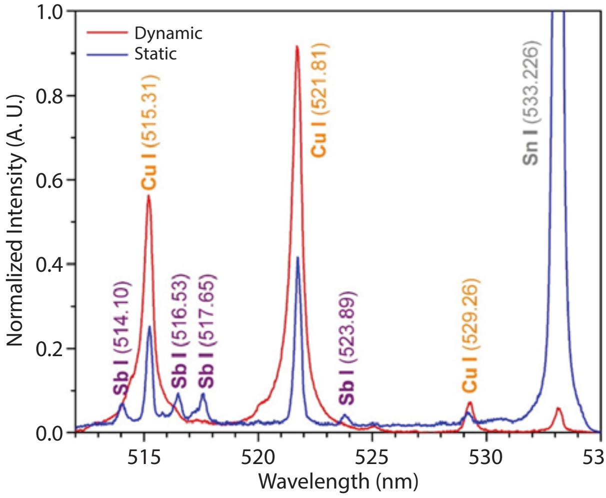

Figure 7. Measurements of the laser beam width (a) before and (b) after the upgrade

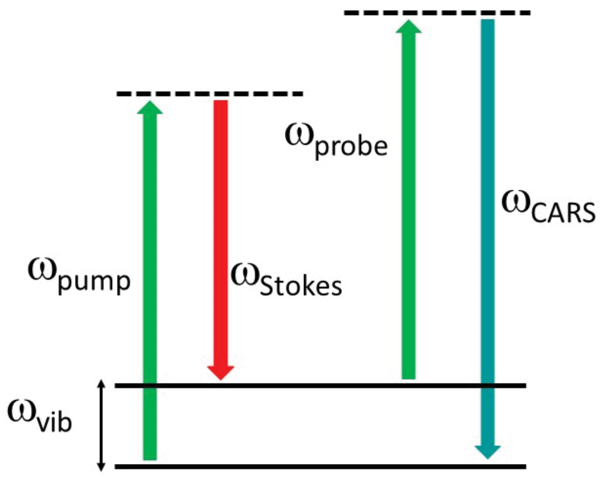

Figure 8. Energy-level diagram depicting the CARS process

images of the free surface and ejecta as they are driven through the field of view at 1.8 and 3 km/s, respectively, as indicated by the PDV measurement shown in Figure 6b. The laser pulse is timed to arrive after the ejecta has had time to separate from the free surface and is evident by a bright spot that appears in the framing camera images (Figure 6c). The interrogated ejecta region can then be seen continuing to travel forward in following frames. The LIBS spectrum is then captured 500 ns after plasma initiation by the ICCD spectrometer system.

The LIBS spectrum obtained in the dynamic experiment is shown in Figure 7 along with a spectrum taken on the sample prior to detonation. There are a number of notable characteristics in these spectra. First, all of the UV lines that were apparent in the static data from Figure 4 are missing in both Figure 7 spectra. This is presumably due to absorption in the thick Boom Box windows. Of greater interest is the change in the ratio of the Sn line at 533 nm and an overall lack of Sb lines throughout the dynamic spectrum. This was the case in each of the three dynamic ejecta experiments performed, although Sb was clearly present in all spectra obtained statically from the bulk sample. A series of experiments was carried out to uncover possible reasons for the different spectra in the dynamic ejecta experiments. Statically, parameters such as camera integration time, gain, slit width, and delay time were varied and found to have no significant or relevant effect on the spectrum; clear Sb lines appeared in all cases. Another dynamic experiment was run in the Boom Box with a slightly earlier delay time to determine if Sb peaks were evident at earlier times. The earlier delay time data show broader lines and a significantly more pronounced Sn line at 533 nm; however, there were still no apparent Sb lines. Static tests were performed on the bulk pewter sample after removing material from the surface to see if surface oxidation might result in different spectra from materials beneath the surface, but there was no observable change. We are continuing to examine how the LIBS spectrum might change when measured with metal powders composed of small (~10 µm) particles, as is the case with ejecta.

Temperature Measurements Using CARS

In the second phase of this work, we plan to use CARS to measure the temperature of a background gas in an ejecta cloud. CARS is a laser-based technique that can provide information about temperature, pressure, and concentration in gases (Kulatilaka 2010). The process involves crossing three laser pulses (pump, probe, and Stokes) spatially, which results in the appearance of a fourth laser beam called the CARS beam. The spectrum of the CARS beam is then measured to obtain information about temperature, pressure, and concentration. Figure 8 shows an energy-level diagram depicting the CARS process. The pump and Stokes laser wavelengths are chosen such that the difference energy matches a vibrational transition in the material of interest. This creates a coherent set of states that are then probed to create the output CARS beam.

To date, a CARS system has been developed and is being used to make static measurements in hydrogen gas. The CARS system in place at the Boom Box and an optical diagram is shown in Figure 9.

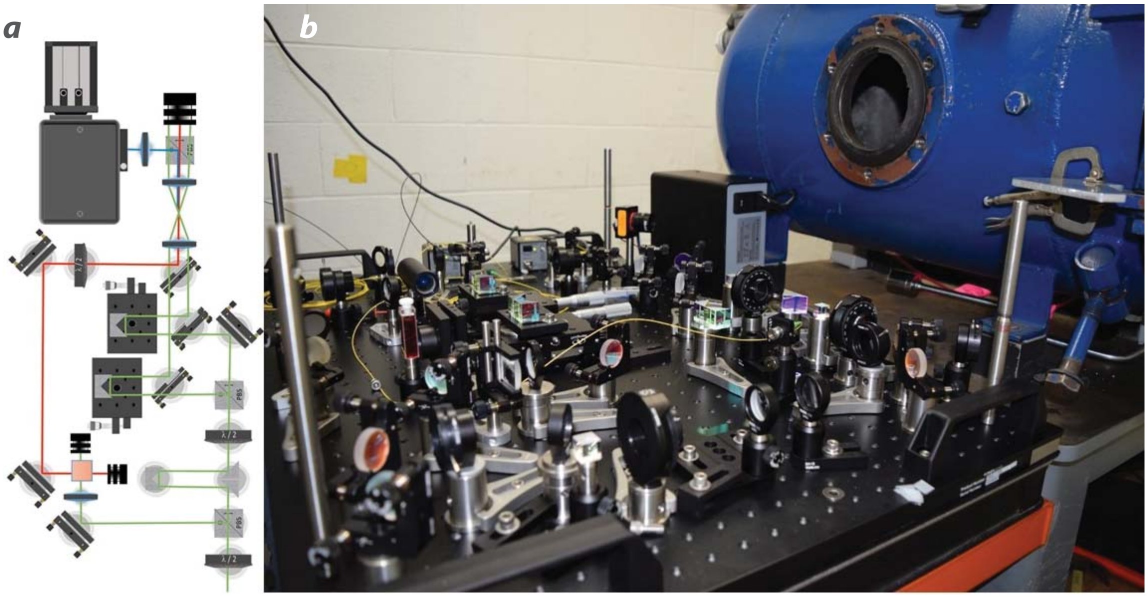

Figure 9. (a) Optical diagram of CARS system and (b) constructed CARS system in place at the STL Boom Box

The CARS system splits a 532 nm, 150 ps pulsed laser into the three beams. Two of the beams are reflected off delay lines adjusted to precisely coincide with the arrival time at the sample while the third leg generates the 683 nm Stokes beam in a dye cell. This wavelength targets the rotational Q-branch Raman shifts in hydrogen that occur in the 4120–4170 cm^{-1} range. We are now extracting temperature information from the data. In FY 2018 we will use the CARS system in a dynamic ejecta experiment.

CONCLUSION

We have demonstrated the capability for using LIBS as a diagnostic to dynamically determine composition in an explosively driven ejecta experiment. Initial results show differences between the dynamic ejecta LIBS spectrum and static spectra taken on the sample before detonation. We continue to investigate the nature of these differences and determine whether they can be attributed to changes in ejecta composition. A CARS optical system has been constructed for measuring the temperature of the background gas in a dynamically reacting ejecta cloud. The CARS system has produced spectra in a hydrogen cell, and data are currently being analyzed. Future experiments are being planned to field CARS dynamically.

REFERENCES

Kulatilaka, W. D., P. S. Hsu, H. U. Stauffer, J. R. Gord, S. Roy. "Direct measurement of rotationally resolved H_2 *Q*-branch Raman coherence lifetimes using time-resolved picosecond coherent anti-Stokes Raman scattering," *Appl. Phys. Lett.* **97** (2010) 081112.

Zellner, M. B., et al., "Effects of shock-breakout pressure on ejection of micron-scale material from shocked tin surfaces," *J. Appl. Phys.* **102** (2007) 013522.

Ultra-Spectral Remote Imaging by Scanning Fabry-Pérot Etalons

STL-036-16 ■ Year 2 of 2

David P. Baldwin,[1,a] **John A. Di Benedetto,**[a] **and Janice Lawson**[a]

[1]baldwidp@nv.doe.gov, (805) 681-2111
[a]Special Technologies Laboratory

We explored designs for compact, rugged, sub-nanometer spectral-resolution spectrometers using fixed-optic Fourier transform spatial interferometers compatible with passive mobile, handheld, or airborne gas and solid chemical detection. During the first year of this project, we assembled and tested Fabry-Pérot–based spectrometer devices and evaluated their application to emission and absorption applications. This experience led us to conclude that Fabry-Pérot spectrometers were much more expensive and less flexible in design than grating and interferometer systems because they are based on relatively narrow bandwidth, high-reflectivity optical coatings. These designs were tested against three applications important to nonproliferation remote sensing: optical emission from thermal or plasma events and sources, passive fluorescence detection of solids, and molecular gas absorption. The project successfully demonstrated that non-imaging spatial heterodyne spectrometers could be used as sensitive detection systems for high-resolution spectrometry of emitting and absorbing gases, and as a detector for Fraunhofer line discrimination of fluorescing solids.

BACKGROUND

In order to passively detect chemical species in several scenarios of importance to NNSS missions, including gas phase molecules in chemical releases, emitting gas phase chemicals in thermal events, and solid materials exhibiting passive solar-induced fluorescence, high-resolution spectroscopy is key. In the presence of complex backgrounds and overwhelming background emission or scattering, these species require detection systems with sub-nanometer resolution to match the line widths of the spectral features of interest for optimum sensitivity and selectivity. Grating-based line scanners either lack the resolution or (if high-resolution) lack the sensitivity at practical integration times to exploit high-resolution spectra of these target

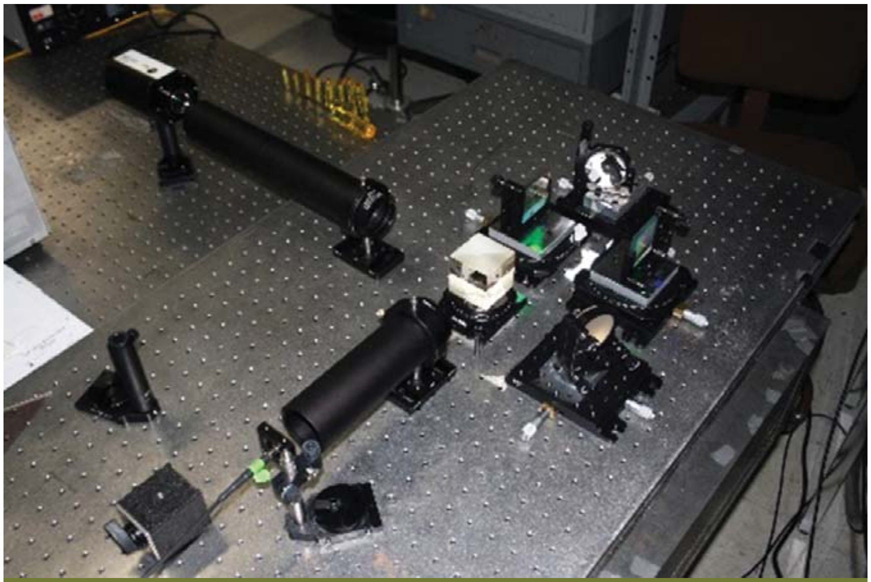

Figure 1. The benchtop LASHIS assembled from COTS components for this project

chemicals. Typically the size of these grating-based systems increases with improved resolution, so very high–resolution grating-based systems tend to be incompatible with portable, handheld, or unmanned aerial system (UAS) implementations.

To address a lack of technologies for these portable, handheld, and UAS-based passive chemical detection methods, this project explored the capabilities of interferometric spectrometers for high-resolution spectroscopy. In FY 2016 we assembled and tested a Fabry-Pérot (FP) interferometer–based system for passive chemical detection. This year we continued to explore alternatives to dispersive grating–based systems by building and testing spatial heterodyne interferometer–based systems having two different high-resolution optical configurations—one imaging and one non-imaging.

PROJECT

Large-Aperture Spatial Heterodyne Imaging Spectrometer (LAHIS)

The first spatial heterodyne system assembled for this project was a large-aperture spatial heterodyne imaging spectrometer (LASHIS) following the published designs from Xiangli (2015) and Cai (2016). The spectrometer was aligned with a heterodyne wavelength of 594 nm using a yellow helium-neon (HeNe) laser. It was assembled with 50 mm aperture optics that included a 200 mm collimating achromatic lens, a 500 nm long-pass filter, and a 600 nm short-pass filter to block out-of-band light and prevent spectral aliasing, non-polarizing beam splitter cube, two 1200 groove/mm plane ruled–gratings (500 nm blaze), two plane mirrors, and a 400 mm imaging achromatic lens. The LASHIS is shown in Figure 1.

In this design, an object or image at the entrance to the spectrometer (lower left in Figure 1, where a fiber bundle is shown) is reimaged at the detector plane (upper left in Figure 1). The collimated beam is split by the beam splitter, and a wavelength-dependent lateral sheer is introduced by the grating pair, creating a wavelength-dependent optical path length difference before the two beams are superimposed at the detector plane. This difference produces an interferogram for a diffuse unstructured object. However, for a structured object, in order to obtain the interferogram for each pixel, one needs to scan the object horizontally across the input aperture and use the intensity of a pixel on that object in many consecutive images to obtain the interferogram for that pixel. For best resolution, one needs to step the pixel across the aperture and measure intensities for that pixel in each of the vertical columns of the detector, in this case over 2000 images. Assuming that the spectrometer were passing over the image scene at a speed that would allow adequate photons to be collected, and in a straight enough line and with enough scene structure to register the pixel locations, this design amounts to an ultra-spectral pushbroom imager. Difficulty in registration could result if the scene lacks sufficient detail for good image indexing. Low-level flights that do not conform to straight lines might also make this registration more complicated.

We assembled a system based on the published design and obtained 4.35 cm^{-1} (~0.14 nm) resolution over a spectral range from 16,756 to 19,786 cm^{-1} using a 1394 × 1040 pixel detector (4.65 × 4.65 µm pitch). We replaced that detector with a larger-format detector (2736 × 2192 pixels at approximately the same pitch, 4.54 × 4.54 µm) and achieved a resolution of 2.21 cm^{-1} (~0.07 nm). This met our goal of spectral resolution of less than 0.1 nm at the wavelengths of the Fraunhofer magnesium (Mg) b1 and b2 lines at around 518 nm. The wavelength calibration for this system was

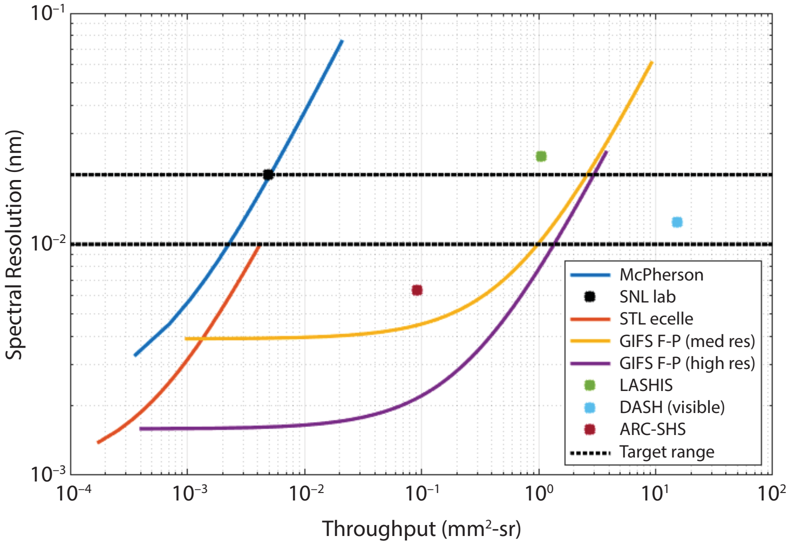

Figure 2. Comparison of resolution and theoretical throughput for a number of ultra-spectral spectrometer designs

performed using defocused emission from neon (Ne), krypton (Kr), and mercury (Hg) gas discharge lamps (eliminating the need for extracting intensities from an image data cube).

Spatial Heterodyne Spectrometer (Non-Imaging)

In other work, Mark W. Smith of Sandia National Laboratories compared literature and experimental values for resolution and theoretical throughput for a number of ultra-spectral spectrometer designs. The comparison included Smith's MacPherson grating spectrometer, the echelle grating spectrometer used in prior studies on Fraunhofer line discrimination by the principal investigators of this project, literature data for FP imagers (Yee 2004), the LASHIS system assembled here, and published literature (Harlander 1991, Englert 2007, Corliss 2015) for non-imaging spatial heterodyne spectrometers (SHSs) with and without field-widening prisms (DASH and ARC-SHS in Figure 2, respectively).

Based on this comparison (and also on limitations to miniaturization of the LASHIS design), we decided to assemble an SHS system to evaluate its applicability to the three remote sensing areas of interest. Our budget did not permit us to acquire the pair of custom wedges we needed to evaluate the increase in throughput from field widening. However, this phenomenon is well documented (Harlander 2002, 2010).

Our benchtop SHS system is shown in Figure 3. It is assembled using all 50 mm aperture optics. Lens 1 (100 mm achromat) collimates light into the SHS. Through different SHS configurations, we used various long-pass, short-pass, or band-pass filters to block light to the red of the heterodyne wavelength, to the blue of the Nyquist cutoff frequency, or to limit the range to a narrow region of interest within the broader range. A non-polarizing beam splitter cube divides the collimated beam into two beams that are incident upon two matched gratings in Littrow configuration for the heterodyne wavelength. The dispersion of these two beams, both tilted in the same direction with respect to the incoming beams, results in a wavelength-dependent path length difference. The dispersing beams are recombined at the splitter, and the gratings are imaged by an achromatic lens pair (lens 2:200 mm and lens 3:100 mm) onto the CCD detector plane. It is important to note that the gratings are imaged at the detector to create the interferogram, but the object image from the input is not imaged at the detector. Therefore, unlike the LASHIS, this is not an imaging spectrometer design.

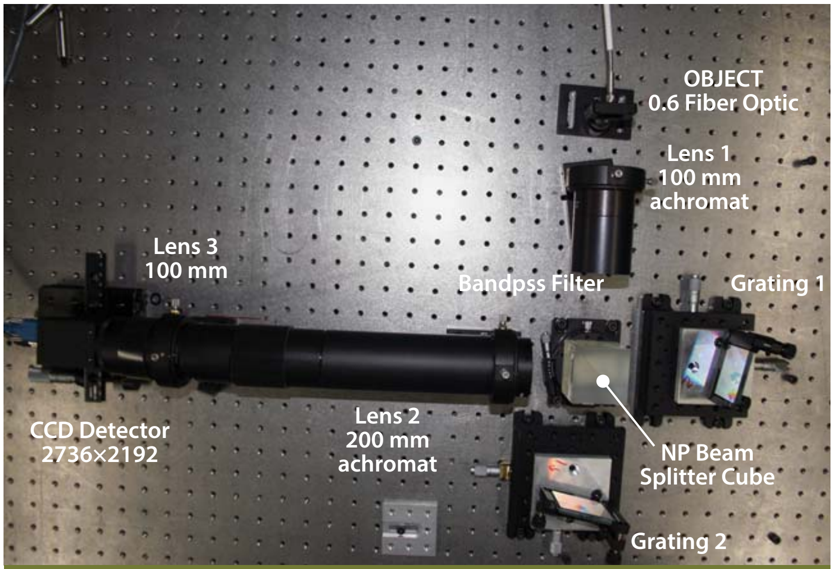

Figure 3. The benchtop SHS. An enclosure was used during data acquisition to cover the central components of the interferometer and reduce stray background light.

The following sections detail the components used for the three applications of the SHS and the performance of the system in these applications. Each application required some customization, such as changes to the gratings, and choice of heterodyne wavelength and spectral filters.

Emission

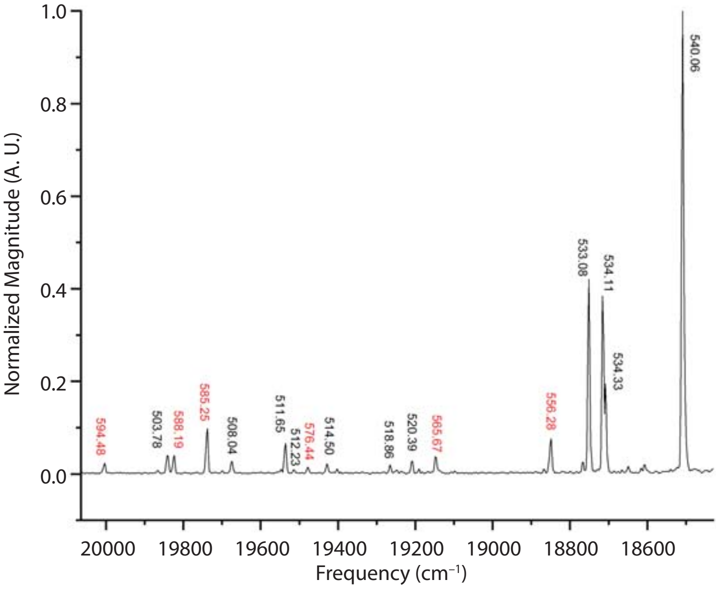

Figure 4. Neon discharge lamp emission spectrum acquired using the SHS with a heterodyne wavelength of 543 nm; red indicates assigned neon line to the red of the heterodyne frequency and to the red of the short-pass cutoff

For spectral emission testing, the SHS was first assembled using a green HeNe laser at 543 nm for the heterodyne wavelength with 300 groove/mm gratings (blazed at 500 nm), a 550 nm short-pass filter to block wavelengths to the red of the heterodyne, and a 500 nm long-pass filter to block wavelengths to the blue of the Nyquist limit. The 1394 × 1040 CCD detector was used at this point in the project (the larger CCD was purchased later). Wavelength calibration and emission testing were performed using a neon discharge lamp. Figure 4 shows the spectrum for this source. The lines labeled in red are assigned neon lines to the red of the heterodyne frequency and to the red of the short-pass cutoff. However, these filters only have an optical density of 2.0, and these lines are very intense compared to the in-band emission features, resulting in spectral wrapping.

In this configuration, the spectral range of the SHS was from 18,416 to 20,075 cm^{-1}, and the resolution of the system was 2.38 cm^{-1} (~0.06 nm). Because there is a tiny amount of residual tilt between the two gratings that could not be removed with the manual stages and mounts, the interferogram had a small amount of left-to-right shift from the top to the bottom of the detector. To use all of the accumulated signal from the detector without smearing the spectra, the collected 2-D interferogram was grouped into ten regions (each 1394 × 1040) and summed for each range. Each sum was Fourier transformed to obtain frequency spectra before summing the regions.

Fluorescence of Solids

We also tested the SHS's ability to detect the passive, solar-pumped, fluorescence of solids. There are two strong Fraunhofer absorption lines of Mg (b1 and b2) at 518.36 and 517.27 nm. By comparing the contrast ratios for these lines in solar radiation scattered from a non-fluorescing surface to that scattered from a fluorescent (inelastic scattering) surface, one can calculate the amount of fluorescence generated by the target material. In order to best detect this small amount of inelastic scattering in the presence of a large amount of elastic scattering, the resolution of the spectrometer needs to nearly match the line width of the Fraunhofer lines being collected.

For this application, the heterodyne frequency of the SHS was shifted to 532 nm using a doubled Nd:YAG (neodymium-doped yttrium aluminum garnet) laser. The gratings were changed to 600 groove/mm (500 nm blaze). At first, the SHS was assembled using 550 nm short-pass and 500 nm long-pass filters. However, compared to emission applications where the lines or interest constitute a small amount of signal against a dark background (resulting in very high signal-to-noise ratios and high-contrast ratio interferograms), these solar spectra highlighted an important limitation of spatial heterodyne spectrometry. Photons at wavelengths across the entire spectral region contribute to noise across the entire 2-D interferogram. Also, as a larger wavelength range is included in the spectral transmission of the interferometer, the difference in intensity between the peak at the center burst (zero path length difference position for all wavelengths) and the intensity at large path length difference positions in the interferogram increases. This increased intensity difference can limit the fidelity of spectral line shape and depth reproduction for detectors that typically have a limited dynamic range. These characteristics are critical to detecting small differences in contrast ratios as required in this application.

Because of these noise and dynamic range limitations, the SHS was assembled using a narrow band-pass interference filter (518 nm, 2 nm bandwidth) to block light within the Nyquist range of the SHS that would otherwise generate noise in this region and limit the dynamic range response of the detector.

In this setup, we used a larger 2736 × 2192 pixel CCD. Without the band-pass filter, the spectral range was from 18,795 to 19,658 cm^{-1}. The resolution was 0.631 cm^{-1} (~0.017 nm), approximately four times higher than in the previous emission application, as we doubled the grating groove density and had nearly twice the number of pixels in each row of the detector. Figure 5 shows the normalized solar-scattered spectra from a non-fluorescing Teflon target and from a fluorescing glass material (placed in front of the Teflon target). This amount of difference in the depth in the scattered line shapes is sufficient to calculate fluorescence yield for this material.

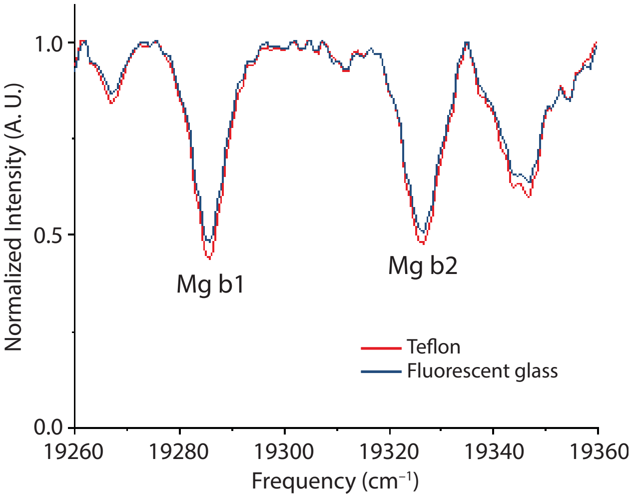

Figure 5. Solar spectra scattered from fluorescing and non-fluorescing targets collected using the SHS

Molecular Gas Absorption

The final application of the SHS was tested using atmospheric absorption lines of water and oxygen. For this application, the gratings were replaced with 600 groove/mm gratings (750 nm blaze). A continuous wave laser diode was temperature- and frequency-tuned to 700.16 nm and provided the heterodyne source for alignment of the SHS. This precise wavelength of this source was not critical and not well known until the spectrometer was aligned and the wavelength calibration determined using neon lamp spectra. We anticipate using a similar procedure for aligning SHS devices in other spectral regions where fixed-frequency laser sources are not readily available. The spectral range of the system was from 14,283 to 14,919 cm^{-1} with a resolution of 0.464 cm^{-1} (~0.022 nm). Because we were using solar radiation, as in the fluorescence application above, we obtained a 692 nm, 5 nm band-pass filter to limit the out-of-band noise and dynamic range limitations for this application.

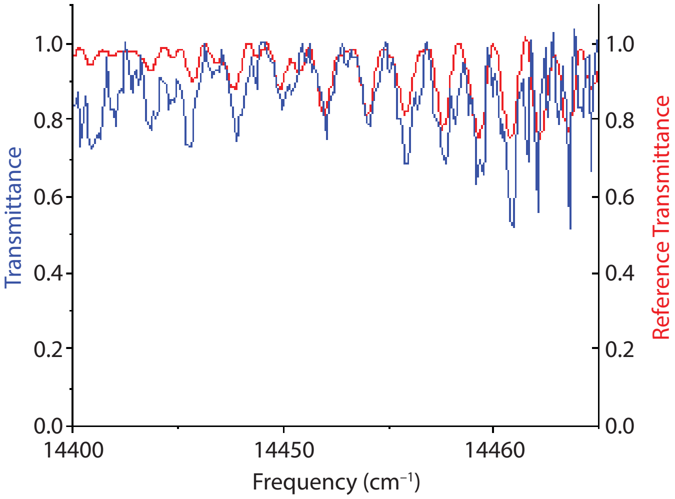

Figure 6. Transmittance spectra of solar radiation absorbed by molecular water vapor and oxygen in the atmosphere measured using an SHS

Figure 6 shows the transmittance spectra obtained in this application (in blue) by collecting solar radiation scattered from a Teflon target (subject to absorption by atmospheric gases) compared to a reference solar spectrum (Delbouille 1972) that has been computationally deresolved from the 0.001 nm reference for comparison. The regularly spaced features from the middle to the right of this spectrum are oxygen absorption features, which are actually line doublets at higher resolution. The less regular features on the left of the spectrum are water vapor absorption features. They are relatively intense here, although it was noted that the weather was somewhat humid in Santa Barbara on that day.

This experiment was conducted very late in the project and was subject to very little optimization. Additional work might include laboratory cell experiments to determine detection limits and better comparisons to reference spectra. However, these experiments did allow us to test the use of tunable lasers and poorly collimated sources for heterodyne alignment, which worked very well. It also allowed us to test the design in a different spectral region where alignment by eye was more difficult. Despite these challenges, this early result was very positive.

CONCLUSION

During the final year of this project, we assembled and tested two spatial heterodyne spectrometer systems. The imaging system performed as expected. Field implementation of this type of system would require that each pixel be tracked and registered in each of over 2000 images so that the elements of the spectral interferogram for that location could be combined to extract a spectrum for that pixel. While this is certainly possible, it would be computationally complex. It would be made even more so if the instrument were implemented on an aircraft where straight line flight for remote sensing is the exception rather than the rule. This instrument is much more promising for satellite applications.

The non-imaging system was assembled and tested for all three of the anticipated applications. The use for detecting emission from excited gas species is perhaps the most straightforward and was tested using gas plasma lamps. The resolution was sufficient for resolving emissions from complex mixtures of materials and would be amenable to characterization of physical properties in energetic events, such as temperature measurements based on line intensity ratios, or for isotopic ratio measurements. It would also work well as a Raman spectrometer where resolution may be at a premium due to chemical mixtures or dense spectra. The non-imaging system was tested as a detector for solid material fluorescence by measuring contrast ratios of solar Fraunhofer lines from scattered sunlight. The system is now being used as a testbed for an NNSS mission activity related to this application. Finally, the system was used to detect molecular species absorption. In particular, we measured atmospheric water and oxygen absorption lines. Proposals are being prepared to extend this application into other spectral regions for remote sensing of fugitive gas emissions.

ACKNOWLEDGMENTS

We would like to thank Dan Zamzow and Dr. Stan Bajic of Ames Laboratory and Mark W. Smith of Sandia National Laboratories for their contributions to this work.

REFERENCES

Cai, Q., B. Xiangli, Y. Fang, “Optical simulation of large aperture spatial heterodyne imaging spectrometer,” *Opt. Commun*. **366** (2016) 136–141.

Corliss, J. B., W. M. Harris, E. J. Mierkiewicz, F. L. Roesler, “Development and field tests of a narrowband all-reflective spatial heterodyne spectrometer,” *Appl. Opt.* **54**, 30 (2015) 8835–8843.

Delbouille L., L. G. Roland, L. Neven, Photometric Atlas of the Solar Spectrum from λ 3000 to λ 10000, Institut d’Astrophysique de l’Universite de Liege, Cointe-Ougree, Belgium, 1972, http://bass2000.obspm.fr/solar_spect.php, accessed on June 8, 2017.

Englert, C. R., D. D. Babcock, J. M. Harlander, “Doppler asymmetric spatial heterodyne spectroscopy (DASH): Concept and experimental demonstration,” *Appl. Opt.* **46**, 29 (2007) 7297–7307.

Harlander, J. M., “Spatial heterodyne spectroscopy: Interferometric performance at any wavelength without scanning,” PhD thesis, University of Wisconsin, Madison, 1991.

Harlander, J. M., F. L. Roesler, J. G. Cardon, C. R. Englert, R. R. Conway, “SHIMMER: A spatial heterodyne spectrometer for remote sensing of Earth’s middle atmosphere,” *Appl. Opt.* **41**, 7 (2002) 1343–1352.

Harlander, J. M., C. R. Englert, D. D. Babcock, F. L. Roesler, “Design and laboratory tests of a Doppler Asymmetric Spatial Heterodyne (DASH) interferometer for upper atmospheric wind and temperature observations,” *Opt. Express* **18**, 25 (2010) 26430–26440.

Xiangli, B., Q. Cai, S. Du, “Large aperture spatial heterodyne imaging spectrometer: Principle and experimental results,” *Opt. Commun*. **357** (2015) 148–155.

Yee, J.-H., M. F. Morgan, R. DeMajistre, E. R. Talaat, J. F. Garten, W. H. Swartz, W. R. Skinner, “Geostationary Imaging Fabry-Pérot spectrometer (GIFS),” *Proc. SPIE* **5660** (2004) 14–22.

Next-Generation Photomultiplier Detectors Using Transmissive III-Nitride Semiconductor Electrodes

NLV-049-16 ■ Continuing in FY 2018 ■ Year 2 of 3

Robert Buckles[1,a] and Ke-Xun (Kevin) Sun[a,b]

[1]bucklera@nv.doe.gov, (702) 295-0323
[a]North Las Vegas
[b]University of Nevada, Las Vegas

Detectors for high-energy gamma and neutron prompt diagnostics are critical technologies for many applications at the NNSS and elsewhere. Unfortunately, legacy, high-quality standard photomultiplier tube technology is becoming outdated and difficult to maintain. This project has been addressing an ongoing need to move toward more advanced solid-state detector concepts. In the first year of this effort, we created a photocathode design based on an indium galium nitride/aluminum nitride (InGaN/AlN) heterostructure. This year we developed a novel, ultrafast AlGaN photoelectron multiplier that will integrate with the photocathode. Fabrication and initial characterization of these structures is described. In FY 2018, we will complete growth and fabrication of the multiplier wafers, and bond the photocathode and multiplier stack, culminating in an operational test of the prototype detector.

BACKGROUND

The NNSS has provided prompt gamma/neutron diagnostics for Stockpile Stewardship, high-energy density physics applications, and defense programs throughout the NNSA complex, the Defense Threat Reduction Agency, and other agencies for decades. While we have endeavored to improve our techniques, methods, and instruments since legacy days, the photomultiplier tube (PMT) industry has stagnated, vastly dwindling to a point of collapse, while solid-state technologies have almost completely supplanted vacuum tube technology. And recently, the lighting, power, and broadcast industries have embraced the advent of high-performance Nobel-winning Group III-nitride semiconductors. Leveraging these advanced technologies, we seek to produce a novel device to surpass the aging vacuum tube detector, while surmounting the limitations of intermediate technologies such as glass microchannel plates. The high-mobility semiconductor "mesh" multiplier we are developing is our response to the PMT quandary.

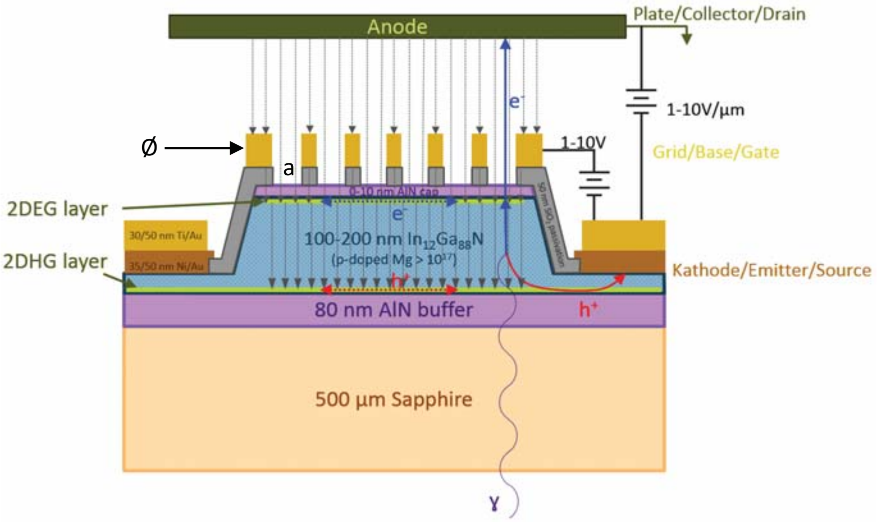

Figure 1. Photocathode device cross section with illustrated operational bias, field lines, and photoelectronic flow (not to scale). Passivation openings (a) are 100 µm inscribed hexagons. Overall diameter Ø is 1 to 20 mm. The configuration is that of a planar triode or vertical field-effect transistor (FET).

Prompt neutron/gamma signatures are high-speed analog signals, too fast for counting electronics but too low in light yield for typical amplifiers, and are typically converted to near-UV light using a fast scintillator material. The PMT can apply greater than 1 million gain with good linearity and temporal response. Our semiconductor mesh photomultiplier should exceed the typical characteristics of vacuum PMT.

PROJECT

The conceptual work in FY 2016 culminated in our photocathode design (Buckles 2017), and processes were finalized for fabrication in FY 2017. Figure 1 shows the epitaxial (epi) thicknesses, interfaces, and contacts with illustrated operational bias, field lines, and photoelectronic flow. The external anode represents the multiplier layer in a stacked PMT assembly, which has an applied field strength of 1 to 10 V/µm. The grid electrode is intended to promote hot electron transport, increasing the local field within the active region, possibly exceeding the free-space field, with ready emission through the vacuum barrier. The heterojunction interfaces provide 2-D electron gas (2DEG) or hole gas (2DHG) layers with high mobility. Due to a quantum-mechanical eigenstate cusp that exceeds the Fermi level energy, these layers provide essentially free carriers and therefore behave unimpeded, much as would flow in a true conductor. High electron mobility transistors are constructed in this fashion to produce extremely fast or wideband switches for power millimeter wave components. It is our expectation that these layers will provide high current-mode charge replenishment to forestall charge saturation. The aluminum nitride (AlN) cap is a very experimental idea—we are testing whether it will resist oxidation better than gallium nitride (GaN) and provide a more stable cesium activation layer. Surface cleanliness and preparation are the most critical parts of cesiation, and a strong (but very thin) nitride barrier may play a key role in transport and quantum efficiency (QE) depending on its conduction band level relative to vacuum. We are attempting zero cap thickness (none) for some of the trials.

Three photocathode thicknesses of 100, 150, and 200 nm were made. The optimal thickness of the photocathode is estimated based on a 200 nm diffusion length for GaN and similar estimates from other research (Siegmund 2006, Pau 2008, Wang 2012). Choosing an optimal thickness involves a trade-off among optical absorption, electron transport, and recombination. UV photons will excite valence electrons into upper conduction bands with a long

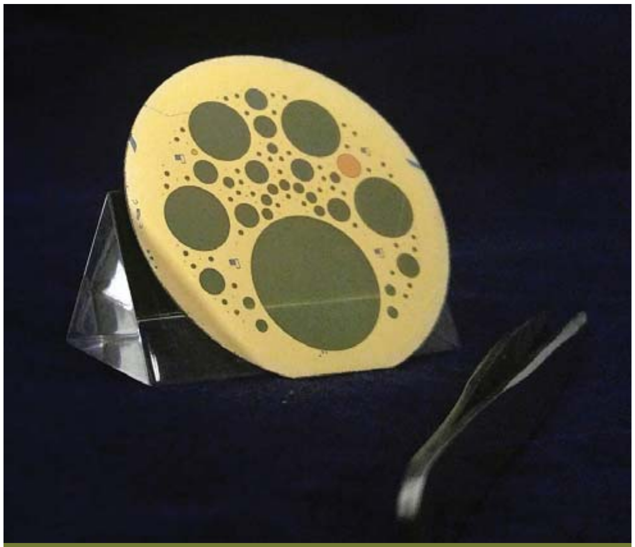

Figure 2. InGaN photocathode devices on 2″ sapphire wafer with a range of sizes (20, 10, 4, 2, 1, and 0.4 mm) for testing purposes and eventual detector assembly with a multiplier stack

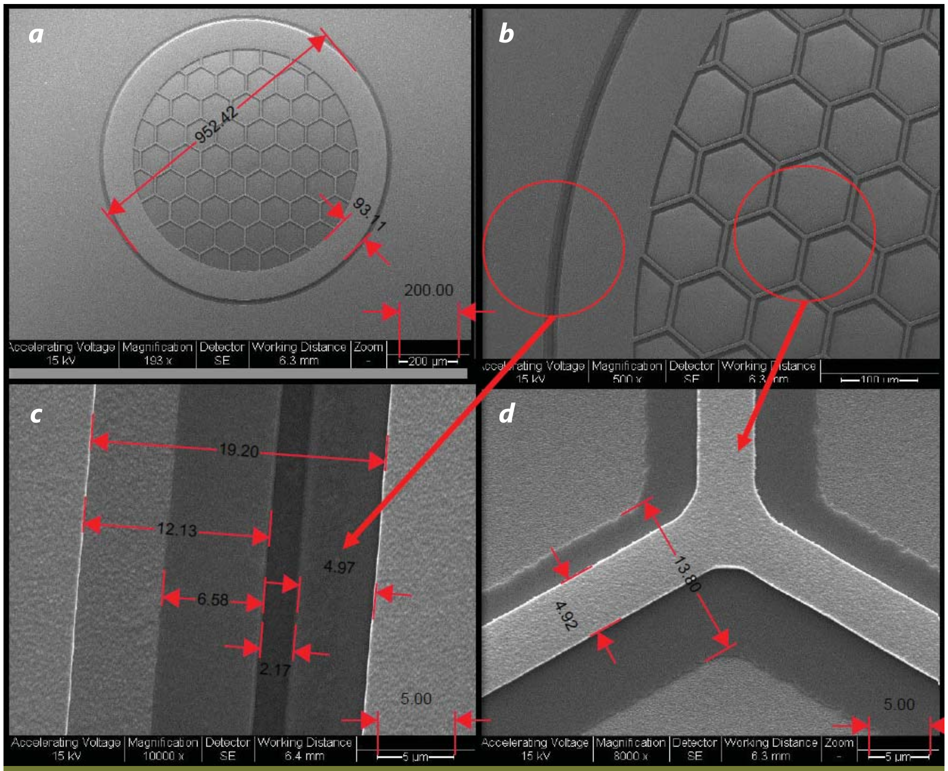

Figure 3. Micrographs of one small InGaN photocathode device with progressively finer magnification. Units are microns. (a) 1 mm device showing circular mesa structure and surrounding plane. Top contact ring is 100 µm wide. (b) Circled regions of interest, edge, and plateau. (c) Mesa edge. Bright white stripes show the silicon dioxide (SiO_2) edge passivation covering the mesa edge. The darkest band is the mesa edge with its bottom toward left and plateau toward right. The brightest regions are bare gold contacts. (d) The honeycomb metallized plateau is a 5 µm wide strip of gold suspended on SiO_2 passivation. This plateau acts as a control "grid" for enhancing the under-surface field for emission without allowing strong conduction to grid. This is very much an optical planar triode, given a collector anode.

lifetime, while photoelectrons just over the band gap (450 nm in our work) may lose energy and recombine before being extracted. Wang (2012) suggests an optimal thickness of 90 nm for 290 nm light and a peak from 13% to 16% internal QE; these parameters fit a model that maintains spectral sensitivity over the UV range. It is a fitted absorption/electron diffusion solution with recombination and escape probability, first proposed by Spicer 50 years ago (Spicer 1958, 1993). Other developmental works in UV GaN avalanche photodiodes (Pau 2008) advise a thickness of 150 nm for 360 nm light. However, Siegmund states that thinner photocathodes have better yield due to the faster extraction. Our work spans a range of thicknesses, as we are using 400 nm light with a band gap shifted to 450 nm. Three sample thicknesses will provide a reasonable benchmark to measure directly without a model fit to see how the high field extraction changes the QE behavior.

Device Fabrication and Characterization

Wafers were produced by Kyma Technologies starting near the end of FY 2016. This proved a fruitful partnership that yielded not only the mixed III-V material growth, but also in-depth knowledge in device fabrication. Final wafer-level photocathode devices were completed this year. These devices are 12% indium gallium nitride ($In_{0.12}Ga_{0.88}N$) epi layers on a 2″ sapphire wafer (Figure 2). Devices with etched mesa structures and metallized contacts are shown in Figure 3. For this transmissive-mode photocathode, the open circles appear brown in color (absorbing blue light) but have a metal patina from the honeycomb grid feature. Each wafer includes a range of photocathode diameters: one 20 mm, four 10 mm, and fourteen 4 mm devices principally for making a full PMT, and several smaller pieces for testing: fourteen 2 mm, fifty 1 mm, and sixty-four 0.4 mm, the smallest of which encompasses just one cell of the honeycomb pattern. (See Figure 3 for metallization detail.)

We characterized the field emission of the photocathodes despite not having yet activated the semiconductor negative electron affinity (NEA) with cesium, expecting small but measureable field-assisted emission. We constructed a custom wafer probe stage and anode (Figure 4), and adapted a large excessed sputter machine for a vacuum test chamber (Figures 5a–5b). Using a Cryotorr pump, we attained a range of temperatures from 30 K to 40 K and low base pressures of 10^{-8} Torr for the field emission tests. All parts were precision cleaned and then conditioned in situ using a repeatedly cycled 1 Torr nitrogen DC plasma discharge for several days, elevating the wafer

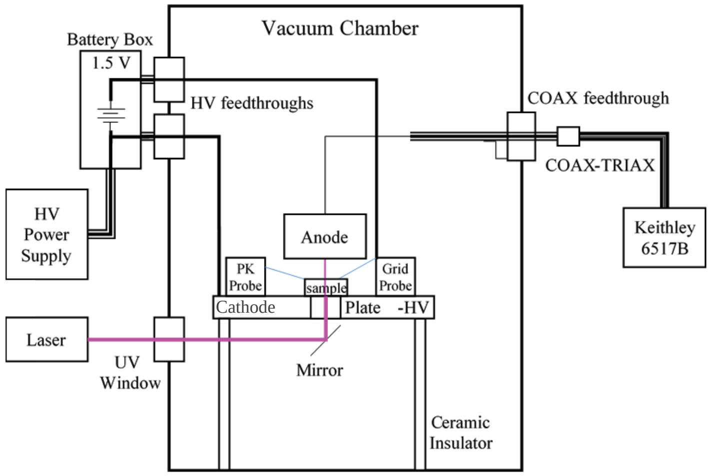

Figure 4. Field emission wafer probe station setup. The cathode is biased negative for ease of reading current, and the anode is near ground for precision current measurement. Chamber wall is ground, but could be made a guarding shield with a more elaborate high-voltage triaxial feedthrough, biased internally from the Keithley electrometer. The high-voltage anode must not interfere with probe manipulators and needs redesign.

stage at +1200 V relative to the chamber (Figures 5c–5d). The experimental setup is shown in Figure 6. Figure 6a shows a sample loaded into the vacuum emission test probe stage, and Figure 6b shows the 405 nm Sacher diode laser illumination and UV window mounted to vacuum chamber.

Although we have yet to do conclusive field emission measurements, we observed a causal response to illumination on the order of 10 to 100 pA. But random fluctuations of the same order were present and difficult to isolate. No amount of averaging could eliminate the fluctuations, as low frequency drift was still present, swamping our measurement. Lock-in detection may solve this issue but was not set up in time for this report. Knowing that field-assisted emission would not be nearly as strong as NEA emission, we anticipated low current measurement and used a Keithley 6517B electrometer with 100 aA resolution and a ±1000 V internal source. However, we hoped to avoid the need for guarded measurements as the vacuum chamber itself is a good electrostatic shield, no interfering source is present within, and a guarded triaxial high-voltage vacuum connector is untenable. We took great pains to limit the sporadic emission from the base to anode and any probe parts, and biased the base negative with the anode and electrometer near ground (two separate ports).

In hindsight, the external bias was likely the cause of the fluctuation we noted; we will address this by directly connecting the stable internal bias of the electrometer to a positive anode before continuing. Chopped, lock-in detection may also be necessary to remove the low-frequency drift. We were also limited in our approach distance and applied field, and we will need to reduce the anode to more of a broad point probe that avoids the wafer probes used for photocathode and grid bias. At the time of this report, we have successfully achieved <1 fA noise levels and optical transport measurements, and will report these successes in the next fiscal cycle.

In parallel with the photocathode production and measurements, we finalized the design of the multiplier wafer section and received preliminary feedback from Kyma Technology regarding the process constraints. Much of the patterning is retained from the photocathode production, and the operation is similar in principle to the photocathode, but the photoelectrons are produced from an adjoining device (Figure 7). The gain mechanism is provided by the collisional impact within the AlGaN material due to the free-space bias field between devices. It can achieve a secondary electron yield of at least 10 for 100 V impact energy and will scale linearly with bias at roughly one-third electron for every band gap unit of primary kinetic energy. This is a practically a universal constant thermodynamic efficiency for stochastic processes. For example, the x-ray radiation yield in silicon is about 1 electron for every 3.6 eV of energy, having a bandgap of 1.12 eV. Other semiconductors behave similarly (Klein 1968). However, metal dynode PMTs are fixed at about two secondaries for 100 eV of impact energy, and only those within a few dozen angstroms of impact surface can escape.

Although the maximum bias remains to be seen, 3 V/µm is the breakdown strength of air (which can be encapsulated) and 30 V/ µm is the breakdown strength of silicon. Conservatively, we estimate 1–10 V/µm to be a reasonable operating range, which projects an impact energy of 200 to 2000 V for a secondary gain of 20 to 200. At full bias, just three of the stacked crystalline meshes would have a gain of 200^3 = 8 million; at low bias, five stacked meshes would have a gain of 20^5 = 3.2 million. This is typical of metal dynode PMTs (with many more dynodes) and would likely represent a saturation level depending on the particular model. The current is modest because 1 A is 0.6×10^{19} e^-/s (6 billion per nanosecond), which indeed seems large from a counting perspective. For a

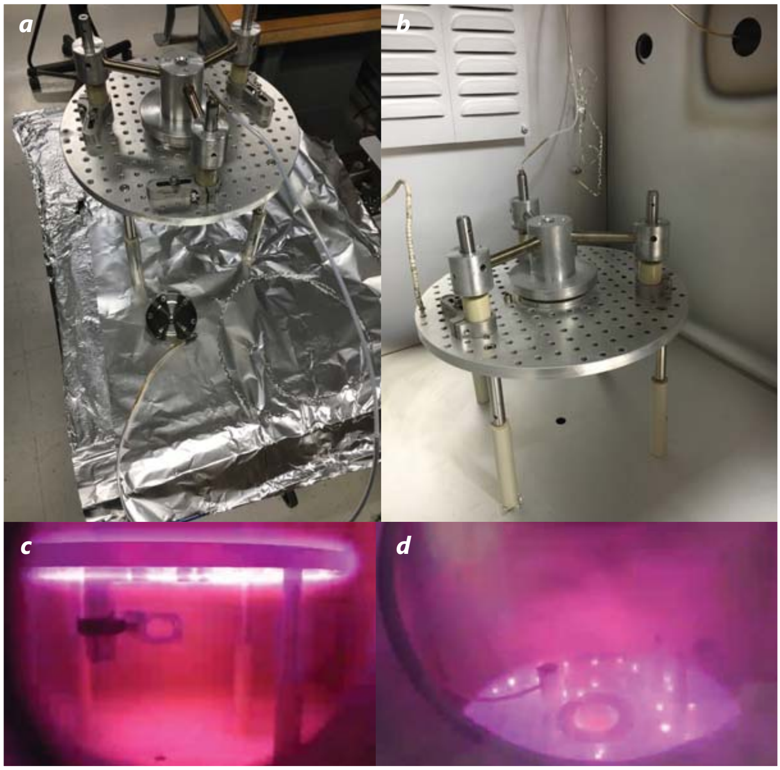

Figure 5. (a) Improvised wafer probe station for in-vacuum high-field emission measurements, showing anode collector and feedthrough. All components are vented high vacuum parts with mostly prefabricated vacuum-compatible parts from Thorlabs. (b) Inside chamber view with probe station. It is important to have a large degree of freedom for moving the stage in and out of the chamber and configuring the probe points on the wafer manually. A large volume places challenges on the vacuum system but is manageable. (c and d) Plasma discharge conditioning of all parts, noting points of high-field discharge and the turning mirror mount underneath the base plate. Discharge was discontinued after all arc points terminated.

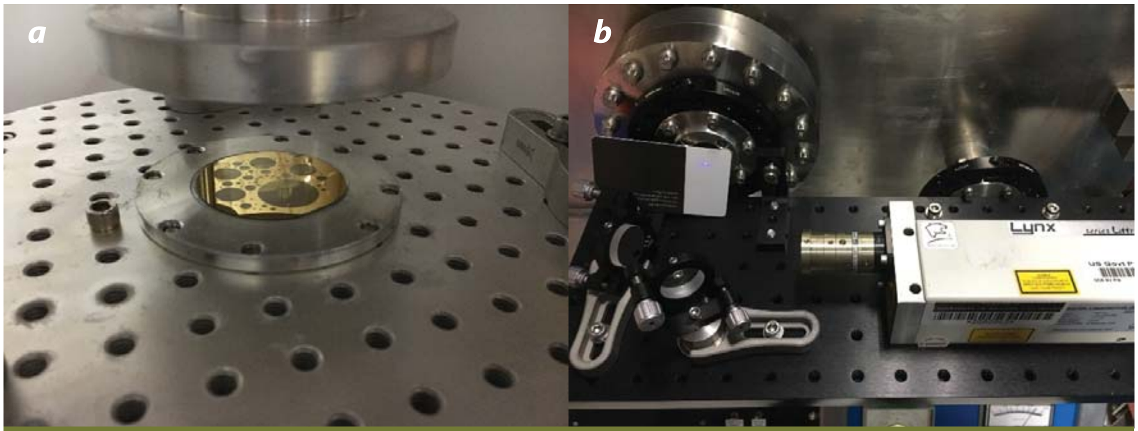

Figure 6. (a) Loading a sample wafer in the vacuum emission test probe stage. Probes (not shown) are low profile and mounted at a convenient placement on the large base. The center holder is precisely made for the rim of the wafer and has a large enough clear aperture to reach any spot for illumination from underneath. (b) 405 nm Sacher diode laser illumination and UV window mounted to vacuum chamber.

50-ohm transient recorder, the current would be 50 V, a typical linear limit for a fine-mesh PMT. But run-of-the-mill PMTs tend to have a linear limit closer to 5 V, or 100 mA (600 million electrons per nanosecond), so a gain of a few million is not outlandish. We hope that a metal semiconductor multiplier can transport that much charge, though we are concerned about its transport properties and, hence, include the grid electrode to supply high field and heterojunctions to provide the 2DEG and 2DHG interfaces for enhanced mobility. We choose AlGaN as the multiplier material for its greater mechanical strength and immunity to all but deep UV light that might result from residual interaction from the high-speed electrons, knowing that this choice will require more kinetic energy due to the higher band gap.

The gain layer thickness must not be so thin that it is fragile, and not so thick that it cannot be grown without cracking. We have estimated the electron

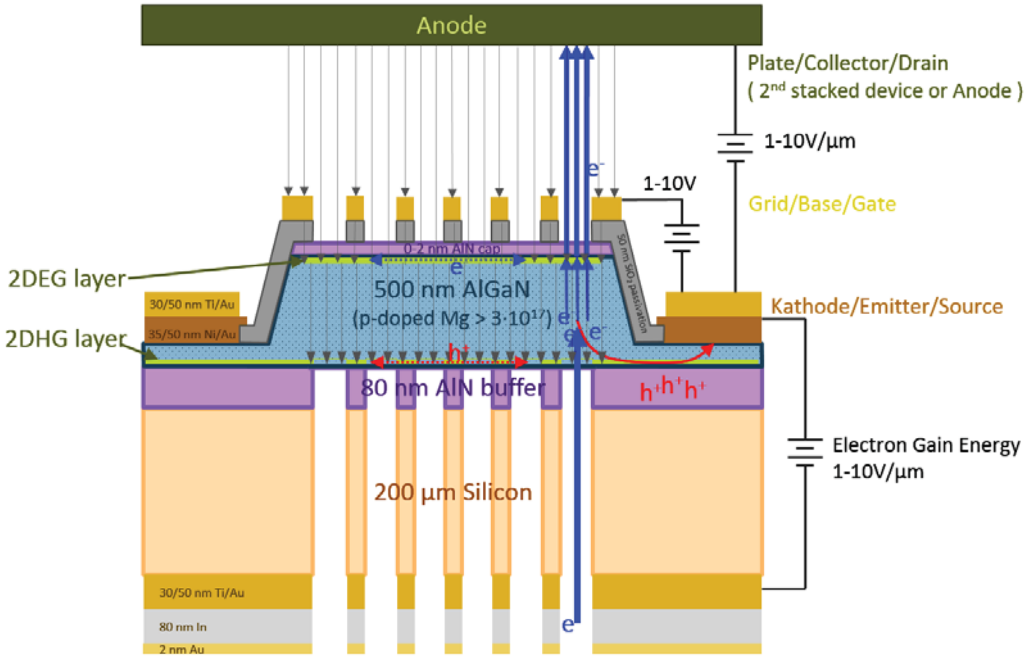

Figure 7. Electron "crystalline mesh" multiplier device cross section with illustrated operational bias, field lines, and electronic flow (not to scale). Passivation and acceleration openings are 100 µm circles with exactly the same pattern as the photocathode. Overall widths are 1 to 20 mm. The configuration is that of a planar triode, or vertical FET, but with collisional gain. Multipliers can be stacked; each 1 mm stack will give a geometric gain of about 1 million.

penetration of AlGaN and mean free path (MFP) based on ionization coefficients, mobility, and saturated velocity. Assuming a mobility estimate, starting from rest rather than having initial energy, one may predict a maximum MFP of 900 nm, which seems too large. By extrapolating the (high-energy) NIST ESTAR database (Berger 2005) for electron collisional cross section and continuous slowing down approximation range, we may expect a 500 eV electron to have a range around 10 nm, which seems too small. However, the NIST data are presumed to be inaccurate below 1 keV, as they do not account for electronic structure band theory. Instead, using measured electron-hole impact ionization coefficients for GaN provides reasonable estimate (Özbek 2012). This method, which follows an avalanche breakdown Chynoweth model, is measured via electron beam–induced current technique and yields a quasi-continuous model of acceleration from rest followed by impact expressed in terms of inverse electric field. If we presume that an infinite electric field (breakdown) also represents our case of high impact energy, the ionization coefficient for electrons in GaN would be 6.4×10^5/cm, a mean free path of 67 nm. The same but less precise result is obtained (Tut 2006) for $Al_{0.4}Ga_{0.6}N$ when inferred from avalanche photodiode gain characterizations.

About 3 to 4 MFP for a thermalization range would disperse the energy well enough to capture it all, which amounts to 250 nm. Our design should span a range of 250 to 1000 nm, but the final range will be determined by initial growth tests. The NIST extrapolation of 10 nm seems worrisome, at least for the prospect of punching through the buffer AlN layer, so we plan to etch through the buffer as well as the silicon substrate.

Silicon plays an important role for the multiplier as a mechanical substrate, having half the thermal expansion of AlGaN. Upon cooling from epi deposition, the AlGaN epilayer remains under tension, and if it does not rupture, it can remain under tension as a free-standing film after etching through the substrate. Estimates of the stress and stability of a stretched membrane suggest that AlGaN is very strong in terms of tensile strength (we must be careful of substrate warping if the epilayer is too thick), and its critical stress intensity factor (fracture toughness) is high enough to be stable against crack formations that could nucleate out of lattice defects in the epilayer. The material must be protected from gross puncture contact and handled with more care than a typical wafer. Furthermore, silicon is very easy and cost effective to etch through chemical means (unlike AlGaN). A definite disadvantage of silicon is its finite conductivity at room temperature (a concern even for high-resistivity intrinsic silicon), which causes leakage from biasing and may set the maximum voltage and gain.

CONCLUSION

In the second year of this project, we completed the fabrication of the prototype InGaN photocathodes and created a vacuum high-voltage wafer probe station for field emission measurements. Vacuum field emissions are verified but noisy, and further improvements in guarding and biasing will be carried out in FY 2018. We plan to measure the transport and internal QE properties on a clean bench wafer probe station before returning to vacuum field emission measurement. Design of the crystalline mesh multiplier wafer devices were completed; with process knowledge gained from the photocathode processing, we will confidently move forward with the multiplier fabrication in early FY 2018. At the time of this publication, the etch processes and suspended epilayer were proven, and two thickness chosen, 250 and 500 nm, with the 1000 nm being deemed too thick for stable growth.

ACKNOWLEDGMENTS

We would like to thank Dr. Jacob Leach, Kyma Technologies, Raleigh, North Carolina, for expertise and steadfast commitment to III-Nitride growth and device fabrication of a very unconventional design.

REFERENCES

Berger, M. J., J. S. Coursey, M. A. Zucker, J. Chang, "Stopping-power and range tables for electrons, protons, and helium ions," National Institute of Standards and Technology, Gaithersburg, Maryland, 2005, https://www.nist.gov/pml/stopping-power-range-tables-electrons-protons-and-helium-ions, accessed September 30, 2017.

Klein, C. A., "Bandgap dependence and related features of radiation ionization energies in semiconductors," *J. Appl. Phys.* **39** (1968) 2029.

Özbek, A. M., "Measurement of impact ionization coefficients in GaN," PhD Dissertation in Electrical Engineering, North Carolina State University, Raleigh, North Carolina, 2012.

Pau, J. L., C. Bayram, R. McClintock, M. Razeghi, D. Silversmith, "Back-illuminated separate absorption and multiplication GaN avalanche photodiodes," *Appl. Phys. Lett.* **92** (2008) 101120.

Plaut, R. H., "Linearly elastic annular and circular membranes under radial, transverse, and torsional loading. Part I: Large unwrinkled axisymmetric deformations," *Acta Mech.* **202** (2009) 79–99.

Siegmund, O., J. Vallerga, J. McPhate, J. Malloy, A. Tremsin, A. Martin, M. Ulmer, B. Wessels, "Development of GaN photocathodes for UV detectors," *Nucl. Instrum. Methods Phys. Res. A* **567** (2006) 110–113.

Spicer, W. E., "Photoemissive, photoconductive, and optical absorption studies of alkali-antimony compounds," *Phys. Rev.* **112**, 1 (October 1958) 114.

Spicer, W. E., A. Herrera-Gomez, "Modern theory and applications of photocathodes," *Proc. SPIE* **2022** (1993) 158575.

Tut, T., M. Gokkavas, B. Butun, S. Butun, E. Ulker, E. Ozbay, "Experimental evaluation of impact ionization coefficients in AlxGa1−xN based avalanche photodiodes," *Appl. Phys. Lett.* **89**, 18 (2006) 183524.

Wang, X.-H., S. Feng, G. Hui, H. Cang-Lu, C. Hong-Chang, C. Ben-Kang, R. Ling, D. Yu-Jie, Z. Jun-Ju, "The optimal thickness of a transmission-mode GaN photocathode," *Chin. Phys. B* **21**, 8 (2012).

This page left blank intentionally

Drone Video Platform—Collision Avoidance, Situational Awareness, and Communications

STL-039-17 ■ Continuing in FY 2018 ■ Year 1 of 2

**Daniel Frayer,[1,a] Mary D. O’Neill,[b] Mace Mavroleon,[c] Craig Hollabaugh,[d]
Janice Lawson,[b] Rusty Trainham,[b] and Samuel Fall[b]**

[1]frayerdk@nv.doe.gov, (505) 663-2090
[a]New Mexico Operations–Los Alamos
[b]Special Technologies Laboratory
[c]Pure Engineering
[d]Keystone International

Unmanned aerial systems (UASs) operating in consequence management (CM) scenarios can obtain and transmit critical information on various hazards and inform real-time decision making while reducing risks to first responders. In this project we utilized the Sandstorm UAS, a fixed-wing development platform that is part of a complementary SDRD effort. Although a fixed-wing platform can enable longer travel and operational times, maneuverability limitations complicate the collision avoidance required to avoid post-disaster hazards. A modular situational awareness and communications infrastructure is required to support autonomous UAS mission needs. This year we developed the infrastructure requirements, designed the core module central to this concept, and began developing a collision avoidance system for the Sandstorm. When this project completes next year, we expect the UAS to field CM-relevant sensors and function as a test bed for other sensors with minimal integration. The modular infrastructure is expected to mitigate many integration issues and facilitate autonomous operations.

BACKGROUND

In July 2016, an SDRD deep dive meeting resulted in a proposed mission to develop and operate, within two years, an unmanned aerial system (UAS) carrying sensors and communications equipment, allowing real-time situational awareness of hazards and demonstrating the ability to respond to a complex radiological disaster. The proposed UAS would fly autonomously, sufficiently low and slow to allow for radiological detection, but at a high enough altitude to

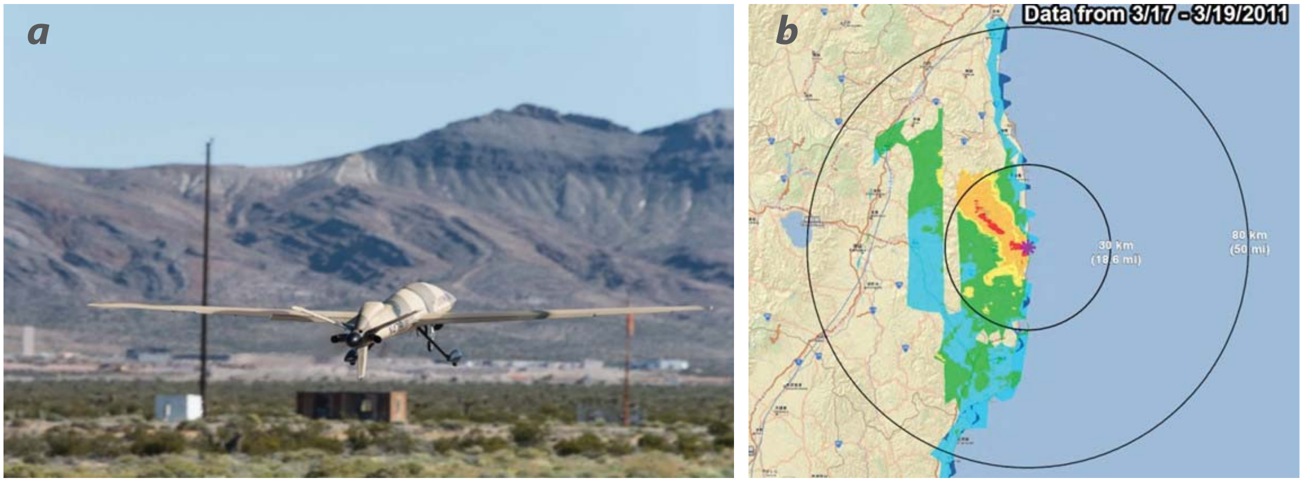

Figure 1. (a) Sandstorm, an integral part of a recent strategic initiative project, and (b) a radiological map from the Fukushima disaster produced from RSL data. This project leverages experience in these areas.

avoid unexpected obstacles. An onboard sensor suite would allow navigation in post-incident geometries and would ideally include onboard processing and algorithms for employing sensor data to react intelligently to unexpected static obstacles. Preferably, the system would field a suite of sensors that report on radiological, chemical, and biological hazards, or at least provide the flexibility to rapidly swap out sensors in the field. The system infrastructure should be standardized, simple, and flexible so that new detectors could be added by non-expert users, both for the aforementioned flexibility, and for new sensor development. The summary goal of the initiative was that we capitalize on our existing consequence managment (CM) mission and technical expertise to enable quicker and more effective response in future radiological emergencies.

From its inception, the initiative sought to leverage core capabilities and previous investments. Under the strategic initiative SDRD project "Unmanned Aircraft System for Remote Contour Mapping of a Nuclear Radiation Field" (Guss 2016, McCall 2017, Malchow 2018), we explored UAS platforms. Among the platforms purchased were two fixed-wing Sandstorms (Figure 1a), which were used in tests with radiological and chemical sensors to determine limits in mapping and detection. This strategic initiative project established a baseline for our UAS capabilities. Furthermore, the Remote Sensing Laboratory (RSL) has long operated the Aerial Measuring System (AMS) and enjoys demonstrated experience and expertise in CM and Radiological Search, among other missions. Figure 1b shows mapped data from the response to Fukushima (ca. 2011), in which many RSL personnel participated. In addition to leveraging these investments and missions, the initiative sought to incorporate the technical expertise borne of existing standard communications and video interfaces developed on other projects, such as development of EagleRay interfaces and similar technologies.

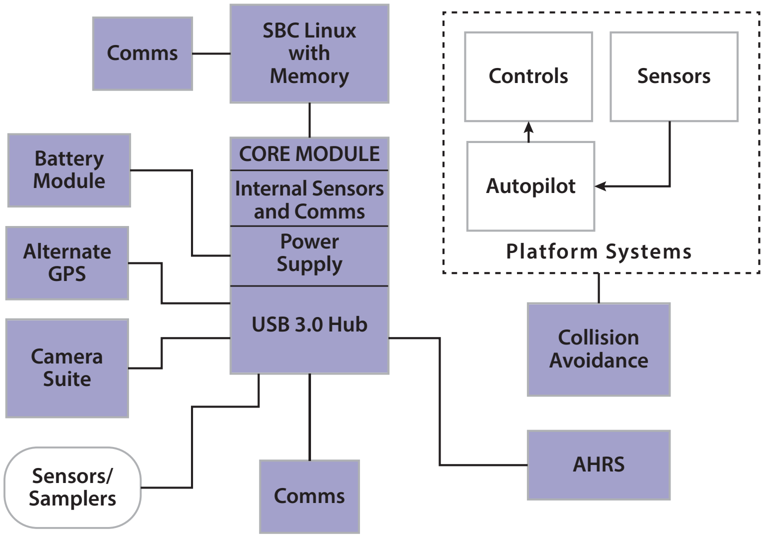

Figure 2. Blocks of the infrastructure from the interface control document (ICD) are shown in blue. These should interface with the platform, sensors, and samplers with standard interfaces, ensuring integration into any platform is rapid.

This SDRD has focused on creating an enabling infrastructure for the Sandstorm, but has, where possible, made decision choices to allow for ready scaling on other platforms. The components of this infrastructure are shown in Figure 2. Early discussions revealed the possibility of a wide array of technologies and systems that could be fielded on UASs within our core mission spaces; the core module was envisioned as providing a power, communications, and basic computing backbone necessary for most of these. Where possible, we incorporated firmware for interfacing directly with radiological sensors we possess. This module can accept an optional single-board computer (SBC) with memory if more onboard computing power is required or a sensor is already able to interface to an SBC. Multiple USB 3.0 hubs are available for attitude and heading reference systems (AHRS), communications, cameras, alternate GPS, and sensors. The battery module provides power for anything that needs power on the UAS. A distinction was made between the core module, on the one hand, and platform systems, such as the autopilot, on the other. The collision avoidance module will communicate directly with the autopilot.

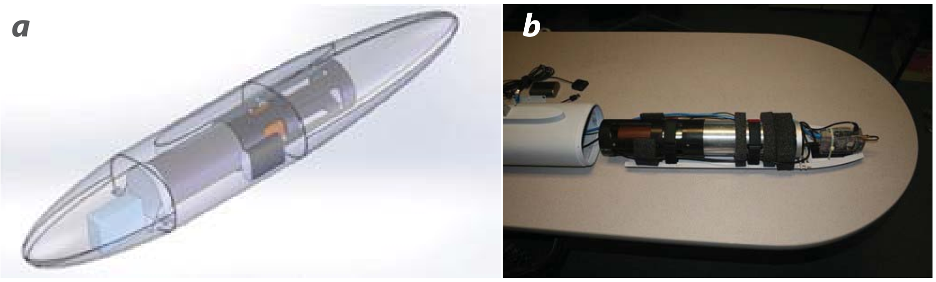

Figure 3. (a) Solid model of 3″ × 6″ NaI:Tl detector in its pod and (b) the 3" × 6" NaI:Tl detector

Figure 4. Sandstorm with the pod on the belly of the platform

Project

This two-year project consists of developing an infrastructure and performing the required staged verifications. The Sandstorm UAS flies at airspeeds from 40 to 70 knots and has a 15-foot wing span. Based on conversations with Unmanned Systems, Inc., we planned for a 5-pound budget for infrastructure and an additional 10-pound budget for sensor pay-loads. Early in FY 2017, we conducted various liter-ature and technology searches, to determine which envisioned components or subsystems might be commercially available, and to incorporate current approaches to development. We developed an interface control document (ICD) and subsystem requirements based on what was learned. As dictated by the ICD and requirements, we then completed the design for the core module, and developed the collision avoidance framework. While originally out of scope for this project, we tested a UAS to empirically determine the performance of in-house radiological sensors at heights and speeds beyond those in which we had previous experience. In FY 2018, we plan to fabricate and fully test the core module, and assemble it and the subsystems in a Sandstorm. We also plan to test collision avoidance technology on a low-cost platform and then integrate it on the Sandstorm. In addition, we plan to demonstrate modular system performance, optical/gamma data fusion, autonomous execution, and autonomous systems collaboration. At the end of the project, we will conduct a mission-relevant test.

Radiological and Chemical Testing on a UAS

As part of this SDRD, we conducted radiological testing on a UAS. In February and March 2017, we flew a 3″ × 6″ thallium-doped sodium iodide (NaI:Tl) gamma detector on a Sandstorm. This detector had a 695 mL active detector volume and 7% gamma energy resolution. It is suited for radiological surveys and localizing hot spots. Figure 3 shows the solid model of the pod used to develop the installation of the 3″ × 6″ NaI:Tl.

Figure 4 shows a Sandstorm with the pod installed on the belly of the platform. The use of this pod allows different configurations to be tested without modifying the platform. The sources for the February 2017 test were two 50 mCi ^{137}Cs sources side-by-side. Example data are shown in Figure 5.

Real-time spectral strip chart recorders for detection of the 662 keV spectra confirmed that the source

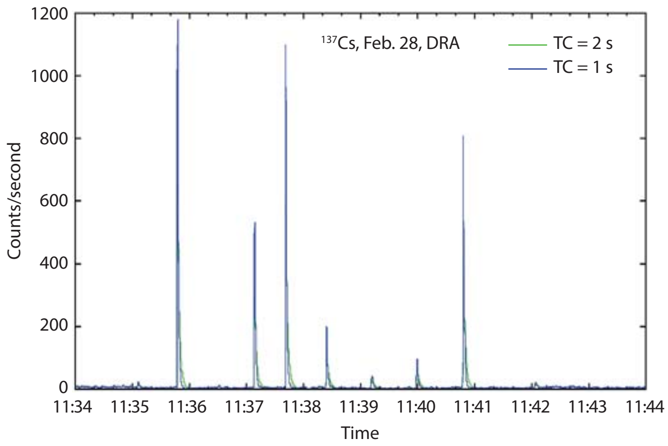

Figure 5. Example data collected on February 28, 2017, for two 50 mCi ^{137}Cs sources side-by-side. This plot shows the seven radiation hits recorded while in flight.

was ^{137}Cs. Seven above-threshold radiation hits were recorded from the air. Three below-threshold hits were also recorded: two during takeoff and landing (11:35:07 and 11:42:04) and one during flight (11:36:30).

For all tests, a Raspberry Pi was configured to acquire the data in lieu of the core module under development. It should be noted that the core module processor will provide at minimum the same basic interfaces with lower weight and power than the Raspberry Pi. Conceptually, a prototype board can be available ahead of time to allow development of the direct interface to any new sensors that might be suitable for smaller platforms.

In August 2017, we flew a chemical sensor and sampler, also developed under this project, on the Sandstorm platform. This real-time volatile organic compound sensor had six sampling tubes for post-flight mass spectrometry and allowed for on-runway post-flight chemical analysis via a Sionex unit. The solid model for this sensor is shown in Figure 6.

In September 2017, as part of an SDRD feasibility study, we flew an H3D Apollo sensor. This sensor has four CZT (cadmium zinc telluride) crystals in a 20 × 20 × 15 mm package, a 24 mL active detector volume, and a 1% gamma energy resolution. This sensor provides gamma directional and imaging capability, which can help with many of our missions in locating radiation sources.

In September 2017, we also flew a 2×2 NaI:Tl gamma detector on a 3DR Solo Quadcopter, as shown in Figure 7. This test allowed us to determine the ability of flying radiation sensors on a small platform. This sensor has a 103 mL active detector volume, with a 6.5% gamma energy resolution. Because this quadcopter has the ability to hover in place (or land), it can integrate signal much longer than on the fixed-wing platform, and may thus expand our UAS capability for the radiological mission. An example spectrum for a 20-second integration time is shown in Figure 8.

Infrastructure

The infrastructure consists of the following subsystems, as shown in Figure 2:

- Core module
- SBC
- Battery module
- Communications
- AHRS
- Camera suite
- Collision avoidance subsystem

To minimize integration issues during actual testing, we purchased a Sandstorm fuselage and are using it to set up and test electronics in situ at STL.

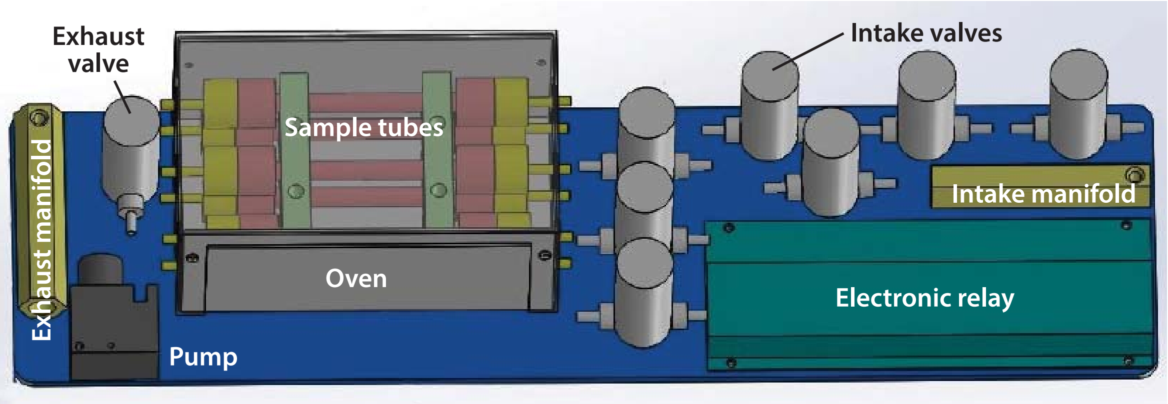

Figure 6. The chemical sensor measures 4″ × 15″

Figure 7. 2×2 NaI:Tl gamma detector on the 3DR Solo Quadcopter

The core module is the key subsystem for the UAS system. The core module and the battery subsystem will be used in all UAS platforms, and a prototype of the core module has been designed as a single circuit board; however, the final article will have three PCBs, internal sensors, comms, a power supply, and a USB PCB (Figure 9), minimizing its overall size. The three PCBs will stack using built-in connectors; allowing each PCB to be tested or replaced separately. The board design is complete, all parts have been purchased and will be assembled and tested in FY 2018.

While the core module can perform basic computing, it will not be able to perform image processing or provide sensor data overlay capability; the optional SBC will provide this capability. Processors such as a Raspberry Pi or ODroid, along with "stick" computers such as those shown in Figure 10, can be connected to this core module. It should be noted that the core module can enable deployment of sensor systems with built-in processing capability, but need external power and communications.

The core module will also provide basic comms with a low data rate of about 100 kbps. The modular infrastructure allows the addition of longer range or higher data rate comms, or cellular sticks such as those shown in Figure 11, according to mission needs.

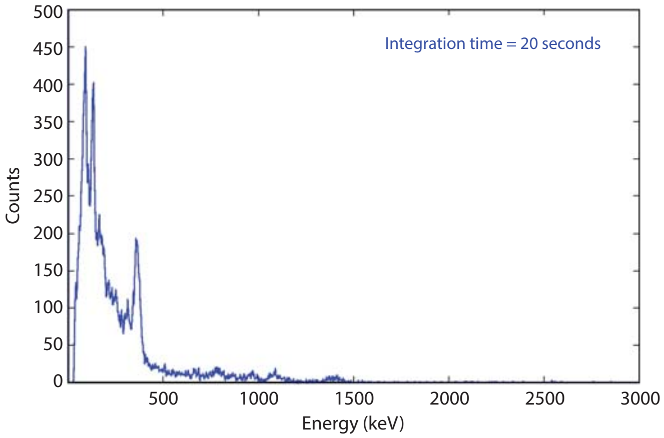

Figure 8. Spectra from a 2×2 NaI:Tl gamma detector on 3DR Solo Quadcopter using a 20-second integration time

Table 1. Power budget by subsystem. This conservative estimate indicates that we can design for 50 W.

SUBSYSTEM	CURRENT AT 5 V (A)	CURRENT AT 3.3 V (A)	CURRENT AT 12 V (A)	SYSTEM POWER NEED (W)
Core module	0.05	0.11		0.613
AHRS		0.25		0.825
Collision avoidance		5		16.5
Cameras	1.2			6
Communications			0.35	4.2
Radiological sensors	0.32			1.6
CPU modules	1			5
Chemical sensors	0.4			2
Subtotal total nom (I)	2.97	5.36	0.35	
85% power supply efficiency	0.4455	0.804	0.0525	
Total nom (I)	3.4155	6.164	0.4025	
Total nom	17.0775	30.82	2.0125	49.91

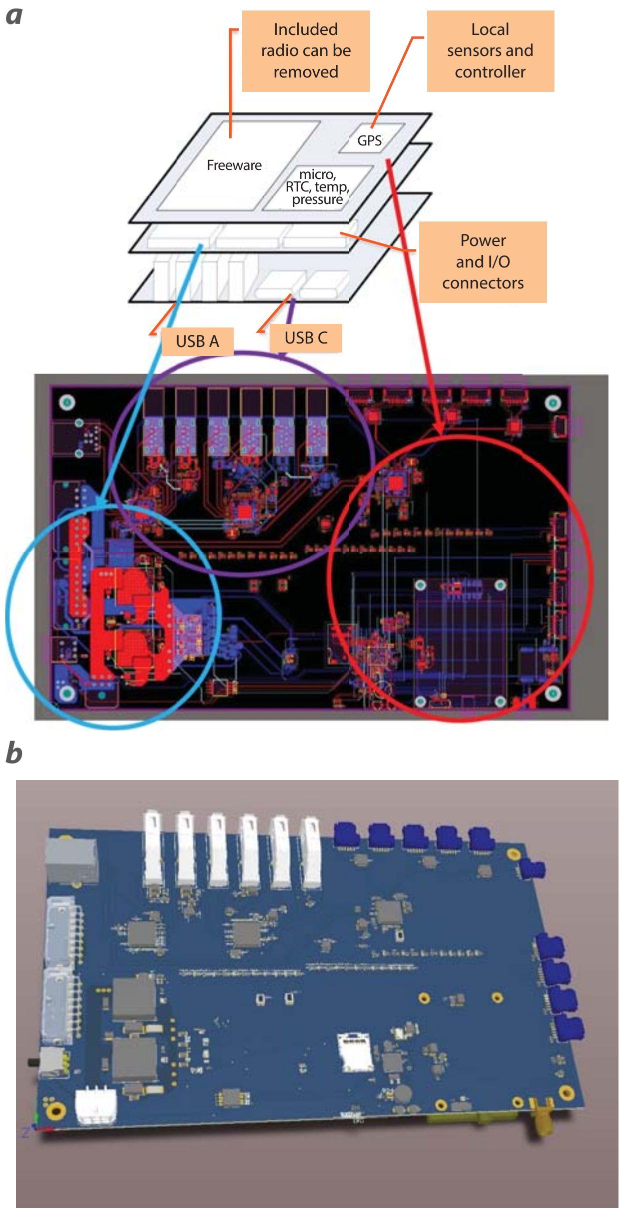

Figure 9. (a) Prototype core module layout shows internal sensors and how the single PCBs will evolve into three—a comms PCB, a power supply PCB, and a USB PCB. (b) The single 8″ × 5″ board will be tested on the Sandstorm.

The power budget we developed is shown in Table 1. The budget is conservative, and assumes that all subsystems are both powered and drawing their maximum rated power. This assumption results in a power requirement of about 50 W. We designed the power distribution system to allow flexibility for growth. Modular battery packs of 18650 Li-Ion cell batteries were incorporated into the design. These packs can be stacked to provide voltage in multiples of 3.3 V, and the power distribution system can take these battery outputs and distribute the 3.3, 5, and 12 V required for subsystems and sensors for a given mission. This modularity allows only the battery weight needed for a given mission to be installed on the platform.

The AHRS subsystem provides attitude information including pitch, roll, and yaw. AHRS data can be converted from an aircraft coordinate system to an earth coordinate system as the platform flies through a scenario. A traditional inertial measurement unit (IMU) does not include the processing to provide attitude and heading. This system will be purchased or the AHRS data may be provided by the onboard autopilot. The derived requirements for this subsystem are given in Table 2.

The camera subsystem will provide situational awareness for a pilot and context imagery for sensors that have directionality, but is not a substitute for a high-resolution imagery required for mapping. The camera module may be a single camera or a suite of cameras that provide hyper-hemispheric coverage. This subsystem will be mounted on the underside of the platform and fit in a 4″ diameter dome that protrudes no more than 2.5″ from the platform skin. A standard USB data cable using a micro USB-B connector connects this subsystem to the main processor. The data interface is intended to allow downlink of low-rate video with directional sensor detection overlay via the UAS comms. Specifications for the camera subsystem are given in Table 3.

A number of COTS standard gimbal configurations are under consideration for this module. Possible gyro-stabilized, low-weight, low-power cameras are shown in Figure 12. The original SDRD proposal included the concept of developing a “virtual” gimbal camera system as a desirable camera subsystem. A virtual gimbal would have multiple cameras that could be tasked depending on the desired direction of imaging. Among those shown, the VIOOA camera includes

Figure 10. Example stick computers; typical size is 4″ × 1.5″ × 0.5″ and weight of 1.9 oz

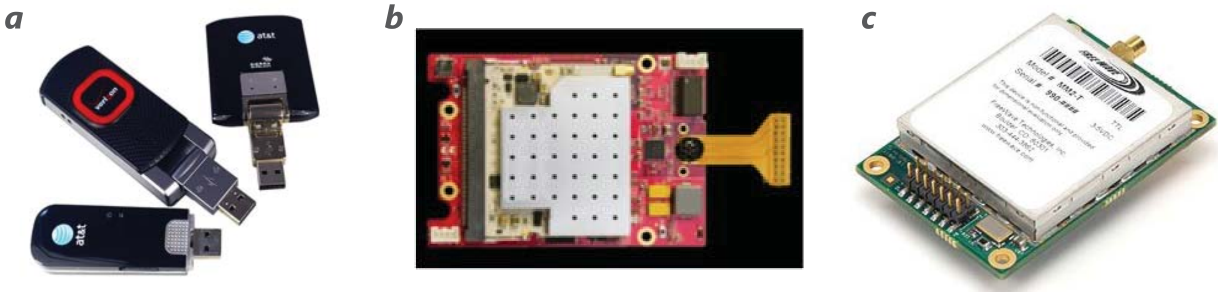

Figure 11. Optional added capabilities include (a) cellular sticks; (b) WaveRelay with long-range, high-rate capability; and (c) a low data–rate, long-range FreeWave comm module

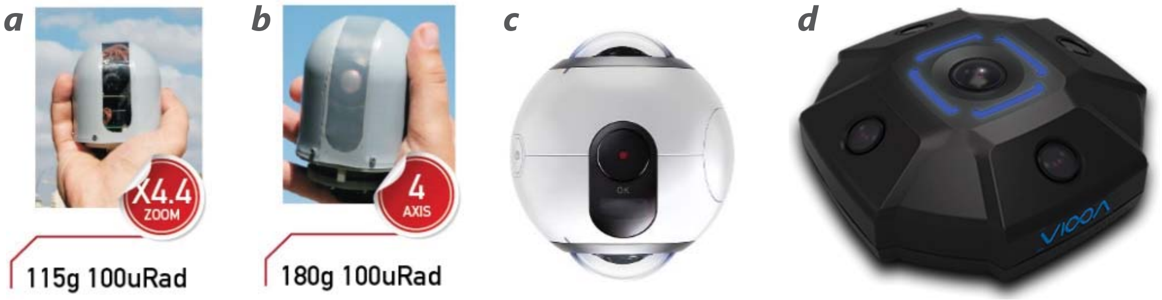

Figure 12. Example cameras include the (a) TOR Robotics, (b) TOR MCD, (c) TOR MCU, and (d) Samsung Gear 360 SM-C200 virtual gimbal camera VIOOA for drones (176 g+110g adapter)

Table 2. Key AHRS Requirements

PARAMETER	VALUE
Update rate (selectable)	1 × 100 Hz
Startup time	<1 second
Full accuracy warm-up time	<30 seconds
Pitch range	±90°
Roll range	±180°
Heading range	0° to 360°
Pitch, roll, and heading resolution	<0.01°
Pitch, roll accuracy	<0.4°
Heading accuracy	<0.1°
Noise (@100 Hz)	<0.025° RMS
Operating temperature	0°C to 40°C
Weight	<3 oz
Power	<0.5 W
Size (l × w × h)	<2.2″ × 1.1″ × 1.1″

what they also call a virtual gimbal, negating our need to develop this subsystem. More investigation and final selection of the configuration will be done in FY 2018.

While collision avoidance is available for rotary-wing platforms, it is not commercially available for fixed-wing platforms. Research into viable solutions for the Sandstorm revealed two candidates, the high-speed, autonomous, pushbroom stereo method (Barry 2014, 2017) and Opto-Knowledge Systems, Inc.'s proprietary research for the U.S. Navy. The work by Barry is open source, and was demonstrated on a small UAS flying at approximately 25 knots (Barry 2015), about half that of the Sandstorm, but the Sandstorm's 15-foot wing span is more than five times that of the 34-inch platform used by Barry. We modeled performance of a scaled-up, at higher speeds but with cameras farther apart, and determined that this approach is viable for use on the Sandstorm. Because it is open source and readily scalable, we decided to use Barry's collision avoidance method.

Barry's method places one camera on each wing such that the depth can be determined by pixel shifts between the images. Traditional algorithms search the obstacle field through multiple distances, making the computation time too lengthy to allow for typical fixed-wing fights. Barry's method recognizes that at

Table 3. Camera Subsystem Requirements

PARAMETER	VALUE	NOTES
Power	<6 W	
Instantaneous field of view	<0.5 mrad	0.5 m at 1 km resolution
Field of regard	>85° diagonal	
f/#	<3	
Shutter speed	4–1/8000 second	At 70 knots, 400 ft altitude, 0.35 ms, ~0.1 mrad
Frame rate	≥30 fps	
Full angular coverage	>240 Az × 60º El	Forward-looking hemispheric coverage
Connector interface	USB3	
Storage	>128 Gbytes	
Operating temperature	0°C to 40°C	
Weight	<10 oz	
Size (l × w × h)	<4″ × 4″ × 5″	Dome protrudes from the fuselage

drone speeds, the images do not significantly change between frames. This method allowed a smaller subset of obstacle field depth measurements. The distance between these measurements is dictated by the minimum distance to avoid objects, and is specific to a given platform. In Barry's demonstration, the distance between measurements was 10 meters. As his UAS traveled, this 10-meter horizon was pushed forward (as in sweeps of a pushbroom); this feature allows the software to build a full map of the surroundings. This method allowed real-time computation and the ability to fly through, and avoid, trees at 25 knots (Barry 2015).

This project was originally formulated as a combination of COTS or on-hand components and methods with development of a wayfinding and collision-avoidance system. It turned out that, just after the project started, MIT published on just such a system. We are attempting to duplicate the system, based on the MIT material, so that we can scale it up for our platform and application.

CONCLUSION

This SDRD was driven by the need to operate UASs with sensors to return high-value data in disaster scenarios. This mission requires the ability to avoid post-disaster hazards and communicate pertinent information to the ground. In the first year of this project we developed an ICD and system architecture for the required modular situational awareness and communications infrastructure to support this UAS mission. We designed the core module, which is central to this infrastructure. We began work on the collision avoidance subsystem based on the work of A. Barry of the MIT Computer Science and Artificial Intelligence Laboratory (CSAIL) (Barry 2014, 2017). Requirements were drafted and COTS components were researched for those most suitable for this infrastructure.

In FY 2018 we will complete infrastructure fabrication, test the core module, and integrate the collision avoidance subsystem into our Sandstorm fuselage at STL and then into the full platform. On the Sandstorm, we will perform modular system testing, optical/gamma data fusion testing, autonomous execution, and systems collaboration.

Completion of this project next year will allow a nearly plug-and-play capability for many DOE-specific sensors onto UAS platforms. It will create a test bed for other sensors with minimal integration, and it will eliminate many integration issues due to the modular infrastructure with established interfaces and capabilities.

ACKNOWLEDGMENTS

The authors wish to thank Karen McCall and Eric Wagner for their insights related to development of platform capabilities. We would also like to thank Lance McLean for his expertise related to the AMS and other radiological missions.

REFERENCES

Barry, A. J., R. Tedrake, "Pushbroom stereo for high-speed navigation in cluttered environments," https://arxiv.org/pdf/1407.7091.pdf, 2014, accessed February 10, 2017.

Barry, A. J., "Flight code for MIT CSAIL Robot Locomotion Group flying-through-forests project," https://github.com/andybarry/flight, 2015, accessed February 20, 2017.

Barry, A. J., P. R. Florence, R. Tedrake, "High-speed autonomous obstacle avoidance with pushbroom stereo," *Journal of Field Robots, Special Issue on High-Speed Vision-Based Autonomous UAVs*, 2017, http://groups.csail.mit.edu/robotics-center/public_papers/Barry16a.pdf, accessed March 28, 2018.

Guss, P., et al., "Multiple unmanned aircraft system for remote contour mapping of a nuclear radiation field," in *Site-Directed Research and Development*, FY 2015, National Security Technologies, LLC, Las Vegas, Nevada, 2016, 1–13.

McCall, K., et al., "Multiple unmanned aircraft system for remote contour mapping of a nuclear radiation field," in *Site-Directed Research and Development*, FY 2016, National Security Technologies, LLC, Las Vegas, Nevada, 2017, 11–22.

Malchow, R., et al., "Multiple unmanned aircraft system for remote contour mapping of a nuclear radiation field," in *Site-Directed Research and Development*, FY 2017, National Security Technologies, LLC, and Mission Support and Test Services, LLC, Las Vegas, Nevada, 2018, 9–18.

This page left blank intentionally

Man-Portable Dense Plasma Focus for Neutron Interrogation Applications

NLV-009-17 ■ Continuing in FY 2018 ■ Year 1 of 2

Brady Gall,[1,a] Nichelle Bennett,[b] Tim Meehan,[a] Michael Heika,[a] Michael Blasco,[a] Vincent DiPuccio,[a] Joseph Bellow,[a] Adam Wolverton,[a] James Tinsley,[c] and Robert O'Brien[d]

[1]gallbb@nv.doe.gov, (702) 295-3117
[a]North Las Vegas
[b]New Mexico Operations–Sandia
[c]Special Technologies Laboratory
[d]University of Nevada, Las Vegas

The reliable detection of special nuclear materials continues to be a primary goal of global security programs conducted by Defense Nuclear Nonproliferation agencies. While these programs are diverse, many of them share a core need for a small, robust, pulsed neutron generator. This project addresses this need by building a man-portable dense plasma focus (DPF) neutron source. Because it is often quite large and requires heavy machinery for transport, DPF technology seems an inconsistent choice for a compact generator. Nevertheless, it offers many benefits that are infeasible using conventional neutron sources: it can generate intense neutron pulses, operate at relatively low voltage, and be scaled to a lightweight form factor. In FY 2017 we designed a new compact DPF plasma source using particle-in-cell simulations and tested a novel tabletop pulsed power driver system. In FY 2018 we will perform measurements of neutron output and configure the tabletop system into a field-portable device.

BACKGROUND

The dense plasma focus (DPF) device has long been considered an inexpensive, compact source for generating pulsed neutrons (Mather 1964, 1965; Bernard 1977), and it is currently being explored for a range of applications from activation analysis and plasma nanotechnology to radiography and material detection (Gribkov 2006, Zhang 2007, Hussain 2010, Krishnan 2012, Rawat 2013). Recent DPF developments have focused on increasing the device's portability and pulse repetition rates (Lee

1998, Rapezzi 2004, Shukla 2015, Niranjan 2016). This project is leveraging these advances in portable pulsed power technology and our existing expertise in large-scale DPF systems to build a compact device capable of meeting the needs of global security's neutron-based programs, including nuclear search, warhead confirmation and monitoring, and render safe (Office of Defense Nuclear Nonproliferation 2018). These programs involve an object or container under investigation to be probed with neutron radiation. For many reasons, it is not practical for test objects to be brought to a central location for neutron probing. Therefore, a reliable, high-flux neutron source must be developed that can be brought to the object's location instead. The source must produce at least 10^6 neutrons per second, be reasonably portable and rugged, and be simple to operate (NNSS 2016). Such a source would enable us to accomplish these mobile applications.

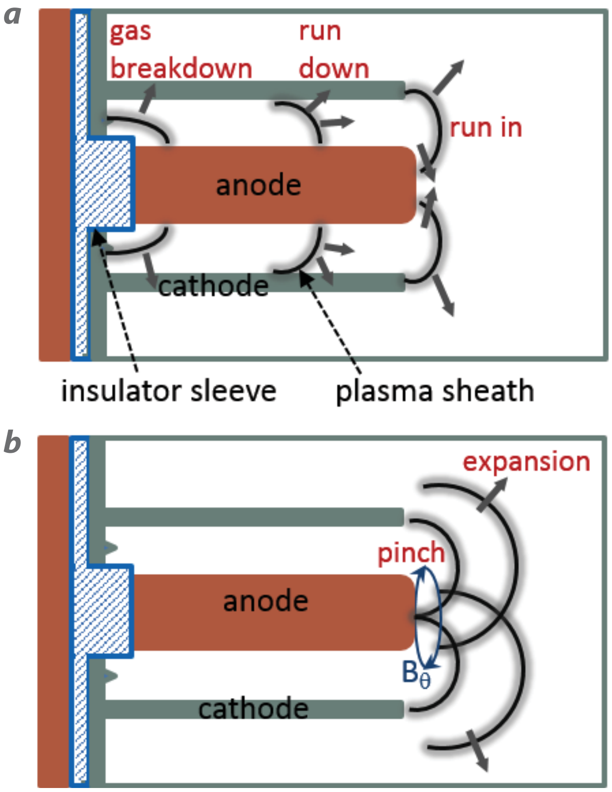

Figure 1. The DPF operation illustrated in four phases. During gas breakdown, the voltage pulse is injected through the insulator sleeve (blue), and a plasma sheath (black) is formed between the anode tube (brown) and the cylindrical cathode (grey). This sheath is accelerated axially during run-down and radially during run-in. After the pinch, the plasma expands radially and axially to the walls of the vacuum chamber (not pictured).

Most commercial compact neutron sources, such as the Adelphi DT108API, operate in continuous mode to achieve neutron flux rates up to 10^8 neutrons/second (deuterium-tritium [D-T]) (Adelphi Technology 2016). However, continuous operation is not ideal for active interrogation applications. Rather, the preferred source is a pulsed generator because it provides a low background window of generator off-time for measuring prompt and delayed target responses. Another benefit of pulsed operation is that the sensing instrumentation can be synchronously gated with the active duty cycle of the source, increasing the signal-to-noise ratio of the interrogation system. To remain competitive with the average yield of continuous sources, the instantaneous yield of the pulsed generator must be very high.

Categorically, the DPF is an ideal candidate for mobile, neutron-based applications for many reasons. First, as a pulsed source, it is favorable for target response sensing applications like special nuclear material detection. Next, DPFs are potent neutron sources, especially considering their size compared to other technologies. According to modeling results, we expect our optimized DPF design to generate up to 10^8 neutrons/pulse. Finally, DPF systems operate between 10 and 30 kV, which is 3 to 10 times lower than conventionally energized neutron sources. As a result, the auxiliary components can be minimal, enabling a compact form factor. These strengths support characteristics necessary to accomplish mobile neutron interrogation.

PROJECT

This project is a two-year endeavor to design and build a portable DPF for Defense Nuclear Nonproliferation (DNN) applications. In this first year we designed a new DPF plasma source geometry, procured compact high-voltage hardware, developed control system software, and assembled and tested a tabletop pulsed power prototype. In FY 2018 we will test the new DPF source and shrink the tabletop system into a portable form factor. The end result will be a rugged, easy-to-operate, and portable DPF neutron source.

This section describes work completed this year. First a brief overview of the basic principles of the dense plasma focus is presented. Then the modeling and optimization methodology is discussed. The details of the hardware design and configuration for the benchtop pulsed power prototype and the test results of the prototype are given. Finally, we present the radiological safety analysis operating at the nominal output field of 1 × 10^8 neutrons per pulse.

DPF Operation

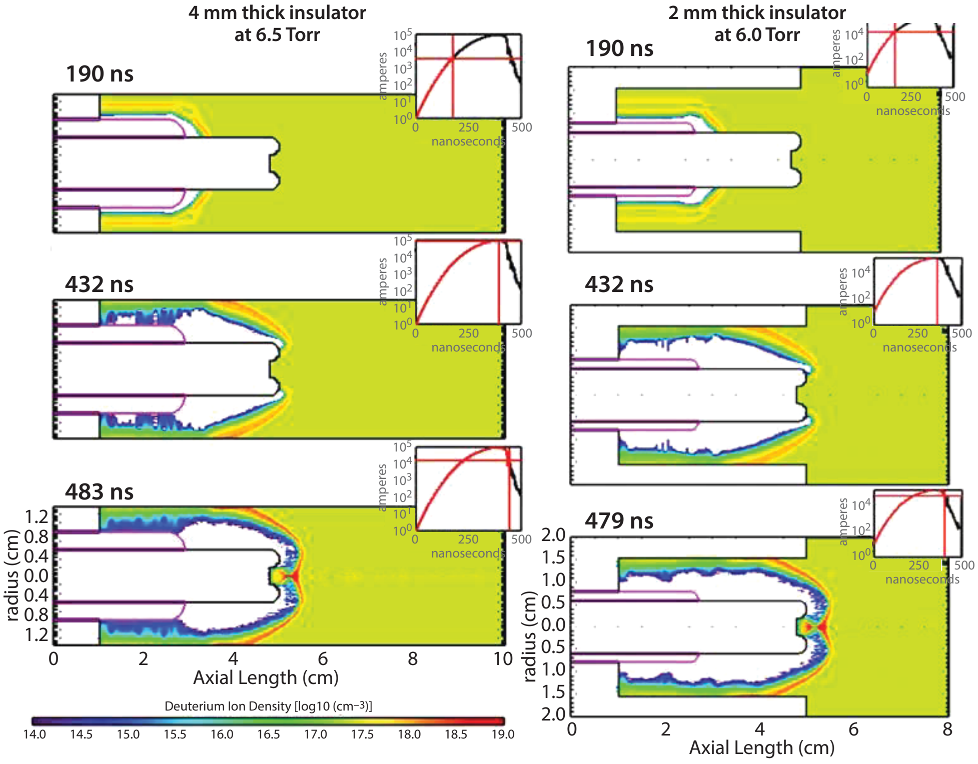

Figure 2. Simulated ion density contours for two DPF designs with toroidal anodes and insulators that are 4 mm and 2 mm thick. Densities are plotted (on a log scale) during run-down (190 ns), run-in (423 ns), and pinch (480 ns). Inset plots show anode input current with crosshairs indicating progress in the run-down phase. The x-axis limits are from 0 to 500 ns, and the y-axis limits are from 0 to 1 × 10^5 A.

The DPF device is a coaxial accelerator with a blunt anode termination that is filled with a low-density gas, typically deuterium (labeled DD [deuterium-deuterium] for the interacting ions), or a D-T mixture. The cathode is a hollow cylinder comprising either a solid wall or bars of conductor with an open area fraction of approximately 50%. As the accelerator is pulsed, the gas ionizes and accelerates through the $\boldsymbol{j} \times \boldsymbol{B}$ force to the end of the anode. The plasma pinches at the anode tip with sufficient velocity to create neutrons by fusion processes.

Four phases comprise DPF operation, as shown in Figure 1. The gas ionizes in the first phase with the arrival of a high-voltage pulse. The conductivity increases rapidly as the current-carrying plasma sheath is formed. As the current rises and the $\boldsymbol{j} \times \boldsymbol{B}$ force increases, the plasma sheath is accelerated to the end of the anode. This second phase is referred to as run-down. The third phase, or run-in, occurs after the plasma sheath reaches the end of the anode and is accelerated radially inward. In the final pinch phase, the plasma densities and temperatures (energies) have increased sufficiently to enable fusion reactions.

DPF Tube Optimization

The DPF hardware design described in the previous section has remained relatively unchanged since it was first fielded. In a recent paper, we demonstrated that the Mather-type DPF must adhere to a narrow range of anode and cathode dimensions and operating pressures to ensure gas breakdown and still be compatible with low-impedance operation for a given capacitor bank (Bennett 2017a). Therefore, as we investigate design changes for optimizing the neutron yield, we are making only modest changes to the shape of the anode termination. We did not change the cathode and elected to only investigate a bar-shaped cathode geometry. We first describe the simulation technique and then the simulation results for five anode shapes.

The simulations of the DPF are performed using the fully relativistic magnetohydrodynamic (MHD) particle-in-cell (PIC) code, Chicago, from the developers of LSP (Welch 2001, 2004, 2007; Rose 2002). Using a hybrid fluid/kinetic treatment (Offermann 2016), the plasma is modeled as a quasi-neutral, Eulerian fluid during the run-down and run-in phases, after which the particles are transitioned to a kinetic treatment for the pinch (Bennett 2017b). A single fluid particle is transitioned to thousands of electron and ion particles per cell in a manner that conserves momentum and charge. These kinetic particles are then advanced via their individual momenta, binary collision frequencies, and fusion interactions with no assumed distributions.

The simulations are initialized with deuterium plasma. All D-D and D-T fusion reactions are modeled, and the resulting proton, tritium, ^{3}He, and neutron particles are treated kinetically. The simulations are conducted in

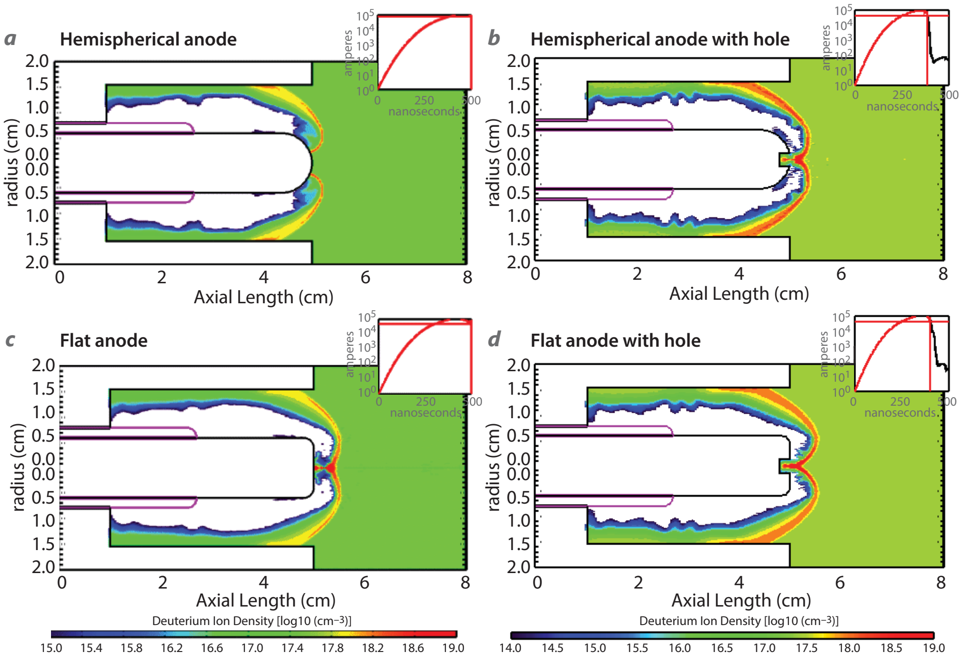

Figure 3. Simulated ion density contours during the pinch phase for four anode shapes: (a) hemispherical, (b) hemispherical with a 15 mm radius hole, (c) flat, and (d) flat with a 15 mm radius hole

2-D cylindrical coordinates (*r*,*z*). The resolutions in the pinch region are 100 µm and 107 µm in the radial and axial directions, respectively. Plasma motion through the cathode bars is approximated in 2-D using a transparency model by which a prescribed fraction of incident particles are absorbed.

The simulation technique described above was applied to nine simulation geometries. The first five were used to identify the best anode length and gas pressure for the capacitor bank with a 400 ns quarter wave discharge and 120 kA peak current. Anode lengths of 4, 5, and 7 cm were tested with densities of 6, 6.5, and 2 Torr. The best correspondence of peak current and plasma pinch is achieved with the 5 cm long anode at 6 Torr. We then determined the best insulator wall thickness for this small geometry and concluded that 2 mm provided a slightly better sheath shape compared to a 4 mm thick insulator. The test simulations for the insulator thickness use a toroidal anode termination, as illustrated in Figure 2. This figure shows the ion densities during run-down, run-in, and pinch. The thinner insulator appears to provide some mitigation of plasma restrike, but both insulators appear acceptable.

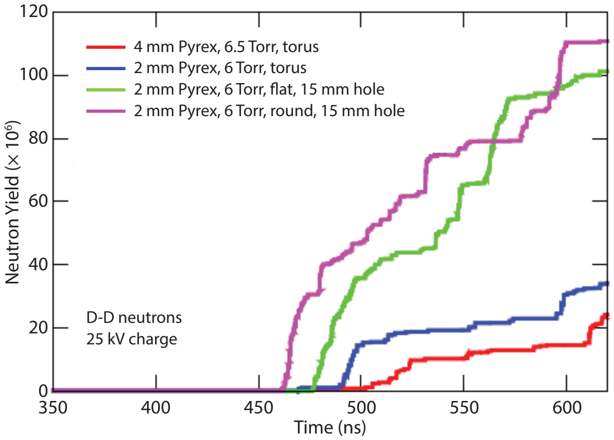

Figure 4. Neutron yields for the toroidal, hemispherical, and flat anodes with 15 mm holes on axis, as shown in Figures 2 and 3. The flat and hemispherical anodes generate three times the yield of the toroidal anode.

Focusing on a 5 cm long anode with a 2 mm thick insulator at 6 Torr, we investigated four additional anode terminations: hemispherical, hemispherical with a 15 mm radius hole on axis, flat, and flat with a 15 mm radius hole. The hole diameter was determined in a prior optimization study. These geometries are illustrated in Figure 3, which shows the ion densities during the pinch phase (after 450 ns).

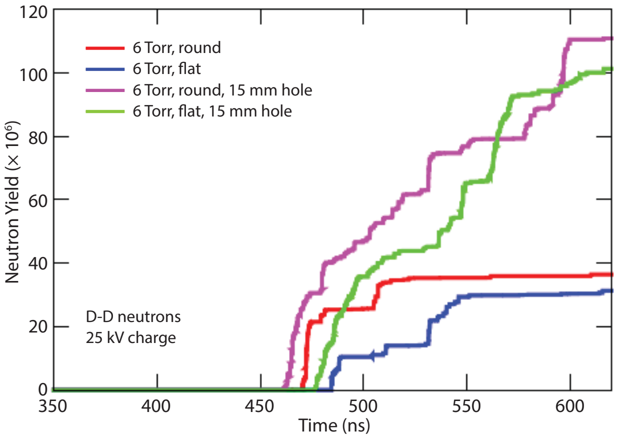

Figure 5. Neutron yields for the hemispherical and flat anodes with and without holes. Neutron yield is markedly increased by the anodes with holes.

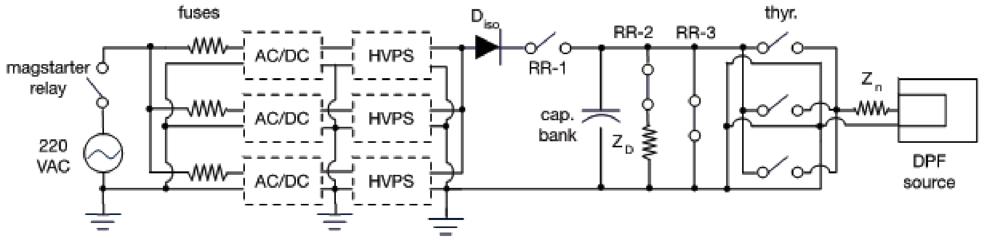

Figure 6. Circuit diagram for portable DPF system

The neutron yields for all the geometries with holes (toroidal, flat, and hemispherical) are compared in Figure 4. The flat and hemispherical anodes generate three times the yield of the toroidal anode. The plasma sheath thins prematurely in the toroidal design, tens of nanoseconds prior to the initiation of fusion reactions. It is possible to reduce the diameter of the hole interior to the torus, but this design would appear very similar to the flat anode with a hole.

Finally, Figure 5 plots the neutron yields for the hemispherical and flat anodes with and without holes. The holes perturb the plasma, seeding an $m = 0$ instability, which enhances beam-target fusion by increasing the high-energy tail of the ion energy distribution.

Pulsed Power Test Bed

At a minimum, the final embodiment of the delivered system must meet two requirements to satisfy the needs of a portable neutron generator for DNN applications. The first requirement is that it must generate at least 10^6 neutrons per second. The second requirement is that it must be sufficiently portable for field use. These requirements conflict with one another; smaller systems generate lower neutron yield. This is because neutron yield is largely a function of the maximum current that can be delivered to the DPF load. For example, large-scale machines such as the 1 MJ DPF located in North Las Vegas (NLV) operate at 2.2 MA and generate up to 10^{11} neutrons per pulse. While the neutron output is indeed prolific, the machine weighs approximately 25,000 lb and is prohibitively large for conventional portable applications. Fortunately, only a fraction of the nominal output of the NLV DPF is necessary to accomplish most portable neutron interrogation applications (NNSS 2016). A machine that can generate 10^7 neutrons once every ten seconds is all that is required to meet DNN applications specifications. This reduces the peak current required to approximately 100 kA (Lee 1996, 2010; Krauz 2012), greatly reducing the physical size of the system. This section details the design and construction of a pulsed power test bed made entirely from components that can fit into a small, portable case, operate on battery power, and deliver the necessary peak current to drive a DPF to produce sufficient neutron yield for portable active interrogation applications.

Figure 6 shows the basic circuit diagram for the pulsed power module. The prototype was powered by single-phase 220 VAC power. This was selected in favor of 120 VAC to reduce the current draw of the system and allow it to operate on a single circuit breaker. A magstarter relay controlled the flow of power to a parallel arrangement of three Mean Well NES 350 analog-to-digital converters (ADCs). A 5 A slow-blow fuse was installed at the input of each ADC for front-end electrical protection. When configured for 220 V, the ADC supplies each drew a nominal current of 4 A and supplied 24 V at 14.4 A DC. Power monitors installed at the AC power source provided real-time measurement of the power draw of the system, which typically reached approximately 700 W. Using this system, the 3.0 µF capacitor bank was charged to 25 kV in approximately 6 seconds, which is an appropriate repetition rate for portable active interrogation applications. Furthermore, the power draw of the system was compatible with high-capacity lithium ion batteries, enabling a portable form factor for future evolutions of the pulsed power system.

An array of three parallel Ultravolt 30C24 high-voltage power supplies were used to deliver high voltage to the capacitor bank. A 50 kV TDK diode was used to isolate the power supplies from negative-going high-voltage reflections that can occur when the capacitor bank is discharged into the plasma load. A suite of three E40-DT-40 Ross relays were used to provide multiple layers of fail-safe protection. Ross relay 1 (RR-1) was located between the isolation diode and the capacitor bank and was configured to be normally open. This provided an air gap between the high-voltage power supplies and was a visual confirmation that the power supplies were physically disconnected from the capacitor bank. RR-2 was a normally closed relay that was used to dump residual stored energy in the capacitor bank to a water resistor and inductive load. Finally, RR-3 was a backup normally closed relay

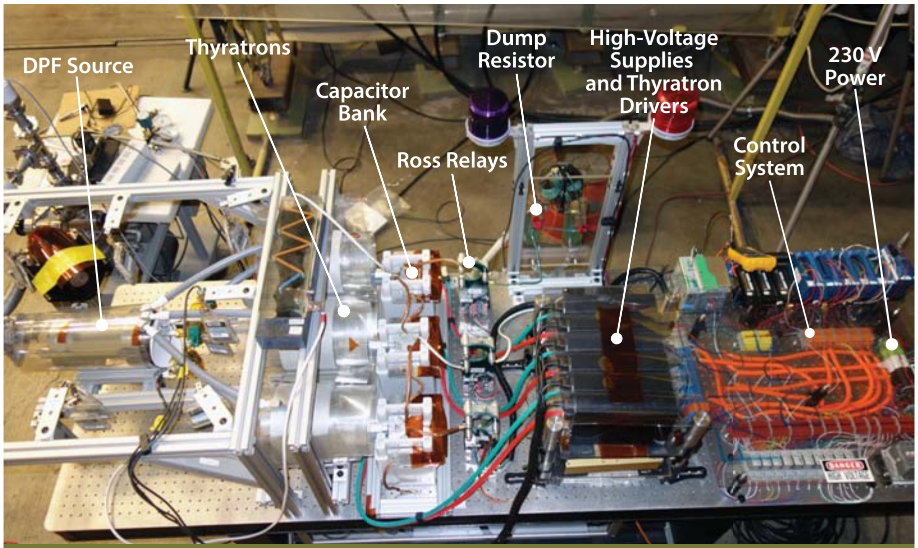

Figure 7. Benchtop prototype of the portable DPF system

that directly shorted the capacitor bank to ground. In the case of a total loss of power or communications, spring-loaded solenoids would revert the system to a safe, stable configuration. The capacitor bank comprised six parallel General Atomics S/SS 31150 0.5 μF capacitors with a total capacitance of 3.0 μF. High-voltage switching was achieved using a parallel arrangement of three Pulsed Power Solutions TDI4-100k/45H thyratrons. The thyratrons were triggered simultaneously using a Stanford Instruments 535 delay generator and driver units supplied by the vendor. The network had complex loss terms (shown as Z_n), and it primarily consisted of a series inductance and resistance with nominal values of 40 nH and 0.1 Ω, respectively. The DPF plasma source was housed within a 6″ CF vacuum chamber, and high-voltage isolation was provided with layered sheets of Mylar.

The DPF anode and cathode geometry used in the preliminary testing was reclaimed from a previous experiment and was not the optimized geometry described in the previous section. Fabricating a new DPF tube is non-trivial and was deferred to the second year of the project. While not an exact match, the fielded DPF tube was similar to the optimized geometry, with a length of 10 cm and radius of 0.5 cm.

Low-voltage logic was implemented using the National Instruments Compact Field Point platform. A custom control system was developed for the DPF using the LabVIEW environment. Safety was the first priority in operating the prototype system. Fiber-optic communications allowed for the system to be operated remotely in a control room, and closed-circuit television was used to monitored the system during operations. A two-key system was used to ensure that the machine could not be energized during maintenance operations. The Ross relay system ensured the capacitors were in a shorted configuration whenever either key was removed from the control panel. As an added precaution, personnel would manually confirm absence of voltage on the capacitor bank using a resistive shorting hook prior to maintenance activities. The prototype DPF test bed in place in the NLV A1 high bay is shown in Figure 7.

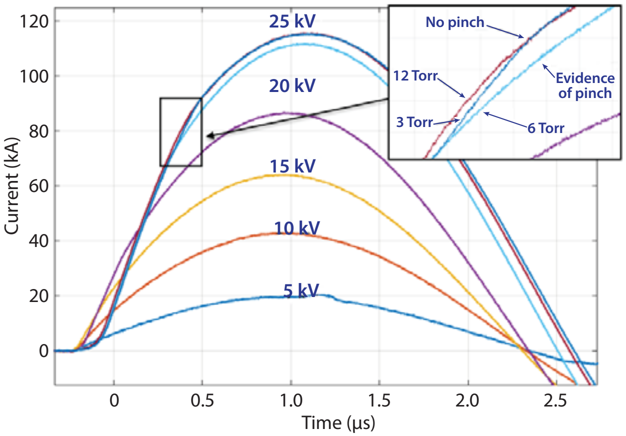

Figure 8. Discharge current waveforms from 5 to 25 kV at 5 kV intervals charging potential on the benchtop prototype DPF system

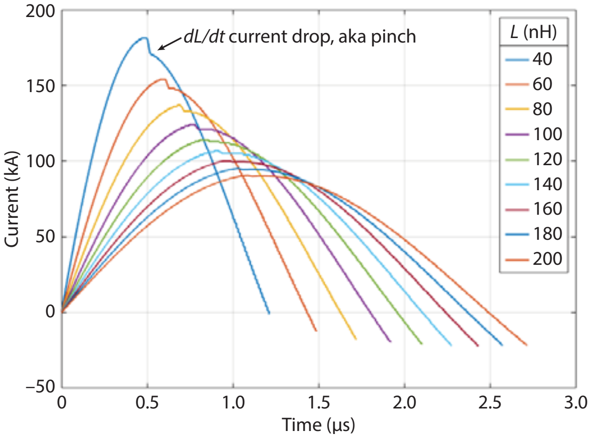

Figure 9. Modeled discharge current waveforms for a 3.0 μF capacitor bank and 4 cm long DPF anode with increasing system inductance

Experimental Results

On September 28, 2017, the compact pulsed power bank was first energized to high voltage. A suite of diagnostics were used to measure the output of the system. A 1200:1 voltage divider measured the charge voltage of the capacitor bank. Three Pearson 8631 current monitors with 2000A/V sensitivity measured the shot current of each thyratron. Two neutron time-of-flight Hamamatsu photomultiplier tubes coupled to an Eljen EJ 232 scintillator, positioned 15 cm and 1 m from the pinch, detected gamma and neutron pulse waveforms. Data were recorded using Teledyne LeCroy HDO 6104 12-bit, 2.5 GS/s digitizers. An array of eight facility area monitors were positioned around the device to measure the dose as designated by the radiation-generating device (RGD) project manager. The pressure of deuterium gas supplied to the plasma chamber was measured using a Baratron pressure transducer.

A high-voltage integrity test was conducted on the capacitor bank prior to discharging to the plasma chamber load. The bank was energized in 5 kV increments from 5 kV up to the nominal shot voltage of 25 kV. After each test, the bank was discharged into the water resistor load, and the crew inspected the machine for signs of damage. At approximately 20 kV, the capacitor bank arced from anode to cathode due to a surface flashover on the Kapton insulator. We reconfigured the insulator to prevent surface flashover and resumed the test; no further flashovers were observed. With the high-voltage integrity test complete, the machine was ready for discharging into the plasma chamber load.

The thyratron vendor recommends conditioning the thyratron switches prior to operating at full voltage. The conditioning process was similar to the high-voltage integrity test, consisting of incrementally stepping the units to higher voltage. The first shot was at 5 kV charge potential. The Pearson monitors returned current traces on each of the thyratrons, showing the characteristic underdamped series RLC (resistance-inductance-capacitance) waveform. The current waveforms were summed, and a peak current of 20 kA was measured. After 12 shots, the bank voltage was increased to 10 kV and the experiment was repeated. Figure 8 shows the waveforms for each of the tests conducted.

As shown in Figure 8, the peak current of the shot increased in step with the charge voltage of the bank. At 5, 10, 15, 20, and 25 kV, peak currents of 20, 43, 64, 86, and 115 kA were measured, respectively.

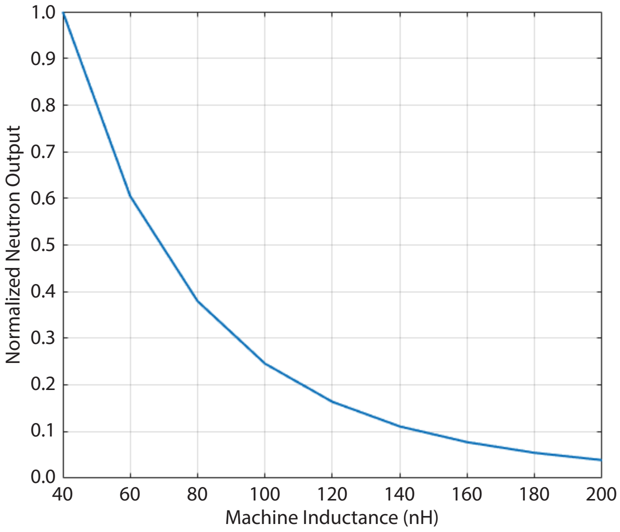

Figure 10. Modeled neutron yield for a 3.0 µF capacitor bank and 4 cm long DPF anode with increasing system inductance

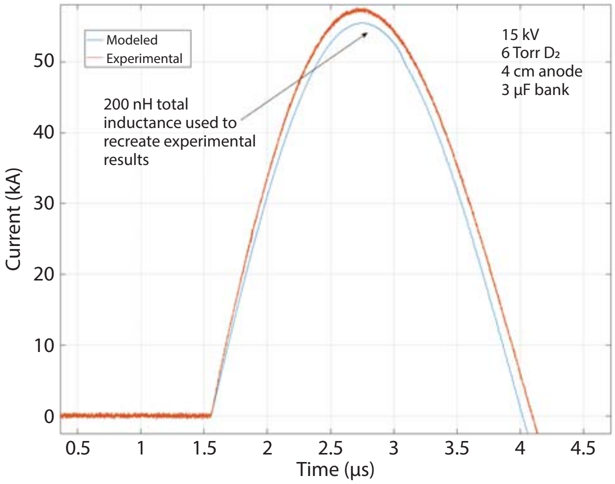

Figure 11. Experimentally measured current waveform compared to a simulated current waveform for a 200 nH, 3.0 µF system

A pressure scan was also conducted at 25 kV. The inset in Figure 8 shows a zoomed-in view of three overlapped waveforms, showing data from shots at a fill pressure of 3, 6, and 12 Torr of deuterium. The lower-amplitude curve corresponds to the 3 Torr shot, and the higher amplitude curves are from the 6 and 12 Torr shots. While all three waveforms approximately follow one another, the 3 Torr shot is noticeably lower in amplitude than the other two pressures. Furthermore, the three curves separate from one another at approximately 450 ns after t = 0, which is when modeling predicted the pinch to occur. The electrical response of the pinch is a sharp change in

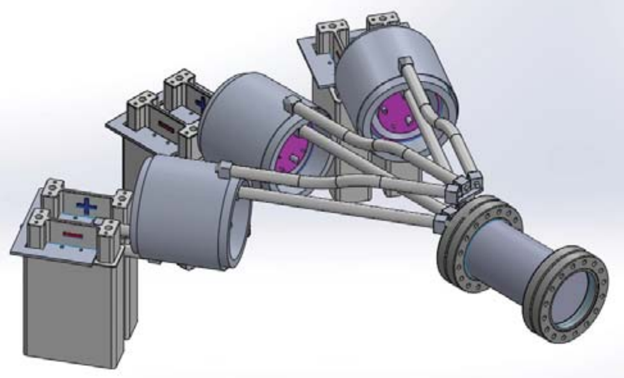

Figure 12. 3-D render of the pulsed power system for the benchtop prototype DPF, showing three capacitor sub-banks, three thyratron switches, and the DPF vacuum chamber

inductance, or *dL*/*dt*, which causes a drop in current. This evidence suggests that a weak pinch may have occurred at 25 kV and 3 Torr. The neutron time-of-flight diagnostics did not, however, capture any neutron pulse waveforms above background.

While the shot current, voltage, and pressure were appropriate for neutron production, the bank inductance was significantly higher than what is typically observed in DPF systems. Inductance, a parasitic property of the pulsed power bank, largely depends on the length and separation of current-conducting paths. It is impossible to eliminate all inductance from a circuit, but an optimized DPF system will have 40 nH or lower total bank inductance. Figure 9 shows the current waveform of the DPF system modeled using the Lee model (Lee 2014) for different values of inductance.

As shown in Figure 9, as the inductance increases, the quarter-period (peak) of the current waveform is increasingly delayed in time. At 40 nH the quarter-period occurs at approximately 500 ns and increases to 600 ns at 60 nH of bank inductance. At 200 nH the quarter-period is delayed to 1.2 µs. In addition to delaying the quarter-period, increased inductance also reduces the peak amplitude of the current waveform, from up to 180 kA at 40 nH to approximately 80 kA at 200 nH. These effects combined cause a strong response in *dL*/*dt*, which directly corresponds to pinch energy and, subsequently, total neutron yield. Figure 10 shows how inductance reduces the total yield of the DPF system.

As shown in Figure 10, the total neutron output of a DPF system decreases exponentially as a function of system inductance. The plot is normalized to the yield of the system at 40 nH, which is the desired inductance of the bank. Increasing the inductance to 60 nH reduces the total neutron yield to 60%, and at 200 nH the yield is only 3% of the 40 nH case. Clearly, designing a bank with low inductance is critical to the performance of the system as a potent neutron source. Figure 11 shows a measured current trace from the prototype pulsed power machine alongside a model of the same bank. A value of 200 nH was required to match the modeled current waveform to the experimental measurement, indicating that the inductance of the machine was excessively large to generate significant neutron yield.

As previously mentioned, the inductance of the pulsed power module is primarily dependent on the size of the device. The benchtop prototype was intentionally designed to be large to aid with assembly and reduce the complexity of the initial design. Figure 12 shows a 3-D rendering of the prototype used in FY 2017. As shown, the system has many features that increase the inductance of the bank, in particular, the long stretches of high-voltage transmission lines that connect the thyratrons to the DPF source tube. While not optimal, this design was important in the development of the system, as it provided a platform to test a new control system and high-voltage equipment that will ultimately lead to a portable pulsed power generator. With the benchtop prototype tested, we will develop an optimized DPF pulsed power unit in FY 2018.

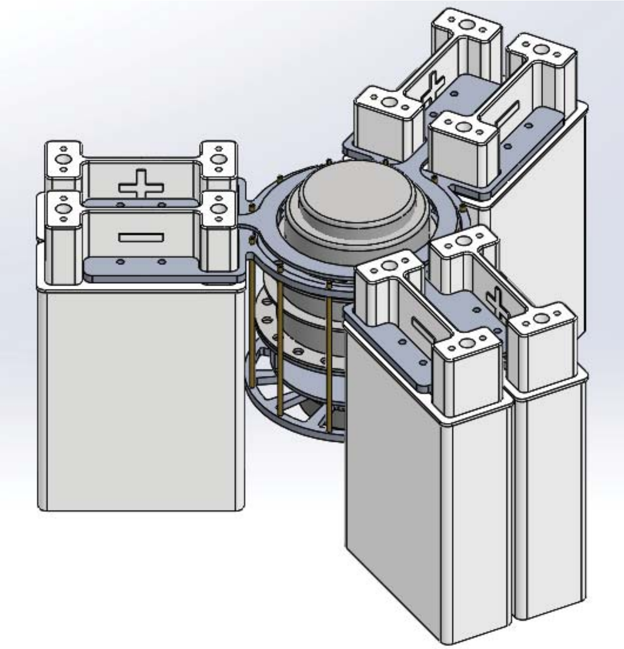

Figure 13. 3-D render of the next-generation portable DPF system, showing three capacitor sub-banks arranged radially around a single thyratron switch

The conceptual design for the new, lower-inductance unit was completed, and a 3-D render of the unit is shown in Figure 13. The new design is much smaller in form-factor than the FY 2017 benchtop prototype. The number of thyratrons has been reduced from three to one, which allows for a radial arrangement of capacitors around it. This shape eliminates the need for long current-carrying transmission lines and allows for very compact component spacing. The system will be potted in a high-strength silicone epoxy to prevent electrical breakdown. These changes will certainly reduce the inductance of the bank, but the actual value of the inductance cannot be measured until the machine is energized and fired next year.

Radiological Analysis

The final embodiment of the portable DPF neutron source will be compact system capable of producing up to 10^8 neutrons/pulse. Because people will use the machine, it is important to understand the risks inherent in operating an RGD. When the system is completed, the dose will be measured using a thermoluminescent dosimeter; however, while the system is still under construction, it is useful to model the device to anticipate the approximate dose that can be expected. This section describes the modeling procedure used to determine the radiological dose of the portable DPF.

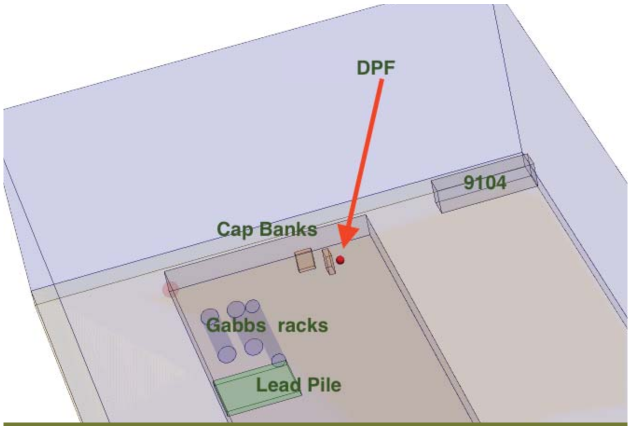

Figure 14. Diagram of simulation space for DPF system in Geant4 model

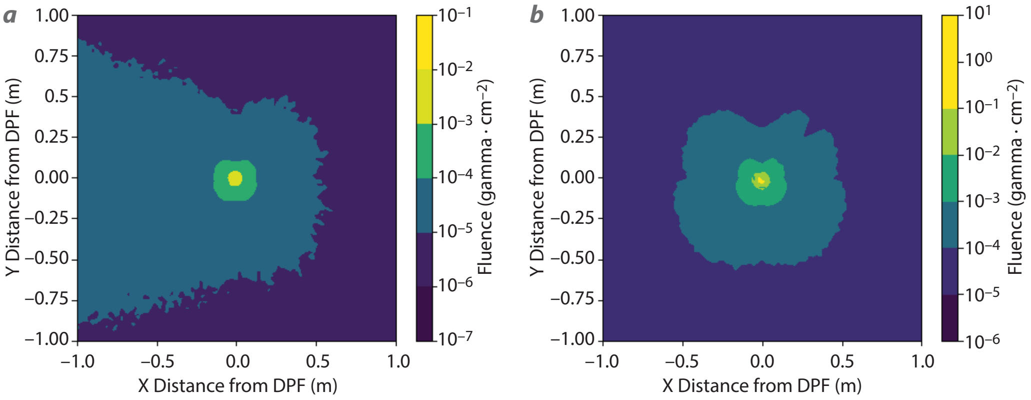

Figure 15. Comparison between (a) gamma and (b) neutron fluence profiles (all energies) for the DPF prototype in the A1 high bay in North Las Vegas

The modeling was conducted using Geant4, which is an open source radiation transport program maintained by the European Organization for Nuclear Research (CERN) (Allison 2016). Geant4 is a C++ toolkit that allows users to write radiation transport applications that leverage the massive amounts of existing work that has been put together by CERN. It is designed to be flexible and extensible, so that users can add their own functionality without much trouble.

Conventionally, radiation transport modeling is often conducted using MCNP. With MCNP, simulations are driven by a text file known as an input deck. A user would describe the geometry, physics, and various simulation parameters to obtain outputs of various types. Geant4 handles the simulation process somewhat differently. A programmer would create a small simulation application using the Geant4 toolkit, and the simulation parameters and outputs would be requested either directly in the source code (hard-coded) or in a script file that the application would read. This is rather convenient if the user wishes to run different configurations. For small simulation efforts, such as the portable DPF input deck, MCNP input decks are not hard to understand, but when more realistic simulations are performed, with large amounts of realistic geometry in the simulation domain, Geant4's geometry subsystem handles this much more easily than MCNP would. While Geant4 can be interfaced with CAD programs (via the GDML interface), MCNP does not come with a native CAD capability.

The DPF dose-field simulation was written to be as similar to the existing MCNP model as possible, to allow for a comparison between the results of the two simulations. Curiously, Geant4 did not have a dose-field output option, so one had to be written. This process was straightforward but time-consuming, and involved writing several C++ classes that interface with Geant4. Once these classes were compiled and tested against some model dose data, we were able to generate a dose-field to submit to Radiological Control in support of our DPF radiation safety plan. Figure 14 shows a 3-D rendering of the simulation space of the Geant4 model. The region modeled was the NLV A1 high bay. The portable DPF was positioned just to the south of a large capacitor bank used for the existing large DPF system. Other large sources of scatter included the concrete floors, large stacks of lead bricks, and a legacy underground nuclear test rack (Gabbs). Personnel were located in a trailer located outside of the building, approximately 100 feet from the source.

Figure 15 shows the neutron fluence produced by the portable DPF operating at 10^7 neutrons/pulse. The plot of the fluence field of secondary gammas produced by the neutron pulse (Figure 15a) has an asymmetric distribution. This asymmetry is caused by scatter from the nearby large-scale capacitor bank. Figure 15b shows the neutron fluence field, which is a relatively symmetric field. Neutrons at 2.45 MeV produce approximately ten times the dose of gamma particles; therefore, this dose analysis considers only neutron radiation (International Commission on Radiological Protection 1973). The neutron fluence at 1 meter from a source operating at the portable DPF's peak modeled yield of 10^8 neutrons/pulse is calculated in Equation 1,

$$\frac{10^8\ \mathrm{n}}{4\pi\times100^2\ \mathrm{cm/m}} = 795.8\ \mathrm{n\cdot cm^{-2}}. \tag{1}$$

Using conversion factors from Table 4, Appendix 6 of ICRP-21 (International Commission on Radiological Protection 1973), the neutron fluence at 1 meter results in 1.55 mrem per pulse. The portable DPF will be operated at a repetition rate of 0.2 Hz, resulting in an average dose of 1116 mrem/hr. The OSHA whole-body annual dose limit is 5,000 mrem, so a worker could only operate the machine for approximately 4.5 hours per year at a standoff of 1 meter (U.S. Department of Labor 1996). Increasing the distance to 18.3 meters reduces the dose to 4.62 µrem/pulse or 3.3 mrem/hr, which will exceed the OSHA limit in approximately nine months under continuous operation. This analysis shows that the portable DPF should be treated with care because it may present a radiological hazard. However, if operators practice ALARA principles by limiting time near the device and maximizing distance from the device, the health impact from operating the system can be significantly reduced.

CONCLUSION

The first year of this project was dedicated to building a new pulsed power module to drive a portable dense plasma focus neutron source for DNN applications such as active interrogation. These applications require a neutron source capable of producing 10^6 neutrons/second that can be reasonably carried and deployed in the field by an individual. Hybrid MHD PIC simulations have been used to design a new DPF anode that can maximize the neutron yield of a compact capacitor bank; modeled results predict a neutron yield of up to 10^8 neutrons/pulse. A compact pulsed power generator was then designed that can operate the DPF at a repetition rate of 0.2 Hz, resulting in a peak average neutron yield of 2×10^7 neutrons/second. Furthermore, the generator is compact and lightweight, and can be operated on battery power, making it a truly portable device. At peak output, the system produces a significant neutron dose to personnel, but near-field exposure below one hour is well below OSHA limits, and far-field exposure can be sustained for over one thousand hours with minimal radiological risk.

A benchtop prototype of the design was constructed and tested this year. A pair of neutron detectors were fielded at the source, but no neutron signal was measured. The primary reason for this was excessively high inductance. An optimized DPF will have approximately 40 nH of inductance throughout the system, but our prototype had an estimated inductance of 200 nH, which resulted in an approximately 97% reduction in neutron yield. While not the preferred outcome, this result emphasizes the need to further shrink the footprint of the DPF since inductance is proportional to length and separation of conductors.

A next-generation DPF system was designed and will be fabricated early in FY 2018. Testing will be done in the first half of FY 2018. In tandem, we are constructing the external housing, modular battery systems, ruggedized control hardware, and basic user interfaces to enable a working portable DPF prototype by the end of FY 2018. Once complete, the system will be available for global security or other organizations to test in further research initiatives or incorporate into broader mission space.

ACKNOWLEDGMENTS

The team would like to thank Stephen Molnar for greatly assisting with design and construction, E. Chris Hagen for project planning guidance, Gladys Arias-Tapar for designing an RGD registration plan and work package, Nathan Sipe for accommodating the team to set up and deconflict work in the A1 high bay, Anthony Montoya for eagerly and rapidly delivering excellent machining and fabrication services for building the benchtop prototype, and M. Krishnan for welcoming our team to his laboratory at the AASC (Alameda Applied Sciences Corporation, San Leadro, California) to learn about compact DPF design techniques.

REFERENCES

Adelphi Technology, "DT108API associated particle imaging neutron generator," 2016, http://www.adelphitech.com/products/dt108api.html, accessed July 15, 2016.

Allison, J., et al., "Recent developments in Geant4," *Nucl. Instrum. Methods Phys. Res. A* **835**, 1 (2016) 186–225.

Bennett, N., et al., "Kinetic simulations of gas breakdown in the dense plasma focus," *Phys. Plasmas* **24** (2017a) 062705.

Bennett, N., et al., "Development of the dense plasma focus for short-pulse applications," *Phys. Plasmas* **24** (2017b) 012702.

Bernard, A., P. Cloth, H. Conrads, A. Coudeville, G. Gourlan, A. Jolas, C. Maisonnier, J. Rager, "The dense plasma focus—A high intensity neutron source," *Nucl. Instrum. Methods* **145** (1977) 191–218.

Gribkov, V., A. Dubrovsky, L. Karpiski, R. Miklaszewski, M. Paduch, M. Scholz, P. Strzyewski, K. Tomaszewski, "The dense plasma focus opportunities in detection of hidden objects by using Nanosecond Impulse Neutron Inspection System (NINIS)," *AIP Conf. Proc.* **875** (2006) 415–418.

Hussain, S., S. Ahmad, M. Z. Khan, M. Zakaullah, A. Waheed, "Plasma focus as a high intensity flash X-ray source for biological radiography," *J. Fusion Energy* **22**, 3 (2010) 195–200.

International Commission on Radiological Protection, *Data for Protection against Ionizing Radiation from External Sources: Supplement to ICRP Publication 15: A Report*, Pergamon Press, 1973.

Krauz, V., K. Mitrofanov, M. Scholz, M. Paduch, L. Karpinski, E. Zielińska, P. Kubes, "Experimental study of the structure of the plasma-current sheath on the PF-1000 facility," *Plasma Physics and Controlled Fusion* **54**, 2 (2012) 025010.

Krishnan, M., "The dense plasma focus: A versatile dense pinch for diverse applications," *IEEE Trans. Plasma Sci.* **40**, 12 (2012) 3189–3221.

Lee, S., A. Serban, "Dimensions and lifetime of the plasma focus pinch," *IEEE Trans. Plasma Sci.* **24**, 2 (1996) 1101–1105.

Lee, S., P. Lee, G. Zhang, X. Feng, V. A. Gribkov, M. Liu, A. Serban, T. K. S. Wong, "High rep rate high performance plasma focus as a powerful radiation source," *IEEE Trans. Plasma Sci.* **26**, 4 (1998) 1119–1126.

Lee, S., S. H. Saw, "Numerical experiments providing new insights into plasma focus fusion devices," *Energies* **3**, 4 (2010) 711–737.

Lee, S., "Plasma focus radiative model: Review of the Lee model code," *J. Fusion Energ.* **33** (2014) 319–335.

Mather, J. W., "Investigation of the high-energy acceleration mode in the coaxial gun," *Phys. Fluids* **7**, 11 (1964) S28.

Mather, J. W., "Formation of high-density deuterium plasma focus," *Phys. Fluids* **8**, 2 (1965) 366.

Nevada National Security Site, "SDRD Technology Needs Assessment R&D," National Security Technologies, LLC, Los Alamos, New Mexico, 2016.

Niranjan, R., R. K. Rout, R. Srivastava, T. C. Kaushik, S. C. Gupta, "A 10^9 neutrons/pulse transportable pulsed D-D neutron source based on flexible head plasma focus unit," *Rev. Sci. Instrum.* **87** (2016) 033504.

Offermann, D. T., D. R. Welch, D. V. Rose, C. Thoma, R. E. Clark, C. B. Mostrom, A. E. W. Schmidt, A. J. Link, "Transition from beam-target to thermonuclear fusion in high-current deuterium Z-pinch simulations," *Phys. Rev. Lett.* **116** (2016) 195001.

Office of Defense Nuclear Nonproliferation (NA-22), "DNN R&D Call for Proposals," 2017.

Rapezzi, L., M. Angelone, M. Pillon, M. Rapisarda, E. Rossi, M. Samuelli, F. Mezzetti, "Development of a mobile and repetitive plasma focus," *Plasma Sources Science and Technology* **13**, 2 (2004) 272.

Rawat, R. S., "High-energy-density pinch plasma: A unique nonconventional tool for plasma nanotechnology," *IEEE Trans. Plasma Sci.* **41** (2013) 701–715.

Rose, D. V., D. R. Welch, B. V. Oliver, R. E. Clark, D. L. Johnson, J. E. Maenchen, P. R. Menge, C. L. Olson, D. C. Rovang, "Coupled particle-in-cell and Monte Carlo transport modeling of intense radiographic sources," *J. Appl. Phys.* **91**, 5 (2002) 3328.

Shukla, R., A. Shyam, R. Verma, E. Mishra, M. Meena, K. Sagar, P. Dhang, "Results of ultracompact plasma focus operating in repetitive burst-mode," *IEEE Trans. Plasma Sci.* **43** (2015) 2354.

U.S. Department of Labor, 29 CFR 1910.1096, Ionizing Radiation, (b)(1), https://www.osha.gov/pls/oshaweb/owadisp.show_document?p_table=STANDARDS&p_id=10098 (1996) September 30, 2017.

Welch, D. R., D. V. Rose, B. V. Oliver, R. E. Clark, "Simulation techniques for heavy ion fusion chamber transport," *Nucl. Instrum. Methods Phys. Res. A* **464**, 1–3 (2001) 134–139.

Welch, D. R., D. V. Rose, R. E. Clark, T. C. Genoni, T. P. Hughes, "Implementation of a non-iterative implicit electromagnetic field solver for dense plasma simulation," *Comp. Phys. Comm.* **164** (2004) 183.

Welch, D., T. Genoni, R. Clark, D. Rose, "Adaptive particle management in a particle-in-cell code," *J. Comp. Phys.* **227**, 1 (2007) 143–155.

Zhang, T., et al., "Optimization of a plasma focus device as an electron beam source for thin film deposition," *Plasma Sources Sci. Tech.* **16** (2007) 250.

Silicon Strip Cosmic Muon Detectors for Homeland Security

RSLN-018-16 ■ Continuing in FY 2018 ■ Year 2 of 3

J. Andrew Green,[1,a] David D. Schwellenbach,[b] Ron Lipton,[c] Paul M. Rubinov,[c]
Cristinel V. Gingu,[c] Michael J. Utes,[c] William E. Cooper,[c]
Johnny B. Green,[c] Humberto Gonzalez,[c] and Miguelangel Marchan[c]

[1]greenja@nv.doe.gov, (702) 295-9803
[a]Remote Sensing Laboratory–Nellis
[b]New Mexico Operations–Los Alamos
[c]Fermilab

Muon tomography and radiography are important detection technologies used to locate special nuclear materials in shielded containers for homeland security applications (Morris 2008). The current technology uses gas-filled drift tubes for position-sensitive charged particle detection and tracking. Drift-tube systems are prohibitively large in size and mass as well as having high development and maintenance costs. Due to the ambiguity of hit location and hit time, the tracking and calibration software needed for industrial-scale drift-tube systems is complex, labor-intensive, and costly. The purpose of this project is to build, test, and evaluate a muon tracking system based on silicon microstrip detectors similar to those used in the particle and nuclear physics communities for high-resolution tracking. To date we have built detector planes, and we have successfully read and analyzed LED and laser data from microstrip sensors. Next year we will complete the 1 ft^2 demonstration tracker capable of collecting cosmic-ray data; we will also explore how our system can be adapted for other applications.

BACKGROUND

High-energy protons and nuclei constantly bombard Earth's atmosphere from many different sources. Much of the sun's low-energy flux is captured by Earth's magnetic field, but higher-energy flux enters from outside the solar system. This flux of high-energy particles interacts with the upper atmosphere to create short-lived mesons that then decay into many different particles, principally muons/anti-muons, photons, and electrons/positrons. At sea level the muon flux, which dominates, is approximately 10,000/min/m^2 (Figure 1). The spectrum falls exponentially with energy (Grieder 2001).

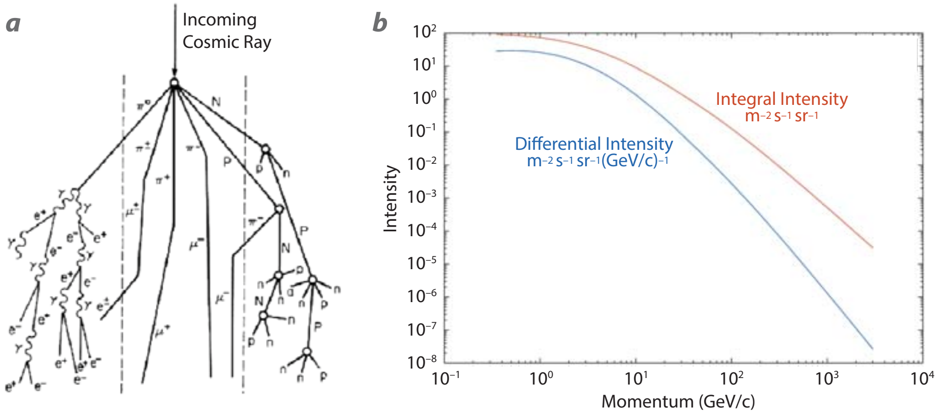

Figure 1. (a) A diagram illustrates how a high-energy cosmic hadron from outer space impacts Earth's atmosphere to create a flux of muons at sea level; (b) fitted differential and integral spectra of vertical muon data at sea level (data from Grieder 2001)

Muons are similar to electrons but have about 200 times the mass (m_μ = 106 MeV/c^2). Unlike protons and neutrons, muons are subject only to weak and electromagnetic forces. The decay of a muon is described as $\mu+ \rightarrow e^+ + \upsilon_e + \overline{\upsilon}_\mu$, with a lifetime of τ = 2.2 μs at rest. The mean cosmic ray muon energy is about 4 GeV (Patrignani 2016), which means they have an effective lifetime of $\gamma\tau = (38) \times (2.2\ \mu s) = 83\ \mu s$. The properties of the muon make it a great candidate for passive imaging. At GeV and higher energies, the muon is highly penetrating through matter because of its high mass and low relative energy loss. A 4 GeV (relativistic) muon has a range of about 3 meters in iron or 18 meters in water (Groom 2001). Muon multiple scattering through matter depends on density and atomic number. Hence, tracking the muons above and below a scene allows us to see locations in space where most scattering occurs. The zenith-angle distribution of these particles is roughly $\cos^2(\theta)$, where θ is from the zenith (Grieder 2001, Patrignani 2016). This angular variation allows 3-D imaging with muons since the object is being illuminated from multiple directions. Furthermore, about 55% of the muons are positively charged (μ^+), and 45% are negatively charged (μ^-). The negatively charged muons can interact with atomic electron shells and nuclei, and they can create secondary coincident x-rays, gammas, and neutrons that may also be used for special nuclear material detection (Nagamine 2007).

Multiple modes of tracking and detecting secondaries may be employed, and these were discussed in numerous prior works (Morris 2008, Schwellenbach 2013, Erlandson 2016). Regardless of the method to reconstruct via secondaries and/or multiple-scattering methods, an excellent tracking capability is required.

The focus of this work is to develop a much more compact and efficient tracking technology for detecting muon positions and trajectories when they enter or exit a scene of interest.

Though significant resources have been spent on drift-tube systems for cargo scanning, drift-tube detectors continue to present significant hardware, software, and physical stability/quality issues. While silicon detectors of the same scale will have a higher initial production cost, we expect that over time the long-term costs should decrease in some cases. High channel density (factor of ~400 compared to drift tubes) allows silicon detectors to be used very compactly.

Additionally, silicon-based tracking opens up the field for the use of smaller, human-portable trackers. For demonstration purposes, one of our goals is also to construct a tabletop (or small rack-mount) system that may be used to demonstrate the capability.

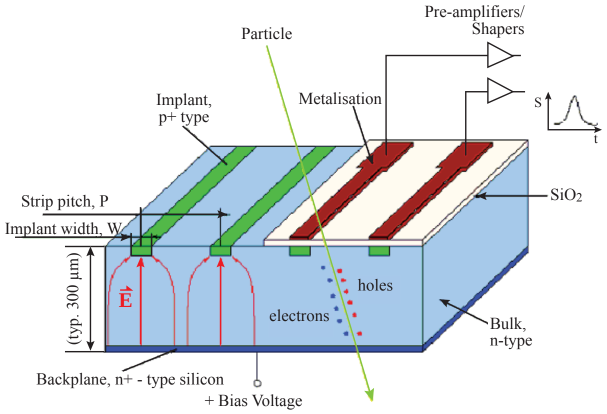

Figure 2. Cross section of a silicon strip detector (image from High Energy Physics Department of Firenze). The bias voltage is delivered at the bottom, and the electrodes are at the strip locations on top. Each silicon strip channel has a metallic pickup, giving an image-charge response to a minimum-ionizing particle in the bulk silicon. This yields position in one dimension via center-of-charge of channel numbers hit. Another sensor layer with orthogonal strips will yield the other needed hit coordinate. Multiple *X*–*Y* layers allow measurement of position and direction.

Silicon sensors (Figure 2) are typically created from 0.3 or 0.5 mm thick silicon wafers that are several inches on a side (depending on crystal growth and fabrication technology), using lithography methods. The sensors for this project were designed, mounted, assembled, and tested at Fermilab. They are fabricated with many aluminum microstrips on top to locate charged particles passing through the silicon below. The detection medium is the depletion layer (about 0.3 mm for 0.5 mm wafer), which is created by reverse-biasing the sensor (as one would reverse-bias a diode) with a nominal voltage of 200 V. The solid-state medium is advantageous over gas-filled drift tubes due to the larger particle energy deposition (an order-of-magnitude higher than 2″ of argon at one atmosphere) (Groom 2001). The hit location of the particle is determined by taking a weighted-mean position of the hit, where the weights come from the pedestal-subtracted analog-to-digital converter (ADC) readout of each microstrip by a front-end chip called an ASIC (application-specific integrated circuit). ASICs are critical components in the design of high-density detection systems, and their properties must be tuned to the problem at hand. For instance, the detector capacitance that the ASIC "expects" must be part of the design. Also, the expected event rate and whether self-triggering and other logic will be required both affect how the chip is designed.

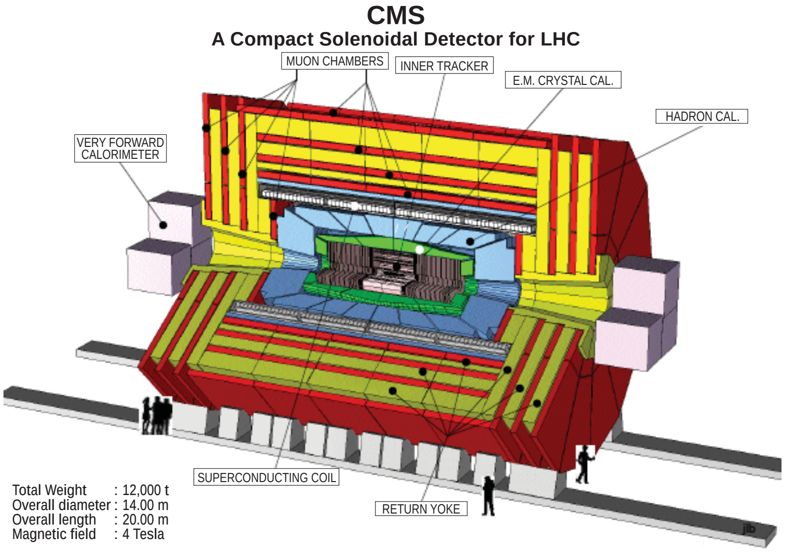

Figure 3. The sensors for this project were originally developed for the Compact Muon Solenoid (CMS) collider-detector at CERN (Krammer 2011), partly funded by the DOE Office of Science. Many tens of square meters of silicon sensors have been built to instrument the CMS central tracking system. This SDRD project leverages the same U.S.-based expertise and test equipment.

PROJECT

Conceptual Design

We are designing a small-scale system of nominal tracking area, ~1 ft^2, with an emphasis on developing lower-cost scaling and maintaining the desirable aspects of silicon-strip detectors: high spatial resolution, ease of use, and compactness. We are investigating performance, feasibility, tracking capabilities, applications, cost-scaling, and reliability. To do this, we have teamed with detector experts in the Particle Physics Division at Fermilab. This project seeks to develop variations that will reduce cost and area for cosmic muon tracking as opposed to the expense related to high-rate/radiation beam experiments on which they are typically used.

Our sensors, which are 0.5 mm thick with 122 μm pitch (Figure 2) between microstrips, work by immediate charge response (<1 ns); therefore, they do not depend on timing resolution or drift calibration to obtain good position-resolution tracking (as is the case for drift tubes). The small pitch is needed to allow the silicon layers to be a few centimeters apart vertically and achieve the same or better angular resolution as the current drift-tube detectors. Hence, detector thickness goes from about 2 feet (for the case of drift tubes) to about 1 inch (for the case of silicon microstrips). The 1 ft^2 detector will be composed of multiple 3 × 3 arrays of 10 cm square silicon microstrip sensors arranged for 3-D tracking. The sensors we are using were originally fabricated for the Compact Muon Solenoid (CMS, Figure 3) detector at the Large Hadron Collider at CERN. There are sufficient quantities of these sensors in dry storage to complete this project. The tracking detector conceptual design is composed of multiple perpendicular layers of silicon strips to compute the cosmic-ray trajectories. To reduce risk, smaller sub-units are being prototyped to better understand how multiple detectors are wire-bonded to each other and to the ASICs, to produce the data acquisition readout, and to check performance and noise pedestals.

The Fermilab team has selected a path forward to complete the first detector string, which is based on

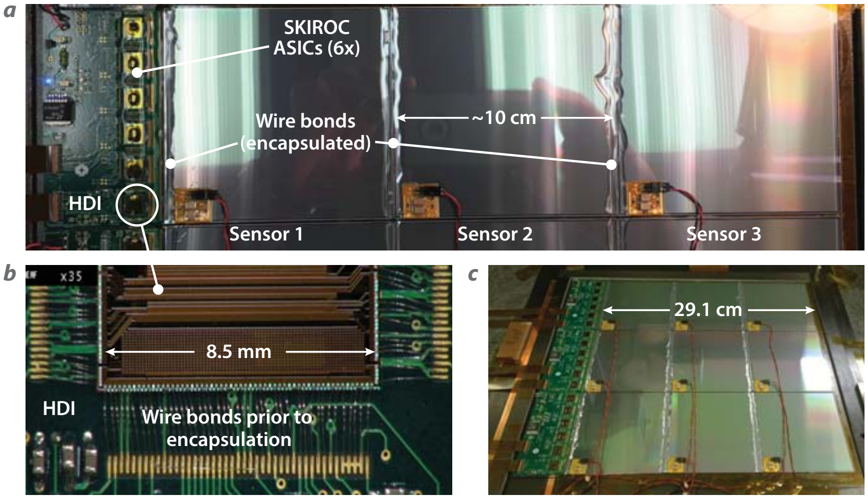

Figure 4. (a) One of the first fully assembled and tested detector strings assembled with readout chips on the left with three sensors wire-bonded in series. The microstrips run left to right and are 122 µm pitch. (b) Magnified view of part of a SKIROC chip and wire-bonds that interface the chip to the high-density interface (HDI) board. The same wire-bonding is also used to connect the sensor microstrips across the 1 mm gap between sensor squares. (c) Fully assembled 1 ft^2 sensor-plane all mounted on a carbon-fiber board.

an ASIC called the SKIROC (Silikon pin Kalorimeter Integrated ReadOut Chip) and shown in Callier (2011). This component was originally developed for current and future high-energy physics experiments. The SKIROC is a 64-channel front-end interface that amplifies and digitizes the microstrip signals. Each channel reads out one microstrip. To provide greater dynamic range, high-gain and low-gain analog-to-digital conversion is provided. Internal or external triggering (triggers cause an event to be digitized and stored) is possible. Each chip is about 1 cm^2 in size. The SKIROC was designed for the CMS and International Linear Collider (ILC) programs to read out a fine-grained silicon-based calorimeter (Omega 2016).

Sensor data in this project are read by a hybrid of custom and off-the-shelf data acquisition architecture called a Zedboard, a Xilinx-based field-programmable gate array (FPGA) board running Linux.

The minimum unit of this tracking system is called a detector string (Figure 4). Each string consists of three daisy-chained microstrip sensors (about 30 cm in total length) with sufficient ASICs on one end to read out the microstrips (Figures 4a and 4b). Three in a daisy-chain and three columns populate the ~1 ft^2 tracker (Figure 4c). Two such orthogonal detectors, an *X–Y* plane, fix one cosmic muon track point. Three *X–Y* planes is more ideal to allow track-fitting redundancy, but two are expected to be sufficient. In the future, many such small *X–Y* planes might compose a larger-area tracking panel. A muon tomography detector will consist of at least two top and two bottom panels, with sufficient space between the major sections for an object to be scanned.

The current silicon-strip sensors in use in high-energy physics (HEP) and associated ASICs were designed to function in high particle occupancy, event rate, and radiation damage environments. Being exposed to high radiation, typical sensors need to be cooled to low ambient temperatures, such as –10°C. While our type of sensor does need a relatively high channel density and robustness, it will not operate in such a challenging environment. To reduce cost and area, we will pursue efficiencies that optimize our detectors for operation with cosmic-ray rates/occupancies and for room-temperature operation.

Electronics and Readout

Basic Architecture

The overall architecture to build the 1 ft^2 detector is as follows: A scintillator "paddle" will be used to trigger the tracker externally, at least for now. Self-triggering is certainly possible, but scintillator triggering is very simple and good for prototyping. A 3 × 3 array of 10 cm square sensors will measure one of the *X* or *Y* components of the particle tracks. Two orthogonal arrays will give one *X–Y* hit coordinate. The *X–Y* sensors will be mounted on carbon-fiber boards, which have a favorable coefficient of expansion and low mass. Each of the 3 × 3 arrays is composed of three columns of three sensors wire-bonded in series. Each column is read out by six SKIROC chips mounted on a high-density interface (HDI) board (Figures 4 and 7). This was previously called a "carrier" board in prior reports. A similar pair of *X–Y* sensor planes will be placed about 2 cm below the first plane-pair. These will create a tracking module. Another tracking module for the region below the object being scanned (target) will be assembled to allow cosmic ray tracking above and below the target object.

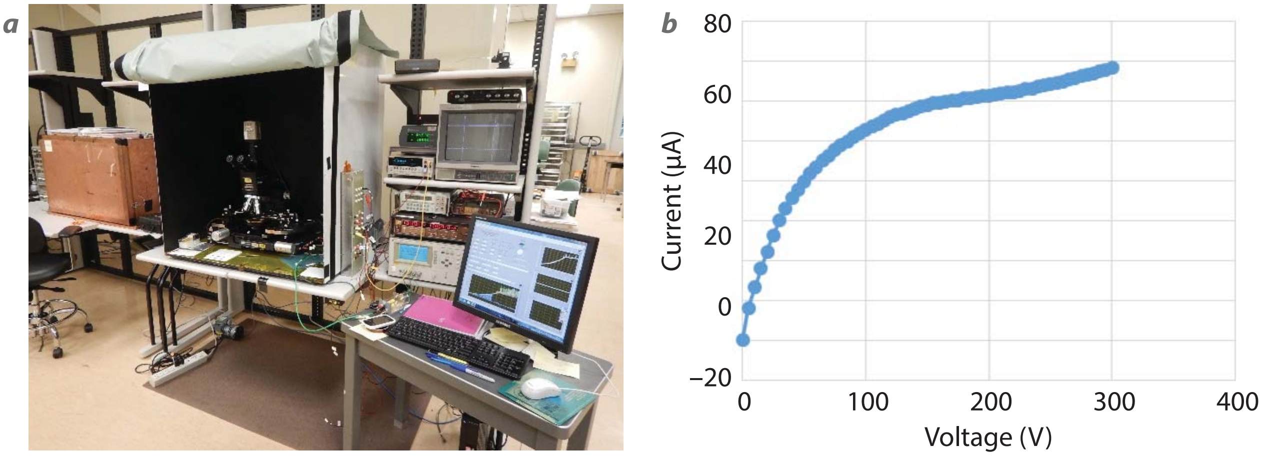

Figure 5. (a) Test-stand at Fermilab SiDet facility used to evaluate our sensors for current and capacitance vs. applied bias voltage. Each sensor has its own current-voltage curve plotted so that the operating bias voltage and sensor health may be determined. The typical value for bias voltage is 180–220 V. Sensors that do not have a normal plateau curve are rejected. (b) An example of a normal plateau curve.

Adaption of Previously Designed Electronics

This project adapts previously developed technology to build our tracker. The silicon microstrip sensors, “CMS ST” sensors, have been in dry storage for over 10 years. Testing (Figure 5) has shown them to be in good condition for this project, and they are in sufficient supply. The SKIROC ASIC chip for front-end readout of the microstrips was originally designed not for tracking, but for silicon-based calorimetry upgrades for the HEP program. However, the properties of the SKIROC are expected to be sufficient for readout of our microstrips. A Xilinx FMCIO (FPGA Mezzanine Card IO) board, interfaced to a readout board, is currently used to read data from the HDI, then push the data to an off-the-shelf Zedboard. This readout architecture was largely developed for test-beam setups that are used to develop detectors for the previously mentioned HEP efforts.

Because the SKIROC was not originally developed for reading out our microstrips, the pitch between the SKIROC signal pads is such that we can only read out every other microstrip. This will end up giving us effectively a 244 µm pitch instead of the more ideal 122 µm. The resulting tracking angular resolution is conservatively 5 mrad, which is sufficient for proof-of-concept, as typical high-Z material scattering is in tens of milliradians. This is just one of the number of adaptations required to make forward progress. However, typical hit resolution with charge sharing is likely to be below 100 µm (competitive with the best drift tubes). While several ASICs were considered for our project, the SKIROC was the best combination of price and capability. The alternative would have been to purchase chips that are ~10 times the cost of the SKIROC, or worse, to design and fabricate our own ASIC, which is outside the scope of this SDRD.

Components and Software Development

Some components have been adapted to meet the needs of early prototyping, and some have been designed. Our re-engineering of the components carefully considered proper electrical and mechanical interfaces needed for high-resolution tracking. In FY 2016 we developed the flex board, HDI board, mechanical design, carbon-fiber base, and FPGA firmware (Green 2017).

In FY 2017 we also addressed inadequacies in the designs developed in FY 2016. For instance, after we fabricated the first version of the HDI board, we noted problems with reading all six SKIROC chips. Furthermore, the chips were light sensitive, but only the sensors that they read out should be light sensitive. We modified the wire-bond traces to eliminate these problems. Additional modifications improved footprint, component layout, noise, and board diagnostics. The newest HDI design is now reliable and performs well on reading out chips and sensors. Additionally, the flex board required modification to reduce vertical height and ensure that the flex circuit was not under stress. Also in FY 2017, the techniques in detector fabrication were developed to ensure mechanical alignment, electrical contact, and protection from the environment. Finally, changes were made to the software to correctly read and analyze the data. A C++ set of classes has been written to allow convenient exploration and plotting

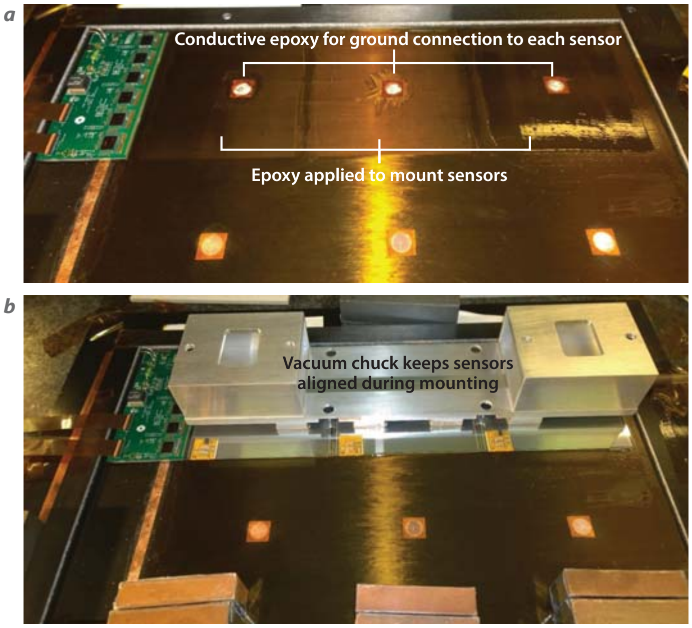

Figure 6. (a) Preparing a set of three sensors for gluing onto the carbon-fiber base. (b) The three sensors are pre-aligned and then placed together with a vacuum chuck, a device that uses a vacuum to preserve the alignment of the sensors while being glued and moved into position.

of the data. These tools were used to determine signal-to-noise ratios as a function of high voltage, measure pedestals and response to laser and LED light pulses, and test proper detector function. The processes and procedures in this project are being further documented to maintain continuity.

Detector Fabrication

Significant capital machinery, materials, technical experience, and preparation are required to fabricate the detectors. The coordinate measurement machine aligns components prior to gluing or mounting. Automated wire-bonding machines make the hundreds of ultrasonic soldering connections possible between the ASIC, HDI, and sensor microstrips. An encapsulation machine correctly applies the encapsulant silicone, Sylgard 186, to protect wire bonds and chips. Numerous diagnostic microscopes are used for repair and characterization. A "vacuum chuck" is used to maintain alignment of three sensors in a column prior to gluing (Figure 6). Masks are used to control where glue is applied, and conductive epoxy is used to maintain certain connections to each sensor.

Mechanical Design

Figure 7 presents a side view of a tracking module. Two such modules are to be made. The enclosure includes light shielding as well as ventilation. Unlike photomultiplier systems, rigorous light shielding is not needed. An *X*–*Y* plane will be made from two 1 ft^2 planes mechanically mounted back to back and with the microstrips running perpendicularly. The distance between two *X*–*Y* planes per tracking module is set to about 2 cm. This distance is set so that for a conservative 100 μm hit resolution, the angular resolution will be approximately 0.1 mm/20 mm = 5 mrad. Due to this spacing, the solid angle acceptance of this system will be a few-to-several times the solid angle of our prior drift-tube detectors, depending on configuration. This results in more valid tracks per unit time from cosmic rays, greater ratio of tomographic coverage area to detector area, and reduced Z-smearing of target images.

Software and Analysis

The data acquisition system (DAQ) consists of FPGA firmware and embedded Linux software. We use firmware running on Xilinx FPGAs on the

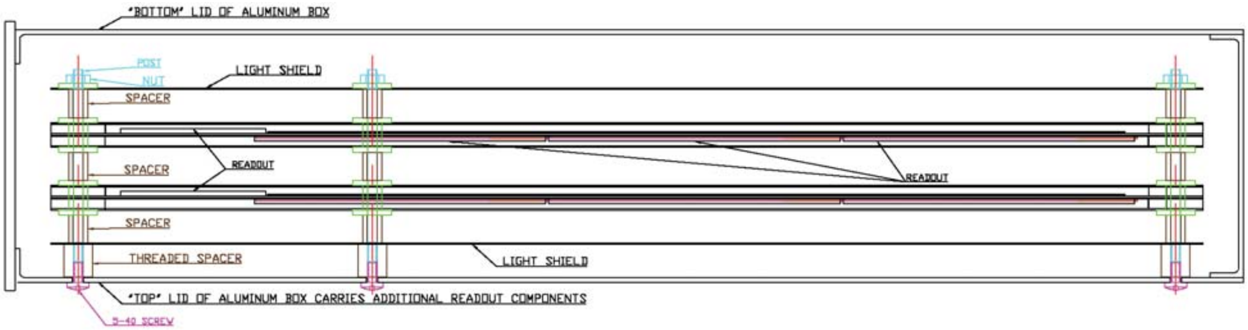

Figure 7. Side-view mechanical drawing of one full detector assembly. Shown are the outer enclosure and two stacked *X*–*Y* planes edge-on. Their vertical spacing will be about 20 mm. Two such assemblies will be produced.

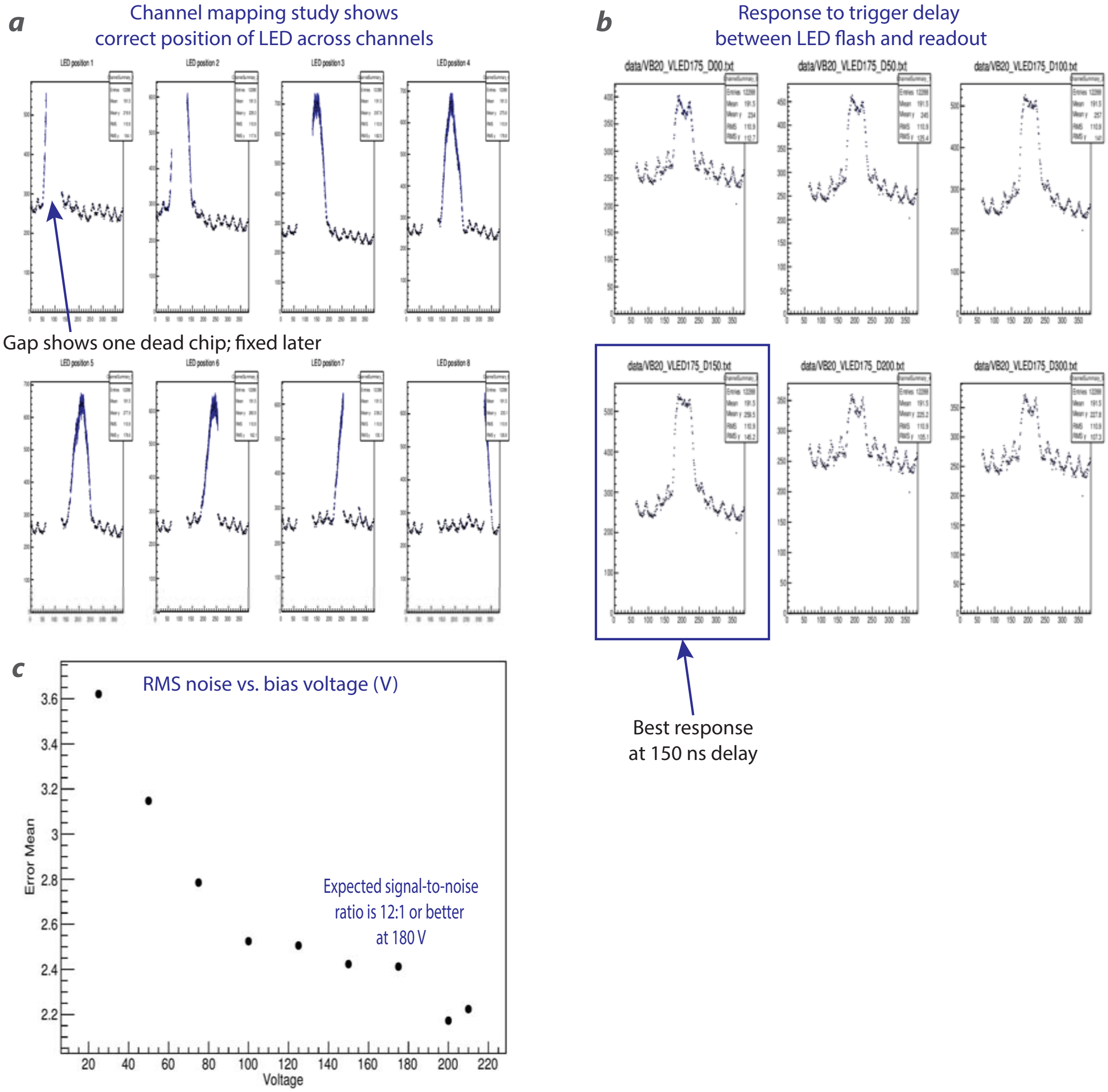

Figure 8. Among the analyses performed were a (a) channel mapping study, a (b) trigger delay study, and a (c) noise pedestal study

Zedboard as well as on the FMCIO. These are used to respond to signals coming directly from the SKIROC chips reading out the silicon microstrips. The FMCIO FPGA pulls the SKIROC ADC data, then pushes it via high-definition multimedia interface (HDMI) cable to the Zedboard. The FPGA on the Zedboard responds to the HDMI signals and puts the data into local memory. This memory is read using a Linux program running on the Zedboard turning the data into files. The files are pulled from the Zedboard and analyzed.

We have also developed codes needed to analyze data. The code is used to make plots and perform diagnostics on the data stream that result from each trigger event. Each event contains each microstrip's ADC values, headers that provide coarse- and fine-time, board addresses, and health information. All data are used to ensure event integrity. The plots can also show systematic problems, such as when certain channels are not present in the readout, do not respond correctly to LED or laser light, or have unusually high noise. These result in repairs to the affected hardware and firmware. One of these hardware modifications is referred to above in a fix to the HDI board; see also Figure 8.

CONCLUSION

We are building a tabletop silicon microstrip muon-tracking system that uses adapted high-energy physics detectors previously developed at Fermilab. This experience will lead to larger-scale cosmic muon tracking and associated applications. We have established the detector fabrication, the board electronics, the firmware, and subsequent software needed to take data from many sensors. In FY 2018 we will add more detector planes, fabricate and install electronics, and produce hit- and track-finding software. Demonstrations of simple scenarios are also planned once the detector is built.

REFERENCES

Callier, S., F. Dulucq, C. de La Taille, G. Martin-Chassard, N. Seguin-Moreau, "SKIROC2, front end chip designed to readout the Electromagnetic CALorimeter at the ILC," Topical Workshop on Electronics for Particle Physics, 2011, Vienna, Austria, http://iopscience.iop.org/article/10.1088/1748-0221/6/12/C12040/meta, accessed November 10, 2016.

Erlandson, A., S. Livingstone, V. Anghel, C. Jewett, O. Kamaev, M. Thompson, "Cosmic ray inspection and passive tomography: Recent results from Canada's unique Muon Scattering Tomography system," Poster 2B-7, SORMA West, University of California, Berkeley, May 22–26, 2016.

Green, J. A., D. D. Schwellenbach, R. Lipton, P. M. Rubinov, C. V. Gingu, M. J. Utes, W. E. Cooper, J. B. Green, "Silicon strip cosmic muon detectors for homeland security," in *Site-Directed Research and Development*, FY 2016, National Security Technologies, LLC, Las Vegas, Nevada, 2017, 73–80.

Grieder, P. K. F., *Cosmic Rays at Earth: Researcher's Reference Manual and Databook*, Elsevier Science Press, Amsterdam, The Netherlands, 2001, 363–364.

Groom, D. E., N. V. Mokhov, S. I. Striganov, "Muon stopping power and range tables 10 MeV–100 TeV," *Atomic Data and Nuclear Data Tables* **78**, 2 (2001) 183–356.

High Energy Physics Department of Firenze, "Silicon Detector.gif," http://hep.fi.infn.it/CMS/sensors/Silicon_Detector.gif, accessed December 5, 2016.

Krammer, M., "Silicon detectors," Institute of High Energy Physics, Vienna, Austria, 2011, http://www.hephy.at/fileadmin/user_upload/Lehre/Unterlagen/Praktikum/Halbleiterdetektoren.pdf, accessed November 10, 2016.

Morris, C. L., et al., "Tomographic imaging with cosmic ray muons," *Science and Global Security* **16** (2008) 37–53.

Nagamine, K., *Introductory Muon Science*, Cambridge University Press, New York, 2007, 40–68.

Omega Corporation, "SKIROC front-end chip," 2016, http://omega.in2p3.fr/index.php/products/skiroc.html, accessed November 10, 2016.

Patrignani, C., et al. (Particle Data Group), "Review of particle physics," *Chin. Phys. C* **40** (2016) 100001.

Schwellenbach, D., et al., "Passive imaging of warhead-like configurations with cosmic-ray muon tracking scanners," in *Site-Directed Research and Development*, FY 2012, National Security Technologies, LLC, Las Vegas, Nevada, 2013, 129–134.

Development of a High-Performance Digital Multichannel Analyzer for Radiation Detection Applications

RSLN-028-17 ■ Year 1 of 1

Ron Guise,[1,a] Michael Bass,[a] and Krikor Hovasapian[a]

[1]guisere@nv.doe.gov, (702) 295-8666
[a]Remote Sensing Laboratory–Nellis

Multichannel analyzers (MCAs) are used in radiation detection to collect data from a detector and transform the data into a human-consumable format. Our goal was to create an MCA based on a field-programmable gate array (FPGA) to meet the unique and evolving needs of radiation detection in global security applications. Ultimately, we created a highly extensible MCA (XMCA) using a modular architecture that is capable of rapidly integrating new features. In addition, we developed a highly scalable test environment with the flexibility required to support such an elastic technology. Our XMCA consisted of three PCBs: an analog board containing the analog-to-digital converter and front-end circuitry, a digital board hosting the FPGA and microcontroller unit, and a high-voltage board. The XMCA design was first created using Verilog, tested using software simulation, and finally hardware tested using the digital board. We successfully obtained spectral data and have created a physical housing for field use.

BACKGROUND

Commercial multichannel analyzers (MCAs) are costly and lack the flexibility required in a development platform. They are primarily designed for laboratory use with standard PC architectures and non-real-time acquisition rates. But global security applications often require tighter timing characteristics and need to operate on various platforms and in uncontrolled environments; furthermore, commercial units frequently lack features we desire, which are not readily available in the COTS units. In the past, we have had manufacturers modify commercial MCAs to suit our needs. This process takes a year or more to complete and requires lengthy discussions, drafting non-disclosure agreements, and establishing contracts with the manufacturer. As a solution, this project sought to design an in-house custom MCA platform based on a field-programmable gate array (FPGA) that is able to provide custom implementations, filters, algorithms, and interfaces. An FPGA will enable developers to add functionality over time, adapt the platform to new systems, and create custom variations for research. The platform will contain a digital board

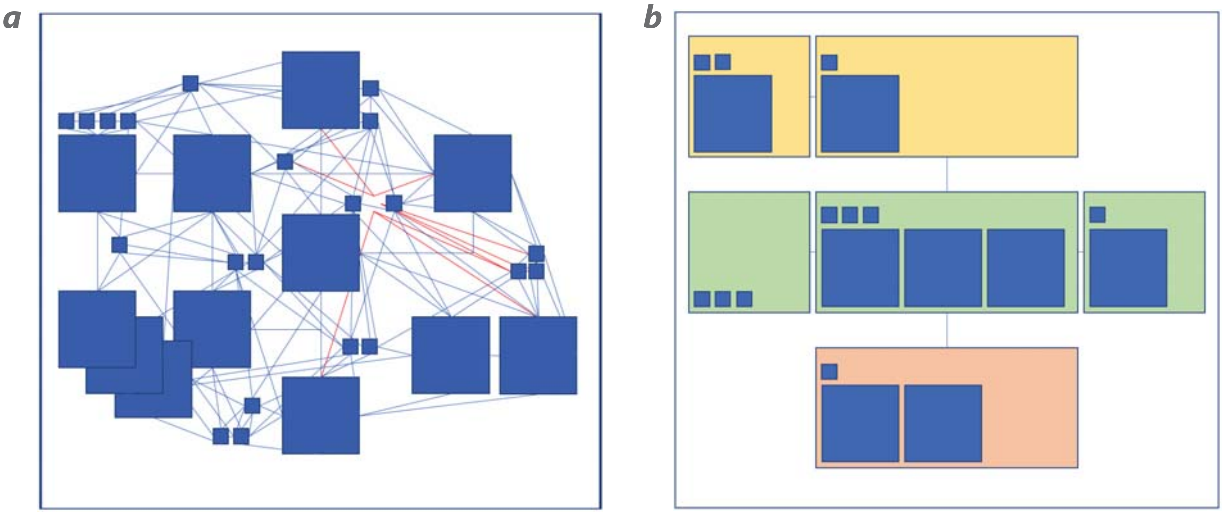

Figure 1. (a) A traditional design has many discrete interconnects that can highly affect the design, even when a simple change is made (red lines), but (b) a well structured design solves this issue

hosting the FPGA MCA and a microcontroller unit (MCU), an analog board performing signal shaping and analog-to-digital conversion, and a high-voltage board. An application programming interface (API) will expose functionality for third-party development. By owning this design and having it in a well-structured architecture and development environment, we will have the ability to rapidly implement features and changes as needed.

PROJECT

For this project, we modified an existing MCA design previously created in an ASIC (application-specific integrated circuit). Using a software design method known as test-driven development (TDD), we restructured the Verilog code, making it very structured and, thus, easy to manage, change, synthesize, and test. Breaking with past practices, the development environment also employed TDD principles. In the past, FPGAs were continually tweaked by developers until some point of completion was established. Future changes were difficult if developers were not intimately familiar with the entire design history. Furthermore, ensuring that a change did not inadvertently affect some other part of the design was very challenging, even for the original developer (Figure 1a).

Using TDD and a well-structured design alleviates much of the difficulties associated with future development. The design, highly structured and parameterized, created an extensible, maintainable framework into which desired specifications and functionality could be integrated (Figure 1b). For example, the current system uses a 12-bit analog-to-digital converter (ADC). To change the ADC to a 14- or 16-bit converter requires changing a single parameter. Once changed, this parameter will propagate throughout the design, changing the width of all affected data paths/busses, memory banks, etc.

In addition to TDD, the design was influenced by modern software engineering principles that include a service-oriented architecture, modular design, do not repeat yourself, and loose coupling.

The project included not only the creation of an extensible MCA (XMCA), but also the testing and design environments required for project longevity. Figure 2 illustrates the XMCA architecture.

The test infrastructure was divided into two parts: (1) software/simulation and (2) hardware. The software/simulation testing environment is hosted on a Linux cluster that contains four Linux servers, each containing 16 processor cores. It is designed using C++, sockets, a custom communications protocol, Linux shell scripts, and Xilinx Vivado. The software/simulation testing environment is designed to be scalable to accommodate testing of iterative changes.

The hardware testing exercises the digital circuitry through a custom XMCA hardware test suite (HTS) application. The HTS generates radiation events with randomized energy values, translates those into Fluid Arduino commands, and then uses an Arduino to electrically stimulate the FPGA inputs. The HTS reads outputs from the FPGA via the MCU, and compares the results with the expected values based on the stimulus (Figure 3).

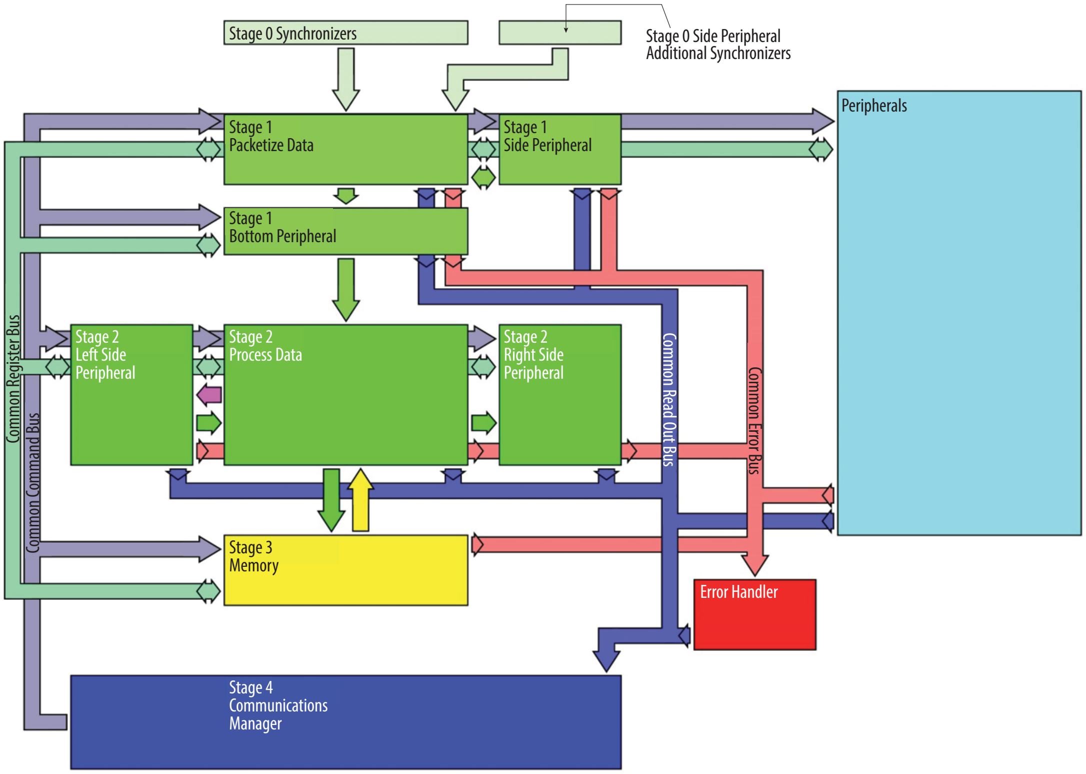

Figure 2. Diagram of the XMCA architecture

The HTS design is focused on separation of concern. The application core was developed separately from the interface. Thus, it can be used with a graphical user interface, terminal, web-based interface, etc. It uses a custom scripting language referred to as XMS. The scripting language can expand as the XMCA design expands, and it can address any number of Arduinos/XMCAs as desired in order to allow faster and/or more thorough testing.

The HTS design allows testing to be done iteratively (Figures 4 and 5) so that thorough hardware tests can run unattended for extended periods. Use of the Arduinos greatly limits the speed at which hardware tests can run and does not allow for tight timing constraints. To address this, the fifth XMCA was added to control the timing constraints needed for testing coincidence mode. Future developments could likely include development of an FPGA-based stimulus board that could be used in place of the Arduino to allow full-speed hardware testing.

RESULTS

The current XMCA design includes the following features: double-buffered short-term histogram, single-buffered long-term histogram, list/event mode, user-settable conversion gain; gain stabilization, pulse pile-up rejection; dual detection, coincidence, and fully synchronized or free run mode.

The XMCA also has several generic counter inputs available as well as full error checking in order to verify viability of selected parameters.

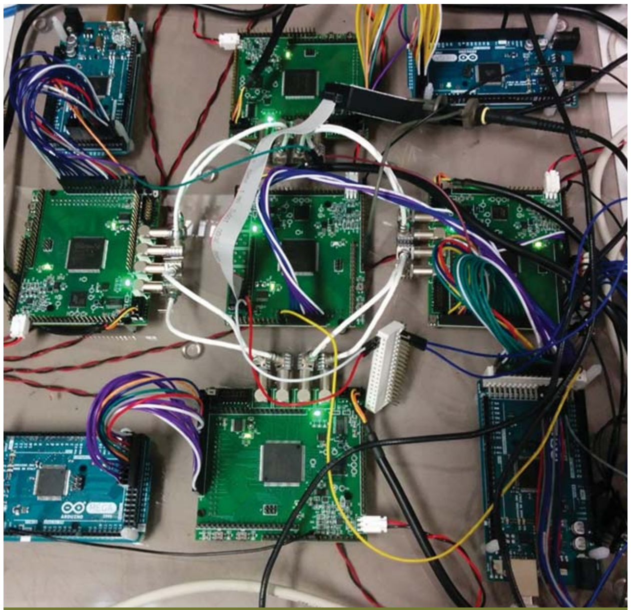

Figure 3. Four XMCAs undergoing coincidence mode hardware tests are stimulated by four Arduinos; a fifth XMCA controls timing

1 - North

```
PASS - Short Term
Histogram Test Passed!
PASS - Short Term
Histogram Test Passed!
PASS - Long Term
Histogram Test Passed!
PASS - Short Term
Histogram Test Passed!
PASS - Short Term
Histogram Test Passed!
PASS - Long Term
Histogram Test Passed!

6 out of 6 Passed
0 out of 6 Failed
```

```
              <**Main Menu**>
     1        : MCA Settings
     2        : MCU Settings
     3        : Board Status
     4        : Advanced Settings
     5        : Reset System
     ?        : To see this menu
Long Term Histogram Test Passed!
```

4294967295 Pulse Pile Up Counter; 8000 Gross Counter; 3 Gain Stabiliz Read Ou; 0 Dead Time Counter

3 - South

```
PASS - Short Term
Histogram Test Passed!
PASS - Short Term
Histogram Test Passed!
PASS - Long Term
Histogram Test Passed!

3 out of 3 Passed
0 out of 3 Failed
```

```
              <**Main Menu**>
     1        : MCA Settings
     2        : MCU Settings
     3        : Board Status
     4        : Advanced Settings
     5        : Reset System
     ?        : To see this menu
Long Term Histogram Test Passed!
```

4294967295 Pulse Pile Up Counter; 6000 Gross Counter; 3 Gain Stabiliz Read Ou; 0 Dead Time Counter

2 - East

```
PASS - Short Term
Histogram Test Passed!
PASS - Short Term
Histogram Test Passed!
PASS - Long Term
Histogram Test Passed!

3 out of 3 Passed
0 out of 3 Failed
```

```
              <**Main Menu**>
     1        : MCA Settings
     2        : MCU Settings
     3        : Board Status
     4        : Advanced Settings
     5        : Reset System
     ?        : To see this menu
Long Term Histogram Test Passed!
```

4294967295 Pulse Pile Up Counter; 6000 Gross Counter; 3 Gain Stabiliz Read Ou; 0 Dead Time Counter

4 - West

```
PASS - Short Term
Histogram Test Passed!
PASS - Short Term
Histogram Test Passed!
PASS - Long Term
Histogram Test Passed!

3 out of 3 Passed
0 out of 3 Failed
```

```
              <**Main Menu**>
     1        : MCA Settings
     2        : MCU Settings
     3        : Board Status
     4        : Advanced Settings
     5        : Reset System
     ?        : To see this menu
Long Term Histogram Test Passed!
```

4294967295 Pulse Pile Up Counter; 6000 Gross Counter; 3 Gain Stabiliz Read Ou; 0 Dead Time Counter

Figure 4. The HTS, showing testing of four XMCAs

1 - North

```
: 1
lowLevelCutOff : 0
shortTermHistogramStart
: 0
shortTermHistogramSize :
2048
longTermHistogramStart :
0
longTermHistogramSize :
2048
Running Fine
Running Coarse
PASS - Testing for non-
empty spectra - Passed!
PASS - Short Term
Histogram Test Passed!
PASS - Short Term
Histogram Test Passed!
PASS - Long Term
Histogram Test Passed!
Testing Dual Detection
Testing Dual Detection
High
PASS - Short Term
Histogram Test Passed!
PASS - Short Term
Histogram Test Passed!
PASS - Long Term
Histogram Test Passed!
Testing Dual Detection
Low
```

```
RSLMCA Interface

              <**Main Menu**>
     1        : MCA Settings
     2        : MCU Settings
     3        : Board Status
     4        : Advanced Settings
     5        : Reset System
     ?        : To see this menu
```

4294967295 Pulse Pile Up Counter; 1543 Gross Counter; 3 Gain Stabiliz Read Ou; 0 Dead Time Counter

3 - South

```
empty spectra - Passed!
PASS - Short Term
Histogram Test Passed!
PASS - Short Term
Histogram Test Passed!
PASS - Long Term
Histogram Test Passed!
Testing Gain Stabilization

Gain Stabilization read
out should show the need
to decrease the gain
PASS - Gain Stabilization
Read Out Test Passed! -
Value: 1

Gain Stabilization read
out should show the need
to increase the gain
PASS - Gain Stabilization
Read Out Test Passed! -
Value: 2

Gain Stabilization read
out should show no need
to change the gain
PASS - Gain Stabilization
Read Out Test Passed! -
Value: 0
Testing Gain Stabilization
with Pulse Pile Up
```

```
Histogram
     4        : Read out Long Term
Histogram
     5        : Read and Clear Long
Term Histogram
     6        : Clear all memory
     ?        : To see this menu
     <-       : Backspace key to go
back
```

4294967295 Pulse Pile Up Counter; 6654 Gross Counter; 1 Gain Stabiliz Read Ou; 0 Dead Time Counter

2 - East

```
enablePulsePileUp : True
enableDualDetection :
True
gainStabilizationChannel :
628
gainStabilizationWindow
Width : 62
shortTermConversionGain
: 1
longTermConversionGain
: 1
lowLevelCutOff : 0
shortTermHistogramStart
: 0
shortTermHistogramSize :
2048
longTermHistogramStart :
0
longTermHistogramSize :
2048
Running Fine
Running Coarse
PASS - Testing for non-
empty spectra - Passed!
PASS - Short Term
Histogram Test Passed!
PASS - Short Term
Histogram Test Passed!
PASS - Long Term
Histogram Test Passed!
Testing Pulse Pile Up
```

```
              <**MCA -> Registers->
Parameter-> Long Term Histogram**>
     1        : Conversion Gain
     2        : Histogram Start
     3        : Histogram Size
     ?        : To see this menu
     <-       : Backspace key to go
back
```

1091 Pulse Pile Up Counter; 8111 Gross Counter; 3 Gain Stabiliz Read Ou; 0 Dead Time Counter

4 - West

```
Parameters :
enableGainStabilization :
True
enablePulsePileUp : True
enableDualDetection :
True
gainStabilizationChannel :
547
gainStabilizationWindow
Width : 372
shortTermConversionGain
: 1
longTermConversionGain
: 1
lowLevelCutOff : 0
shortTermHistogramStart
: 0
shortTermHistogramSize :
2048
longTermHistogramStart :
0
longTermHistogramSize :
2048
Running Fine
Running Coarse
PASS - Testing for non-
empty spectra - Passed!
PASS - Short Term
Histogram Test Passed!
PASS - Short Term
Histogram Test Passed!
```

```
RSLMCA Interface

              <**Main Menu**>
     1        : MCA Settings
     2        : MCU Settings
     3        : Board Status
     4        : Advanced Settings
     5        : Reset System
     ?        : To see this menu
```

5330 Pulse Pile Up Counter; 7785 Gross Counter; 2 Gain Stabiliz Read Ou; 0 Dead Time Counter

Figure 5. The HTS running iterative testing on four XMCAs

The design was based on the Remote Sensing Laboratory's need and is a compromise between throughput speed and power consumption. The front-end circuitry uses a traditional sample and hold, feeding a 1-million-sample-per-second ADC. The FPGA and MCU both run off a 10 MHz clock. The design of the FPGA could easily run much faster if needed. Thought was given to future designs that could achieve much faster sampling; for example, including a phase-locked loop could provide the ability to allow a much faster front end while still running the rest of the digital circuitry at a slower clock frequency in order to provide the best use of speed and power.

The initial spectral results (Figures 6–8), power consumption, and throughput of the design fit our expectations. There was a small noise spike on the low-energy end of the spectra, which was investigated and was reduced to the point that we could clearly see the 60 keV peak from ^{241}Am. However, it was still present and would require a new PC board layout in order to fully resolve the issue.

The flexibility of the design and the system was also proven during the year. At a quarterly review a colleague remarked that the commercial MCA he used only had list/event mode, which made the data processing time lengthy. We asked ourselves if we could provide both histogram data and event mode data simultaneously, decided how it could be implemented, and added that feature within a matter of weeks. Thus, a user could much more quickly analyze the histogram data in order to down-select or prioritize which list/event mode data to analyze first.

Prior to the end of the year, potential users expressed interest in using the XMCA design in several projects. Thus, rather than spend an extensive amount of time testing the first prototypes that had a known noise problem, we decided to focus efforts on a new PC layout to resolve the noise issue. In addition to modifying the PC board layout, we added some useful features and put it in a usable package.

CONCLUSION

This project produced a development platform for an in-house multichannel analyzer that can be customized for radiation detection in global security applications. The initial tests of the

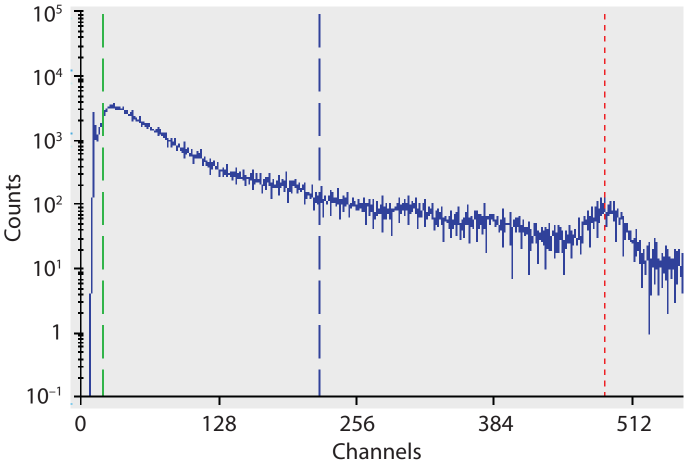

Figure 6. Background spectra collected with the prototype XMCA, showing a noise spike at the low end of the spectra

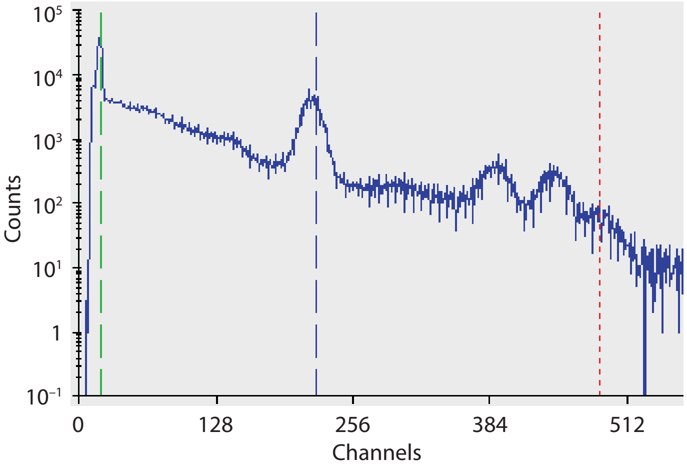

Figure 7. Spectra of ^{241}Am, ^{137}Cs, ^{60}Co collected using the prototype XMCA

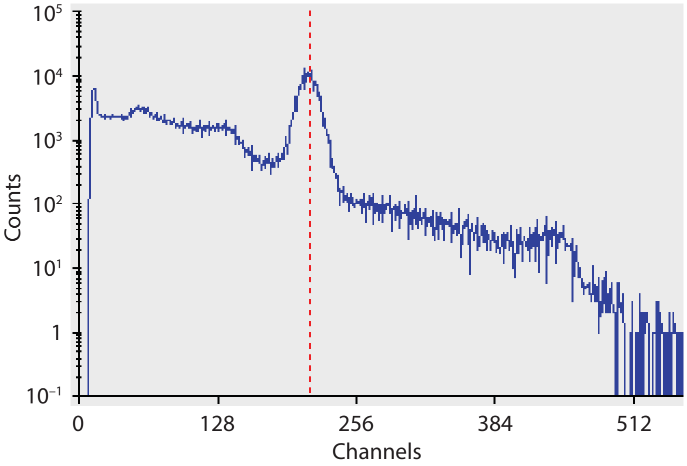

Figure 8. Spectra of small ^{241}Am and stronger ^{137}Cs sources collected with prototype XMCA with approximately 50K counts per second throughput

software and hardware met our expectations for spectral results, power consumption, and throughput.

Through the use of structured design architecture and a highly functional FPGA development environment, we produced an MCA design that will likely be adaptable to a multitude of projects. Because of our approach and development environment, our design is easy to maintain, modify, and reuse, allowing a much more rapid and thorough process to be realized by other members of the engineering and scientific communities in order to further capabilities. We cannot emphasize enough the importance of owning this design; we now have the ability to fairly easily, with rapid turnaround, change the configuration as needed and avoid lengthy delays involved in using commercial MCAs.

ACKNOWLEDGMENTS

We would like to thank Andrew Green, Michael Reed, Paul Guss, and Ken Braithwaite for their advice, input, feedback, and encouragement relating to this work.

Transient RF and Optical Plasma Signatures

STL-024-17 ■ Continuing in FY 2018 ■ Year 1 of 2

Clare Kimblin,[1,a] Ian McKenna,[a] Manuel J. Manard,[a]
Duane Gardner,[a] Xianglei L. Mao,[b] and Gary Walker[c]

[1]kimblicw@nv.doe.gov, (805) 681-2257
[a]Special Technologies Laboratory
[b]Applied Spectra Incorporated
[c]Remote Sensing Laboratory–Nellis

Large-scale high-explosive (HE) tests have characteristic radio frequency (RF) and optical signatures that are useful observables for nonproliferation and treaty verification purposes. We need to better understand the fundamental aspects of these signatures, and we are seeking to develop well-characterized and controlled laboratory conditions to test theoretical predictions. This year we developed test capabilities to support statistically repeatable benchtop experiments. Methods to measure RF emissions and characterize the constituent atoms, ions, molecular species, and carbon clusters produced in HE tests were devised. A specially configured RF-shielded optical test chamber was used in preliminary tests, and a custom high-pressure cluster source was designed and fabricated. In FY 2018, the cluster source will be used as the input to an ion mobility-mass spectrometer (IM-MS) to provide carbon cluster size and charge distributions following laser ablation of graphite and to inform RF and optical measurements. In initial open-air experiments, time-resolved RF, optical emission spectra, and plasma images were collected following laser ablation of graphite. Preliminary tests involving laser ablation of Detasheet were also performed as a gateway to using de minimis quantities of HE in laser ablation/IM-MS, RF, and optical measurements. In addition, we describe information gained from the fielding of RF antennas at the NNSS Forensic Surface Shots campaign.

BACKGROUND

The ability to distinguish high-explosive (HE) package designs based on radio frequency (RF) observables remains a major objective of HE test programs. Experimental data capable of providing validation for chemical and physical processes on sub-micron–length scales and at early times (to microseconds) is lacking, however, and this insufficiency is a major hindrance to developing new models for HE detonation (Willey 2017). Current methods to study RF from large-scale HE experiments also do not allow for the separation of RF emissions originating from fundamentally different sources such as air shock, detonation, and combustion. Furthermore, large-scale HE experiments cannot provide the repeatability required for statistical analysis. This project seeks to address some of these issues using small-scale, repeatable measurements under controlled conditions.

Helios RF modelers seeking to address different aspects of RF generation have a number of theories regarding the origin of RF emissions. Modeling efforts at Sandia National Laboratories are focused on RF generated by individual charges (i.e., where discharge between two molecules or ions can lead to a cascade of discharges) rather than material properties. Solid carbon is a major constituent of product mixtures following detonation of carbon-rich HE (Watkins 2017), and at Lawrence Livermore National Laboratory (LLNL) RF produced by charging carbon particulates is the focus of modeling efforts. The diagram in Figure 1 shows a notional representation of the generation of carbon clusters resulting from propagation of a detonation wave through an explosive. The sequential formation of solid carbon indicated by the diagram may be incomplete. In both large- and small-scale tests, blackbody-emitting carbon particulates are difficult to characterize because they do not have distinct spectral emissions. Although time-resolved small-angle x-ray scattering (TR-SAXS) measurements are now being made in the ~100 ns post-detonation time regime (Watkins 2017), structural studies of solid carbon products, such as scanning and transmission electron microscopies, powder x-ray diffraction, Raman spectroscopy, and x-ray pair distribution function measurements, are the more standard measurements performed on samples retrieved following large- and small-scale detonations. To our knowledge, with all of these methods, particle charges are not identified and transient RF signatures are not collected.

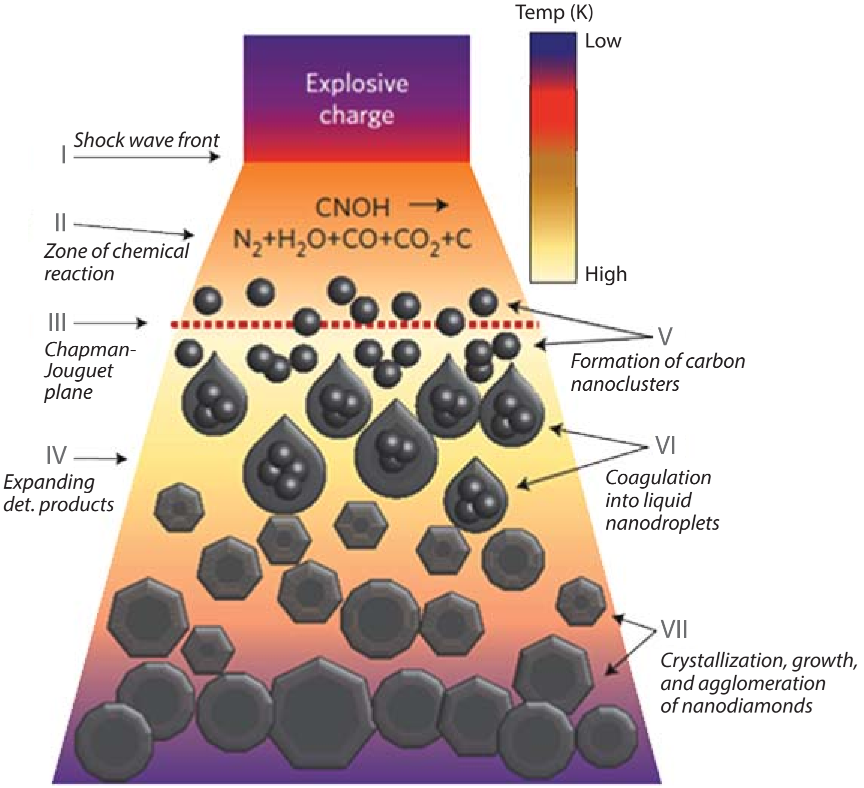

Figure 1. Notional representation of detonation wave propagation indicating the production of a dense fluid of molecular gases and solid carbon following HE detonation. Image from Mochalin (2012).

Using controlled, surrogate experiments we will explore the role of chemical and physical processes in RF generation, mainly on carbon particulates. Processes that are likely to generate electric fields that lead to subsequent discharge and RF emissions during and following laser ablation (LA) of graphite include (1) differential ejection of electrons or ions during the ablation process, creation of an electric field at the graphite surface; (2) charging of delaminated layers of graphite as they separate from the substrate; (3) collective behavior in plasma ionized by shock-heated air; (4) triboelectric contact charging between carbon clusters and separation based on Stokes number; and (5) charging of carbon atoms and clusters while immersed in the plasma (Sears 2017).

In previous work we demonstrated that LA generates species that correspond to some of those observed in HE tests at similar temperatures (Kimblin 2017). When materials are laser ablated, temperatures (>10,000 K) and pressures (tens of GPa) mimicking detonation are reached. In addition to ionic, atomic, and molecular species formed following LA of graphite, carbon clusters are also produced. This project employs laser ablation of graphite as a laboratory method to generate such clusters and explore their role in RF generation. Two systems were designed and fabricated: an RF-shielded stainless-steel optical test chamber for the collection of RF emissions and ultraviolet near infrared (UV-NIR) signatures following laser ablation, and a custom high-pressure cluster source (as the front end to an ion mobility-mass spectrometer [IM-MS]) for the creation and characterization of large carbon clusters. Using the RF/optical chamber, simultaneous RF and UV-NIR emissions will be collected to correlate RF signals and emission from spectroscopically distinct (ionic, atomic, molecular) species. By using the high-pressure cluster source coupled to an IM-MS, spectroscopically indistinct particulate species will be characterized by mass, charge, and allotrope. For integration of results between the RF/optical and IM-MS experiments, the same controlled conditions for plasma generation will be used in both the RF/optical and IM-MS experiments.

Analytic and empirical data from these experiments will be provided to RF modelers to inform their models, and feedback from RF modelers will guide further laboratory experiments. In this way, this project will benefit current nonproliferation and treaty verification programs by providing empirical data from controlled tests that are pertinent to informing and testing predictive RF models.

PROJECT

RF Measurements at the Forensic Surface Shot (FSS) Experiment

Early in FY 2017 the forensic surface shot (FSS) experiment presented an opportunity to field antennas at the NNSS in conjunction with UV-NIR spectrometers, allowing us to become more familiar with RF measurements in the field. The shots ranged in size from 87 to 1000 kg. An active monopole antenna (10 kHz–80 MHz) and passive biconilog antenna (30 MHz–1 GHz) were fielded at distances of 1 km and 300 m from ground zero to prevent damage to antennas and electronics due to the blast. Predicted signal strengths were based on a paper by Harlin et al. (2009) in which RF signals were collected from 10 kg detonations at distances of 37.5 and 75 m from ground zero. In addition, two assumptions were made to account for distance and mass scaling. First, RF field strength drops with distance (r). For low frequencies a drop of $1/r^{2.5}$ between 37.5 and 75 m was noted by Harlin; above $r > 75$ meters the drop was expected to be between $1/r^{2.5}$ and 1/r, depending on where the transition to far field occurs. At the 300 m site, this predicts a reduction in signal as high as 1/180 relative to the signal measured by Harlin (2009). For high frequencies the RF field strength drop was predicted to be 1/r. At the 300 m site, a 1/8 reduction in signal was predicted based on distance. The second assumption was that RF field strength scales with HE blast pressure such that $[\mathrm{Mass}_{(\mathrm{FSS})}/\mathrm{Mass}_{(\mathrm{Harlin})}]^{1/3} \geq \sim$4.6-fold increase at FSS for a 1000 kg explosive.

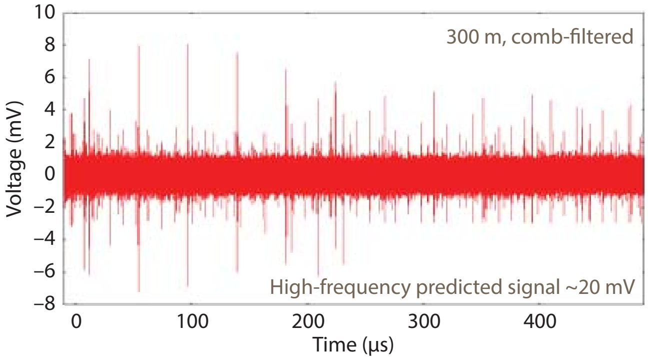

Figure 2. Results from the passive biconilog antenna positioned at 300 m from ground zero. No evidence of HE-related RF emission was observed.

HE-related RF signals were not identified in any of the RF data collected at the four shots. Despite the prediction that the high-frequency signal from the 1000 kg test would be >2x higher than the observed noise level, there was no evidence of an HE-related RF signal in the comb-filtered RF trace collected at 300 m with the passive biconilog antenna (Figure 2). The lack of HE-related RF emission may be due to effects of terrain, scope bandwidth, HE configuration, and unknowns related to scaling with mass.

RF Measurements in the Laboratory

The large-scale, not readily repeatable FSS experiments emphasized difficulties associated with field measurements and the appeal of controlled laboratory experiments. An RF-shielded, vacuum-

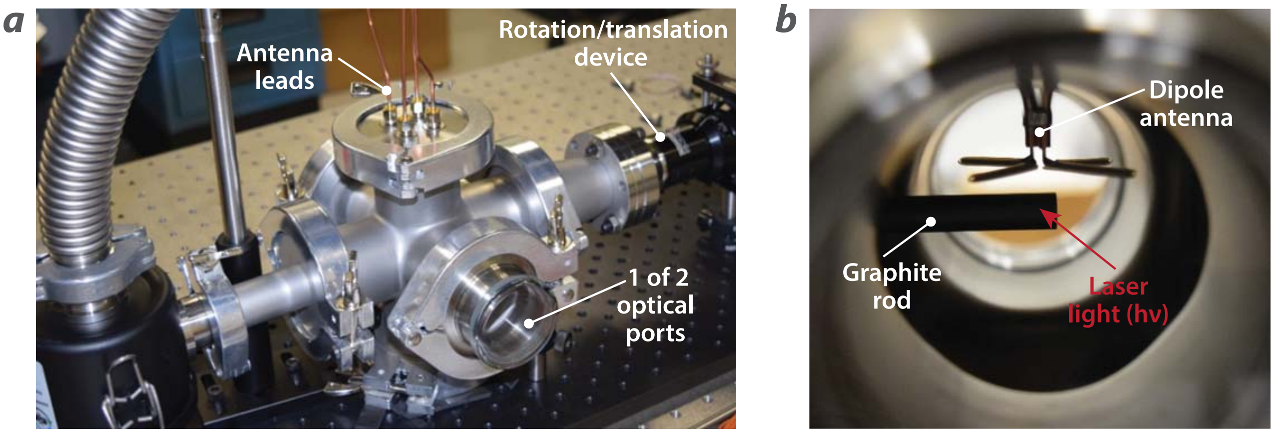

Figure 3. (a) RF/optical vacuum chamber in the lab, (b) view through the rear optical port where the laser beam (hν) enters and creates a plasma normal to the plane of the paper. The dipole antenna can be moved varying distances from the graphite and can be rotated to study the effect of changing the antenna position relative to the plasma.

tight six-way-cross was designed and fabricated from stainless-steel parts (Figure 3) for controlled RF/optical measurements. In the apparatus, antennas are shielded from outside RF noise sources, and conditions can be varied (pressure, bath gas, and substrate) while optical measurements are performed (emission spectra and/or plume imaging).

Initial RF measurements under vacuum and in air were made using the RF/optical vacuum chamber at the Special Technologies Laboratory (STL) and a copper (14 gauge), cross-polarized dipole antenna with a 1 to 500 MHz balun. The antenna response was first tested within the chamber using a reference probe ~2 cm from the graphite rod, and the probe antenna ~3 cm on the opposite side of the rod. Except for apparent resonances at 20 and 300 MHz, the probe exhibited a near ideal linear/log response. Following laser ablation of the graphite rod (Quantel/Brilliant, ~140 mJ/pulse, 4.4 ns pulse width at 1.064 µm) in the RF-shielded chamber, the antenna did not pick up any signal associated with the laser flash lamp, and the observed signal-to-noise ratio was more than 5x higher than that measured at Applied Spectra Incorporated (ASI) (without a test chamber). Additionally, the RF pulse persisted for multiple microseconds (Figure 4).

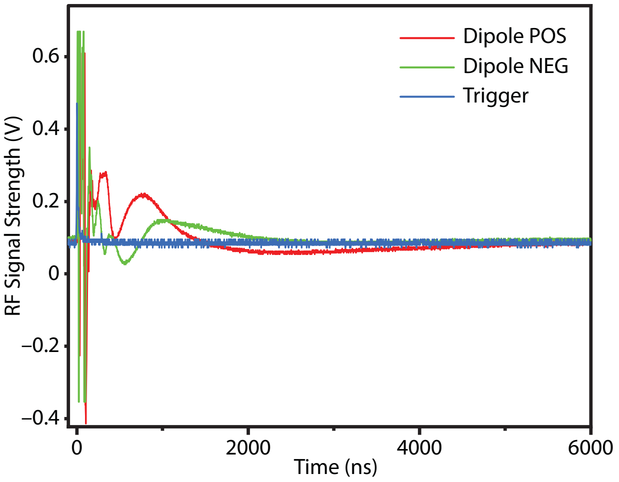

Figure 4. Representative RF trace collected in the RF/optical chamber

While the RF/optical vacuum chamber was being designed and built at STL, a number of RF measurements were made at ASI in open air without a chamber. A dipole antenna identical to the one used in the RF/optical chamber was used at ASI. Results of a study on laser ablation (Quantel/Brilliant B, 153 mJ/pulse, 14 ns pulse width at 1.064 µm) of graphite in air with laser focus 1 mm below the graphite surface to limit laser sparking of air (5 cm focal length and 4.9 cm focal distance, 120 µm estimated spot size) are shown in Figures 5 and 6. Figure 5a shows the laser pulse trigger recorded using a photodiode (black trace) and the background-subtracted RF signal (red trace). The measured RF signal lasts ~150 ns, and the strongest RF is observable in the first ~20 ns. Figure 5b shows plasma images at 10 ns intervals following laser ablation of the graphite. In the first ~20 ns, the plasma size changes most dramatically and only continuum emission is observable spectroscopically. Ionic species, such as C^+ and N^+, start to appear at about 50 ns (Figure 6). These results suggest that the strong early-time RF emission may be caused by the rapid expansion of the plasma, implying that the strong RF comes from the fast-moving charge and/or a rapid drop in charge density. It is possible that the fast-moving charge is associated

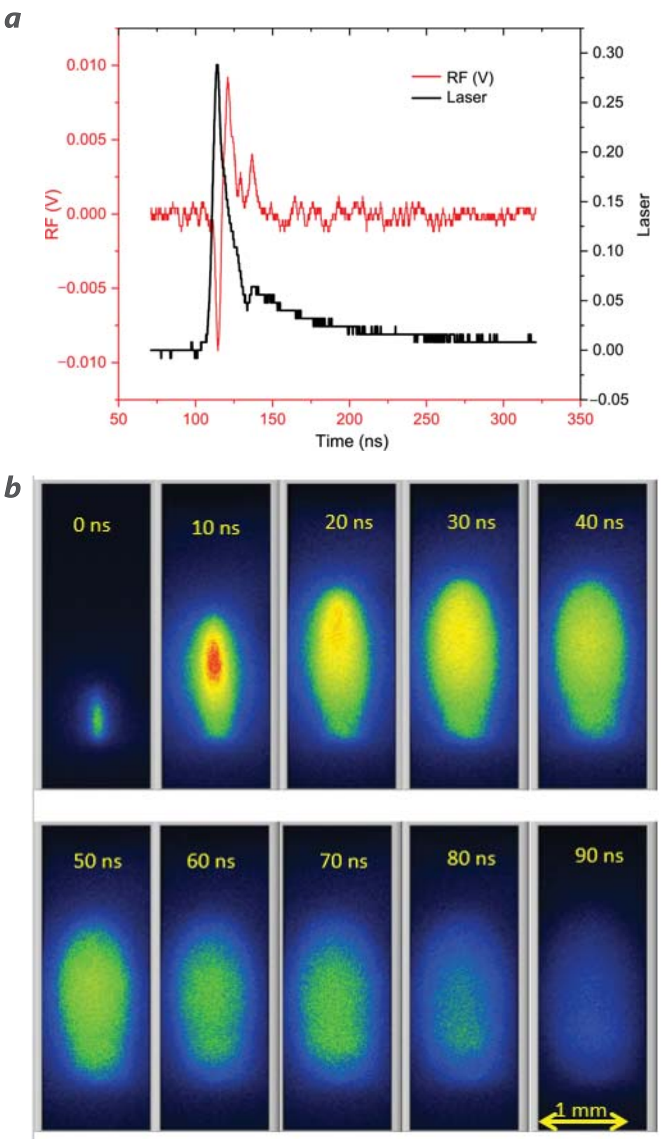

Figure 5. (a) RF emission (red trace) and photodiode response (black trace) –50 to ~250 ns after LA and (b) graphite plasma images at 10 ns intervals

with small ionic species and/or charged carbon clusters. Although we do not have equivalent information for the evolution of carbon clusters following LA of graphite, TR-SAXS studies performed with 10 mg quantities of explosive (PBX 9502) indicate that carbon cluster formation is mostly complete within the first 200 ns following its detonation (Watkins 2017).

In FY 2018 we will collect imagery of the plume and emission spectra using the RF/optical chamber. Emission spectra of C^+ and N^+ will allow us to derive electron density as a function of time, and temperature will be derived spectroscopically.

Cluster Source and Ion Mobility Mass Spectrometer (IM-MS)

Ideally, characterization of carbon clusters by mass, charge, and geometry using IM-MS would occur in concert with RF and optical measurements made in the RF/optical chamber. Before a hybrid RF/optical–IM-MS chamber can be proposed, demonstration of a custom, high-pressure cluster source is needed.

Usually cluster ionization sources are operated under vacuum (~10^{-4} Torr) with the result being that low molecular weight clusters are produced. For the creation of large carbon clusters, such as carbon nano-onions (CNOs), and others created from detonations, higher operating pressures and specific heating and cooling techniques have been used. For instance, Dorobantu et al. (2014) report on the fabrication of CNOs following laser ablation of graphite into a 900°C furnace at 7 Torr. Ablation products were collected by condensation on a water-cooled cold finger. To directly create higher molecular weight carbon clusters as input to the IM-MS, we designed and fabricated a high-pressure cluster source that will operate at five orders of magnitude higher pressures than a typical cluster source (Figure 7). Buffer gas will be introduced to collisionally cool the plasma and provide variable pressures, likely ranging from about 10 to 1000 Torr.

Near the end of this fiscal year, fabrication of the cluster source was complete, and testing is scheduled for FY 2018. This year, to provide a baseline result, a conventional pulsed-valve cluster source was used to create clusters following laser ablation of graphite at approximately 10^{-2} Torr.

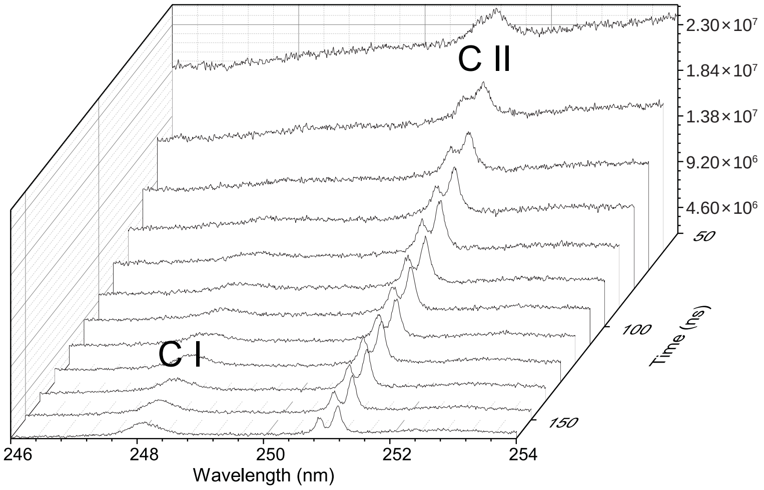

Figure 6. UV emission, 50 to 160 ns after LA, single pulse

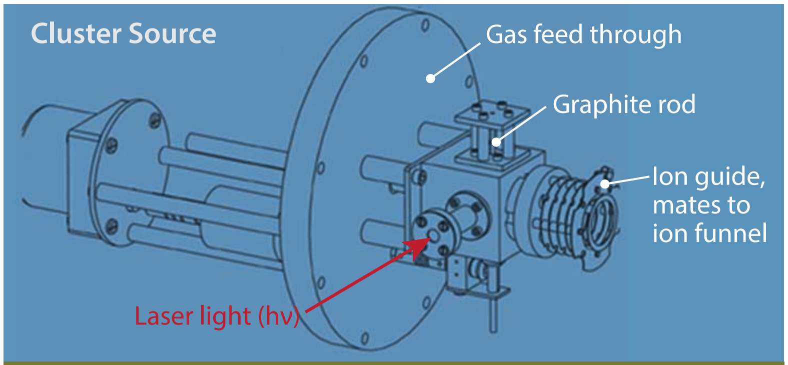

Figure 7. Custom cluster source designed to operate at pressures up to five orders of magnitude higher than a conventional cluster source. The cluster source will reside in the IM-MS source chamber.

As shown in Figure 8, cluster sizes ranged from about C_9^+ to C_{14}^+ using the lower pressure cluster source. Significantly larger cluster sizes are expected with our custom high-pressure source in FY 2018. Carbon cluster sizes and geometries will be compared to those from structural studies of solid carbon products retrieved following detonations, based on literature reports.

Laser Ablation of Detasheet Experiments

Research from the Army Research Laboratory suggests that with laser-ablated HE, chemical reactions in the vapor plume, behind the shock front, affect the air shock front velocity as measured by the speed of propagation of air above the ablated material (Gottfried 2014). For energetic materials Gottfried observed a strong correlation to calculated energies of detonation (Figure 9). By laser ablating HE we would like to cause it to deflagrate, after which we would compare the clusters and RF generated in this manner to the clusters and RF generated by LA of graphite. We can then compare the LA-produced carbon clusters to those reported as produced from true detonations (based on the literature) to see how different the species' distributions are.

We performed some preliminary tests with a 10 mg sample of Detasheet in the STL Boom Box to determine if deflagration could be observed using significantly lower laser power than reported by Gottfried (2014). Detasheet is ~63% PETN (pentaerythritol tetranitrate) in an inert binder, and though not a pure explosive, it was used for preliminary experiments because it was readily available in de minimis quantities (10 mg and less for a secondary explosive) that can eventually be removed from the Boom Box area. A Schlieren imaging configuration with a 9-frame camera was used to image the shock wave front and compare air shock velocities from a laser-ablated energetic material (Detasheet) to those from a laser-ablated nonenergetic material (control). Two Nd:YAG (neodymium-doped yttrium aluminum garnet) lasers, first of a lower power (Big Sky/CFR400, 90 mJ, 5–10 ns pulse width at 1.064 μm) then a higher power (Quantel/Brilliant, ~250 mJ, 4.4 ns pulse width at 1.064 μm), were used to target the Detasheet (~0.8 mm diameter spot size). For the experiments using the higher-powered laser, Detasheet was confined on all but one side in a narrow cylinder cut into an aluminum block. No evidence of deflagration was observed with either laser. As shown in Figure 10, the distance between the substrate surfaces (Detasheet and control) and vertical air shock wave fronts are the same by 22 μs. Based on visual inspection of the Detasheet, there was also no evidence of deflagration. We expect that this is due to the dilution of PETN (63%) in the binder and the lower laser powers used in this work compared to Gottfried's 900 mJ, 6 ns pulse width (1.064 μm). In FY 2018 the tests will be repeated with a <10 mg sample of pure explosive. If deflagration is observed, we will laser ablate PETN in the cluster source and the RF/optical chamber.

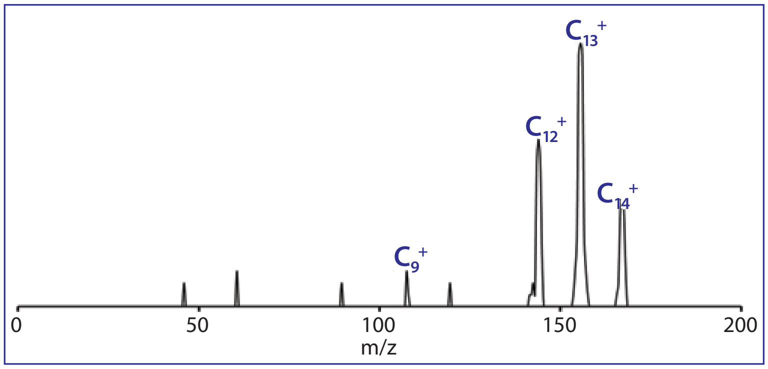

Figure 8. IM-MS pulsed-valve cluster source result, showing carbon clusters produced by LA of graphite under vacuum at conventionally low pressure (~10^{-2} Torr, t = ~1 μs)

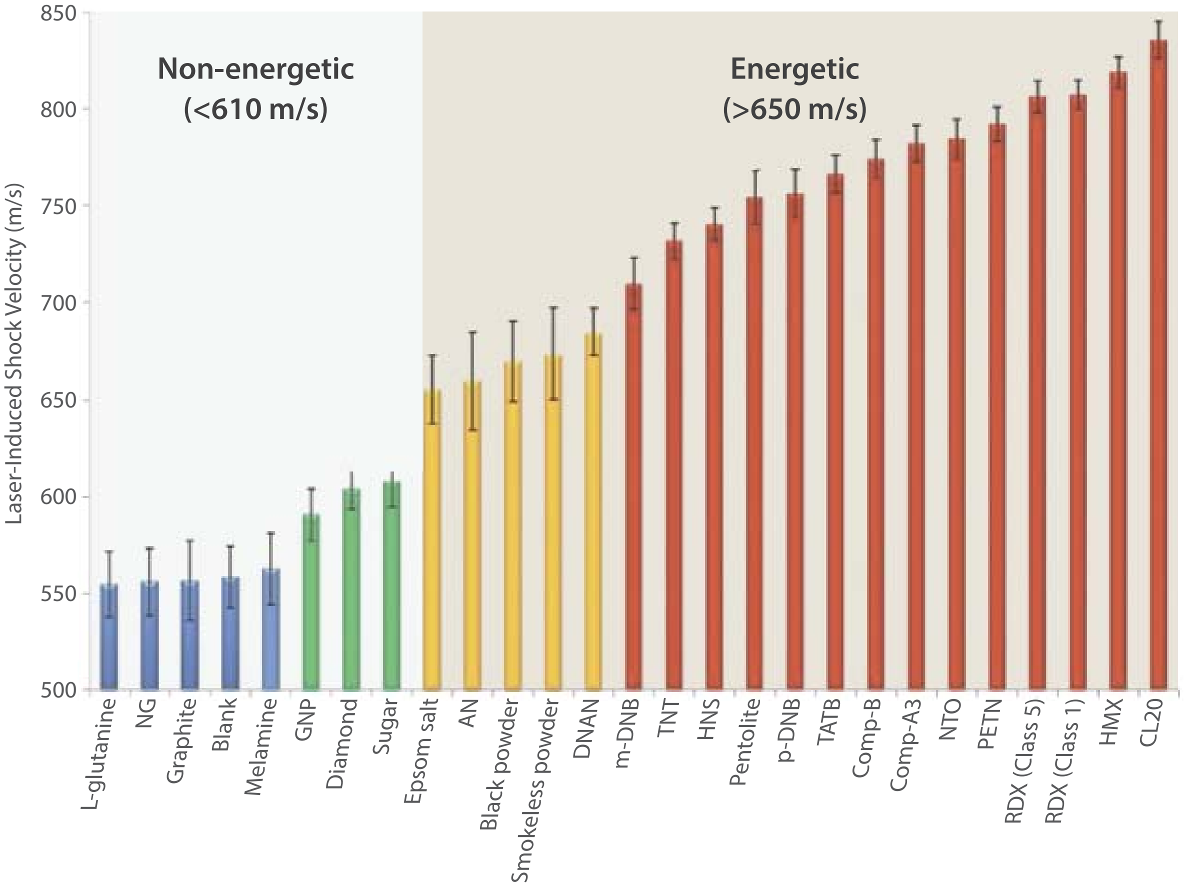

Figure 9. Characteristic laser-induced shock velocities measured following laser ablation of nonenergetic and energetic materials. Plot based on Gottfried (2014).

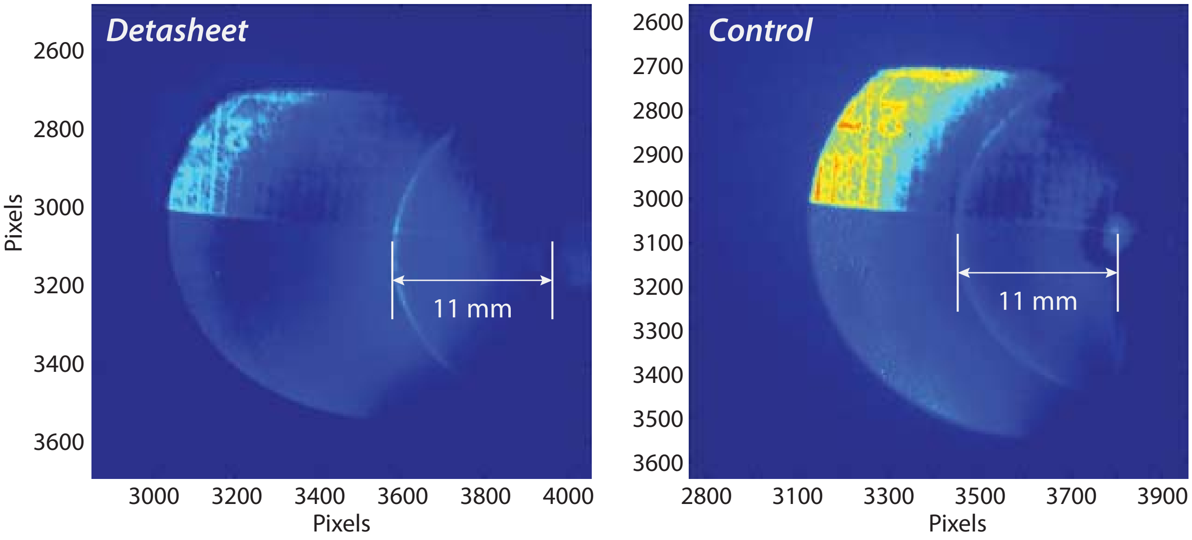

Figure 10. Schlieren images of air shock wave above target surfaces at t = 22 µs (1064 nm laser, 90 mJ, no sample confinement)

CONCLUSION

In the first year of this two-year project, we have set the stage for controlled RF/optical and mass spectrometry experiments to be performed in FY 2018. We have designed and built an RF/optical chamber and a custom high-pressure cluster source. The shielding of the RF/optical chamber is such that we do not observe interference from the laser flash lamp, and RF signal strength is higher than in the experiments performed without an RF-shielded chamber. Initial results from the RF/optical work performed in air without RF shielding indicate that the strongest RF coincides with the fastest growth of the plasma plume.

In FY 2018 the custom high-pressure cluster source will be placed in the IM-MS source chamber, and cluster sizes will be compared to those reported from true detonations. If signs of deflagration are seen with PETN, distributions of species and RF produced following laser ablation of HE will be compared to those from laser ablation of pure carbon substrates. Using like conditions in the RF/optical chamber and cluster source IM-MS, we will probe the contents of the plasma and look for correlations between species, conditions characterized, and RF signatures. Data and analytic results will be shared with Helios RF modelers to facilitate further study.

ACKNOWLEDGMENTS

We would like to thank Ben Valencia and Tom Keenan for design and fabrication support; Michael Grover, Jason Mance, Brandon La Lone, Gene Capelle, and Jason Scharff who supported the setup and execution of Boom Box experiments; and Jason Sears (LLNL RF modeler) for his contributions.

REFERENCES

Dorobantu, D., P. M. Bota, I. Boerasu, D. Bojin, M. Enachescu, “Pulse laser ablation system for carbon nano-onions fabrication,” *Surface Engineering and Applied Electrochemistry* **50**, 5 (2014) 390–394.

Gottfried, J. L., “Influence of exothermic chemical reactions on laser-induced shock waves,” *Phys. Chem. Chem. Phys.* **16** (2014) 21452–21466.

Harlin, J., R. Nemzek, “Physical properties of conventional explosives deduced from radio frequency emissions,” *Propellants Explos. Pyrotech.* **34** (2009) 544–550.

Kimblin, C., R. Trainham, G. A. Capelle, X. Mao, R. E. Russo, “Characterization of laser-induced plasmas as a complement to high-explosive large-scale detonations,” *AIP Advances* **7** (2017) 095208.

Mochalin, V. N., O. Shenderova, D. Ho, Y. Gogotsi, “The properties and applications of nanodiamonds,” *Nature Nanotechnology* **7** (2012) 11–23.

Sears, J., personal communication, June 2017.

Watkins, E. B., et al., “Evolution of carbon clusters in the detonation products of the triaminotrinitrobenzene (TATB)-based explosive PBX 9502,” *J. Phys. Chem. C* **121**, 41 (2017) 23129–23140.

Willey, T. M., et al., “Measurement of carbon condensates using small-angle x-ray scattering during detonation of high explosives,” *AIP Conf. Proc.* **1793** (2017) 030012-1–030012-5.

Gas-Phase Ion-Neutral Interactions of Cerium Ions with Deuterium

STL-002-17 ■ Continuing in FY 2018 ■ Year 1 of 2

Manuel J. Manard,[1,a] Paul R. Kemper,[b] and Rusty Trainham[a]

[1]manardmj@nv.doe.gov, (805) 681-2121
[a]Special Technologies Laboratory
[b]University of California, Santa Barbara

The gas-phase interactions of cerium (Ce) cations and deuterium neutrals have been investigated using a temperature-dependent reaction cell that is embedded between two quadrupole mass analyzers. Ce_m^+ clusters (m = 1 – 24) have been generated with our instrumentation, and rate constants have been acquired for the dissociation of deuterium by insertion Ce^+ as a function of temperatures ranging from approximately 275 K to 525 K. A negative temperature dependence is observed, indicating the reaction becomes less efficient as the temperature is increased. A combination of experimental and theoretical analyses suggests that the overall reaction is exothermic for insertion of Ce^+ into the deuterium bond. Electronic structure calculations were performed using density functional theory at the B3LYP level to characterize all reactant and product species as well as to generate a transition state structure for the insertion reaction. In FY 2018, we will seek to extend these methods to larger Ce clusters.

Background

Ejecta contributions to weapons performance remains an active area of research. Validation and verification of nuclear weapon simulations, specifically transport models, can be limited if uncertainty in the composition of the ejecta cloud exists. Ejecta density and size distributions are measured using dynamic holography, Mie scattering, x-ray radiography, and piezoelectric pins. None of these techniques can be used to determine the time evolution of the chemical composition of an ejecta field. Instrumentation developed at the Special Technologies Laboratory has recently been used to investigate these chemical phenomena. As such, detailed studies of the gas-phase thermodynamic and kinetic properties of these species have been carried out to provide insight into the fundamental processes governing reactivity of ejecta at the molecular level in support of ongoing stockpile stewardship research efforts. Specifically,

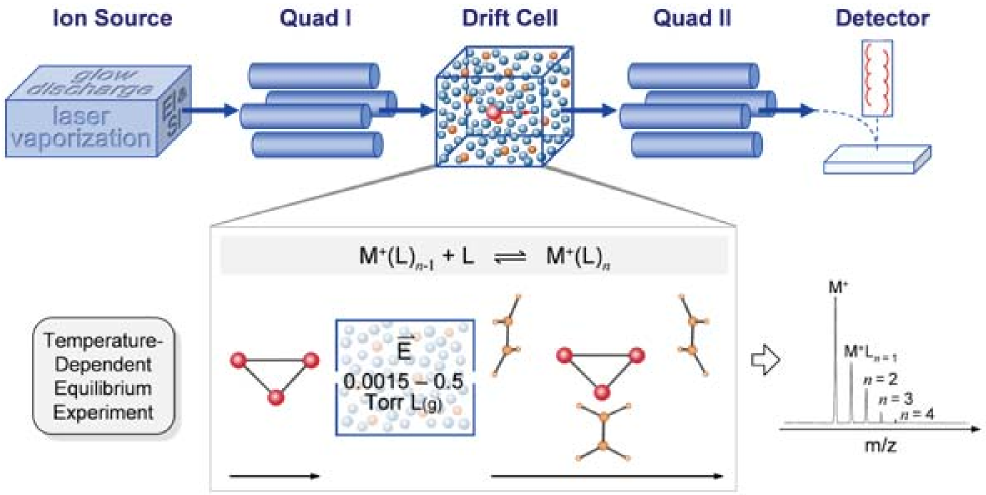

Figure 1. A schematic representation of the quadrupole-cell-quadrupole mass spectrometer

by probing the reactions that occur when shocked material interacts with other chemical species in their surroundings, the results acquired here could provide information leading to improved diagnostic capabilities for the stockpile science and technology community as well as provide experimental data for simulation benchmark research.

PROJECT

Experimental Method

A schematic representation of the instrument and an illustration of the type of data that is generated by the system are shown in Figure 1. The design details of the components that make up the various regions of the instrument were described previously (Manard 2014, 2015). Thus, only a brief discussion of the design of the system will be provided. Ce_m^+ clusters are generated by pulsed laser vaporization of a translating/rotating cerium rod in a high-pressure argon (Ar) bath gas. The desorbed cerium plasma is cooled by collision with the inert bath gas. The timing of the Ar pulse is synchronized with the laser using a Stanford Research Systems delay generator (DG535). The typical Ar pulse width is on the order of 200 µs with a backing pressure of 40 psi. Cerium clusters exiting the source are then mass selected by the first quadrupole mass filter and injected into the reaction cell.

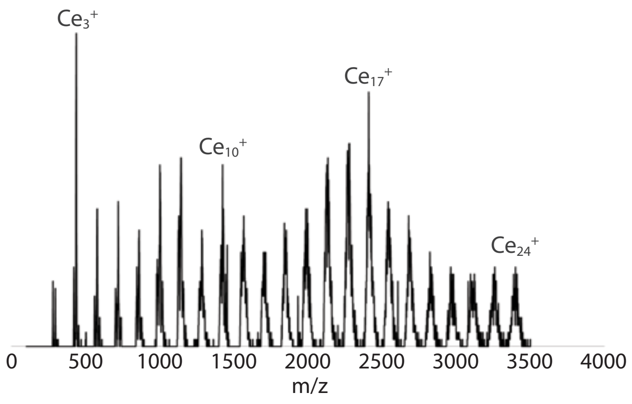

Figure 2. A mass spectrum of the Ce_m^+ ($m = 2 – 24$) clusters

The reaction cell is a copper (Cu) block 4 cm long with an entrance and exit orifice measuring 0.5 mm in diameter. The cell can be filled with either inert (helium, He) and or reactive (deuterium, D_2) gases kept flowing to maintain constant pressure. The typical gas pressures in the cell range from 2 to 4 Torr. Pressures in the cell are measured using a capacitance manometer. The experimental temperature range of the cell is variable from 80 K to 800 K. The temperature is monitored by three thermocouples placed at various locations on the cell. Multiple thermocouples are used to verify no significant temperature gradients exist across the cell. Ions are drawn though the cell under the influence of a weak electric field (drift voltage). The field is weak enough so that the thermal energy of the ions is not significantly perturbed. Ions exiting the cell are mass selected by a second quadrupole mass filter and detected using a Channeltron electron multiplier. The amount of time ions spend in the cell is controlled by adjusting the drift voltage and/or the pressure in the cell. If the relative ratio of the product to reactant peaks does not change with time, then temperature-dependent equilibrium methods can be used to obtain thermodynamic properties of the system. If the relative ratio of the product to reactant peaks does change with time, then reaction rate constants can be acquired and how the rate constants vary with temperature can be determined.

A mass spectrum of the Ce_m^+ (m = 2 – 24) clusters generated by the system is shown in Figure 2. The data shown were acquired by allowing all cluster ions produced by the source to pass through the first quadrupole and scanning the second quadrupole. The cell was filled with 2 Torr of He, so no reaction products are formed. The size distribution of the clusters shown in Figure 2 is unique to the set of experimental conditions used to generate the mass spectrum. Varying the parameters can shift the distribution to favor formation of smaller clusters, such as the Ce^+ monomer and dimer. These data show the current system is capable of generating a wide range of Ce_m^+ species.

Atomic cerium cations were initially studied to gain a fundamental understanding of the cerium-deuterium interactions. Accordingly, mass spectra of Ce^+, obtained with 2 Torr of He present in the cell are shown in Figure 3. The upper spectrum shown in Figure 3 was acquired with quadrupole one set to allow all ions to pass through, and thus all naturally occurring isotopes of Ce are observed. The lower spectrum was acquired by mass selecting m/z = 140, which corresponds to the Ce isotope having the greatest relative abundance. These data illustrate the ability of the instrument to select specific isotopes to prevent any potential mass inferences from being injected into the reaction cell.

Figure 4 shows mass spectra of Ce^+ acquired with 2.5 Torr of D_2 filling the reaction cell at a temperature of 325 K. Both spectra were obtained by mass selecting m/z = 140 (Ce^+) with the first quadrupole and scanning the second quadrupole over the mass range shown. It is clear from these spectra that a single D_2 (m/z = 4) is bound to the core ion, which corresponds to the peak shown at m/z = 144. It is also clear that a peak is present at m/z = 142, a result of an H_2 isotope impurity present in the cylinder of D_2. The impurity is present at a relatively small concentration (approximately 2000 ppm according to manufacturer specifications) and is compensated for in the analysis as described in a later section.

The upper spectrum of Figure 4 was acquired at a reaction time of 21.7 μs and the lower spectrum at a reaction time of 127.2 μs. It is apparent from these data that the relative ratio of Ce^+ reactant and the CeD_2^+ products peaks are changing significantly with time. These data suggest that the system has not reached equilibrium because the ratios of these peaks are not time independent. Thus, time-dependent rate constants can be acquired for this system.

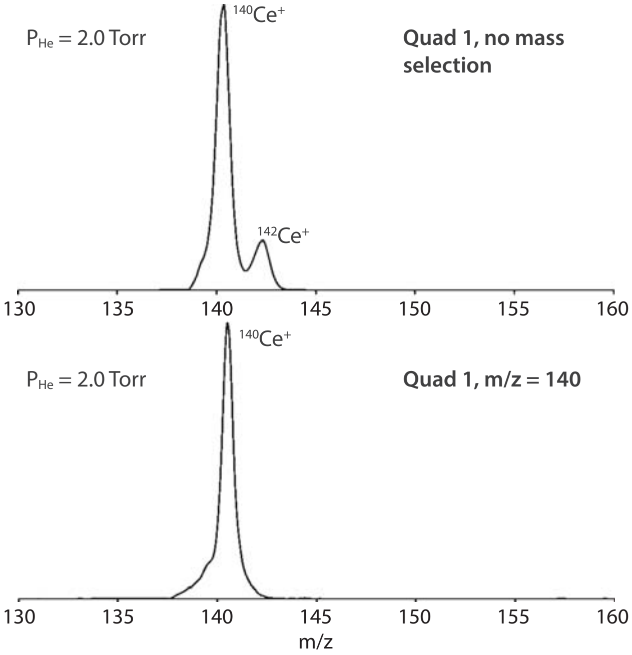

Figure 3. Mass spectra acquired for Ce^+. For the upper spectrum, no mass selection is used. The lower spectrum show mass selection of m/z = 140.

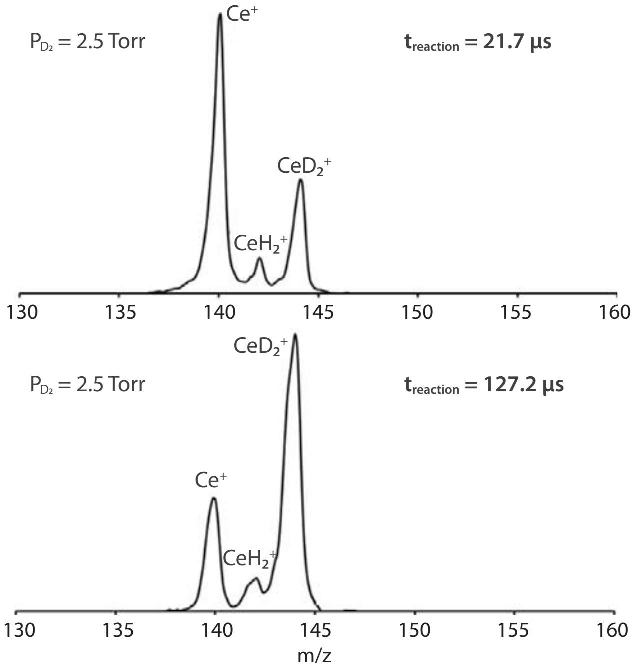

Figure 4. Mass spectra illustrating the time-dependent relative concentrations of Ce^+ to CeD_2^+ acquired at T = 325 K and a D_2 gas pressure of 2.5 Torr. The reaction times for the upper and lower spectra are provided.

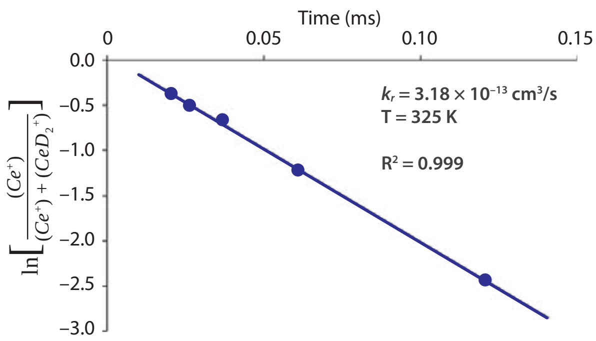

Figure 5. A plot of the natural log of the relative concentrations of reactant and product ions versus time acquired at T = 325 K. The resulting rate constant and the R^2 value of the plot are also provided.

Reaction Mechanism

Rate constants for the pseudo-first order reaction

$$Ce^+ + D_2 \xrightarrow{k_r} CeD_2^+ \tag{1}$$

were determined from the expression

$$\ln\left[\frac{Ce^+}{Ce^+ + CeD_2^+}\right] = -k_r \times \rho_L \times t, \tag{2}$$

where $[Ce^+]$ is the concentration of unreacted Ce^+, $[Ce^+ + CeD_2^+]$ is the sum of the concentration of unreacted Ce^+ and the CeD_2^+ concentration (representing the concentration of Ce^+ at time t = 0), ρ_L is the number density of D_2 in the reaction cell at a given pressure and temperature, t is time in seconds, and k_r is the rate constant for the reaction.

The concentrations used in Equation 2 are directly proportional to the peak intensities in the mass spectra acquired after the ions exit the cell. Rate constants for the overall reaction of Ce^+ with D_2 were acquired by varying the amount of time the Ce^+ ions spend in the cell and plotting the left-hand side of Equation 2 as a function of time. The resulting plots are approximately linear with slopes that are proportional to $k_r(T)$. An example of such a plot is given in Figure 5. The temperature of the cell was varied over a wide range to determine the effect of temperature on the experimental rate constants. These data are shown in Figure 6.

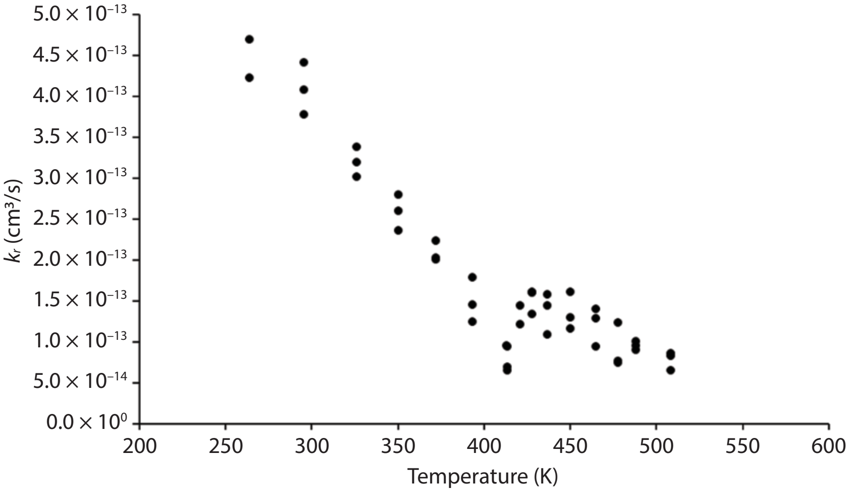

Figure 6. Experimentally measured rate constants for Ce^+ reacting with D_2 as a function of temperature. The text includes a detailed analysis of the data.

Theoretical Method

All reactant and product species were characterized theoretically to determine atomic and molecular parameters needed to analyze the experimental data and to identify factors important in the bonding of Ce^+ with D_2. Density functional theory (DFT) calculations were carried out using the B3LYP hybrid functional and the NWChem software package. For all calculations reported here, deuterium was described using the standard 6-31++G** basis set. The basis set and effective core potential (ECP) used to treat cerium were developed by the Stuttgart-Dresden group and is referred to as Stuttgart RSC 1997 ECP. For heavier elements, atomic basis sets make use of ECPs to replace a certain number of core electrons with an effective potential to reduce the complexity of the calculation. Here, 28 of cerium's core electrons are replaced by the ECP, while all remaining electrons are explicitly treated by the basis set.

Geometry optimizations of CeD_2^+ were performed for multiple candidate structures to determine a true global minimum. To confirm the geometry obtained from the calculation was a true minimum, vibrational frequencies and rotational constants were also calculated to ensure the geometry did not actually correspond to a saddle point, which would manifest itself as a negative vibration frequency in the calculation.

Discussion

The data shown in Figure 6 indicate that a negative temperature dependence is observed for the measured rate constants. This condition implies that the reaction becomes less efficient as the temperature is increased. Phenomena such as this may seem counterintuitive. However, similar situations have been observed for reactions that are exothermic, where a tight transition state is located along the reaction coordinate at lower energy than the reactants at infinite separation. A tight transition state results from a saddle point along the potential energy surface (PES) that the reactants must pass through to proceed to products.

The data in Figure 6 strongly suggest that an exothermic reaction is occurring between Ce^+ and D_2 that must proceed to products (CeD_2^+) through a tight transition state that is lower in energy than the reactant species. This observation also indicates that a more intricate bonding interaction is at play between the reactants. Specifically, when an atomic cation interacts with a neutral diatomic molecule, two types of bonds can form. The first is primarily electrostatic in nature, where a largely unperturbed D_2 ligand is relatively weakly bound to the Ce^+ core ion. With these types of bonding interactions, a small amount of electron density that comprises the σ bond of the two deuterium atoms may be donated to an unoccupied valence orbital of Ce^+. Or, it is possible that a covalent bond between Ce^+ and one or both of the deuterium atoms in D_2 may form. Here, a significant amount of electron density is shared between the cerium cation and one or both of the deuterium atoms. In order to form these new covalent bonds, the existing σ bond in D_2 may be significantly altered or completely broken. It should be noted that the electrostatic interactions described above reach equilibrium extremely quickly, on timescales that are much faster than those achievable with the current design of the reaction cell (<<10 μs). Thus, the fact that rate constants can be measured on the timescale of the experiment strongly suggest the bonding interaction is not of an electrostatic nature.

Figure 7 shows the CeD_2^+ complexes calculated from DFT for an electrostatically D_2 ligand bound to Ce^+ (left) and a species where Ce^+ has inserted itself into the D_2 molecule, breaking the σ bond between the two deuterium atoms and forming two equivalent Ce^+-D covalent bonds. Using the reaction formula given in Equation 1, the energy of the bond formed for the electrostatically bound complex is –7.2 kcal/mol, while the energy of the bonds formed for the inserted CeD_2^+ molecule is –33.1 kcal/mol. It is clear that the inserted species is energetically favored. However, the thermochemistry associated with the insertion process was examined, using DFT energies, to ensure this mechanism is physically plausible.

First, DFT suggests that the energies required to dissociate the D_2, as shown in Equation 3, is approximately 108 kcal/mol.

$$D_2 \rightarrow D + D \tag{3}$$

Thus, in order to break the D_2 bond, an energy in excess of this amount must be available in the Ce^+ insertion mechanism. Now, consider the dissociation reaction shown in Equation 4,

$$CeD_2^+ \rightarrow CeD^+ + D, \tag{4}$$

where one of the covalent Ce^+-D bonds in the inserted CeD_2^+ species (Figure 7b) is broken to release a deuterium atom. DFT suggests that the energy required to break this bond is approximately 70.3 kcal/mol. Because both Ce^+-D bonds are equivalent, the energy released by forming these two bonds is approximately –140.6 kcal/mol. When the cost of breaking the deuterium bond is removed from this value, DFT suggests the overall insertion reaction is exothermic by approximately –33 kcal/mol. This strongly supports the hypothesis that the mechanism giving rise to the experimental rate constants is insertion of Ce^+ into the D_2 bond.

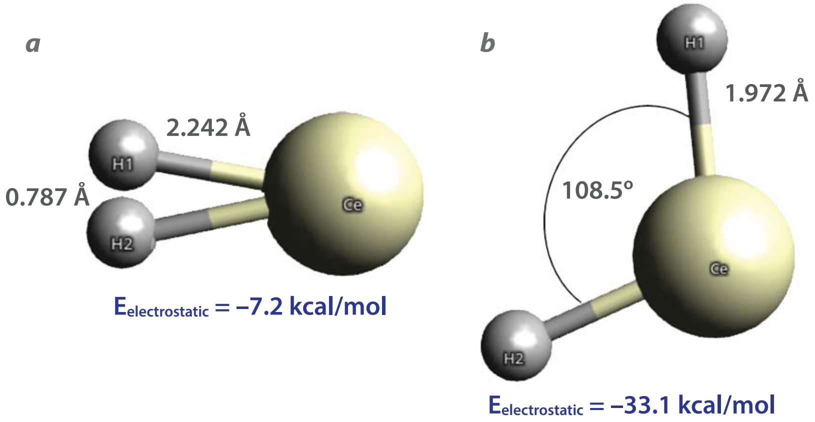

Figure 7. Theoretical geometries of CeD_2^+ complexes calculated at the DFT B3LYP level. Bond lengths are in angstroms, and angles are in degrees. The energies shown for the electrostatically bound molecule and the inserted molecule are calculated relative to the reactant energy asymptote (Equation 1).

Further examination of the valence electronic configuration of Ce^+ also provides evidence in support of the insertion mechanism. Ce$^+$ has the ground-state electronic configuration $5d^24f^1$. It has been previously shown that the interactions of lanthanide atomic cation with neutral species are dominated by the $5d$ or $6s$ electrons and not significantly influenced by the $4f$ electrons (Manard 2017). Thus, the $4f$ electron is not expected to directly participate in the Ce$^+$-D bond formation process. Instead, the two electrons occupying the $5d$ orbitals of Ce$^+$ could directly interact with the electron associated with each deuterium atom to form two Ce$^+$-D covalent bonds. DFT suggests that the bonds formed in the inserted CeD_2^+ molecule are composed of electron density originating for the $5d$ orbitals of Ce$^+$ and the $1s$ orbital of the deuterium atoms. It is this overlap of the $1s$ orbitals with the $5d$ orbital of Ce$^+$ that likely leads to the geometry calculated for the inserted CeD_2^+ species. The 108.5° bond angle of inserted CeD_2^+ indicates the natural orientation of the d orbitals (excluding the d_{z^2} orbital).

We must now explain the negative temperature dependence that occurs for the rate constants of reaction 1. As previously stated, a negative temperature dependence would result from the presence of a tight transition state along the reaction coordinate that lies lower in energy relative to the Ce$^+$ + D_2 asymptote. Accordingly, DFT was used to determine if a tight transition exists along the PES for the insertion of Ce$^+$ into D_2. A series of saddle-point calculations were performed to evaluate if a maximum exists along the reaction coordinate for reaction 1 and the energy of the maximum relative to the reactants and products. The resulting PES is shown in Figure 8. DFT suggests a saddle point exists on the PES at 12.6 kcal/mol below the reactant asymptote. The transition state structure is shown at the saddle point in Figure 8. Here, the deuterium-deuterium bond is beginning to stretch (1.090 Å for the transition state structure versus 0.766 Å for unbound D_2). Additionally, the D-Ce-D bond angle is just beginning to expand at 31.5° versus 108.5° for the final inserted CeD_2^+ structure. Lastly, the vibration frequencies of the transition state were calculated and one negative vibration frequency, corresponding to the stretching of the deuterium bond, was observed. This result strongly supports the hypothesis that there is a tight transition state along the reaction coordinate.

The reaction rates become less efficient as the temperature increases occurs because of the density of available states at the reactant orbiting transition state (where the reactants initially begin to interact with one another) and the tight transition state. As the temperature increases, the Boltzmann distribution of available states at both locations on the PES increase. However, as the temperature rises, the density of states accessible at the reactant orbiting transition state increase faster than those at the tight transition state. This leads to more available pathways for the back reaction than for the reaction to proceed to products. Thus, the back reaction becomes more favorable as the temperature increases, leading to the negative temperature dependence of the rate constants.

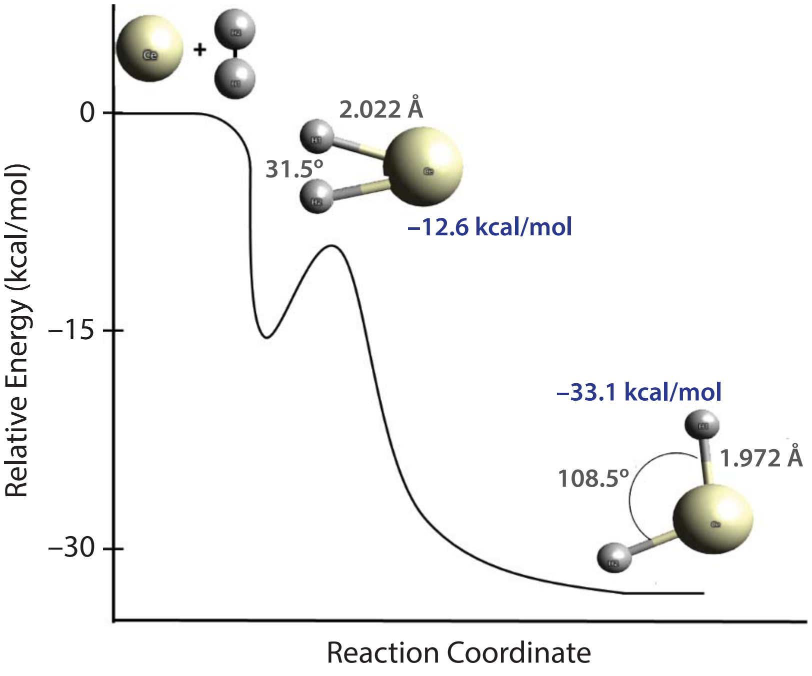

Figure 8. A potential energy surface for the insertion of Ce$^+$ into the D_2 σ bond, calculated using DFT. The calculation suggests a saddle point exists along the reaction coordinate that is lower in energy than the reactant energy asymptote, resulting in a tight transition state at the saddle point. Theoretical geometries of the reactants, products, and the transition state are also shown.

CONCLUSION

Ce_m^+ clusters (m = 1 – 24) have been generated with our instrumentation, and rate constants have been acquired for the dissociation of D_2 by insertion Ce^+ as a function of temperature ranging from approximately 275 K to 525 K. A negative temperature dependence is observed, indicating the reaction becomes less efficient as the temperature is increased. Combined with DFT (B3LYP level), these data have revealed that the reaction is exothermic and that a tight transition state exists along the reaction coordinate. The transition state lies lower in energy than the reactant asymptote and is rate determining because the density of accessible states increases more slowly at the tight transition state, relative to the reactant orbiting transition state, as the temperature increases. This generates more available pathways for the back reaction as the temperature rises, leading to a decrease in reaction efficiency.

The fundamental physical information attained as part of this effort will be used to understand similar data that will be acquired for larger cerium clusters as this effort continues in FY 2018.

REFERENCES

Manard, M. J., "An experimental and theoretical investigation into the chemical properties of uranium and thorium ions in the gas-phase and on surfaces," in *Site-Directed Research and Development*, FY 2013, National Security Technologies, LLC, Las Vegas, Nevada, 2014, 103–107.

Manard, M. J., "An experimental and theoretical investigation into the chemical properties of uranium and thorium ions in the gas-phase and on surfaces," in *Site-Directed Research and Development*, FY 2014, National Security Technologies, LLC, Las Vegas, Nevada, 2015, 139–147.

Manard, M. J., P. R. Kemper, "Reduced mobilities of lanthanide cations measured using high-resolution ion mobility with comparisons between experiment and theory," *Int. J. Mass Spectrom*. **412** (2017) 14–19.

This page left blank intentionally

Large-Area PDV for Characterizing Explosive Particle and Fragment Velocity Distributions

STL-023-17 ■ Year 1 of 1

Ian McKenna,[1,a] **Gerald D. Stevens,**[a]
Jason Mance,[a] **and Brandon La Lone**[a]

[1]mckennij@nv.doe.gov, (805) 681-2273
[a]Special Technologies Laboratory

Large-area photonic Doppler velocimetry (PDV) is applied to dynamic shock measurements to provide early-time velocimetry of particle acceleration and velocity distribution. Current verification methods for explosive dispersal predictive models leave significant gaps in experimental data, in particular the ability to measure particle velocities with high precision for large-volume experiments. In this project we developed a PDV system that can measure over an area of 80 cm^2, as opposed to the traditional point-sampling PDV. Ultimately the large-area PDV could be used to characterize the morphological evolution of a high-explosive event over the complete event, from very early stages (source terms) to an equilibrium state. We found in this work that very high laser powers, on the order of tens of kilowatts, are required to obtain even modest signals when illuminating an 80 cm^2 target area. We present the results of several laboratory experiments using the high-power, laser-illuminated, large-area PDV.

BACKGROUND

Predictive models for improvised chemical explosive devices require realistic source term input to better determine initial conditions and constrain calculations. Current models of the explosive dispersal of liquid constituents, vessel breakup, and shock propagation through airborne particulate suspensions are underdetermined (Theofanous 2011, 2016), and current fluorescent imaging and high-speed camera methods have significant gaps in experimental data. In particular, the ability to measure particle velocities with high precision for large-volume experiments is lacking. In this work we investigated photonic Doppler velocimetry (PDV) techniques applied to centimeter-scale targets to help characterize the morphological evolution of a high-explosive (HE) event over the complete event, from very early stages (source terms) to an equilibrium state.

PDV was the enabling technology that led to the latest generation of experiments at the NNSS U1a Complex, and it holds enormous potential for other dynamic experiments within the DOE enterprise, such as the Helios HE test series and future subcritical experiments. Extending the technology to larger, integrated experiments, without the need for hundreds of PDV channels, as in the current subcritical program, will help improve modeling capabilities and broaden our application space to other experimental areas in shock physics and nonproliferation research. In particular, HE modelers have expressed interest in obtaining dynamic, early-time (~microseconds) velocimetry measurements of shocked materials and metal fragments to bound model inputs of long duration, shock, detonation, and combustion models for HE and metals. Building a capability to more accurately measure HE drive profiles for large-scale explosive tests will facilitate increased model confidence and longer duration model runs.

PROJECT

We develop and apply large-area PDV to dynamic shock measurements to provide early-time velocimetry of particle acceleration and velocity distribution. PDV has previously been used on small-scale experiments with very high precision (<0.1%). We extend the basic PDV methods to larger-scale objects distributed over significantly larger volumes (few to several liters). This project leverages prior DOE and NNSS development of PDV systems to investigate the use of alternative large-optic PDV probe configurations that will allow for larger area sampling, longer standoff distances, and greater target size distributions.

Experimental Approach and Modeling

Our initial exploratory designs for large-area PDV were based on an existing single-channel PDV diagnostic having a two-fiber probe to separate the laser launch from the receiver, thus providing greater beam coverage due to increased beam divergence. We developed a model to estimate how well the two-fiber probe collects reflected light from a target as a function of illumination and distance. The model assumed Lambertian surface scattering from the target and 1550 nm wavelength with an initial numerical aperture (NA) of 0.14 on an 8 µm diameter fiber. To best account for the complexities of mode matching into the single-mode receiver probe, we used Zemax optical software; this software also allowed us to vary parameters such as distance and light intensity. While qualitative in nature, the model showed that for Lambertian target reflectance, the two-fiber receiver would collect reasonable signal levels at distances of several centimeters, a result that met or exceeded more rudimentary illumination area calculations (ignoring single-mode fiber coupling). The model results (Figure 1) also provided a basis for comparison with empirical data collected on a two-fiber probe, which showed a ~15 dB drop in collection efficiency over a 3 cm distance from a specular target.

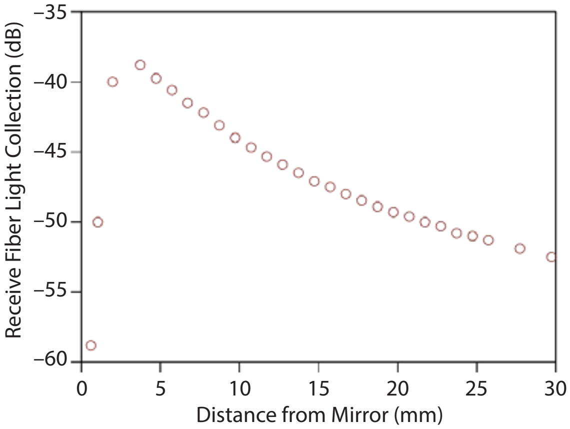

Figure 1. Two-fiber probe return efficiency (in dB) vs. distance from specular reflector

Initial Experiments— Static Target Testing

To experimentally verify the model predictions for returned laser reflection in a two-fiber probe, we added a frequency upshift (ν_0 + 100 MHz) using an acousto-optic modulator (AOM) prior to mixing the return signal with the local oscillator. This provides a means to measure the static intensity of return in real time while manipulating variables such as probe placement and target size. Several specular reflective spherical targets were fabricated to investigate the limits of target size and target-to-probe distance ranging in diameter from 1 to 5 mm in 1 mm increments. The spheres were suspended from 100 µm fiber optics to minimize any scattered light (Figure 2). The probe was a dual-purpose (send/receive), bare, single-mode fiber with an NA of 0.14 and a core diameter of 8 µm. The laser power was 100 mW and the wavelength was 1550 nm.

Beginning with the largest (5 mm) sphere, we investigated the return from the probe. The upshifted static return signal amplitude from the sphere was measured at multiple distances from the probe tip along the beam axis as well as laterally across

Figure 2. Static test spheres (suspended from thin optical fibers) sized from 1 to 5 mm

the beam axis at three different distances. The results plotted as signal-to-noise ratio (SNR) versus distance overlaid with laser spot diameter versus distance are shown in Figure 3a, and as SNR versus lateral (horizontal) distance in Figure 3b. SNR is recorded as the ratio of the 100 MHz peak height to the average amplitude of the noise floor in the FFT power spectrum. In Figure 3a, as the ratio approaches unity at approximately 10 mm, the laser spot size is still considerably smaller than the 5 mm diameter of the target sphere, and even at the closest distance measured laterally, the SNR goes to unity at just over 1 mm off center. This indicates that while the largest spherical target is visible statically at close range, considerably higher power will be required to obtain usable signals dynamically at distances greater than tens of millimeters.

Initial Experiments—Dynamic Target Testing

Utilizing a large-area PDV probe configuration similar to that used in the static tests, we performed initial dynamic tests to determine ability to distinguish larger (cm-scale) targets moving in an extended field of view of several centimeters. For these experiments, a manually actuated titanium plate impacted an elastomer sphere ~4 cm in diameter. To initiate recording of the oscilloscope traces for these experiments, an ambient light interrupt was set to trigger as the titanium plate approached the sphere initially at rest. The two-fiber large-area PDV probe was placed approximately 20 cm in front of the sphere with the continuous wave (CW) illumination laser fiber outputting ~1 W. The resulting velocity profile showed excellent distinction between the titanium plate moving at constant velocity through the field of view and the rapidly accelerating sphere after impact (Figure 4). However, the laser spot size was not quite large enough to view both objects simultaneously.

Dynamic HE (Boom Box) Experiments—Comparison with Standard Collimated PDV

In conjunction with an experiment to examine material behavior under shock loading, a large-area PDV probe was added to an HE test series performed at the Special Technologies Laboratory Boom Box. The experiment was designed to produce an ejecta cloud from a shocked pewter metal sample. The sample, which had grooves machined into the free surface of the pewter to create the ejecta after shock breakout, is described in detail in "Dynamic Measurement of Chemical Composition and Chemical Reaction with Surrounding Gas of Shock Wave–Generated Ejecta Particles," another FY 2017 SDRD project (Turley 2018). The large-area PDV probe was mounted normal to the free surface of the coupon face adjacent to a standard PDV probe in order to compare the ability

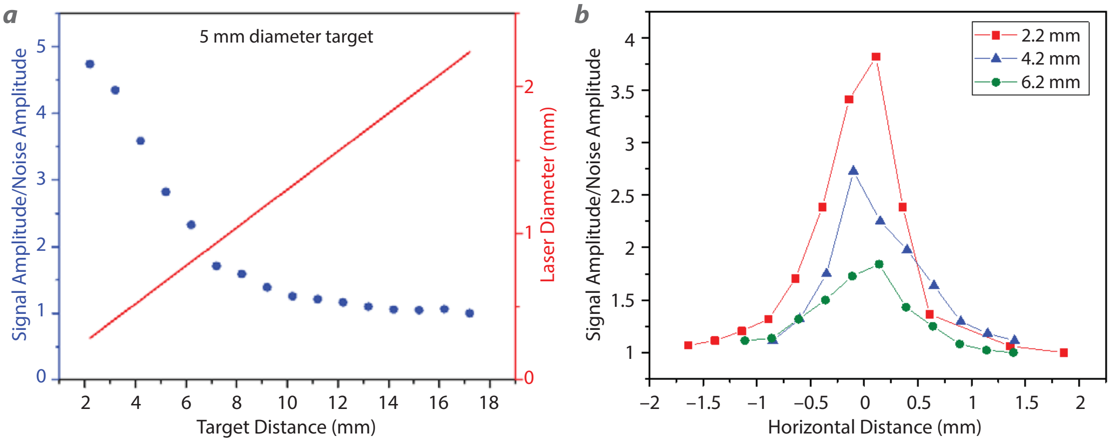

Figure 3. Static upshifted return SNR vs. distance measured (a) axially and (b) laterally

to track a cloud of micron-scale ejecta particles. Both the PDV and large-area PDV probes were the same distance from the target. The PDV laser power was 100 mW, and the output was a collimated 100 µm diameter beam. The large-area PDV laser power was 1 W delivered from a bare single-mode fiber with an NA of 0.14. Two experiments were carried out with probe distances of 30 and 50 mm. The initial distance of 30 mm showed that both PDV types could track the fastest ejecta and the moving surface beneath, with collimated PDV showing a slight gain in SNR at the earliest times, but with large-area PDV tracking particles over the entire distance and with better SNR later in time. The large-area PDV probe also returns a continua of ejecta velocities at all times while they tend to come in and out of the field of view of the collimated PDV probe. Results are plotted in Figure 5.

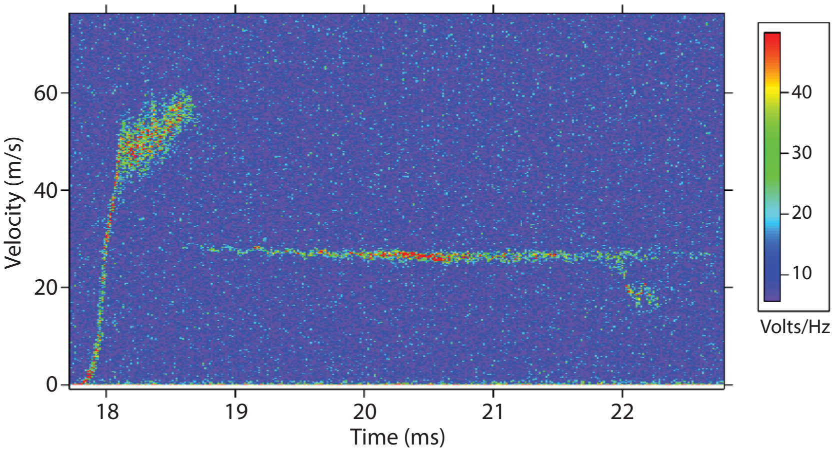

Figure 4. Dynamic test velocity profile showing 4 cm sphere initially at rest (steep curve at left) accelerating after impact from constant velocity titanium plate (horizontal line near 30 m/s)

A second experiment with the same target type was performed with the probes placed approximately 50 mm above the free surface. In this instance, the collimated PDV showed considerably improved SNR over the large-area PDV over most of the record length (Figure 6).

As with the 30 mm experiment, the large-area PDV at 50 mm showed improved SNR at the later times in the experiment, potentially providing clearer results compared to standard PDV where objects that move in and out of the field of view can create misleading features in the spectrogram data.

High-Power Laser Dynamic Experiments

Based on results from the static and dynamic testing, we determined that increased laser launch power would be the most effective means to increase illumination coverage and provide a larger field of view to the large-area PDV probe with equal or greater power density on target. For these experiments, a Continuum Nd:YAG (neodymium-doped yttrium aluminum garnet) laser was selected for operation at its base wavelength of 1064 nm. The laser outputs ~6 J of energy into a ~300 µs pulse with an average power of ~20 kW. A negative lens was added to the beam path followed by a 10 cm diameter positive lens to provide a low-divergence 10 cm diameter beam for target illumination. The receive-only probe collects

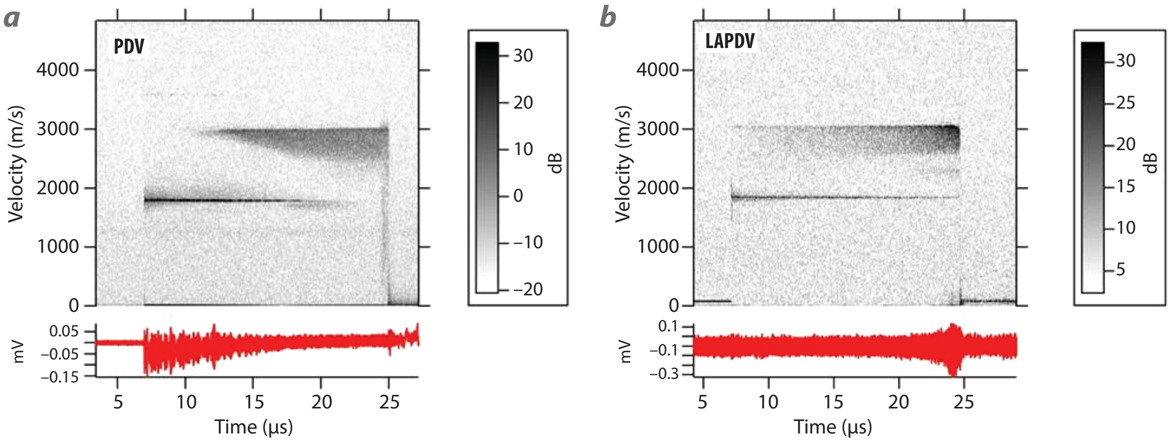

Figure 5. Results comparing (a) collimated PDV and (b) large-area PDV probe measurements on pewter HE shock experiments at 30 mm from surface to probe. The recorded time domain data are shown below their spectrograms.

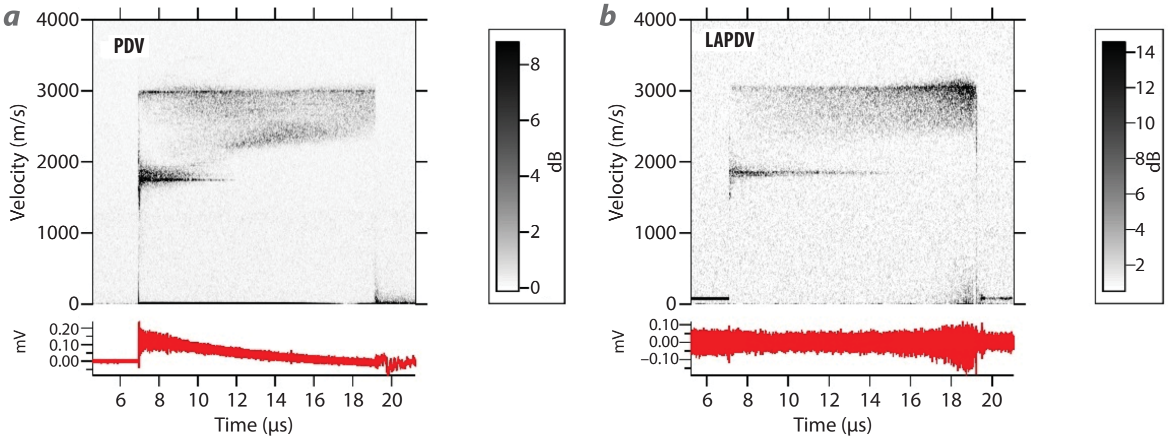

Figure 6. Results comparing (a) collimated PDV and (b) large-area PDV probe measurements on pewter HE shock experiments at 50 mm from surface to probe. The recorded time domain data are shown below their spectrograms.

Doppler-shifted reflections off the moving target and is combined with the local oscillator using a 90/10 fiber splitter. The probe was single-mode 6 µm core bare fiber with an NA of 0.14. It was placed approximately 0.6 m from the target in order to overlap the probe field of view with the 10 cm diameter beam area.

A 10% beam split was taken from the seed laser (prior to the AOM stage and amplifiers) and used as the local oscillator. The AOM shifts the signal beam 40.7 MHz, which, when combined with the unshifted local oscillator, results in a static 40.7 MHz beat frequency on light returned from non-moving objects. This corresponds to a velocity of 21.7 m/s. Therefore, increased velocities in the PDV signal begin at 40.7 MHz; they decrease initially, bounce off the zero frequency floor, and then increase. A schematic of the setup is shown in Figure 7 along with an image of the Continuum laser system used in the experiments.

Using this system we measured targets with velocities ranging between approximately 50 and 100 m/s. Target sizes ranged from several centimeters to as small as 3 mm. Materials of similar size but different masses were selected to provide dissimilar acceleration after impact with a single common object. To accelerate the targets, we used a PVC pipe-based vacuum launcher assembly to launch a ping pong ball that impacted the targets. Timing to trigger the laser and collection probe was obtained with a light interrupt photodiode on the barrel of the launcher. Data were collected on several target configurations, including the one shown in Figure 8.

A velocity spectrogram taken with this setup is shown in Figure 9. As can be seen, several object velocities are simultaneously apparent with reasonable signal levels.

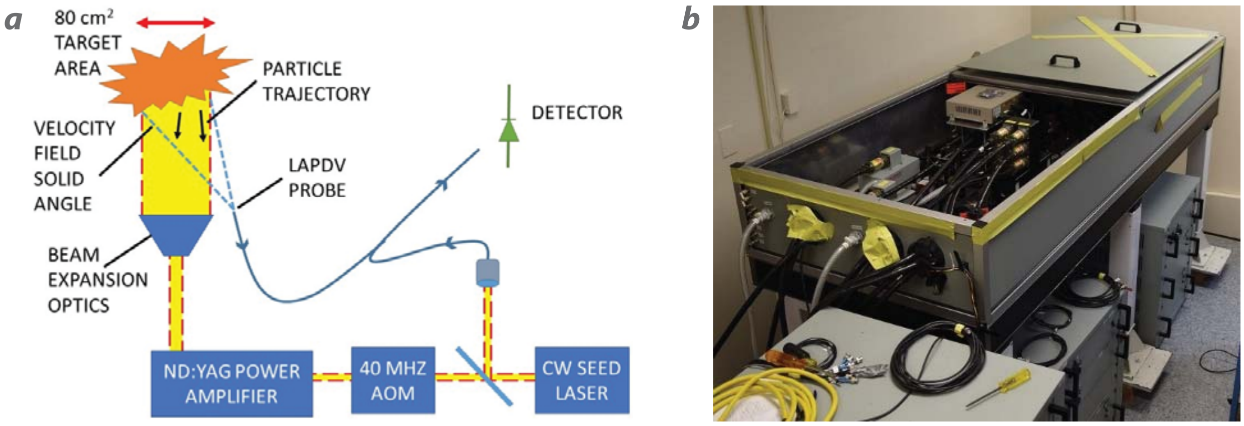

Figure 7. (a) Collection schematic for the large-area PDV experiments and (b) the Continuum 1064 nm laser system used in experiments

Figure 8. PVC vacuum launcher configured with lead, steel, and plastic targets

Qualitatively, the lines seen below the 21.5 m/s static return in Figure 9b are indicative of moving objects; however, significantly higher SNR would be required to identify all of the individual targets or even make distinctions between object types (i.e., plastic vs. lead). However, there are at least two objects clearly distinguished, which, assuming the signal has bounced through the zero frequency floor, are traveling with velocities from 31 to 34 m/s and from 21 to 27 m/s, respectively.

In a second experiment, five larger (1–2 cm), lower-mass targets were positioned over the barrel seal in a manner similar to that shown in Figure 8. The targets consisted of a 2 cm diameter foam ball, two (each) 1 cm diameter plastic beads, and 2 cm diameter lightweight fabric balls. The static and dynamic results are shown in Figure 10, with frequency fringes omitted from the plot for clarity. Optimization of the launcher resulted in significantly higher velocities, and two objects are clearly distinguished traveling at 120 and 140 m/s. The faster object, initially in the field of view, exits as the slower object enters, and both objects are simultaneously recorded briefly.

In contrast with the CW laser system used in the initial dynamic target tests, the Continuum pulse width was only on the order of 300 µs, making timing the target impact with the laser critical. Significant timing jitter, along with lack of secondary diagnostics such as shadowgraph or a high-speed camera, prevented timing of the target impact with the laser pulse to any better than millisecond-level accuracy. Future work would need to include secondary diagnostics and improved timing techniques to reduce timing jitter to tens of microseconds or less depending on target velocity. The technique also appears to suffer from effects of frequency smear, presumably due to laser speckle, wherein the target surface dynamics contribute to smearing of the measured frequencies in the probe return (Warren 2014). This appeared particularly evident on larger targets (>1 cm) and was much more prevalent in the free-space Nd:YAG laser–based experiments as opposed to the CW fiber laser experiments, although further study would be needed to confirm the origins of the effect.

CONCLUSION

We have analyzed the performance of large-area PDV in a variety of experimental conditions and compared our results with standard collimated PDV performance. We demonstrated the technique both with a diverging CW fiber laser and with a high-energy pulsed free-space Nd:YAG laser.

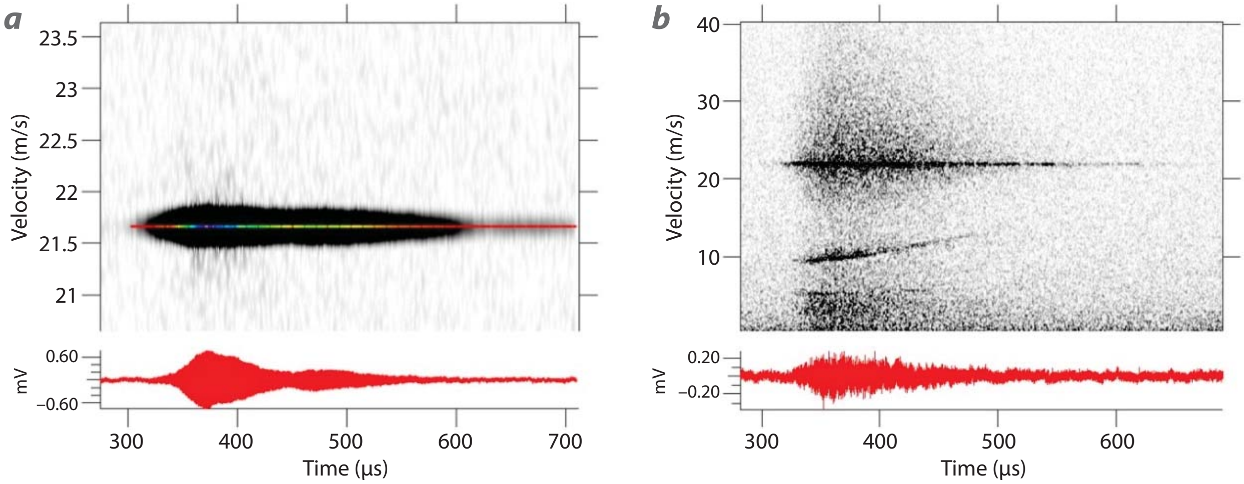

Figure 9. (a) Static velocity field showing v_0 = 21.65 m/s, associated frequency fringes at 40.7 MHz upshift and (b) dynamic return showing multiple moving targets in velocity field

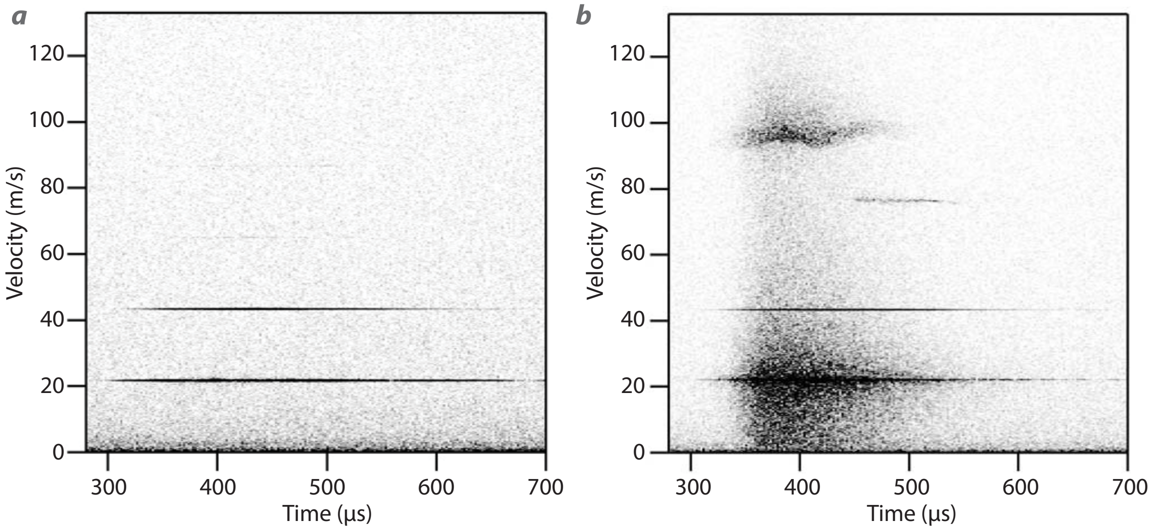

Figure 10. (a) Static velocity field showing v_0 = 21.7 m/s, associated frequency fringes at 40.7 MHz upshift and another static beat at 43.4 m/s and (b) dynamic return showing multiple moving targets in velocity field

Comparison of standard PDV to large-area PDV in an explosively driven cloud of ejecta with a CW fiber laser shows that the larger collection volume can provide longer track lengths than PDV for a given target size and velocity, and that signal-to-noise ratio levels are comparable to what is typically achieved using standard PDV. Experiments carried out to measure large-area PDV performance using a high-power pulsed laser delivered through free space demonstrate it is possible to simultaneously resolve multiple objects in a relatively large (80 cm^2) field of view. In the free-space laser experiments, signal-to-noise ratio was comparable to that of standard PDV, but velocity resolution was poor. It is unclear if this is a result of poor timing, laser speckle, target geometry, or other factors, and additional work would be required to obtain improved timing and target distinction.

Further applications of large-area PDV could include additional free surface shock experiments, where it may better facilitate disambiguation of adjacent ejecta stream velocities, and applications including medium to large hydrodynamic testing and shock wave dispersal of solid and liquid suspended media.

ACKNOWLEDGMENTS

The authors would like to thank Rachel Posner for her contributions to modeling the large-area PDV performance, Gene Capelle for laser selection and setup, and Ed Daykin for technical contributions and support of the follow-on experiments. Also a special thanks to Emeritus Professor Theo G. Theofanous (University of California, Santa Barbara, Chemical Engineering) for the initial research motivation.

REFERENCES

Theofanous, T. G., “Aerobreakup of Newtonian and viscoelastic liquids,” *Annu. Rev. Fluid Mech.* **43** (2011) 661–690.

Theofanous, T. G., V. Mitkin, C.-H. Chang, “The dynamics of dense particle clouds subjected to shock waves. Part 1. Experiments and scaling laws,” *J. Fluid Mech.* **792** (2016) 658–681.

Turley, W. D., J. Mance, G. Capelle, B. La Lone, M. Grover, R. J. Valencia, “Dynamic measurement of chemical composition and chemical reaction with surrounding gas of shock wave–generated ejecta particles,” in *Site-Directed Research and Development*, FY 2017, National Security Technologies, LLC, and Mission Support and Test Services, LLC, Las Vegas, Nevada, 2018, 49–54.

Warren, W., L. Ott, E. Elmore, E. Moro, M. Briggs, “Laser speckle in dynamic sensing applications,” in *Special Topics in Structural Dynamics, Volume 6. Conference Proceedings of the Society for Experimental Mechanics Series*, G. Foss, C. Niezrecki, eds., Springer, 2014.

This page left blank intentionally

Low-Power, Self-Organizing Reporting Devices: Situational Awareness Using Distributed Arrays

STL-102-16 ■ Year 2 of 2

E. Kirk Miller[1,a] and Hart Kornell[a]

[1]millerek@nv.doe.gov, (805) 681-2237
[a]Special Technologies Laboratory

We have developed Canary, a small, inexpensive sensing and communications device meant for persistent monitoring in a wide range of circumstances. It provides light, IR, infrasound, sound, ultrasound, magnetometer, accelerometer, temperature, pressure, humidity, and GPS sensing. For communications, it includes a nearby mesh and a long-range radio that can also mesh. The Canary board has a standard I2C connector to make daughtercard attachment straightforward. Canary was built to enable multi-sensor situational awareness, as a platform for ubiquitous (potential) CBRNE monitoring, and as an experimental platform for empirical investigation of complex networks and algorithms. Canary used open source interfaces and standards in the design, and the Canary design itself is also open source—a significant change in design approach. In FY 2017 we refined calibration and collected performance data. We also used Canaries to determine whether they could differentiate between the on and the off status of Lawrence Berkeley National Laboratory's 88-inch Cyclotron. Data analysis of the results were very promising.

BACKGROUND

Recent publications from U.S. government agencies strongly advocate the use of novel thinking and methods to tackle remote sensing national security missions. The short history of remote sensing as it relates to nuclear nonproliferation has been about finding places, that is, physical locations and facilities, where there might be proliferation-relevant activities. But, over time, changes in technology have shifted this fundamental perspective to studying the relationships between places.

To illustrate, let us consider the nuclear fuel cycle (NFC). Each succeeding stage of the NFC is more difficult to locate (from a distance) than the preceding. While it is hard to hide the mining of ore, enrichment and reprocessing can be done in bland,

Figure 1. The Canary, a small, inexpensive sensing and communications device meant for persistent monitoring in a wide range of circumstances

undistinguished industrial buildings or in underground facilities. To find the latter, the networks connecting them to the former must be detected; these networks represent relationships, the core of future proliferation detection.

For example, to learn where our attention should be put when monitoring a nuclear fuel cycle using the network of relationships approach, we identify the staging facility, use our knowledge of NFC practices and practicalities to sense when a shipment is likely to be leaving, and track the shipment to a destination (noting that the material is the concern, not necessarily the vehicle on which it is carried). When this identification process is deemed reliable, the patterns of relationships therein lead us to one point of focus. In that way, the long investment in place-centered remote sensing can be brought fully to bear. Said differently, we cannot look closely at everything, so understanding the networks of relationships can (potentially) allow us to decide our points of focus.

The Canary device responds to this method, as described in this report.

PROJECT

Research Program and Device Design

Canary (Figure 1) was built to support this mission in three ways: first, as a vehicle to support other, higher-sensitivity/selectivity sensors physically attached to Canaries and using their capabilities; second, as a source of tips and cues to high-value sensors; and, third, as a capable, stealthy, inexpensive, easily embedded stand-alone device.

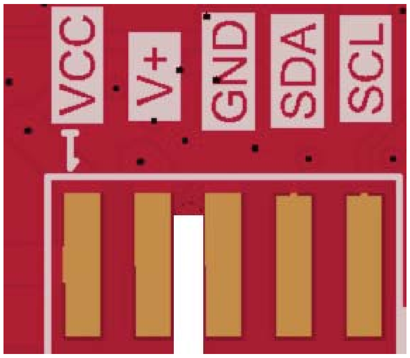

Figure 2. I2C connection showing the back, which has five GPIO pins. The I2C connector makes daughter-board attachment simple.

In the first role, Canary provides both straightforward extensibility via the I2C daughtercard connector and by providing general context and communications services, allowing the sensor developer to focus on his or her area of specialization. Context may be, for example, the temperature, pressure, and humidity needed by a chemical sensor.

The second role for Canary is as a source of tips and cues, tips being informational notifications and cues specific directives. For example, Canaries on a roadway can cue Oak Ridge National Laboratory's high-resolution Humble Oracle system that a potentially high-value target is approaching, and give its current location and speed.

Thirdly, Canary may be deployed as an independent device or as an array. Canaries self-organize in meshes and as a network self-heal by automatically regenerating the mesh when devices come online or go offline. The combination of sensors on individual Canaries may be adequate to uniquely identify vehicles; if the probabilistic reliability of identification is lower than desired, classification into categories should be achievable. Using the LoRa long-range mesh, we can potentially follow vehicle routes for hundreds of kilometers.

This specific application is speculative, as field testing was not performed. However, even a lesser role could

Table 1. Summary of Density-Based Clustering Data

		PREDICTED CLASS	
		On	Off
ACTUAL CLASS	On	88.2%	11.8%
	Off	26.5%	73.5%

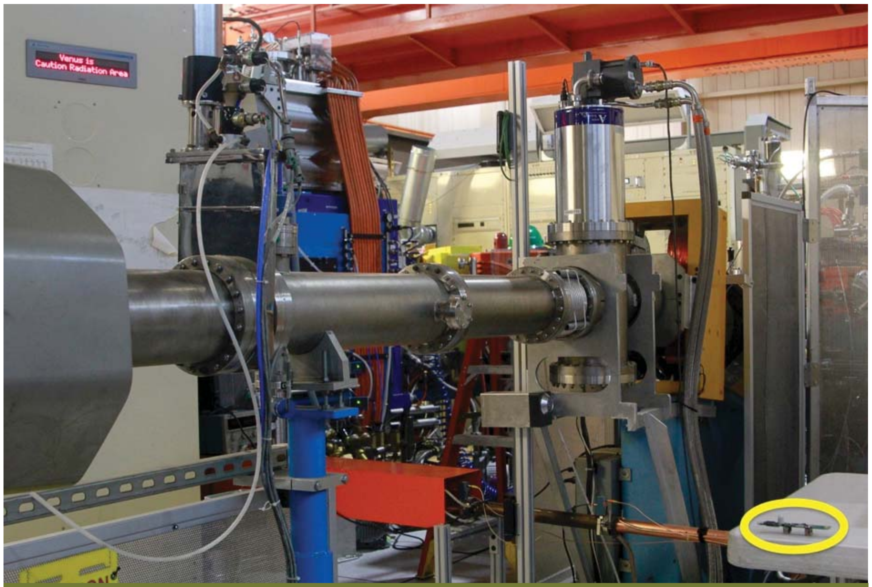

Figure 3. The Lawrence Berkeley 88-inch Cyclotron with one of the Canaries shown circled in yellow at bottom right

still be of value to the mission (e.g., by transmitting vehicle signatures and estimated transit times to Canaries emplaced near roads leading to “enigma” facilities to report matches).

Open Source and Standards Architecture

Regarding the code architecture, two important things should be noted: (1) in every possible case we used widely used open-source interfaces and standards such as Contiki, MQTT, ProtocolBuffers, and I2C connection for the architecture (Figure 2), and (2) Canary is itself fully open source code, including both hardware design and firmware.

Experiment Results

Two experiments performed in FY 2017 are described.

Inferring Behavior from Outside

An ongoing problem in proliferation detection is inferring the activities inside a building using sensors outside the building. Taking advantage of an opportunity, we chose to determine whether an earlier prototype pair of Canaries could differentiate between the on and the off status of Lawrence Berkeley National Laboratory’s 88-inch Cyclotron, which provides well-characterized beams of protons, heavy ions, and other medium-energy particles. We gathered 50 hours of data from June 20 to 23, 2017. Two Canaries were set near the Venus ion source and atop the Cyclotron. These were static locations for the duration of the experiment (Figure 3).

We applied two analysis methods to the data. In the first case, we used unsupervised learning, first preprocessing the data using 3-D principal component analysis (PCA) and then applied a density-based clustering algorithm (Figures 4 and 5).

We performed density-based spatial clustering using the standard DBSCAN algorithm with arbitrary cluster shapes and noise detection. Our results were quite good: 85% accuracy with an F-score = 0.71. F-score is a (kind of) Bayes for analyzing sensor data, combining both sensitivity and selectivity for an overall “goodness” rating. Results are summarized in Table 1.

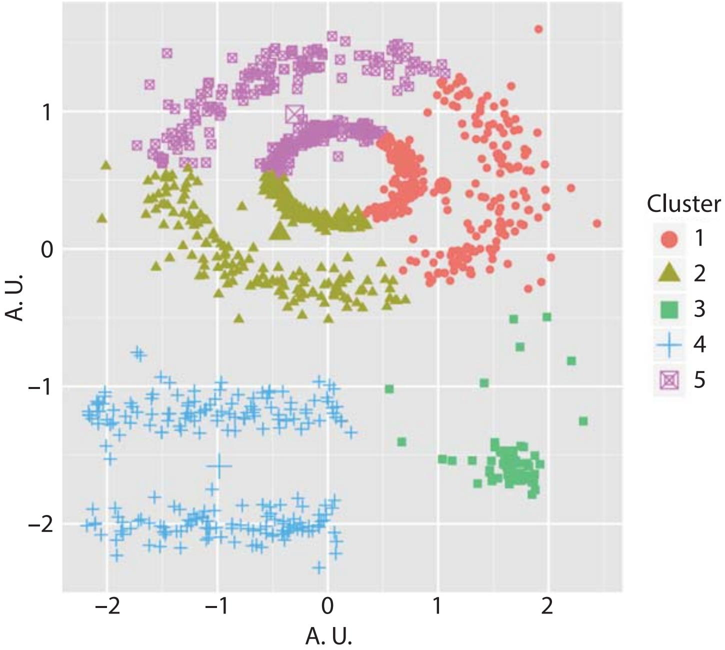

Figure 4. Density-based clustering applied to data collected at the Lawrence Berkeley 88-inch Cyclotron

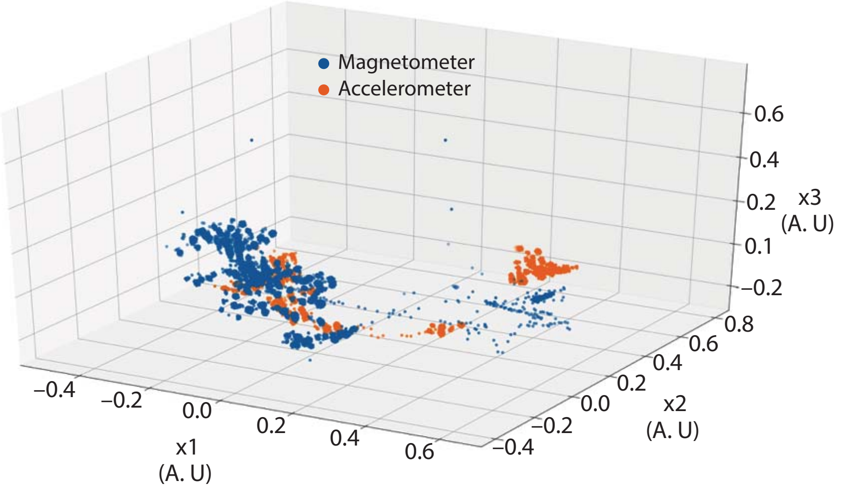

Figure 5. Density-based spatial clustering analysis of the Lawrence Berkeley 88-inch Cyclotron data

We independently analyzed the data with supervised learning (Figures 6 and 7). Data were preprocessed using standardization (Figure 6) and then analyzed with a feed-forward neural network for label classification (Figure 7). Hyperparameters (parameters of the learning algorithm, which autonomously derives the actual data parameters) of the model were set at three hidden layers (dimension 100, 50, 100): Sigmoid activation, Sigmoid cross entropy loss, and Adam optimizer (learning rate 0.01). We trained 70% of the data and tested on 30%. Our results indicated 97% accuracy with an F-score = 0.99 (Table 2).

This surprised us in two ways. First, we thought the PCA approach would yield better results, and the superiority of the feedforward NN was quite unexpected. Second, and more important, we used only a single sensing modality of the Canary in this experiment. We believe superior results could be obtained, even with less-advantageous positioning, by using the full set of sensing modalities completed in the final quarter of FY 2017.

Table 2. Summary of Supervised Learning Experience

		PREDICTED CLASS	
		On	Off
ACTUAL CLASS	On	99%	1%
	Off	5%	95%

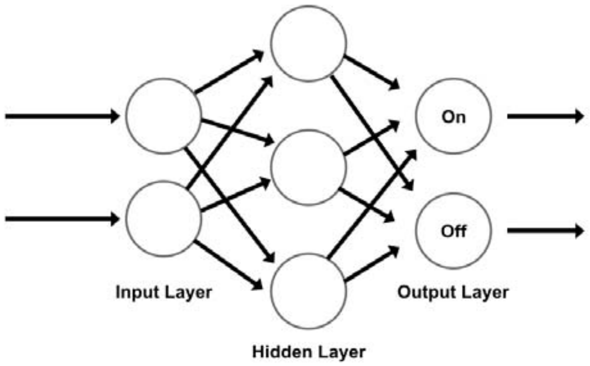

Figure 6. A generalized network shows how internal processing traverses multiple layers

Air Canary

We attached a Canary to a weather balloon and sent it to an elevation of 103,000 feet (Figure 8). The data gathered were used for sensor calibration and performance assessment. We must point out that a key design benefit is illustrated with this experiment: we devoted thought and effort into making Canaries individually cheap, which is what allowed us to send one on a trip from which we had no assurance it could return. Although we did recover it, our general point is that experiments with the Canary can be performed that would pose unacceptable risk with

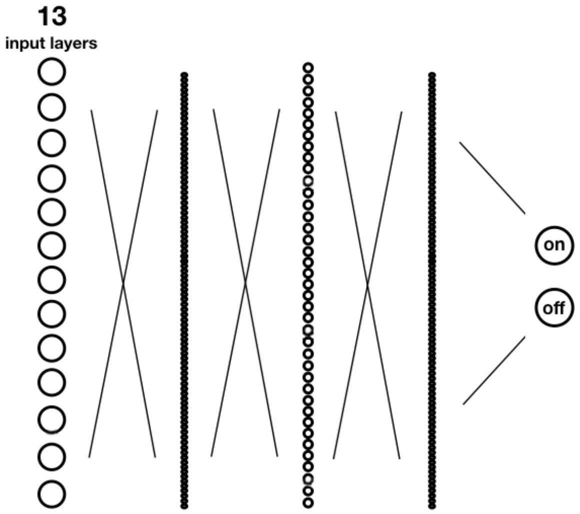

Figure 7. Label classification of supervised learning data

Figure 8. A Canary was launched with a weather balloon to 103,000 feet; data were used for sensor calibration and performance assessment

higher-cost devices. Our sponsors and customers (and we ourselves) can encircle a facility with one hundred Canaries at relatively low cost.

CONCLUSION

Over the past two years, the Canary is proving its capability as a sensing and communications device for persistent monitoring. Canaries have been distributed to Los Alamos, Sandia, Oak Ridge, Pacific Northwest, Lawrence Berkeley, and Savannah River National Laboratories. Canary has also been distributed to a variety of laboratories, universities, and industrial partners. The Canary's open source interface and standards architecture makes it a hallmark in sensor array development. Data analysis of this year's experiment at the Lawrence Berkeley 88-inch Cyclotron showed a 97% accuracy in the device to predict on and off states for the instrument. The long-term plan for Canary is to be a platform for persistent monitoring of CBRNE threats.

ACKNOWLEDGMENTS

We acknowledge Sashi Ono, Jon Steelsmith, Daniel Ng, Furqaan Afzal, Bethany Goldblum, Austin Wright, Yara Mubarek, Elie Katzenson, Pam Rangel, and Stephan Weeks for their creative and tenacious support.

This page left blank intentionally

Gas Gun–Configured Magnetic Compression Generator

NLV-013-17 ■ Year 1 of 1

Stephen E. Mitchell,[1,a] Melissa Matthes,[a] Jeff Cates,[a] James Wilson,[a] Russell Howe,[a] Tim Meehan,[a] Cameron Hawkins,[a] Brendan O'Toole,[b] Mohamed Trabia,[b] Dylan Williams,[b] and Richard Jennings[b]

[1]mitchese@nv.doe.gov, (702) 295-3065
[a]North Las Vegas
[b]University of Nevada, Las Vegas

This project explored the concept of achieving current amplification by principles of high-explosive magnetic compression generation but without high explosives. Moreover, the project was designed to prove that a gas gun or launcher could be configured to provide the input energy and action necessary for magnetic compression generation performance in a more controlled, cost-effective manner and to improve safety.

BACKGROUND

Many applications, such as in Z-pinch–driven experiments, depend on large peak currents (e.g., >> MA or one million amperes) to drive D-X reactions to produce useful neutron yields. Such reaction yields are nonlinear (e.g., powers of 2–4) functions of peak current, thus >> MA is generally desired to compensate for inefficiencies and losses to achieve targeted yields. Other areas and applications are found in high-power magnetic generation, high-power lasers, oil well exploration, drivers for high current and high magnetic field experiments, and a variety of military applications (Pavlovskii 1994a, 1994b; Novac 1998).

Producing adequate current is not trivial; it largely depends on the state of the art for producing high currents (e.g., ~10 MA range) commonly achieved in gigantic multi-stage Marx sources and low-impedance, inductive voltage adder–driven machines. Extremely high currents (e.g., >>10 MAs) necessary for liner and reactor-type applications have been achieved using high-explosive magnetic compression generation (HEMCG) technologies. HEMCG was first demonstrated by Andrei Sakharov (1966a, 1966b) in the early 1950s by means of explosively driven metallic conductors and conservation of magnetic flux to achieve tremendous current amplification unobtainable by conventional capacitor bank systems. In nearly the same period, Fowler (1960) independently demonstrated an HEMCG plate generator configuration. Decades later (circa 1990s), a joint American-Russian collaborative effort would be forged to advance the technology (Younger 1996).

But HEMCG technology is a prohibitively costly alternative to conventional pulsed power technology, and it carries an often unacceptable safety risk. HEMCGs are by default, "one and done"—everything

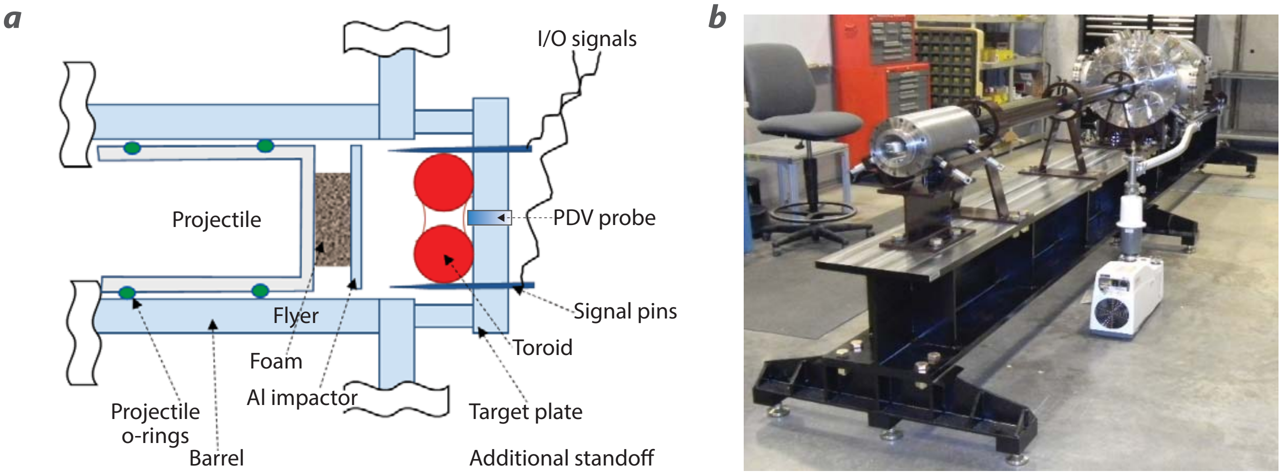

Figure 1. (a) Cross-section illustration of C3 launcher and toroid MCG components relative position and locations. The toroid MCG is mounted on the target plate within the containment vessel with three switching pins described in further detail along with the projectile's flyer. (b) View of the C3 launcher.

in the local vicinity of the generator is lost. Needless to say, the operational duty cycle for conventional HEMCGs is prohibitively low, thereby disqualifying such an option from any aggressive experiment schedule. The trade-off is choosing between one-time-only use and the superior energy density of magnetic compression generators (MCGs) compared to conventional pulsed power sources.

Fundamentals and Baseline Criteria

The physical principle that enables MCGs is conservation of magnetic flux with rapid field compression, which is described elsewhere (Fowler 1975) in detail; however, compression need not be driven by high explosives (HE) for requisite short time scales. Instead, a gas gun projectile with sufficient energy could drive the rapid expansion of the armature both radially and longitudinally within a helical stator or compress a plate generator-like configuration.

From first principles this can be shown by solving an ordinary differential time-dependent $L(t) - R$ circuit that a current amplification expression can be described as

$$I(t) = I_0\left[\frac{L_T(0)}{L_T(t)}\right]^{\left(1-\frac{Rt}{L_0}\right)}, \qquad (1)$$

where I_0 is the initial capacitor bank "seed" current, $L_T(0)$ is the initial inductance at time = 0, $L_f(t)$ is final inductance at "burnout" time t when the inductor value is essentially zero, and R is the total line resistance. Burnout time is the displacement length in the inductor divided by the HE burn speed in that displacement direction. Note that the expression to the right of I_0 in Equation 1 is interpreted as amplification gain factor, G.

Also, from the derivation, an important and necessary performance criteria is determined by requiring the time change in inductance or dL/dt to be greater than the total load and line resistance. By applying chain rule and baseline conditions, such as projectile speed and inductor displacement, dL/dt is rewritten as $v_p dL/dq$; now, in terms of the gas gun and inductor parameters, v_p is the projectile speed and q is a generalized coordinate (either radially or longitudinally) in the inductor. Hence, the threshold requirement for amplification is $v_p dL/dq > R$.

PROJECT

The two sections of this report reflect the two principal project paths, each using a different gas gun and different MCG configuration: (1) North Las Vegas (NLV) C3 gas launcher (Figure 1b) and a toroid MCG and (2) the University of Nevada, Las Vegas (UNLV) Mechanical Engineering Department's two-stage gas gun facility and helical (e.g., solenoid) MCG.

NLV C3 Gas Launcher and a Toroid MCG

In this phase of the project, we electrically energized a toroidal inductor (aka MCG in this configuration), compressed it by a large 75 mm bore single-stage gas launcher at nominal projectile velocity of 480 ms^{-1} at the NLV C3 Launcher, and measured/verified current amplification response. Figure 1a is a cross section of the launcher primary components in relation to a toroidal MCG.

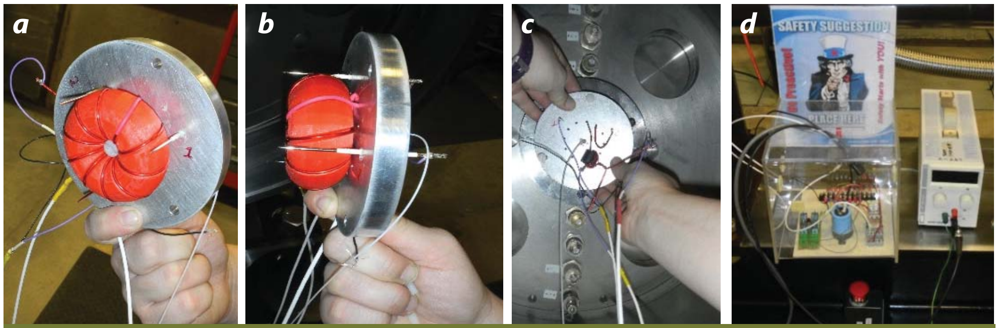

Figure 2. (a, b) Various views of the 75 mm full-diameter, 25 mm wide toroid MCG mounted to the C3 launcher's target plate and (c) the MCG being installed within the containment vessel. (d) The charge and discharge electrical circuit is shown for reference.

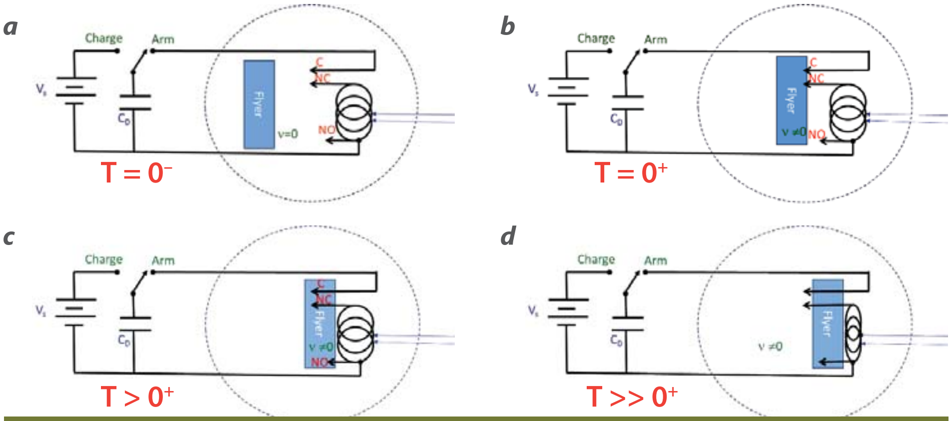

Figure 3. (a) At T = 0^- the arming switch is engaged and the flyer plate has not connected the armed discharging power (C_D) through the inductor to set up the initial current and magnetic field. (b) At T = 0^+ the flyer plate has connected the *armed* discharging power (C_D) through the inductor to set up initial current and magnetic field via C and NC connections. (c) At T > 0^+ the flyer plate has shorted the input connections to the inductor via C, NC, and NO connections. (d) At T >> 0^+ the flyer plate compresses the toroid.

The 75 mm full-diameter toroid MCG was fabricated from a 3-D printed, thin, toroid shell form, 50 mm and 25 mm primary and secondary diameters, respectively, with an evenly spaced 10-turn 16 AWG wire wound coil (Figure 2). The inductive value was calculated and verified to be 1.2 µH. Switching and controlling electrical energy into the MCG was challenging; for example, solid-state switches are easily controllable but prohibitively slow for the timescales needed for current amplification. Hence a unique electro-mechanical switching scheme was developed, and it is explained below.

Figure 3 shows a cartoon representation of a time-phase solution for MCG theory of operation in this configuration. The flyer plate and the three pins (also shown above in Figures 2a and 2b) make up the unique three-way switch. The C (common) and NC (normally closed) pins are exactly the same length. The NO (normally open) pin is 0.5 mm shorter than both the C and NC pins.

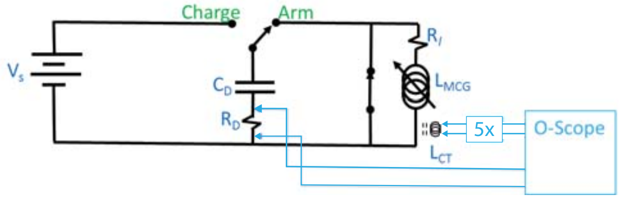

Figure 4. V_s is the supply voltage (100 VDC), C_D is the discharge capacitor (1 mF), R_D is the discharge current sensing resistor (1 Ω), R_l is the line resistance (0.018 Ω), L_{CT} is current transformer (N_{CT} = 6, L_{CT} = 1.6 µH), L_{MCG} is the toroid MCG (1.2 µH). Oscilloscope input terminators are at high-Z (1 MΩ).

Results: NLV C3 Gas Launcher and a Toroid MCG

Figure 4 shows the electrical condition and the states when the MCG is charged; the electrical energy is "trapped" inside the MCG 1 µs after it is charged, and the toroid inductance decreases due to compression.

Figure 5 shows a plot of measured (orange trace) and calculated (blue trace) voltage signals representing the amplified current in the toroid MCG through compression. The measured signal is a 5x attenuated current transformer voltage signal scaled to the current

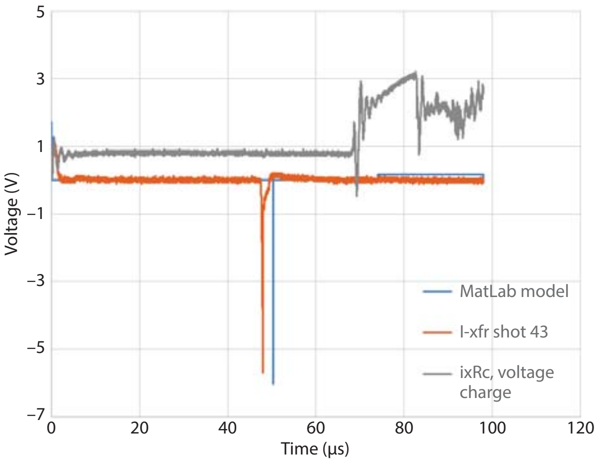

Figure 5. Measured voltage from current transformer (orange) and calculated voltage response (blue). Gain = 5.3. The measured voltage through the IR resistor voltage drop in capacitor line is also shown (grey).

as 42.017 A/V. The first voltage peak, occurring at approximately 0 µs, corresponds to a peak current of 462 A; this peak occurs when the flyer plate and C-NO connection first energizes the LCR circuit. The input to the toroid MCG is shorted 1 µs later through the flyer plate and NO-C pin connections, thus isolating the remaining LR circuit components. The 1 µs time delay is due to the physical difference in the pin NO and NC-C switch lengths and the projectile nominal speed of 480 ms^{-1}. The calculated amplified negative-going 60 V peak (blue trace, voltage-to-scaled current of 2.52 kA), occurring at 50 µs, is late by 2 µs compared to the measured 59 V peak (measured signal voltage-to-scaled current of 2.48 kA). The calculated and measured amplification factors are 5.45 and 5.30, respectively. The time delay discrepancy is most likely due to the reflected wave and additive compression effect off the target plate; compression is occurring earlier than simple kinematics predict, and we are still investigating this.

Finally, at maximum compression of the toroid MCG which occurs just before 50 µs, the flyer plate fractured in small pieces (verified by post-shot forensics). This unexpected but desirable event occurs around 70 µs or 20 µs after full compression and acts like a fast opening switch enabling the electrical return path of amplified current to be measured through the current sensing resistor (shown in Figure 5 as a grey trace).

UNLV Gas Gun and Helical MCG

For these tests, we envisioned a scaled-down helical MCG (Figure 6) that could use a gas gun's projectile to initiate the armature expansion.

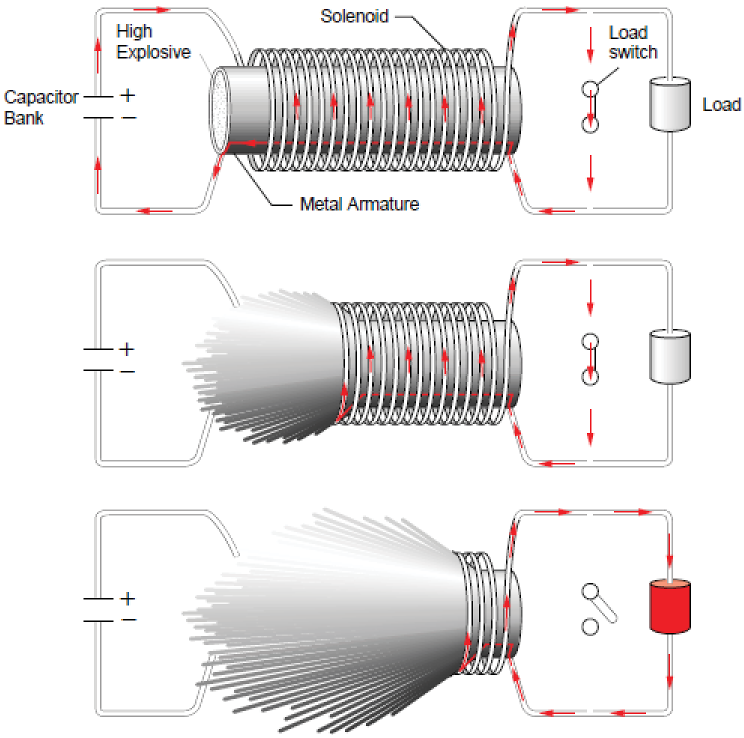

A helical MCG has a long metal armature that is packed with HE and placed within a solenoid. As the capacitor bank discharges, the current generates a magnetic field in the space between the solenoid and the armature. The load switch is initially in the closed position, preventing the current from flowing through the load.

The HE is detonated at one end, and the armature expands—like an inflating long balloon. The volume between the solenoid and the armature decreases in both the radial and longitudinal directions, compressing the magnetic flux.

Flux conservation results in an enhanced magnetic field, which induces a large current in the remaining loops of the solenoid. At peak flux compression, the load switch is opened, and a greatly enhanced current is delivered to the load.

Figure 6. A proposed, scaled-down helical MCG that could use the UNLV gas gun projectile to initiate the armature expansion

The UNLV two-stage gas gun, configured for a velocity of >2 kms^{-1} with a .38-caliber Lexan projectile launcher, was employed (Figure 7) as the gas gun driver. The UNLV gun's projectile speeds are within an order of magnitude of HE burn velocities (e.g., >7 kms^{-1}), making it a worthy surrogate to HE.

This project benefited greatly by developing accurate shock wave simulations that guided design and fabrication of components necessary for the helical solenoid MCG. Team members took full advantage of learning Sandia National Laboratories' multi-material, Eulerian, large-deformation, strong shock wave, solid mechanics code CTH for this purpose. We modeled a process similar to that described in Figure 6 and arrived at the dynamic compression depicted in Figure 8.

Based on the information from the CTH simulations, we fabricated Lexan-packed aluminum armatures at the UNLV Mechanical Engineering's machine shop along with a special fixture support mount to secure the armature during projectile impact within the containment vessel. The high-speed 5 Mfps Kirana video camera used to observe and witness the event and an inside view of the containment vessel are shown in Figure 9.

The 5 Mfps video capture of a .38-caliber Lexan projectile fired at 2.039 km^{-1} into the Lexan-packed aluminum armature device was parsed for single images. These images (Figure 10) were in good agreement with the CTH model (Figure 8), qualitatively

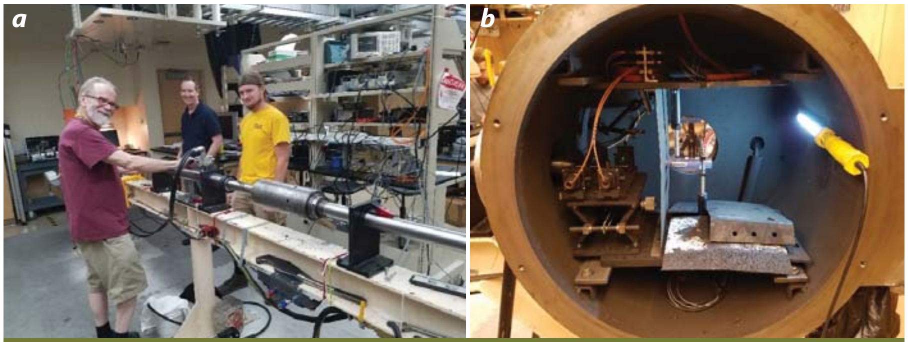

Figure 7. (a) UNLV two-stage gas gun along with UNLV team members Richard Jennings, Dr. Brendan O'Toole, and Dylan Williams. (b) Inside view of the containment vessel.

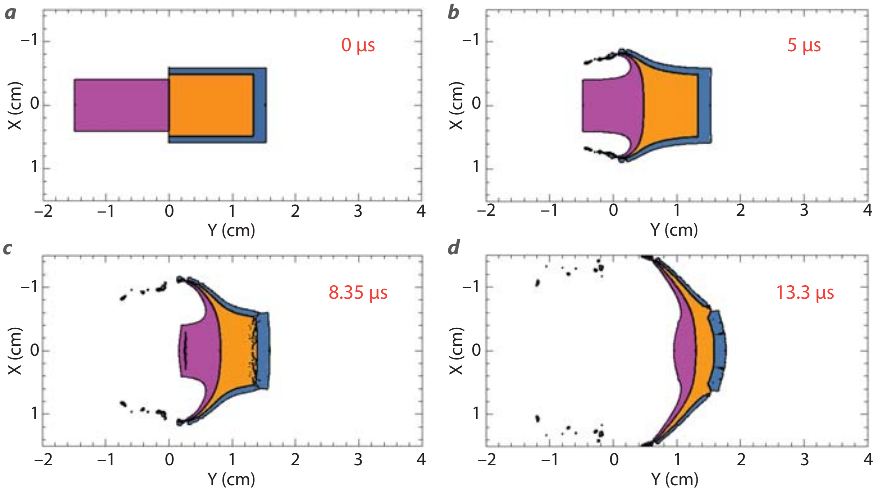

Figure 8. Time-phased depictions of the radially and axially expanding armature at (a) 0, (b) 5, (c) 8.35, and (d) 13.3 µs. Blue is the 1 mm thick, 9.5 mm inner diameter aluminum armature shell; orange is Lexan fill, and violet is .38-caliber Lexan projectile at 2.039 km^{-1}.

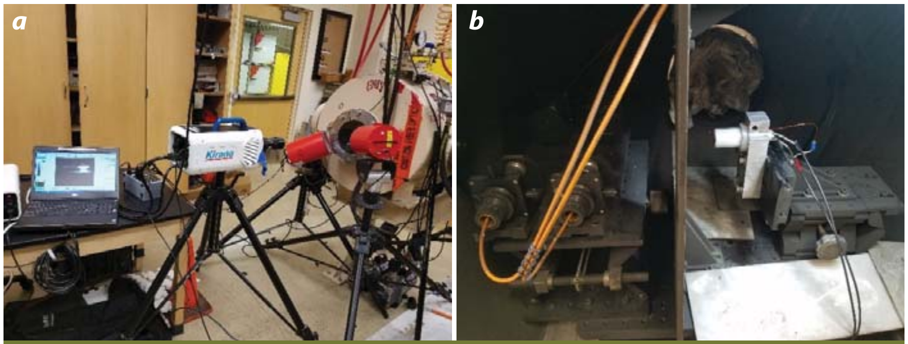

Figure 9. (a) High-speed 5 Mfps Kirana video camera arranged for best field of view of the containment vessel. (b) Inside of the containment vessel; at the left are the special start-stop beam break components and assembly; at the right is the special fixture support mount that secures the armature during projectile impact within the containment vessel.

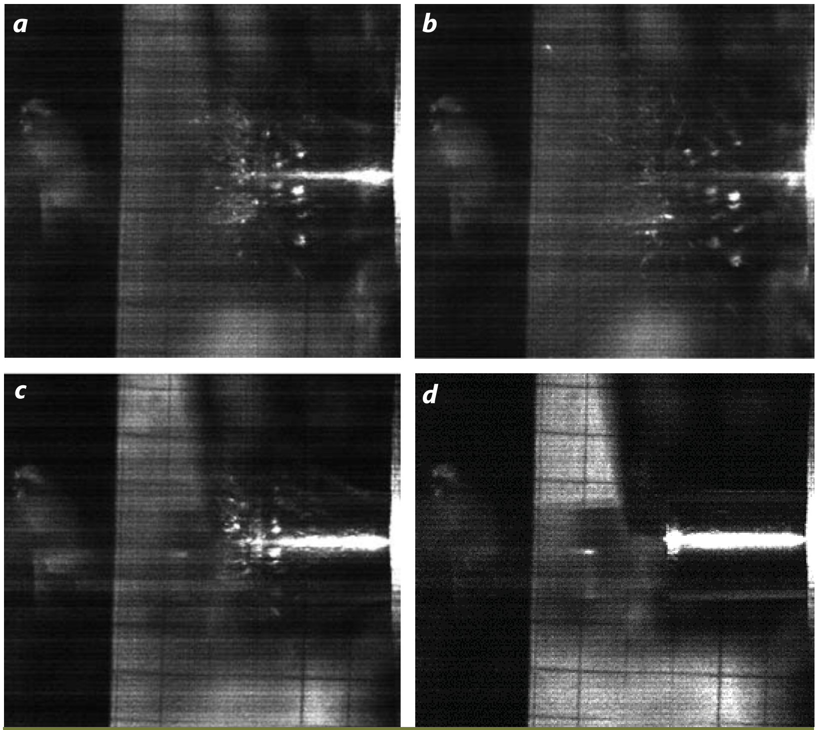

Figure 10. Time-phased frame slices at (a) 0, (b) 5, (c) 8.35, and (d) 13.3 µs from the video capture of radially and axially expanding armature. Each photo is a rough time phase match and verification to simulation results shown in Figure 8. The .38-caliber Lexan projectile was fired at 2.039 km^{-1}.

in dynamic metal-conic wave propagation and quantitatively in time phase of event.

Results: UNLV Gas Gun and Helical MCG

Full helical MCG device configurations were fabricated shortly after concluding satisfactory expansion response in the armature during the .38-caliber Lexan projectile and Lexan-filled aluminum armature impact test mentioned above.

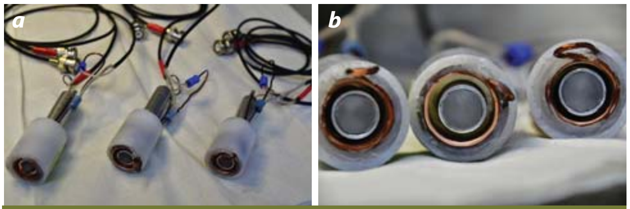

Figure 11. (a) Various helical MCG configurations with electrical cabling and connections and (b) close-up cross-section views of various helical MCG configurations with three different stator OD to armature OD aspect ratios: 1.2, 1.4, and most common 1.6, respectively

Three helical MCGs with varying stator-to-armature outer diameters (OD) were fabricated (Figure 11). However, only the helical MCG whose stator-to-armature OD aspect ratio of 1.6 (e.g., the armature OD = 0.38″ and the stator OD = 0.608″) was used in full test configuration for current amplification verification.

The electrical circuit schematic diagram is shown in Figure 12. The time-of-flight of a nominal 2 kms^{-1} projectile from the end of the launch tube to the helical MCG is about 125 µs. Therefore, the oscilloscope external trigger was set for a 100 µs delay to capture the full event plus an additional 25 µs leading up to the event. This setting was based on the CTH simulations, the inelastic collision of the 1.159 g Lexan projectile, and the 1.4 g Lexan-filled aluminum armature results in a longitudinal velocity of about 900 ms^{-1}, as shown in Figure 13. Thus, in terms of burnout times (e.g., armature length divided by compression speed), the 2 kms^{-1} projectile velocity is not correct and not used. The 900 ms^{-1} speed is appropriate and is used in current amplification calculation. This also agrees with a burnout time of the entire magnetic compression event, ~13 µs, as estimated in the CTH simulations.

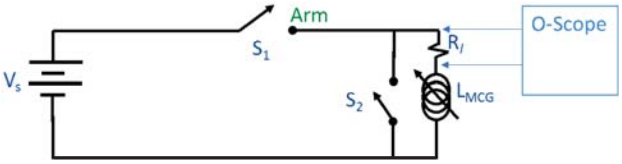

Figure 12. For logistical reasons unimportant to this report, a capacitive charge-discharge circuit was not used. Instead, a nominal unregulated power supply, V_s, energized the helical MCG, LMCG, through switch S_1. During Lexan projectile and armature impact, and subsequent armature expansion and magnetic compression, the switch S_2 closure symbolizes the helical MCG input shorting out. R_l, which was a 1″ length of wire in series to the MCG, acted like a current-viewing resistor measuring current amplification.

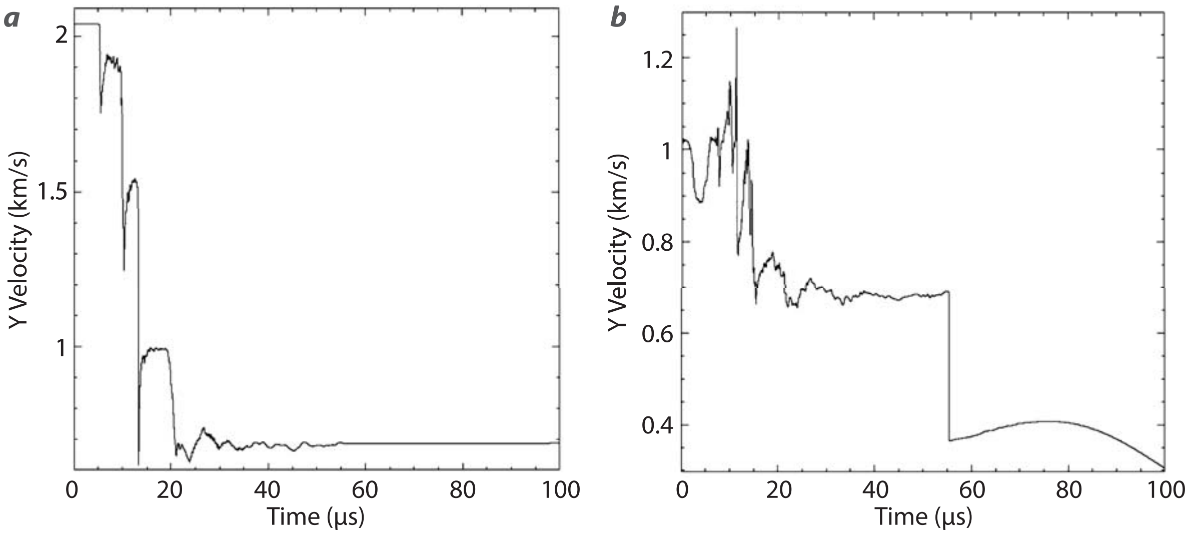

Figure 13. (a) CTH-simulated velocity of the Lexan projectile's course of impact with the Lexan-filled armature. (b) CTH-simulated velocity of the Lexan-filled armature. Both plots of velocity with respect to time are in the axial y direction of travel.

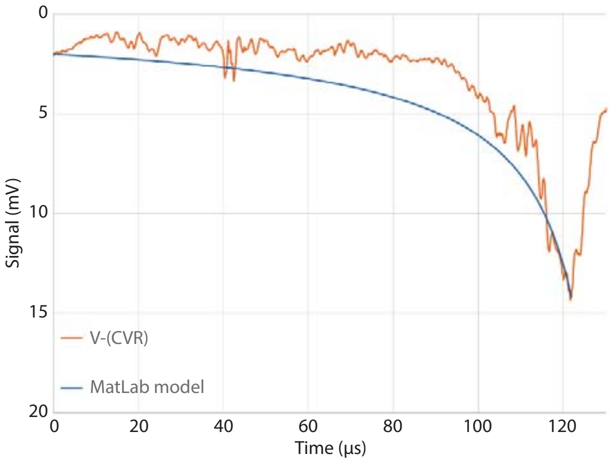

Figure 14. Voltage signal of the IR voltage drop across 1″ of exposed wire from the helical MCG circuitry (orange) and calculated voltage response of the current amplification (blue). Gain = 4.3.

Figure 14 shows a plot of measured (orange trace) and calculated (blue trace) voltage signals representing the amplified current in the helical MCG during the projectile-armature impact and expansion. The orange trace is the voltage signal measuring the IR voltage drop across 1″ of exposed wire from the helical MCG circuitry. The initial current scales to the measured voltage across the 1″ of exposed wire as 3000 A/V, which corresponds to 1″ length of 16 AWG wire, which has a current of 133 mA. The peak amplified current of 0.638 A (or 0.012 V measured on the oscilloscope) occurs just beyond 12 μs and represents a current amplification of 4.3 in this helical MCG configuration. The calculated current amplification shows fair agreement; the peak value and occurrence time matched well, but the rising edge values disagreed. Possibly this is due to our not correctly accounting for the deceleration of the Lexan projectile into the Lexan-filled aluminum armature and back-reflected wave.

CONCLUSION

Current amplification was achieved in two different types of MCG configurations without HE by using different types of gas gun launchers as the principal driving mechanisms. The NLV C3 single-stage gas launcher, whose projectile speed was 480 ms^{-1}, produced a current amplification of 5.3; whereas the UNLV two-stage launcher, whose projectile inelastic collision and momentum transfer resulted in an effective HE burn speed of 900 ms^{-1}, produced a current amplification of 4.8. A possible explanation to the disparity in the descending gain values for the apparent ascending driving speeds is efficiency in compression; the toroidal MCG areal cross section compressed essentially 100%, but in the helical MCG, the areal cross-section change varies as the square of the difference in stator to armature ODs.

Finally, to achieve practical MA range current amplification in gas gun–configured MCGs would require either large projectile cross sections to compress an equally large toroid (e.g., large initial inductance value) MCG and/or much faster gas gun projectile speeds to compensate for inelastic collision and non-energy conservation momentum transfer in a helical MCG geometry.

ACKNOWLEDGMENTS

We would like to thank Ed Daykin, Mike Pena, and Aaron Luttman for their encouragement and insightful suggestions and contributions to this work.

REFERENCES

Fowler, C. M., W. B. Garn, R. S. Caird, "Production of very high magnetic fields by implosion," *J. Appl. Phys.* **31** (1960) 588.

Fowler, C. M., R. S. Caird, W. B. Garn, "An introduction to explosive magnetic flux compression generators," LA-5890-MS, Los Alamos Scientific Laboratory, Los Alamos, New Mexico, March 1975, https://www.osti.gov/scitech/servlets/purl/4218822, accessed on March 21, 2004.

Novac, B. M., I. R. Smith, "Autonomous compact sources for high power microwave applications," presented at the Megagauss VII Conference, Tallahassee, Florida, 1998.

Pavlovskii, A. I., et al., "EMG magnetic energy for superpower electromagnetic microwave pulse generation," in *Megagauss Magnetic Field Generation and Pulsed Power Applications*, Commack, New York, Nova, 1994a, 961–968.

Pavlovskii, A. I., R. Z. Lyudaev, V. N. Plyashkevich, N. B. Romanenko, G. M. Spirov, L. B. Sukhanov, "MCG application for powered channeling neodym laser," *Megagauss Magnetic Field Generation and Pulsed Power Applications*, Commack, New York, Nova, 1994b, 969–976.

Sakharov, A. D., *Sov. Phys.-Doklady* **10** (1966a) 1045.

Sakharov, A. D., *Sov. Phys.-Usp.* **9** (1966b) 294.

Younger, S., I. Lindemuth, R. Reinovsky, C. M. Fowler, J. Goforth, C. Ekdahl, "Lab-to-lab scientific collaborations between Los Alamos and Arzamas-16 using explosive-driven flux compression generators," *Los Alamos Science* **24** (1996).

RGB Wavefront Sensor for Turbulence Mitigation

STL-078-16 ■ Year 2 of 2

Mary D. O’Neill,[1,a] David Terry,[b] and Janice Lawson[a]

[1] oneillmd@nv.doe.gov, (805) 681-2477
[a] Special Technologies Laboratory
[b] Fifth Gait Technologies, Santa Barbara

Atmospheric effects reduce the ability to detect or identify objects of interest due to spatial and spectral scintillation. Algorithms alone cannot correct for turbulence over long-range horizontal paths. While adaptive optics methods work well for astronomical viewing, they are not readily adapted for complex imagery over long-range horizontal paths. In this two-year research project, we combine an off-the-shelf high-frame-rate USB3 color camera with a compact 90 mm Maksutov-Cassegrain telescope and an OKO deformable mirror (DM) to create a portable red/green/blue (RGB) wavefront sensor and turbulence mitigation system. The telescope’s aperture is covered with an aluminum plate holding three separate narrowband color filters. These filters, specifically matched to the relative spectral response of the sensor’s Bayer mask, provide nearly complete separation of the three color images. This device enables portable imaging through atmospheric turbulence and analysis thereof, where relative motion of the three-color Bayer-pixel video provides real-time wavefront information on the second-order statistics of Kolmogorov turbulence. In our second year, we incorporated an OKO DM with 96 actuators into our sensor. We measured relative RGB pixel shifts and controlled this mirror using an ODROID single-board computer. We developed a bench setup to calibrate the relationship between pixel shifts and the deformable mirror actuators. We demonstrated the feasibility of this system on a benchtop and are preparing for a relevant outdoor environment with very high turbulence.

BACKGROUND

The atmosphere has three major effects on a propagating wave: absorption, scattering, and refractive-index fluctuations, commonly referred to as atmospheric turbulence. Image degradation caused by atmospheric turbulence presents a significant problem in extended-range surveillance and signal processing because, in many critical applications, these effects are far more restrictive than limitations induced by optics or camera sampling.

Turbulence is strongest when there is a large temperature differential between the earth (ground) and the surrounding air. When the earth is warmed by the sun, energy is radiated back, locally warming the air and causing convection. Wind mixes the created buoyant warm cells of air with adjacent cooler air. As energy dissipates into the next layer, convection cells are reduced in size. Whereas larger cells act as refractive elements, the smaller cells act as diffractive elements. In general, the smallest and largest cells determine the inner (l_0) and outer (L_0) scales of turbulence (Max 2010). The inner scale defines the size of the smallest inhomogeneities in the turbulence, below which we use fluid viscosity to describe flow. The outer scale defines the point beyond which the turbulence becomes anisotropic, resulting in structural and refractive index effects (Tofsted 2000).

Fried's atmospheric coherence length, r_0 (Fried 1967), is the standard parameter used to characterize the point spread function (PSF) for imaging through the atmosphere (*seeing* conditions, Martinez 2010). This can be computed from the path-length integrated $c_n{}^2$ as

$$r_0^{-5/3} \equiv \frac{2.91}{6.88}\left(\frac{2\pi}{\lambda}\right)^2 \int_0^L \left(1-\frac{z}{L}\right)^{5/3} c_n^2 dz \equiv \frac{2.91}{6.88}\left(\frac{2\pi}{\lambda}\right)^2 \left(\frac{3}{8}\right) \langle c_n^2 L \rangle . \quad (1)$$

Here, λ is the monochromatic wavelength, L is the integrated line-of-sight (LOS) path length, and we have defined the "constant-equivalent" average index of refraction structure constant $\langle c_n{}^2 L\rangle$ as if $c_n{}^2$ were constant along the entire path. Note that r_0 is inversely proportional to $c_n{}^2$ and thus to the strength of turbulence. Algorithms used to analyze signals and mitigate image degradation are increasingly dependent on the character and strength of the turbulence. Figure 1 contains images of a standard target (USAF 1951 resolution test chart) taken during a warm day in California as the sun heated the atmosphere and LOS turbulence increased such that the aperture diameter to the coherence radius D/r_0 increased. Even though the image is not monochromatic, it is apparent that *perceived image quality correlates with* D/r_0. Consequently, D/r_0 can be used as a dimensionless, macroscopic turbulence strength parameter. In practice, we find a D/r_0 of ~20 produces images that have insufficient high spatial frequency detail and cannot be reliably improved by image processing.

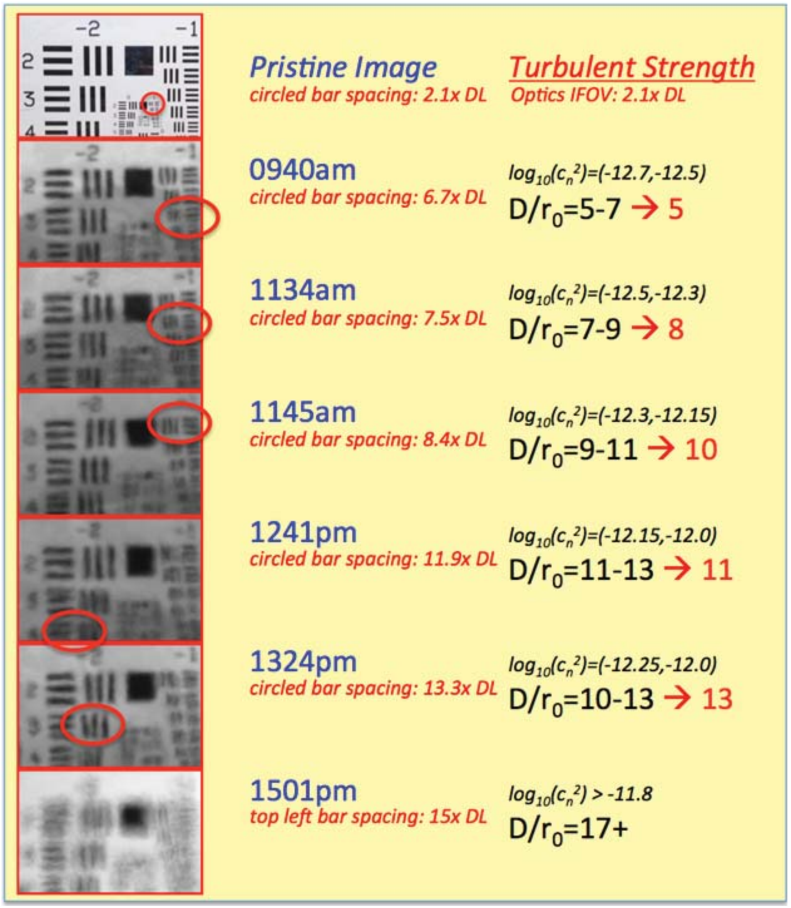

Figure 1. Turbulence strength chart. The target is taken through increasing levels of turbulence characterized by D/r_0 shown on the right. The USAF 1951 resolution test chart aids in extracting an "apparent turbulent resolution" that can be directly compared to a scintillometer measurement.

Fried (1978) postulated that there is some probability of getting a lucky or clear image through turbulence. Many algorithms rely on this probability to get high spatial frequency content. Hufnagel (1989) determined that if wavefront distortion could be corrected, the probability would increase. Zernike polynomials are used for describing aberrations in optical systems and

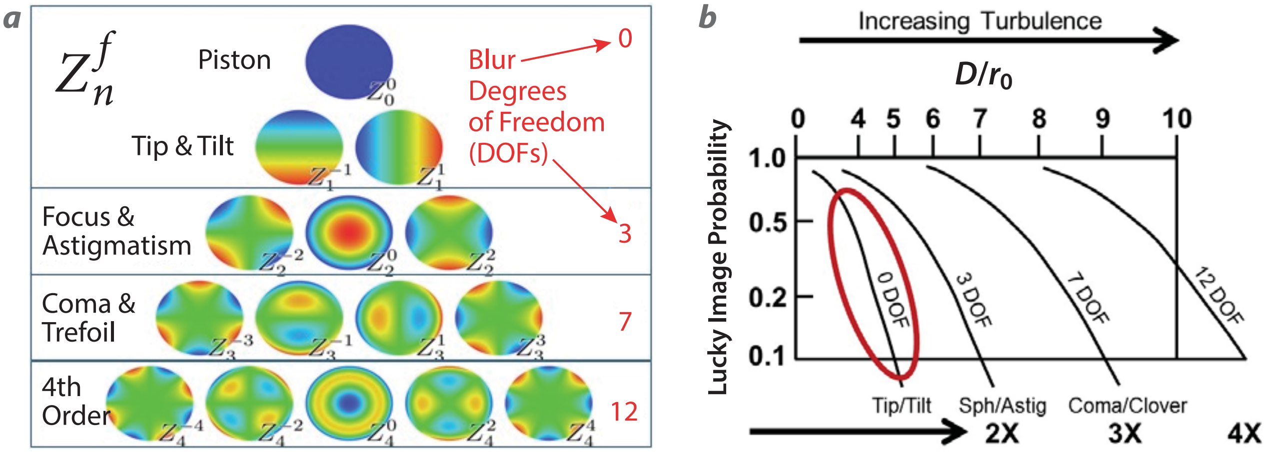

Figure 2. (a) The first twelve Zernike degrees of freedom (DOFs), and (b) the probability of getting a lucky image with different DOFs of Zernike corrections

are often used to describe the wavefront distortion associated with atmospheric turbulence (Born 1965, Noll 1976). The first twelve Zernike degrees of freedom (DOFs) are shown on the left in Figure 2a. Figure 2b shows the improvement in the probability of getting a lucky image with different DOFs of Zernike corrections.

Adaptive optics (AO) systems have been used for years in astronomy to correct for the wavefront distortion associated with atmospheric turbulence (Beckers 1993). For scene-based Shack-Hartmann AO systems, the source is not completely coherent, so interferometers are not used. Instead, an image of the pupil is projected onto a lenslet array, such that each lenslet represents a different portion of the entrance aperture. Each lenslet images the scene onto a different portion of an image plane. In the absence of turbulence, the images of the point source are uniformly distributed based on the lenslet configuration. With wavefront distortions, the images of the point source will shift from their nominal positions. The corresponding pixel shifts are related to the slopes of the phase of the wavefront for each aperture location. Algorithms for extracting the wavefront distortion exist, but these all rely on high spatial frequency content and typically require a point source in the scene. The phase map derived from these algorithms generates the commands to a deformable mirror (DM) that corrects for the wavefront distortion associated with turbulence. The algorithms for detecting the shifts must be fast enough to change the mirror as the turbulence changes.

While AO works well for astronomical viewing, the same methods do not work well for complex imagery from long-range horizontal paths. Some Shack-Hartmann analysis has been done for astronomical extended sources with this sensor type (Sidick 2007, 2013; Lukin 2010; Rais 2016), but this work has not been extended to horizontal paths. Work at Lawrence Livermore National Laboratory (Poyneer 2003) indicated applicability to horizontal paths using a cross-correlation technique. The Army Research Laboratory passive adaptive imaging is specifically designed to mitigate horizontal path turbulence (Tofsted 2016), but its implementation includes moving parts not suitable for a compact AO system. Each of these methods for extended sources uses the received imagery to a separate wavefront sensor to compute pixel shifts associated with wavefront distortion, and all suffer from the same lack of high spatial frequency content characteristic of high turbulence. Currently, no adequate compact, motion-tolerant AO solution exists for significant long-range horizontal path–induced degradation.

PROJECT

The goal of this project is to develop a compact AO system for long-range horizontal paths that improves severely degraded images. To do this, we are leveraging the statistical tools developed as part of an earlier NNSS SDRD project (O'Neill 2014, Terry 2014) and AO work from literature.

There are two key aspects to this research. First, instead of using a lenslet array, we are leveraging COTS cameras and filters to create a red/green/blue (RGB) wavefront sensor (WFS). This allows the same imagery used for obtaining the wavefront distortion to be provided seamlessly to the user while being tolerant to platform motion. It also allows us to access second- and third-order statistics via RGB color separation.

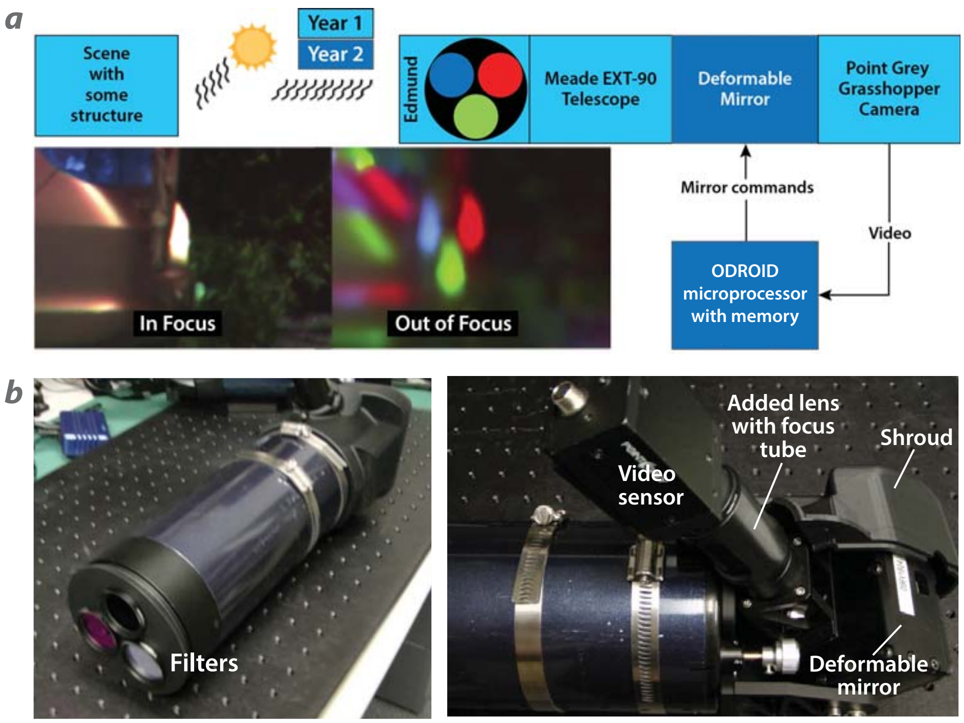

Figure 3. (a) RGB wavefront sensor FY 2015 block diagram and (b) hardware. The sun illuminates the scene with some structure. The reflected light enters the three filters at the entrance to the telescope. When in focus all three images align, but out of focus the pixel shifts correspond to the slope of the phase errors. These errors can be used to compute commands to a DM.

We use the method to obtain temporal variance images developed in an FY 2013 SDRD project "Passive Method to Characterize Atmospheric Turbulence" (O'Neill 2014, Terry 2014) to extract high spatial frequency content associated with the scintillation index; this helps determine wavefront distortion, even with limited high spatial frequency content in the scene. By updating this variance image at each frame, new pixel shifts can be obtained on a frame-by-frame basis.

Figure 3a shows the RGB WFS block diagram and Figure 3b shows the hardware developed in FY 2015 and FY 2016. Solar illumination reflects off the scene and enters the three sub-apertures. When the telescope is focused and no turbulence is present, the three images align perfectly. Because individual light rays go through different points of a plane before or behind focus, any defocus shows up as a pixel shift. When in focus, the pixels are oriented to the same point on the image plane, but when out of focus, the shifted pixels indicate degrees of focus error.

In our first year, we selected a Meade EXT-90 Maksutov-Cassegrain telescope and a Point Grey Grasshopper camera for our first breadboard. We verified the operation of this camera with a COTS mobile Samsung-based 8-CPU single-board computer (SBC) that drives the USB3 camera, runs Linux, operates on battery, and offers Wi-Fi hot spot connectivity. This year we integrated a DM into our telescope making the RGB wavefront sensor a portable AO system that improves overall image quality and will enable existing algorithms to further that improvement. A new shroud was made using our 3-D printer to enclose the DM. Because we placed the DM at the location of the current mirror, we are not at a pupil and thus not imaging the entrance aperture (i.e., the DM is located at a defocus plane). Figure 4 shows the mirror piston positions, mirror, and the mirror installed in the RGB WFS.

We ran Zemax to determine the ray bundle sizes. Because the bundle sizes were smaller than desired, the overall focal length was lengthened by adding a lens between the mirror and the camera, thus increasing the ray bundle sizes. This lens allows us to fix the focus knob of the telescope, and instead focus by rotating this added lens. We developed software to control the DM and compute the variance images.

As seen in Figure 3, the filter assembly reduces the apertures and thus increases the *f/#* of the system; in FY 2017 we updated our filters to improve both spectral bandwidth and *f/#*. We used the measurement of the relative spectral response of the Point Grey Grasshopper taken in FY 2016 (O'Neill 2017) and ran our selection algorithm considering COTS filters. Because the optimum filters were from two different manufacturers, during initial testing we discovered that the path lengths for these sets were significantly different. This resulted in the focal distance for blue being significantly different from red and green. We replaced this blue filter with one from the same manufacturer as for the red and green, resulting in reduced sensitivity.

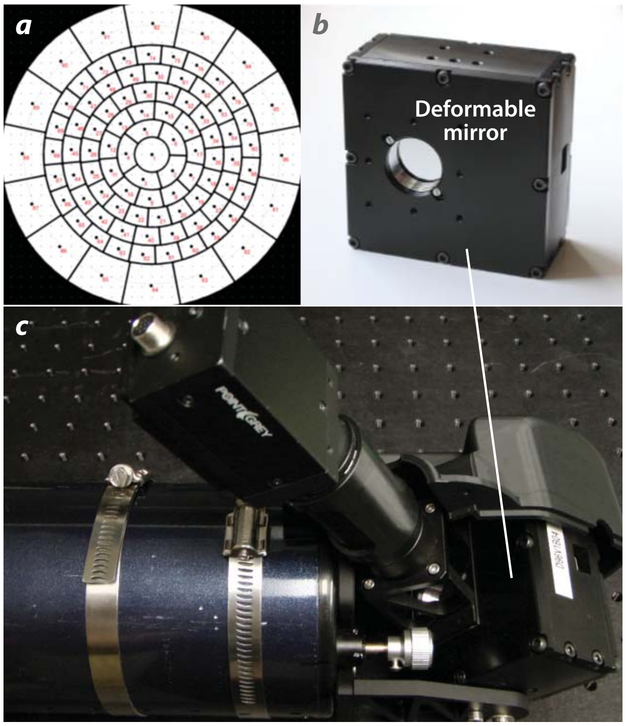

Figure 4. (a) 96 mirror piston positions, (b) mirror, and the (c) mirror installed in the RGB WFS

The bench setup shown in Figure 5 allowed us to calibrate and more easily test the system without taking it outside.

The Ocean optics lamp provides the illumination to the diffuser/grid assembly. We used our spare telescope as a collimator by reversing its direction. By placing our grid assembly at the focus of the collimator, the rays leaving this collimator are parallel and, thus, the target appears to be in the far field. The RGB WFS only needs to be placed at the appropriate angle with respect to this ray bundle. Because of the use of the Maksutov-Cassegrain telescope as the collimator, focusing artifacts including astigmatism were noted in the setup. This was advantageous in that it gave us the ability to verify that we could correct for more than defocus. Using the focus knob on the collimator allows us to make the target appear at different ranges. The ODRIOD (small blue box) that uses the Samsung Exynos-5422 processor (the system-on-chip [SoC] common to Samsung Galaxy tablets) does all the computing, including the variance image, pixel shifts, and mirror control. At the time of this writing, we were in the process of determining the limitations of this platform. Development on this platform will make transition to a tablet more realizable, and enable improvement as Samsung improves SoC capability on new Galaxy tablets.

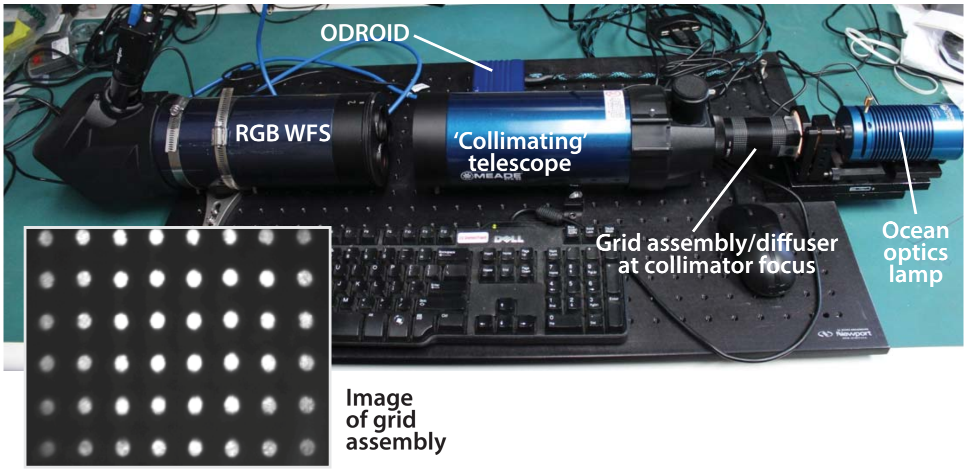

Figure 5. Bench setup. Illumination is provided by the Ocean optics lamp, which floods the grid assembly at the point of focus of the collimating telescope. The parallel rays leave the collimating telescope making the target appear to be in the far field. These enter the RGB wavefront sensor and are imaged on the Point Grey camera. The ODROID processes the images and commands the DM.

In order to mimic on the bench the degradation induced by atmospheric turbulence, we manufactured a phase plate whose transmitted wavefront phase statistics replicates the statistics of turbulence. To do this, we first generated the desired phases using a computer program developed by Dr. David Terry of Fifth Gait Technologies. The program creates a phase screen (an N×M array of phases with correct statistical properties) based on the grid size and the coherence radius, r_0. The original calculations correspond to an r_0 of 0.5085 cm (c_n^2 ~10–13, $L = 1$ km) similar to the conditions at the White Sands Missile Range (WSMR) at 800 m. Because the actual depth was too small to be easily patterned into any optical medium, we utilized the phase difference in two materials to allow for a much larger pattern to be milled into acrylic (aka Plexiglas) assuming an index-matching adhesive filled the voids. Due to the three apertures of the RGB hardware, we could not place a single screen in front of the telescope, so we replicated the pattern in front of each sub-aperture. A phase screen color-contour heat map for a 4.5″ × 4.5″ plate and for the actual phase

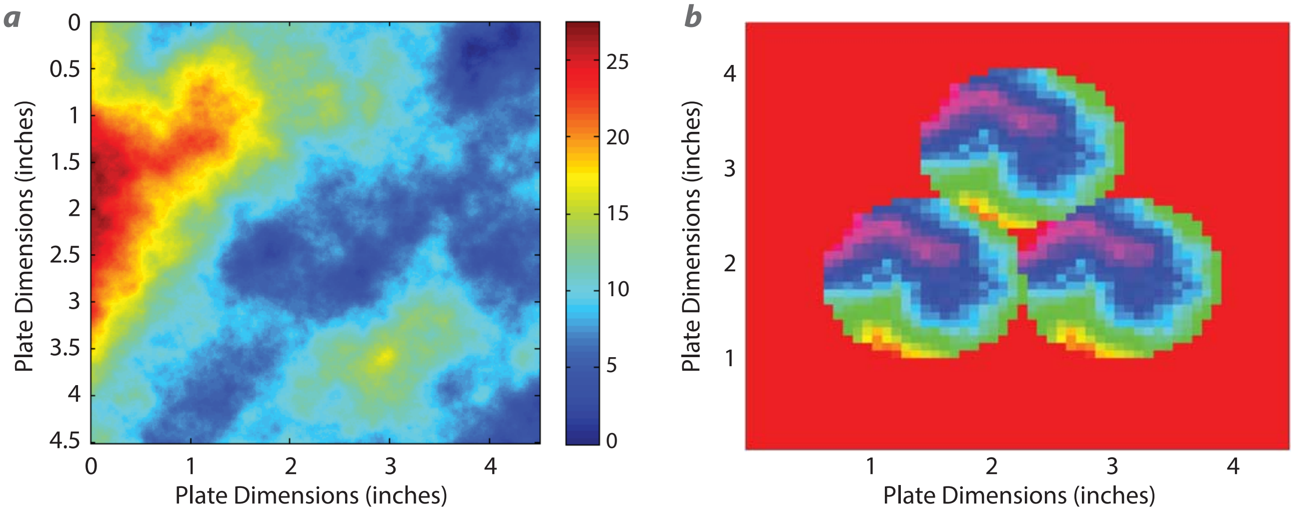

Figure 6. Heat maps of (a) full phase screen (levels = 0.001″) and for (b) repeated screen to be placed in front of the RGB sensor. Dimensions are the physical plate size to be placed in front of the sensor.

plate created for the RGB sensor are shown in Figure 6.

Because the UV-cured epoxy is a permanent bond, we investigated substituting corn syrup for the epoxy. Corn syrup has a similar viscosity and index match to the epoxy, so it provided an excellent surrogate for practice. This allowed us the opportunity to disassemble and reassemble the phase plate until a good result was obtained. Initial use of the phase plate revealed possible issues with assembled flatness. More work needs to be done to make this fully mimic actual turbulence, and ideally we should make optical measurements of its corresponding second-order structure function. The assembled phase plate is shown in Figure 7.

The variance image developed in the earlier SDRD project enhances the turbulent flows even with minimal image contrast and, thus, provides pixel shifts even in extremely high turbulence. While other AO methods rely on the structure in an image, using the variance image relies on the variation over time of the turbulence. Because we have three co-aligned apertures, the pixel shifts in the variance image correspond to the phase shifts associated with the sub-aperture locations. In our current implementation, we compute pixel shifts via a phase shift in the Fourier domain. Given an intensity measurement at a focal plane at pixel location x, y, at time t, and based on proportionality to Kolmogorov's ansatz (Kolmogorov 1941), we define the received flux variance as the normalized variance over all pixels on the focal plane over n samples in Δt increments as

$$\sigma_z^2\,(x,y,t) = \frac{\langle I(x,y,\tau)^2\rangle_{\tau\,=\,t_0 \text{ to } t_0+\,n\Delta t} - \langle I(x,y,\tau)\rangle^2_{all\ x,\ y,\ \text{and}\ \tau}}{\langle I(x,y,\tau)\rangle^2_{all\ x,\ y,\ \text{and}\ \tau}}. \qquad (2)$$

In this equation, the variables x, y, and t represent the x pixel location on the detector, the y pixel location on the detector, and the time of the frame. The variable I represents radiant flux at the pixel in counts.

To extract only the turbulence information, and not the scene or sensor noise, for each row, r, or column, c, in the image, the 1-D Fourier transform is computed to obtain the 1-D power spectral density (PSD) of turbulence, $\varphi(k)$. In practice, a fast Fourier transform is used. For horizontal calculations we define k as the spatial frequency in radians/pixel, and the estimated 1-D

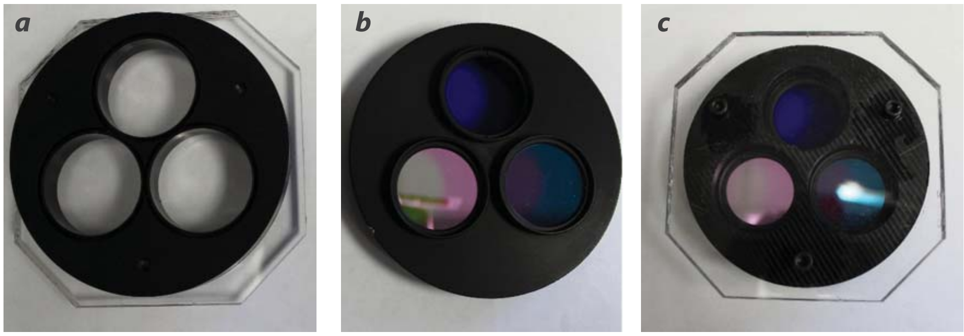

Figure 7. (a) Back side of phase plate with holder, (b) RGB filter assembly, and (c) phase plate press fit onto RGB holder for test

PSD for each row, *r*, for the Bayer red (R) channel, is computed as

$$\varphi_R(k_x,y=r,t)=\sum_{x=0}^{N-1}\sigma^2_{z\_R}(x,y=r,t)e^{-ik_x x/N}. \tag{3}$$

This is repeated for green (G) and blue (B). Because we use the relative shifts between colors, any platform motion is cancelled out, which is a critical requirement for compact operation. We compute the relative phase shift in the image in radians for red to green as

$$\alpha_{R/G}(k,r,t)=argMax(FT^{-1}[\varphi(k_x,y=r,t)\varphi^*_G(k_x,y=g,t)]). \tag{4}$$

This process is repeated for G-B and B-R to get all three cases. To get the horizontal pixel shifts, we then multiply by the frequency such that

$$\Delta x(r,t)=\Sigma_{k_x}\alpha_{R/G}(k_x,r,t)/k_x. \tag{5}$$

This process is repeated for all columns to get the vertical shifts.

To determine if the mirror was suitable for a relevant scenario, data from the September test at the WSMR at 800 meters to target were analyzed (O'Neill 2016). Color cameras automatically demosaic imagery by converting Bayer pixel color planes to RGB so the user sees only a color picture, which typically has mixing of the original color planes. Our processing is done on the raw Bayer pixels; therefore, the color separation remains intact, producing images directly associated with the three apertures. A first-order calculation of the vertical pixel shifts was done on the whole image to determine the range of the DM motion. The R-G and B-R show shifts at the peak of about 5 and 10 pixels. We measured the relative pixel shifts associated with the full range of piston motion of the OKO DM to be 10 pixels, which is compatible with the 800-meter 2.4×10^{-13} $m^{-2/3}$ turbulence levels measured at the WSMR.

Because we did not place the mirror at a pupil (it is at a defocus plane, i.e., near, but not at, an image plane), we speculated that we could measure the relative pixel shifts for the different actuator positions and determine a linear solution.

Consider a point in the object plane. Because the object is in the far field, rays from this point intersect the entrance aperture with a single angle of incidence. The location of these ray bundles at subsequent positions within the telescope depends on this angle of incidence, such that the location on the entrance aperture is $[x(px,py), x(px,py)]$. Figure 8 shows a cartoon of ray bundles for a given object point, at the entrance aperture, the DM, and the detector (focal plane array, FPA) plane. Note that, in the absence of turbulence (or any defocus), this bundle will be focused to a point at the image plane; because the detector has been defocused, however, the bundle has a finite area at the FPA. If the entrance aperture is divided into several sub-apertures, the bundle at the FPA will be separated into the equivalent number of smaller bundles, each with the appearance of the object point, albeit blurred. With focus errors (such as those induced by turbulence), these multiple images shift apart.

If the DM were at an exit pupil, the bundle in Figure 8b would look the same as those in Figure 8a. The effect of defocus on the colors is illustrated in the extreme case shown in Figure 9, where we manually took an image of a specular reflection off a bumper through focus.

We developed a method to separate the image into a number of blocks in order to determine the relationship between the relative pixel shifts in these blocks and the required voltages to counter these shifts. Using a number of assumptions, based on the PSFs derived from the wave equation and the literature provided by OKO, we mathematically determined a likely relationship between the measured R-G pixel shifts and DM deformation in *z*,

$$\begin{aligned}&(x_r(b)-x_g(b))k_{x_{fpa}}+(y_r(b)-y_r(b))k_{y_{fpa}}\\&\quad=2(k(g)-k(r))(z(x_{DM},y_{DM},V)+c),\end{aligned} \tag{6}$$

where (x_r, y_r) is the pixel location for the red color plane in block b, (x_g, y_g) is the pixel location for the green color plane in block *b*, *k* is the wavenumber $= 2\pi/\lambda$, *z* is the mirror deformation at (x_{DM},y_{DM}) for voltage *V*, and *c* is a constant related to the original angle corresponding to the position of the point at the object. This calculation is performed for every block, color plane, and direction. A correction factor is required for each shift to

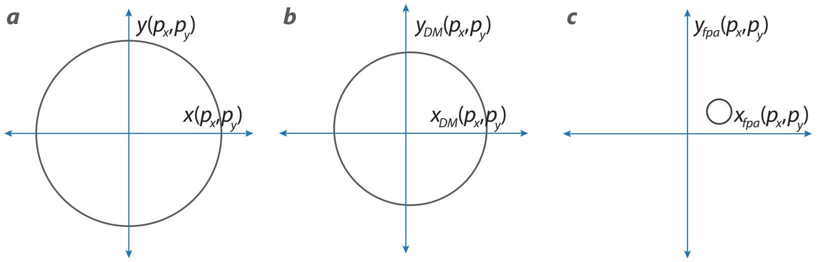

Figure 8. (a) Ray bundle at entrance aperture, (b) ray bundle at DM (note that this is off center as it moves toward (c) ray bundle (PSF) at the FPA

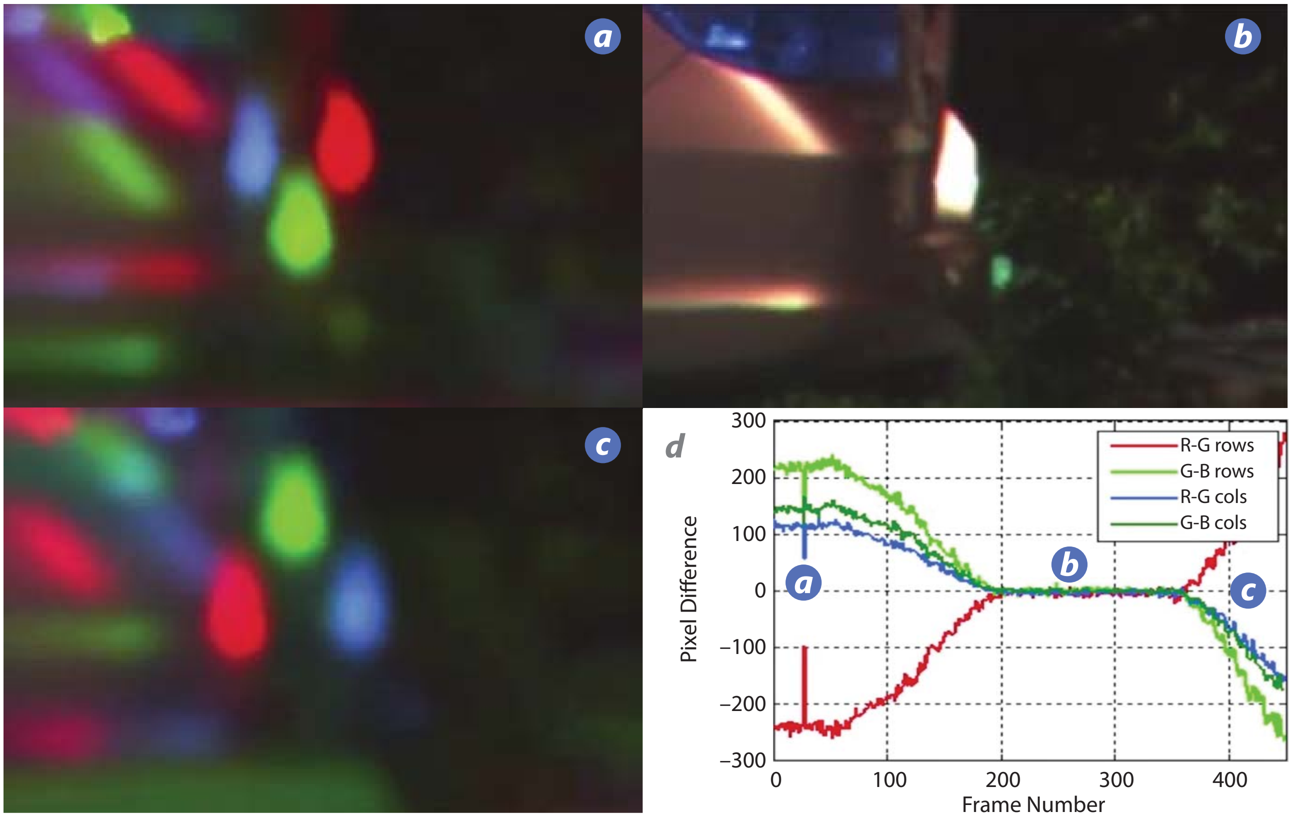

Figure 9. (a) Defocus forward of image plane, (b) at image plane, and (c) in aft of image plane. (d) The plot shows pixel shifts as the video went through focus that can be exploited when caused by turbulence.

account for the fact that the four color planes (R, G1, G2, B of the Bayer mask) are a pixel apart.

From the OKO literature, z is proportional to V^2 (Vdovin 2013). Because this quadratic is based on an approximation between electrostatic pressure and voltage, we changed the exponent to be a variable, resulting in the matrix equation

$$sign\,(\Delta\vec{V}) \cdot |\Delta\vec{V}|^{e} = A\Delta\vec{p}, \qquad (7)$$

where e is the exponent power between 0 and 2, initially set to 1.0, $\Delta\vec{p}$ is the relative shift as a Mx1 vector where M = (# of dimensions, xy) (# of colors, clr) (# of blocks, b); A is an N×M matrix of coefficients, where N is the number of actuators positions; and $\Delta\vec{V}$ is an N×1 vector of delta voltages.

Because the pixel shifts have polarity, care is required to determine the actual delta voltages. We began with a linear solution to see if it would converge. We found the relationship between delta shifts and delta voltage to be crucial; thus, the calculated delta shifts between colors needed to be offset from delta shifts corresponding to

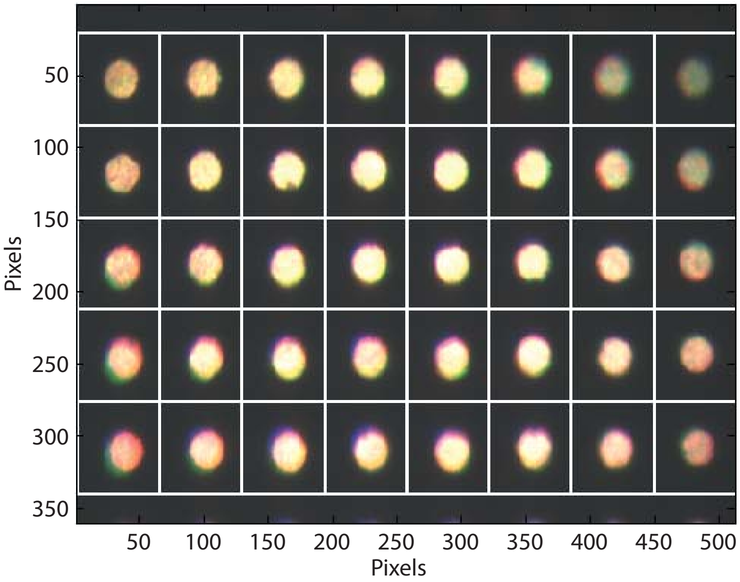

Figure 10. Grid pattern used for calibration. We set each block to be 64 × 64 pixels in the raw color planes. Note that using the raw data results in half the number of pixels that result from Bayer interpolation.

the center voltage. To obtain the coefficients, we used the grid pattern from the bench set to provide 40 blocks (8×5) as shown in Figure 10.

We collected images for 36 unique mirror actuator combinations and five different delta voltages. We analyzed these images for the relative pixel shifts corresponding to delta voltages to create vector, Δp. We then compute the solution for A, with $e = 1$ as

$$A = (\overrightarrow{\Delta p})^{-1}\,(sign\,(\overrightarrow{\Delta V})\cdot|\overrightarrow{\Delta V}|^{e}). \qquad (8)$$

Once matrix A was computed, we tested this set of coefficients by slightly defocusing the collimating telescope within the range of motion of the DM. We added a relaxation parameter for our implementation to determine if the solution would converge. For each block, we use our phase correlation registration algorithms (that were implemented on an SBC in FY 2016) on received variance images (or static images on the bench) to extract pixel shifts. The program then computed the estimated voltage error associated with the measured shifts as

$$\widehat{\Delta V} = rA\overrightarrow{\Delta p}, \qquad (9)$$

where r is a relaxation parameter between 0 and 1. Using this estimate, we compute the new mirror voltage as

$$V(t) = V(t-\Delta t) - (sign(\widehat{\Delta V})\cdot|\widehat{\Delta V}|^{e}), \qquad (10)$$

where e was equal to 1 for our initial test. Using multiple mirror initialization voltages, we saw this method converge in about eight frames using a relaxation parameter of 0.25, as indicated in Figure 11.

The images associated with the starting point, frame 4, and frame 8 for this initial test are shown in Figure 12.

Figure 12a shows the image at the initialization voltage. Note that all three colors are well separated, indicating defocus. By about the fourth frame, the error is cut in half, and by the eighth frame it is within the measurement error of the phase correlation

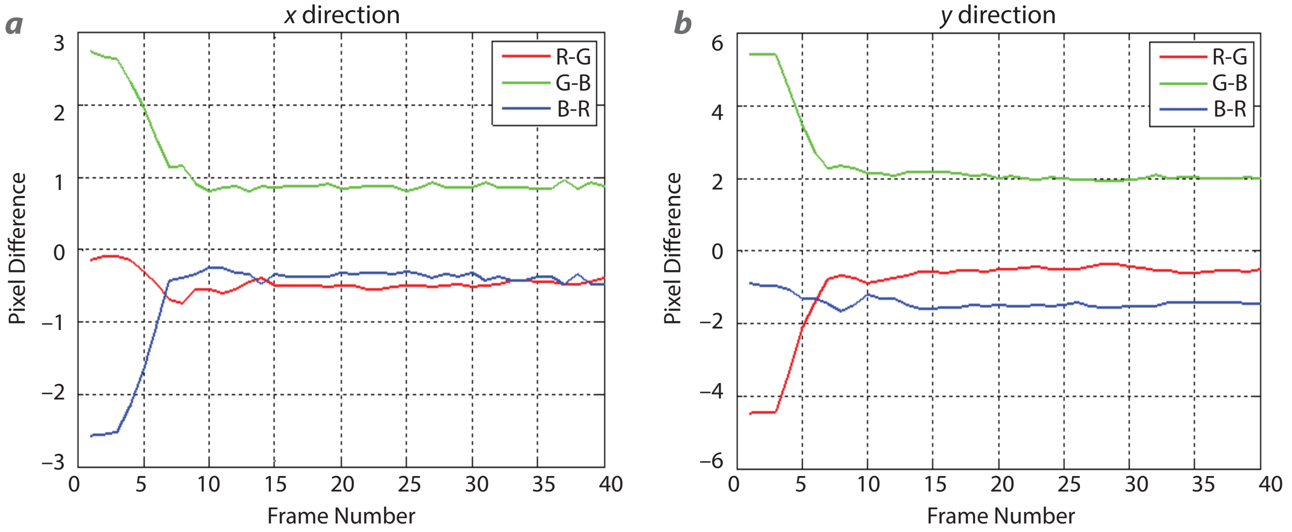

Figure 11. Pixel difference equal to focus error versus frame number for (a) x and (b) y directions. The solution converges in about eight frames.

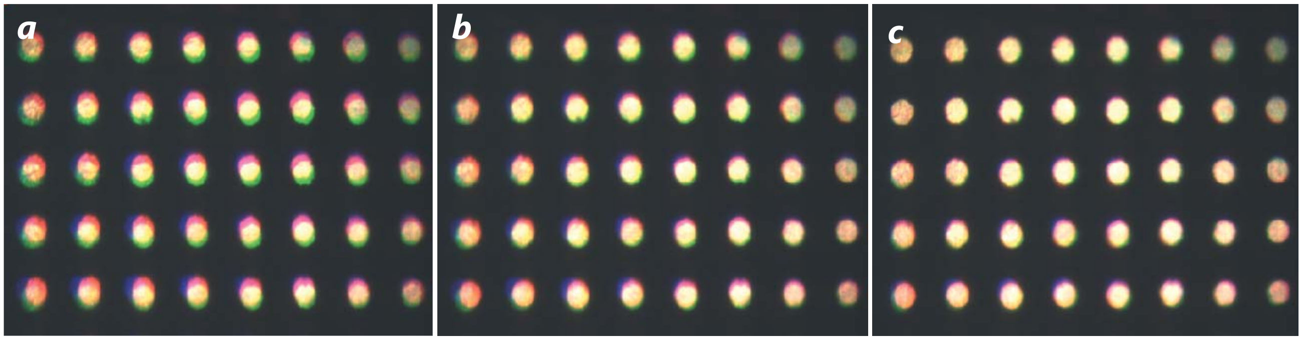

Figure 12. Example mirror control results for bench test case with 0.25 relaxation. (a) No correction (>8 total pixel error), (b) four frames of correction (<4 pixel error), and (c) 8 frames of correction (~2 pixel error)

registration algorithms with the exception of the G-B shifts. We believe using an exponent of 1.5 can improve these results.

Further bench testing and optimization is required to verify the capability of this system in outdoor scenarios. At the current time, we have refocused the telescope to a particular target range (about 250 m) and are recomputing the coefficients of Equation 8 for an exponent of 1.5.

CONCLUSION

We have created a prototype portable AO system using low-cost COTS components. The keys to this work are the three-color aperture configuration and the use of the temporal statistics associated with the variance image to improve the ability to get pixel shifts even in high turbulence. This year we selected and integrated a DM and a suitable SBC into our system. The fold mirror in the telescope was replaced with the DM, and a shroud, printed on our 3-D printer, replaced the original. Because the mirror is not at a pupil plane, typical AO correction methods using Zernike polynomials could not be used. We created a bench setup that allowed us to directly correlate pixel motion to mirror commands and verify our ability to correct for focus errors on the bench. We hope to finalize this solution for demonstration in a relevant turbulent environment, perhaps outside with a target range of about 0.25 km in very high turbulence ($c_n^2 \sim 10^{-12} m^{-2/3}$).

ACKNOWLEDGMENTS

The authors wish to thank Ian McKenna and Dr. Rusty Trainham for their help in data collection and sensor characterization. The authors also wish to thank Dr. David Tofsted of the Army Research Laboratory for his insights into AO and turbulence.

REFERENCES

Beckers, J. M., “Adaptive optics for astronomy: Principles, performance, and applications,” *Ann. Rev. Astron. Astrophys.* **31** (1993) 13–62.

Born, M., E. Wolf, *Principles of Optics*, Section 9.2, Pergamon Press, New York, 1965.

Fried, D. L., “Optical heterodyne detection of an atmospherically distorted signal wavefront,” *Proc. IEEE* **55** (1967) 57–77.

Fried, D. L., “Probability of getting a lucky short-exposure image through turbulence,” *J. Opt. Soc. Am.* **68** (1978) 1651–1658.

Hufnagel, R. E., “The probability of a lucky exposure,” Tech. Memo, REH-0155, Perkin-Elmer, Norwalk, Connecticut, February 1989.

Kolmogorov, A. N., “The local structure of turbulence in incompressible viscous fluid for very large Reynolds numbers,” *Dokl. Akad. Nauk SSSR* **30**, 4 (1941) 301–305.

Lukin V. P., N. N. Botygina, O. N. Emaleev, P. A. Konyaev, “Wavefront sensors for adaptive optical systems,” *Meas. Sci. Rev.* **10**, 3 (2010) 102–107.

Martinez, P., J. Kolb, M. Sarazin, A. Tokovinin, “On the difference between seeing and image quality: When the turbulence outer scale enters the game,” *European Southern Observatory Messenger* **141** (2010) 5–8.

Max, C., Lecture 3 of Astronomy 289C: Adaptive Optics and its Applications, University of California, Santa Cruz, April 8, 2010.

Noll, R. J., “Zernike polynomials and atmospheric turbulence,” *J. Opt. Soc. Am.* **66** (1976) 207–211.

O’Neill, M. D., D. Terry, A. Potter, I. McKenna, “Passive method to characterize atmospheric turbulence,” in *Site-Directed Research and Development*, FY 2013, National Security Technologies, LLC, Las Vegas, Nevada, 2014, 125–135.

O’Neill, M. D., D. Terry, “Portable COTS RGB wavefront sensor,” *MSS Passive Sensors*, Gaithersburg, Maryland, 2016.

O’Neill, M. D., D. Terry, “RGB wavefront sensor for turbulence mitigation,” in *Site-Directed Research and Development*, FY 2016, National Security Technologies, LLC, Las Vegas, Nevada, 2017, 109–117.

Poyneer, L. A., K. La Fortune, C. Chan, “Scene-based wave-front sensing for remote imaging,” UCRL-JC-154654 Lawrence Livermore National Laboratory, Livermore, California, 2003.

Rais, M., J.-M. Morel, C. Thiebaut, J.-M. Delvit, G. Facciolo, “Improving the accuracy of a Shack-Hartmann wavefront sensor on extended scenes,” 6th International Workshop on New Computational Methods for Inverse Problems (NCMIP), Cachan, France, May 2016, https://hal-enpc.archives-ouvertes.fr/hal-01344949/document, accessed October 5, 2016.

Sidick E., J. J. Green, C. M. Ohara, D. C. Redding, “An adaptive cross-correlation algorithm for extended scene Shack-Hartmann wavefront sensing,” in *Adaptive Optics: Analysis and Methods/Computational Optical Sensing and Imaging/Information Photonics/Signal Recovery and Synthesis Topical Meetings on CD-ROM*, OSA Technical Digest (CD) (Optical Society of America, 2007), paper JTuA7, http://www.meripet.com/Papers/JTuA7.pdf, accessed October 5, 2016.

Sidick, E., “Extended scene Shack–Hartmann wavefront sensor algorithm: Minimization of scene content dependent shift estimation errors,” *Appl. Opt.* **52** (2013) 6487–6496.

Terry, D., M. D. O’Neill, “Passive method to characterize atmospheric turbulence,” *MSS Passive Sensors*, Gaithersburg, Maryland, 2014.

Tofsted, D. H., “Turbulence simulation: Outer scale effects on the refractive index spectrum,” ARL-TR-548, Army Research Laboratory Technical Report, November 2000, https://www.arl.army.mil/www/default.cfm?technical_report=294, accessed April 6, 2015.

Tofsted, D., “Passive adaptive imaging through turbulence,” *Proc. SPIE* **9833** (2016) 98330B.

Vdovin, G., O. Soloviev, M. Loktev, V. Patlan, “OKO Guide to Adaptive Optics,” 4th edition, OKO Technologies, May 2013.

This page left blank intentionally

A Semiconductor-Based High-Yield X-Ray Photocathode

LO-007-17 ■ Continuing in FY 2018 ■ Year 1 of 3

**Kathy Opachich,[1,a] Andrew MacPhee,[b] Otto Landen,[b] Ning Chen,[c]
Ashwini Gopal,[c] Salah Udin,[c] Terry Hilsabeck,[d] Eric Huffman,[d]
Jeffrey A. Koch,[a] Jun Feng,[e] Dave Bradley,[b] and Sabrina Nagel[b]**

[1]opachiyp@nv.doe.gov, (925) 960-2520
[a]Livermore Operations
[b]Lawrence Livermore National Laboratory
[c]NanoShift LLC
[d]General Atomics
[e]Lawrence Berkeley National Laboratory

In this two-year project, we are developing a silicon-based high-yield x-ray photocathode for use in the spectral energy range from 1 to 30 keV. In our previous work (Opachich 2016a, 2017), we fabricated and tested a structured photocathode that showed an improvement of 3x in measured secondary electron yield. This concept can be extended to increase the yield up to an order of magnitude higher than what was previously demonstrated. The design necessitates use of structures with wall angles from 1° to 3°. Unlike the previous 10° wall angle design, when coated with gold this geometry introduces a loss of electric field and, thus, loss of signal from the photocathode. This can be circumvented with the use of dielectric materials, or with a solid-state approach by generating a charge depletion region within a doped silicon substrate. Several cathode designs were modeled in FY 2017. In FY 2018 we plan to fabricate a set of test devices and characterize the cathode performance. Here we discuss the device design and modeling results.

BACKGROUND

Time-resolved x-ray diagnostics are widely used at the National Ignition Facility (NIF) (Miller 2004). Currently the facility uses streak camera detectors, such as the Diagnostic Insertion Manipulator Imaging Streak Camera (Opachich 2012), Streaked Polar Instrumentation for Diagnosing Energetic Radiation (SPIDER) (Khan 2012), and time dilation imaging tubes (Hilsabeck 2010, Nagel 2012) for imaging in the 5 to 10 keV range. The introduction of the Advanced Radiographic Capability on NIF will provide imaging

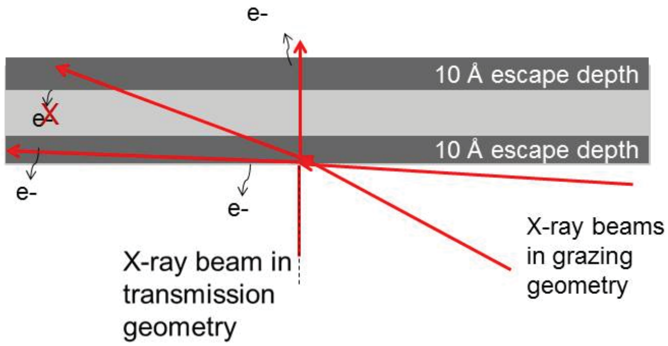

Figure 1. Example of the grazing incidence and transmission geometry. The electron escape depth (not to scale) is shown on both sides of the photocathode. Electrons that are generated within the bulk do not contribute to the measured yield.

sources that extend well above 10 keV. However, current detectors rely on photocathode materials to convert photon signals to electrons, which are then dispersed temporally with the use of voltage ramps and magnetic fields. The imager detector efficiency and operational range drops significantly above 10 keV due to a sharp reduction in quantum efficiency (QE) of most photocathode materials (i.e., gold and cesium iodide) (Hara 2000, Khan 2013, Opachich 2014). Geometrically enhanced photocathodes provide a potential solution, and they can be easily integrated into existing detectors without compromising performance.

The electron yield can be improved by better matching the x-ray path length to the very thin top-most emission layer of the photocathode, defined as the electron escape depth. This is accomplished by changing the incidence angle of x-ray photons to a very shallow, near-grazing geometry, as shown in Figure 1. The secondary electron escape depth is typically very thin; for example, in gold it is limited to the top 10 Å of the photocathode surface (Henke 1981, Fraser 1992). Incidence angles below ~20° are needed to provide significant enhancement. Grazing incidence detectors have utilized this geometry and demonstrated improvement in photocathode QE by a factor of 15–20 times in the soft x-ray range (Feng 2010). This effect can also be extended to the 10–30 keV range, as predicted by the semi-empirical model by Fraser (1983a, 1983b).

Changing the incidence angle of current NIF detectors is costly and may not be possible due to engineering design constraints; however, it is fairly simple to change the design of the photocathodes by introducing geometrically enhanced surfaces such as pillars, cones, or recessed cavities. In our previous SDRD effort, we have modeled, fabricated, and tested a recessed pyramid photocathode (Opachich 2014, 2015, 2016b). The photocathode used a 10° structure wall angle, and showed a yield increase of 3x. The predicted yield and recessed pyramid photocathode designs are shown in Figures 2a and 2c. For comparison, the yield from a standard planar photocathode is shown in Figures 2a and 2d. An increase of an order of magnitude is predicted with the use of a 3° wall angle in the same recessed structure, as seen in Figures 2a and 2b. Such shallow angles require the recessed pyramids to be much longer than those previously fabricated and necessitates a new design. The longer structure depth and use of a metal cathode coating will introduce a

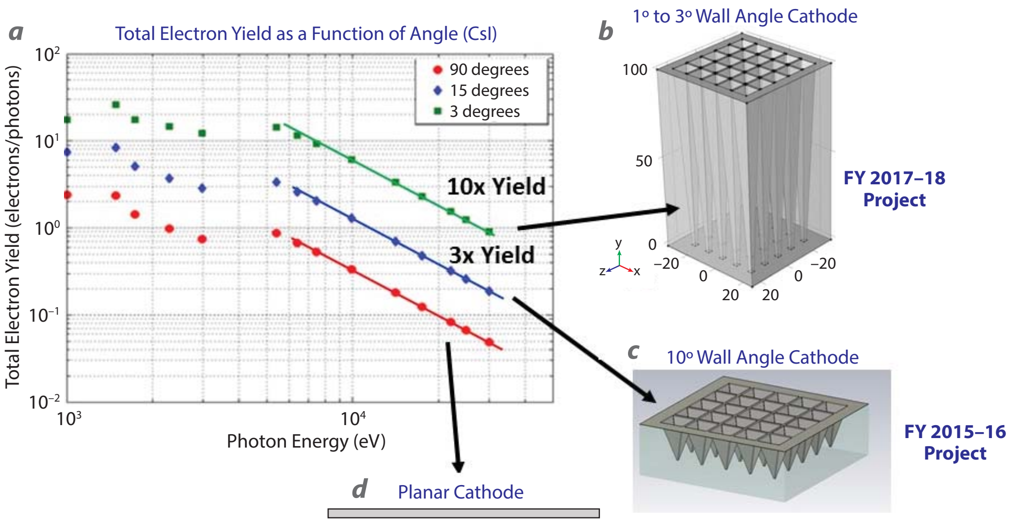

R&D 100 winner, 2017
Patent application, 2016
Publications, 2014–2016

Figure 2. Predicted yield for planar, 10°, and shallow-angle cathode designs. (a) Calculated expected secondary electron yield as a function of energy. Three incidence angles are shown. (b) A structure with a 1°–3° wall angle. (c) A structure with a 10° wall angle has improved yield by 3x. (d) An example of a planar photocathode.

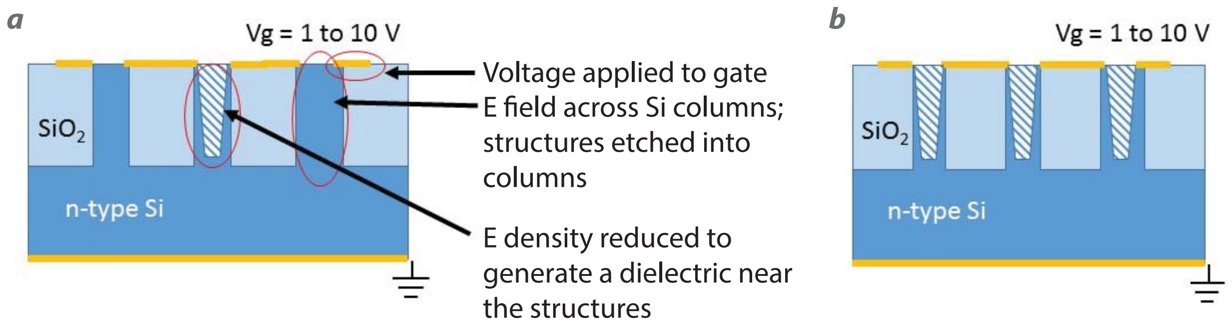

Figure 3. Proposed solid-state photocathode design, showing (a) the various parts of the photocathode and a description of the functionality, and (b) the final design. Structures will be etched into the Si columns.

loss of electric field within the recessed cavities. This negates any yield improvements from the structure, because the field is needed to extract and accelerate photoelectrons out of the cavities. One solution is to use a dielectric material as a substrate and an alkali metal photocathode. A dielectric condition known as a depletion region can also be generated within a semiconductor device with the use of metal/oxide/silicon layers. Here electron carrier densities can be manipulated with the selection of an appropriate device design and voltage (Velasquez-Garcia 2011a, 2011b). The feasibility of such an approach was validated with COMSOL modeling software. This year we focused on investigating several types of structures to identify a potential cathode design. This included modeling the electric field along with electron and hole densities in n- and p-type silicon. We also developed a second design that uses a glass substrate with high-density etched recessed pyramid microchannels.

PROJECT

Semiconductor and High-Density Microchannel Photocathode Concepts

The proposed solid-state photocathode uses an n-doped silicon (Si) substrate into which columns are etched (Figure 3a) and the areas between columns are filled with an oxide (SiO$_2$). Metal contacts are placed along the top and bottom of the photocathode. Recessed pyramid structures are etched into the Si columns (Figure 3b), and the entire top surface is coated with a layer of cesium iodide (CsI). The metal contacts create an electric field within the Si substrate. The two contacts act as a switch when voltage is applied to the top contact (V_g), and the bottom one is grounded. When the electron density is reduced within the columns near each structure, a dielectric condition exists and a voltage gradient needed to extract electrons from the CsI photocathode is present. After the emission process is completed, the cathode could then be biased to reverse the effect to help replenish charge within the CsI emission layer. Such a cathode would be operated in pulsed mode.

Several unknowns exist for the semiconductor-based design. The behavior of electron and hole carriers in a large external electric field introduced by the detector in the acceleration gap region needs investigation. The design requires pulsed operation and timing that takes into account carrier transport through the bulk of the material. Finally, the full-scale design will be costly to fabricate due to cathode size and pattern density. For these reasons we also developed a high-density microchannel cathode design as an alternative solution.

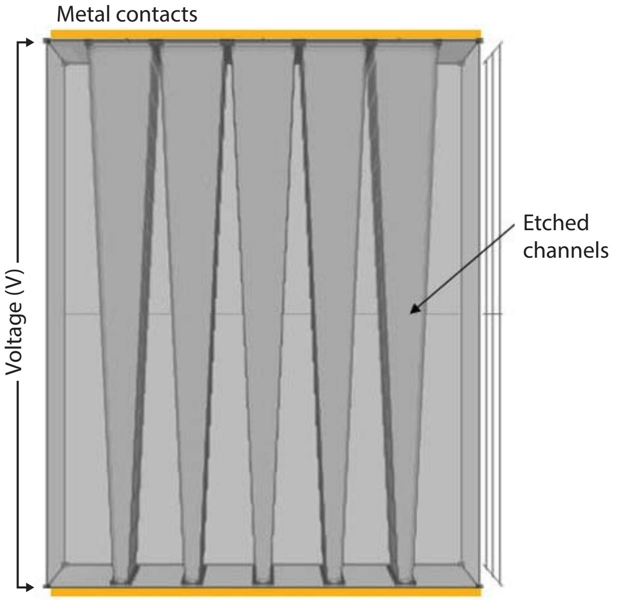

Figure 4. Alternate high-density microchannel cathode design. High-density channels are etched into a glass substrate. The top and bottom of the device are coated with a conductive layer, and then the entire emission surface, including the walls of the recessed pyramids, is coated with CsI.

In the alternative high-density microchannel cathode design, a glass substrate is used with structures etched along the top of the device. The top and bottom of the device are coated with metal where voltage is applied to generate an electric field within the recessed pyramids. The entire cathode surface, along with the recessed pyramid walls, is then coated with a CsI emission layer. The design is shown in Figure 4.

Photocathode Modeling Results

Both designs were modeled in COMSOL to assess performance. The solid-state photocathode was modeled using the semiconductor and AC/DC COMSOL modules. The results, shown in Figure 5, present a single Si column with a ground plane at the bottom and two metal contacts at the top of the structure. Several voltages were applied to the device to study electric field and electron density. Figure 5 shows a selection of voltages. At $V_g = 0$ V the device shows the initial electron density and electric potential. As the voltage on V_g is increased to 10 V, the electric potential increases along the column and the electron carrier density reduces, as expected. This relationship shows that such a design can potentially generate a depletion condition near the recessed pyramid structure within the column.

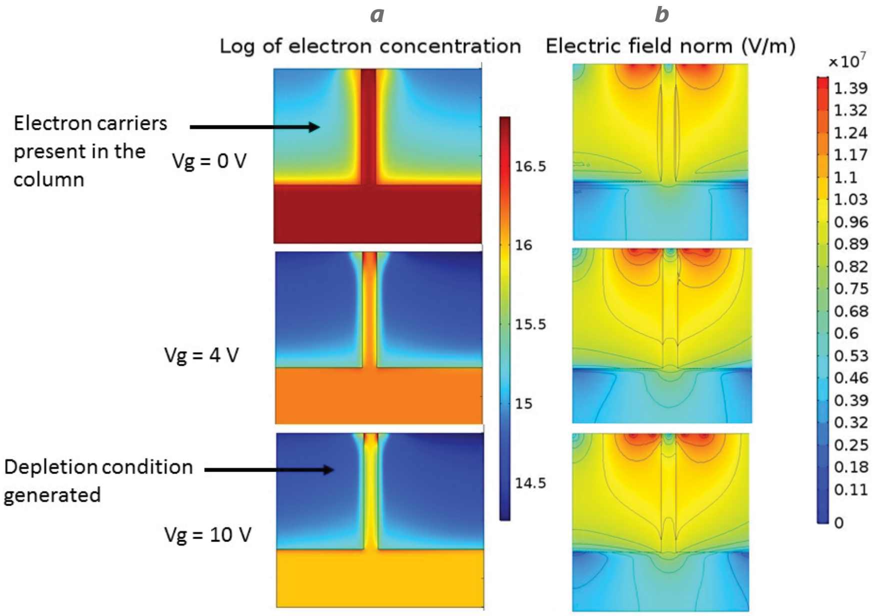

Figure 5. Results of the COMSOL model for the semiconductor-based design, showing (a) the electron concentration result and (b) the electric field as a function of applied gate voltage

The simulation results for the high-density microchannel device are shown in Figure 6. Because the device's substrate is made from a dielectric oxide, SiO_2, the electric potential shown in Figure 6a is uniform within the channels and the substrate. When photons are incident onto the photocathode, the resulting photoelectrons are generated at the wall surface of the channels and must escape the photocathode without secondary interactions. Electron trajectories are influenced by the amount of voltage applied to the device and the depth of the channels. The resulting electron trajectories for a 40 μm deep structure held at –200 V are shown in

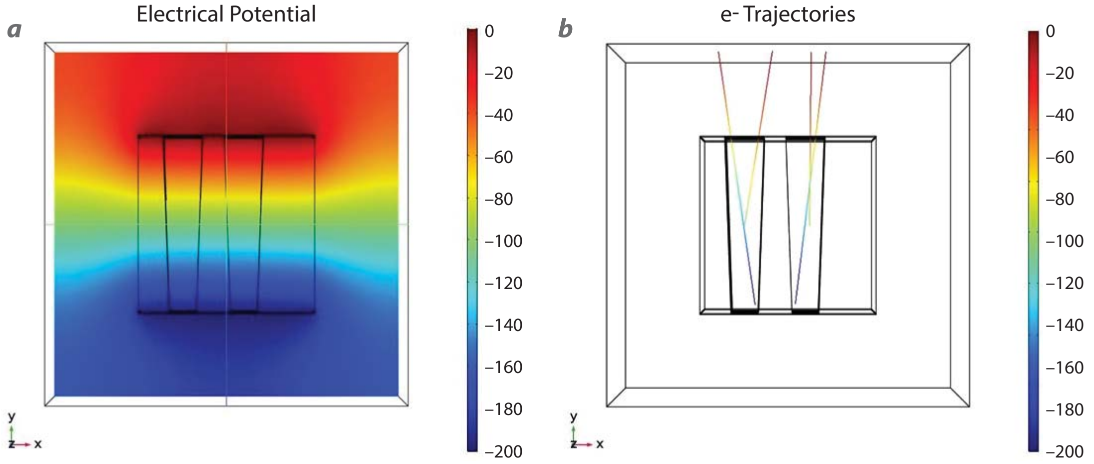

Figure 6. High-density microchannel cathode modeling in COMSOL showing (a) electric potential within the channel and substrate and (b) electron trajectories

Figure 6b. Here we see that, for our given cathode thickness and voltage, electrons that are generated at the bottom of the structure are able to clear the outer aperture of the channel. We plan to use these modeling results in FY 2018 to finalize both prototype designs.

CONCLUSION

A new photodiode concept has been identified in order to improve photoelectron yield by an order of magnitude in the 1 to 30 keV range. COMSOL modeling software was used to investigate the feasibility of semiconductor-based photocathode and high-density microchannel designs. The modeling results show that both designs are feasible. We will begin developing a fabrication process for both devices in parallel and plan to test device performance at the end of FY 2018.

To date, related work (spanning several years) resulted in a patent application (Opachich 2016c), several presentations at the High Temperature Plasma Diagnostics Conference (Opachich 2014, 2016b), a talk at the SPIE Optics and Photonics Conference (Opachich 2015), and two talks at the National Inertial Confinement Fusion Diagnostics Meeting (Opachich 2014, 2015). The project on which this research is based received an R&D 100 Award in 2017. The modeling work discussed in this report and subsequent device fabrication will help improve this technology even further.

REFERENCES

Feng, J., K. Engelhorn, B. I. Cho, H. J. Lee, M. Greaves, C. P. Weber, R. W. Falcone, H. A. Padmore, P. A. Heimann, “A grazing incidence x-ray streak camera for ultrafast, single-shot measurements,” *Appl. Phys. Lett.* **96**, 13 (2010) 134102.

Fraser, G. W., “The characterisation of soft x-ray photocathodes in the wavelength band 1–300 Å: I. Lead glass, lithium fluoride and magnesium fluoride,” *Nucl. Instrum. Methods Phys. Res.* **206**, 1–2 (1983a) 251–263.

Fraser, G. W., “The characterisation of soft x-ray photocathodes in the wavelength band 1–300 Å: II. Caesium iodide and other insulators of high photoelectric yield,” *Nucl. Instrum. Methods Phys. Res.* **206**, 1–2 (1983b) 265–279.

Fraser, G. W., M. T. Pain, J. E. Lees, C. R. Binns, J. F. Pearson, P. R. Houghton, “The characterization of gold x-ray photocathodes,” *Nucl. Instrum. Methods Phys. Res. A*, **321**, 1–2 (1992) 385–391.

Hara, T., Y. Tanaka, H. Kitamura, T. Ishikawa, “Performance of a CsI photocathode in a hard x-ray streak camera,” *Rev. Sci. Instrum.* **71**, 10 (2000) 3624–3626.

Henke, B. L., J. P. Knauer, K. Premaratne, “The characterization of x-ray photocathodes in the 0.1–10-keV photon energy region,” *J. Appl. Phys.* **52**, 3 (1981) 1509–1520.

Hilsabeck, T. J., et al., “Pulse-dilation enhanced gated optical imager with 5 ps resolution,” *Rev. Sci. Instrum.* **81** (2010) 10E317.

Khan, S. F., et al., “Measuring x-ray burn history with the Streaked Polar Instrumentation for Diagnosing Energetic Radiation (SPIDER) at the National Ignition Facility (NIF),” *Proc. SPIE* **8505** (2012) 850505.

Khan, S. F., et al., “Characterization of the x-ray sensitivity of a streak camera used at the National Ignition Facility (NIF),” *Proc. SPIE* **8850** (2013) 88500D.

Miller, G. H., E. I. Moses, C. R. Wuest, “The National Ignition Facility: Enabling fusion ignition for the 21st century,” *Nuclear Fusion* **44**, 12 (2004) S228.

Nagel, S. R., et al., “Dilation x-ray imager a new/faster gated x-ray imager for the NIF,” *Rev. Sci. Instrum.* **83**, 10 (2012) 10E116.

Opachich, Y. P., et al., “High performance imaging streak camera for the National Ignition Facility,” *Rev. Sci. Instrum.* **83**, 12 (2012) 125105.

Opachich, Y. P., P. W. Ross, A. G. MacPhee, T. J. Hilsabeck, S. R. Nagel, E. Huffman, P. M. Bell, D. K. Bradley, J. A. Koch, O. L. Landen, “High quantum efficiency photocathode simulation for the investigation of novel structured designs,” *Rev. Sci. Instrum.* **85**, 11 (2014) 11D625.

Opachich, Y. P., et al., “Precision fabrication of large area silicon-based geometrically enhanced x-ray photocathodes using plasma etching,” *Proc. SPIE* **9591** (2015) 95910O.

Opachich, Y. P., et al., “High-yield x-ray photocathodes for next-generation imaging detectors,” in *Site-Directed Research and Development*, FY 2015, National Security Technologies, LLC, Las Vegas, Nevada, 2016a, 147–152.

Opachich, Y. P., P. W. Ross, A. G. MacPhee, T. J. Hilsabeck, S. R. Nagel, E. Huffman, P. M. Bell, D. K. Bradley, J. A. Koch, O. L. Landen, “Structured photocathodes for improved high-energy x-ray efficiency in streak cameras,” *Rev. Sci. Instrum.* **87**, 11 (2016b) 11E331.

Opachich, Y. P., A. MacPhee, “Photocathode,” U.S. Patent Application 15,24,9197, filed August 26, 2016 (2016c).

Opachich, Y. P., et al., “High-yield x-ray photocathodes for next-generation imaging detectors,” in *Site-Directed Research and Development*, FY 2016, National Security Technologies, LLC, Las Vegas, Nevada, 2017, 119–126.

Velasquez-Garcia L. F., S. A. Guerrera, Y. Niu, A. I. Akinwande, “Uniform high-current cathodes using massive arrays of Si field emitters individually controlled by vertical

Si ungated FETs—Part 1: Device design and simulation," *IEEE Trans. Elect. Dev.* **58**, 6 (2011a) 1775–1782.

Velasquez-Garcia L. F., S. A. Guerrera, Y. Niu, A. I. Akinwande, "Uniform high-current cathodes using massive arrays of Si field emitters individually controlled by vertical Si ungated FETs—Part 2: Device fabrication and characterization," *IEEE Trans. Elect. Dev.* **58**, 6 (2011b) 1783–1791.

Spectral Reconstruction from Compton Crosstalk Applied to Large PVT Scintillators

STL-008-17 ■ Year 1 of 1

Rusty Trainham[1,a] **and James Tinsley**[a]

[1]trainhcp@nv.doe.gov, (805) 681-2248
[a]Special Technologies Laboratory

Preliminary simulations of gamma absorption by plastic scintillators suggest that improved sensitivity and energy resolution could be achieved by high-Z metal doping of the plastic and by implementing a Compton reconstruction algorithm on the data stream. Additionally, the use of gadolinium (Gd) as the high-Z dopant would likely permit neutron detection via correlated gamma emissions induced by neutron absorption within the scintillator. Experimental verification of the simulations has been problematic because we have been unable to acquire large high-Z–doped plastic scintillator panels for testing. The limited experimental results we obtained from the Gd-doped liquid scintillator have been disappointing, and may signify that the energy resolution modeling of our simulations was inadequate.

BACKGROUND

Plastic scintillators are the detectors of choice for portal monitors, not because of any radiation physics advantage, but because plastic is cheaper, lighter, and easier to manufacture in large sizes. Polyvinyl toluene (PVT) is about three and a half times lighter than sodium iodide (NaI) and about an order of magnitude cheaper for large detectors. For screening trucks crossing a border, the weight and cost reduction of PVT compared to NaI is compelling; however, sensitivity and energy resolution are sacrificed. Plastics do not make good detectors for isotope identification. The gamma sensitivity of PVT is lower than NaI, and the energy resolution is worse. In fact, the energy resolution is so poor that PVT is used primarily for gross counting applications and not for spectroscopy.

Heavy metal–doped plastic scintillators are commercially available, and they are used primarily for x-ray detection. A few percent of lead (Pb) added to the PVT (e.g., 2% to 5% by weight of Pb for Saint Gobain's BC452) improves the radiative stopping power of the plastic without drastically reducing its transparency. The high-Z doping does not significantly change the density of the PVT, but the high Z of the dopant increases the radiative interaction of the bulk plastic. As a function of the atomic number, Z, the scattering/absorption cross section behaves as Z^4 (Evans 1955, Bethe 1957), so a small amount of

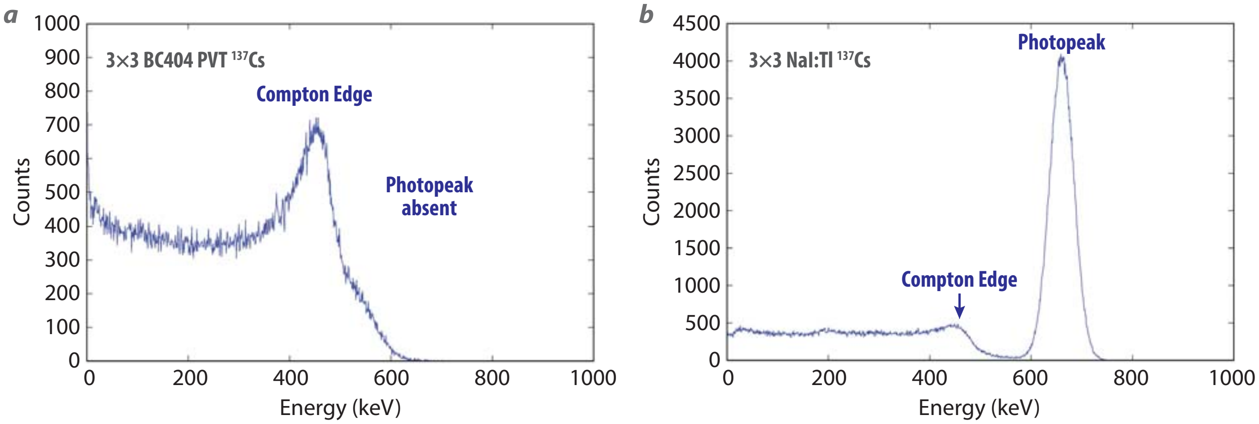

Figure 1. Geant4 simulations of gamma absorptions demonstrate the photopeak performance of PVT and NaI. (b) The spectrum produced by NaI has a photopeak, but (a) the spectrum from PVT does not.

a high-Z dopant can have a significant impact upon sensitivity. Improved gamma absorption moves the top energy of resolvable photopeaks to higher values. If Compton reconstruction is applied to the data, then that top energy value is nearly doubled. Thus, mapping of Compton counts into photopeaks can be achieved for relevant spectroscopic applications as long as the numbers are favorable.

A scintillator converts absorbed gamma rays into visible photons that are counted by a photomultiplier tube. Consequently, the number of photons generated by gamma absorption is proportional to the gamma's energy. The gamma-photon conversion for PVT is 10 photons per keV absorbed, whereas for NaI it is 38 photons per keV. The statistics of a gamma measurement generally follow a Poisson distribution; thus, by counting statistics alone, PVT should have an energy resolution of about a factor of 2 worse than NaI (i.e., $1/\sqrt{3.8}$). Other factors come into play for energy resolution, such as photomultiplier efficiency, detector geometry, scintillator transparency, electron noise, etc. If counting statistics alone were responsible for energy resolution, NaI would have a resolution of about 0.6% for the 662 keV gamma of ^{137}Cs. In reality, the energy resolution is an order of magnitude worse (~6% to 7%). Assuming no radical differences in the other energy resolution factors for PVT (similar transparency, geometry, phototubes, noise, etc.), the energy resolution of PVT could be expected to be on the order of 12% to 14%.

It is generally assumed that PVT has an energy resolution of about 20% at 662 keV; however, PVT detectors do not produce photopeaks at that energy. This is due to the low density and low Z of PVT. The stopping power for gamma rays in a detector is proportional to the density of electrons of the detector material, or, in other words, to the mass density, and, as mentioned earlier, there is a strong dependence upon the Z of the atomic constituents of the detector. Of the three major interaction mechanisms of gammas with matter (photoelectric effect, Compton scattering, and pair production), Compton scattering predominates for most relevant detection scenarios. Higher-density scintillators such as NaI can more readily fully absorb a gamma by means of several Compton scatters before the gamma exits the detector, and the full gamma absorption produces a distinct photopeak in a spectrum. With a lower-density detector such as PVT, a Compton gamma–scattered gamma has a greater chance of exiting the detector before subsequent scatters and full absorption. The partial energy left in the detector from the incomplete absorption contributes to the Compton continuum. Figure 1 shows simulated spectra from PVT and NaI of a ^{137}Cs source. The spectrum from NaI contains a photopeak, and that from PVT does not. Unless a PVT scintillator panel is very large and thick, it will not produce a 662 keV photopeak. Consequently, the determination of an energy resolution for PVT at 662 keV is problematic. It is still meaningful to have an energy resolution number for modeling the Compton continuum, but it is less straightforward to evaluate, and it relies on assumptions about the linearity of detector response.

PROJECT

The project compared Geant4 (Allison 2016) simulations of gamma and neutron absorption by PVT and NaI detectors. Because we had difficulty obtaining large PVT detectors, our experiments were conducted late in the fiscal year with a pair of gadolinium (Gd)-doped liquid scintillators. We simulated doping levels of various high-Z metals (Pb, Gd, bismuth [Bi]), detector size, and geometry. These simulations

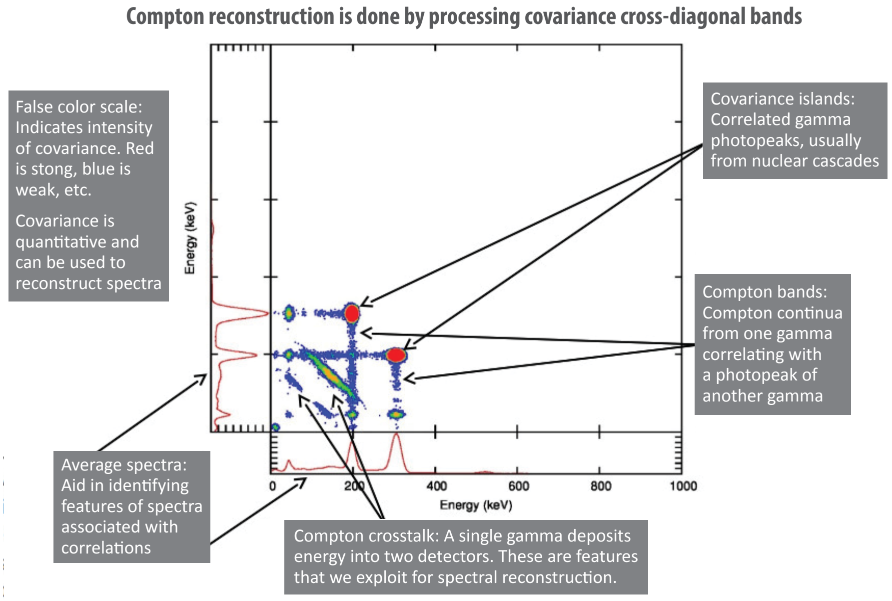
Compton reconstruction is done by processing covariance cross-diagonal bands

False color scale: Indicates intensity of covariance. Red is stong, blue is weak, etc.

Covariance is quantitative and can be used to reconstruct spectra

Covariance islands: Correlated gamma photopeaks, usually from nuclear cascades

Compton bands: Compton continua from one gamma correlating with a photopeak of another gamma

Average spectra: Aid in identifying features of spectra associated with correlations

Compton crosstalk: A single gamma deposits energy into two detectors. These are features that we exploit for spectral reconstruction.

Figure 2. This covariance map of data from a pair of NaI detectors measuring a ^{176}Lu has various correlation features labeled, including the Compton crosstalk (cross-diagonal) bands used to generate Compton-reconstructed spectra

produced list mode data from which we could generate average spectra as well as Compton-reconstructed spectra. An average spectrum is produced by binning the data as they are collected. Compton-reconstructed spectra are generated by summing the energies of time-correlated data from a pair of adjacent detectors. This concept is visualized in Figure 2, a covariance map of correlated data collected from two NaI detectors measuring a ^{176}Lu (lutetium) source (real data). The center panel of the figure is a false color map of covariance (or correlation) where red is high correlation and blue is lesser correlation, and green, yellow, and orange are degrees of correlation in between blue and red. Insignificant correlation is the background color (white). At the left and at the bottom of the center panel are average spectra for the data that aid in identifying the features within the covariance map. Various correlation features are labeled in the covariance map, but the features used for Compton reconstruction are the cross-diagonal bands, called Compton crosstalk bands because they represent interactions where a gamma is Compton scattered in one detector and the energy down-shifted gamma is completely absorbed by the other detector. The Compton crosstalk bands have axis intercepts at locations of photopeaks of the average spectra.

Geant4 simulations of high-Z–doped PVT confirmed that Compton reconstruction was not effective for small detectors. As mentioned, a low-density detector needs to be of a certain size to absorb a significant amount of energy from multiple Compton scatters. Because the Compton reconstruction method uses the covariance of signals from a pair of detectors, to be able to produce photopeak spectra there must be a significant probability of capturing the total gamma energy within those two detectors. Small detectors result in Compton scattering in both detectors without complete absorption, and those correlated signals remap Compton events into other Compton events. Simulations with 3″ cubic detector blocks, even with high-Z doping of the PVT, demonstrated that photopeaks were not significantly produced in the Compton reconstructed spectra. However simulations with 18″ × 18″ × 6″ PVT blocks did produce photopeaks with 2% Pb doping by weight. Figure 3 shows the effect of the Pb doping for large, 18″ × 18″ × 6″, PVT detector panels. In the Geant4 simulations the panels are sandwiched such that the source is located in front of one detector and the second detector is shielded by the first. This particular geometrical arrangement was chosen to optimize the interception of forward Compton scattered–gammas from the front detector into the second detector where the down-shifted gammas have a greater probability of being fully absorbed.

The simulations of gamma absorptions with different doping elements were all similar, and the effect was indifferent to the atomic and nuclear structures of the high-Z dopant. What was important was the density of electrons and the effective Z of the material. For gamma energies from about 100 keV to several MeV, atomic and nuclear resonances contributed little to the overall effect.

The prospect of detecting neutrons with a Gd-doped detector inspired us to propose this project. The idea of using induced gammas from neutron absorption by Gd was proposed by a colleague, Raymond Keegan, about a decade ago. But we would have to address the problem that Gd produces gammas over a large spectral spread from a few keV up to several MeV, and there was no good method proposed to distinguish a neutron-induced gamma from a background gamma. The idea emerged that correlated cascade gammas

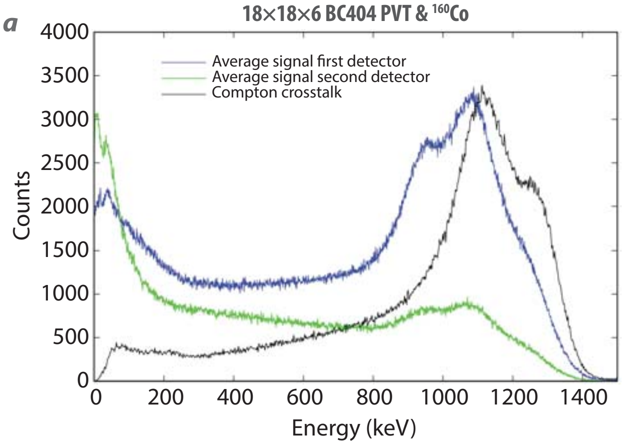

Figure 3. A small amount of high-Z metal doping allows a pair of large 18″ × 18″ × 6″ PVT detector panels to produce a Compton-reconstructed spectrum with resolvable photopeaks of the ^{60}Co doublet for (a) undoped and (b) Pb-doped PVT

from the neutron-Gd interaction could be separated from background by the covariance approach. The covariance maps from the Geant4 simulations shown in Figure 4 display correlations from gammas emitted by Gd upon neutron absorption. Figure 4a shows a map for 2.45 MeV neutrons (e.g., D-D STNG tube), and Figure 4b for thermal neutrons. The spectra at the bottom of the maps are average spectra from the front detector facing the neutron source; they show broad continua of gammas from low energy up to about 2.3 MeV. Such continua would be difficult to distinguish from normal background; however, the covariance bands in the maps would be distinct from background and could be used for neutron detection. As the neutron absorption cross section is greater at low energy, thermalizing the neutrons before entering the detectors would be important.

Experimental Results

The simulations looked very promising, but it was unclear if the Geant4 modeling captured all the relevant physics. Geant4 does not include the physics of conversion of Compton cascade electrons into scintillation photons, so the detector resolution modeling was crude and somewhat ad-hoc. Also,

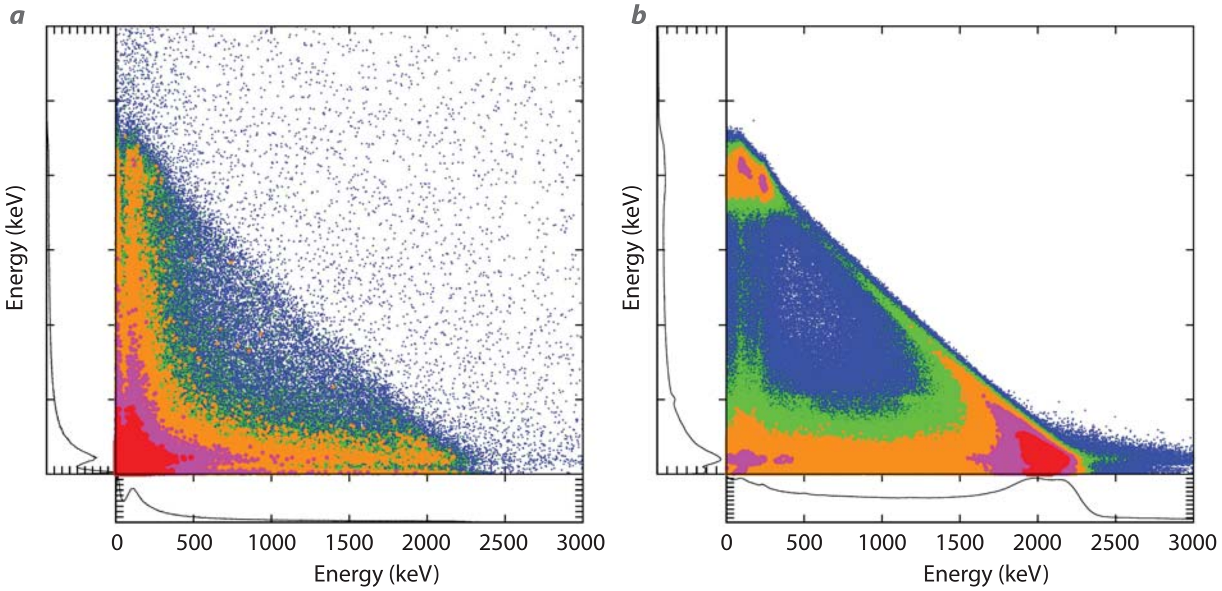

Figure 4. Covariance maps of neutron absorption by Gd doping of PVT show correlated gammas that can potentially be separated for background. (b) The effect is most dramatic when the neutrons are thermalized before reaching the detectors.

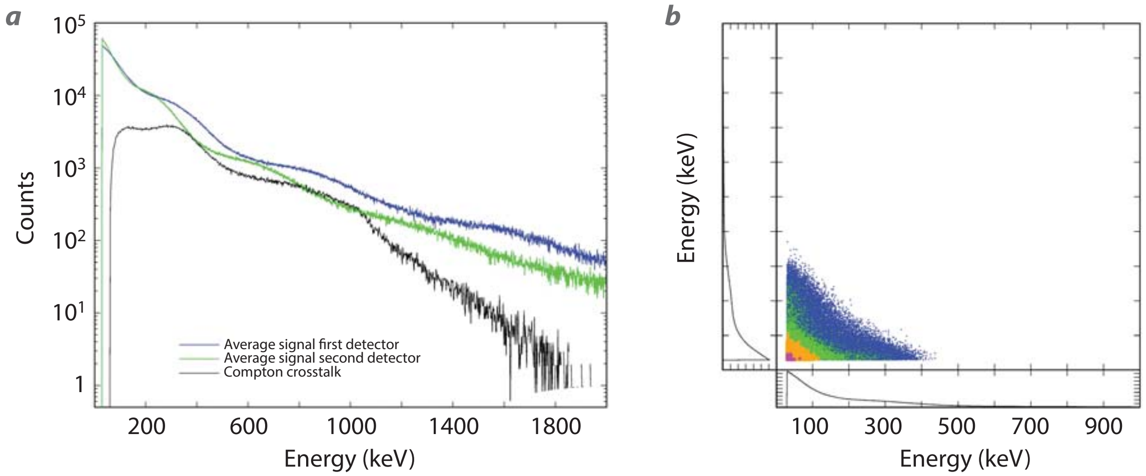

Figure 5. (a) Average and Compton-reconstructed spectra of a ^{137}Cs source measured by a pair of detectors containing Gd-doped EJ-331 liquid scintillator and (b) the covariance map of the same data; the data are largely featureless

it was unclear if the neutron libraries contained all the relevant gamma correlations for the neutron-Gd interaction.

We intended to devote half of the project to confirm the model results with experiments. In the first quarter of FY 2017, we approached both Saint-Gobain and Eljen about purchasing large panels of Pb- and Gd-doped PVT scintillators, but found that Pb-doped scintillators are special order items available only in smaller sizes. For example, at Saint-Gobain, the largest sample of BC452 available is 2″ × 2″ × 18″. Though we proposed a design and Saint-Gobain considered it (piecing together bars and attaching a light pipe at a cost-prohibitive sum of ~$50,000), ultimately we did not procure a large detector from them. At Eljen the situation was similar; their largest block of EJ-256 was 4″ × 4″ × 4″, and we were advised against combining these panels. Eljen suggested the liquid scintillator EJ-331 as an alternative. In the second quarter of FY 2017, we procured 75 liters of EJ-331 Gd-doped liquid scintillator and two large tanks for assembling a pair of detectors, which we received in late August; therefore, the results presented here are preliminary.

Figure 5 shows results from a pair of detectors containing Gd-doped EJ-331 liquid scintillator. Figure 5a contains average spectra along with the Compton-reconstructed spectrum for a ^{137}Cs source, and Figure 5b is a covariance map of the same data. These results are disappointing, as there are no correlation features beyond very low energy correlations commonly found

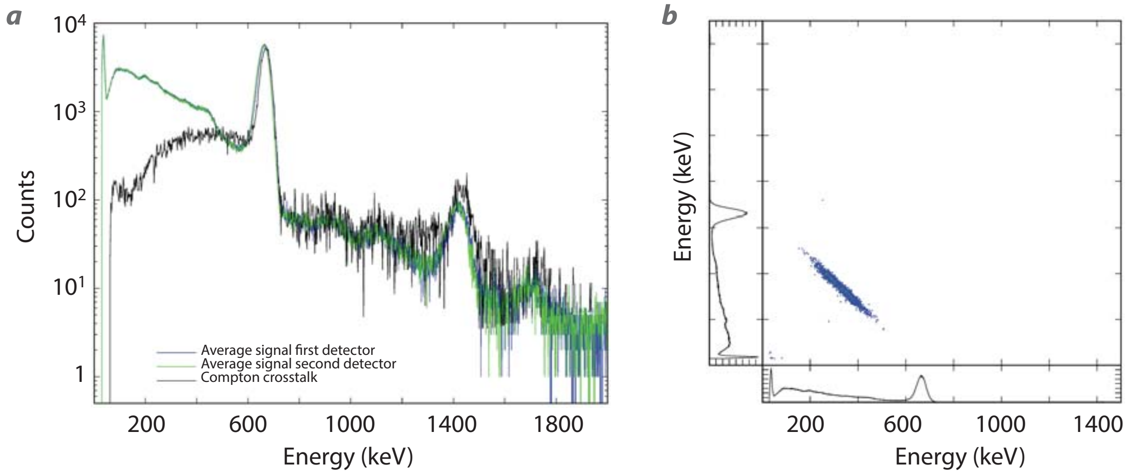

Figure 6. Properly calibrated detectors produce (a) a Compton-reconstructed spectrum with photopeaks located at the correct energies and widths the same as in average spectra and (b) a covariance map with a 90° cross-diagonal Compton crosstalk band with axes intercepts at the correct gamma energies

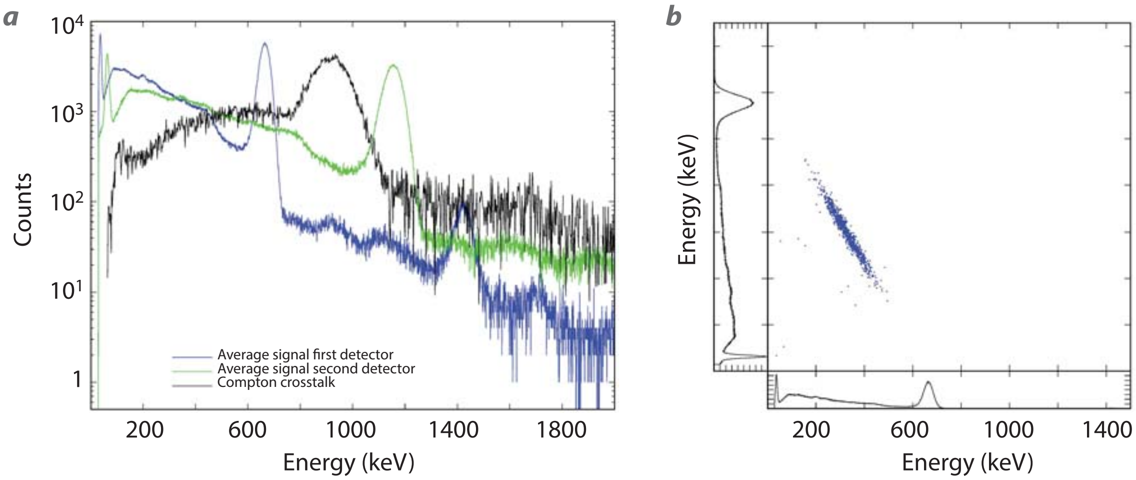

Figure 7. A mistuned energy calibration produces (a) a Compton reconstructed peak at the wrong energy and (b) a Compton crosstalk band that is not at 90° to the main diagonal of the covariance map

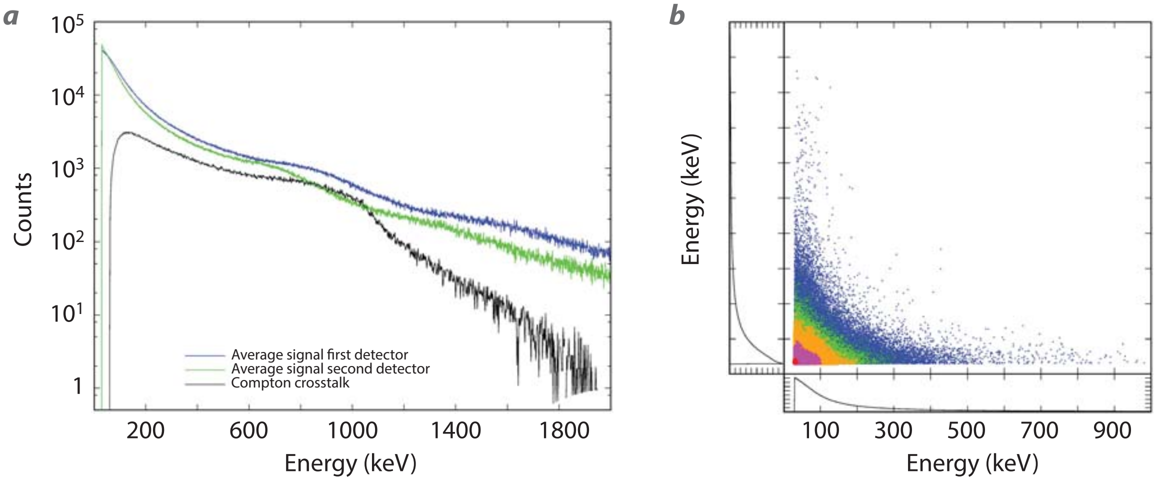

Figure 8. (a) ^{252}Cf neutron-induced signals from Gd-doped EJ-331 liquid scintillator (b) do not show the expected covariance features. The energy calibration of these plots is a best guess, and the detector biases were probably too high for the measurement.

in background spectra. Because there is neither a photopeak nor a Compton edge in the data to use for calibration, the energy scale in the plots is a best-guess calibration.

Two problems became immediately apparent when working with EJ-331 in large tanks. Detector dead time from background, which introduces a negative correlation into the data, was very significant (~10%), and this, in turn, caused issues with the covariance method. The other problem was the lack of energy calibration of the two detectors. The usual application of the covariance method requires the same calibration for both detectors. The method can be applied for different calibrations, but the calibrations must be known. Because EJ-331 performs worse than bare PVT, there were absolutely no features to indicate the energy calibration for any of the phototube biases we attempted. Figure 6 shows how a properly calibrated pair of detectors should appear for ^{137}Cs measured by NaI, and Figure 7 shows what happens when the detectors are improperly calibrated. These spectra are real data produced by a pair of 3″ × 3″ NaI detectors and a ^{137}Cs source. In the covariance map in Figure 6b, the crosstalk band is a 90° cross-diagonal band with respect to the main diagonal, and it intercepts the axes at the photopeak energy. The spectral plot (Figure 6a) shows the Compton reconstructed spectrum, which has the photopeak at the correct energy and a width that is identical to the average spectra.

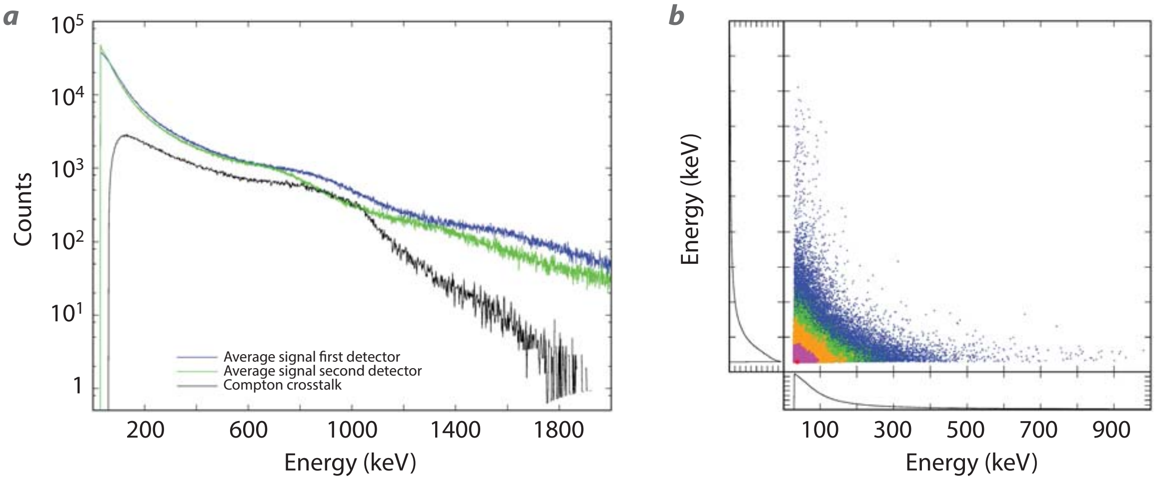

Figure 9. A thermalizing barrier of 4 inches of high-density polyethylene (HDPE) does not affect the spectra of neutron-induced gammas from Gd-doped EJ-331 liquid scintillator exposed to a ^{252}Cf source

In Figure 7, the energy calibration was intentionally mistuned to demonstrate what occurs in a Compton-reconstructed spectrum. In the spectral plot in Figure 7a, the average spectrum of one detector has the photopeak at the correct energy of 662 keV, but the other detector has its photopeak at 1150 keV. The Compton reconstruction placed the photopeak somewhere in between those two energies, and the width of the reconstructed photopeak is much larger than the widths of average spectra. The covariance map (Figure 7b) shows that the Compton crosstalk band is not at 90° to the main diagonal of the map.

The mistuned energy calibration of Figure 7 demonstrates the problem of calibration, and since the average spectra have clearly defined photopeaks, it is easy to determine the necessary calibration adjustment (or detector gains) to produce correct Compton-reconstructed spectra. When the data are as featureless as those shown in Figure 5, however, it is not obvious how to calibrate the detectors. During the brief time we exercised our detectors, we did not find an appropriate way to calibrate them.

Although the detectors were uncalibrated, we decided, nevertheless, to look for neutron-induced gamma correlations. The liquid scintillator EJ-331 contains Gd at 1.5% by weight. This Gd concentration was not as high as desired, nor is the density of EJ-331 as high as PVT, so the results would not be as good as the original modeling. Yet the modeling suggested that we should see something. Data collected from a ^{252}Cf source, shown in Figure 8, indicate that the expected covariance features are not present, or are, at least, not obvious.

The simulations indicated that thermalizing the neutrons would produce better results, so we collected data with 4″ of high-density polyethylene (HDPE) to moderate the neutrons and 2″ of lead to block the gammas from the ^{252}Cf. The moderator was placed between the source and the detectors. The results, shown in Figure 9, are nearly identical to the data plotted in Figure 8.

The experimental configuration was not exactly what we wanted, and all of the experimental results were disappointing. The liquid EJ-331 is a lower-density material than PVT; the Gd doping was less than desired; the air-liquid interface inside the detectors reduced photon yield somewhat, degrading the energy resolution; and the phototubes had not been previously tested to confirm correct performance. Most significantly, the poor performance of the experiment very likely points to an inadequacy of our modeling of the detector energy resolution. This could be an insurmountable barrier for applying the Compton reconstruction technique to plastic scintillators. The details are particularly important here, and the intrinsic energy resolution of the scintillator can make or break the technique.

A recent development of great interest is that doping levels of 15% by weight of Bi in PVT and energy resolutions of 11% have been achieved at Lawrence Livermore National Laboratory (Cherepy 2017). Bismuth is an interesting dopant because it is the heaviest element without any radioactive isotopes. The chemistry for dissolving Bi in PVT is relatively straightforward, and it makes a reasonably transparent plastic. If large detector panels can be made of Bi-loaded PVT, then Compton reconstruction could be a valuable technique for spectroscopic applications.

CONCLUSION

Using Geant4 we modeled Compton reconstruction of correlated signals from pairs of scintillators. The results indicated that greatly improved sensitivity and energy resolution were possible for PVT plastic scintillators, provided that they contain a few percent of a high-Z dopant and that the covariance Compton reconstruction method be implemented on the data stream. Although lead-doped PVT is a catalog item at both Saint-Gobain and Eljen, we were unable to acquire scintillator panels large enough to collect laboratory data to compare to the simulated results. Late in the project we acquired large detectors with a Gd-doped liquid scintillator, but issues with energy calibration and detector dead time marred the results. Also, the experimental results from the liquid scintillator may indicate that we had not properly modeled detector resolution in our simulations.

ACKNOWLEDGMENTS

We would like to thank Ray Keegan for initially suggesting that detecting neutron-induced gammas from gadolinium could be a viable neutron detection mechanism. We would also like to thank Nerine Cherepy and Steve Payne for several discussions about high-Z doping of PVT.

REFERENCES

Allison, J., et al., “Recent developments in Geant4,” *Nucl. Instrum. Methods Phys. Res. A* **835** (2016) 186–225.

Bethe, H. A., E. E. Salpeter, *Quantum Mechanics of One- and Two-Electron Atoms*, Plenum Publishing Corporation, New York, 1957, 313.

Cherepy, N. J., R. D. Sanner, P. R. Beck, E. L. Swanberg, T. M. Tillotson, S. A. Payne, C. R. Hurlbut, “Bismuth- and lithium-loaded plastic scintillators for gamma and neutron detection,” *Nucl. Instrum. Methods Phys. Res. A* **778** (2015) 126–132.

Evans, R. D., *The Atomic Nucleus*, McGraw-Hill Book Company, New York, 1955, 698.

Enhancements to Rad/Nuke Search Algorithms

RSLA-004-17 ■ Year 1 of 1

Michael Hornish,[1,a] Thomas McCullough,[a] and Sarah Bender[a]

[1]hornismj@nv.doe.gov, (301) 817-3347
[a]Remote Sensing Laboratory–Andrews

The search for anomalous radiation signatures, especially from illicit special nuclear material, is of extreme importance in national security and global safeguards. In this project, we investigated new ways to improve the radiological/nuclear (RN) detection performance (gamma ray and neutron) in deployed emergency response equipment. The objective was met via more efficient and effective use of advanced algorithms, including spectral anomaly detection schemes that are designed to exploit modern-day enhancements to sensors, data quality, and computing resources. These efforts have resulted in enhanced performance, such as longer detection distances and more reliable alarm triggers. The new methods we developed are now implemented in tool suites used for rapid post-processing of RN search data.

BACKGROUND

During radiological/nuclear (RN) search operations (e.g., as part of security support to a special event or as part of a targeted, intelligence-driven search), the ability to detect threat sources—especially challenging configurations involving special nuclear material (SNM)—is somewhat limited by gamma ray and neutron alarm algorithms that are outdated, ineffective, or not sufficiently optimized in terms of sensitivity. Improvements in threat detection are absolutely necessary for effective protection of national security interests and more efficiently meeting mission-specific requirements of emergency response assets, such as the Nuclear/Radiological Advisory Team (NRAT) and the Radiological Assistance Program (RAP).[2] Moreover, implementing these enhancements in operational tools that take full advantage of all resources available today (computing resources, detection equipment, sophisticated algorithms) will make impactful gains in threat detection possible; these tools can also be implemented in the relatively short period.

Traditional gross count alarm triggers have been used for decades in detection equipment used during search operations, and while they can be effective in some applications, they are inherently plagued by

---

[2] NRAT and RAP are managed by NNSA NA-84 Office of Nuclear Incident Response. NRAT is operated out of the Remote Sensing Laboratories at Andrews and Nellis Air Force bases.

uncertainties in local gamma ray naturally occurring radioactive material (NORM); furthermore neutron (cosmic) backgrounds vary substantially from place to place and in time. Therefore, responders must choose between high sensitivity and high false (or nuisance) alarm rates that come from low alarm thresholds, or low sensitivity and low false alarm rates that arise from high alarm thresholds. Because responders often use aging detection equipment, gross count alarms were the only reasonable option.

As technology advances, and computing resources have become miniaturized and faster, detection equipment nowadays provides gamma ray spectral data (typically 0–3 MeV full scale at 1 Hz) that contain a wealth of gamma ray information beyond count rates, even though it is typically from low-resolution scintillator materials like thallium-doped sodium iodide (NaI:Tl) crystals. Algorithms that are designed to search for changes from typical NORM spectral features (photopeaks, continua, low-energy phenomena that alter the shape or features of spectra) are commonly referred to as spectral anomaly detection algorithms (SADA). Many studies over the years have successfully demonstrated that significant improvements in likelihood of threat detection of RN materials or devices of concern can be realized by enhancing and operationally implementing newer, more powerful algorithms that take more effective advantage of available information and deployed resources (Hornish 2016). These advancements allow more rapid anomaly characterization, threat detection, and increased efficiency in rejecting nuisance alarms.

DOE search teams such as NRAT and RAP currently solely use the SADA nuisance-rejection spectral comparison ratios for gamma ray anomaly detection (NSCRAD). The algorithm was developed by Pacific Northwest National Laboratory (Pfund 2007, 2010) to distinguish low-count sources of interest from benign naturally occurring radiation and irrelevant nuisance sources. It uses a number of broad, overlapping energy regions of interest to statistically compare each newly measured spectrum with the current estimate for the background to identify anomalies. NSCRAD augments traditional and simplistic gross count alarm algorithms and has been implemented in the operational platform utilized by NA-84 search assets, namely the Advanced Visualization and Integration of Data (AVID) program developed at the Remote Sensing Laboratory (RSL).

While NSCRAD has proven to be a valuable tool with significantly improved sensitivity to gross count alarms, its current implementation in AVID is by design simplistic and does have inadequacies (e.g., it provides a single figure of merit with no supporting information to point an end user to the underlying spectral cause of an anomaly; it is relatively insensitive to certain spectral energies of interest). In addition, other SADAs are complementary to NSCRAD and superior in terms of performance and detection range. These other algorithms are generally more complex and sophisticated but are not readily available in AVID, thereby constraining the capabilities of the search teams sent out to find the most challenging of source configurations.

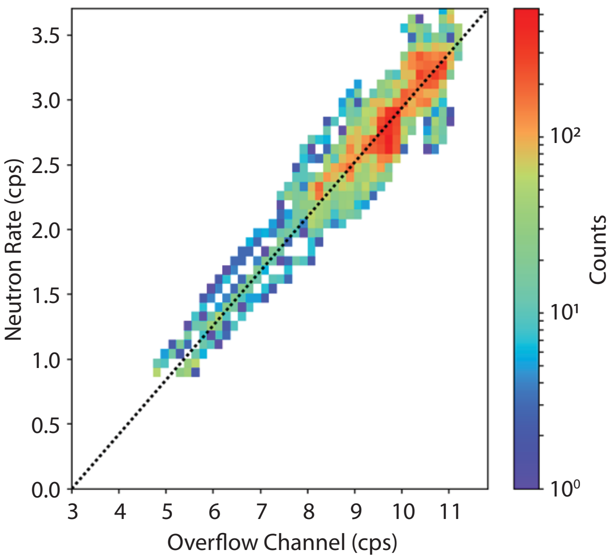

Figure 1. Linear relationship between count rates of NaI:Tl scintillator systems above 3 MeV on the horizontal axes and the ^{3}He neutron arrays on the vertical axes. The example shown is for a vehicle-mounted system driven in an urban environment.

A prime example of a very powerful SADA is the wavelet-assisted variance reduction anomaly detection (WAVRAD) algorithm (McCullough 2012), whose design premises are that detection of radiological anomalies is a much easier problem to solve than their identification, and that the two need not (and in most cases should not) be intrinsically linked. WAVRAD provides a general algorithmic approach for real-time anomaly detection that is resistant to common detector imperfections (e.g., poor calibration or resolution, thermal drift), avoiding the limitations of any source or template library, and providing immediate, easily interpreted, actionable user feedback. The algorithm uses continuous wavelet transform for variance reduction, forms an expectation from recent measurements, and evaluates the deviation between the current measurement and the expectation using methods from linear algebra. The generality and simplicity of these concepts yield an algorithm that is flexible, easily applied, not overly computationally demanding, and effective. Much of our effort to enhance gamma ray anomaly detection focused on more comprehensive and robust application of the WAVRAD algorithm for improved performance.

At the same time, a parallel independent effort was undertaken to study and improve neutron anomaly detection. We explored exploitation of the overflow channel of NaI:Tl-based detectors used in mobile, man-portable systems to predict the corresponding neutron count rate in ^{3}He detectors. This overflow channel captures events that have energies higher than approximately 3 MeV gamma ray equivalent energies. In the absence of a strong or nearby neutron point source, which can contribute neutron-induced high-energy gamma rays through capture and scatter processes, the dominant feature in this >3 MeV energy range is the signature associated with cosmic-ray muons traversing through the detector crystal. These muons are created in the upper atmosphere when the primary cosmic-ray flux of hadrons impinges the upper atmosphere to create pions that rapidly decay into muons. Muons have extremely high energies in these contexts, which leads to minimum ionization in the scintillator material and a detectable signature well above 3 MeV for the detector volumes in the mobile or backpack systems in use. The multichannel analyzers embedded in the detection systems used by emergency response assets will count events in that energy range in the overflow channel.

Meanwhile, the background neutrons that are, in general, detected in the ^{3}He detectors are dominated by secondary and tertiary cosmic-ray neutrons and their corresponding interactions in matter that can result in additional neutrons through spallation and (n,2n) reactions. Because cosmic-ray muons and cosmogenic neutrons are inherently related in origin, the amount of muons detected is generally linearly related to the amount of cosmogenic neutrons detected for the count rates encountered on the earth's surface (Figure 1).

This relationship is an important factor because neutrons originating from a man-made neutron point source, as from ^{252}Cf, alpha-n sources (say Am-Be) or SNM, are likely only readily detected at standoff distances in the ^{3}He neutron detectors rather than the gamma ray detectors where secondary effects involving neutron activation or capture events contribute low-probability gamma ray signatures. As a result, an algorithm that monitors the relative recent historical rates of overflow channel counts (i.e., muons) and neutron counts in ^{3}He detectors in a given area or environment can be used to establish a prediction of expected neutron counts. Therefore, a neutron anomaly (i.e., a man-made neutron source) will manifest itself as an excess of counts in the ^{3}He detector arrays above the rates predicted by trends in the muon flux as measured with the gamma ray detectors. The advanced neutron algorithm employed here enables much more effective neutron search operations that adjust to the local environment, whereas current approaches of static background thresholds inevitably suffer from false positives or negatives, depending on when the background threshold is established.

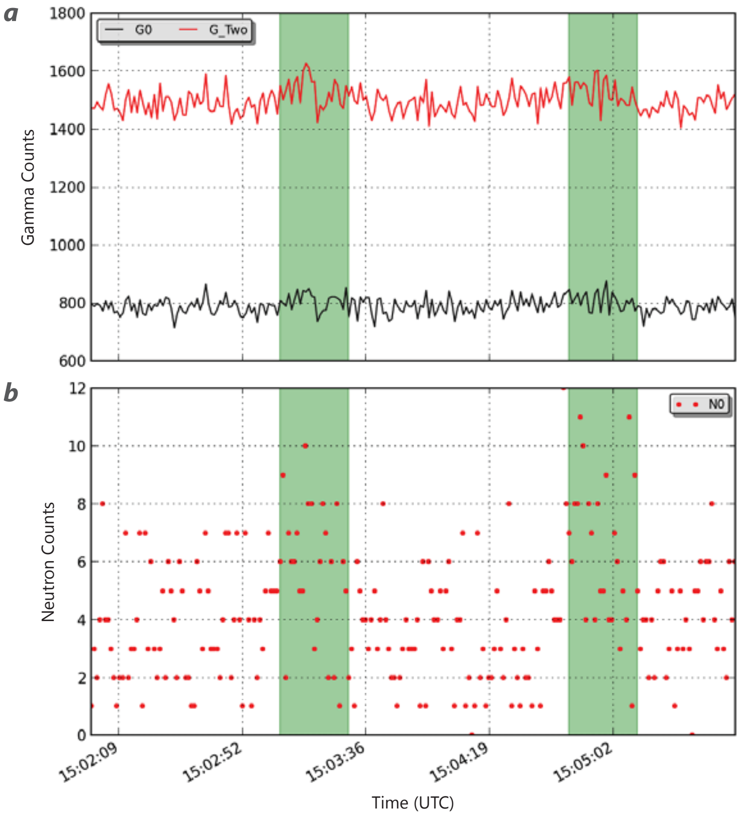

Figure 2. Vehicle-mounted mobile system drive-by of a weak, shielded source with subtle (a) gamma ray and (b) neutron signatures. Green-shaded areas show data points when the system was in source range; the unshaded areas are background only. The gamma ray plot shows the response of a single detector log (G0) and the summation of two logs (G_Two).

PROJECT

We decided to pursue two anomaly detection approaches: (1) more powerful applications of WAVRAD and (2) a broader use of a new dynamic neutron alarm threshold via exploitation of the relationship of cosmic muon data (collected in gamma ray scintillators) with neutron data collected with collocated ^{3}He tube arrays. Our main focus was to leverage previous work to develop advanced application of these algorithms, largely by applying the algorithms over a wide array of sample times. This nuance enables greater sensitivity to longer-lived anomalies that may be due to a very slow approach of a nearby source or a passby of a source at large standoff distance, which are the very kinds of problems that typically escape detection through current methodologies that focus on very small integration times and are sensitive to only rapid, short-duration encounters. This approach of concurrently monitoring short, medium, and long integration times enables effective detection of short-lived and long-lived anomalies.

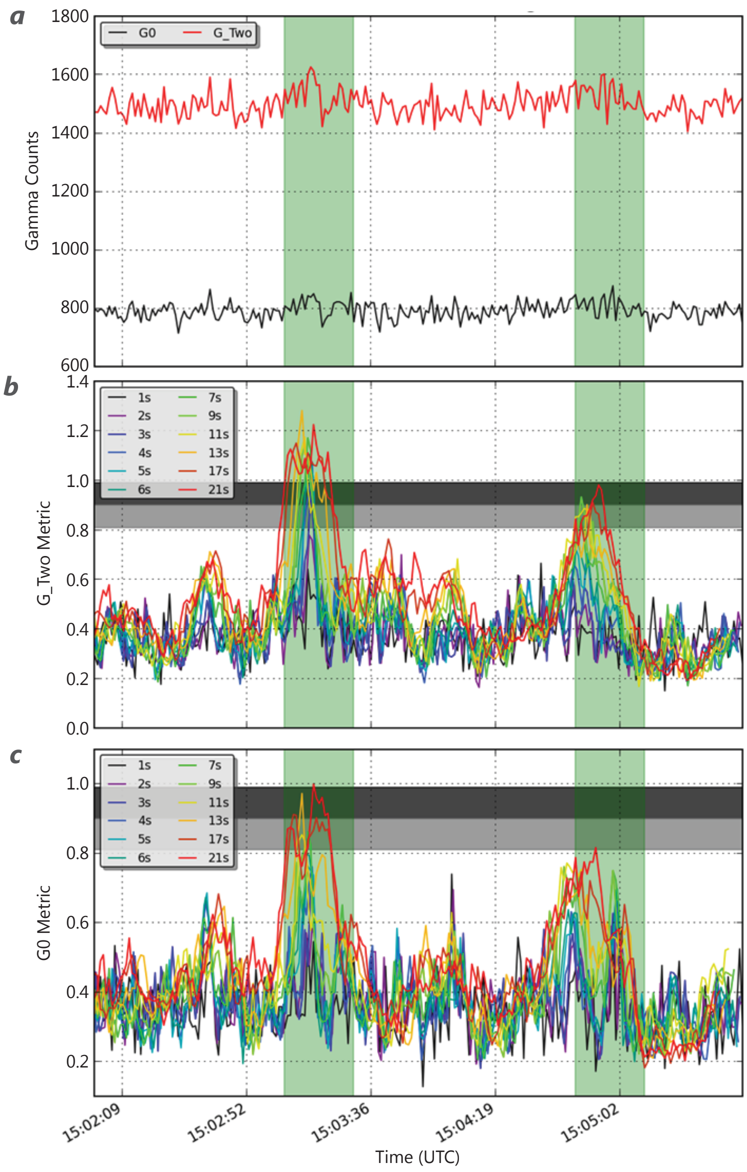

Figure 3. (a) Gamma ray time series data for the source drive-by for one (G0) and two (G_Two) detector logs and (b and c) the WAVRAD figure of merit applied over different sample times shown in the plot legends. The gray bars indicate a typical alarm threshold of 0.9 for the WAVRAD alarm metric (with 10% above and below, indicating the typical tolerance for that threshold).

The ability to simultaneously run multiple algorithms applied against a wider range of integration times for 1 Hz data on faster processors with efficient algorithms was studied in depth. To test the approach, we analyzed a large dataset from vehicle-mounted mobile and backpack systems. An example of that data is provided in Figure 2, which was collected with a commercial vehicle-mounted mobile detection system containing two 1-liter logs of NaI:Tl scintillator for gamma ray detection and two arrays of slightly moderated ^{3}He tubes for neutron detection. In this particular example, the mobile system is driven by a gamma-neutron source at standoff distance, and the count rates of the gamma and neutron detectors are shown as a function of UTC timestamp. The times at which the source is encountered by the detector are highlighted in green, a 25-second window for this example. The background count rates measured outside of the green windows of the source encounter are typical, and they highlight the difference between gamma ray count rates (hundreds or thousands of counts per second on average) and neutron count rates (less than 20 cps) for detectors of this size. It is important to note that the signal strength from this particular standoff distance and source configuration highlight the futility of gross count and NSCRAD alarming (that only look at very small sample times), which never come close to alarming.

The result of applying the WAVRAD algorithm to this dataset for a number of different sample times is shown in Figure 3. The first detector had a stronger signal than the second; this was caused by the statistical fluctuations of the two encounters. However, both encounters registered WAVRAD metrics that approach or exceed a typical alarm threshold (normalized to generate around one false alarm per hour). Of particular importance for the summation of the two detector logs (middle plot), is that short samples of one or two seconds never reach the alarm threshold, whereas the longer sample times do for at least the first encounter and, in most cases, the second encounter.

If we apply the same techniques to neutron time series data using the neutron cosmic correlation approach, we see similar results, as shown in Figure 4. As in the gamma data, this example is one in which the traditional approaches used by DOE search teams (gross count alarming with short sample times) never approach an alarm threshold typically employed during search operations. The use of cosmic correlation of muons and cosmogenic muons and longer time windows significantly increases the likelihood of detection. In this case, the short sample times of a few seconds are not very sensitive, but the intermediate sample times (5–30 seconds) are very sensitive, and the long sample times (>30 seconds) are still fairly effective.

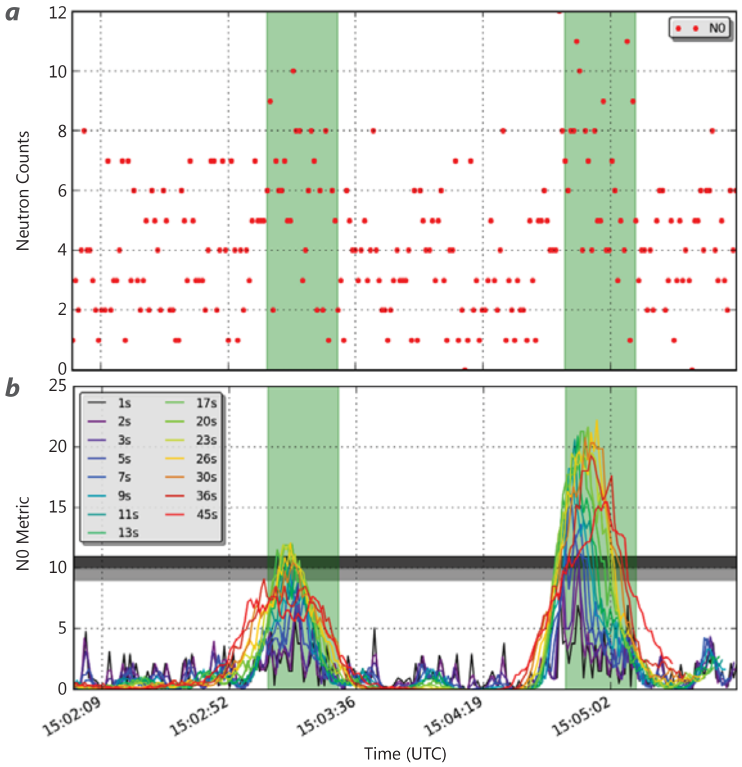

Figure 4. (a) Neutron time series data for the source drive-by and (b) neutron anomaly figure of merit applied over different sample times shown in the plot legend. The gray bars indicate a typical alarm threshold of 10 for the neutron cosmic correlation metric (with 10% above and below, indicating the typical tolerance for that threshold).

While this example is only one demonstration of the sensitivity enhancements achieved by use of sophisticated anomaly detection algorithms applied over multiple sample times, it illustrates trends we noted across the large numbers of datasets we analyzed in which backpack and vehicle-mounted systems were exposed to target sources at distance with diminishing signals. For the gamma ray datasets, we observed an increase on the order of 20% to 50%. In some cases a greater increase occurred in detection distance over the current operationally implemented algorithm (NSCRAD) when using this applying the WAVRAD algorithm over multiple time windows. The exact improvements vary depending on target isotope (and associated energy signatures) and background environment. For the examples involving encounters with neutron sources, we similarly observed improvements in detection distance from 20% to 75% and greater increase for all cases but the short-duration encounters.

Furthermore, the results of this work were accomplished with a series of Python scripts that are designed to efficiently execute these calculations and can be easily run on a number of computing platforms. The resources in computing time and capacity needed to execute these calculations are miniscule, and the calculations can be processed on large sets of data quickly, which make them much more useful for potential end users and eventual integration into real-time data analysis tools. We provided this tool kit to a number of potential end users for them to become familiar with the capability that likely will eventually be standard operating procedures.

CONCLUSION

During this project, we explored advanced applications of sophisticated anomaly detection algorithms and achieved marked improvements in detecting anomalies. The use of multiple, concurrent sample times significantly increases the likelihood of detection for sources that evade detection by traditional alarm algorithms. Improvements from 20% to 50% or higher (up to 75%) of detection distance for gamma ray (neutron) source encounters occurred. We developed a set of tools that, in their current form, can provide impactful gains for post-processing anomaly detection, and with additional future work can be integrated as real-time tools. The ability to detect anomalies with greater sensitivity and to distribute these tools to users conducting search operations are important contributions to the national security preparedness of our country in the protection against radiological or nuclear terrorism.

Acknowledgments

We would like to thank Claude Concolato and Eric Moore for their contributions to this work.

References

Hornish, M. J., et al., “Evaluation of spectral anomaly detection algorithms for radiological/nuclear search,” DOE/NV/25946--2782, National Security Technologies, LLC, Las Vegas, Nevada, April 2016.

McCullough, T. L., M. R. Kiser, M. S. L. K. McLean, “Wavelet assisted variance reduction anomaly detection (WAVRAD),” Internal paper, National Security Technologies, LLC, Las Vegas, Nevada, 2012.

Pfund, D. M., R. C. Runkle, K. K. Anderson, K. R. Jarman, “Examination of count-starved gamma spectra using the method of spectral comparison ratios,” *IEEE Trans. Nucl. Sci.* **54**, 4 (2007) 1232–1238.

Pfund, D. M., K. R. Jarman, B. D. Milbrath, S. D. Kiff, D. E. Sidor, “Low count anomaly detection at large standoff distances,” *IEEE Trans. Nucl. Sci.* **57**, 1 (2010) 309–316.

Dynamic Test Prediction and Characterization through Modeling-Informed, Multi-Source Data Fusion

NLV-006-17 ■ Continuing in FY 2018 ■ Year 1 of 3

Aaron Luttman,[1,a] Jared Catenacci,[a] Kevin Joyce,[a]
Joe Paulson,[b] Collin Montenegro,[a] and Doug L. Trone[a]

[1]luttmaab@nv.doe.gov, (702) 295-0303
[a]North Las Vegas
[b]Montana State University

Multi-intelligence (MINT) analysis is the science of fusing multiple data modalities for the purpose of event or threat detection. MINT has been used in the intelligence community for over a decade, and it is now becoming an important component of the NNSA's nuclear nonproliferation activities and facility threat assessments. In this project, we are designing a MINT approach to detect and characterize experimental activities at the NNSS, using data from the information technology infrastructure, power grid, and standing seismic array. In FY 2018 we will add data from a new multi-modal sensor, called Canary (Kornell 2017, Miller 2018). By fusing these different data streams to analyze NNSS activities, we are characterizing the timelines, types, and scales of experiments at the different NNSS locations. This will add a new component to NNSS threat assessments and provide the NNSA with methods that can be applied at other facilities across the complex and more broadly in the Defense Nuclear Nonproliferation mission to characterize activities at foreign sites.

BACKGROUND

Multi-source data analysis has become a standard approach in situational awareness and real-time defense applications. In multi-source or multi-intelligence (MINT) analysis, when various forms of data are merged, they provide more information than the data sources independently. Across the DOE, MINT is becoming a core component in threat analysis to reveal vulnerabilities present in seemingly innocuous data. In particular, there is an interest in understanding what experimental activities at the NNSS can be detected and to what extent they can be characterized.

Multi-source data analysis has a broad range of challenges, including identifying features, understanding the importance and contribution of each data type, determining how to combine features from different data streams, assessing and quantifying the uncertainties and errors associated with each data stream, dealing with missing data, and communicating the results of the analysis with appropriate confidence levels to the end users and decision makers (Simonson 2016). In order to address these issues, we are implementing a multi-resolution approach to identifying and characterizing activities at the NNSS, where the different levels of resolution correspond to different levels of detail in the analysis. At the coarsest level of resolution, we identify activities at the NNSS, which is to say that we answer the questions of whether something occurred at the NNSS and where. For surface explosions, such as the Source Physics Experiment (SPE) series, this is straightforward, but we have also demonstrated that we can identify experiment activity by using patterns of life analysis for other facilities. We intend to resolve the analysis even further, for example, by characterizing a U1a experiment as integral or focused. In order to perform experimental characterization at this level, blackbox features are insufficient; therefore, we will rely on the physics-based records, such as seismic and infrasound data, and in FY 2018 data provided by the recently developed Canary sensor (Kornell 2017, Miller 2018). These methods will capitalize on physics-informed features, such as the relative timing of signatures.

PROJECT

This year we established access to seismic and infrasound data (both the standing array archived with the University of Nevada, Reno [UNR] and the array fielded by the NNSS), domain name server (DNS) and firewall activity logs, and power grid data. The DNS and firewall logs, shared with us by NNSS's cyber security, consist of hourly counts associated with individual facilities. NNSS Operations and Infrastructure (O&I) collects the power grid data by facility from local meters, which provide energy usage in 15-minute intervals. The Integrated Project Team includes members of cyber security and O&I, giving the project seamless access to continuous data. This year we identified various data sources, obtained data, and developed methods for analyzing each of the streams individually. We have had noteworthy successes with newly developed methods for estimating location and yield of surface explosions through near-field, openly available seismic data; identifying dates of insertion and explosion of subcritical experiments (SCEs) at U1a; and correlating network usage periods of high and low activity to experimental campaigns with the dense plasma focus (DPF) activities at Area 11. Each of these new methods allows us to better understand how an adversary could predict and characterize experiments at the NNSS, and each of the methods is detailed below.

Assessing and Characterizing SPE from Seismic Data

Six SPEs were executed in Area 15 over the past few years. During an SPE, chemical explosives are detonated underground, and the data are used to calibrate and improve detection and characterization methods of subsurface explosions (Snelson 2013). Our goal was to discover the day and approximate time of SPEs 4Prime, 5, and 6—without any explicit knowledge about when the experiments occurred—through interpreting seismic signals. In order to remain in a semi-blind setting, the analysts were given data in one-month periods to analyze, but were not told if these periods actually corresponded to the occurrence of an SPE.

We considered data collected from 44 seismic stations located across southern and central Nevada and 3 stations in southern California. Each of these stations include three seismometers that measure ground velocity. One of the three sensors measures vertical motion, and the other two measure lateral motion in orthogonal directions. The data are transmitted automatically and stored in a repository at UNR, and we downloaded these files to our local machines.

In order to "telescope in" on events of interest, we first reduced the resolution of the data, forming a single dataset that was an amalgamation of each of the sensors. For each sensor, we computed the maximum of the absolute velocity over non-overlapping 15-minute intervals throughout the month-long period. Then these values were normalized so that the largest maximum that occurred during the month was equal to unity. This step accounted for different sensitivities across various sensors. Finally, the reduced data, containing only the maxima over the 15-minute periods, were averaged together for all available sensors, resulting in a single dataset. From this single dataset, outliers were identified. Note that because the reduced data from each sensor falls between 0 and 1, the maximum possible value in the single dataset is 1 and the minimum possible value is 0. A value closer to 1 indicates that a large ground velocity was measured on a large percentage of the sensors over the 15-minute period. Detecting outliers in this way allows us to quickly incorporate all of the available data to determine 15-minute periods of interest to inspect more carefully. Figure 1 is an example image of the reduced data from May 2015. The four largest values are circled in the figure; notice that the two largest values were generated by minor earthquakes in Nevada.

After outlier intervals were identified, the next step was to progress through the time periods (15-minute windows) and estimate the epicenter for the event or events that resulted in the high-intensity signals. Typically, epicenter location methods rely on determining the separation of the primary (P-wave) and secondary (S-wave) waves (Spence 1989). From the separation time of the two waves, the distance between the sensor and the epicenter can be estimated by comparing to either reference output from ground motion geophysics models or reference tables derived empirically (Jeffreys 1959, Bolt 1960). With the distance between the sensor and epicenter known for three or more sensors, multilateration (Norrdine 2012) can be used to estimate the epicenter. However, all of the seismic detectors we have access to are within the local region of the NNSS (less than 200 km). Due to the close proximity of the sensors to the events of interest, the P- and S-waves do not have enough time to fully separate, so we cannot reliably use standard methods to estimate the epicenter. Rather, we exploit the fact that the seismic waves do not travel a long distance before reaching the sensors by assuming that the wave speed is constant over this range. This allows us to make use of a simple linear model to estimate the source location. This was accomplished by maximizing the correlation of the arrival time of the seismic wave for each sensor with the (unknown) distance between the sensor and the epicenter. That is, we solve

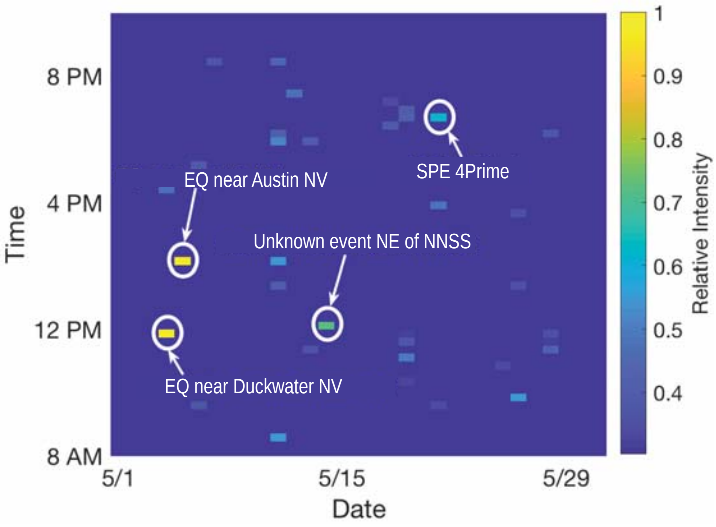

Figure 1. The seismic data are reduced from a collection of many sensors to a single data product, showing relative seismic intensity as a function of time. Two earthquakes and SPE 4Prime are correctly detected, and another seismic event of unknown origin is detected northeast of the NNSS.

$$\tilde{x} = \underset{x}{\operatorname{argmax}}\, \rho(\mathbf{t}, d(x,\mathbf{y})), \tag{1}$$

where $\mathbf{t}$ is an $n \times 1$ vector of arrival times for each of the n sensors, $\mathbf{y}$ is an $n \times 2$ vector of GPS coordinates for each of the n sensors, $d(x,\mathbf{y})$ is the azimuthal distance between the sensor and the location x, and $\rho(\mathbf{t}, d(x,\mathbf{y}))$ is the correlation coefficient between the arrival times and the distance of the sensors from the location x. The arrival time of each signal was found using an automatic detection method for determining the onset of seismic waves (Akazawa 2004).

For regional events that produced strong motion records, we typically are able to estimate the source location to within 3 to 5 km. This level of accuracy is sufficient to determine whether an event originated from within the NNSS boundary, and if so, where. Using this method for event identification and epicenter estimation, we were able to correctly identify the occurrence of SPEs 4Prime, 5, and 6 to within 2 seconds, and we estimated the origin location correctly to within 2 km (Table 1).

To characterize the SPEs beyond simply detecting their occurrence, the relative yield of each of the three SPEs was estimated. To estimate the magnitude, we adopted the magnitude model from Lee (1972), given by

$$\text{Magnitude} = c_1 + c_2\, log_{10}(T - c_3) + c_4 D, \tag{2}$$

where c_1, c_2, c_3, c_4 are parameters to determine, T is the duration of the seismic wave, and D is the distance of the detector from the epicenter. To compute the duration of the wave, a decaying exponential is fit to the signal envelope after the arrival of the S-wave, and the end of the wave is determined by finding where the exponential crosses the baseline noise level. An example waveform is shown in Figure 2; the total duration of the wave is the length of time indicated by the vertical dashed lines, and the exponential fit to the wave envelope is the red curve.

To determine the unknown parameters in Equation 2, the model was calibrated using known earthquakes in southern California and southern Nevada that produced seismic waves with similar amplitudes as those observed for the SPEs. Each sensor was calibrated independently, resulting in a unique set

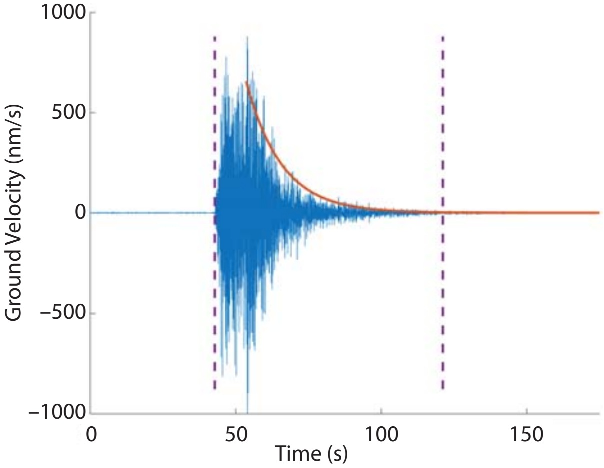

Figure 2. An example seismic waveform; the time duration of the wave is indicated by the dashed vertical lines and the estimated wave code is the red curve

of calibration parameters c_1, c_2, c_3, and c_4, with the final yield estimate being the mean of the individual estimates. The estimated relative sizes, along with the true relative sizes computed from the known yield in TNT equivalent, are given in Table 1. Normalizing to the largest SPE, SPE 5, we were able to accurately estimate the relative sizes of SPEs 4Prime and 6. If ground truth is known from previous seismic events in the area, these relative yields could be converted to absolute yields using standard seismic amplitude scaling relationships.

Determining Facility Activities from Patterns of Life

Patterns of life analysis exploits data gathered about day-to-day routines to gauge activities. NNSS patterns of life data can indicate when a particular facility is operational and how many people are there. For example, when there are no experiments at the Tactical Demilitarization Development (TaDD) facility in Area 11 (where the DPF is located), there are also no people at the facility. Internet activity at Area 11 indicates people are present, which further implies that an experimental campaign is active. The same is not true for the Joint Actinide Shock Physics Experimental Research (JASPER) facility, where people are stationed year-round regardless of whether a campaign is in progress. The two primary data streams we used to characterize patterns of life at the NNSS are the DNS logger and load profiles from the power grid for each facility. The DNS logger gives us a total number of “counts” for each NNSS subnet per hour, which correspond to Internet activity, and the load profiles show power usage in 15-minute intervals. In this report, we describe results for U1a, JASPER, and TaDD, as these three facilities represent the breadth of knowledge, or lack thereof, that can be obtained from the patterns of life.

U1a

One of the core missions of the NNSS is to perform SCEs, dynamic experiments that study the behavior of materials under extreme temperatures and pressures. The primary facility for SCEs is the U1a Complex, an experimental laboratory of tunnels approximately 960 feet underground in Area 1 at the NNSS. There are several important questions that one would be interested in asking about the activities at U1a. Basic questions include postdicting and predicting experiments. In the first year of this project, we successfully characterized prior U1a experiments using DNS and power grid data.

The daily energy consumption for U1a is shown in Figure 3a, with yellow indicating high power usage and blue indicating low power usage. The facility has a baseline energy consumption level for overnight periods and weekend/holiday days, but, on regular work days, the arrival and departure of personnel can be inferred from the spike in energy consumption in the morning and the return to the baseline level in the afternoon. The approximate start times for daily operations, defined as the time when the energy

Table 1. Comparison of the known and estimated relative sizes of SPEs 4Prime, 5, and 6

EVENT	DATE	TIME (Known)	TIME (Estimated)	YIELD (kg)	RELATIVE SIZE (Known)	RELATIVE SIZE (Estimated)
SPE 4Prime	5/21/2015	18:36:00	18:36:02	89	0.0177	0.0192
SPE 5	4/26/2016	20:49:00	20:49:01	5035	1	1
SPE 6	10/12/2016	18:36:00	18:35:59	2245	0.4459	0.4377

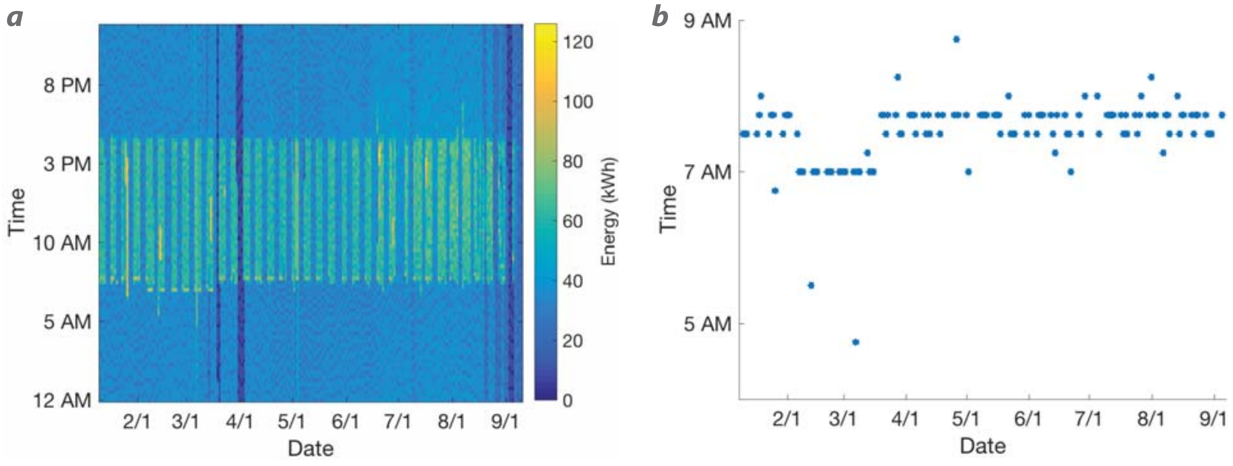

Figure 3. (a) The energy consumption of U1a in 15-minute intervals and (b) the estimated time for the start of operations

consumption rises above the overnight baseline, are shown in Figure 3b.

As seen in the figure, the cluster of days at the end of February and beginning of March show power usage beginning earlier in the day; on February 13 and March 7 power usage began extremely early in the day. This cluster of early starts—and the two extreme days—will be further characterized in the work that follows, demonstrating that we can accurately postdict the most important experimental activities at U1a.

To predict when an experiment will occur in the future, it is necessary to develop models to classify operations each day at a facility and to provide a statistical measure of certainty along with the classification. Classifying the state of the facility requires a model for operations in each of the modes of interest and training data in each of the modes to calibrate the model. The training data can be actual observed data over a period during which the state of the facility is known or from simulated datasets that mimic the data produced for each state. In our case, because the standard energy profiles are relatively simple, we chose to simulate the facility's energy consumption in each operational mode of interest. The operational modes incorporated into our model were closed, normal day, and early starts. The closed class describes days in which the energy consumption never rose above baseline levels. Normal days are defined as days in which the facility operations begin at approximately 7:30 a.m., increasing the energy consumption from baseline to a constant level, and then returning to baseline at approximately 4:30 p.m. Early starts, though nearly identical to normal days, denote facility operation beginning by 7:00 a.m. Of course, from Figure 3 we see that these three classes will not encapsulate every observed profile, but these classes are sufficient to characterize high-value experiments. The training data for each of the considered classes is shown in Figure 4. Each day is described by a feature vector with the four components: (1) time of initial rise of power consumption, (2) level of consumption throughout the day, (3) time of the return to baseline, and (4) baseline level.

For the simulated training data, values for each of the four features were sampled from normal distributions whose means and variances are equal to the sample means and variances of the measured data. For each of the profiles, random noise was added at every time point, and the training data were incorporated into a linear discriminant analysis (Fisher 1936, Rausch 2009) in order to predict the operational mode for the U1a facility for each day of observed data. Table 2

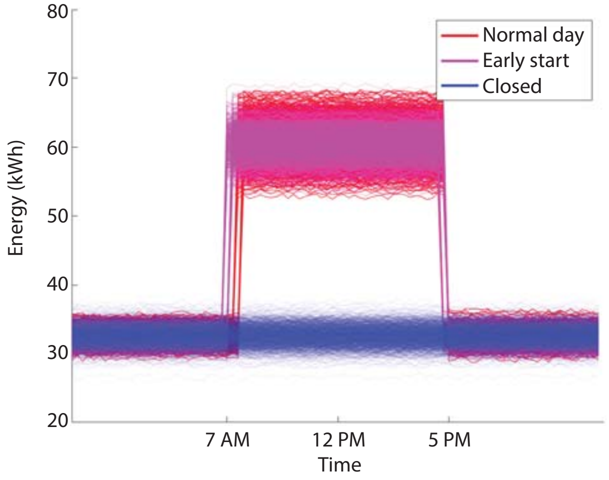

Figure 4. The simulated training data of the energy consumption profiles for the three operational modes of interest

Table 2. Success rate of classifier using a linear discriminate analysis

	CLOSED	NORMAL DAYS	EARLY START
Correctly Classified	95	101	25
Incorrectly Classified	12	9	1
Percent Correct	89%	91%	96%

summarizes the results of this classification, and the closed and normal states are correctly classified for approximately 90% of the days, with early starts correctly identified for 96% of the days. Most of the misclassifications are a result of days in which the profile was not adequately described by the model for energy consumption profiles. Yet, the days we are most interested in are the early starts, and we correctly identified 25 of the 26 of these days. The timeline of the operational mode of the U1a facility is shown in Figure 5, where the solid dots represent the predicted class or operational mode, and the circles depict the true class.

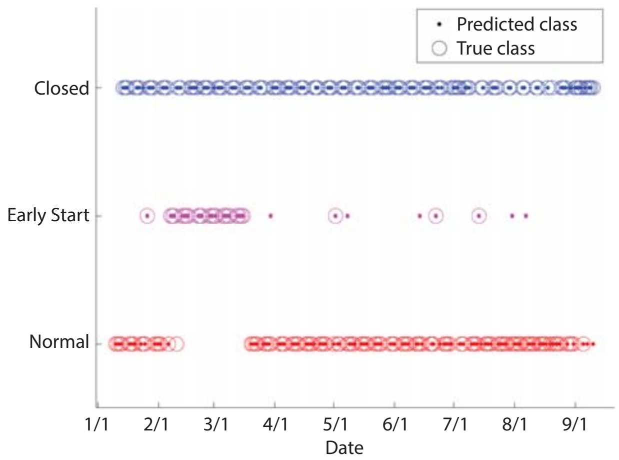

Figure 5. Predicted operational mode of U1a compared to the true class

After using individual data streams and predictive modeling, the next step in the analysis is to combine multiple data streams to resolve discrepancies that cannot be resolved by a single data modality. The two most extreme days in power usage are February 13 and March 7, but the start times are pretty similar, making them difficult to distinguish solely from the power grid data. These two days show very different characteristics in network usage data, measured by firewall counts, which can be seen in Figure 6. On February 13, the network usage was very low, which suggests that there were few people at U1a, but, from the power usage, we know that those few people showed up very early. On March 7, there was a very large number of people, as shown from network usage, and those people showed up early, as we learn from power usage. That SCEs are carried out at the

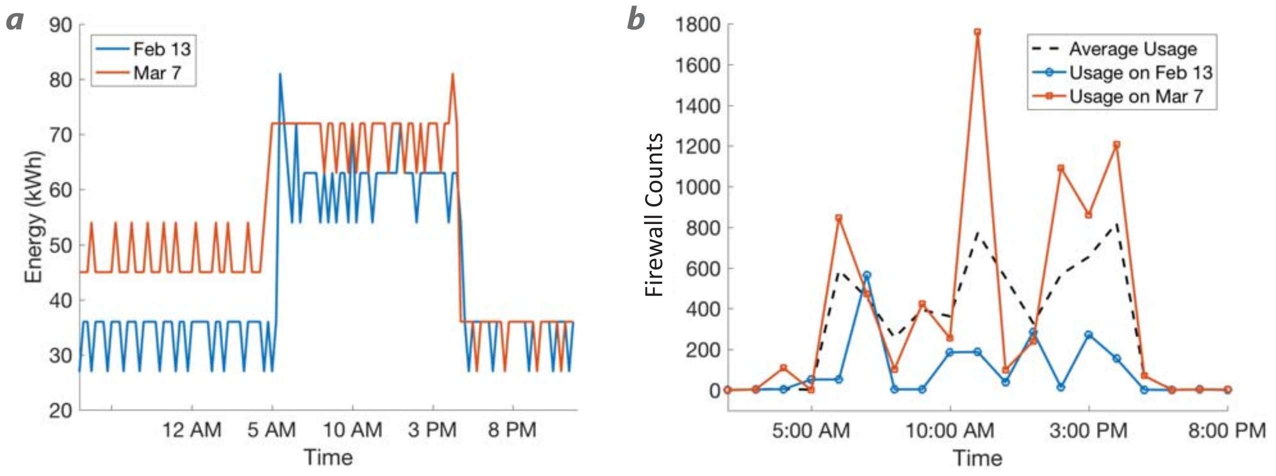

Figure 6. The (a) energy consumption and the (b) Internet usage at U1a on February 13 and March 7 used to postdict an experiment

NNSS U1a facility is publicly available information, so an outsider with general understanding about the experimental process involved in carrying out an SCE would be able to identify these characteristics as an indication that February 13 was the day of package insertion for the Eurydice confirmatory experiment, on which only essential personnel were present at U1a. That allows one to further deduce that March 7 was the day of the Eurydice confirmatory experiment. The distinction of these days is clear using both data streams, but not clear with either stream individually. We will monitor both data streams closely on the upcoming Vega and Lamarck experiments set to take place in FY 2018.

JASPER

Understanding the dynamic properties of plutonium under extreme temperatures and pressures is essential for understanding performance of the nuclear weapons stockpile. The JASPER facility is a two-stage powder gun for measuring the properties of plutonium in relevant regimes. In contrast to the U1a facility, where a high level of detail and experimental activities could be inferred from patterns of life monitoring, the JASPER facility yields very little information from the same data streams. Whether executing an experiment or not, the JASPER facility workday starts and ends at roughly the same time and the population does not vary enough to create a detectable increase in power consumption or network traffic.

TaDD

An important component of the NNSS's Stockpile Stewardship mission is the development of diagnostic systems for SCEs. The newest class of SCEs, neutron-diagnosed SCEs, will use a high-flux pulsed neutron source that is currently being developed at TaDD. Observing TaDD provides an interesting case study, as there are a wide range of operational modes: periods when the facility and personnel are at maximum capacity during experimental campaigns, periods of medium activity during repairs and dry runs leading up to experiments, and periods where there is little or no activity. During FY 2017 there were two high-profile experimental campaigns involving the use of special nuclear materials (SNM); the first took place over a span of two weeks in February, and the second was spread out over three weeks in August, with the middle week being a period during which the DPF was under repair.

When an experiment is being executed, due to potential radiation, the DPF is cleared of personnel. The only indoor location suitable for staff during a shot is inside the remote-control trailer, which is powered by diesel generators. Because the presence of personnel in the facility does not increase the energy consumption above baseline levels, the power data contains no relevant information regarding operations.

Figure 7 shows the firewall and DNS counts for January 5 through March 20 and March 1 through July 31, respectively. The first SNM campaign occurred during the weeks of February 13 and 20 and was preceded by two weeks of dry runs. The second

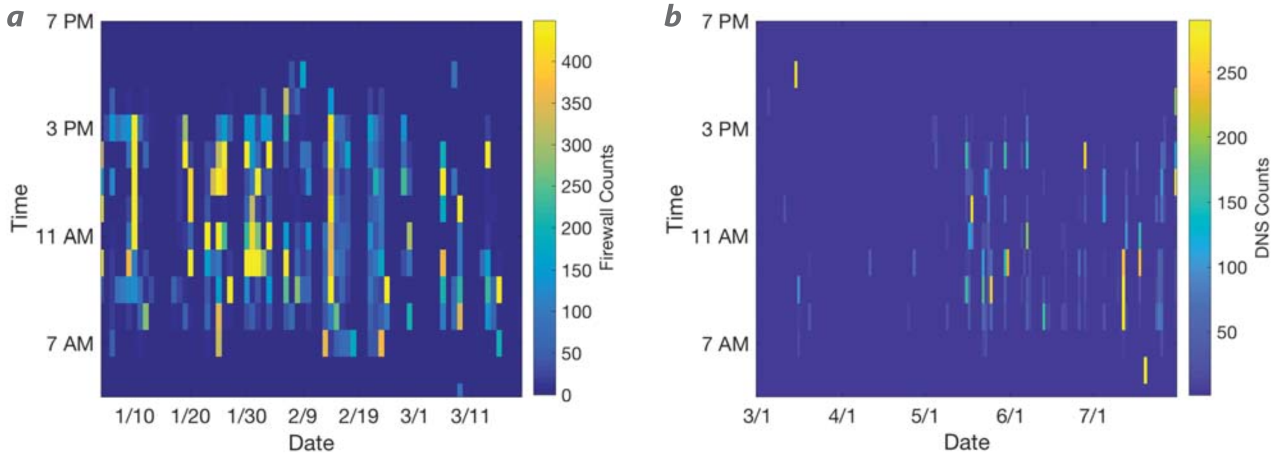

Figure 7. The hourly network activity levels at Area 11. (a) For the period of January through March the network activity is represented using firewall counts and (b) for May through August the activity is determined by the DNS counts (note the different intensity scales).

week of the campaign only consisted of Tuesday, Wednesday, and Thursday because Monday was President's Day. The activity levels during the dry run period and the SNM campaign are similar, with the SNM series only being distinguishable by the consecutive days for which there is an increased level of activity beginning at 7 a.m. Extremely low DNS counts were observed from March until mid-May. In March, the Area 11 DPF was down and there were no activities at the facility. Beginning in April the DPF crew began repairing the DPF capacitor bank, and the repairs were completed during the second week of May. On May 16 the DPF was fired for the first time since the end of the SNM campaign in February, and experiments were conducted through the end of May, at which point operations stopped and were not resumed until August. Notice that even once repairs began on the DPF, the network activity did not increase significantly until experiments resumed on May 16. This is because the repairs were conducted within the Area 11 DPF compound, where there are no network connections. Yet, once experiments began, the network activity increased because the crew was stationed in the remote trailer, which has network access. Even after the series concluded at the end of May, the network levels remained intermittent during June and July as repairs and upgrades were made to the facility. These repairs were not made by the DPF crew; however, crew members had to be present to oversee the facility. Because the DPF crew members were not assisting in the facility upgrades, portions of the day were spent in the remote trailer.

CONCLUSION

Our initial efforts have illustrated that through patterns of life monitoring using benign data, much can be learned about facility operations and experimental activities for facilities where the mode of operations changes for experimental activities. A facility such as JASPER, which rarely deviates from its standard mode of operations, is fairly immune to such event detections. For the SPE shots, we were not only able to detect events, but also able to infer information about the scale of the experiments. Finally, by tracking a subset of experiments that occurred in FY 2017, we have identified trends that can be incorporated into the prediction of experiments at facilities, such as SCEs at U1a and high-value experiments at TaDD. Thus, we are making significant progress in developing the ability to detect, predict, and characterize experimental activities at various sites across the NNSS.

In FY 2018 we will use Canary sensors developed under the SDRD program (Kornell 2017, 2018) at STL to expand the number of measurement modalities. The Canaries will be fielded at various sites of interest at the NNSS. Collecting data from Canary sensors placed in the field presents challenges in both bringing the sensors online with the ability to collect and record data continuously as well as handling the administrative issues that will allow us to place the sensors at various locations on the NNSS. When combined with the seismic, cyber, and power data that we have established access to in FY 2017, we will have a true multi-modal dataset in which to apply and develop data fusion techniques to test the detection and prediction capabilities possible concerning NNSS facilities and experiments.

ACKNOWLEDGMENTS

The authors would like to thank Jesse Bonner, Bob White, and Hart Kornell for their useful insight and suggestions with regards to this project.

REFERENCES

Akazawa, T., "A technique for automatic detection of onset time of P- and S-phases in strong motion records," 13th World Conference on Earthquake Engineering, August 1–6, 2004, http://www.iitk.ac.in/nicee/wcee/article/13_786.pdf, accessed on May 18, 2017.

Bolt, B. A., "The revision of earthquake epicenters, focal depths and origin-times using a high-speed computer," *Geophys. J. Int.* **3**, 4 (1960) 433–440.

Fisher, R. A., "The use of multiple measurements in taxonomic problems," *Ann. Eugenics* **7** (1936) 179–188.

Jeffreys, H., *The Earth: Its Origin, History and Physical Constitution*, Cambridge University Press, Cambridge, UK, 1959.

Kornell, J., P. Rangel, S. Ono, "Canary: Low-power, self-organizing reporting devices: Situational awareness using distributed sensor arrays," in *Site-Directed Research and Development*, FY 2016, National Security Technologies, LLC, Las Vegas, Nevada, 2017, 97–101.

Lee, W. H. K., R. E. Bennett, K. L. Meagher, "A method of estimating magnitude of local earthquakes from signal duration," U. S. Geological Survey, 1972, https://pubs.usgs.gov/of/1972/0223/report.pdf, accessed on June 2, 2017.

Miller, E. K., H. Kornell, "Low-power, self-organizing reporting devices: Situational awareness using distributed sensor arrays," in *Site-Directed Research and Development*, FY 2017, National Security Technologies, LLC, and Mission Support and Test Services, LLC, Las Vegas, Nevada, 2018, 129–133.

Norrdine, A., "An algebraic solution to the multilateration problem," 2012 Conference on Indoor Positioning and Indoor Navigation, November 13–15, 2012.

Rausch, J. R., K. Kelley, "A comparison of linear and mixture models for discriminant analysis under nonnormality," *Behavior Research Methods* **41**, 1 (2009) 85–98.

Simonson, K., R. Hansen, T. LaBruyere, M. Van Benthem, R. D. West, "A frequentist approach to multi-source classification," Conference on Data Analysis, March 3, 2016, https://www.osti.gov/scitech/servlets/purl/1364857, accessed on August 5, 2017.

Snelson, C. M., R. E. Abbott, S. T. Broome, R. J. Mellors, H. J. Patton, A. J. Sussman, M. J. Townsend, W. R. Walter, "Chemical explosion experiments to improve nuclear test monitoring," *Eos* **94**, 27 (2013) 237–239.

Spence, W., S. A. Sipkin, G. L. Choy, "Measuring the size of an earthquake," *Earthquakes and Volcanoes* **21**, 1 (1989) 58–63, https://pubs.usgs.gov/unnumbered/70039068/report.pdf, accessed on June 1, 2017.

This page left blank intentionally

Algorithm Development for Targeted Isotopics

RSLA-002-17 ■ Continuing in FY 2018 ■ Year 1 of 3

Eric Moore,[1,a] Bill Ford,[a] Emma Hague,[a] and Johanna Turk[b]

[1]mooreet@nv.doe.gov, (301) 817-3381
[a]Remote Sensing Laboratory–Andrews
[b]Former employee

Unlike some previous attempts at utilizing machine learning approaches to solve the problem of isotopic identification that have created new machine learning algorithms, we are emphasizing a data-driven approach to the problem. Rather than creating new machine learning techniques, we are drawing on an existing framework for better data exploitation by using well-established techniques. Using multiple libraries and software packages to train over much larger quantities of data than have been used in the past, we have demonstrated in FY 2017 that predictive models can not only accurately identify isotopes, but can also provide additional information about the radiation background. In FY 2018, a detailed comparison of predictive model and human isotopic identification accuracy will be performed.

BACKGROUND

There have been a number of attempts to use machine learning approaches to solve the problem of isotopic identification, typically by creating new algorithms. Conversely, we are using the right data, or to be more accurate, using the data the *right* way. While earlier efforts had limited successes, they have never consistently outperformed a good template-matching algorithm well enough to be worth implementing. By exercising the data, we hope to create a paradigm of continual improvement as more data become available.

Computers are now better at solving well-defined image recognition problems than humans; the machine learning community has been on the cusp of this achievement for years. The infrastructure developed, mostly by industry, to realize this and many other capabilities (natural language processing, recommender systems, etc.) is mostly open source. This study exploits these methods to develop robust capabilities for identifying targeted isotopics.

The importance of automated radiation identification (ID), especially in the context of brief source encounters, is hard to overstate. Two decades ago very few of the sensors deployed during search operations had spectral capabilities, and those that did were usually deployed by teams with substantial knowledge of spectroscopy; now a greater number

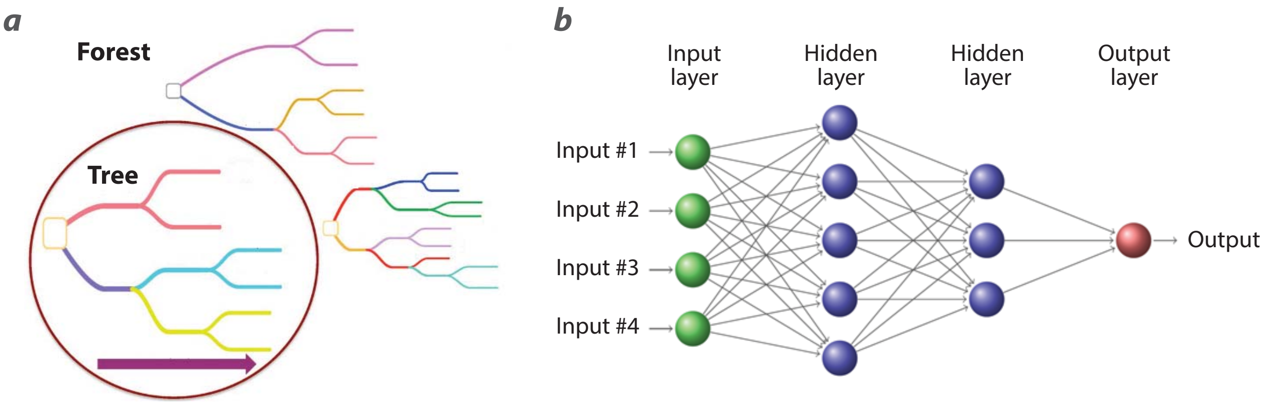

Figure 1. (a) A decision tree structure and (b) an artificial neural network

of "searchers" have no knowledge, or very limited knowledge, of in situ radiation detection techniques. Now many—soon to be most—detectors used during dynamic (e.g., the source and detector are moving relative to each other) search operations (in the sense that the source and detector are moving relative to each other) use microchannel analyzers (MCAs) that continually collect spectral data second by second. This creates new problems for low-statistics IDs (i.e., when the detector is exposed to the source for a very short period of time, or the signal-to-background is very low).

Too many people are needed to support the number of sensors that are fielded during radiological/nuclear search operations. And sensors need to be better at pre-filtering nuisance alarms so a single operator can monitor multiple sensors. Despite the large number of personnel, the probability of encountering a threat source (should one exist) during a major public event is low. This is true even if one assumes that a close approach would result in detection. The sensor-to-person ratio is too small to provide coverage during standard preventive radiation/nuclear detection search operations.

Many high-priority search operations are no longer unfocused but are target-specific threat/intelligence–driven searches. Hence, there is significant opportunity to exploit the information known about the search, as one may have a priori knowledge of the isotopics, time, and target location.

PROJECT

For all the reasons stated above, good automated ID is badly needed, and this project takes a data-driven approach to addressing the challenge. Using algorithms for the statistical learning from open source libraries, we will focus on the data and develop a sustainable method to incorporate new data. Wherever it makes sense to do so, a priori specifics will be utilized to improve accuracy or increase the level of information gleaned from the machine algorithms employed.

Equipment and Data

Data collections from an NA-22 project were used to characterize the generic detector system[2] used for this project, a sodium iodide (NaI) 2″ × 4″ × 16″ crystal with an Ortec DigiBase. The same system has been added to some ongoing measurement campaigns for DOE NA-84 in order to create a near-zero cost efficiency in data collection. In addition to the NA-22 datasets, we are acquiring existing datasets from other labs and projects. This same canonical sensor is used for all the modeling discussed in this paper.

The fact that both the testing and training sets are modeled using the same basic methodology, and in fact that the test set is modeled data at all, are the greatest shortfalls in this proof-of-concept study. As it must be assumed that any test set derived from real data will perform worse, addressing this shortfall is the highest priority. The next step in creating more independent test and validation datasets will be to model these using MCNP while continuing to model the training datasets in GADRAS. Once measured (real) datasets are available, they will be used for validation. This effort has already begun for small samples of isotopes.

Regardless of how much data is collected, we will not be able to fill all our requirements for data, as machine learning is extremely data intensive. In order to fill the "holes" in our datasets and to augment them, we are doing a significant amount of modeling. Most of the

---

[2] A DOE NA-22 project (Signal Studies, Algorithms, and Methods FY17–19) system was leveraged for this purpose.

training datasets are being modeled in GADRAS, and at this point the MCNP modeling is being reserved for testing and/or validation of built models. There is a significant amount of modeling effort to accomplish, especially in MCNP.

General Machine Learning

The objective in any machine (statistical) learning process is to map some input vector (predictor space) onto an output vector (response space) (Figure 1b). We may refer to the input as predictors (p) or features, and the output as response (y) or classes. When we refer to training data, we mean the observations, whether modeled or measured, used in the statistical learning process. This means, for example, that observations of a neural network feed into the learning process while the weights and general architecture are still being adjusted. The testing data are those observations used to determine the performance of the machine thus trained; they may be used to select from various built machines the one that gives the best result for the particular classification or regression problem in question. Once the selection of the final model (machine) is made, the test dataset will likely be combined with the training dataset, and this newer, larger dataset will be used to retrain the model that was selected using the test data. After this training and testing process is complete, a last holdout dataset, the validation data, is fed through the finalized model to establish the final performance. This validation process is the last opportunity to abandon or adjust the model and should only be done once a selection of a final model is made or new data become available to fill the place of the validation dataset.

Thus far, researchers have used modeled data for all training, testing, and validation, but true validation requires actual data. In some small-scale examples actual data were used for the validation, and the performance is encouraging (Figure 4).

In this project all available datasets will be used to create and test the models. It is hoped that from this and subsequent work, a sustainable framework for continuous model improvement will be established, so that as additional data become available, the machine will become an ever-improving "spectroscopist." It is reasonable to believe this is possible, as other areas of pattern recognition are demonstrating success. Ultimately, the machine should learn to consistently outperform human spectrocopists, especially when more than just gamma data are being considered.

The criterion for the assessment of models during training and testing depends on the machine architecture being employed, but once training of the final model is complete, we have used accuracy as the criterion throughout, defined as

$$Accuracy = \frac{TP + TN}{TP + FP + TN + FN}, \tag{1}$$

where TP is the number of true positives and FN the number of false negatives. Our criterion may change depending on the demands of the problem case—for example, we may have a very low tolerance for type II errors (false negatives). If this is the case, the more appropriate criterion may be recall, defined as

$$Recall = \frac{TP}{TP + FN}. \tag{2}$$

Maximizing recall will ensure that the false negative rate is correspondingly minimized. For our current purposes the accuracy has been a sufficient metric.

Specific Machine Learning Architectures

Twenty years ago machine learning aimed to develop highly specialized, domain-specific, solutions to individual problems; however, today the industry trend is to produce general solutions to "classes" of problems. Much of these are available from online open source libraries filled with free machine learning computation solutions. (A list of libraries is provided as an appendix.) As these open source libraries provide all the varying machine architectures that are likely to be needed for this project, we are leveraging the available tools to address our domain-specific problem.

Some architectures used in this work are artificial neural networks (ANNs), support vector classifiers/machines (SVCs, SVM)s, random forests (RFs), and k-nearest neighbors (k-NNs). These common methods of machine learning are employed in the most frequently used open source libraries. Every statistical learning method has its own challenges related to use, and many different parameters must be considered during implementation. Rather than describing each architecture in detail, we will describe how we use RF, which will serve as an example of the other methods.

Example: Decision Trees

Tree-based methods of statistical learning concentrate on the segmentation, or partitioning, of the predictor space into regions related to some threshold, or trigger, associated with the predictors involved. By predictor space we mean the p-dimensional space that spans all the input parameters used, or anticipated to be used, to predict the output (y). In our case, y is an isotopic identification. The raw channel inputs from the MCA are predictors. So one can imagine an algorithm that would ask for each channel whether or not some threshold was exceeded. Every time a threshold query occurred, a branch is created in the tree (Figure 1a). While it is trivial to show that this can result in a parameter space that has been subdivided into as many as 2^p pieces, in reality this is tightly constrained by the number of observations n. The set of splitting rules can be represented as a tree; therefore, the methods are generically referred to as decision trees (Figure 1).

For the purpose of this example, we assumed that all techniques are employed as supervised, meaning the answers (y) for some training dataset are known and used in the training process; this was not true for all aspects of our research. After every training iteration, results of how all the observations were classified[3] are compared to the correct classification for that observation. To establish how correct a given iteration is, we look at the classification error rate, or the proportion of misclassified observations. This is one of many metrics used during training, and is not to be confused with the final validation metric, which is still accuracy. In practice for classification problems, one frequently used metric is the Gini index, which is

$$G = \sum_{k=1}^{K} \hat{p}_{mk}(1 - \hat{p}_{mk}), \tag{3}$$

where $\hat{p}_{mk}$ is the proportion of the events in the m^{th} region that are from the k^{th} class. The Gini index gives a measure of the total variance across the K classes. It is also common to use the cross entropy for a measure of this variance (Hastie 2017).

Random forests make a large number of classification trees based on some random subset of the possible predictors to build trees. So instead of all predictors being used in a given tree, some subspace of the whole predictor space generates the forest. The Gini will then select the best method tree given all observations.

When building an RF model, we consider parameters such as the number of trees, or how many random, with replacement, subspaces of predictors are generated; or of the many pieces into which the observations are divided, how many can be described in terms of k-folds or samples with replacement (cross-validation).

Setting RF parameters during training in any given method is fairly simple. Now we will discuss a much more important aspect to the process—choosing predictors called features.

Feature Engineering and Selection

Thus far, only raw channel data have been discussed, but many different predictors were examined to help in spectral identification. We rebinned the channel data from 1024 channels roughly linearly in energy space to 256 channels linearized in resolution space, meaning the peaks are all roughly the same width. This preprocessing step is analogous to calibration. The input vector to an ANN would still be channel count rate data. Although for a human spectroscopist channel count data (i.e., a spectrum) is the best way to classify gamma ray data, this need not be the case for a machine. Moments of the spectra (mean, variance, skewness, kurtosis, etc.) are a good example of an engineered feature. Using higher-order parameters can be a concern when dealing with low-sampled distributions.

Ratios of various parts of the spectrum were studied. Although some of the regions were physics motivated,

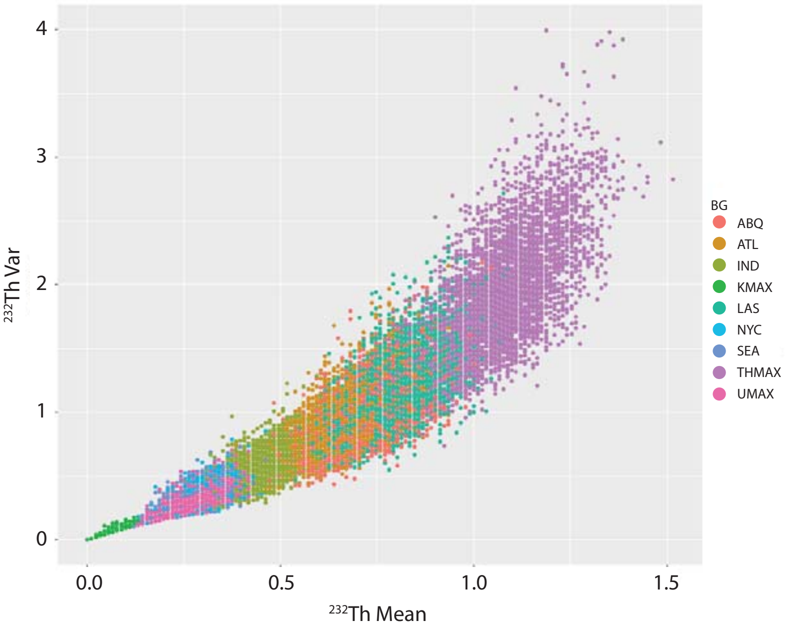

Figure 2. Even with a variety of isotopes and shielding, these features (mean and variance of a window specific to ^{232}Th) would be useful in classifying background type

---

[3] The method, as described, is a classification not regression problem. This need not be the case in general for RFs.

predominantly we rastered across the first 3 MeV of the energy space and used the means and variants of the net counts in those regions as input features into various machine methods.

The power of these features can be seen in the class separation that they provide even without a machine algorithm applied, as in the case of background separation. Nine background compositions were chosen corresponding to extremes in the potassium-uranium-thorium (*K-U-T*) ratios as well as six mixtures corresponding to different cities. These backgrounds were then mixed in various source/background quantities to several different source isotopes to cover a range of different signal-to-noise ratio levels. Thousands of such combinations were generated.

Although no machine learning algorithm was generated to separate these data by class, it is clear by inspection of some of the features (i.e., the thorium mean and variance) that such an algorithm could be generated (Figure 2).

In summary, the general methodology employed is to examine correlation in any available data types: gamma, neutron, or other sensor data. Correlations between the desired response and the available predictors must be found or suspected to include features that are "engineered" from the set of available data. The features are selected and trained/tested against modeled datasets then validated on real datasets, when available, and on independently modeled datasets when necessary.

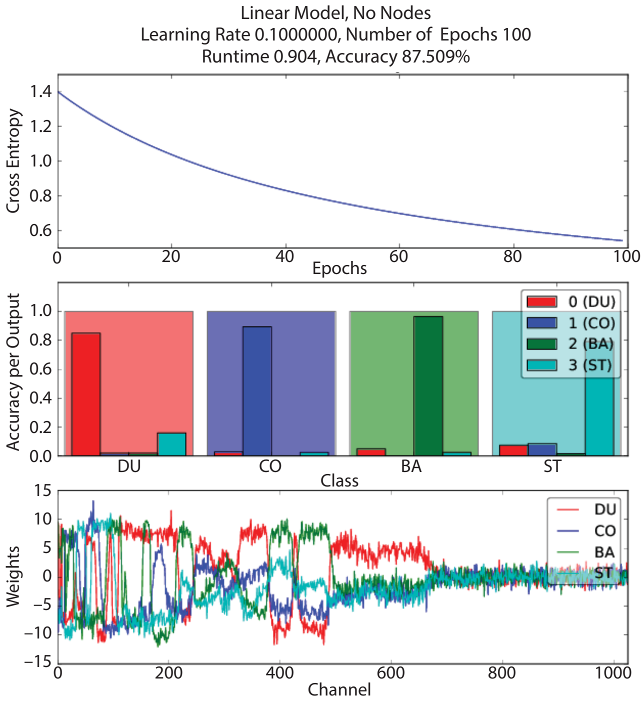

Figure 3. Trained response classes of shielding over various isotopes and distances. The shielding used is one of four classes: bare (BA), concrete (CO), steel (ST), and depleted uranium (DU).

RESULTS

In addition to looking at isotopic ID algorithms, we have also trained a dataset to classify by shielding, backgrounds, and enrichment (uranium). First, we trained an ANN to categorize by shielding (Figure 3).

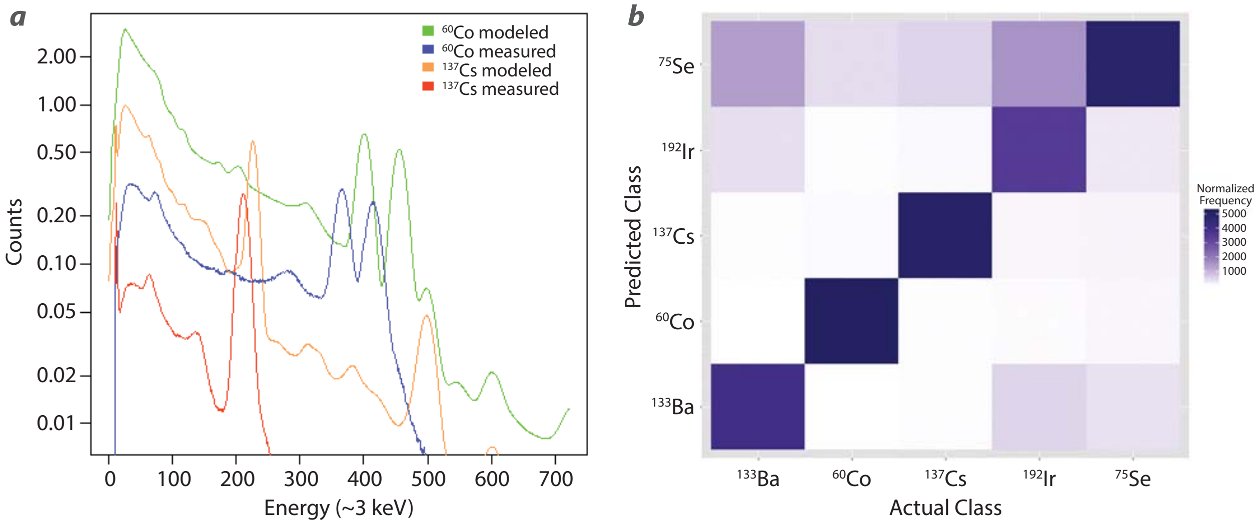

Figure 4. A training dataset, GADRAS, including six isotopes with different combinations of backgrounds and shielding was used to train an RF algorithm to classify by isotope. A validation set was used of measured data. (b) The confusion matrix indicates good class separation, despite the poor agreement in (a) calibration. (Note: The x-axis is in units of 3 keV.)

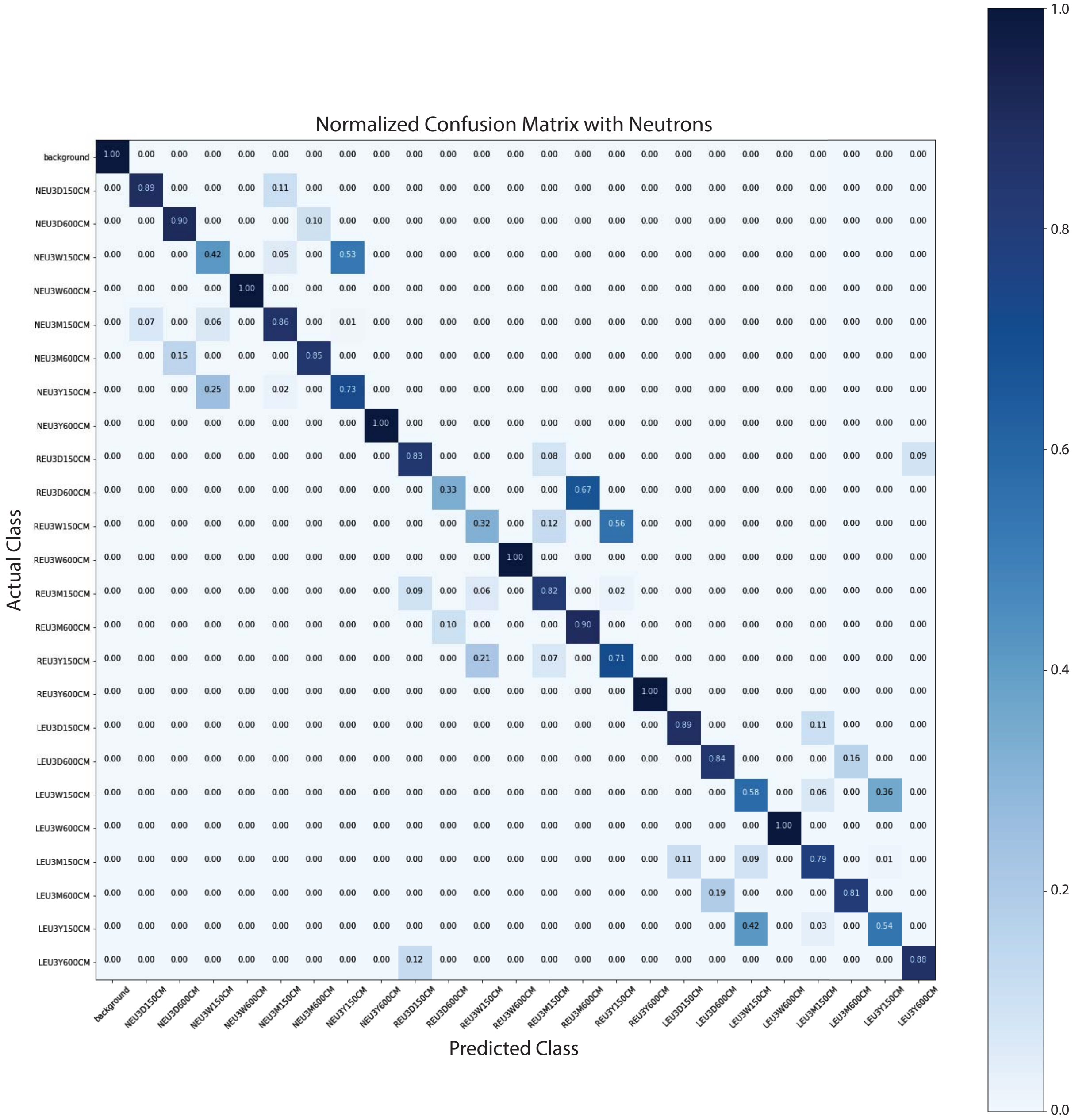

	background	NEU3D150CM	NEU3D600CM	NEU3W150CM	NEU3W600CM	NEU3M150CM	NEU3M600CM	NEU3Y150CM	NEU3Y600CM	REU3D150CM	REU3D600CM	REU3W150CM	REU3W600CM	REU3M150CM	REU3M600CM	REU3Y150CM	REU3Y600CM	LEU3D150CM	LEU3D600CM	LEU3W150CM	LEU3W600CM	LEU3M150CM	LEU3M600CM	LEU3Y150CM	LEU3Y600CM
background	1.00	0.00	0.00	0.00	0.00	0.00	0.00	0.00	0.00	0.00	0.00	0.00	0.00	0.00	0.00	0.00	0.00	0.00	0.00	0.00	0.00	0.00	0.00	0.00	0.00
NEU3D150CM	0.00	0.89	0.00	0.00	0.00	0.11	0.00	0.00	0.00	0.00	0.00	0.00	0.00	0.00	0.00	0.00	0.00	0.00	0.00	0.00	0.00	0.00	0.00	0.00	0.00
NEU3D600CM	0.00	0.00	0.90	0.00	0.00	0.00	0.10	0.00	0.00	0.00	0.00	0.00	0.00	0.00	0.00	0.00	0.00	0.00	0.00	0.00	0.00	0.00	0.00	0.00	0.00
NEU3W150CM	0.00	0.00	0.00	0.42	0.00	0.05	0.00	0.53	0.00	0.00	0.00	0.00	0.00	0.00	0.00	0.00	0.00	0.00	0.00	0.00	0.00	0.00	0.00	0.00	0.00
NEU3W600CM	0.00	0.00	0.00	0.00	1.00	0.00	0.00	0.00	0.00	0.00	0.00	0.00	0.00	0.00	0.00	0.00	0.00	0.00	0.00	0.00	0.00	0.00	0.00	0.00	0.00
NEU3M150CM	0.00	0.07	0.00	0.06	0.00	0.86	0.00	0.01	0.00	0.00	0.00	0.00	0.00	0.00	0.00	0.00	0.00	0.00	0.00	0.00	0.00	0.00	0.00	0.00	0.00
NEU3M600CM	0.00	0.00	0.15	0.00	0.00	0.00	0.85	0.00	0.00	0.00	0.00	0.00	0.00	0.00	0.00	0.00	0.00	0.00	0.00	0.00	0.00	0.00	0.00	0.00	0.00
NEU3Y150CM	0.00	0.00	0.00	0.25	0.00	0.02	0.00	0.73	0.00	0.00	0.00	0.00	0.00	0.00	0.00	0.00	0.00	0.00	0.00	0.00	0.00	0.00	0.00	0.00	0.00
NEU3Y600CM	0.00	0.00	0.00	0.00	0.00	0.00	0.00	0.00	1.00	0.00	0.00	0.00	0.00	0.00	0.00	0.00	0.00	0.00	0.00	0.00	0.00	0.00	0.00	0.00	0.00
REU3D150CM	0.00	0.00	0.00	0.00	0.00	0.00	0.00	0.00	0.00	0.83	0.00	0.00	0.00	0.08	0.00	0.00	0.00	0.00	0.00	0.00	0.00	0.00	0.00	0.00	0.09
REU3D600CM	0.00	0.00	0.00	0.00	0.00	0.00	0.00	0.00	0.00	0.00	0.33	0.00	0.00	0.00	0.67	0.00	0.00	0.00	0.00	0.00	0.00	0.00	0.00	0.00	0.00
REU3W150CM	0.00	0.00	0.00	0.00	0.00	0.00	0.00	0.00	0.00	0.00	0.00	0.32	0.00	0.12	0.00	0.56	0.00	0.00	0.00	0.00	0.00	0.00	0.00	0.00	0.00
REU3W600CM	0.00	0.00	0.00	0.00	0.00	0.00	0.00	0.00	0.00	0.00	0.00	0.00	1.00	0.00	0.00	0.00	0.00	0.00	0.00	0.00	0.00	0.00	0.00	0.00	0.00
REU3M150CM	0.00	0.00	0.00	0.00	0.00	0.00	0.00	0.00	0.00	0.09	0.00	0.06	0.00	0.82	0.00	0.02	0.00	0.00	0.00	0.00	0.00	0.00	0.00	0.00	0.00
REU3M600CM	0.00	0.00	0.00	0.00	0.00	0.00	0.00	0.00	0.00	0.00	0.10	0.00	0.00	0.00	0.90	0.00	0.00	0.00	0.00	0.00	0.00	0.00	0.00	0.00	0.00
REU3Y150CM	0.00	0.00	0.00	0.00	0.00	0.00	0.00	0.00	0.00	0.00	0.00	0.21	0.00	0.07	0.00	0.71	0.00	0.00	0.00	0.00	0.00	0.00	0.00	0.00	0.00
REU3Y600CM	0.00	0.00	0.00	0.00	0.00	0.00	0.00	0.00	0.00	0.00	0.00	0.00	0.00	0.00	0.00	0.00	1.00	0.00	0.00	0.00	0.00	0.00	0.00	0.00	0.00
LEU3D150CM	0.00	0.00	0.00	0.00	0.00	0.00	0.00	0.00	0.00	0.00	0.00	0.00	0.00	0.00	0.00	0.00	0.00	0.89	0.00	0.00	0.00	0.11	0.00	0.00	0.00
LEU3D600CM	0.00	0.00	0.00	0.00	0.00	0.00	0.00	0.00	0.00	0.00	0.00	0.00	0.00	0.00	0.00	0.00	0.00	0.00	0.84	0.00	0.00	0.00	0.16	0.00	0.00
LEU3W150CM	0.00	0.00	0.00	0.00	0.00	0.00	0.00	0.00	0.00	0.00	0.00	0.00	0.00	0.00	0.00	0.00	0.00	0.00	0.00	0.58	0.00	0.06	0.00	0.36	0.00
LEU3W600CM	0.00	0.00	0.00	0.00	0.00	0.00	0.00	0.00	0.00	0.00	0.00	0.00	0.00	0.00	0.00	0.00	0.00	0.00	0.00	0.00	1.00	0.00	0.00	0.00	0.00
LEU3M150CM	0.00	0.00	0.00	0.00	0.00	0.00	0.00	0.00	0.00	0.00	0.00	0.00	0.00	0.00	0.00	0.00	0.00	0.11	0.00	0.09	0.00	0.79	0.00	0.01	0.00
LEU3M600CM	0.00	0.00	0.00	0.00	0.00	0.00	0.00	0.00	0.00	0.00	0.00	0.00	0.00	0.00	0.00	0.00	0.00	0.00	0.19	0.00	0.00	0.00	0.81	0.00	0.00
LEU3Y150CM	0.00	0.00	0.00	0.00	0.00	0.00	0.00	0.00	0.00	0.00	0.00	0.00	0.00	0.00	0.00	0.00	0.00	0.00	0.00	0.42	0.00	0.03	0.00	0.54	0.00
LEU3Y600CM	0.00	0.00	0.00	0.00	0.00	0.00	0.00	0.00	0.00	0.12	0.00	0.00	0.00	0.00	0.00	0.00	0.00	0.00	0.00	0.00	0.00	0.00	0.00	0.00	0.88

Figure 5. This confusion matrix indicates the frequency for the actual class on the *y*-axis of being classed in the predicted class on the *x*-axis. The diagonal indicates a correct classification, and most of the off-diagonal elements with data are still correct enrichment classifications.

The same dataset used above was trained to find given classes of shielding, even though the training data were of many differing isotopic compositions.

Some of the simpler machine algorithms have proved to be robust against gain and calibration issues. Although this has only been demonstrated in the case of a small sample of classes (five isotopes and background), it has been validated against measured data (Figure 4). Only two of the isotopes measured are shown in the figure for clarity, but the two classes shown are clearly well distinguished by an RF. This is a promising result, but we cannot say if this method will remain robust for a much broader range of classes. It may be that good calibration is always a prerequisite to successful identification where many classes (isotopes) are concerned; there are reasons to believe this to be so for low-statistics cases. For now we are concentrating mostly on well-calibrated datasets.

The results of our test on a dataset created specifically to demonstrate our ability to create a machine learning method to determine uranium enrichment is discussed next. This dataset, created using GADRAS, consists of three different enrichments at different distances in a fixed background scenario with neutrons empirically determined based on the work of Berndt, Franke, and Mortreau (2010). The uranium enrichment levels (NEU, REU, LEU) correspond to natural, reactor grade, and low-enriched (Figure 5). The distance is the impact parameter for a source in motion passing a stationary sensor and varies from 1.5 to 6 meters. In all cases the source encounters are assumed to be brief; only a single second of integrated data is used in our canonical sensor with an assumed quantity of material of 25 kilograms. Asymptotic spectra are Poisson sampled to create the "observed" encounters. We then used a separate testing dataset, also modeled in GADRAS, in the same background environment but at a different, intermediate distance.

In this final example of our work this year, the importance of machine learning models is shown. The relevant two classes to be trained to were "everything else" versus "shielded ^{137}Cs," which served as a surrogate for a soil density gauge. We expected to create a method of rejection on a common nuisance object in search operations. In our first attempt, the SVM created to separate the two classes had almost no success, but when the same dataset and features were trained to using an ANN, it displayed excellent accuracy in the execution of the same classification (Figure 6). In this case the validation set was also modeled data.

CONCLUSION

In FY 2017 we created a preliminary dataset for the training of predictive models and explored the relative performance of a variety of model types. The most successful models can not only accurately identify isotopes, they can also provide additional information about the radiation background. In relation to machine learning methods, it may be that the best technique in terms of accuracy will not be the one(s) finally adopted due to the requirement of sustainability in the face of new data over time. It is also likely the best solution is actually some ensemble of standard methods utilized together.

In FY 2018, a detailed comparison of the predictive model and human isotopic identification accuracy will be performed. An attempt will be made to quantify the irreducible error associated with the problem in order to have a baseline of comparison for the algorithms being worked on. And some data augmen-tation techniques will be explored to help with the training process. Finally, an exploration of the supplemental information the models can provide (background characterization, distance to source, shielding indications, etc.) will begin.

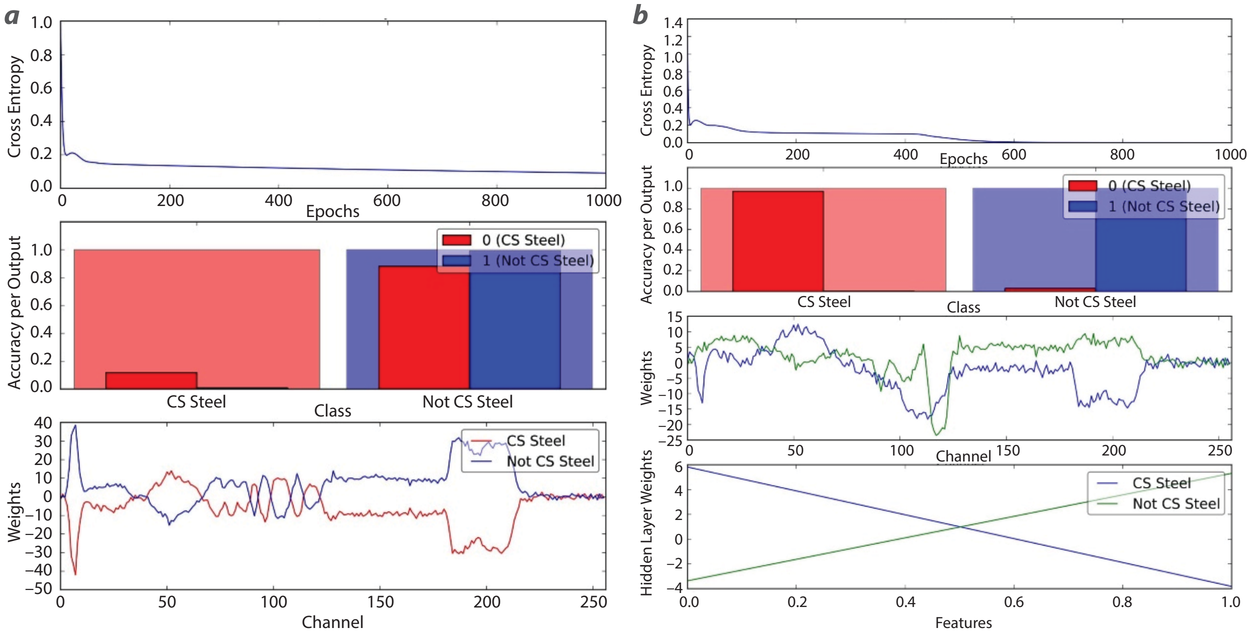

Figure 6. Shielded ^{137}Cs was used as a surrogate for a soil density gauge; both figures show the result of training an algorithm to classify as source or non-source. If the column and the "background" are the same color, the classification is correct; if not, the classification is incorrect. The results of (a) an SVC and (b) an ANN on the same dataset.

ACKNOWLEDGMENTS

We would like to thank Sarah Bender, Emily Jackson, Tom McCullough, and Julia You for their contributions to this work.

REFERENCES

Berndt, R., E. Franke, R. Mortreau, "^{235}U enrichment of UF_6 mass determination on UF_6 cylinders with non-destructive analysis methods," *Nucl. Instrum. Methods Phys. Res. A* **612**, 2 (2010) 309–319.

Hastie, T., R. Tibshirani, J. Friedman, *The Elements of Statistical Learning: Data Mining, Inference, and Prediction*, 2nd Edition, Springer, New York, 2017.

APPENDIX:
MACHINE LEARNING LIBRARIES

1. TensorFlow: https://www.tensorflow.org/
2. TMVA: http://tmva.sourceforge.net/
3. SciKitLearn: http://scikit-learn.org/stable/index.html
4. caret: https://cran.r-project.org/web/packages/caret/index.html
5. e1071: https://cran.r-project.org/web/packages/e1071/index.html

X-Ray Phase Contrast Imaging for Dynamic Material Mix Experiments

LAO-003-17 ■ Continuing in FY 2018 ■ Year 1 of 2

**Daniel J. Clayton,[1,a] David D. Schwellenbach,[a] Craig Kruschwitz,[a]
Dan Stutman,[b] Kevin Tritz,[b] and Pia Valdivia[b]**

[1]claytodj@nv.doe.gov, (505) 663-2153
[a]New Mexico Operations–Los Alamos
[b]Department of Physics and Astronomy, Johns Hopkins University

X-ray phase contrast imaging with transmission gratings for density profile measurements is being developed for dynamic experimental applications. Talbot-Lau deflectometry is a new method of measuring x-ray refraction in addition to attenuation and ultra-small angle scattering that has recently been developed for static imaging, primarily for medical and industrial applications. A flash x-ray source, with a spot size much larger than the continuous microfocus sources of static imaging systems, must be used to obtain density profiles from fast-evolving systems, and only a single exposure can be obtained. The challenges to measuring electron density profiles of two mixed elements from a single-image, low spatial-resolution system are addressed, and initial results from the first of these systems, built and successfully tested on the bench in FY 2017, are presented. This system will be installed on a gas gun and tested during dynamic shock physics experiments in FY 2018.

BACKGROUND

In experiments with dynamically evolving solids, liquids, or high-density plasmas, densities are typically probed with x-ray radiation. This usually takes the form of x-ray radiography, in which x-ray attenuation by a sample is measured and used to infer material density. Alternatively, x-ray phase contrast imaging (PCI), in which the phase shift of x-rays passing through a sample is analyzed, may also be used to infer density, as the index of refraction of x-rays through a sample depends on the density of the material. X-ray PCI has several advantages over traditional radiography, including a linear dependence on density, rather than an exponential dependence, that increases the range of densities over which the technique is applicable for a given x-ray source with a particular spectrum. Also, x-ray attenuation scales

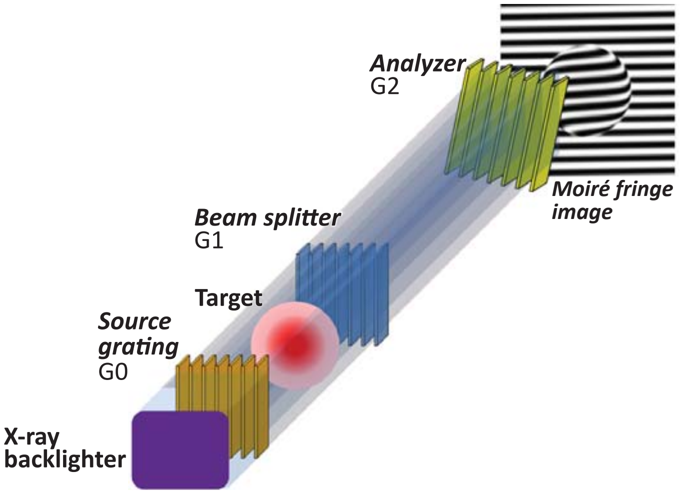

Figure 1. A Talbot-Lau x-ray deflectometer (TXD) with three transmission gratings. G0 and G2 are x-ray amplitude gratings, and G1 is an x-ray phase grating.

more strongly with atomic number Z than PCI; thus, PCI is a more sensitive density diagnostic for low-Z materials. X-ray PCI can thus be used to image low-Z samples using high-energy x-rays that can penetrate high-Z material surrounding the samples.

One potential disadvantage of x-ray phase contrast imaging is the requirement for a coherent, monochromatic light source, historically only available at facilities such as x-ray synchrotrons. Recent advances in the manufacture of x-ray transmission gratings led to the development of Talbot-Lau x-ray deflectometry (TXD) PCI diagnostics, which use compact, incoherent x-ray sources. A Talbot-Lau x-ray deflectometer consists of three transmission gratings with equal, micron-scale slit spacing (Figure 1) (Pfeiffer 2006). The basic principle of the instrument is that spatially coherent, monochromatic light passing through a diffraction grating forms images of the grating at periodic distances. This is referred to as the Talbot effect, and the images are formed at multiples of the Talbot length $z_0 = 2g^2/\lambda$, where g is the slit spacing and λ is the x-ray wavelength. When a sample is placed in front of (or behind) the grating, x-rays deflected by the changing index of refraction create fringe shifts in the image. We refer to this phase grating as the beam splitter, or simply G1.

In the absence of a monochromatic, spatially coherent light source, the Lau effect can be relied upon to simulate such a source while using a polychromatic incoherent source (Jahns 1979). An amplitude grating with the same slit spacing as G1, referred to as the source grating or G0, is placed in front of the x-ray source. Each slit of G0 can be thought of as an individual coherent light source. When placed a Talbot length $z_0 = (\lambda)$ in front of G1, each slit of G1 sees a coherent source of wavelength λ due to constructive interference (Figure 2). With the source grating, it is thus possible to do dynamic x-ray phase contrast imaging in a small lab setting using a compact flash x-ray tube.

Finally, another amplitude grating, referred to as the analyzer or G2 grating, allows micron-scale fringes to be imaged with a standard camera system. The G2 grating also has the same slit spacing as the G0 and G1 gratings and is placed a Talbot length after G1. The grating is rotated about the optical axis by a small angle θ, creating a moiré pattern on the detector. These moiré fringes have a period $p_M \sim g/\theta >> g$. The angle θ can thus be chosen to optimize spatial resolution on the detector.

One major advantage of TXD is that it provides three separate measurements in a single image: x-ray attenuation and ultra-small-angle x-ray scattering (USAXS) are measured in addition to refraction (Pfeiffer 2008). Refraction and attenuation both depend on the line-integrated density of the sample, but with different Z dependencies. The two measurements together can deconvolve the density profiles of a mix of elements. USAXS, caused by micron-scale variations in density, results in a loss of fringe contrast. The effects of all three phenomena on a background fringe pattern are shown in Figure 3.

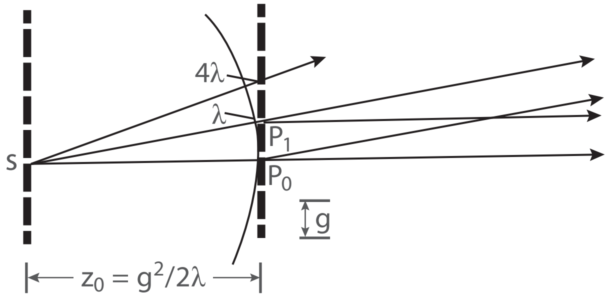

Figure 2. A depiction of the Lau effect, where for a given wavelength λ, coherent light from slits along G0 constructively interfere at the slits along G1, which is placed a Talbot length z_0 away. Image from Jahns 1979.

Simulations with the X-ray WaveFront Propagation (XWFP) code (Weitkamp 2004) show how the densities of two elements can be deconvolved. For this simulation, the x-ray source was a 150 kV tungsten tube filtered with 0.25 mm of uranium for optimal

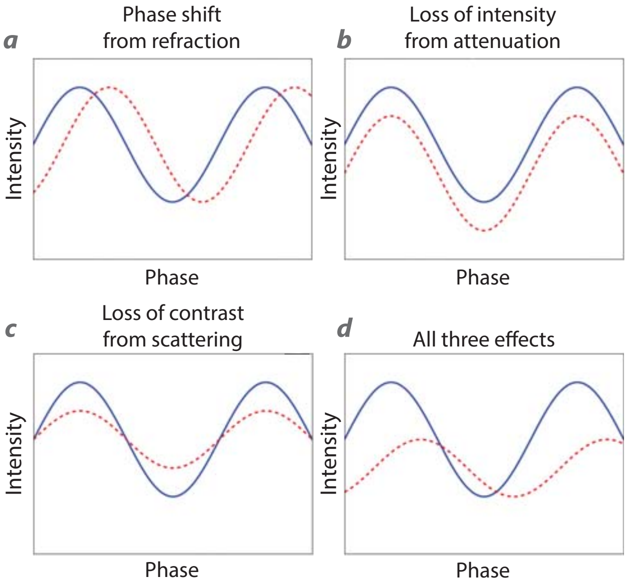

Figure 3. The effects on the background fringe pattern from (a) refraction due to a differential phase shift, (b) attenuation, (c) USAXS, and (d) some combination of the three. The solid blue lines represent the unperturbed background fringe pattern, and the dashed red lines represent changes due to the sample being measured.

imaging at 100 keV. The sample was a 1.5 mm diameter cylinder of mixed material. The resulting TXD images were simulated, and the ratios of attenuation to phase shift for the middle 50% of the cylinders were computed and plotted as a function of elemental fractions. Both the simulated images and resulting ratio curves are shown in Figure 4. These ratio curves, or those obtained from measurements of known samples, can then be used to determine the densities of two elements in an unknown mix independently.

While TXD has only been considered for static imaging, except in a few unique cases (Valdivia 2016), dynamic PCI is only performed at synchrotrons. Dynamic experiments introduce new challenges to TXD. Typically, these systems achieve high spatial resolution by using continuous, microfocus x-ray sources with spot sizes less than 10 µm. By comparison, commercially available flash x-ray sources typically have a spot size greater than 1 mm. Previous TXD systems have used phase scanning (Pfeiffer 2008) or fringe scanning (Momose 2006) to obtain separate images of refraction, attenuation, and USAXS. These methods require at least three exposures of the same static object, precluding their use for dynamic experiments. A single exposure also limits photon statistics, reducing the usefulness of single-image fringe-fitting routines. Additionally, flash x-ray sources typically have larger shot-to-shot variability in dose and spectra, and require labor-intensive anode replacements between shots.

In addition to the challenges inherent in all dynamic experiments, many experiments of interest have more issues. Many of these experiments have high densities, and the flash x-ray sources used for radiography have end-point energies higher than those typically used in TXD. The absorption gratings can become transparent to the high-energy tail of the source spectra, reducing the contrast of the diagnostic. Additionally, many experiments of interest generate their own x-rays that produce a background on the measured signal. TXDs deployed on these experiments will require shielded, gated cameras to reduce background. Another possible

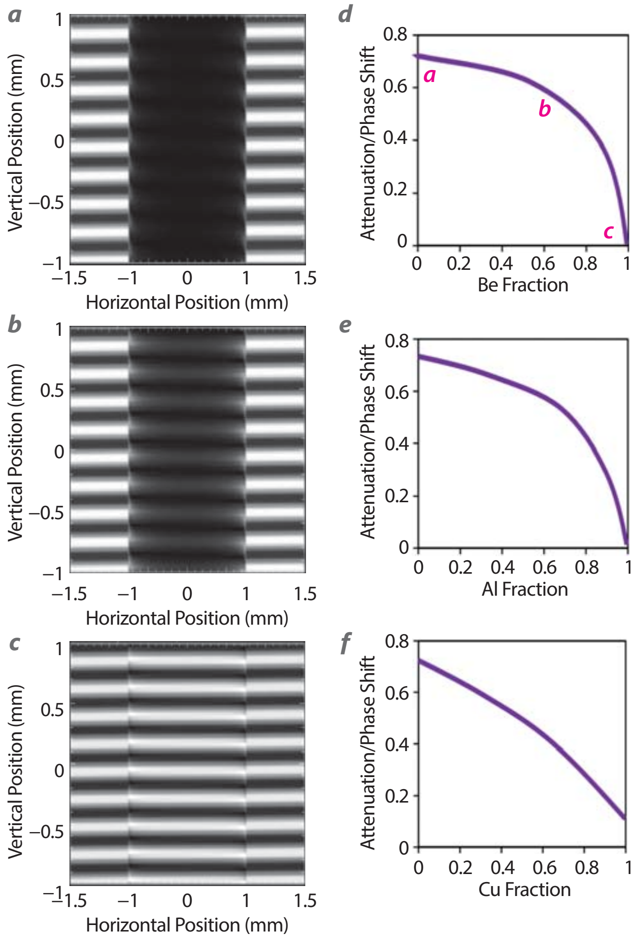

Figure 4. Simulated deflectometry images for (a) pure uranium (U), (b) a mix of 60% beryllium (Be) and 40% U, and (c) pure Be; and the ratios of attenuation to phase shift calculated from simulated images for mixes of (d) Be+U, (e) aluminum (Al)+U, and (f) copper (Cu)+U. Letters on (d) correspond to the images (a), (b), and (c) used to calculate these points.

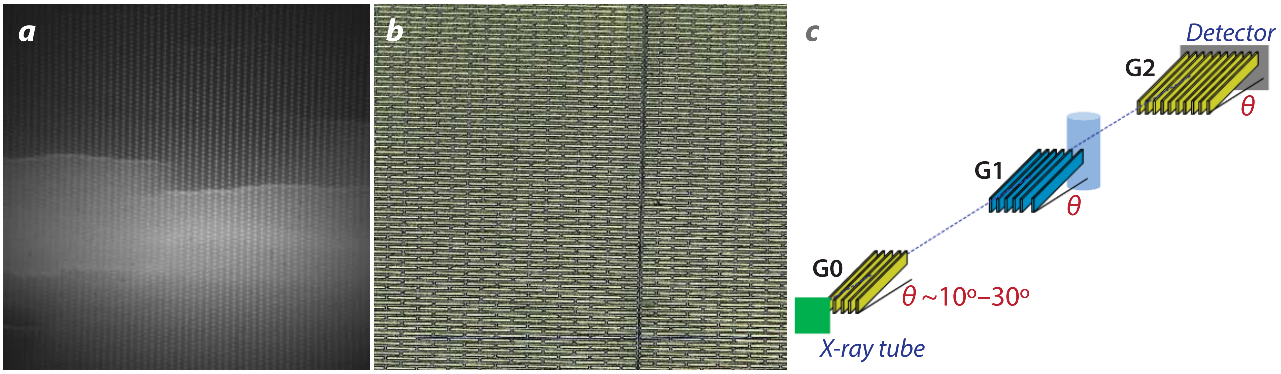

Figure 5. (a) X-ray radiograph, (b) microscope picture of G2 grating, and (c) glancing angle configuration with gratings rotated to increase their effective thickness

solution to reducing x-ray background is to use spectral filtering with multi-layer x-ray mirrors, which will be tested if backgrounds indeed prove bright enough to prohibit accurate density measurements in future experiments. The purpose of this project is to address all of these challenges.

PROJECT

Preliminary studies were performed using a traditional TXD with continuous x-ray source at Johns Hopkins University (JHU). New G0 and G2 absorption gratings were obtained from Microworks GmbH and first tested on this continuous system. Addressing the challenge of using sources with higher end-point energies than are typical, these gratings, with a thickness of 240 µm and slit spacing of 4.8 µm, have an aspect ratio 240/4.8 = 50, greater than any that have previously been produced. These absorption gratings were more difficult to manufacture than the more common lower-aspect-ratio gratings, and microscopy and x-ray radiography revealed a few irregularities (Figure 5). When paired with a previously used G1 phase grating with the same 4.8 µm slit spacing, tests on the JHU continuous TXD demonstrated that these irregularities were not severe enough to inhibit the formation of fringes on resulting images. To further increase the effective thickness of the gratings and thus the fringe contrast of the resulting image, the gratings were placed in a glancing angle configuration (Figure 5), an idea previously patented by JHU (Stutman 2012). The following results were obtained with a glancing angle of $\alpha = 23.5°$; the gratings had an effective thickness of 600 µm.

Preliminary work with the continuous x-ray source at JHU also included studies of the scintillators that will be required for experiments that generate an x-ray background. These scintillators must be bright, have a short decay time, and provide sufficient spatial resolution. Three candidate scintillators were tested: cesium iodide (CsI), lutetium oxyorthosilicate (LSO), and rare-earth garnet $(\mathrm{GdxLu1\text{-}x})^3(\mathrm{GayAl1\text{-}y})^5\mathrm{O}_{12}$:Ce (GLuGAG). CsI provided the best images, with the highest brightness and the best spatial resolution, but the decay time (~1 µs) was deemed too long for most applications. LSO proved to be too dim to produce a useful image at the x-ray energies and doses of interest. This left GLuGAG as the best candidate available. With a short decay time (<100 ns) and sufficient brightness (48,200 photons/MeV at 662 keV) (Wu 2015), the biggest concern with using single-crystal ceramic GLuGAG was the spatial resolution. After finding a 1 mm thick sample of GLuGAG to have a spatial resolution of about 650 µm, Radiation Monitoring Devices, Inc. (RMD), developed new manufacturing techniques to produce thinner crystals. When tested, a 500 µm thick GLuGAG crystal produced an image with near-identical brightness to the thicker crystal but with a spatial resolution of about 460 µm. RMD is now developing even thinner GLuGAG samples for us to test.

One final preliminary study with the continuous source was to conduct the first-ever test of an asymmetric, glancing angle TXD. With a large x-ray source spot size, the spatial resolution of the system can be maximized by building a low-magnification, asymmetric deflectometer in which $L > D$, where L is the distance between G0 and G1, and D is the distance between G1 and G2. In this case, the grating slit spacings differ: $g_0 \neq g_1 \neq g_2$. While asymmetric systems have previously been tested in standard grating configurations, this had not been tried before in a glancing angle configuration. A static benchtop test of an asymmetric, glancing-angle deflectometer was performed using 10 keV x-rays and a glancing angle of $\alpha = 51°$, where α is the angle between the plane of the grating and the optical axis of the system.

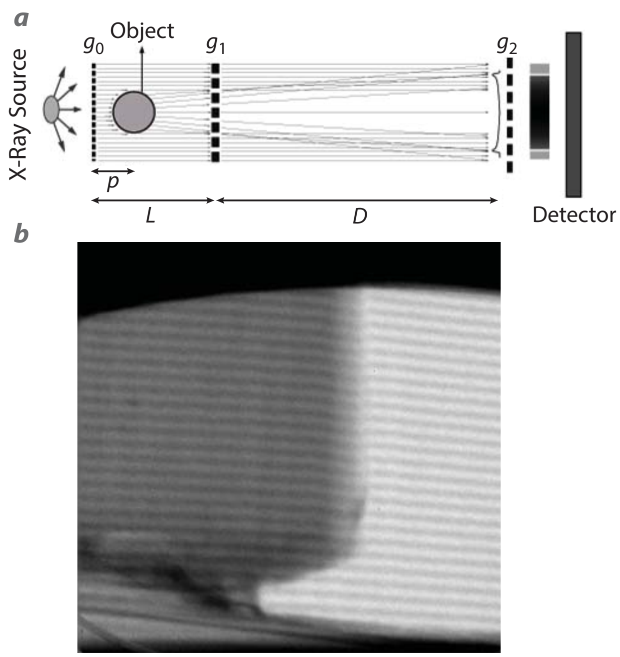

Figure 6. (a) Asymmetric TXD setup and an (b) image of a solid beryllium sample with fringe shifts and attenuation clearly visible

The system was asymmetric, with $L = z_0 = 9.7$ cm, $D = 5$, $z_0 = 48.4$ cm, $g_0 = 2.4$ µm, $g_1 = 4$ µm, and $g_2 = 12$ µm. (Figure 6a). The Talbot order of the system, defined as the number of Talbot lengths between G1 and G2, was $m = 5$. A sample image taken with this system is shown in Figure 6b.

The first TXD system to be used for dynamic experiments was set up on a laboratory bench for initial tests and characterizations. The flash x-ray source is based on a Platts design (Platts 1995) and produces 20 ns pulses with a 25 mrad dose at 1 m and an endpoint energy of 250–300 keV. Molybdenum and tungsten anodes were tested, with all subsequent results obtained with tungsten anodes. The x-ray diode head was set up at one end of an optical breadboard, and the x-ray system was controlled from an adjacent, shielded control room. The gratings were installed on rotational stages along the optical axis that could also be controlled remotely from the control room, and G1 was additionally mounted on a manual linear stage that was used to place it precisely equidistant from G0 and G2. The final spacing between the gratings was 62.5 cm. Finally, a Photometrics CH350 camera fiber-coupled to a P43 phosphor with ~150 µm spatial resolution was installed at the far end of the optical breadboard and used for initial bench tests.

The 240 µm thick G0 and G2 gratings strongly collimated the x-ray beam, and the rotation of each of these gratings was easily aligned by overlapping the bright bands produced on the imaging system by each one. The position and rotation of G1 could then only be aligned by scanning them in very small steps until fringes appeared on the resulting image. Flash x-ray anodes need to be replaced once every 30 to 50 shots, so several weeks are sometimes required to align a TXD system with them; a secondary, continuous x-ray source will be included in future dynamic TXD systems for alignment purposes. Once initial alignment was achieved, it was stable shot to shot, and the sensitivity of the alignment was tested by carefully scanning G1 translation and rotation to map out the boundaries in which fringes could be obtained. It was determined that to measure fringes, the spacing of G1

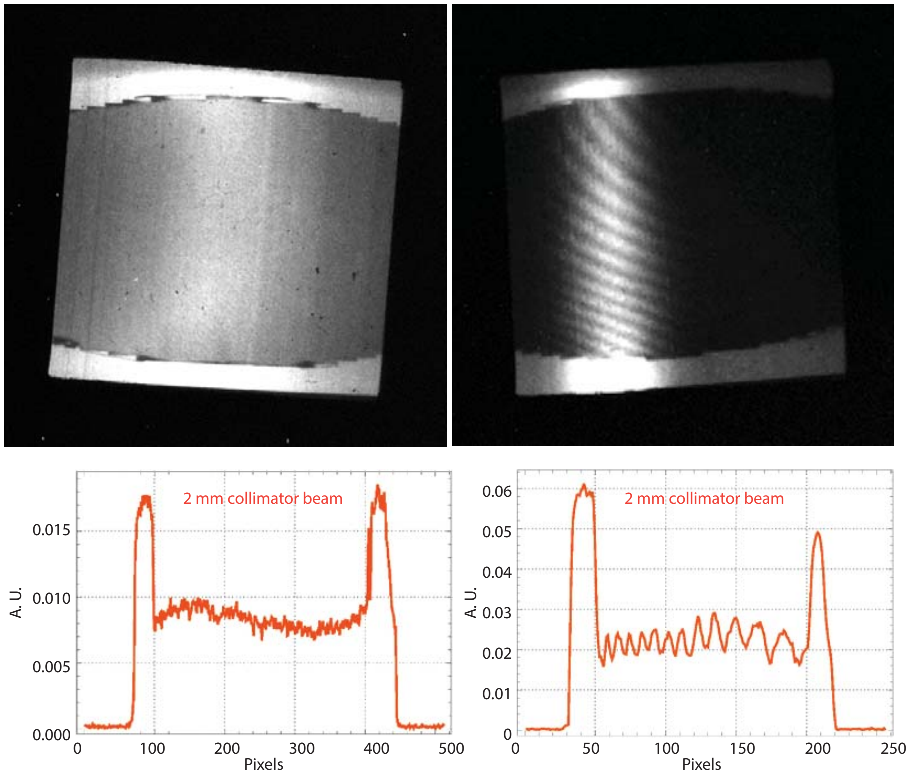

Figure 7. Unprocessed images and lineouts of images taken with 100 µm thick and 240 µm thick gratings

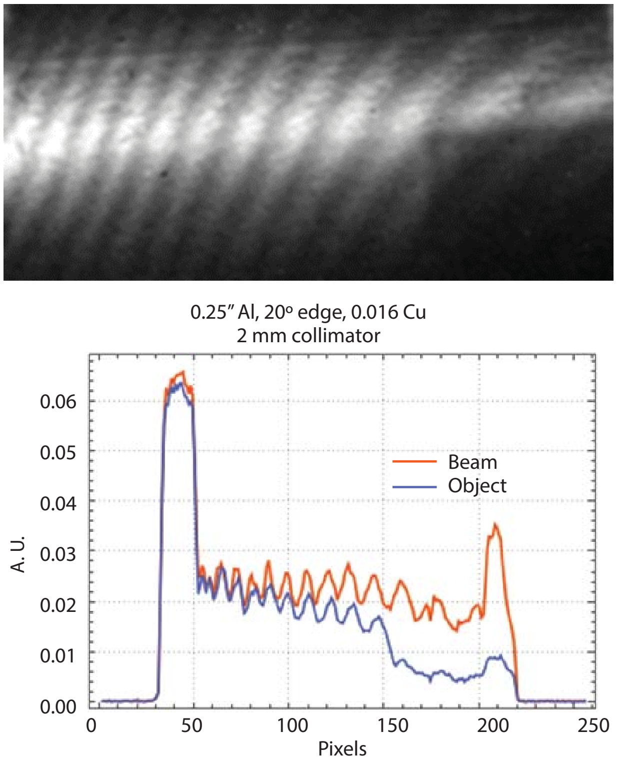

Figure 8. Unprocessed image and lineout from image compared to image without objects

between G0 and G2 must be within about 2 mm and the rotation of G1 must be within about 2 arcminutes of a degree.

Initial images with and without static test objects were collected, and a preliminary analysis was performed. In addition to the 240 µm thick gratings, 100 µm thick gratings at the same 23.5° glancing angle for an effective thickness of 250 µm, were tested for comparison. In baseline images without a test object, collimation from the thick gratings limited the field of view along the horizontal axis, the direction perpendicular to the grating slits, to 7 mm (Figure 7). Fringe contrast, defined as $(I_{max} - I_{min}) / (I_{max} + I_{min})$ where I_{max} and I_{min} are the maximum and minimum intensities of the fringes, was about 17% in these images. By comparison, the 100 µm thick gratings did not limit the effective field of view but produced a fringe contrast of only 3% that was sometimes lost in the noise. In this case the field of view was limited to the size of the imager.

Raw, unprocessed images of an aluminum wedge and copper foil are shown in Figure 8. As expected, the aluminum wedge both attenuates the image and produces a fringe shift. The region of the image covered by the copper foil is strongly attenuated. Comparisons between subsequent shots show that the fringes are extremely stable shot to shot, allowing for easy comparison between experimental images and reference images. This also allows for the averaging of several images for improved photon statistics, though this method could not be used on dynamic experiments. Apertures were tested to see if they could improve the spatial resolution of the images. When a 2 mm aperture was placed on the x-ray diode head, the overall intensity of the image did not change, indicating that the spot size of the source was ≤2 mm. When a 1 mm aperture was installed, the dose dropped significantly and the fringes became noisy (Figure 8). Other aperture sizes will be tested in subsequent experiments.

Preliminary tests have shown that forward modeling, in which deflectometer images are computed from given density profiles and then fit to the raw data, produce more reliable results than the fringe-fitting routines used on high-dose, high-resolution static images. Furthermore, forward modeling has proven to be more robust when experimental images are first deconvolved into separate refraction, attenuation, and USAXS images using Fourier transforms. Both the refraction and attenuation images can then be fit. The experimental data are deconvolved by first applying a 2-D Fourier transform to the image. The attenuation image is simply taken from the absolute value of the

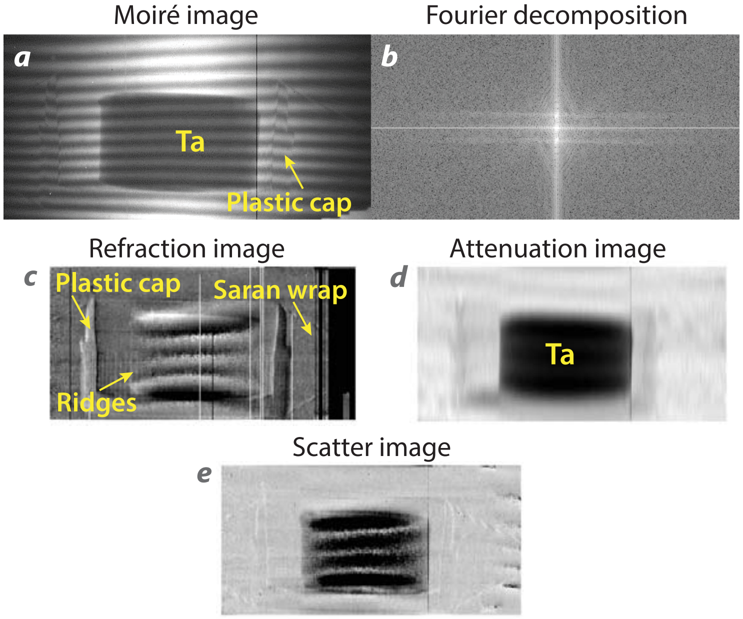

Figure 9. Images of a tantalum aerogel sample, showing (a) raw data with moiré fringes, (b) Fourier decomposition of the raw image, (c) refraction, (d) attenuation, and (e) USAXS

Fourier transform over the interval ±1/2p_M, where again p_M is the moiré period. The refraction image is obtained by taking the argument, or phase shift, of the Fourier transform over the interval of ±1/2p_M about the frequency p_M. While not used in density profile calculations, an USAXS image may be obtained by taking the ratio of the absolute values of the Fourier transforms over these two intervals. Results from a Fourier transform of an experimental image of a static object are shown in Figure 9.

CONCLUSION

Initial tests of a TXD system on a benchtop were successful, and testing and characterization of the system will continue, along with development of the data analysis tools. The system will then be installed on a gas gun experiment to perform dynamic measurements for the first time on shock physics experiments. Results to date were presented at the X-Ray and Neutron Phase Imaging with Gratings 2017 (XNPIG17) meeting held September 11–15, 2017, in Zurich, Switzerland, and a manuscript of this work is being prepared for publication. Three experimental facilities at Los Alamos National Laboratory are interested in their own dynamic TXD systems: DARHT for measuring the density profiles of plasma plumes created when high-intensity electron beam pulses strike a bremsstrahlung target, proton radiography for measuring material mixing in weapon-relevant experiments, and the Chemistry Division for measuring shock waves in detonators in which insensitive high explosives are surrounded by aluminum capsules.

REFERENCES

Jahns, J., A. W. Lohmann, "The Lau effect (a diffraction experiment with incoherent illumination)," *Opt. Commun.* **28**, 3 (1979) 263–267.

Momose, A., W. Yashiro, Y. Takeda, Y. Suzuki, T. Hattori, "Phase tomography by X-ray Talbot interferometry for biological imaging," *Jpn. J. Appl. Phys.* **45**, 6A (2006) 5254–5262.

Pfeiffer, F., T. Weitkamp, O. Bunk, C. David, "Phase retrieval and differential phase-contrast imaging with low-brilliance X-ray sources," *Nat. Phys.* **2**, 4 (2006) 258–261.

Pfeiffer, F., M. Bech, O. Bunk, P. Kraft, E. F. Eikenberry, Ch. Brönnimann, C. Grunzweig, C. David, "Hard-x-ray dark-field imaging using a grating interferometer," *Nat. Mater.* **7**, 2 (2008) 134–137.

Platts, D., M. P. Hockaday, D. Beck, W. Coulter, C. R. Smith, "Compact flash x-ray units," Tenth IEEE International Pulsed Power Conference, Albuquerque, New Mexico, July 3–6, 1995, 892–896.

Stutman, D., M. Finkenthal, "Glancing angle Talbot-Lau grating interferometers for phase contrast imaging at high x-ray energy," *Appl. Phys. Lett.* **101**, 9 (2012) 091108-1–091108-5.

Valdivia, M. P., D. Stutman, C. Stoeckl, W. Theobald, C. Mileham, I. A. Begishev, J. Bromage, S. P. Regan, "An x-ray backlit Talbot-Lau deflectometer for high-energy-density electron density diagnostics," *Rev. Sci. Instrum.* **87**, 2 (2016) 023505.

Weitkamp, T., "XWFP: An X-ray wavefront propagation software package for the IDL computer language," *Proc. SPIE* **5536** (2004) 181–189.

Wu, Y., Z. Luo, H. Jiang, F. Meng, M. Koschan, C. L. Melcher, "Single crystal and optical ceramic multi-component garnet scintillators: A comparative study," *Nucl. Instr. Meth. Phys. Res. A* **780** (2015) 45–50.

This page left blank intentionally

X-Ray Doppler Velocimetry

LO-004-16 ■ Continuing in FY 2018 ■ Year 2 of 3

**Jeffrey A. Koch,[1,a] James A. King,[a] Richard R. Freeman,[a]
Eric C. Dutra,[a] and Eric Huffman[a]**

[1]kochja@nv.doe.gov, (925) 960-2525
[a]Livermore Operations

We are developing a novel technique, x-ray Doppler velocimetry (XDV), for measuring bulk fluid motion in materials particularly applicable to very hot, x-ray–emitting plasmas in the high-energy density physics (HEDP) regime. The XDV technique relies on monochromatic imaging in multiple x-ray energy bands near the center of an x-ray emission line in a plasma using bent imaging crystals. Higher-energy bands are preferentially sensitive to plasma moving towards the viewer, while lower-energy bands are preferentially sensitive to plasma moving away from the viewer. Combining multiple images in different energy bands allows for a reconstruction of the fluid velocity field integrated along the line of sight. In the second year of research, we designed, fabricated, and partially assembled and tested a new dual-crystal imaging instrument. This instrument will be used to demonstrate the XDV concept in experiments at the Sandia National Laboratories Z-Beamlet Facility, and we will also use it at the University of California, San Diego's plasma pinch machines in FY 2018.

BACKGROUND

After several years of focused effort, the National Ignition Campaign (NIC) at the National Ignition Facility (NIF) (Miller 2004) ended in 2012 without achieving the goal of ignition and thermonuclear burn in the laboratory (Lindl 2014). The reasons for this failure are not understood, and a variety of possible explanations have been given, but it is likely that bulk fluid motion in the compressed hot spot (Spears 2014) is contributing to the failure. Bulk fluid motion serves as an energy sink, trapping implosion kinetic energy that could otherwise transfer to thermal heating and neutron production. Currently, there are no diagnostics that quantify bulk fluid motion in the hot spot, and this gap between needs and capabilities motivated the x-ray Doppler velocimetry (XDV) project (Koch 2017a).

Astronomers have long used multi-spectral imaging at radio frequencies to measure bulk motion of gas clouds, for example, in distant galaxies (Shu 1982),

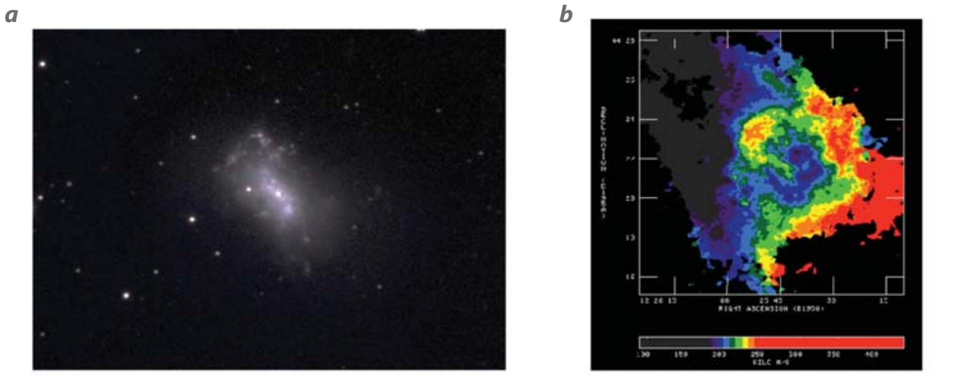

NGC 4449, white-light visible map

NGC 4449, multispectral microwave map

Figure 1. (a) White-light telescope image of galaxy NGC 4449 compared with (b) a multispectral color-coded microwave image of the same galaxy. The multispectral image shows large-scale rotation of gas, suggestive of an ancient merger between counter-rotating galaxies, which is important information that is not present in the white-light image.

and the power of this technique is shown in Figure 1. There, Doppler frequency shifts of the 21 cm hyperfine transition in neutral hydrogen provide information on motion of the emitting atoms, and combining spectroscopy and imaging (multi-spectral imaging) allows a map of gas cloud motion to be generated that shows bulk rotation.

An analogous instrument that can measure Doppler energy shifts of x-rays emitted by plasmas, locally in imaging mode, would allow bulk motion in the plasma to be diagnosed. We intend to accomplish this using near-normal-incidence spherical bent crystals that are already widely used for quasi-monochromatic x-ray imaging applications (Pikuz 1995, Aglitskiy 1998, Uschmann 2000, Koch 2003, Akli 2011, Stoeckl 2012). These systems can provide very large collection solid angles when the angle of incidence is close to normal and the crystal quality is high, and can be very efficient when used with narrow-band emission line sources (Koch 1998). Use of multiple crystals, each tuned to a slightly different energy band, allows a map of fluid velocity (averaged along the line of sight) to be generated, and this is the essential concept behind XDV.

The basic geometry of XDV is shown in Figure 2. Several identical bent imaging crystals (five are shown here), with the same interplanar spacing d, are arranged to view a plasma along a near-common line of sight, and each is configured with a slightly different Bragg angle θB. The Bragg equation $\lambda = 2d\sin\theta_B$ implies that the center bandpass of each crystal falls at a slightly different wavelength λ and therefore a different energy *E*. If we configure the range of energies to run from the red wing to the blue wing of the unshifted center of an x-ray emission line from the plasma, then five quasi-monochromatic images will be generated that emphasize velocities corresponding to the Doppler shifts of the centers of the pass bands of the five crystals. This is shown schematically in Figure 3. Here, the number of crystals is arbitrarily chosen to be five. A lower bound is two crystals, the minimum necessary to show differences between images, while an upper bound will be limited by the complexity of the instrument and ultimately by view differences between lines of sight, necessary due to the non-zero dimensions of the crystals and mounting fixtures. More details on the XDV technique, as well as simulation results, have been published elsewhere (Koch 2017b).

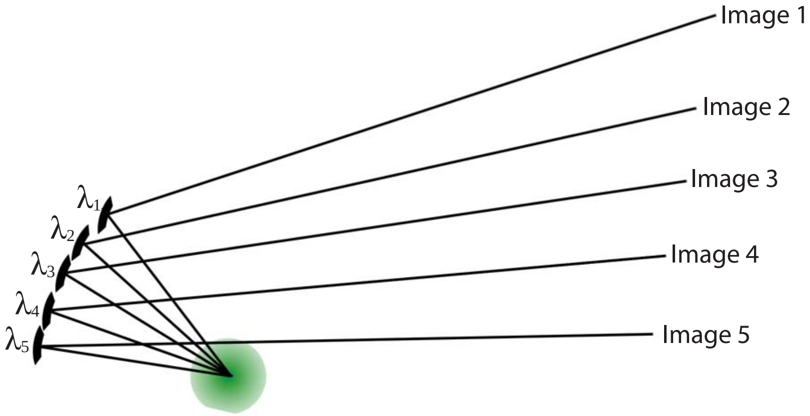

Figure 2. Sketch of one possible implementation of XDV. Here, five identical imaging crystals project five separate images of the source onto a detector. Each crystal is sensitive to different x-ray energies in closely spaced bands near the center of an emission line from the source. Combining the images, for example by color coding, would result in a multi-spectral image similar to that shown in Figure 1b.

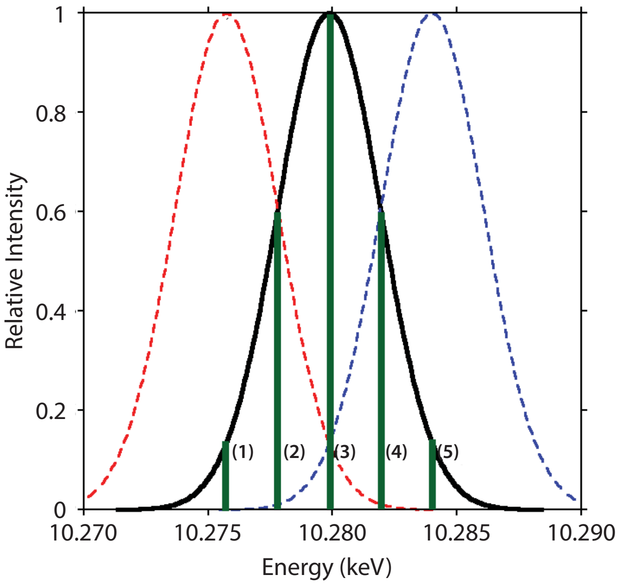

Figure 3. Sketch of the center energy distribution of the crystals shown in Figure 2. An unshifted line would appear brightest in the middle crystal (3). If the source were moving toward the crystal, the line would shift to the right, and the source would appear brightest in the blue-tuned crystal (5), while if the source were moving away from the crystal, the source would appear brightest in the red-tuned crystal (1).

PROJECT

In the second year of the XDV project, we focused on two main issues: Proof-of-principle experiments and the development of a backwards analysis procedure we can use to extract an object velocity map from multiple XDV images. First, we will describe plans and progress towards proof-of-principle experiments at the Sandia National Laboratories (SNL) Z-Beamlet Facility (ZBL). We will then describe how we expect to analyze XDV data from these experiments.

In 2016, SNL constructed a two-crystal x-ray imaging system (Harding 2017), with two wide and widely separated bands intended to provide images of a cobalt-doped Z-produced plasma in the light of cobalt (Co) He-α line emission (7242 eV center, with a 13 eV bandwidth including the entire emission line width) and in the light of continuum emission in a band centered far from the He-α emission line (7265 eV, also with a 13 eV bandwidth). The goal was to map the 2-D location of Co line emission by subtracting the continuum image from the line emission image. A drawing of the system is shown in Figure 4. The system mounts two spherically bent germanium (Ge) (3,5,5) crystals, and two Rowland Circle (RC) apertures next to alignment lasers, on a ring surrounding the target plasma at the center. Each crystal casts an image of the plasma onto a common image plate detector approximately 1 meter away from the target.

This configuration is very nearly a two-crystal version of XDV, so we have decided to redesign the SNL two-crystal system to yield sensitivity to fluid motion while maintaining the same basic geometry. We did this by (1) moving the band center energies much closer together so that they are both within the Co He-α line width, (2) narrowing the bandwidths of the images produced by the crystals, and (3) redesigning the alignment system so that we can reliably select two very closely spaced center energies. We have obtained agreement from SNL to provide beam time at the ZBL laser facility in order to execute these experiments, and the dramatically lower target energy compared with Z, and the much smaller plasma source size, allow us to operate without RC apertures.

A drawing of our new XDV imaging system is shown in Figure 5. We reproduced the ring configuration of the current SNL system, mounting it to a flat base for use in ZBL, but made a number of modifications. First, each crystal mount is broadly adjustable in azimuth, over a range sufficient to cover all realistic Bragg angle choices consistent with imaging x-rays in the Co He-α spectral region with spherical Ge (3,5,5) crystals, by means of a rotation axis passing through the center of the surface of the crystal. The SNL instrument uses flexure mounts with minimal adjustments, pivoting on axes not in the tangent plane of the crystal surface at the center, and uses a different

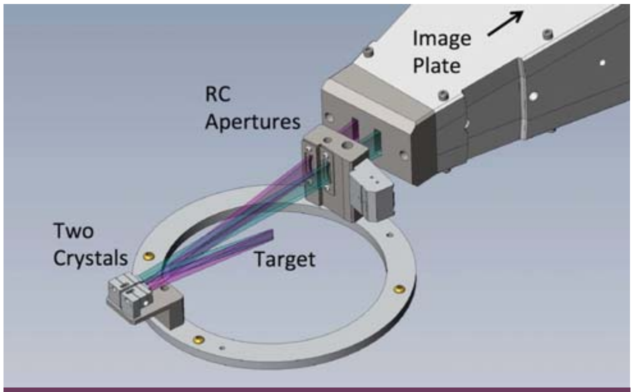

Figure 4. Sketch of the dual-crystal imaging system built by SNL. Target x-rays illuminate two crystals, and each crystal casts an image through a Rowland Circle (RC) aperture onto a distant image plate detector. Alignment lasers mounted next to the apertures aid in correctly adjusting the Bragg angles of the crystals.

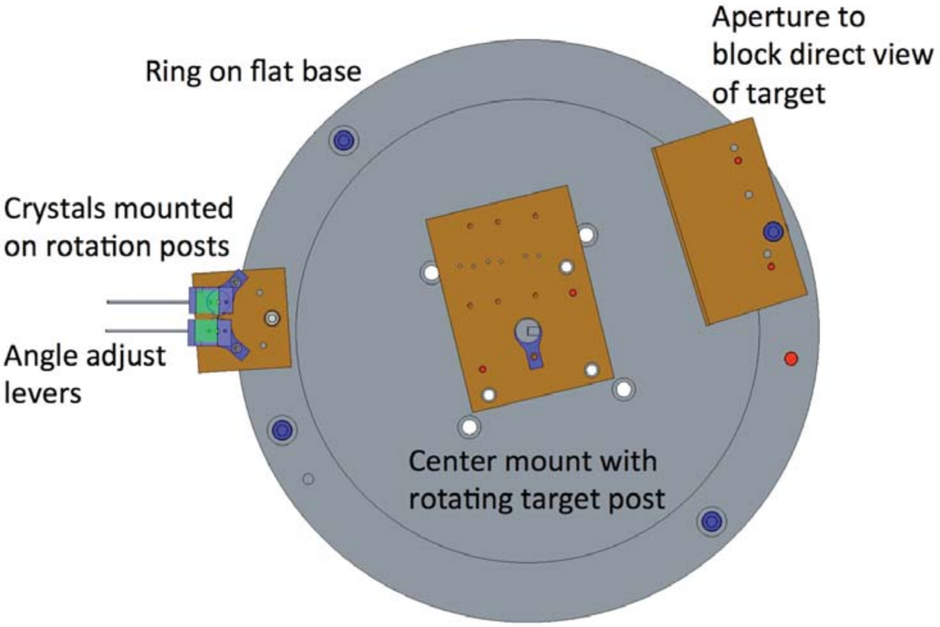

Figure 5. Top view of the ZBL XDV instrument. The laser irradiates the target post from the top of the drawing, and x-rays from the target reflect off each of the two Ge (3,5,5) crystals to form images through the aperture block onto a distant image plate detector that is not shown. The crystal azimuth angles are adjusted using removable lever posts shown at the left.

flexure for each choice of center energy. Second, we are restricting the bandpass of the crystals by means of apertures placed at the crystal surfaces, instead of reflecting off the entire crystal surface and restricting bandpass by aperturing on the RC. RC apertures are necessary for imaging large (many mm) sources, and are important for reducing damage to the detector in high-energy target shots at Z, but neither of these considerations are important for laser-produced plasma experiments at ZBL. Finally, we have redesigned the alignment system, and use a point-like fiber-coupled laser placed at the target location to illuminate the crystals and cast shadows of the apertures onto a reflective reticle (Figure 6). The reticle is placed at a predetermined location where the shadows of the aperture edges coincide as the reflected beams cross at a crossover point. Changing center energies requires only repositioning the reticle to a new crossover point and adjusting the azimuth angles of the crystals until the aperture shadows superimpose at the new predetermined location.

The XDV imaging system is undergoing final fabrication and procurement, assembly, and testing. After completion it will be shipped to SNL for ZBL experiments as their schedule permits. The experiment will be a simple A/B comparison, viewing two experiments with the same system configuration. One experiment will use a target rotated to send the ablation plasma towards the crystals, generating blue-shifted x-ray emission, and the other experiment will send the ablation plasma perpendicular to this viewing angle. We expect velocities of up to 300 km/s based on previous experimental measurements of Doppler shifts from laser ablation plasma (Hall 2017), so we will initially view at two energies corresponding to no velocity (7242 eV, line center) and to 260 km/s blue shift (7248 eV). The results of these experiments will be published elsewhere.

The XDV images will be analyzed to infer the plasma velocity distribution. This problem is complex and constitutes a research topic, given line-of-sight integration, uncertainties in local plasma temperature and density, finite crystal bandwidths, uncertainties in band center energies and crystal reflectivity, and other factors. Nevertheless, by making some reasonable assumptions, we expect to be able to generate quantitative line-of-sight velocity distribution maps from a two-crystal system.

We first assume the emission line is isolated and has a Gaussian functional form characterized by a spatially varying FWHM $\Delta(x,y)$ and a line-center energy E_0. We also assume that the crystal bandwidths are negligibly small, the spatially dependent crystal integrated reflectivity ratio $C(x,y) = R_2(x,y)/R_1(x,y)$ is known, and the central energies E_1 and E_2 are known. In this case, we can calculate the shifted line-center energy $E'(x,y)$ using the ratio map of the two image intensities, $R(x,y) = I_2(x,y)/I_1(x,I)$,

$$E'(x,y) = \frac{\dfrac{\Delta^2(x,y)\ln(C(x,y)R(x,y))}{4\ln 2} + E_2^2 - E_1^2}{2(E_2 - E_1)}. \qquad (1)$$

The local line-of-sight velocity $v(x,y)$ follows simply from the Doppler shift equation,

$$\frac{v(x,y)}{c} = \frac{E'^2(x,y) - E_0^2}{E'^2(x,y) + E_0^2}, \qquad (2)$$

where positive velocities are towards the crystal.

We have explored the importance of the assumptions made above through analysis of a variety of simulated images, generated from a plasma model described elsewhere (Koch 2017b) with peak fluid velocities in excess of 300 km/s. We concentrate on the difference map $\Delta v(x,y)$ between the calculated velocity field $v(x,y)$ and the known velocity field $v_0(x,y)$ at the time of peak emission, and especially the mean value of this map $<\Delta v>$.

Using two monochromatic snapshot (time of peak emission) images at known energies, with $C(x,y) = 1$ and $\Delta(x,y) =$ constant, and ignoring geometrical optics aberrations, yields $<\Delta v> = 10^{-10}$ km/s. This very small number derives from roundoff errors in the coding, and serves as a check on the basic accuracy of the mathematics and the code.

Next, we successively introduced more realism into the simulated images. Using actual local values $\Delta(x,y)$ to generate the images, but using the intensity-weighted spatial average value Δ_{avg} in the analysis, gave $<\Delta v> = 0.2$ km/s. Replacing the perfect images with realistic geometrical ray trace images from crystals having realistic bandwidths yields $<\Delta v> = 0.5$ km/s. Finally, working with time-integrated images instead of snapshots, and with a space- and time-averaged value of Δ_{avg}, yields $<\Delta v> = 5$ km/s and maximum local differences $|v(x,y) - v_0(x,y)|/v_0(x,y)$, averaged over 10 µm spatial regions, of 10%.

We conclude that the simple analysis procedure of Equations 1 and 2 suffices to provide velocity maps accurate to 10% over 10 µm spatial regions, even using time-integrated image data from realistic crystals having realistic bandwidths, provided we also have a space- and time-averaged spectral line width from a high-resolution spectrometer, so that we can substitute this value Δ_{avg} for $\Delta(x,y)$ in Equation 1.

This result drives the desire to couple XDV with simultaneous high-resolution spectroscopy data, an important consideration for future development. Finally, based on these results, we expect that even non-Gaussian line profiles can be analyzed in a similar manner, provided that the line shapes are measured, do not qualitatively change very much across the image field, and can be parametrized by a small number of variables. This again argues for coupling high-resolution spectroscopy with XDV, in order to provide the best quantitative accuracy in the resulting velocity distribution maps.

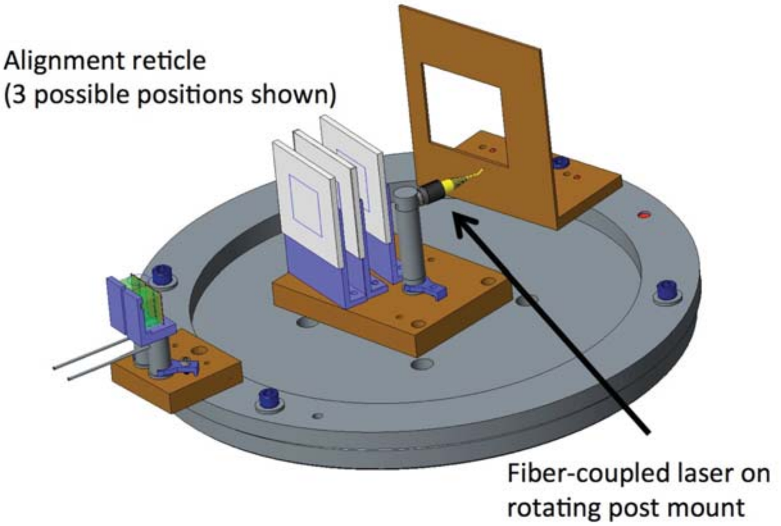

Figure 6. Side view of the ZBL XDV instrument, as configured for alignment. A single-mode fiber-coupled laser emits a beam from a point at the target location, and the shadows of the apertures in front of the crystals superimpose on a reticle that can be placed in several predetermined locations (three are shown). After the crystals are aligned, the reticle and laser are removed, and the laser post is replaced by the target post.

CONCLUSION

We have described a novel technique for measurement of bulk fluid motion in materials that is particularly applicable to very hot, x-ray–emitting plasmas in the HEDP regime. This XDV technique relies on monochromatic imaging in multiple x-ray energy bands near the center of an x-ray emission line in a plasma using bent imaging crystals. Combining multiple images in different energy bands allows for a reconstruction of the fluid velocity field integrated along the line of sight.

In the second year of the project, we designed, fabricated, and partly assembled and tested a new dual-crystal imaging instrument we will use to demonstrate the XDV concept in experiments at ZBL in FY 2018. This instrument will use two Ge (3,5,5) spherically bent crystals, which have already been procured, to image a Co laser–produced plasma onto an image plate detector. We expect these experiments to be performed in Fall 2017, and we expect that they will successfully prove the XDV concept and allow plasma fluid velocity flow fields to be measured in two dimensions for the first time using a data analysis procedure we developed. In the third year, we expect to take the SNL instrument to the University of California, San Diego, and use it to perform physics experiments with their plasma pinch machines. We may also field the instrument on experiments at the University of Nevada, Reno, Nevada Terawatt facility.

We have submitted one technology abstract on the XDV concept, "Method for imaging bulk motional velocities in plasmas" (March 16, 2015). The concept was awarded a provisional patent and has been submitted to the U.S. Patent and Trademark Office as a full patent application (Koch 2016). In the second year of the project, progress was reported at an inertial confinement fusion diagnostic workshop at LLNL, a technical seminar at DOE headquarters, and an SDRD External Advisory Board meeting. Two invited talks were presented at the Radiative Properties of Hot Dense Matter conference in Santa Barbara, and the SPIE: Optics and Photonics Conference in San Diego. A refereed journal article was also published (Koch 2017b).

ACKNOWLEDGMENTS

We thank our collaborators J. Field, G. Hall, and J. Kilkenny at LLNL; E. Harding, G. Rochau, and J. Porter at SNL; A. Covington at the University of Nevada, Reno; and F. Beg at the University of California, San Diego, for their contributions and support.

REFERENCES

Aglitskiy, Y., et al., "High-resolution monochromatic x-ray imaging system based on spherically bent crystals," *Appl. Opt.* **37** (1998) 5253–5261.

Akli, K. U., et al., "A novel zirconium Kα imager for high energy density physics research," *Rev. Sci. Instrum.* **82** (2011) 123503.

Hall, G. N., Lawrence Livermore National Laboratory, private communication (2017).

Harding, E., Sandia National Laboratories, to be published (2017).

Koch, J. A., et al., "High-energy x-ray microscopy techniques for laser-fusion plasma research at the National Ignition Facility," *Appl. Opt.* **37** (1998) 1784–1795.

Koch, J. A., et al., "4.5- and 8-keV emission and absorption x-ray imaging using spherically bent quartz 203 and 211 crystals," *Rev. Sci. Instrum.* **74** (2003) 2130.

Koch, J. A., "Methods and systems for imaging bulk motional velocities in plasmas," U.S. Patent Application 15/090,408, filed April 4, 2016, following U.S. Provisional Patent 62/142,985.

Koch, J. A., E. C. Dutra, R. R. Freeman, M. J. Haugh, J. A. King, "X-ray Doppler velocimetry," in *Site-Directed Research and Development*, FY 2016, National Security Technologies, LLC, Las Vegas, Nevada, 2017a, 173–178.

Koch, J. A., et al., "X-ray Doppler velocimetry: An imaging diagnostic of 3D fluid flow in turbulent plasma," *High Energy Density Physics* **23** (2017b) 184–187.

Lindl, J., O. Landen, J. Edwards, E. Moses, NIC Team, "Review of the National Ignition Campaign, 2009–2012," *Phys. Plasmas* **21** (2014) 020501.

Miller, G. H., E. I. Moses, C. R. Wuest, "The National Ignition Facility," *Opt. Engin.* **43** (2004) 2841.

Pikuz, S. A., V. M. Romanova, T. A. Shelkovenko, T. Pikuz, A. Ya. Faenov, E. Förster, "Use of higher-order reflection from mica crystals in x-ray spectroscopic investigations at 0.1–0.3 nm," *Quantum Electronics* **25** (1995) 16.

Shu, F. H., *The Physical Universe: An Introduction to Astronomy*, University Science Books, Mill Valley, California, 1982.

Spears, B. K., et al., "Mode 1 drive asymmetry in inertial confinement fusion implosions on the National Ignition Facility," *Phys. Plasmas* **21** (2014) 042702.

Stoeckl, C., G. Fiksel, D. Guy, C. Mileham, P. Nilson, T. C. Sangster, M. J. Shoup, W. Theobald, "A spherical crystal imager for OMEGA EP," *Rev. Sci. Instrum.* **83** (2012) 033107.

Uschmann, I., K. Fujita, I. Niki, R. Butzback, H. Nishimura, J. Funakura, M. Nakai, E. Förster, K. Mima, "Time-resolved ten-channel monochromatic imaging of inertial confinement fusion plasmas," *Appl. Opt.* **39** (2000) 5865.

Multi-Frame X-Ray Imaging Using a Streak Camera with a Patterned Photocathode

LAO-008-16 ■ Continuing in FY 2018 ■ Year 2 of 3

Daniel Marks,[1,a] Catalin Filip,[b] and Jeffrey A. Koch[b]

[1]marksdg@nv.doe.gov, (505) 663-2093
[a]New Mexico Operations–Los Alamos
[b]Livermore Operations

We continued development of a time-resolved x-ray imaging system based on compressed ultrafast photography (Gao 2014). The patterned gold-aluminum photocathode developed in our first year (Marks 2017a) was tested; static images were obtained at NNSS's Livermore Operations (LO) Manson source and dynamic images at the Janus laser at Lawrence Livermore National Laboratory's Jupiter facility. The photocathode had a contrast of 20% between the gold and aluminum regions, much lower than anticipated. Despite the disappointing contrast, we proceeded with dynamic experiments while working on alternative photocathode designs. We fielded the camera on a laser-induced plasma experiment at Janus with a 1 ns, 100 J laser pulse. The low contrast made it impossible to get reconstructions from the data, but we learned valuable lessons about fielding the camera that will be applied to experiments in FY 2018. We developed a new photocathode design that provides continuous contact between the gold regions of the photocathode so that the aluminum layer could be eliminated. Using this new design, we again obtained static images at the LO Manson source. The performance was greatly improved, showing a contrast of over 20 to 1. In preparation for our third year, we also revisited and refined our design for a streak camera imaging system that uses a regular 1-D camera slit and made arrangements for optical experiments to test the concept.

BACKGROUND

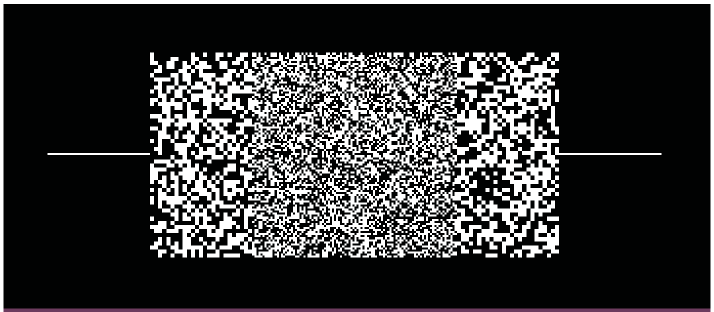

Figure 1. Pattern for the original gold on aluminum photocathode. The smaller squares are 70 × 70 μm and the larger squares are 140 × 140 μm. White areas have 50 nm thick gold deposited on an aluminum and polyimide substrate.

The fastest existing multi-frame x-ray imager is the DIXI camera (Nagel 2012); it uses a time-dilating chamber and variable-voltage photocathode strips to achieve <10 ps images. A separate pinhole is used for each image, which introduces parallax issues. DIXI is constrained to five frames in the configuration used on the National Ignition Facility, which limits the useful continuous time window. The DIXI camera is also an expensive, complicated, heavy instrument, and it incorporates large magnets. There are many applications for which such a camera would be impractical or impossible to field. A simpler, fast multi-frame imaging system using compressed ultrafast photography (CUP), such as we are developing, would be less costly and easier to field, and is likely to be in high demand.

CUP, a recent compressed sensing technique, compresses a time-sequence of images onto a single streak camera image. The original CUP paper (Gao 2014) demonstrated compression of very sparse images onto a single streak camera sweep using a patterned mask to impose fixed high-frequency content onto an image. The full image is streaked using a wide-open streak camera slit. We developed in-house and demonstrated an improved version of CUP in simulations during the FY 2015 effort of the multi-year SDRD project "Ultrafast All-Optical Framing Technology" (Frayer 2016). Having acquired the original source code used by the CUP authors, we found that multiple image copies allow the reconstruction of images that are much less sparse, and we determined that this technique showed promise for capturing data from time-varying phenomena of interest to DOE missions.

In FY 2016 we acquired an unused Kentech x-ray streak camera from Lawrence Livermore National Laboratory (LLNL) and refurbished and mounted a CCD camera on it; worked with Professor Baraniuk at Rice University to improve our reconstruction algorithms, designed and tested a novel rotating-disk compressed imaging system and applied for a patent for it (Marks 2017b), repeated the original CUP experiments with an optical streak camera using the Livermore Operations (LO) long-pulse laser, and designed and constructed our first patterned photocathodes.

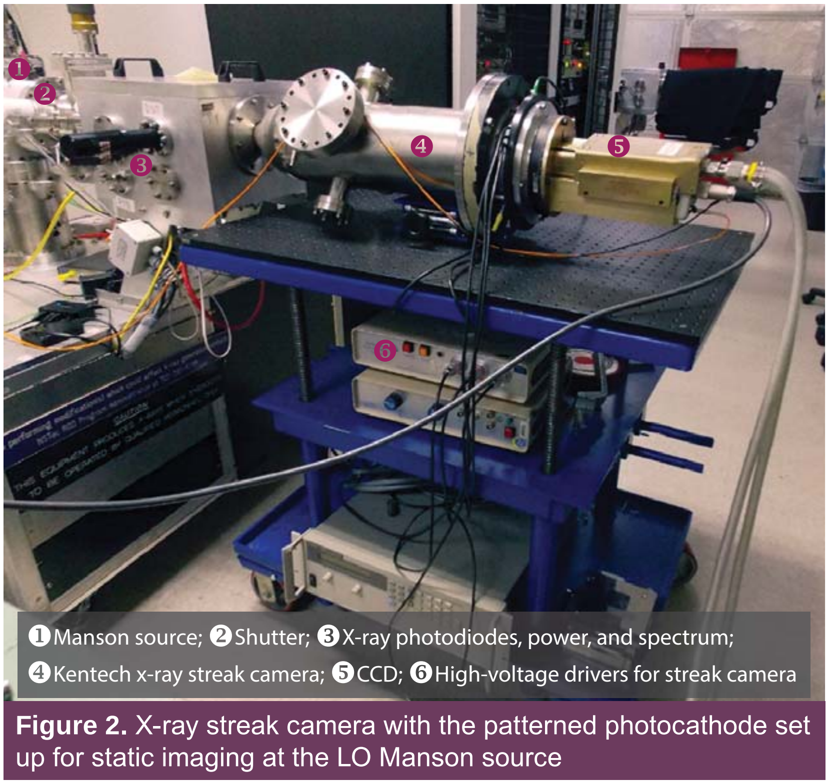

❶Manson source; ❷Shutter; ❸X-ray photodiodes, power, and spectrum; ❹Kentech x-ray streak camera; ❺CCD; ❻High-voltage drivers for streak camera

Figure 2. X-ray streak camera with the patterned photocathode set up for static imaging at the LO Manson source

PROJECT

During our second year we delved into static imaging, dynamic imaging, photocathode design, and preparations for our third year.

Static Imaging

The original patterned photocathode was designed as a 10 × 30 mm pattern of 70 × 70 μm and 140 × 140 μm squares (Figure 1). It is composed of a 100 nm polyimide film with a

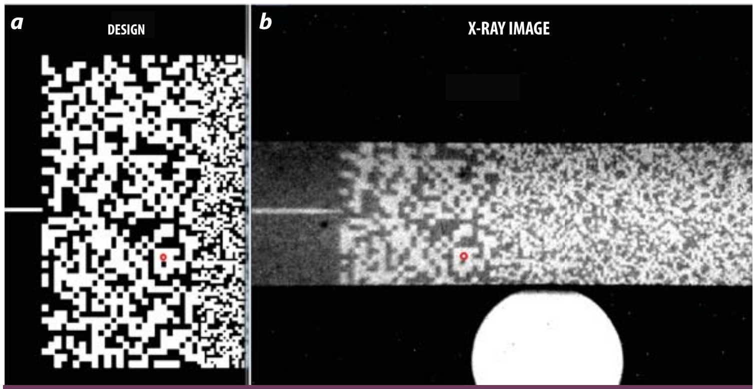

Figure 3. The (a) original gold-aluminum design with its (b) static image. The red circle marks an identical spot in the two images. The large white circle in the static image is due to direct penetration of x-rays through the central aperture in the camera.

25 nm layer of aluminum and a patterned 25 nm thick layer of gold. The gold lines on the edges were intended to acquire an integrated streak of the full experiment, similar to a regular streak camera, but this feature was not tested. We purchased three identical photocathodes.

The gold-aluminum photocathode was installed in the Kentech x-ray streak camera and tested at the LO Manson source, as shown in Figure 2. Exposures of several minutes were required due to the low source strength. Static images were acquired at a constant deflection voltage.

A comparison of the original gold-aluminum pattern with the static image is shown in Figure 3. We see the blur get much worse on the edges. The pattern was designed to have larger squares on the edges to account for the increasing blur. The large circle below the pattern in the static image is due to direct penetration of the x-rays through the central aperture of the camera. The static image does not capture the full pattern due to the limited size of the accelerating grid in the camera. In later tests, we used a larger grid. We used an aluminum anode, which produced lines at ~1.5 keV. The contrast between the gold and aluminum regions was found to be about 20%, which is much lower than the 80% contrast we had expected.

Dynamic Imaging

Dynamic experiments were performed at the Janus laser at LLNL's Jupiter facility. These laser-driven plasma experiments targeted aluminum and silver with 100–200 J, 1 ns laser pulses. The plasma was viewed through an array of 20 µm pinholes to produce multiple images on the photocathode. A diagram of the experiment setup is shown in Figure 4.

First we obtained a static image with no pinhole (Figure 5) to confirm the performance of the photocathode with the spectrum from the experiments. Next we recorded dynamic data with multiple pinholes; data are shown in Figure 6. We attempted the reconstruction of multiple images from the dynamic data but were unable to get anything useful. We always apply constraints to the reconstructions in time and space, and no matter how the data were analyzed, the reconstruction filled out the images to the edge of the

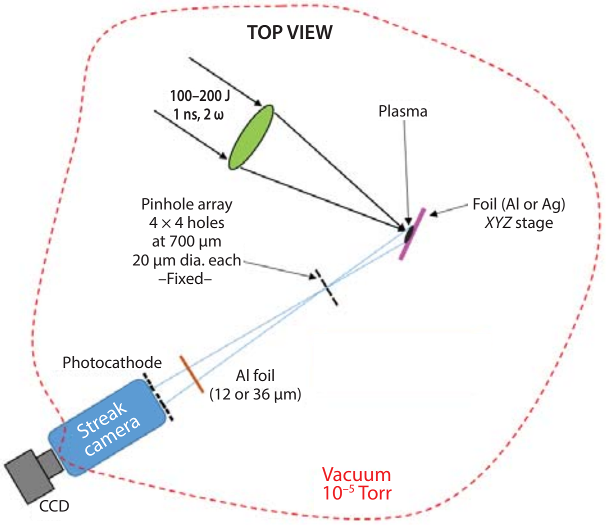

Figure 4. Diagram of dynamic experiments at the Janus laser

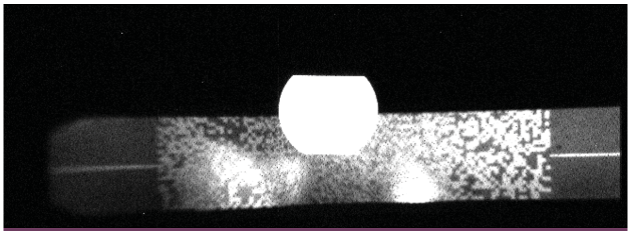

Figure 5. Static image with no pinhole using x-rays from the Janus experiments

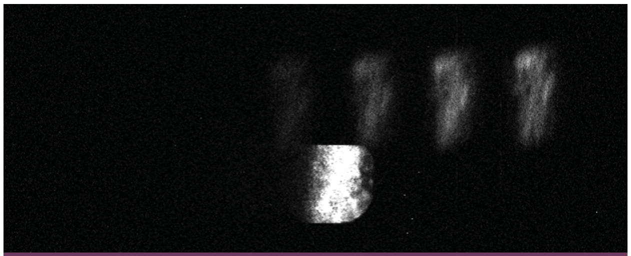

Figure 6. Dynamic image with pinhole array using x-rays from the Janus experiments

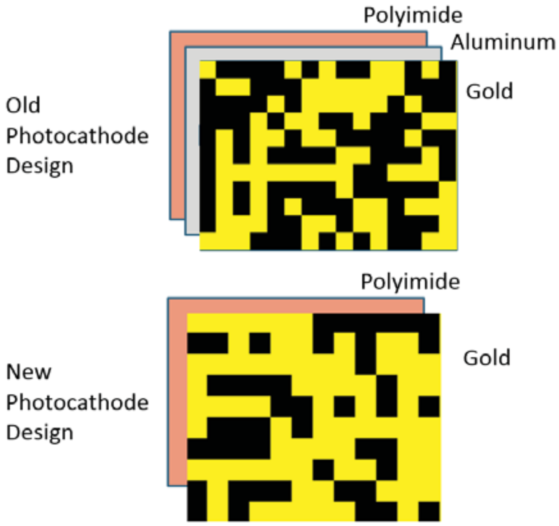

Figure 7. Old and new photocathode layers. In the new design, the gold pattern is continuously connected throughout to provide electrical conductivity without the aluminum layer.

constraints, meaning the data are unusable at this low a contrast. In both the static and dynamic images, there is radiation penetration through the central aperture, spoiling the center of the image where the best resolution resides. In future experiments an angled flange will be added to rotate the camera out of the direct line of sight of the experiment to eliminate this radiation penetration.

New Photocathode Design

The low contrast was caused by excessive photoelectron generation in the aluminum. We do not know why the contrast was so much worse than what we predicted from looking at the literature on the subject, but even the 80% contrast we had predicted would produce problems. If the behavior of the camera is fully characterized, and the experiment is fully understood, we can tolerate some signal from the aluminum, but low contrast becomes a severe problem when there are aspects in the experiment that are not fully characterized. Our goal was to greatly increase the contrast to over a factor of 10 to make the contribution from the non-sensitive areas almost irrelevant.

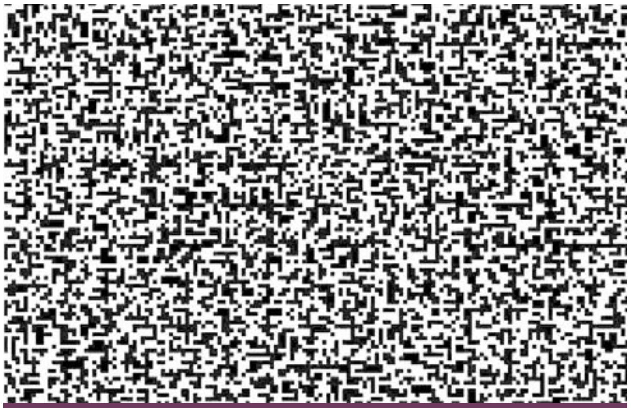

Figure 8. New photocathode pattern. The gold pattern is shown in white with 150 × 150 µm squares.

To improve contrast, we modified the photocathode design; the gold pattern is now connected directly to the polyimide, and the aluminum layer was removed. A diagram comparing the original gold-aluminum and gold-only layers is shown in Figure 7, and the pattern used in the new design is shown in Figure 8.

To increase our chance of getting successful reconstructions, even though the reconstructions will have lower spatial resolution, we changed to a large pattern feature size. Also, new accelerating meshes that are 15 mm high were ordered so that the full pattern can be sensitive.

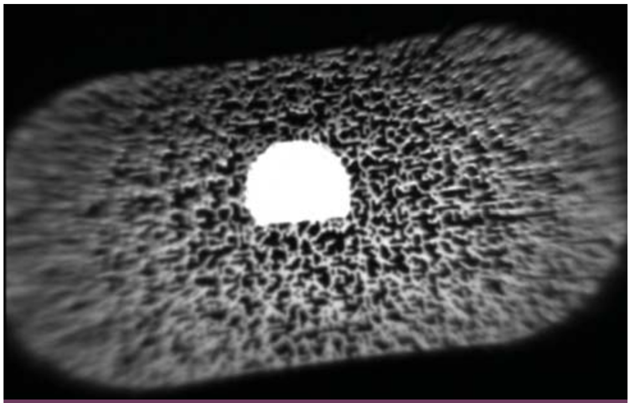

Figure 9. Static image of the new photocathode pattern taken with LO’s Manson source. Contrast was improved to over 20 to 1.

The new photocathodes were tested at the LO Manson source where we obtained static images; the results are shown in Figure 9. Contrast was greatly improved to over 20 to 1, which should make the contribution from the non-sensitive areas almost irrelevant in the analysis. In Figure 9 the spatial resolution at the edges of the static image is worse than that of the original photocathode. Therefore, we plan to use a single pinhole to record one large image in the center to take advantage of the good spatial resolution there. The bright circle in the center will be eliminated by use of an angled flange to rotate the camera out of the direct line of sight of the x-ray source.

FY 2018 Research

In our third year we will re-investigate a method we first explored in the first year of this project—using a regular streak camera with a 1-D input to do 2-D imaging. The concept, based on Li-Sens technology (Wang 2015, Marks 2017a), is illustrated in Figure 10 for x-ray and optical imaging. Each line of the streak camera image encodes a single 2-D image, allowing the reconstruction of hundreds of low-resolution images. This new method and CUP should complement each other. The new method will have lower spatial resolution, and it will not be adversely affected by sudden changes in brightness, whereas with CUP a bright frame can swamp nearby dim frames.

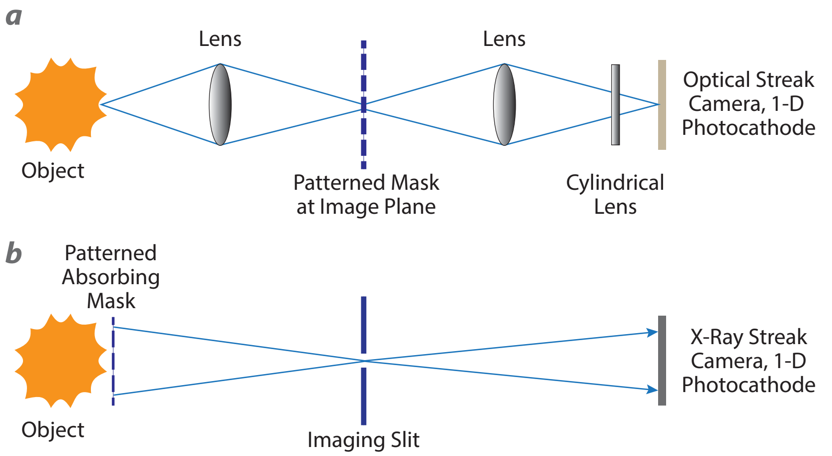

Figure 10. Diagram of (a) optical and (b) x-ray imaging using Li-Sens technology

We have two possibilities for testing our new method with an optical streak camera. First, a Los Alamos National Laboratory detonator group is using a rotating mirror streak camera to investigate detonator initiation. The advantage of using this camera is that it has very good spatial resolution, at least twice as good as a regular streak camera, which will allow reconstructions of higher-resolution images. Second, we will have access to data taken at the University of Nevada, Reno, by Eric Dutra on his current SDRD project, "A Multi-Axial Time-Resolved Spectroscopic Technique for Magnetic Field, Electron Density, and Temperature Measurements in Dense Magnetized Plasmas" (Dutra 2017, 2018).

CONCLUSION

An innovative patterned gold-aluminum x-ray photocathode was tested and found to have contrast less than 20% between the gold pattern and the regions of bare aluminum. This photocathode was tested in dynamic experiments at the Janus laser and was found to have too low of a contrast for acceptable image reconstructions. A new photocathode was designed and constructed that uses a continuously connected gold pattern applied directly to the polyimide substrate with no aluminum layer. This photocathode was tested in static imaging tests at the LO Manson source and was found to have a contrast of greater than 20 to 1, which should produce excellent data for dynamic experiments. In August of 2017, we filed a patent for this work (Marks 2017b).

In FY 2018 the new photocathode will be tested in dynamic experiments at the Janus laser similar to the experiments that were done in FY 2017. A streak camera imaging system with the Li-Sens design, which allows 2-D imaging using an unmodified streak camera with a line input, will be tested on multiple optical streak camera experiments.

ACKNOWLEDGMENTS

We would like to thank Dan Frayer for introducing us to the CUP technique and funding initial development under his SDRD FY 2015 project. Thanks also go to Kathy Opachich, LUXEL, and Gabriel Torres.

REFERENCES

Dutra, E. C., J. A. Koch, R. Presura, W. Angermeier, T. Darling, R. Mancini, A. Covington, "A multi-axial time-resolved spectroscopic technique for magnetic field, electron density, and temperature measurements in dense magnetized plasmas," in *Site-Directed Research and Development*, FY 2016, National Security Technologies, LLC, Las Vegas, Nevada, 2017, 23–32.

Dutra, E. C., J. A. Koch, R. Presura, W. Angermeier, T. Darling, R. Mancini, A. Covington, "A multi-axial time-resolved spectroscopic technique for magnetic field, electron density, and temperature measurements in dense magnetized plasmas," in *Site-Directed Research and Development*, FY 2017, National Security Technologies, LLC, and Mission Support and Test Services, LLC, Las Vegas, Nevada, 2017, 27–34.

Frayer, D., G. Capelle, D. Marks, A. Bernstein, "Ultrafast all-optical framing technology," in *Site-Directed Research* *and Development*, FY 2015, National Security Technologies, LLC, Las Vegas, Nevada, 2016, 205–211.

Gao, L., J. Liang, C. Li, L. V. Wang, “Single-shot compressed ultrafast photography at one hundred billion frames per second,” *Nature* **516** (December 4, 2014) 74–77.

Marks, D., J. A. Koch, R. Tiangco, J. O’Connor, M. Raphaelian, “Multi-frame x-ray imaging using a streak camera with a patterned photocathode,” in *Site-Directed Research and Development*, FY 2016, National Security Technologies, LLC, Las Vegas, Nevada, 2017a, 189–195.

Marks, D., “Compressed video camera with a moving patterned disk,” U.S. Patent Application 15/666,984 filed August 2, 2017b.

Nagel, S. R., et al., “Dilation x-ray imager a new/faster gated x-ray imager for the NIF,” *Rev. Sci. Instrum.* **83** (2012) 10E116.

Wang, J., M. Gupta, A. C. Sankaranarayanan, “LiSens—A scalable architecture for video compressive sensing,” *2015 IEEE International Conference on Computational Photography*, April 2015, 1–9.

Laser-Generated Ultra-High-Energy-Density Plasma for Fast Neutron Pulse Production and Neutron Diagnostic Development

LAO-04-15 ■ Year 3 of 3

James Tinsley,[1,a] Alden Curtis,[b,c] and Jorge Rocca[c]

[1]tinslejr@nv.doe.gov, (805) 681-2282
[a]Special Technologies Laboratory
[b]New Mexico Operations–Los Alamos
[c]Colorado State University

The object of this project is to develop a pulsed neutron source using intense femtosecond laser pulses to generate an ultra high–energy density plasma that is rich in deuterium. Plasma densities that approach that of solid material are obtained through the interaction of the laser with arrays of aligned nanowires. We have measured yields as high as 1.4×10^7 neutrons per laser pulse. This is approximately one order of magnitude higher yield than we achieved last year. The laser upgrade that was done this year can support even higher yields with nanowire targets that have more base material to fully absorb the higher deuteron ion energies.

BACKGROUND

This project is based on work done at Colorado State University (CSU), in which Professor Jorge Rocca and his collaborators have produced hot high-density plasmas through the interaction of high-power density laser pulses and aligned arrays of metal nanowires. The interaction of powerful lasers and solid materials is limited by the barrier to further light penetration that occurs when the critical electron density has been reached. This limits the laser penetration to a thin surface layer and the plasma density to (typically) 0.1% of the solid density. By replacing a solid material surface with an array of nanowires, a much stronger coupling of the incident laser radiation and the target material has been achieved.

In previous work at CSU, electron densities approximately 100 times that of the critical density, multi-keV temperatures, extremely high degrees of ionization and gigabar pressures have been reported using this technique. By substituting highly deuterated polyethylene (CD_2) nanowires for the metals, we produce fast, intense pulses of neutrons through deuterium-deuterium (D-D) fusion.

This project supports a variety of project needs for subcritical experiments and high-energy density physics (HEDP). Specifically, neutron-diagnosed subcritical experiment (NDSE) capabilities need a fast neutron source for detector calibration. Additionally,

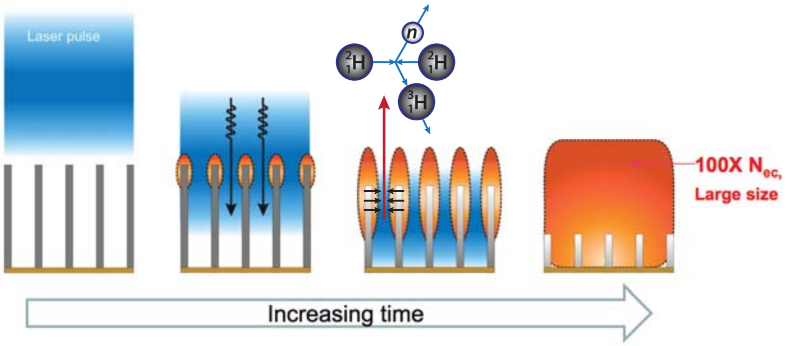

Figure 1. The laser interaction with a bundle of nanowires produces a plasma that is at least two orders of magnitude more intense than the interaction with a solid surface (based on Purvis 2013)

NDSE will benefit from diagnostic development for improved time of flight (TOF) and neutron discrimination measurements, which will be necessary for the plasma characterization. HEDP experiments at the National Ignition Facility and the Z machine will benefit similarly from the development of a diagnostic that can be used for studying neutron burn as well as TOF and neutron discrimination.

PROJECT

The central concept for this project is illustrated in Figure 1. In contrast to a laser pulse hitting a flat surface, a pulse incident on an ordered array of nanowires is able to couple to a much larger volume of material before the free electron density becomes so high that it reflects any further incident laser energy. This makes possible plasmas that have densities close to that of the solid material, very high ionization levels, and gigabar pressures produced with 0.5–0.6 J laser pulses (Purvis 2013). Under such conditions, a plasma is created that contains a sufficient number of deuterons with sufficiently high energies to produce a useful number of neutrons in a pulse on the order of 1 ps duration.

Nanowire Target Systematics

Throughout this project, we made substantial improvements to the nanowire targets (straight wires that are well collimated and have no extraneous material covering them). Beginning last year, we compared nanowire targets made with CD$_2$ from two commercial sources: Polymer Science and Sigma Aldrich (Tinsley 2017). We also made targets with longer nanowire lengths, 10 µm and 15 µm, to compare to the 5 µm nanowires that were the standard earlier in the project (Tinsley 2016). Wires of each length were made with materials from both vendors.

Data from shots taken on 5 µm long and 15 µm long nanowires made using material from both vendors is shown in Figure 2. It is clear that for materials from both vendors the yield is higher on targets with longer wires; with Sigma Aldrich, there is a factor of ~2.5 difference and with Polymer Science, a factor of ~1.4. Yields using 10 µm long nanowires are approximately the same as with 15 µm long nanowires.

Another finding is that targets made with Polymer Science material give better yields overall. We speculate that this is because raw CD$_2$ from Polymer Science tends to be more stiff and slightly more difficult to work with than that from Sigma Aldrich. This makes for wires that keep their shape and

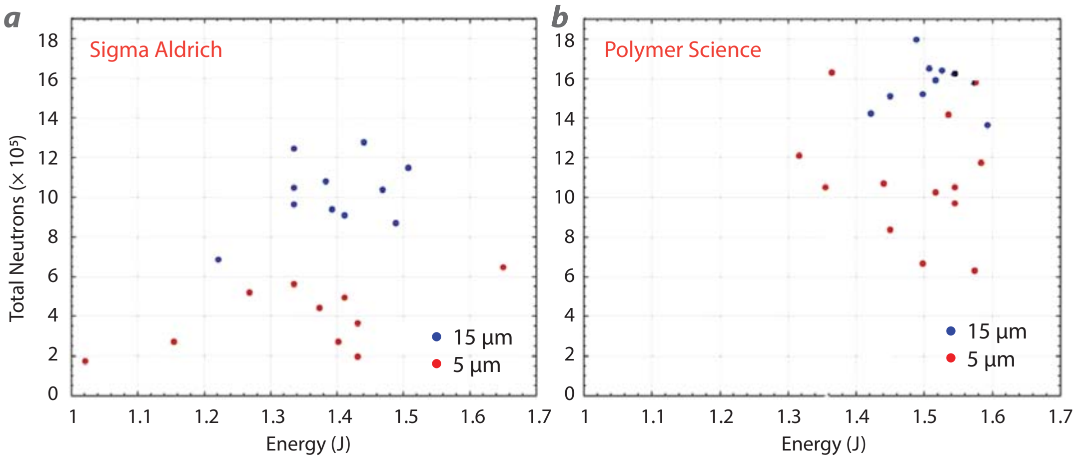

Figure 2. Neutron yields obtained with targets having different nanowire lengths made using (a) Sigma Aldrich and (b) Polymer Science materials

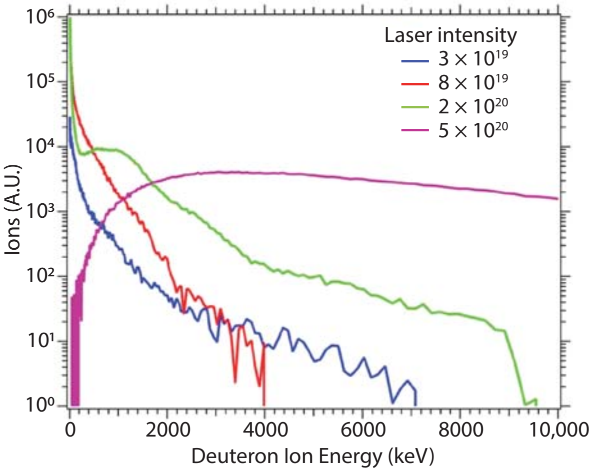

Figure 3. PIC calculations of deuteron ion energy spectra for several laser intensities

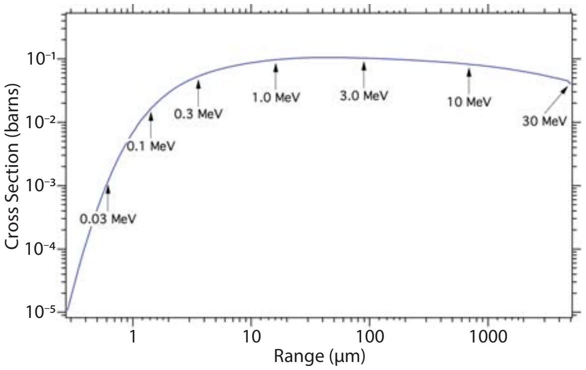

Figure 4. Calculation of deuteron ion range vs. fusion cross section for various ion energies

orientation better than the latter material, resulting in a superior interaction with the laser pulse.

Laser System Upgrade

Particle-in-cell (PIC) simulations done as part of last year's work (Curtis 2016, Tinsley 2017) indicate that as the laser intensity approaches the mid-10^{20} W/cm^2 range, the shape of the deuteron energy spectrum shifts significantly, with a much larger fraction of the ions reaching several MeV, or more (Figure 3). This is important because nearly all D-D fusions occur between energetic deuterons from the plasma interacting with deuterons in the CD_2 material surrounding the interaction volume. (In spite of its very high density, very few D-D fusions take place in the plasma itself, which is quite small in volume, on the order of 100 μm^3.) Because the range of a deuteron ion traveling through CD_2 increases greatly for energies above 200 keV, the probability of fusion increases dramatically. This condition is illustrated in Figure 4, where fusion cross section versus range is plotted for deuteron energies up to 30 MeV. The fusion probability is a product of those two variables: because the probability of an energetic deuteron undergoing fusion increases with the amount of material it passes through, and therefore the number of deuterons at rest that it passes near, the fusion probability is maximized for a deuteron that remains inside the material until it stops (aka "ranges out").

To take advantage of this potential, an upgrade of the laser transport beam line was undertaken this year to increase the laser intensity to the target chamber by more than an order of magnitude. Vital components of the transport system, notably the gratings that comprise the beam compressor and the potassium dihydrogen phosphate (KDP) crystal used to double the frequency of the laser, have a limit to the power density they can withstand. Therefore, it was necessary to increase the beam diameter from 9.5 to 18.5 cm and to obtain larger components to handle the larger beam. This led to a number of changes.

In addition to a new set of larger compressor gratings and a larger KDP crystal, we also obtained larger filters to transmit the doubled (400 nm) light while filtering out the original (800 nm) wavelength and an off-axis parabolic (OAP) mirror to focus the light on the target. Larger vacuum chambers were needed to house these components and to contain the increased beam diameter; therefore, a new chamber for the frequency-doubling system and a new target chamber were also procured (an existing chamber was used for the new compressor). The layout of the improved beam line is shown in Figure 5.

A view of the new target chamber itself is shown in Figure 6 with the lid removed to show the interior.

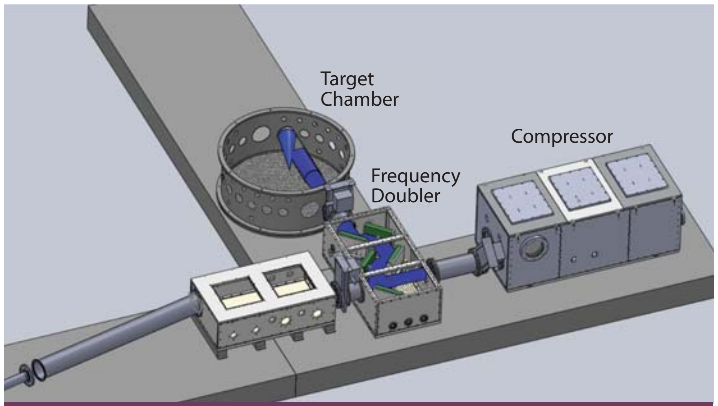

Figure 5. Arrangement of the upgraded laser beam compressor, frequency doubler, and target chamber. The blue cylinder represents the laser beam.

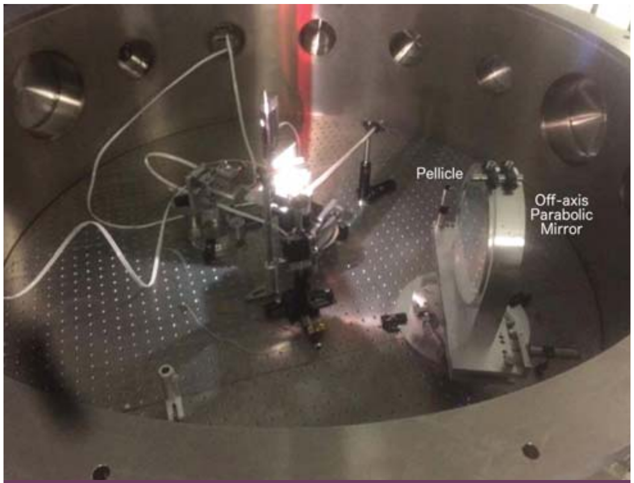

Figure 6. Interior of the target chamber. The bright spot in the center indicates the location of the target holder.

The laser beam enters via a port just out of view at the bottom left of the photo and travels to the right to reflect from the mirror and focus on the target at the center of the chamber. The OAP mirror is coated to reflect light in two very narrow bands at 800 and 400 nm (±6 nm). The plasmas that are produced by laser pulses in these experiments, and others done with metallic nanowires, produce particulate matter that is deposited on surfaces inside the chamber over time. This detritus is insignificant, unless it is deposited on sensitive optics such as the focusing mirror. The mirror is sufficiently expensive ($31,000) and time-consuming (~2–3 months) to obtain that it is imperative to protect it.

To protect the OAP, a very thin nitrocellulose pellicle is set just in front of the reflective surface of the mirror. The first pellicles were 4 µm thick, but after three of these broke within a short period, they were replaced by 7 µm thick pellicles. Having established that the latter had enough strength, more pellicles with anti-reflective coatings on each surface were obtained. This greatly reduces the loss of laser intensity (~15% for uncoated pellicles) that occurs while passing through each surface of the pellicle twice.

After the upgrade, the input energy delivered to the new beam line was gradually increased over a few months of use, finally reaching the design maximum of ~30 J per pulse. This corresponds to $\gtrsim$10 J after transmission through the compressor and frequency doubler. The beam pulse width after the compressor was improved to 30–35 fs from 50–55 fs (Figure 7). The maximum laser intensity is now $\sim 1 \times 10^{21}$ W/cm^2, up from $\sim 9 \times 10^{19}$ W/cm^2 previously. The gradual increase allowed the components, in particular the KDP crystal, to adapt to the power density over time. Because the upgrade was completed late in the fiscal year, our post-upgrade measurements did not have the full benefit of the design laser energy, although we did deliver 4 to 5 times as much laser energy to the target as was possible before the upgrade.

Post-Upgrade Results

Thomson parabola spectrometer images that were made after the laser upgrade are shown in Figure 8. The image in Figure 8a, taken of a flat CD$_2$ target, shows a deuteron spectrum similar to those obtained prior to the upgrade. The image in Figure 8b was taken of a CD$_2$ nanowire target. The spectrum of the deuteron ions is far greater than it was previously,

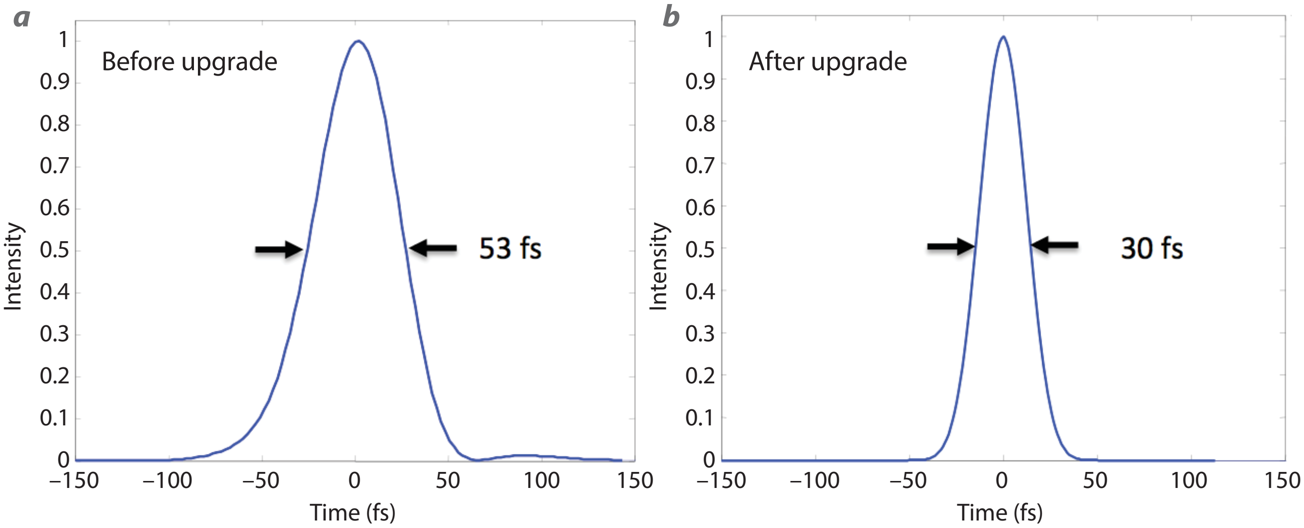

Figure 7. Measurements of the laser beam width (a) before and (b) after the upgrade

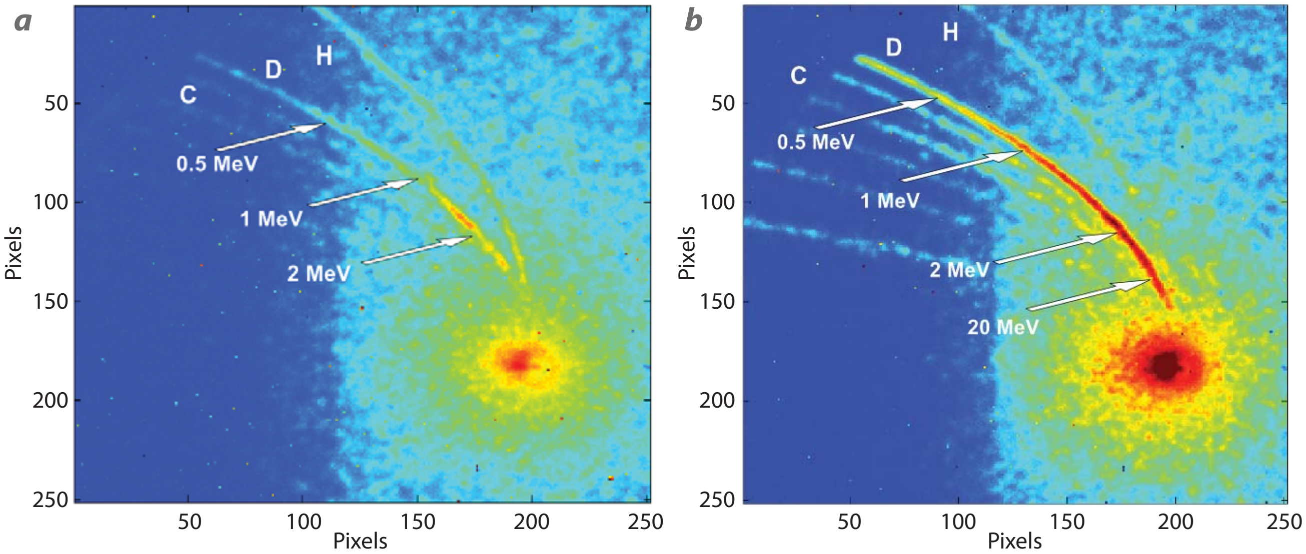

Figure 8. Images of the laser plasma measured on a (a) flat CD_2 target and (b) nanowire CD_2 target recorded with the Thomson parabola spectrometer

especially in the region above 1 MeV in energy. This agrees with the PIC predictions shown in Figure 3.

A summary of the yields obtained with the upgraded laser beam line is displayed in Figure 9 along with FY 2016 results for comparison. While we did achieve neutron yields of almost an order of magnitude greater than last year, we have not yet realized the full potential of the system because it was more difficult than anticipated to produce CD_2 targets with a much thicker backing layer of material (~1 mm) to range out the highest energy deuterons that are generated with the more intense laser pulses. Many of the deuterons with the highest energies passed completely through the material with much of their potential for fusion interactions left unrealized. The apparatus that we have used to manufacture the nanowire targets only supports the inclusion of enough raw material to provide a base of about 200 µm in thickness behind the nanowire surface. It is presently being modified to permit targets with thicker bases to be made.

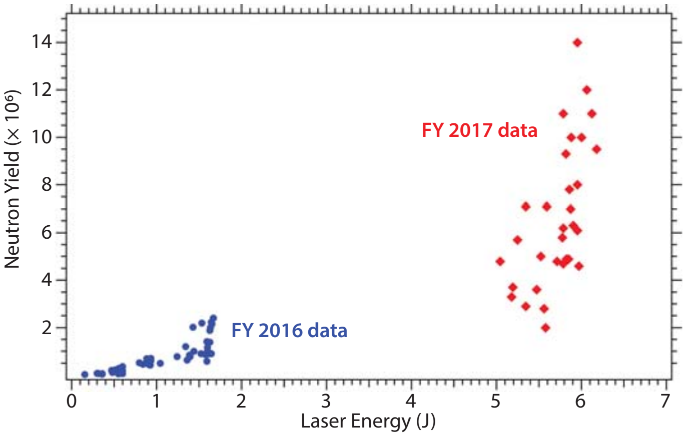

Figure 9. Measured neutron yields obtained before (blue) and after (red) the upgrade profiles

CONCLUSION

This year we continued our systematic study of laser target parameters and saw enhanced yields due to the laser upgrade. Neutron yields from D-D fusion have risen almost one order of magnitude compared with previous results. Even greater yields can be expected in the future with CD_2 nanowire targets that have a thicker base of CD_2 to increase the fusion probability of the highest-energy deuterons now being generated. A paper on this work has been published in *Nature Communications* (Curtis 2018).

ACKNOWLEDGMENTS

We would like to thank Reed Hollinger, Chase Calvi, Soujun Wang, and Vyacheslav Shlyaptsev, all of CSU, for their contributions to this work.

REFERENCES

Curtis, A., et al., "Hot deuteron generation and neutron production in deuterated nanowire array irradiated at relativistic intensity," 58th Annual Meeting of the APS Division of Plasma Physics, October 31–November 4, 2016, San Jose, California, *Bull. Am. Phys. Soc.* **61**, 18 (2016).

Curtis, A., et al., “Micro-scale fusion in dense relativistic nanowire array plasmas,” *Nature Communications* **9** (2018), https://www.nature.com/articles/s41467-018-03445-z, accessed March 14, 2018.

Purvis, M., et al., “Relativistic nano-photonics for ultra-high energy density plasma physics,” *Nature Photonics* **7** (2013) 796–800.

Tinsley, J. R., A. Curtis, J. Rocca, “Laser-generated ultra high–energy density plasma for fast neutron pulse production and neutron diagnostic development,” in *Site-Directed Research and Development*, FY 2015, National Security Technologies, LLC, Las Vegas, Nevada, 2016, 227–233.

Tinsley, J. R., A. Curtis, J. Rocca, “Laser-generated ultra high–energy density plasma for fast neutron pulse production and neutron diagnostic development,” in *Site-Directed Research and Development*, FY 2016, National Security Technologies, LLC, Las Vegas, Nevada, 2017, 205–212.

Site-Directed Research and Development

Appendixes

SDRD Performance Metrics

Mission Support and Test Services–Operated Sites

Acronyms and Abbreviations

This page left blank intentionally

SDRD Performance Metrics

The SDRD program uses quantifiable metrics to track the performance of our R&D investment from year to year. Metrics such as intellectual property, technology transfer to our programs, addressing R&D needs and requirements, and publications are some of the most common types of measureable outcomes. We also consider the importance of other factors, such as follow-on programmatic or external funding received, new methods developed that effectively reduce costs, and overall enhanced staff capabilities. These are further indicators of innovation productivity and are also a direct measure of investment return. SDRD provides our staff with opportunities to explore and exercise creative motivations that ultimately lead to new knowledge and realized technologies. Shown below are some of the more traditional metrics tabulated over the past ten-year period.

Invention Disclosures

Invention disclosures are the first step in our intellectual property pursuit and are often followed by patent applications when deemed appropriate. SDRD has generated well over half of all inventions disclosed company-wide since FY 2002 and continues to do so to this day. On average about one-third of our projects generate new invention disclosures, which is a reasonably high ratio given that projects can vary widely from basic concept, low technical readiness to much higher more applied development efforts. In fact, our programs benefit from a high rate of technology utilization precisely due to this diverse project mix.

	FY08	FY09	FY10	FY11	FY12	FY13	FY14	FY15	FY16	FY17
Number of projects	27	23	25	26	24	24	25	28	27	30
Invention disclosures	6	11	9	7	8	7	7	6	5	4
	22%	48%	36%	27%	33%	29%	28%	21%	19%	13%

TECHNOLOGY TRANSFER

A relatively high percentage of projects, approximately 1 in 3, produce technology that is subsequently adopted by a direct NNSS program. Another measure of program effectiveness and alignment with missions is how well projects address technology needs as identified in the annual *NNSS Technology Needs Assessment*. The ratio of needs addressed to total projects is also indicative of a trend that aligns efforts strategically with the NNSS mission. In addition, a number of projects, but still a small percentage, are targeting emerging fields (of the *Technology Needs Assessment*) and new initiatives intended to incorporate higher risk; these projects explore opportunities for enhanced mission outside of traditional NNSS areas of expertise.

We continue to strive to have SDRD effectively contribute new technology into key programmatic efforts as quickly as possible. New strategic efforts are also providing greater emphasis on forward-looking needs efficiently coupled with long-term visionary goals. As always, SDRD looks to be "ahead of our time by design" and push for SDRD innovations to intersect future and evolving missions with the most impact possible.

	FY08	FY09	FY10	FY11	FY12	FY13	FY14	FY15	FY16	FY17
Number of projects	27	23	25	26	24	24	25	28	27	30
Technology adopted by programs	8	10	10	9	10	9	10	11	10	8
	30%	44%	40%	35%	42%	38%	40%	39%	37%	27%

TECHNOLOGY NEEDS ADDRESSED

The *NNSS Technology Needs Assessment* document continues to be an effective tool for proposal submitters and reviewers. It includes guidance regarding technology gaps and challenges facing mission areas. As mentioned, our directed research emphasis areas this year were similar to last year, and they targeted key investment needs, including nuclear security, information security/assurance, high-energy density physics diagnostics, integrated experiments, advanced analysis, and safeguarded energy. The *NNSS Technology Needs Assessment* is developed from a broad base of input from the national security complex, including laboratories, NNSA, and other external agencies. A minor refresh of the assessment was made this year, building on the previous major revision. The *NNSS Technology Needs Assessment* itself is now in the 13th year of revision, and its utility and effectiveness continues to improve year to year. Of note for 2017, we produced our first broad site announcement (BSA), which contained detailed information on strategic initiatives for our directed research, and also provided further guidance on exploratory research as underpinned by the *Needs Assessment*.

	FY08	FY09	FY10	FY11	FY12	FY13	FY14	FY15	FY16	FY17
Number of projects	27	23	25	26	24	24	25	28	27	30
Gap or need addressed	15	15	13	13	11	14	11	10	10	13
	56%	65%	52%	50%	46%	58%	44%	36%	37%	43%
"Emerging Area and Special Opportunity" effort*	--	--	--	--	--	3	5	5	3	5
	--	--	--	--	--	13%	20%	18%	11%	17%

*per *NNSS Technology Needs Assessment*

PUBLICATIONS

Publications are another indicator of R&D output and provide an archival record of the investments made, which are then available to the broader scientific and technical community. We place a strong emphasis on high-quality, high-impact journal publications. We generally expect about half of all SDRD projects will publish in a given year. An increase in follow-on and co-authored publications has been noted and future prospects for enhanced publishing look promising.

	FY08	FY09	FY10	FY11	FY12	FY13	FY14	FY15	FY16	FY17
Journal publications	3	6	6	5	7	9	8	7	7	8

FY 2002 – FY 2017

NNSS Site-Directed R&D

BY THE NUMBERS

~$100
Total project dollars in funding

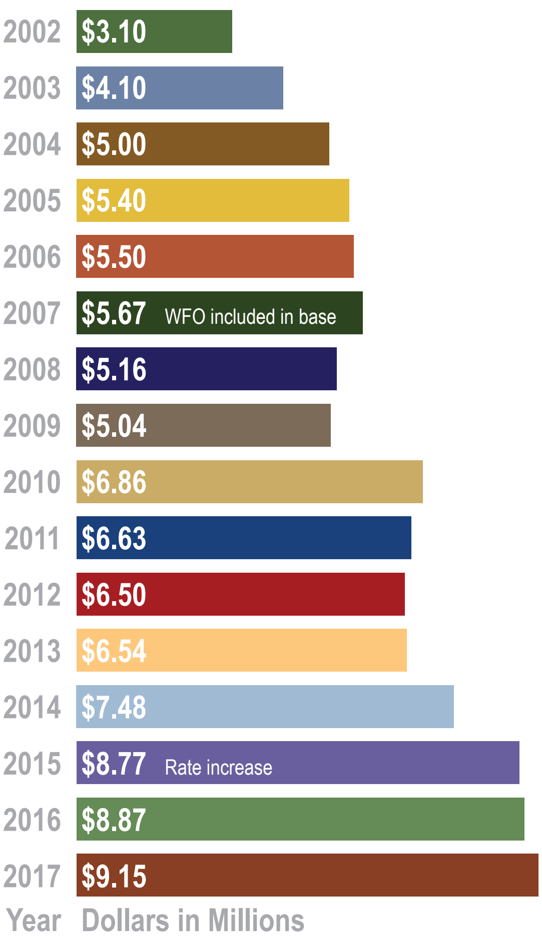

48.5%
Percent of S&T personnel engaged

1362
Proposals

570
Projects

303
Total number of principal investigators with projects

95
New technologies deployed to programs
(FY 2008–FY 2017)

This page left blank intentionally

Mission Support and Test Services – Operated Sites

Livermore Operations (LO)

P.O. Box 2710
Livermore, California 94551-2710

Nevada National Security Site (NNSS)

P.O. Box 98521
Las Vegas, Nevada 89193-8521

New Mexico Operations (NMO) (Los Alamos and Sandia offices)

2900 East Road
Los Alamos, New Mexico 87544

North Las Vegas (NLV)

P.O. Box 98521
Las Vegas, Nevada 89193-8521

Remote Sensing Laboratory–Andrews (RSL–A)

P.O. Box 380
Suitland, Maryland 20752-0380
(Andrews Air Force Base)

Remote Sensing Laboratory–Nellis (RSL–N)

P.O. Box 98521
Las Vegas, Nevada 89193-8521
(Nellis Air Force Base)

Special Technologies Laboratory (STL)

5520 Ekwill Street
Santa Barbara, California 93111-2352

This page left blank intentionally

Acronyms and Abbreviations

1-D	one-dimensional
2-D	two-dimensional
2DEG	2-D electron gas
2DHG	2-D hole gas
3-D	three-dimensional

A

AC/DC	alternating current/direct current
ADC	analog-to-digital converter
AHRS	attitude and heading reference systems
Al	aluminum
ALARA	al low as (is) reasonably achievable
AlGaN	aluminum gallium nitride
AlN	aluminum nitride
Al_2O_3	aluminum oxide
Am	americium
AMS	Aerial Measuring System
ANN	artificial neural network
AO	adaptive optics
AOM	acousto-optic modulator
API	application program interface
APS	Advanced Plasma Source
Ar	argon
ASI	Applied Spectra Incorporated
ASIC	application-specific integrated circuit
AVID	Advanced Visualization and Integration of Data
AWG	American Wire Gauge

B

Ba	barium
bct, BCT	body-centered tetragonal
Be	beryllium
BEEF	Big Explosives Facility
Bi	bismuth
BSA	broad site announcement

C

C	common
C_2H_4	polyethylene
Caltech	California Institute of Technology

CARS	Coherent anti-Stokes Raman Spectroscopy
CBRNE	chemical, biological, radiological, nuclear, and explosive
CCD	charge-coupled device
CD_2, C_2D_4	deuterated polyethylene
CdZnTe	cadmium-zinc-telluride
Ce	cerium
CERN	Conseil Européen pour la Recherche Nucléaire, or European Organization for Nuclear Research
Cf	californium
CH_2, C_2H_4	polyethylene
CM	consequence management
CMS	Compact Muon Solenoid (detector)
CNO	carbon nano-onions
Co	cobalt
comms	comuunications
COTS	commercial off the shelf
CPU	central processing unit
Cs	cesium
CSAIL	Computer Science and Artificial Intelligence Laboratory
CsI	cesium iodide
CSU	Colorado State University
CTH	multi-material, large deformation, strong shock wave, solid mechanics code developed at Sandia National Laboratories
Cu	copper
CUP	compressed ultrafast photography
CW	continuous wave
CZT	cadmium-zinc-telluride

D

D	deuterium
DAC	diamond anvil cells
DAQ	data acquisition
DARHT	Dual-Axis Radiographic Hydrodynamic Test Facility
DC	direct current
D-D, DD	deuterium-deuterium
DFT	density functional theory
DM	deformable mirror
DNN	Defense Nuclear Nonproliferation
DNS	domain name server
DOE	U.S. Department of Energy
DOF	degrees of freedon
DPF	dense plasma focus
D-T, DT	deuterium-tritium
DTRA	Defense Threat Reduction Agency

E

ECP	effective core potential
EBSD	electron backscatter diffraction
epi	epitaxial
EOS	equation of state

F

FET	field-effect transistor
FFT	fast Fourier transform
FMCIO	FPGA Mezzanine Card IO
FP	Fabry-Pérot
FPA	focal plane array
FPGA	field-programmable gate array
FSS	forensic surface shot (experiment)
FWHM	full width at half maximum
FY	fiscal year

G

GaN	gallium nitride
Gd	gadolinium
Ge	gernamium
GLuGAG	rare earth garnet (GdxLu1-x)^3(GayAl1-y)^{5}O$_{12}$:Ce
GM	Geiger-Müller
GOED	Governor's Office for Economic Development
GPS	global positioning system

H

H	hydrogen
HDI	high-density interface
HDMI	high-definition multimedia interface
HDPE	high-density polyethylene
He	helium
HE	high explosive
HEDP	high-energy density physics
HEL	Hugoniot elastic limit
HEMCG	high-explosive magnetic compression generation
HeNe	helium neon
HEP	high-energy physics
Hg	mercury
HMX	cyclothtramethylenetetranitramine
HPCAT	High Pressure Collaborative Access team (Carnegie Science)
HTS	hardware test suite
HV	high voltage

I

ICCD	intensified charge-coupled device
ICD	interface control document
ID	identification
ILC	International Linear Collider
IM-MS	ion mobility-mass spectrometer
IMU	inertial measurement unit
InGaN	indium gallium nitride
InSb	indium antimonide
Ir	iridium
IR	infrared

J

JASPER	Joint Actinide Shock Physics Experimental Research
JHU	Johns Hopkins University

K

KDP	potassium dihydrogen phosphate
k-NN	k-nearest neighbor
Kr	krypton
K-U-T	potassium-uranium-thorium

L

LA	laser ablation
$LaBr_3$:Ce	cerium-doped lanthanum bromide
LANL	Los Alamos National Laboratory
LAPDV	large-area photonic Doppler velocimetry
LASHIS	large-aperture spatial heterodyne imaging spectrometer
LAZE	laser ablation Z-pinch
LED	light-emitting diode
LEU	low enriched uranium
LIBS	laser-induced breakdown spectroscopy
lidar	light detection and ranging
LiF	lithium fluoride
LLNL	Lawrence Livermore National Laboratory
LO	Livermore Operations
LOS	line of sight
LSO	lutetium oxyorthosilicate
Lu	lutetium

M

MCA	multichannel analyzer, microchannel analyzer
MCG	magnetic compression generator
MCNP	Monte Carlo n-particle
MCU	multicontroller unit

	MFP	mean free path
	MHD	magnetohydrodynamic (code)
	MINT	multi-intelligence
	MIT	Massachusetts Institute of Technology
	MSTS	Mission Support and Test Services, LLC
	MWIR	mid-wave infrared
N	NA	numerical aperture
	NaCl	sodium chloride
	NaI	sodium iodide
	NaI:Tl	thallium-doped sodium iodide
	NC	normally closed
	NCAR	Nevada center for Applied Research
	NDSE	neutron-diagnosed subcritical experiments
	Nd:YAG	neodymium-doped yttrium aluminum garnet
	Ne	neon
	NEA	negative electron affinity
	NEU	natural enriched uranium
	NFC	nuclear fuel cycle
	NIC	National Ignition Campaign
	NIF	National Ignition Facility
	NIST	National Institute of Standards and Technology
	NLSF	non-linear least squares fitting
	NLV	North Las Vegas
	NNSA	National Nuclear Security Administration
	NNSS	Nevada National Security Site
	NO	normally open
	NORM	naturally occurring radioactive material
	NRAT	Nuclear Radiological Advisory Team
	NSCRAD	nuisance-rejection spectral comparison ratio anomaly detection
	NSTec	National Security Technologies, LLC
	NTF	Nevada Terawatt Facility
O	O&I	Operations and Infrastructure
	OAP	off-axis parabolic (lens, mirror)
	OD	outer diameter
	OSHA	Occupational Safety and Health Administration
P	Pb	lead
	PC	personal computer
	PCA	principal component analysis

PCB	printed circuit board
PCI	phase contrast imaging
PDV	photonic Doppler velocimetry
PES	potential energy surface
PETN	pentaerythritol tetranitrate
PIC	particle-in-cell (simulation)
PMT	photomultiplier tube
PSD	power spectral density
PSF	point spread function
PVT	polyvinyl toluene
PZT	piezo-electric

Q

QE	quantum efficiency

R

RAP	Radiological Assistance Program
RC	Rowland Circle
RDX	cyclo-1,3,5-trimethylene-2,4,6-trinitamine (explosive)
REU	reactor-grade uranium
RF	radio frequency
RF	random forest
RGB	red, green, blue
RGD	radiation-generating device
RLC	resistance-inductance-capacitance
RMD	Radiation Monitoring Devices, Inc.
RN	radiological/nuclear
ROI	region of interest
RR	Ross relay
RSL	Remote Sensing Laboratory

S

SADA	spectral anomaly detection algorithms
SBC	single-board computer
SCE	subcritical experiment
SDRD	Site-Directed Research and Development
Se	selenium
SEM	scanning electron microscopy
SHS	spatial heterodyne spectrometers
Si	silicon
SiO_2	silicon dioxide
SKIROC	Silikon pin Kalorimeter Integrated ReadOut Chip
Sn	tin

SNL	Sandia National Laboratories
SNM	special nuclear material
SNR	signal-to-noise ratio
SoC	system on chip
SPE	Source Physics Experiment
SPIDER	Streaked Polar Instrumentation for Diagnosing Energetic Radiation
STL	Special Technologies Laboratory
sUAS	small unmanned aerial system
SVC	support vector classifier
SVM	support vector machine

T

TaDD	Tactical Demilitarization Development
TDD	test-driven development
TEM	transmission electron microscopy
TiD_2	titanium deuteride
TNT	2,4,6-trinitrotoluene
TOF	time of flight
TR-SAXS	time-resolved small-angle x-ray scattering
TXD	Talbot-Lau x-ray deflectometry

U

U	uranium
UAS	unmanned aerial system
UNLV	University of Nevada, Las Vegas
UNR	University of Nevada, Reno
USAF	U.S. Air Force
USAXS	ultra-small-angle x-ray scattering
USB	universal serial bus
UTC	coordinated universal time
UV	ultraviolet
UV-NIR	ultraviolet near infrared

V

VTOL	vertical takeoff and landing

W

W	tungsten
WAVRAD	wavelet-assisted variance reduction anomaly detection
WC	tungsten carbide
WFS	wavefront sensor
WSMR	White Sands Missile Range

X

XDV	x-ray Doppler velocimetry
XMCA	extensible multichannel analyzer
XMS	XMCA scripting language
XRD	x-ray diffraction
XWFP	X-ray WaveFront Propagation (code)

Z

ZBL	Z-Beamlet Facility (SNL)